NASA Contractor Report 189192

Flow Interaction Experiment Aerothermal Modeling Phase II

Final Report–Volume II

M. Nikjooy and H.C. Mongia
Allison Gas Turbine Division
General Motors Corporation
Indianapolis, Indiana

and

J.P. Sullivan and S.N.B. Murthy
Purdue University
West Lafayette, Indiana

November 1993

Prepared for
Lewis Research Center
Under Contract NAS3–24350

NASA

TABLE OF CONTENTS

TABLE OF CONTENTS (cont)

LIST OF ILLUSTRATIONS

VOLUME I

LIST OF ILLUSTRATIONS (cont)

LIST OF ILLUSTRATIONS (cont)

LIST OF ILLUSTRATIONS (cont)

LIST OF ILLUSTRATIONS (cont)

LIST OF ILLUSTRATIONS (cont)

VOLUME II

LIST OF ILLUSTRATIONS (cont)

LIST OF ILLUSTRATIONS (cont)

LIST OF ILLUSTRATIONS (cont)

LIST OF TABLES

TABLE OF CONTENTS

IV. DATA PRESENTATION AND DISCUSSION

Detailed concentration and velocity measurements were made in the modified rig. Three configurations were studied: dome annular jets only, primary jets only, and combined dome annular jets and primary jets.

4.1 DOME ANNULAR JETS

Figure 4.1-1* shows the annular jets only configuration. The following two subsections present the concentration and velocity measurements, respectively.

4.1.1 Dome Annular Jets Only - Concentration Measurements

For the annular jets only case, no qualitative information can be collected from the data since all air entering the model was mixed with seed particles. The pictures here do aid in flow visualization.

Pictures for the annular jets only case are presented in Figures 4.1.1-1 through 4.1.1-6. Single and 127 frame averages of the xy plane at z=7.5 in. are seen in Figures 4.1.1-1 and 4.1.1-2. Smoke entering the annular jet is seen to close behind the center portion of the annular jet and travel downstream. Recirculation zones behind the center portion of the annular jet and along the upper and lower walls are present. The pictures at z=7.0 and 8.0 in. have larger recirculation zones along the upper and lower walls.

4.1.2 Dome Annular Jets - Velocity Measurements

Five annular jets were investigated. The three-view drawing in Figure 4.1-1 shows the configuration of the model except all primary jets were removed and replaced with plugs.

4.1.2.1 Inlet Conditions

To establish inlet conditions of the annular jets, velocity scans were made at four edges of the center annular jet. Figure 4.1.2-1 shows a sketch of where the data were taken with respect to the center annular jet.

Figure 4.1.2-2 shows mean and root mean square (rms) velocities at 0.08 in. from the annular jet exit. The results are plotted versus the radius of the annular jet. The mean velocity has a relatively flat profile across the annular gap and agreement between data taken at the different edges. A mean velocity of 23.2 ft/sec exists in the gap. The rms velocity shows larger values for the right and left annular jet edges than the top and bottom edges. This is due to the finite size of the probe volume. The probe volume length was oriented across the annular gap for these two measurements, causing gradient bias to occur due to the existence of a wide range of velocities across the probe volume.

4.1.2.2 Mean Flowfield Results

Figure 4.1.2-3 provides details of the xy plane data sampling grid. The vector plots for the annular jets only case are seen in Figures 4.1.2-4 through 4.1.2-19. Figure 4.1.2-4 shows the rig centerplane vector plot with streamlines. Two regions of high velocity are seen as the fluid discharges into the rig through the annular jets. These peaks spread out and entrain more fluid as the annular jet of fluid develops into the rig. A portion of the fluid from the upper and lower section of the annular jet sets up a pair of counter rotating vortices within the center portion of the annular jet. The main portion of the fluid can be seen converging at the middle of the rig and accelerating as the flow is squeezed between recirculation regions of flow along the upper and lower walls of the rig. Downstream, the main flow then decelerates as the recirculation zones are passed.

---

* Figures for Section IV appear at the end of each subsection. The figure number identifies the subsection in which the figure is discussed.

Recirculating flow along the upper and lower walls of the rig has been observed through flow visualization studies and will be presented in a later section. The vector plot at z=7.5 in. shows some indication of these recirculation zones by the slight turning of the flow at the upper and lower data limits.

Results similar to those at z=7.5 in. are seen at z=7.4 and 7.6 in. (Figure 4.1.2-5). A recirculation zone along the upper wall in the z=7.6 in. plot is more evident than the previous two plots demonstrating asymmetries in the flow. The existence of recirculating flow in the center annular jet region and the convergence and acceleration of the main flow between the recirculating flow along the upper and lower walls still persists.

Similar results are seen farther away from the centerplane between 6.8 in. $\leq z \leq$ 8.2 in., Figures 4.1.2-8 through 4.1.2-19 for planes $z < 7.2$ in. and $z > 7.8$ in. Several general trends can be observed from these figures. First is the movement of the two velocity peaks at the annular jet exit toward the centerline and the disappearance of the recirculation zone behind the center of the annular jet. The cause of both of these is due to the annular jet curvature. The second general trend is the widening of the recirculation zones along the upper and lower walls. Both recirculation zones are clearly evident farther away from the rig centerplane. Third, a decrease in the main flow velocity along the centerline is seen. The flow is still seen to accelerate between the upper and lower recirculation zones but with decreased velocities.

At planes outside of the annular jet, 6.0 in. $\leq z \leq$ 6.7 in. and 8.3 in. $\leq z \leq$ 9.0 in., there is a breakdown of any real organized pattern of flow. Some general trends are still noticeable in the plots. First, downstream flow is reduced and completely disappears by the time the planes at z=6.3 in. and z=8.7 in. are reached. Regions of backflow along upper and lower walls gradually converge at the center of the rig eliminating flow downstream. Second, larger regions of backflow seem to exist along the lower wall of the rig. Initial measurements showed the flow in the rig was very sensitive to the annular jet endplate position. If the plate was not perfectly perpendicular to all the rig walls asymmetries would arise.

No well defined recirculation zone can be seen in any of the previous plots. Sometimes very random, perhaps chaotic, flow velocities are seen in the recirculating flow. The flow was observed to be extremely unsteady during the flow visualization study. Still, general trends in the flow can be discerned.

4.1.2.3 Turbulent Flowfield Results

The yz plane U_{rms} and V_{rms} plots for the annular jets only case can be seen in Figures 4.1.2-20 through 4.1.2-24. Plots at x=0.5 in. (Figure 4.1.2-20) show larger fluctuations in the annular gap of the annular jet with decreased fluctuations in the inner portion of the annular jet and outside the annular jet, $z < 6.8$ in. Larger turbulence levels occur at the exit of the annular jet due to the mixing of the fluid in the rig with that entering the rig. Larger turbulent fluctuations can also be seen at $z > 8.2$ in. in both U_{rms} and V_{rms} plots. Since these levels are not present on the opposite side of the cell, these values may be in error.

At x=1.0 in. similar results are seen, increased magnitudes are evident in the inner portion of the annular jet and a spreading of the turbulence due to the entraining of more fluid by the annular jet. The V_{rms} plot is seen to be spread out over a larger area than the U_{rms} plot and have less defined fluctuations in the annular jet region. Downstream plots show similar development of U_{rms} and V_{rms} profiles in the rig (Figures 4.1.2-23 through 4.1.2-29).

Figures 4.1.2-30 and 4.1.2-31 show the U_{rms} and V_{rms} velocities as they develop downstream of the annular jet in the planes at z=7.0, 7.5, and 8.0 in. The largest U_{rms} fluctuations occur at the annular jet entrance, while smaller fluctuations are present in the center of the annular jet. For the V_{rms} plots, peak values can be seen behind the center of the annular jet. The turbulence spreads toward the upper and lower walls and the cell boundaries with decreasing magnitude farther downstream. Uniform turbu-

lence can be observed at x=6.0 in., but magnitudes are much greater than zero unlike values for the primary jets only case.

The two-dimensional turbulent kinetic energy plots are presented in Figure 4.1.2-32 through 4.1.2-36. Trends existing in the U_{rms} and V_{rms} plots are also seen to occur here. Similar plots are seen at x=0.5 in. and x=1.0 in. Most of the turbulent energy can be seen concentrated at the annular jet exit due to larger velocity gradients in this area because of annular jet flow mixing with the flow already in the rig. At x=1.0 in., the turbulent energy can be seen to spread out more and increases magnitude in the inner annular jet region. Regions of peak turbulence energy can be seen at z > 8.2 in., where peaks existed in the rms plots. Similar results can be seen at downstream stations x=1.5 to 9 in. in Figures 4.1.2-33 through 4.1.2-36.

Figure 4.1.2-37 shows line plots of the K' distribution as it develops downstream for planes at z=7.0, 7.5, and 8.0 in. The greatest turbulence energy can be seen at the annular jet exit, as was seen from the contour plots. Planes at z=7.0 and 8.0 in. have peak values at the rig center, while at z=7.5 in. two peaks are seen on both sides of the rig center. Peak magnitudes diffuse on downstream, but the K' distribution is not quite uniform at x=6.0 in.

yz plane plots of the xy plane Reynolds shear stress are in Figures 4.1.2-38 through 4.1.2-42. The U'V' distribution at x=0.5 in. indicates that the largest magnitude occurs in the annular jet exit region and near the cell edges at z > 8.5 in. Peak fluctuations in the annular jet region occur at the edges of the annular gap where the largest turbulent friction exists due to fluid mixing between fluid entering through the annular jet and the fluid within the rig. Another flat profile can be seen outside the annular jet region, indicating that very little momentum transfer is occurring. Peak fluctuations at z > 8.5 in. may be caused by errors in measurement. Similar results are seen between x=1.0 in. and x=9.0 in. Additional plots for downstream locations are in Figures 4.1.2-39 through 4.1.2-42.

Figure 4.1.2-43 shows Reynolds shear stress distributions in planes at z=7.0, 7.5, and 8.0 in. Largest magnitudes and variations occur immediately downstream of the annular jet, where large velocity gradients and recirculation zones are present. Downstream, the shear stress spreads toward the rig boundaries with decreasing magnitudes. Positive values of U'V' occur in the upper portion of the rig and negative values in the lower portion of the rig.

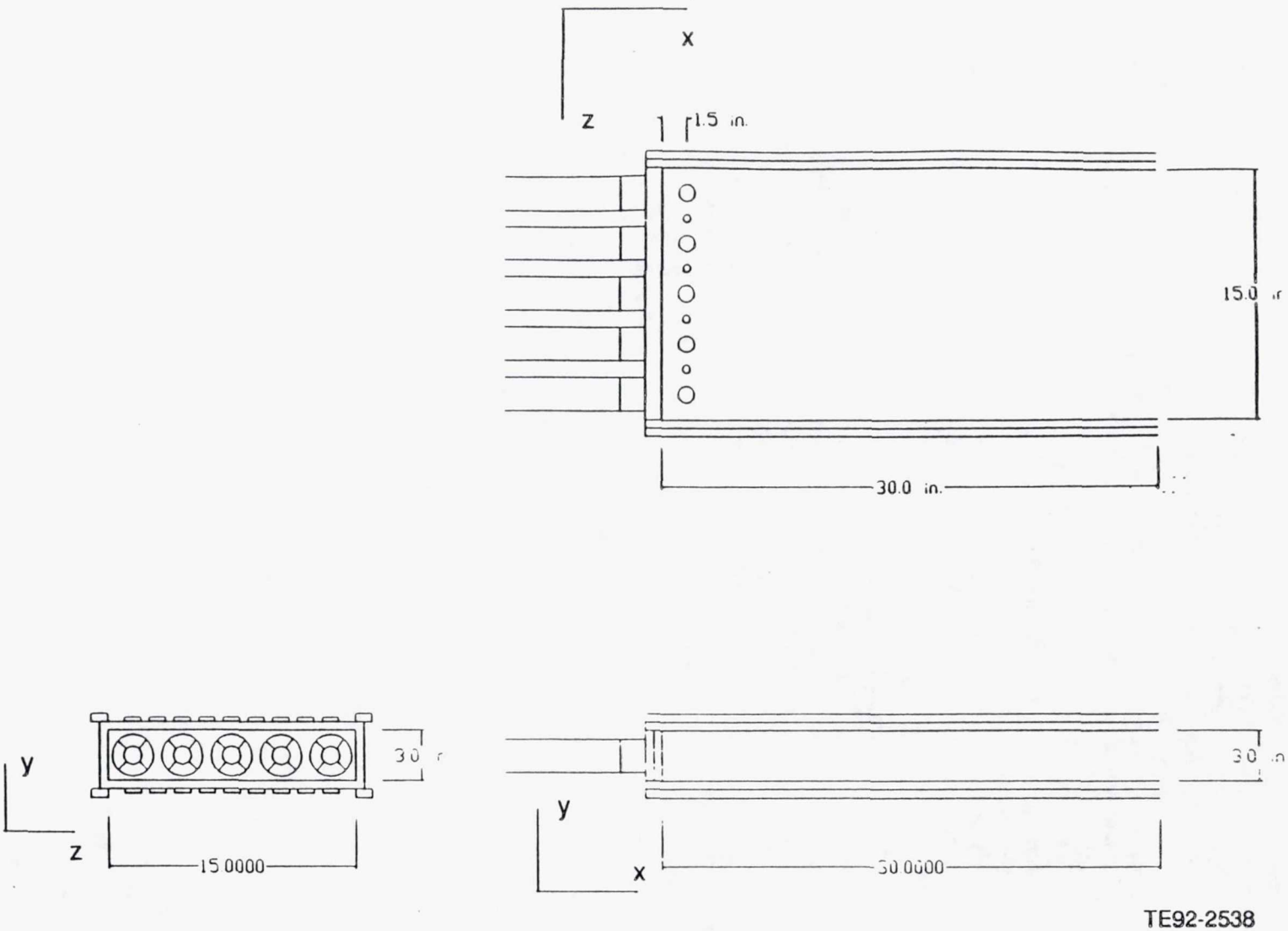

Figure 4.1-1. Annular jets only - three-view drawing.

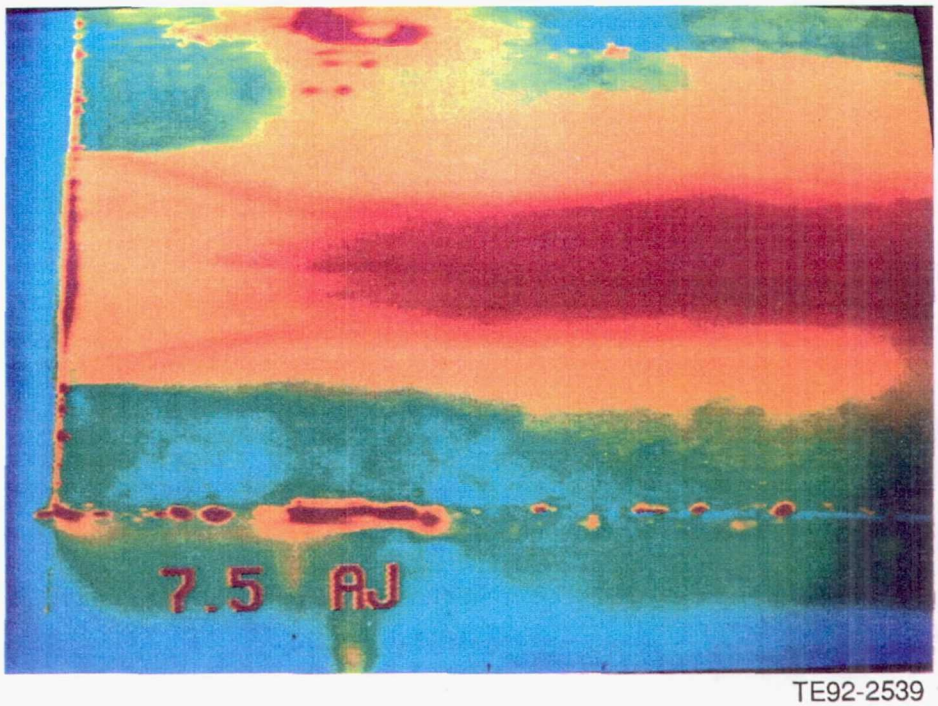

TE92-2539

Figure 4.1.1-1. Annular jets only single frame picture, z=7.5 in.

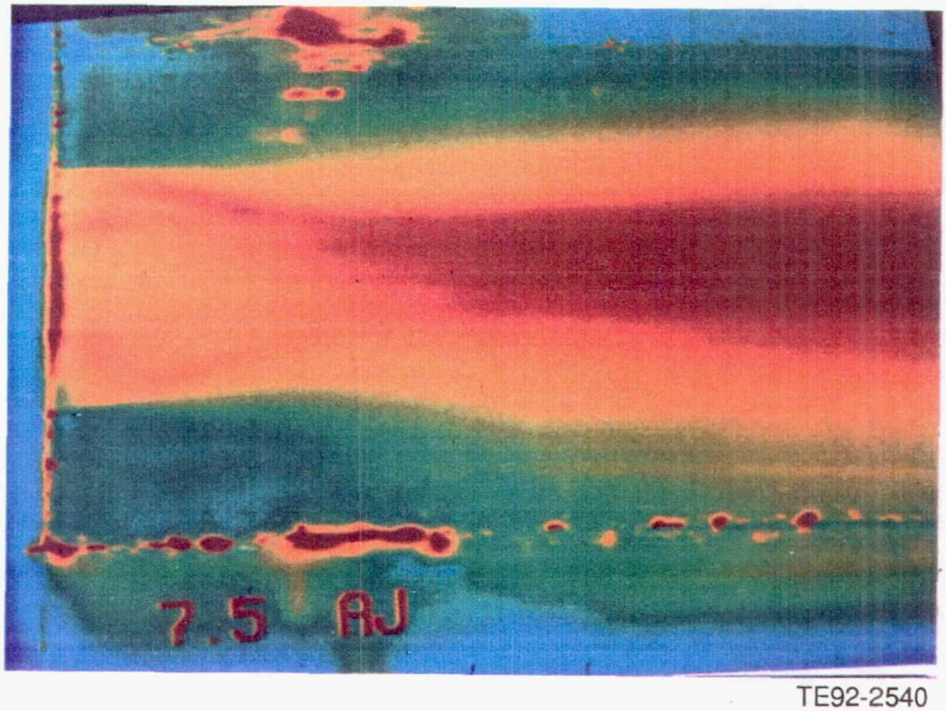

TE92-2540

Figure 4.1.1-2. Annular jets only 127 frame average picture, z=7.5 in.

Page intentionally left blank

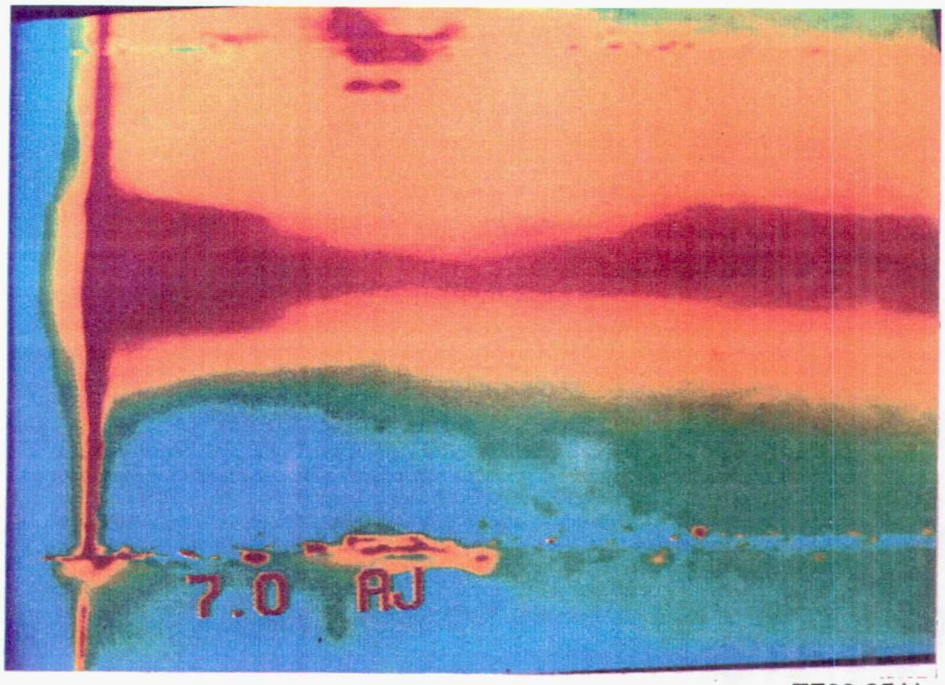

TE92-2541

Figure 4.1.1-3. Annular jets only single frame picture, z=7.0 in.

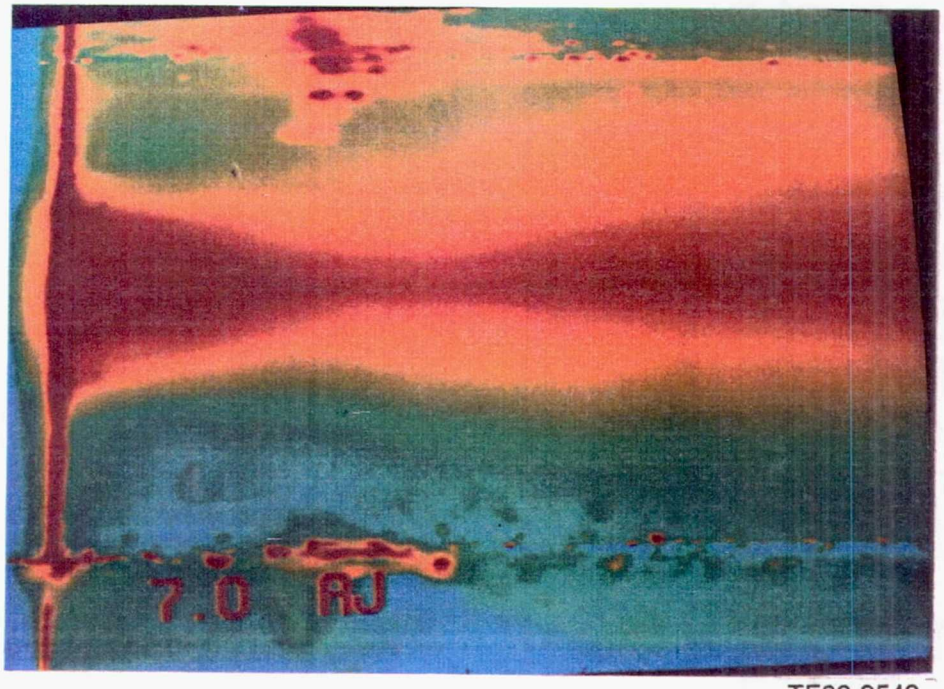

TE92-2542

Figure 4.1.1-4. Annular jets only 127 frame average picture, z=7.0 in.

Page intentionally left blank

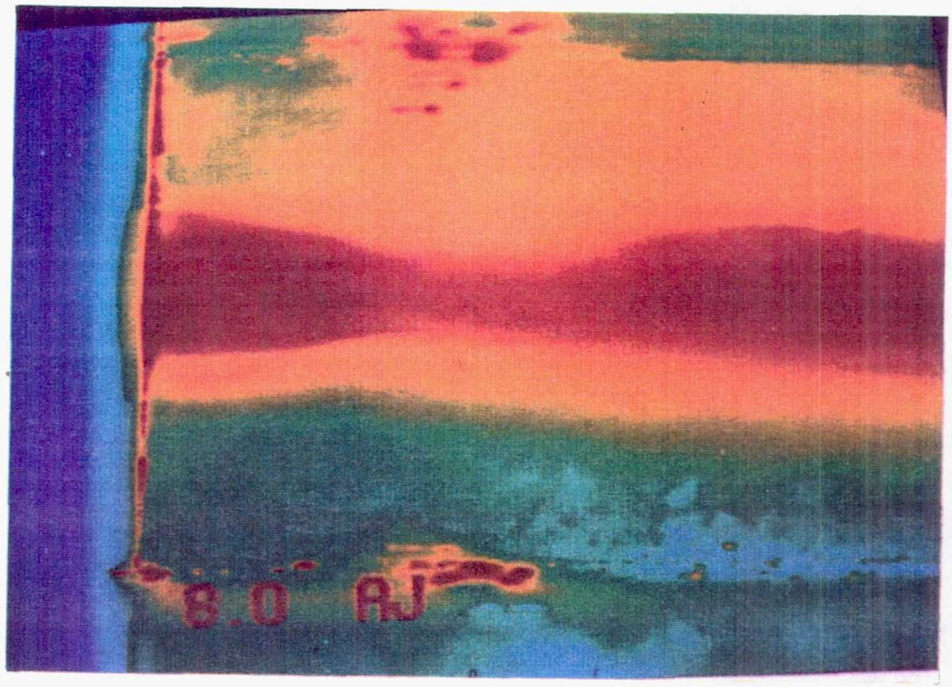

TE92-2543

Figure 4.1.1-5. Annular jets only single frame picture, z=8.0 in.

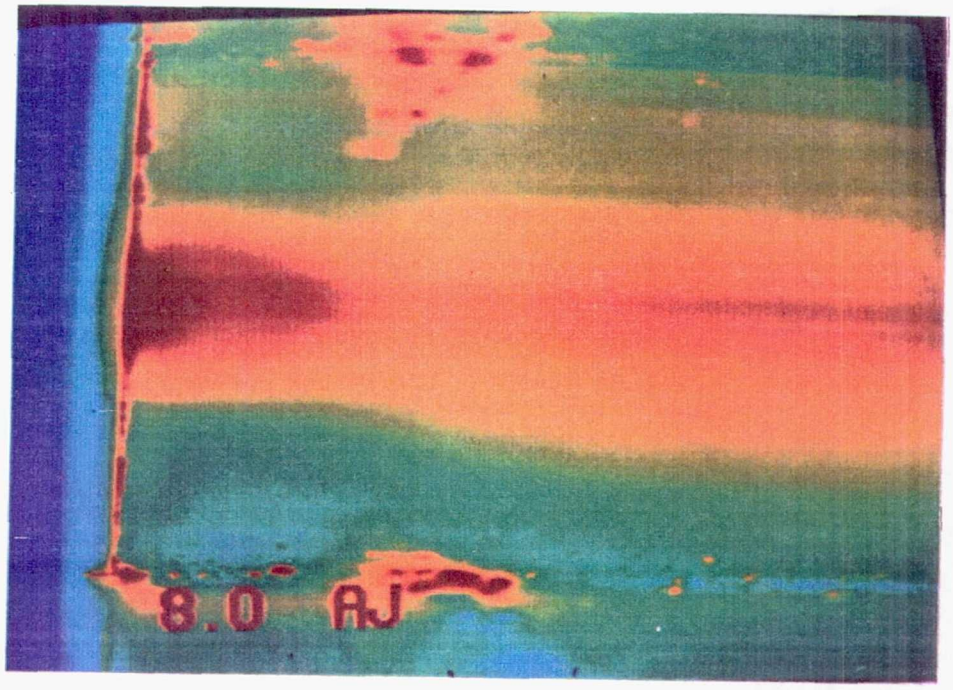

TE92-2544

Figure 4.1.1-6. Annular jets only 127 frame average picture, z=8.0 in.

Page intentionally left blank

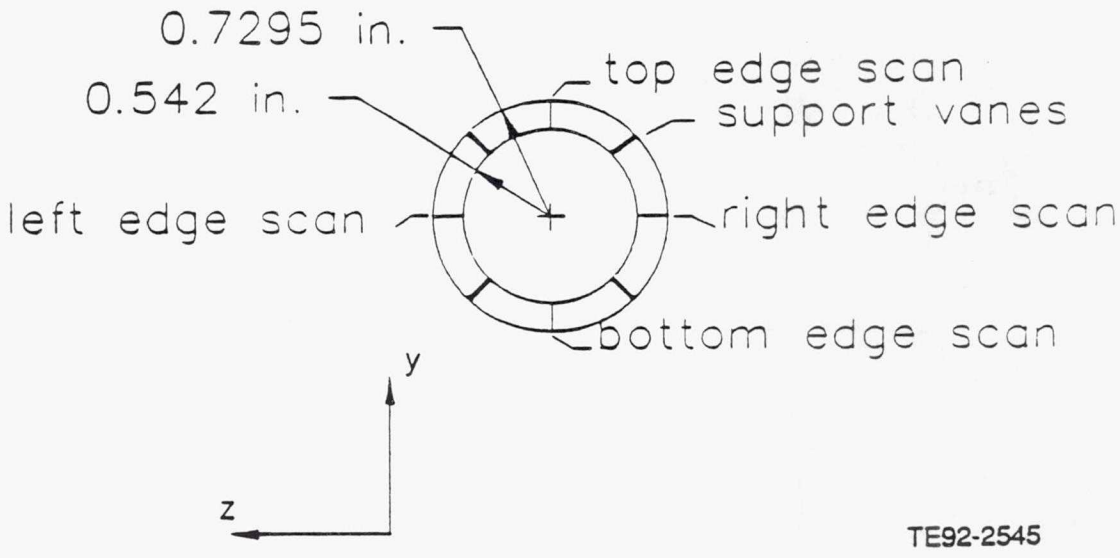

Figure 4.1.2-1. Annular jet scans for inlet conditions.

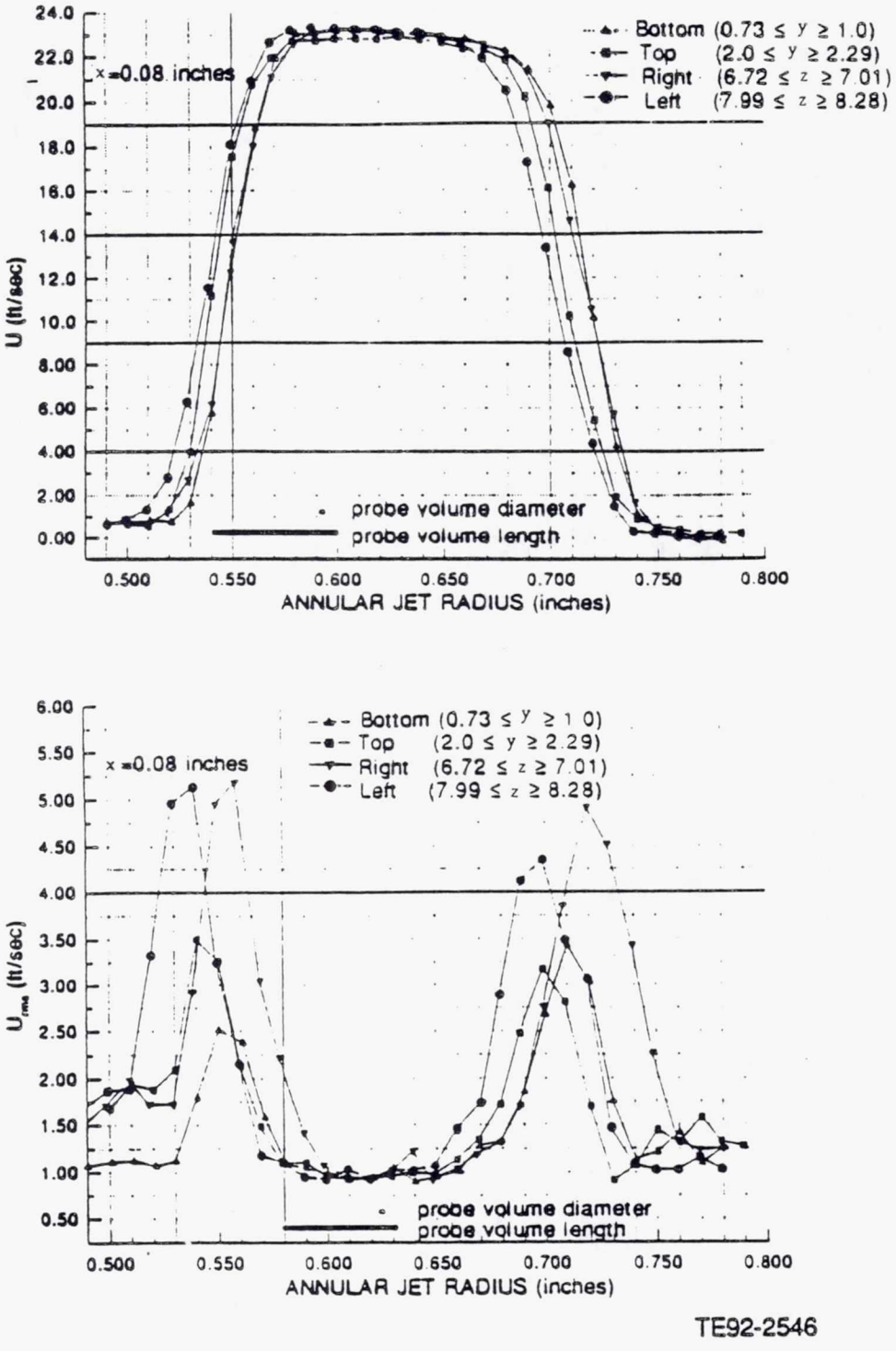

Figure 4.1.2-2. Annular jets only and U_{rms} distribution of the annular jets at x=0.08 in.

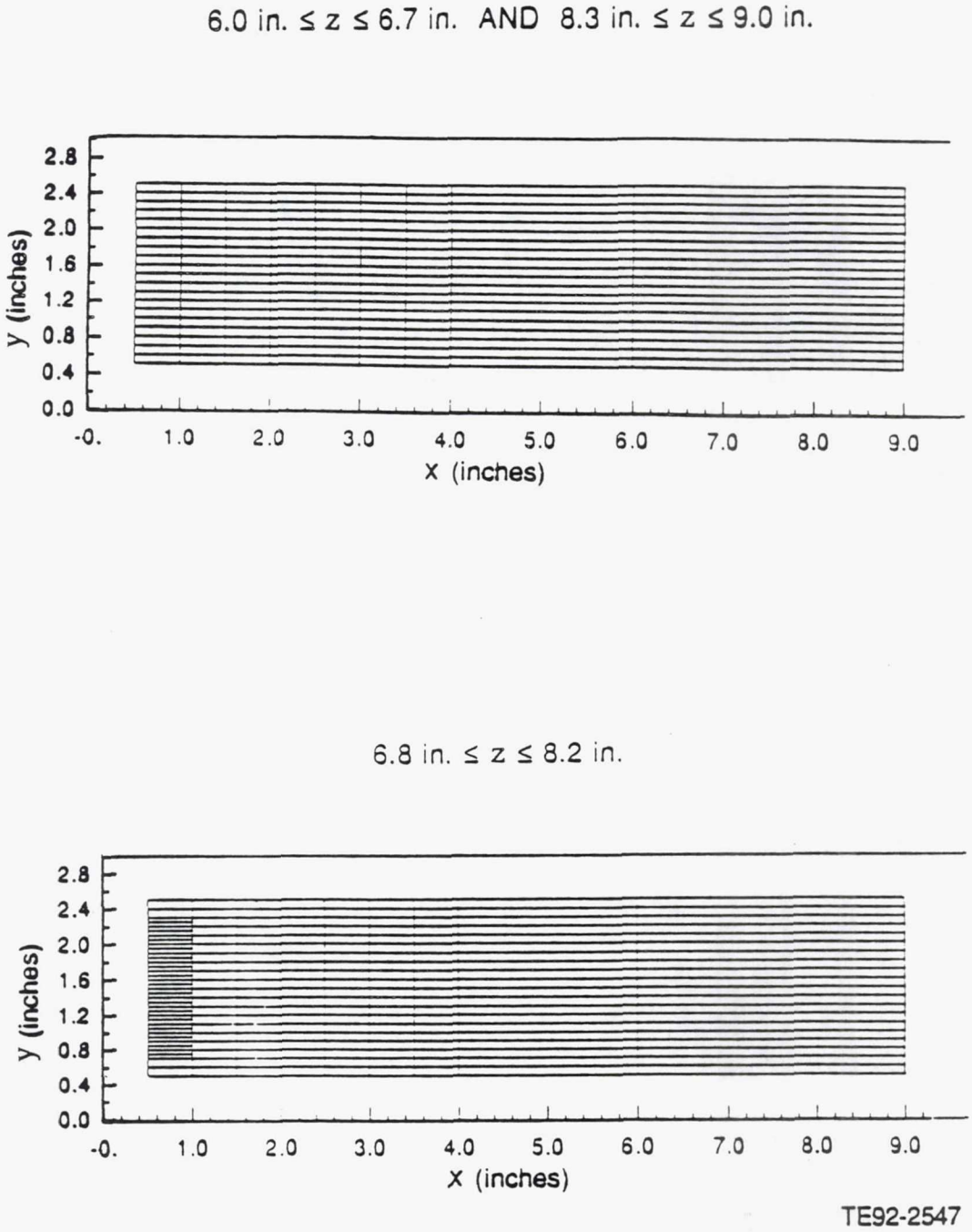

Figure 4.1.2-3. Annular jets only x y plane sampling grids.

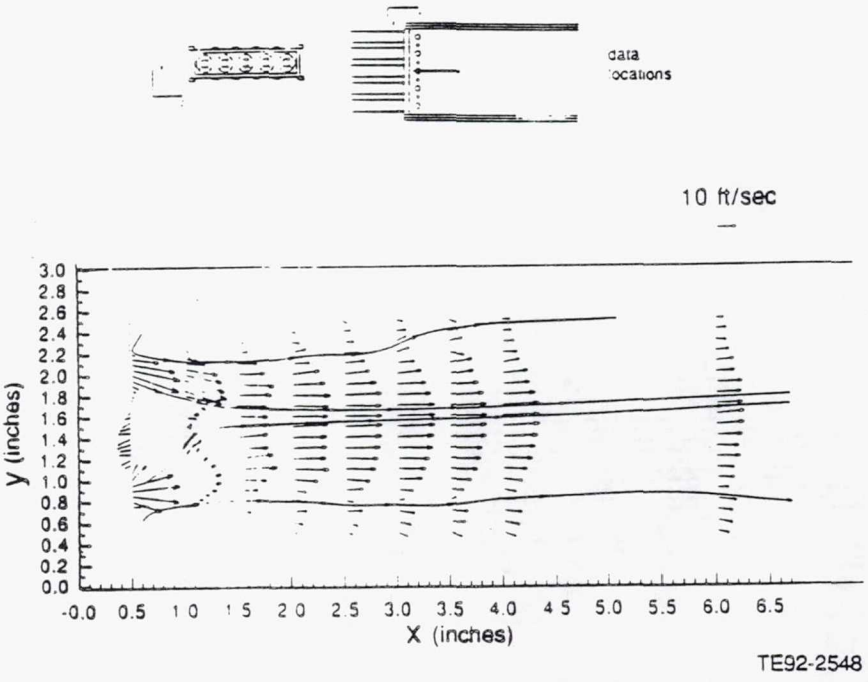

Figure 4.1.2-4. Annular jets only mean velocity vector plot at Z=7.5 in.

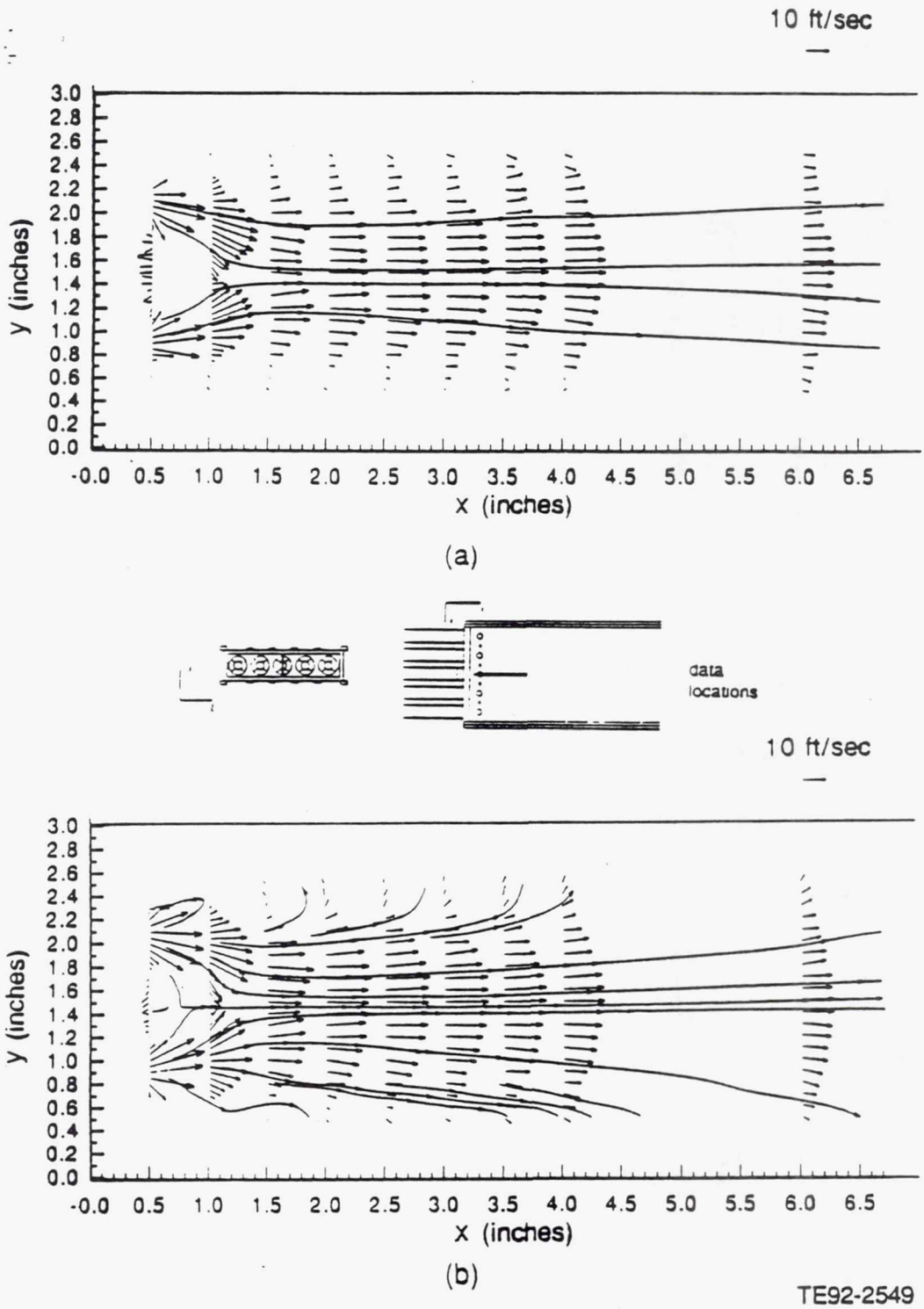

Figure 4.1.2-5. Annular jets only mean velocity vector plots a) Z=7.4 in. b) Z=7.6 in.

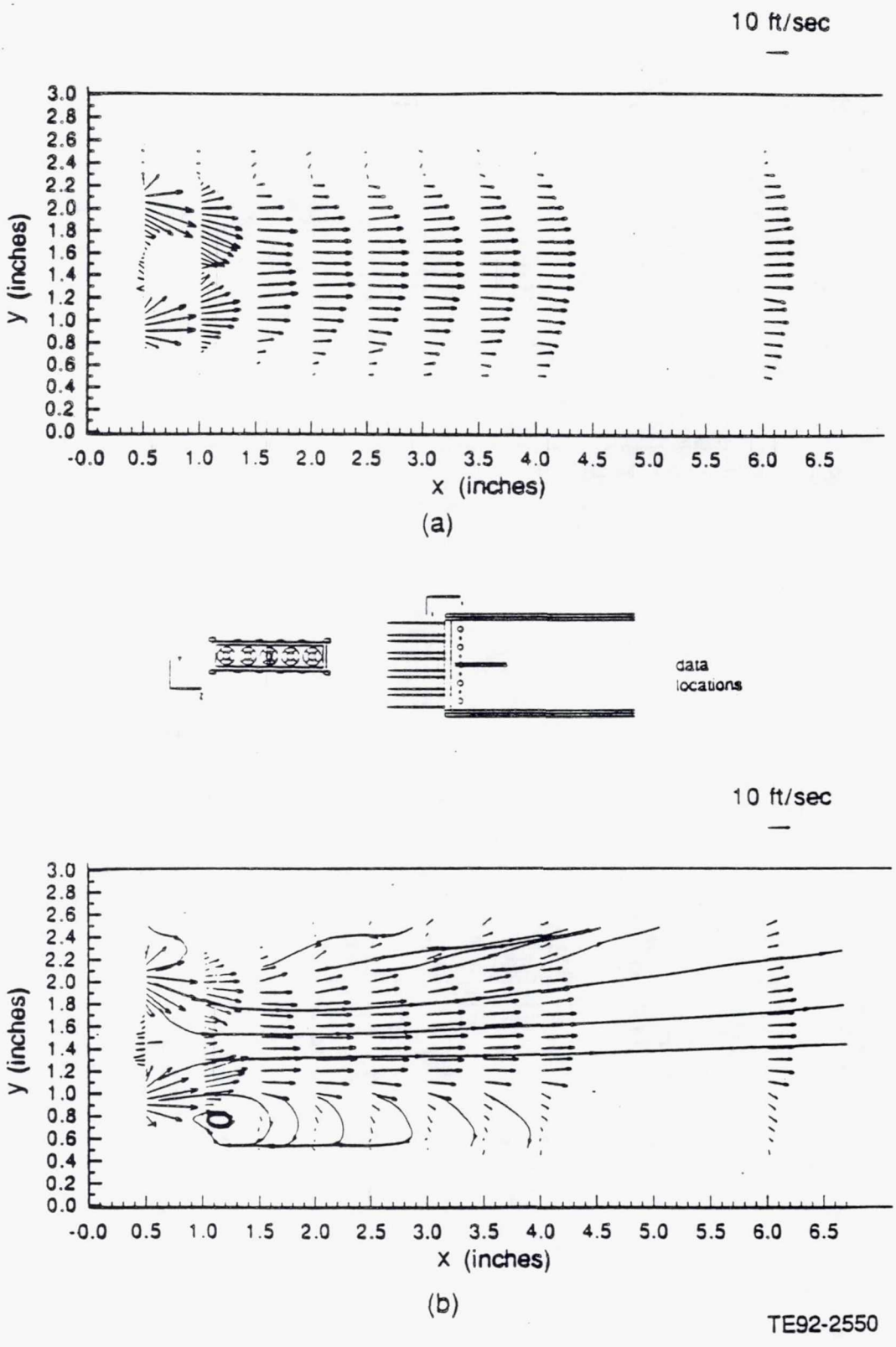

Figure 4.1.2-6. Annular jets only mean velocity vector plots a) Z=7.3 in. b) Z=7.7 in.

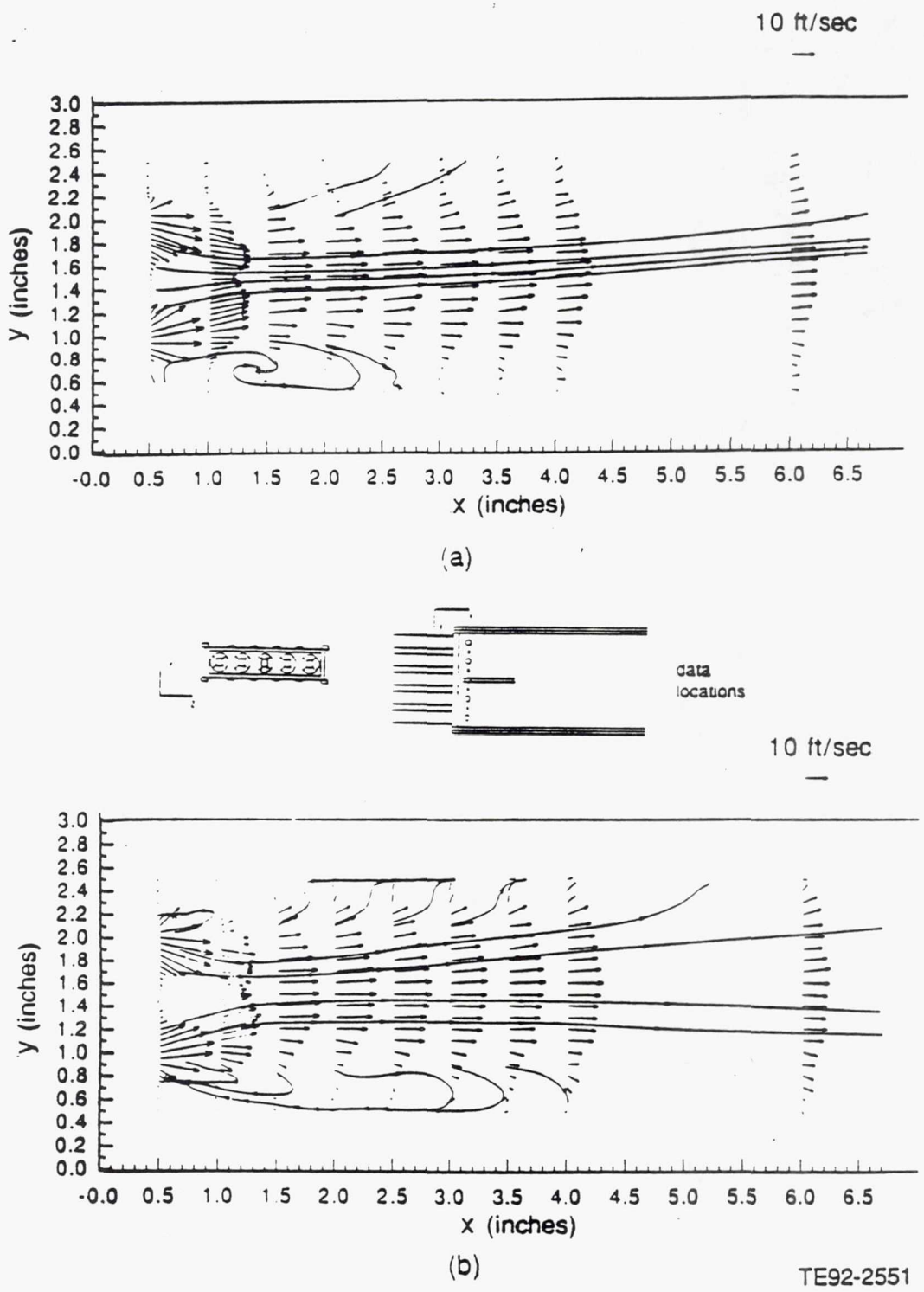

Figure 4.1.2-7. Annular jets only mean velocity vector plots a) Z=7.2 in. b) Z=7.8 in.

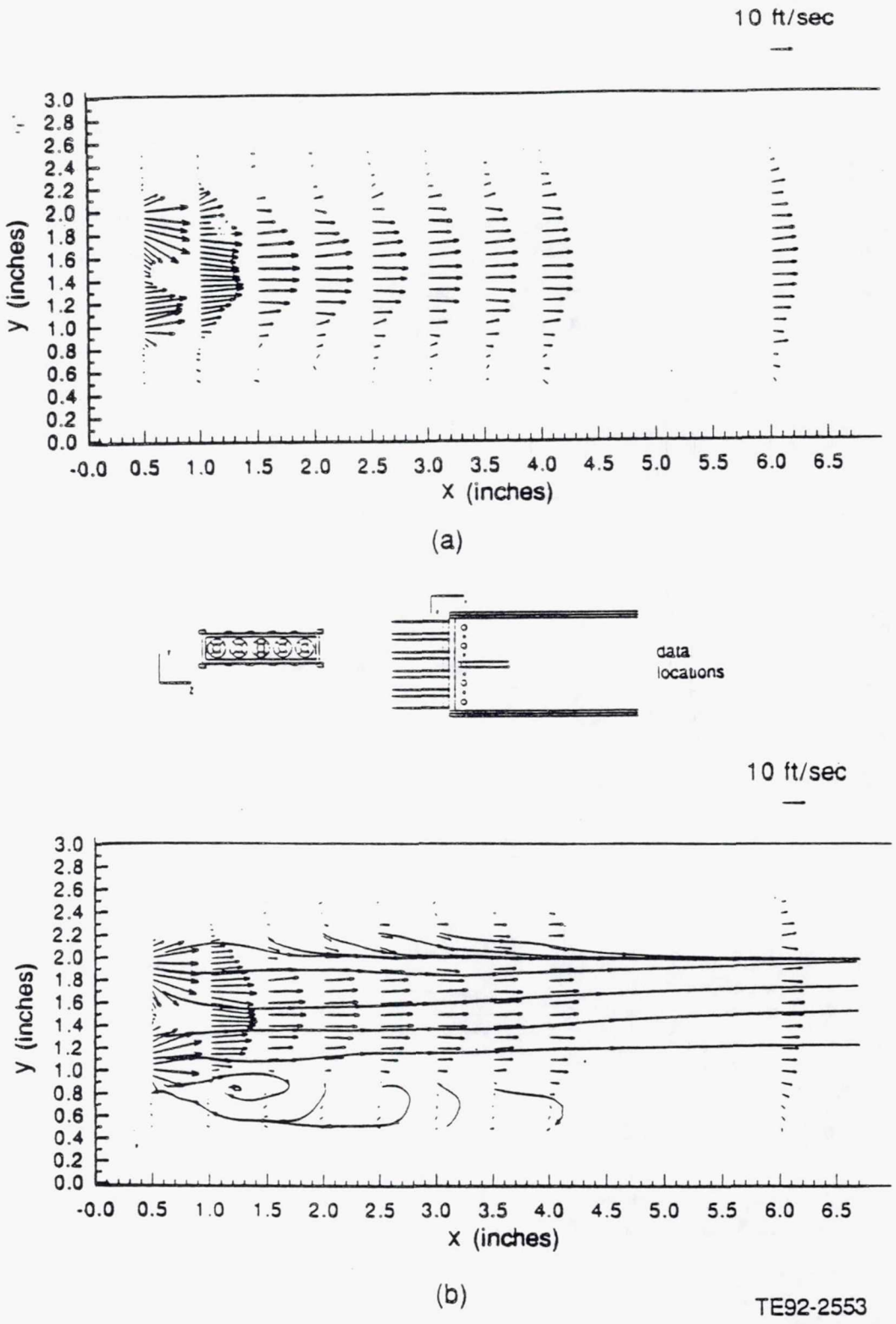

Figure 4.1.2-8. Annular jets only mean velocity vector plots a) Z=7.1 in. b) Z=7.9 in.

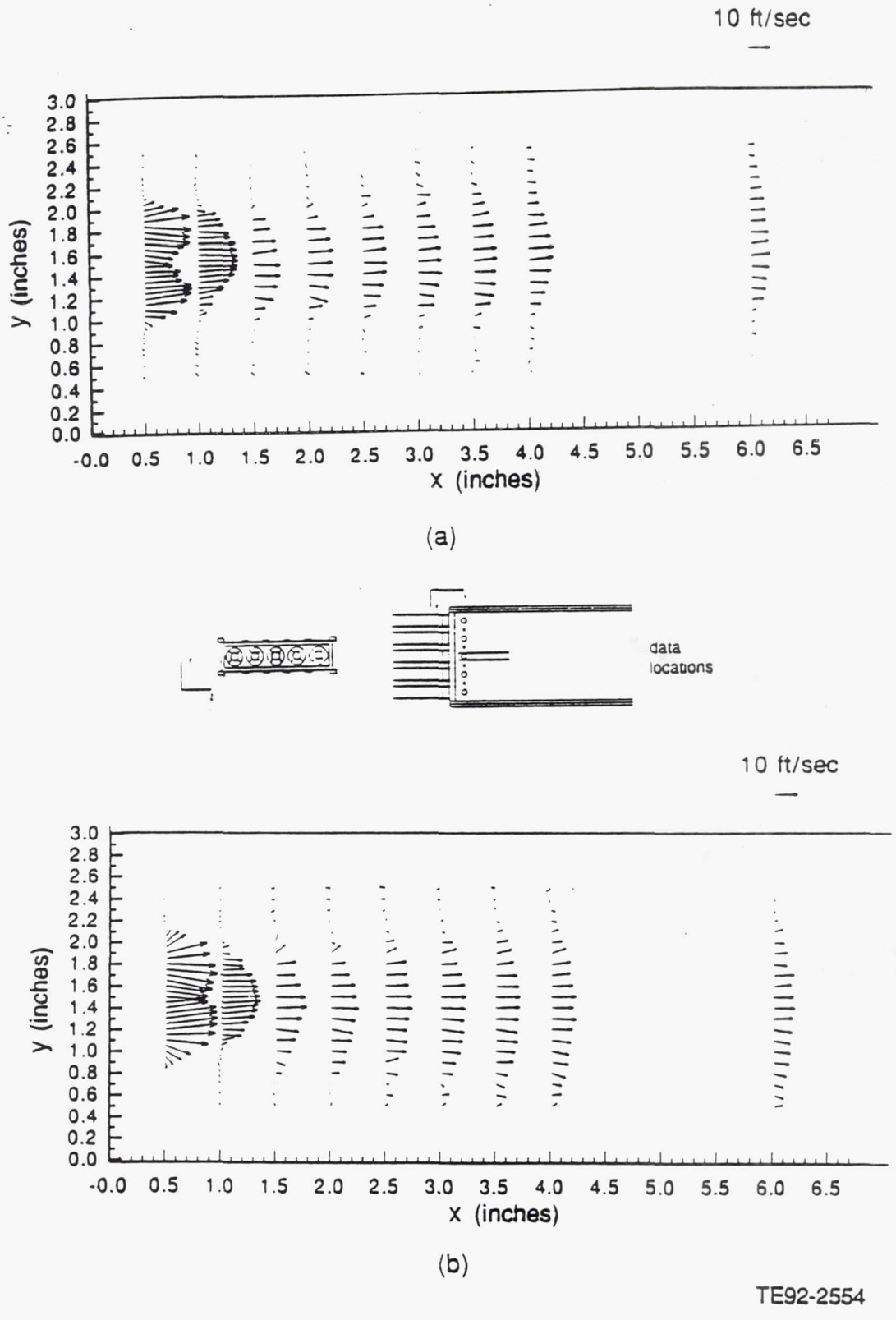

Figure 4.1.2-9. Annular jets only mean velocity vector plots a) Z=7.0 in. b) Z=8.0 in.

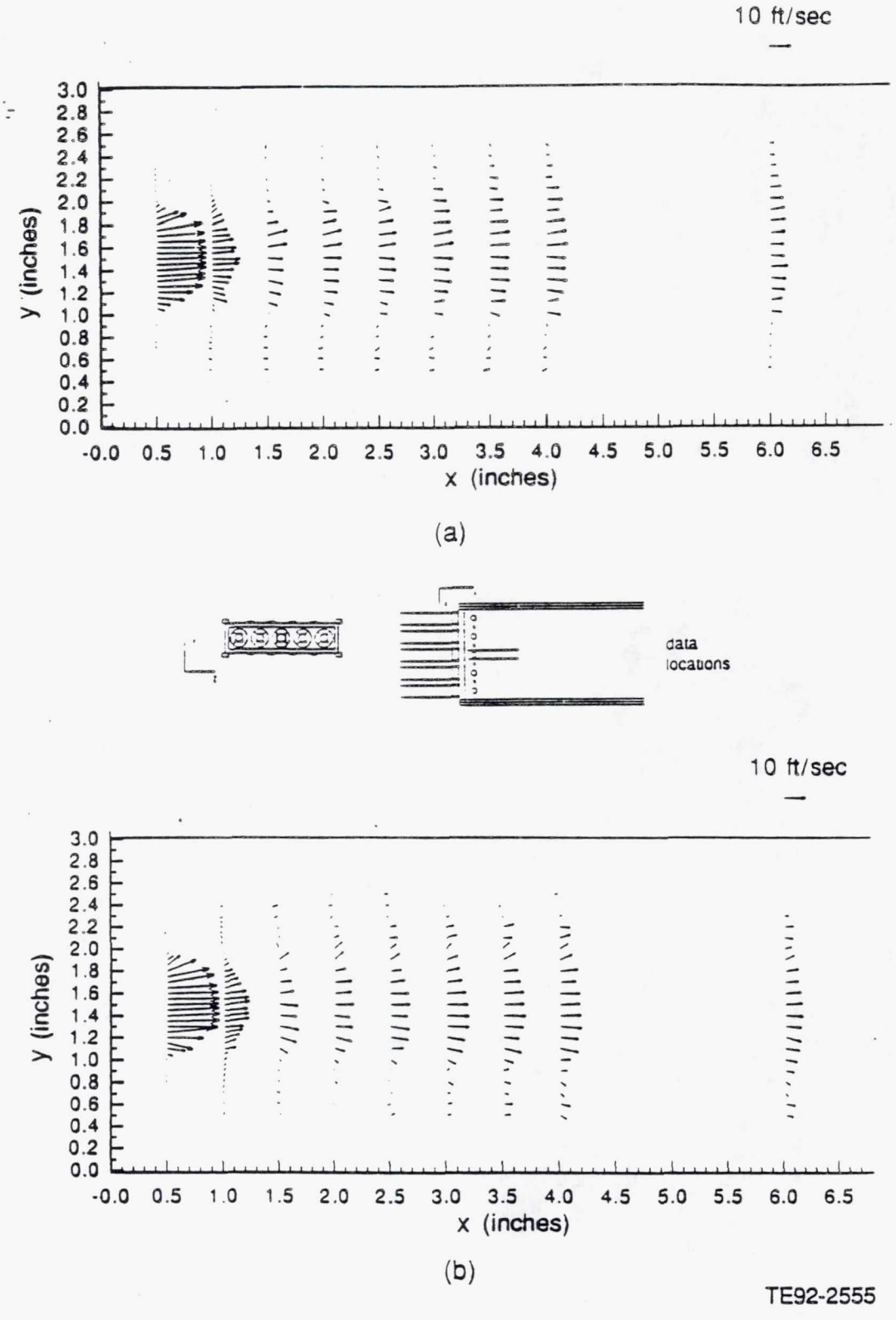

Figure 4.1.2-10. Annular jets only mean velocity vector plots a) Z=6.9 in. b) Z=8.1 in.

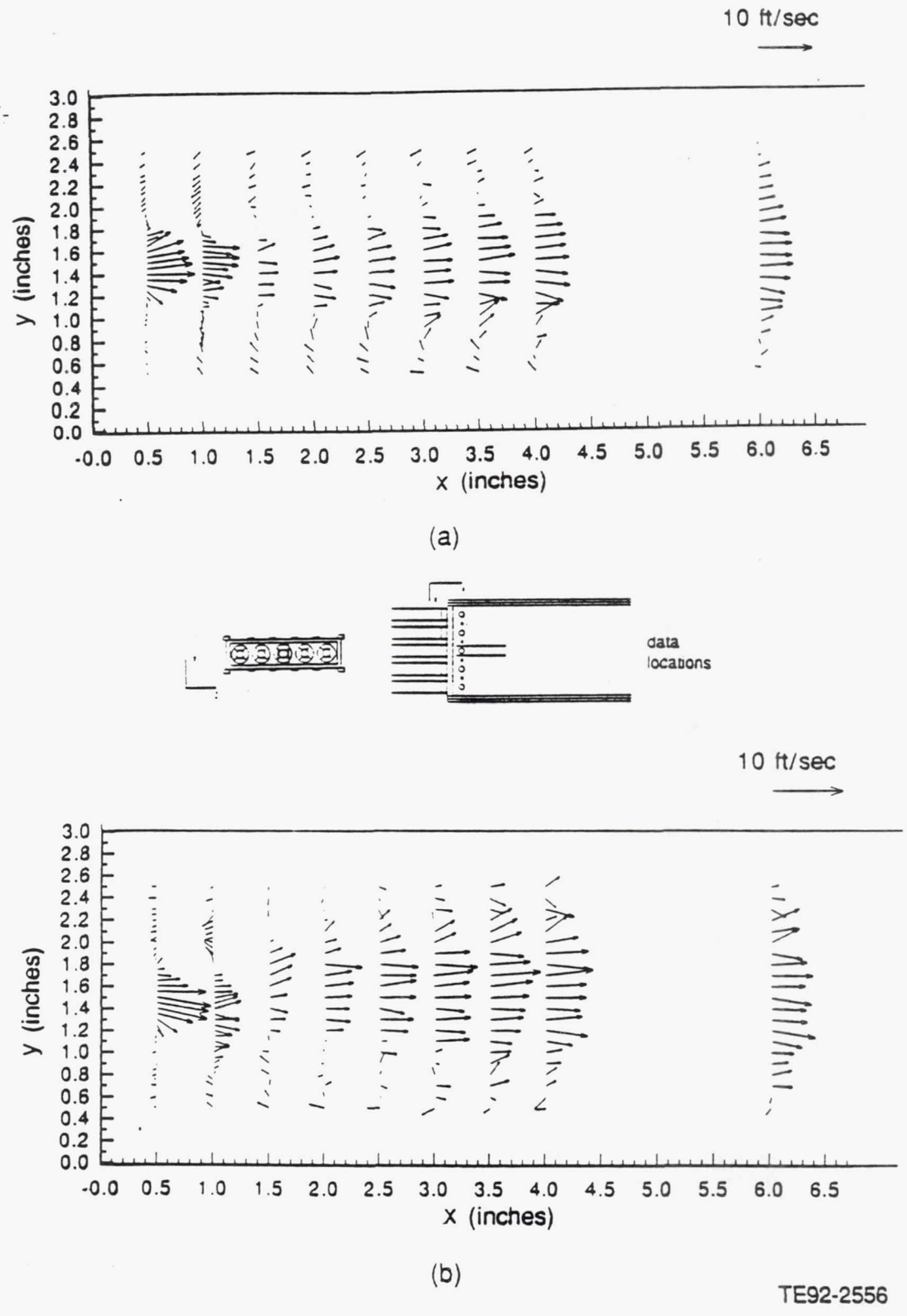

Figure 4.1.2-11. Annular jets only mean velocity vector plots a) z=6.8 in. b) z =8.2 in.

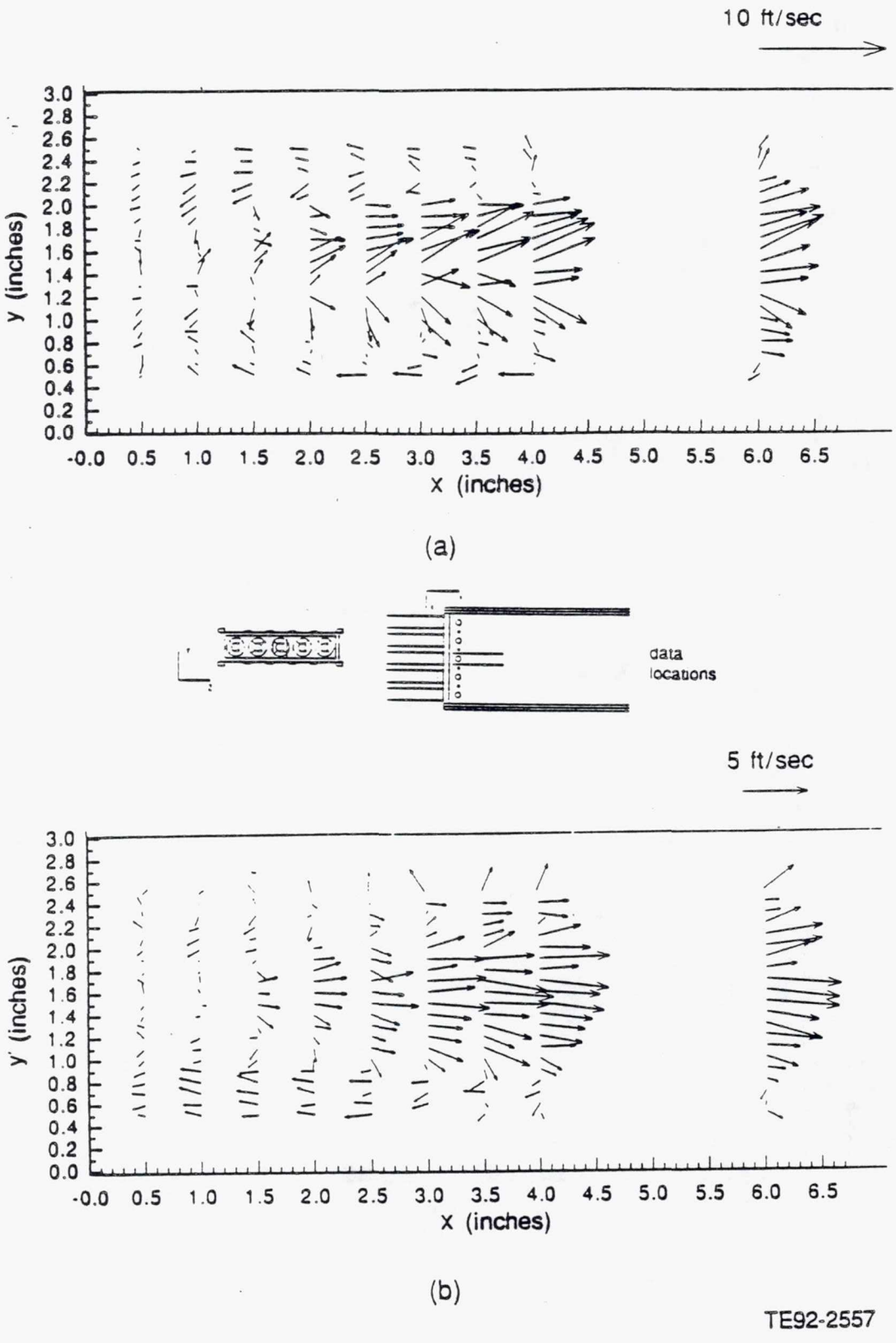

Figure 4.1.2-12. Annular jets only mean velocity vector plots a) Z=6.7 in. b) Z=8.3 in.

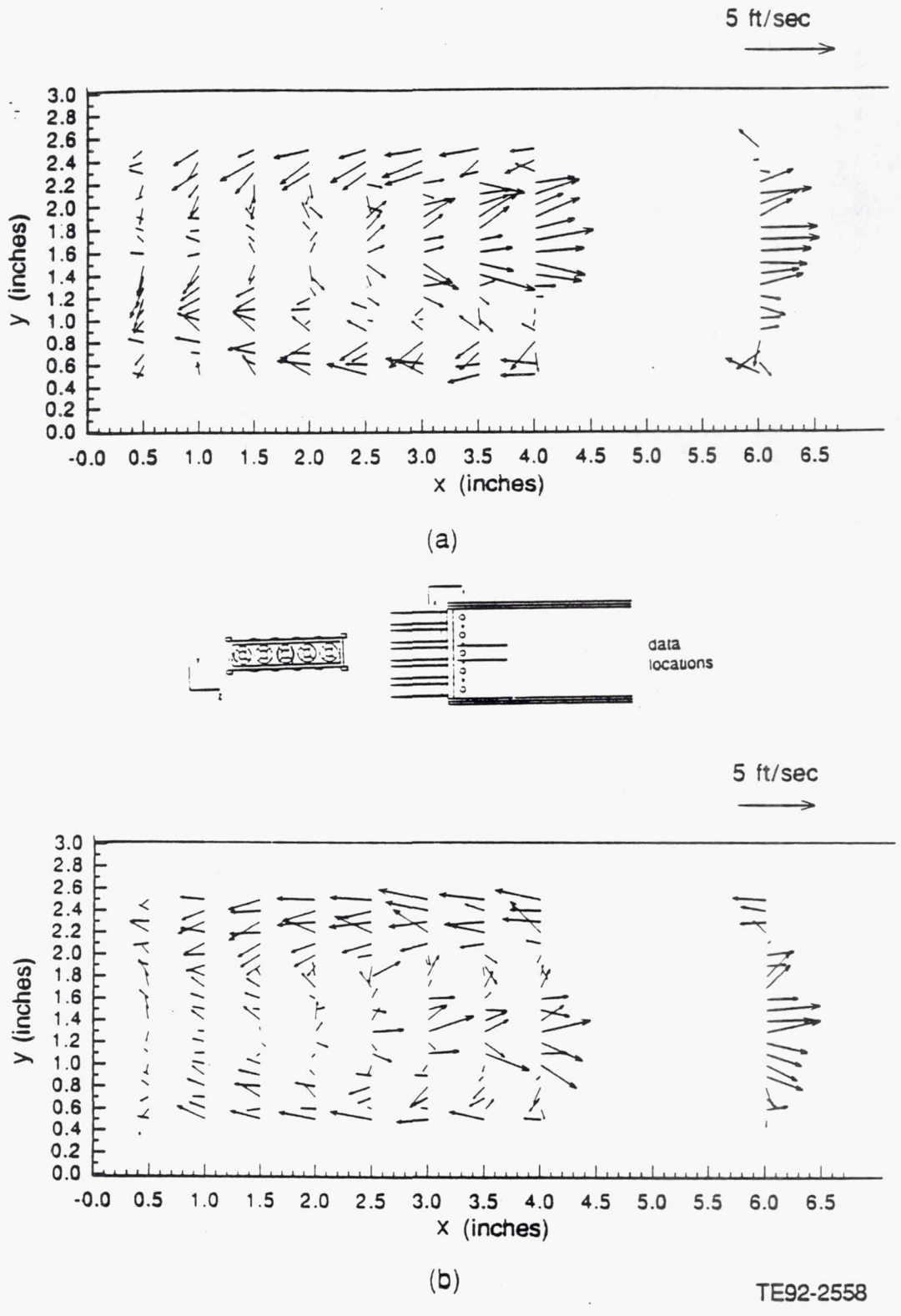

Figure 4.1.2-13. Annular jets only mean velocity vector plots a) Z=6.6 in. b) Z=8.4 in.

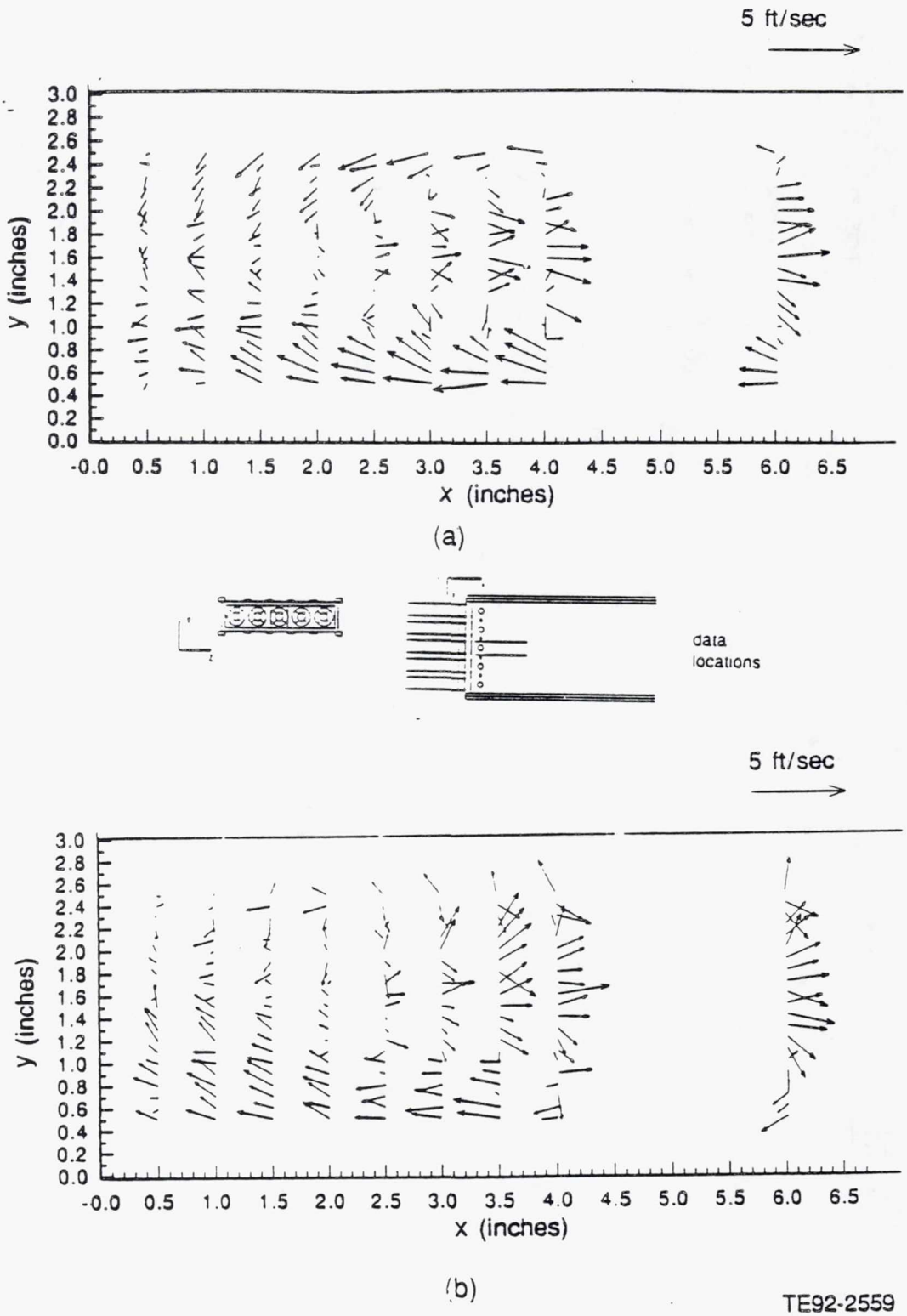

Figure 4.1.2-14. Annular jets only mean velocity vector plots a) Z=6.5 in. b) Z=8.5 in.

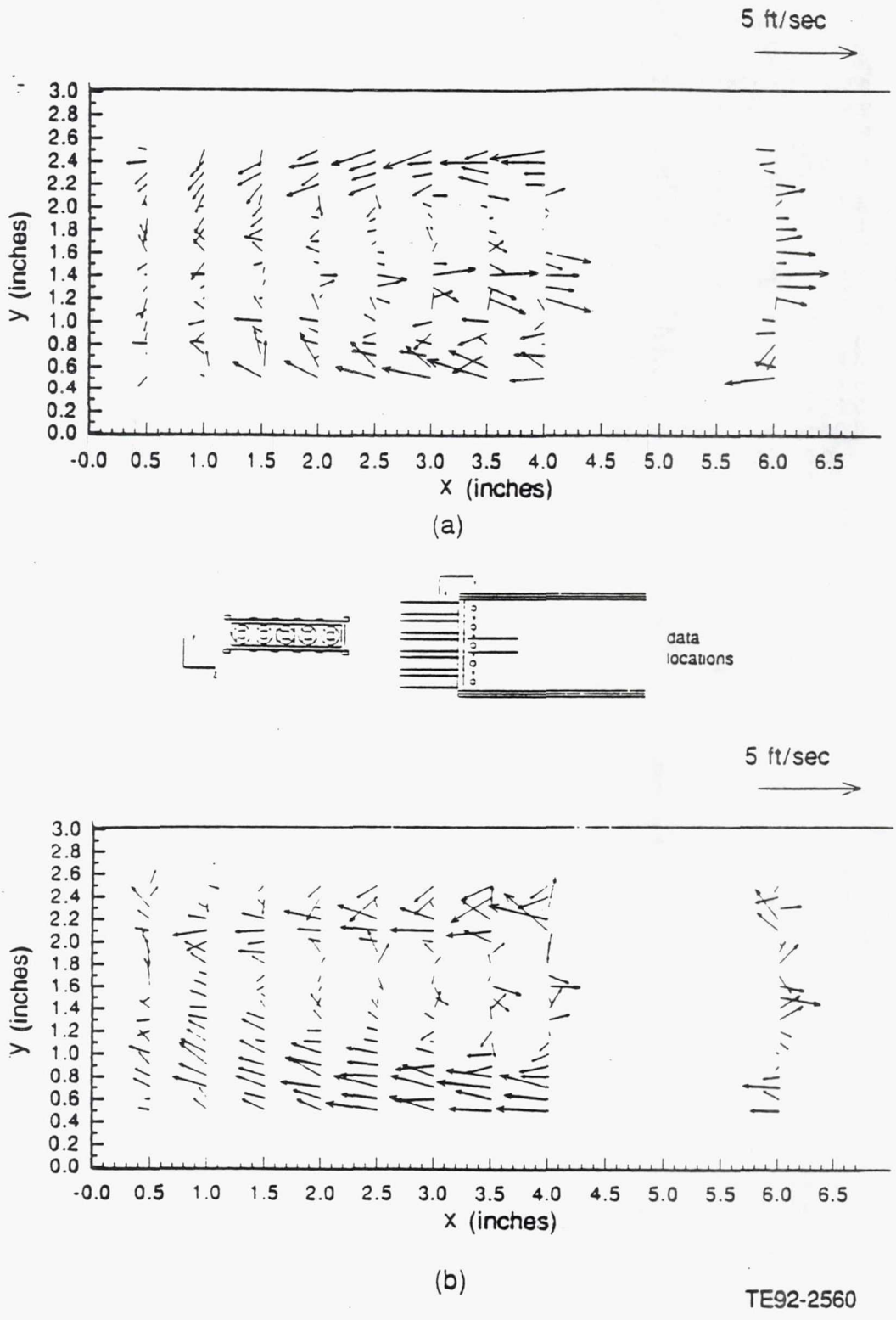

Figure 4.1.2-15. Annular jets only mean velocity vector plots a) Z=6.4 in. b) Z=8.6 in.

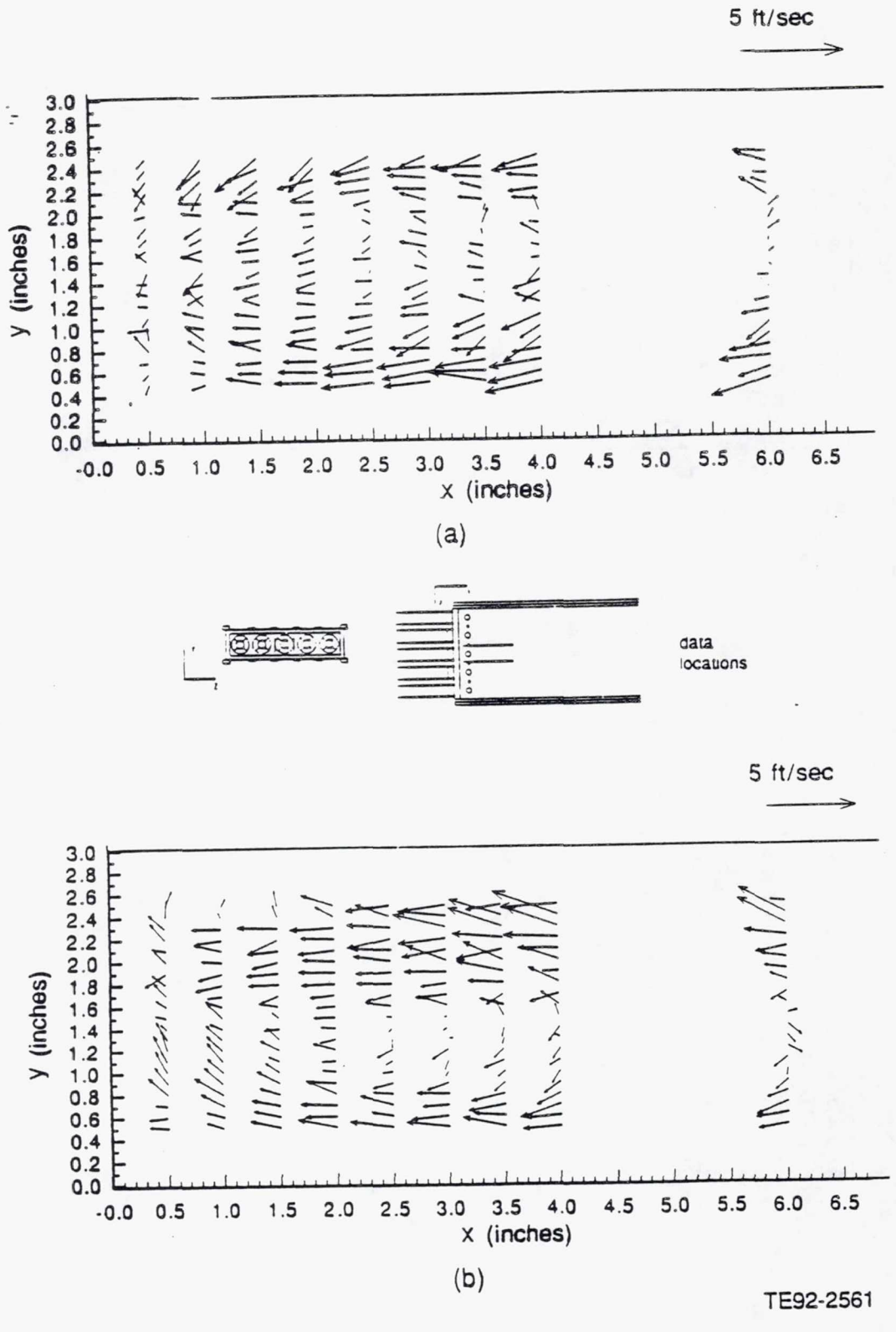

Figure 4.1.2-16. Annular jets only mean velocity vector plots a) Z=6.3 in. b) Z=8.7 in.

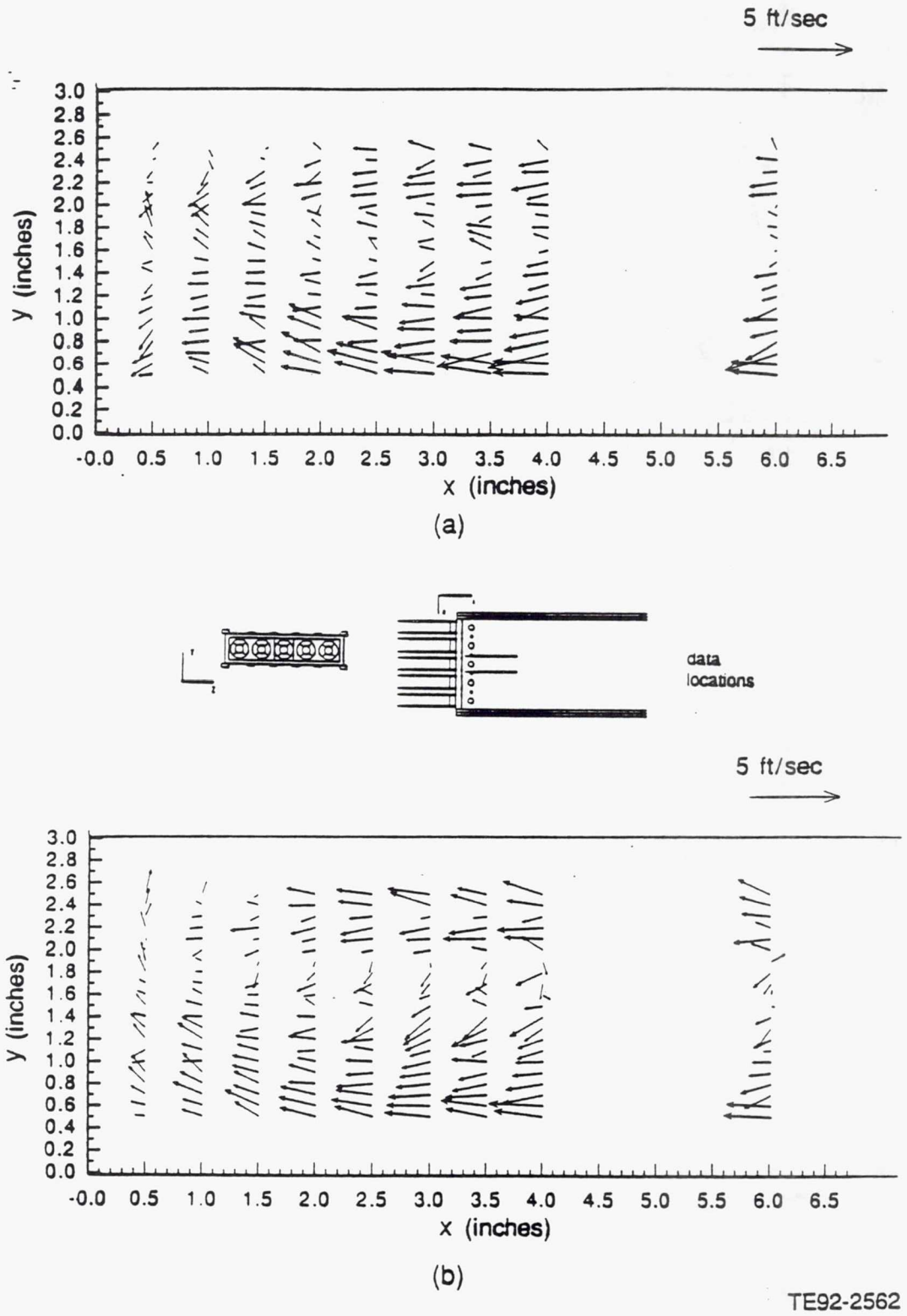

Figure 4.1.2-17. Annular jets only mean velocity vector plots a) Z=6.2 in. b) Z=8.8 in.

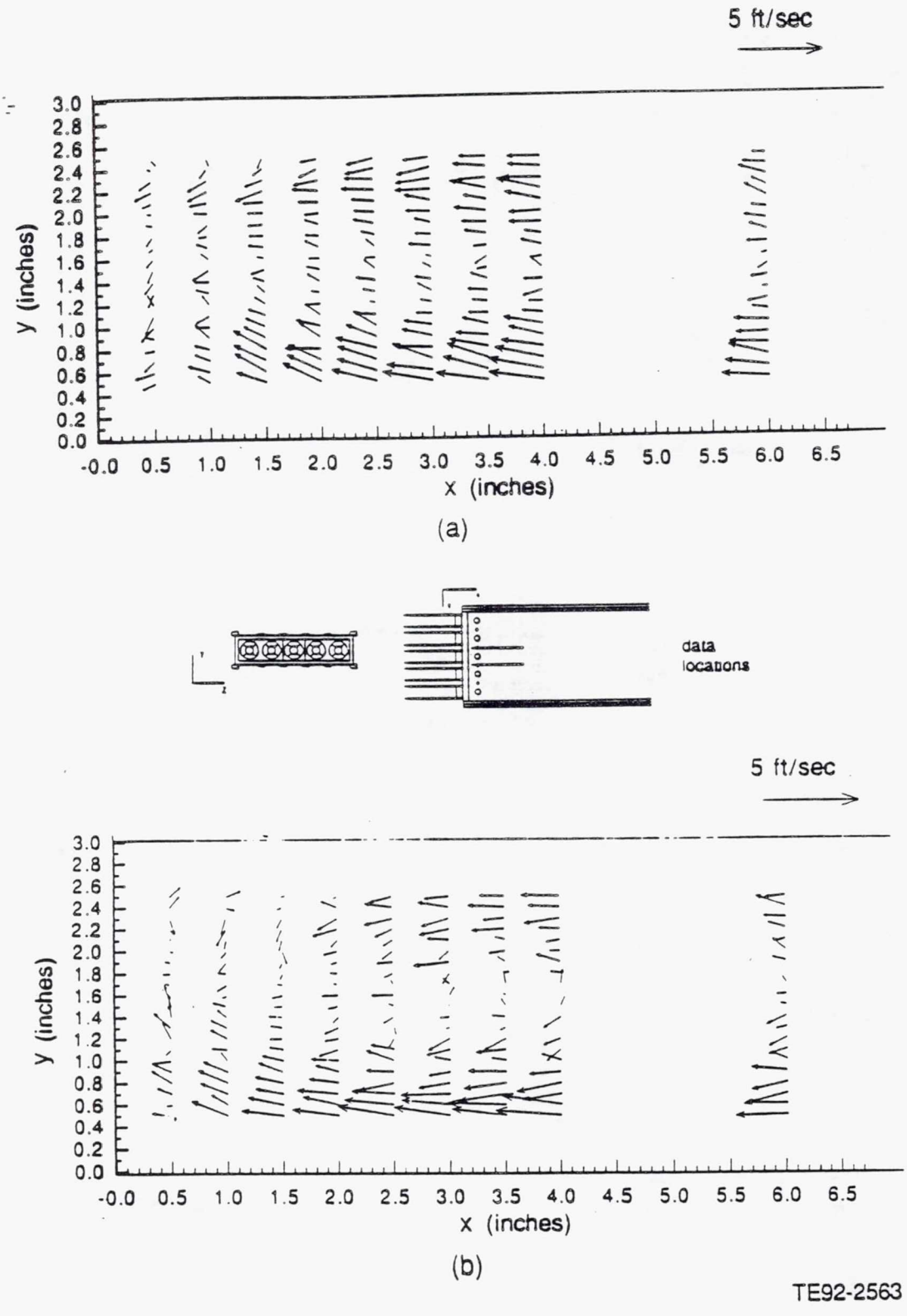

Figure 4.1.2-18. Annular jets only mean velocity vector plots a) Z=6.1 in. b) Z=8.9 in.

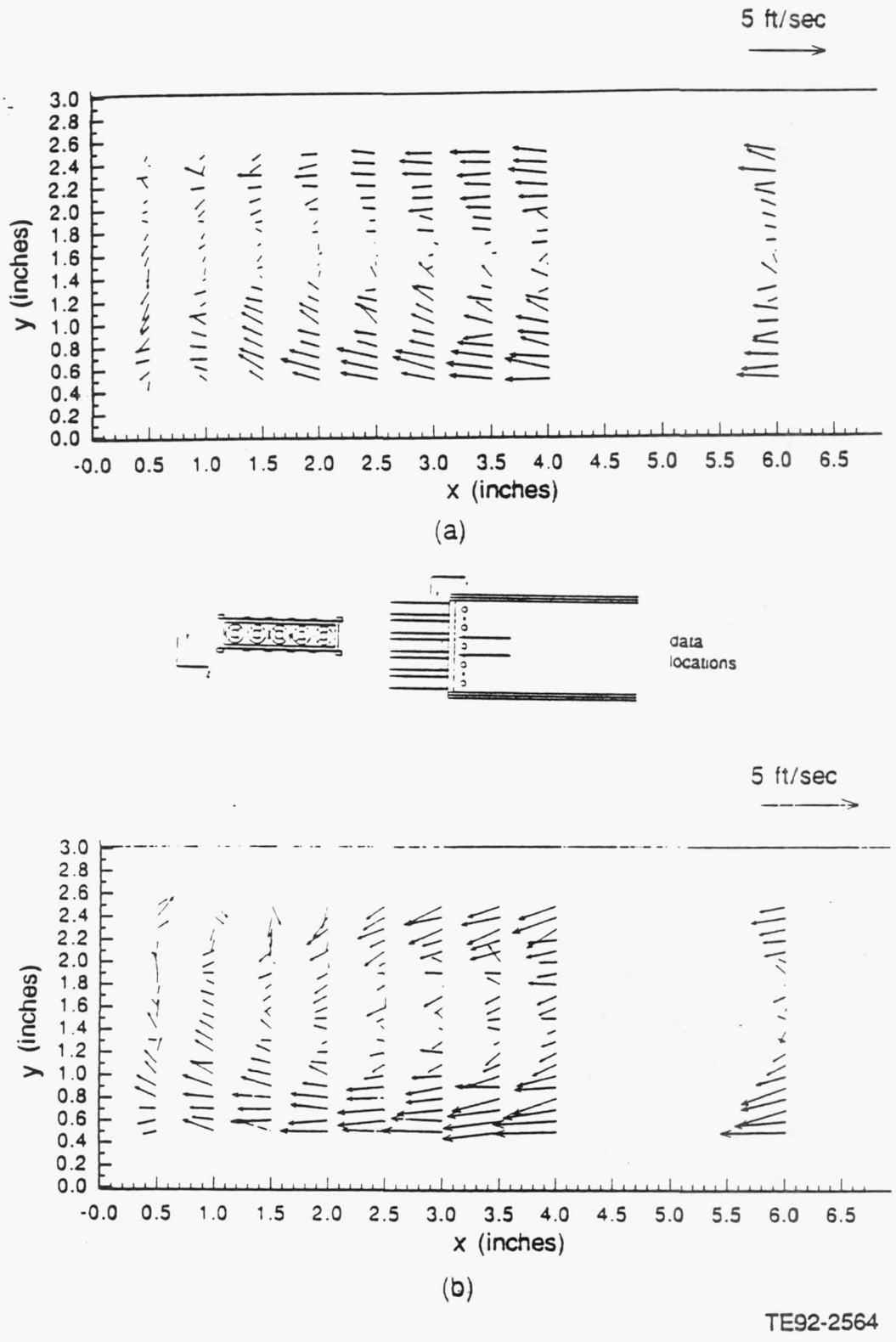

Figure 4.1.2-19. Annular jets only mean velocity vector plots a) z=6.0 in. b) z=9.0 in.

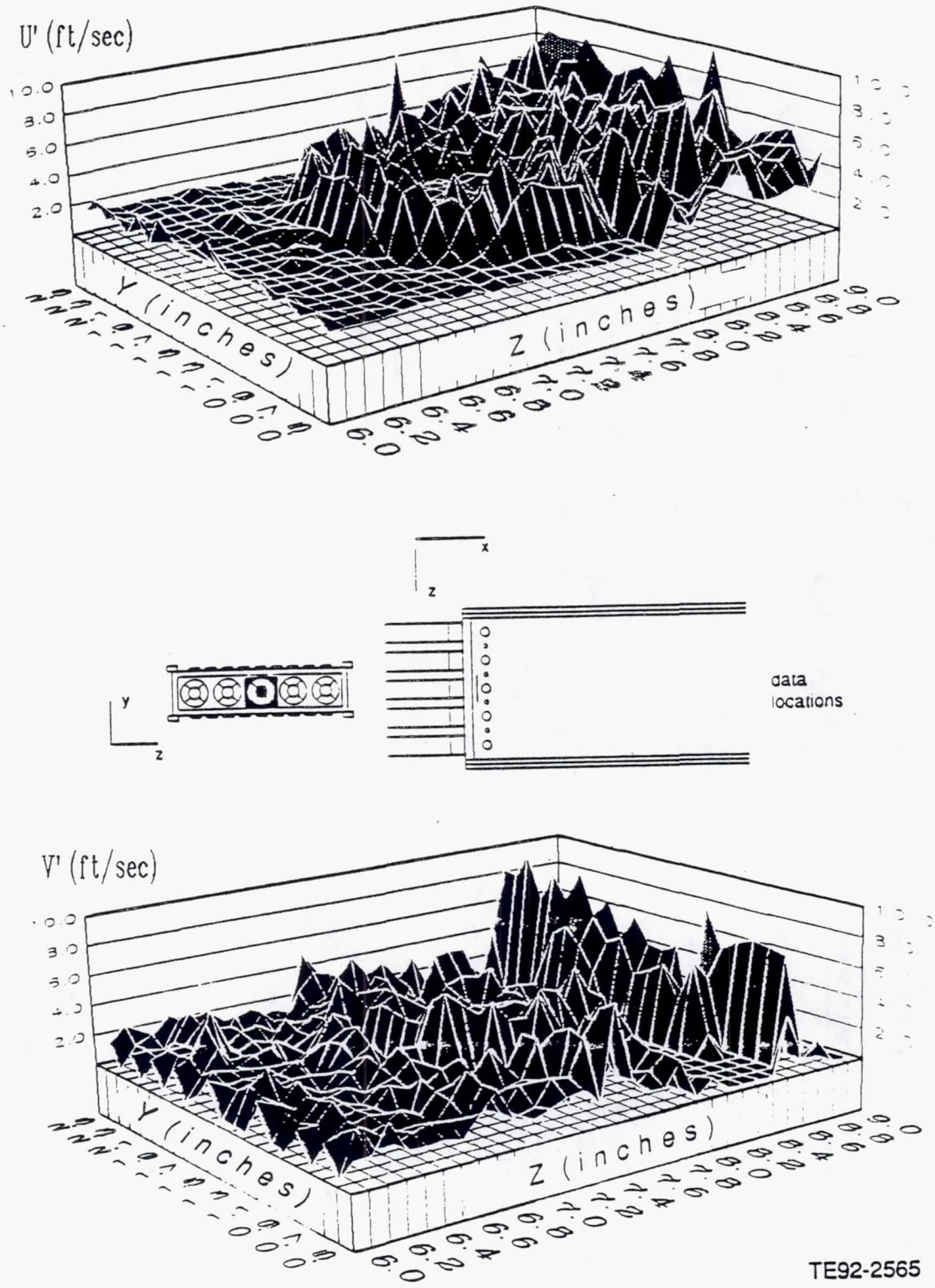

Figure 4.1.2-20. Annular jets only contour plot of U_{rms} and V_{rms} at x=0.5 in.

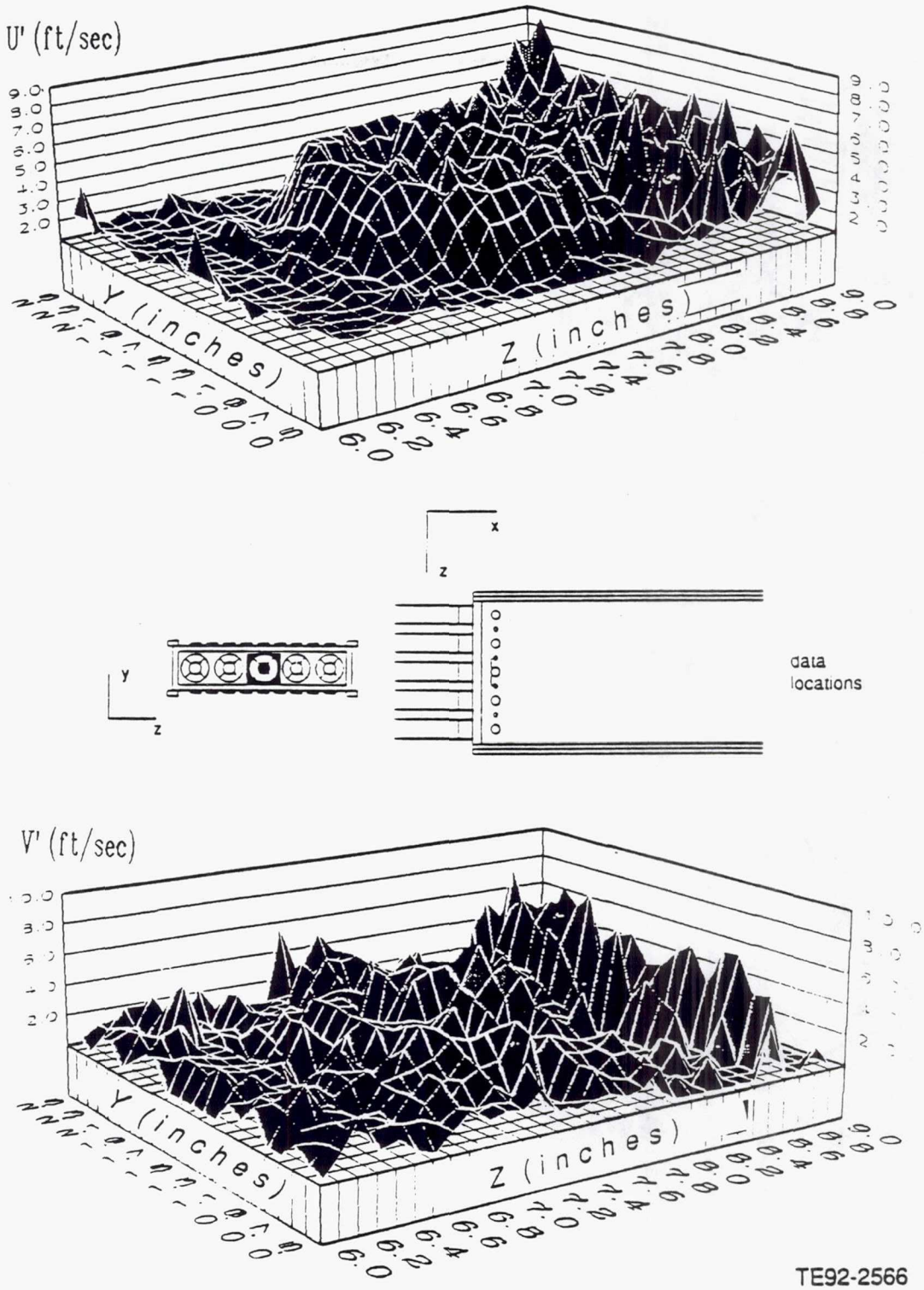

Figure 4.1.2-21. Annular jets only contour plot of U_{rms} and V_{rms} at x=1.0 in.

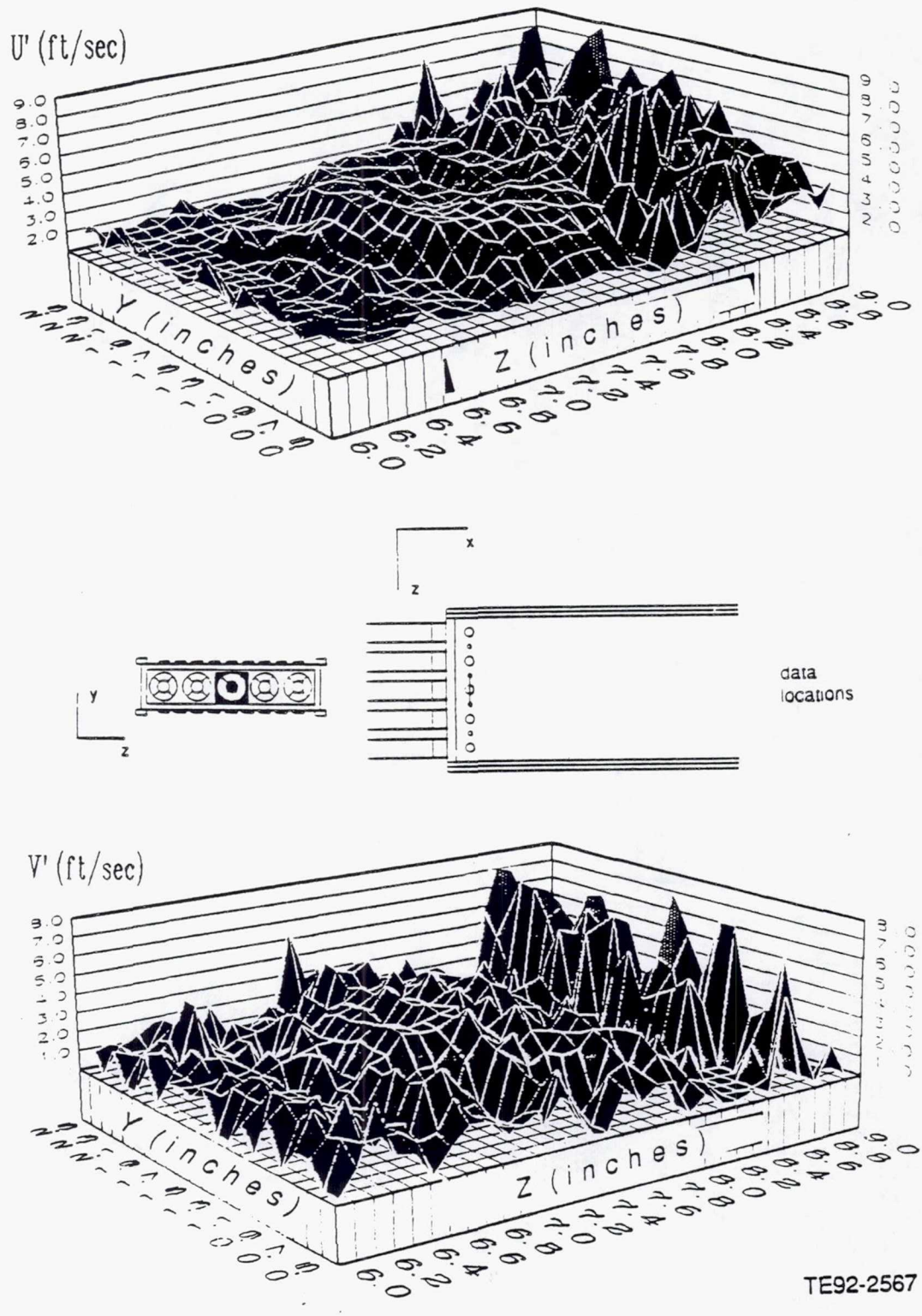

Figure 4.1.2-22. Annular jets only contour plot of U_{rms} and V_{rms} at x=1.5 in.

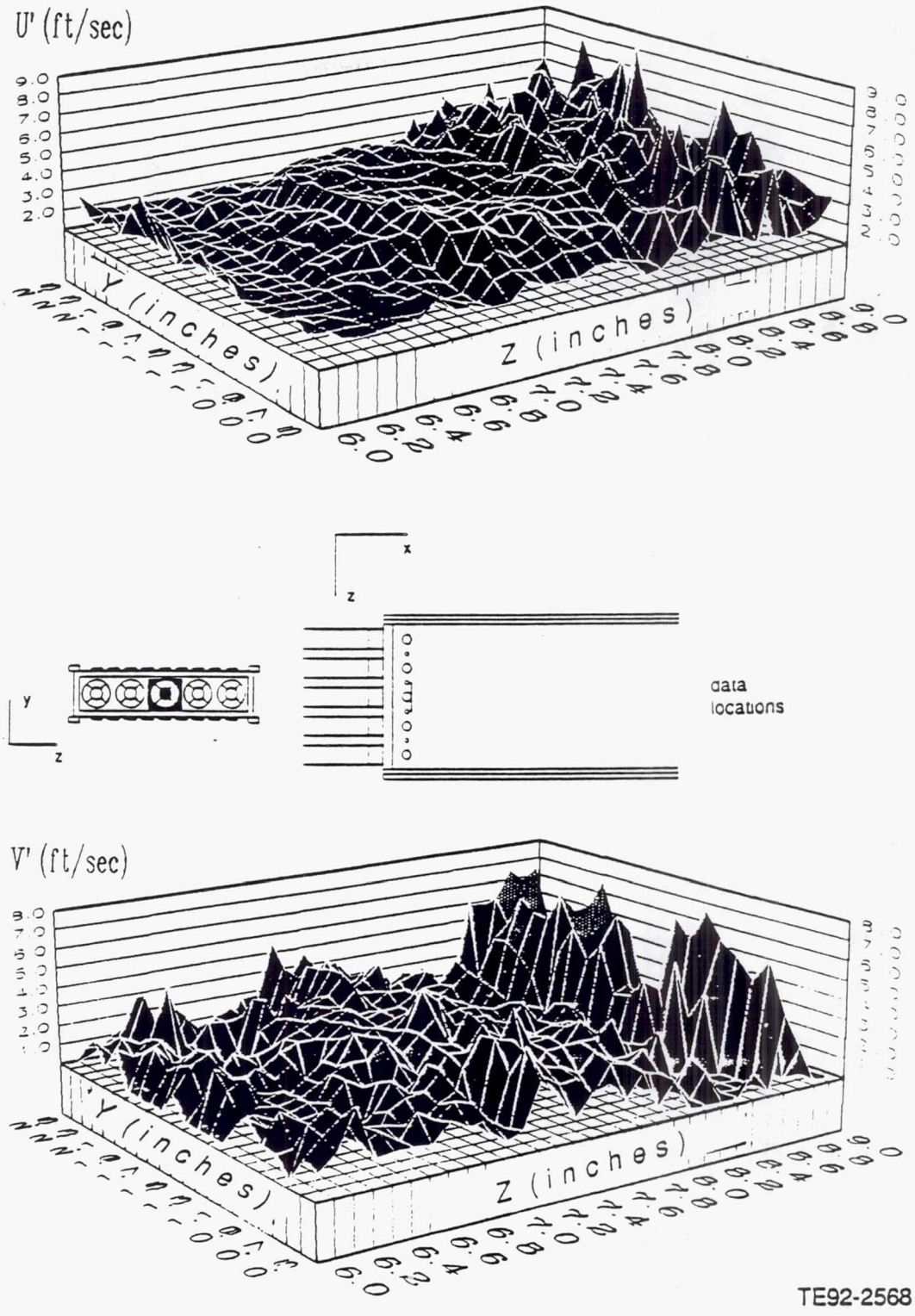

Figure 4.1.2-23. Annular jets only contour plot of U_{rms} and V_{rms} at x=2.0 in.

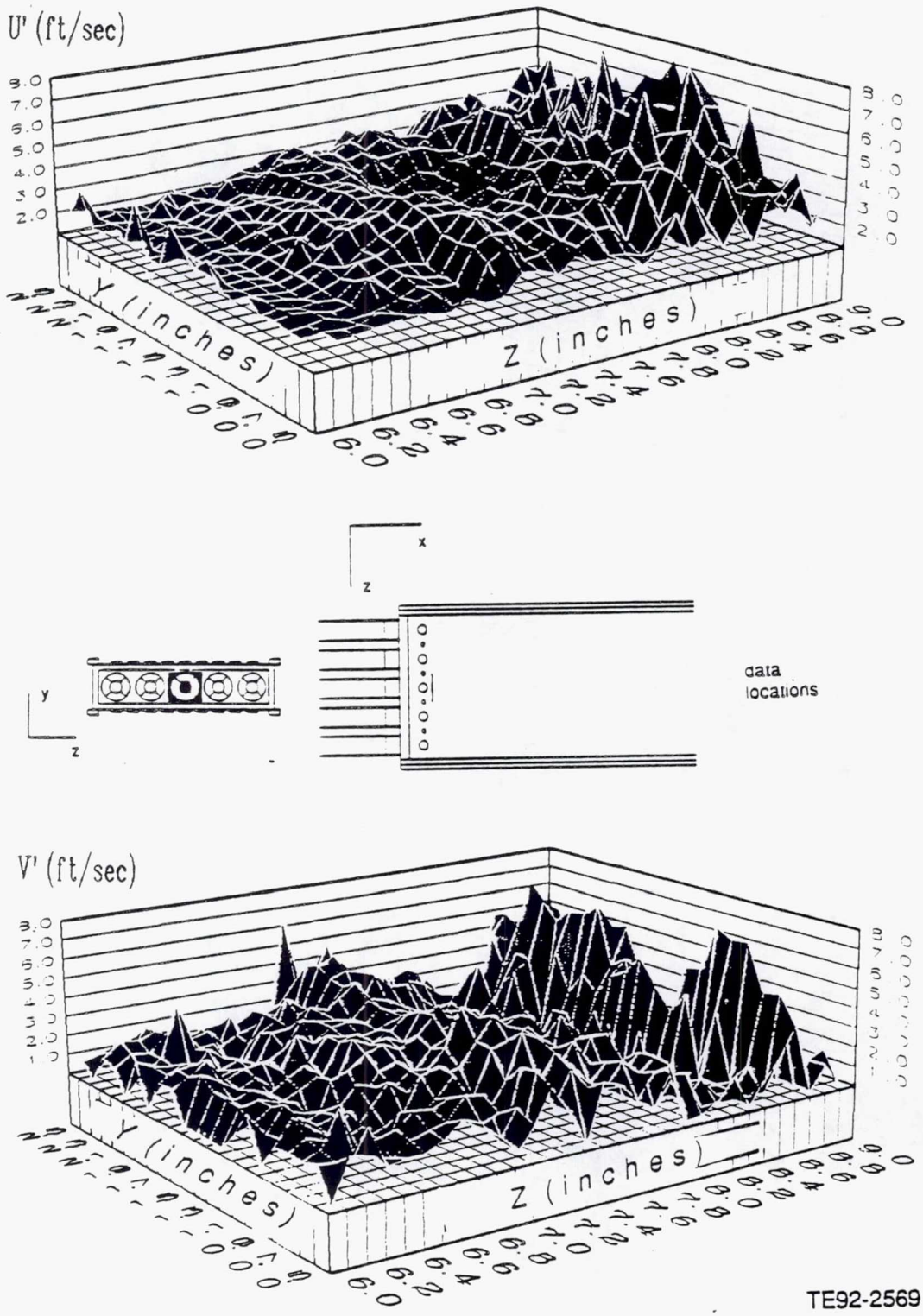

Figure 4.1.2-24. Annular jets only contour plot of U_{rms} and V_{rms} at x=2.5 in.

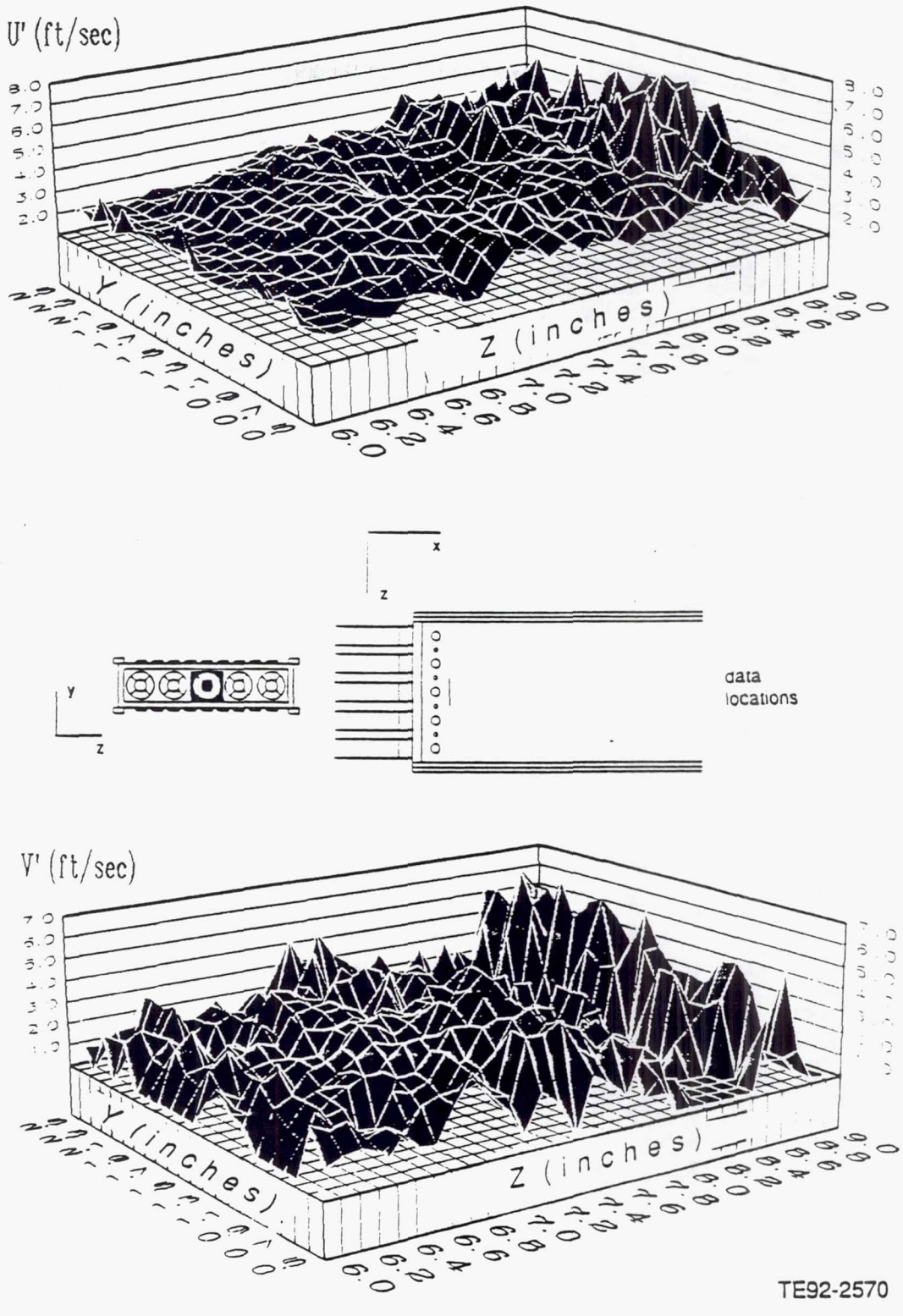

Figure 4.1.2-25. Annular jets only contour plot of U_{rms} and V_{rms} at x=3.0 in.

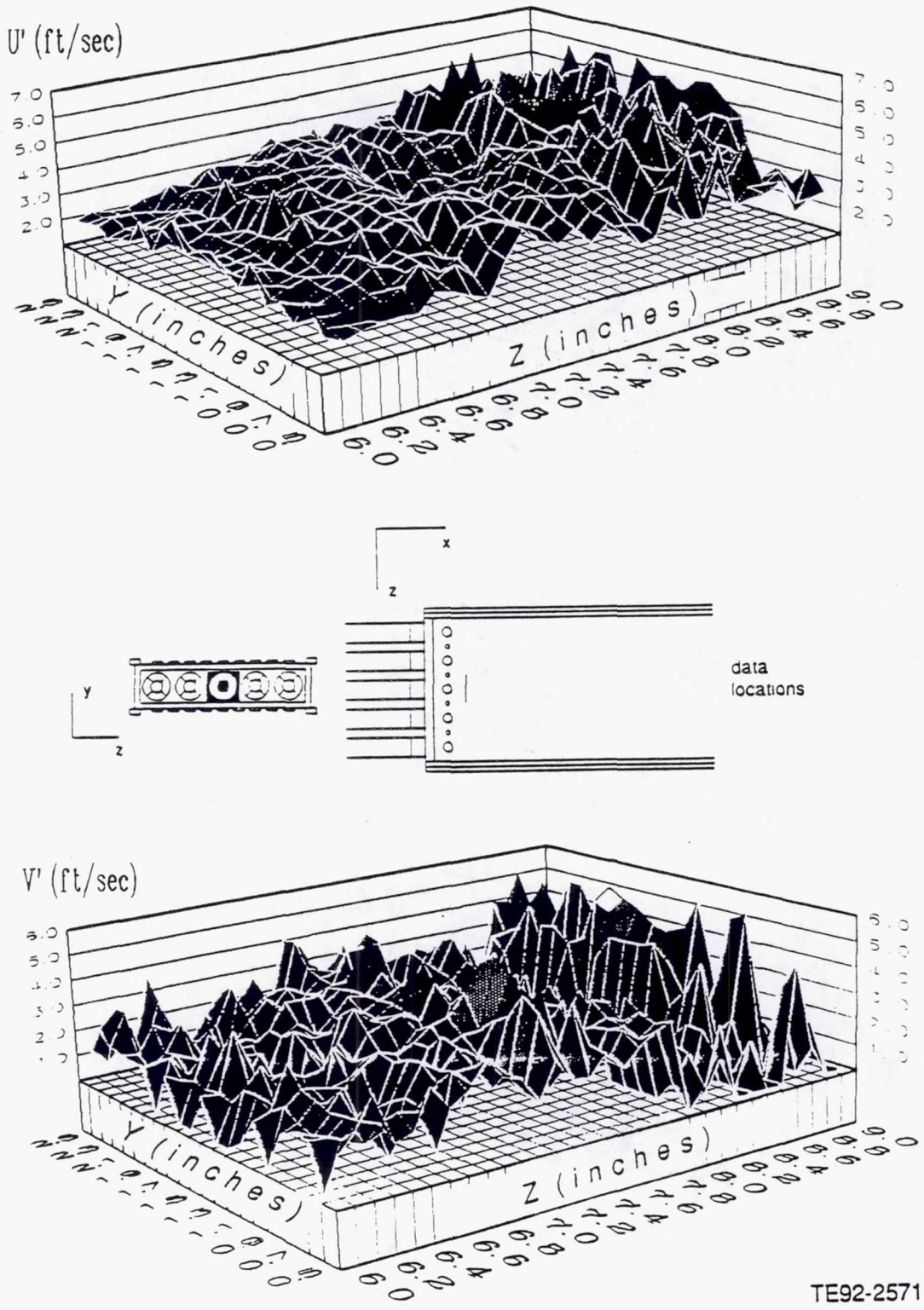

Figure 4.1.2-26. Annular jets only contour plot of U_{rms} and V_{rms} at x=3.5 in.

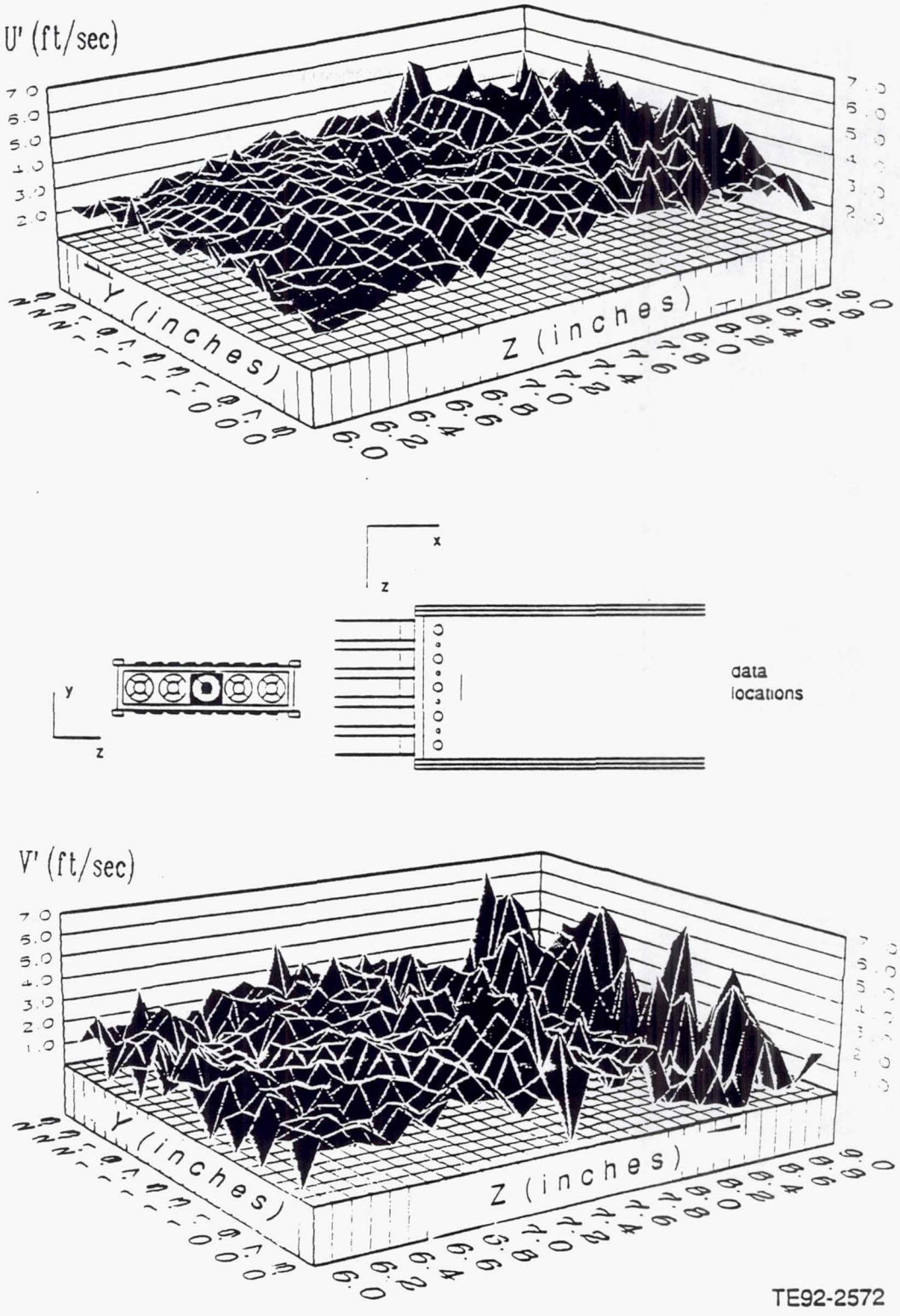

Figure 4.1.2-27. Annular jets only contour plot of U_{rms} and V_{rms} at x=4.0 in.

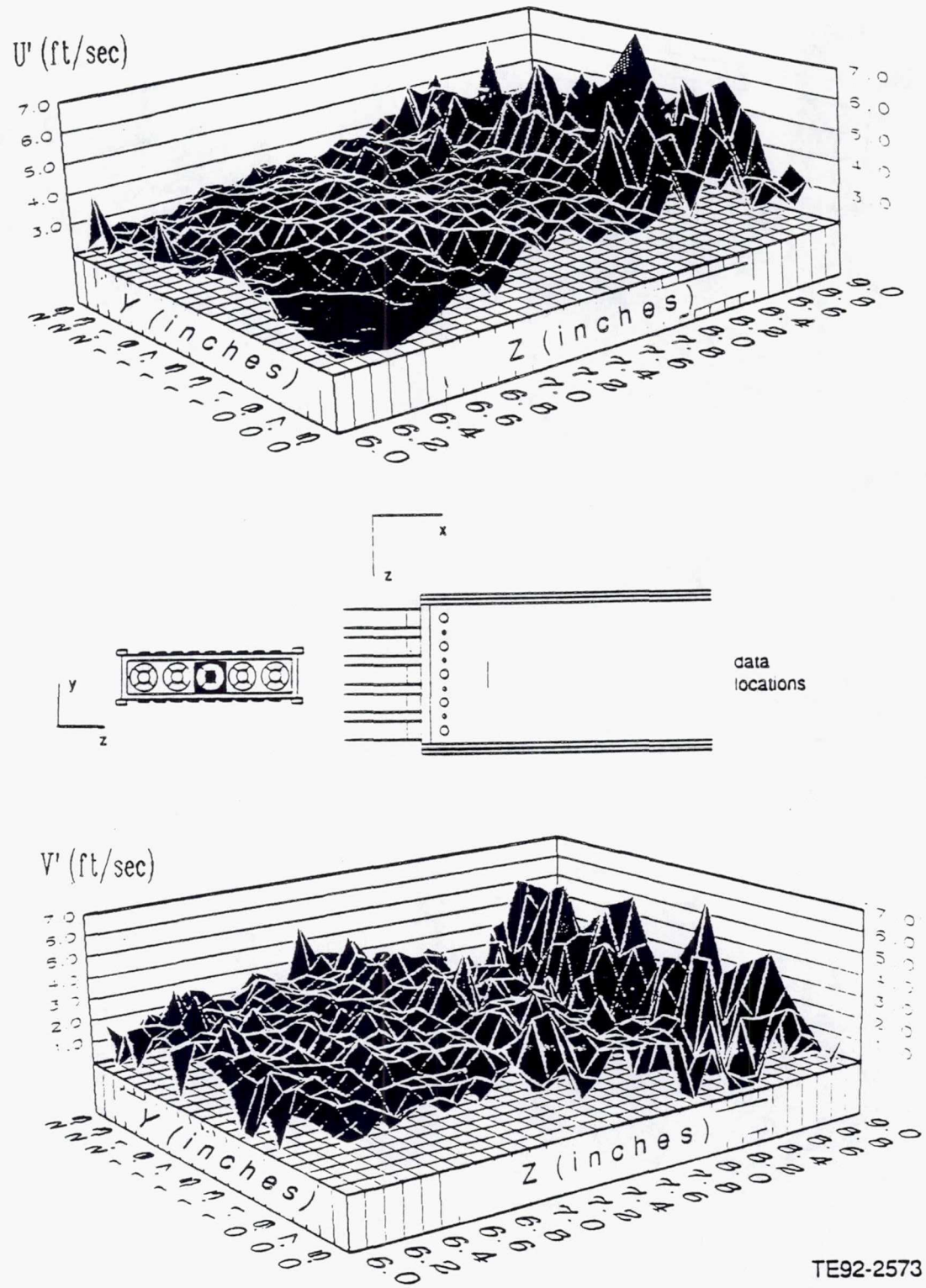

Figure 4.1.2-28. Annular jets only contour plot of U_{rms} and V_{rms} at x=6.0 in.

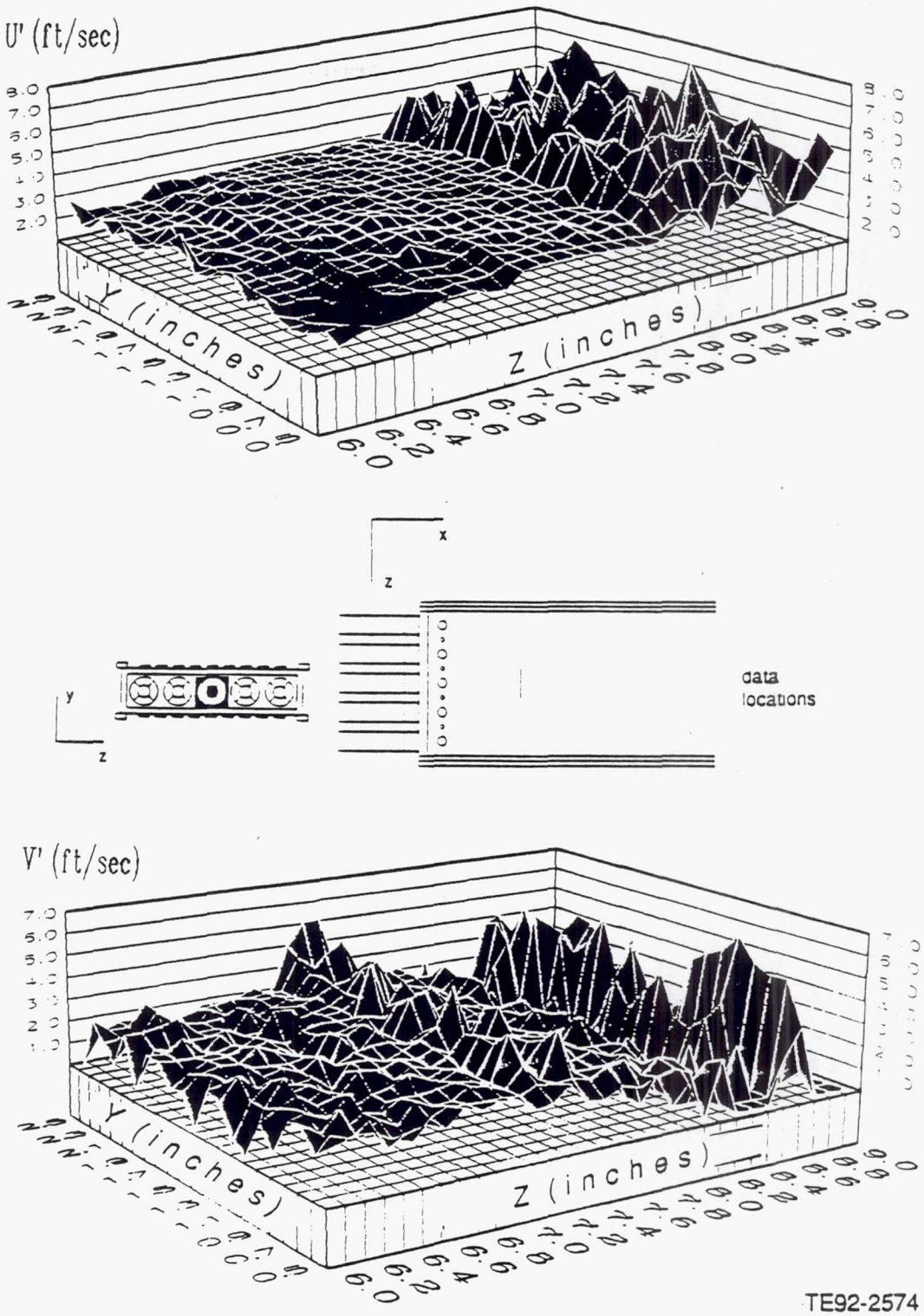

Figure 4.1.2-29. Annular jets only contour plot of U_{rms} and V_{rms} at x=9.0 in.

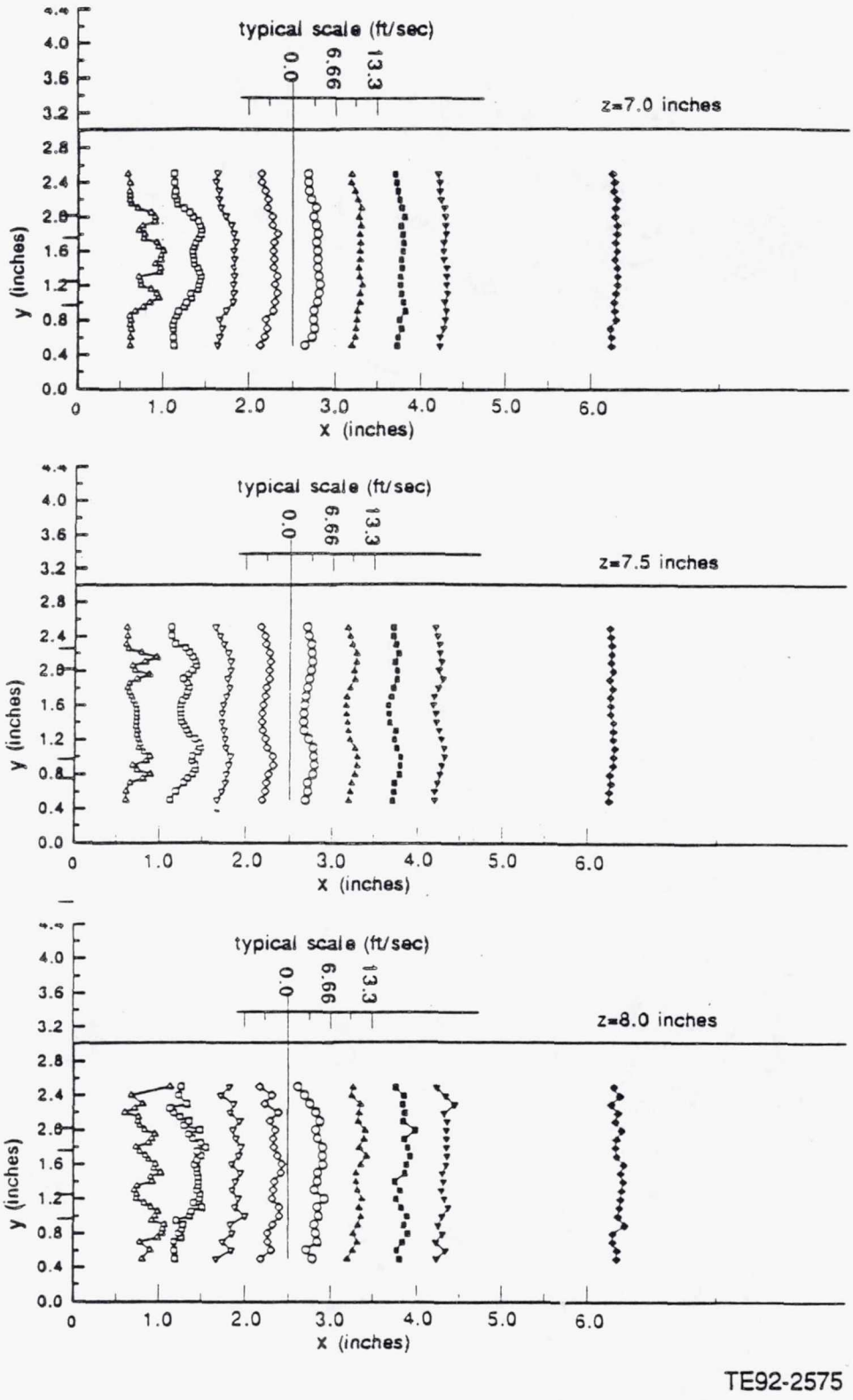

Figure 4.1.2-30. Annular jets only U_{rms} distribution.

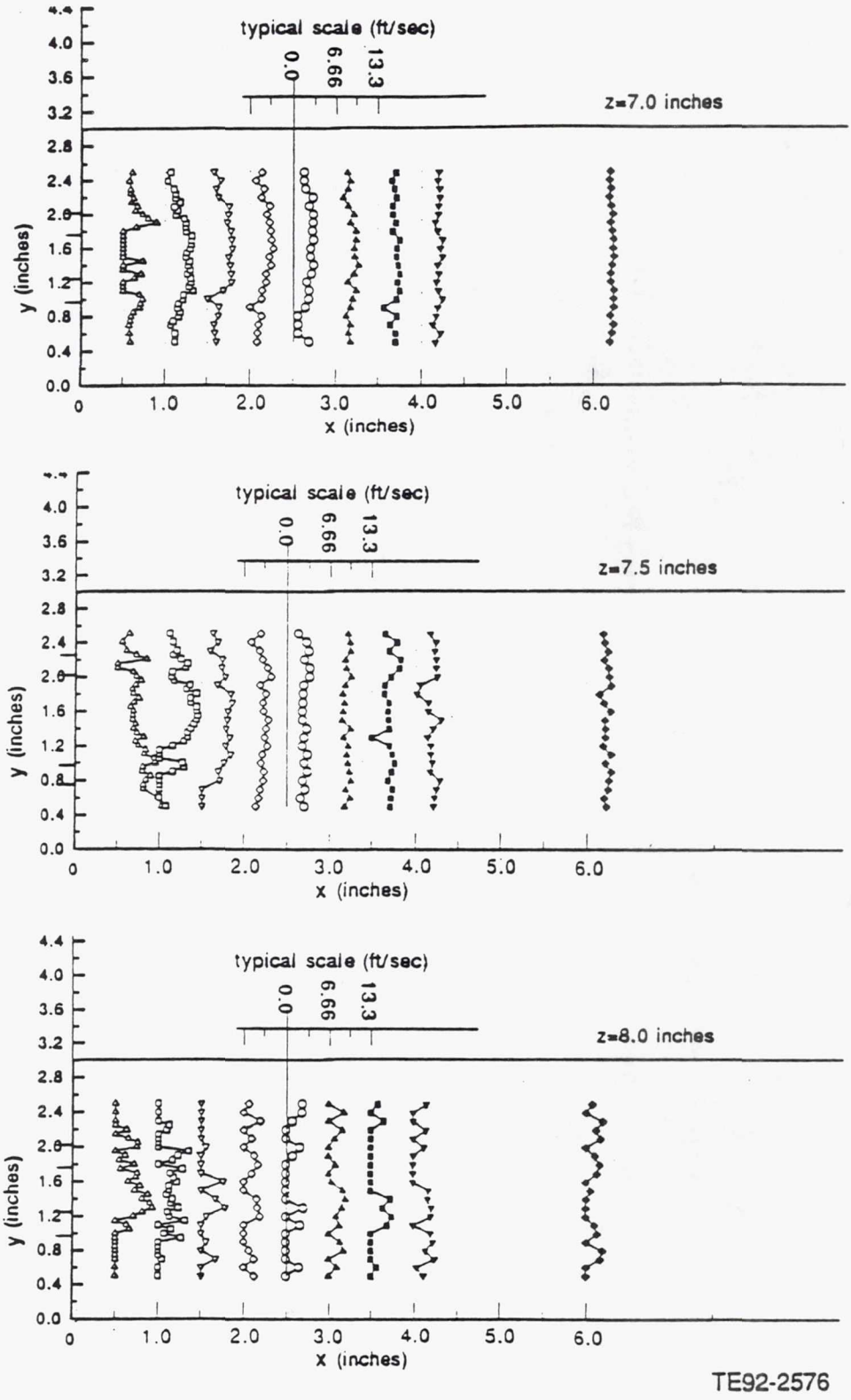

Figure 4.1.2-31. Annular jets only V_{rms} distribution.

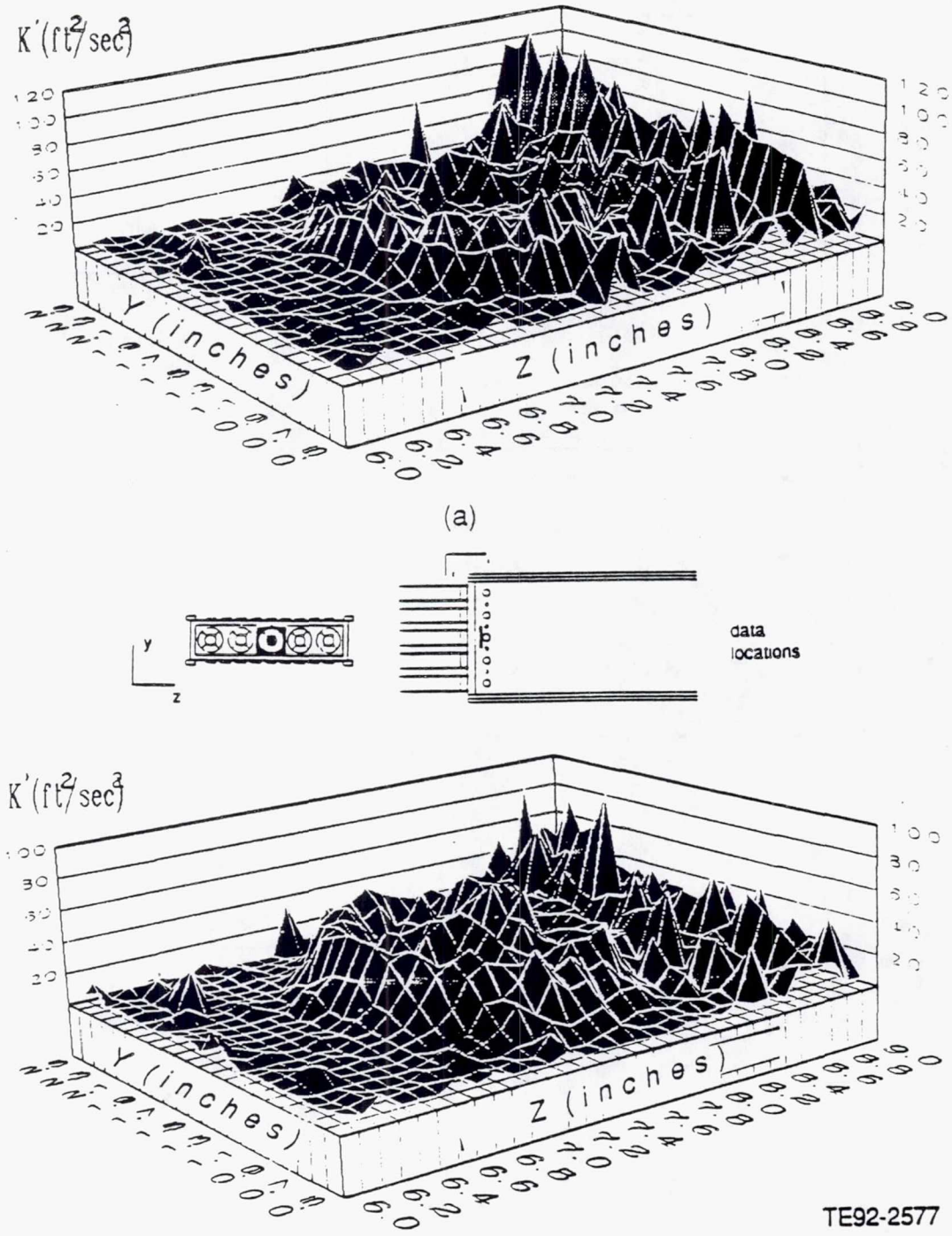

Figure 4.1.2-32. Annular jets only contour plot of K' at a) x=0.5 in. b) x=1.0 in.

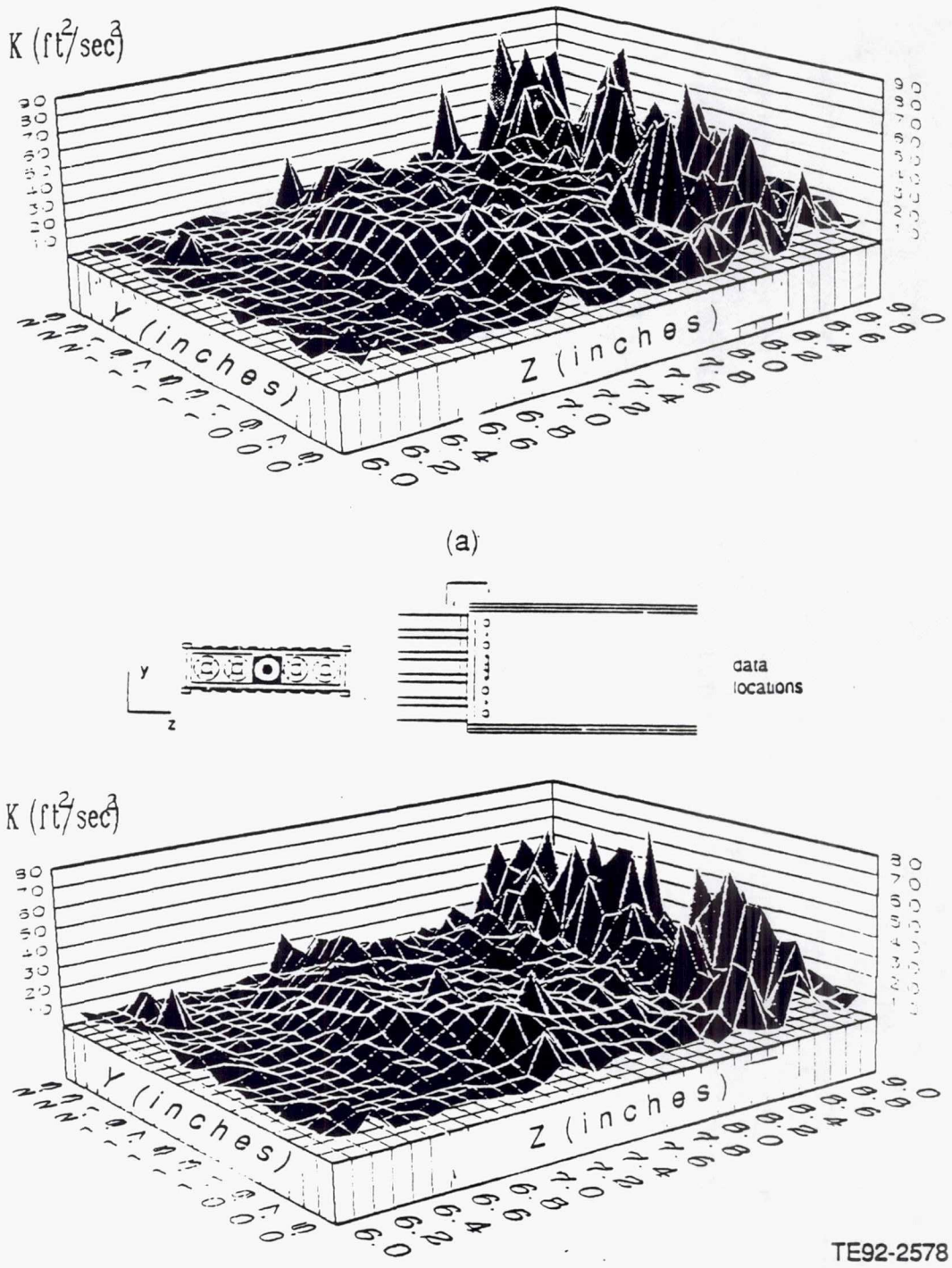

Figure 4.1.2-33. Annular jets only contour plot of K' at a) x=1.5 in. b) x=2.0 in.

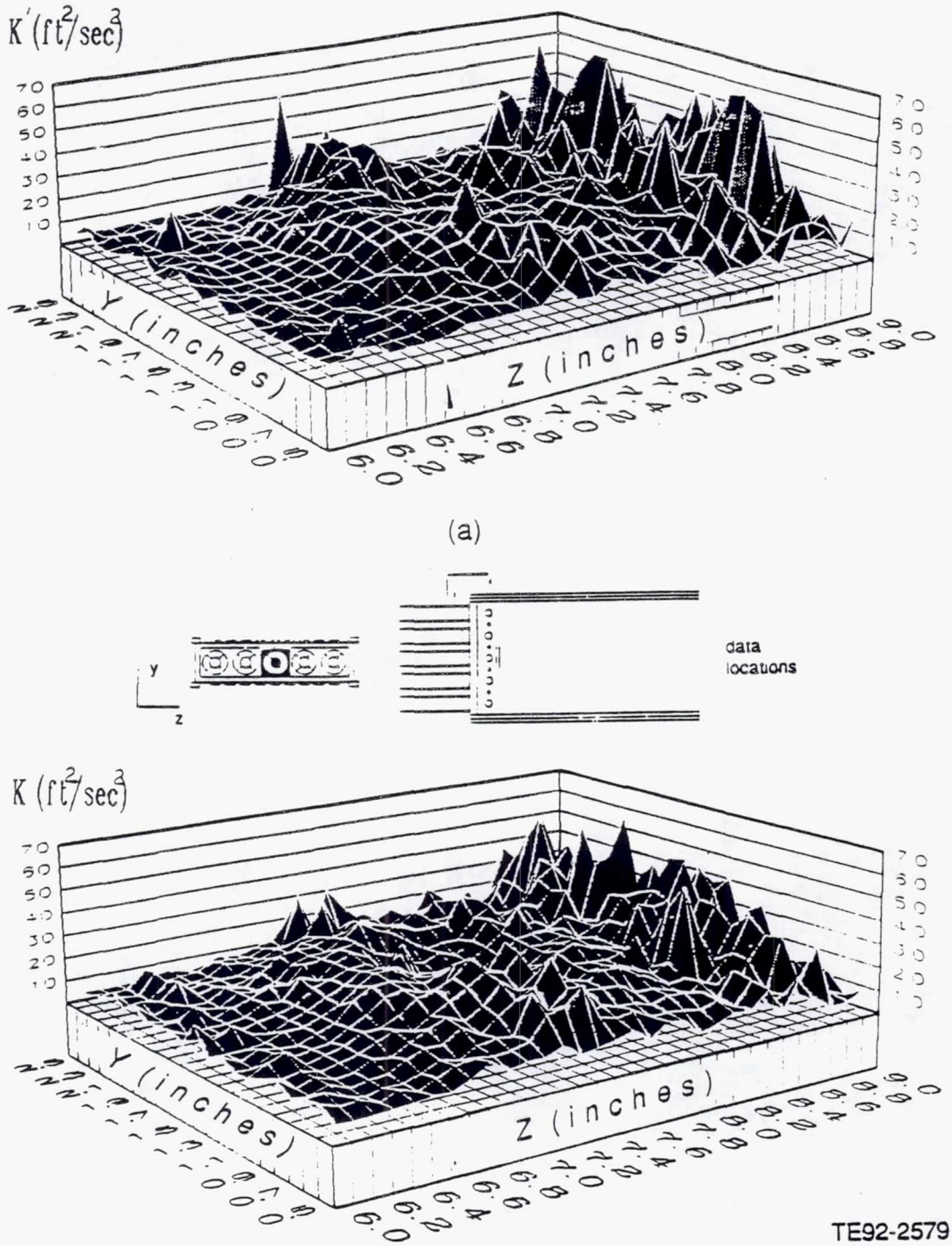

Figure 4.1.2-34. Annular jets only contour plot of K' at a) x=2.5 in. b) x=3.0 in.

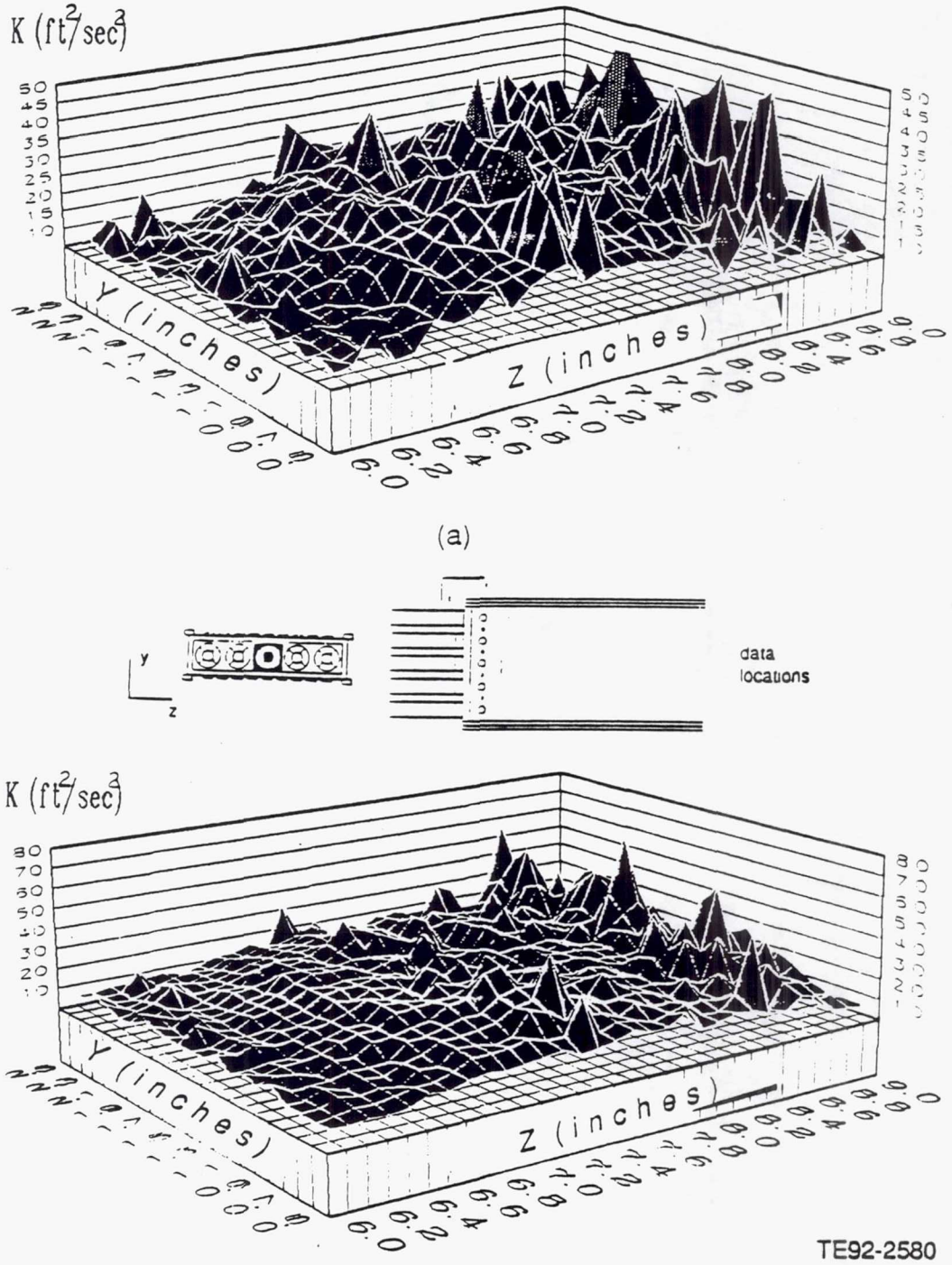

Figure 4.1.2-35. Annular jets only contour plot of K' at a) x=3.5 in. b) x=4.0 in.

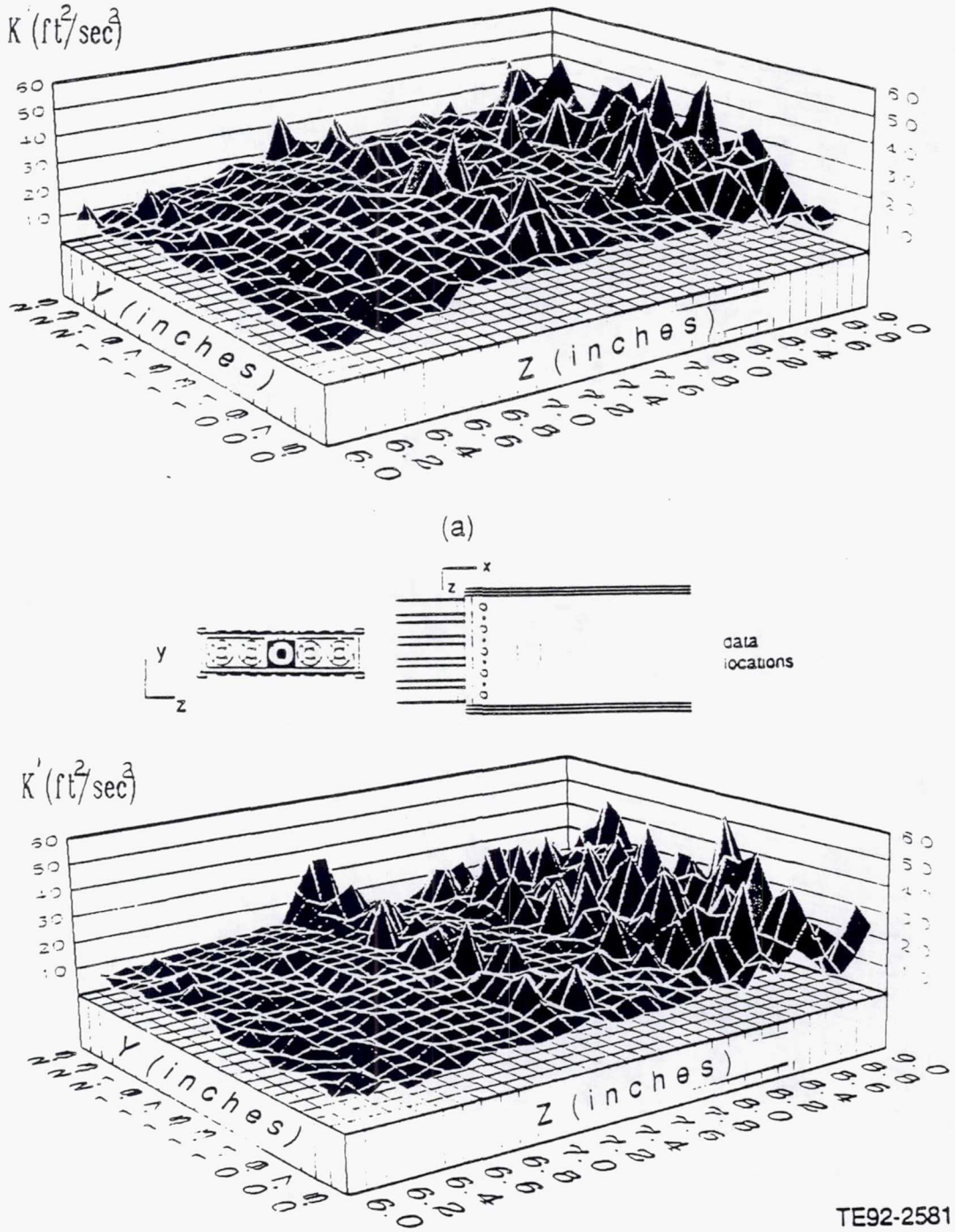

Figure 4.1.2-36. Annular jets only contour plot of K' at a) x=6.0 in. b) x=9.0 in.

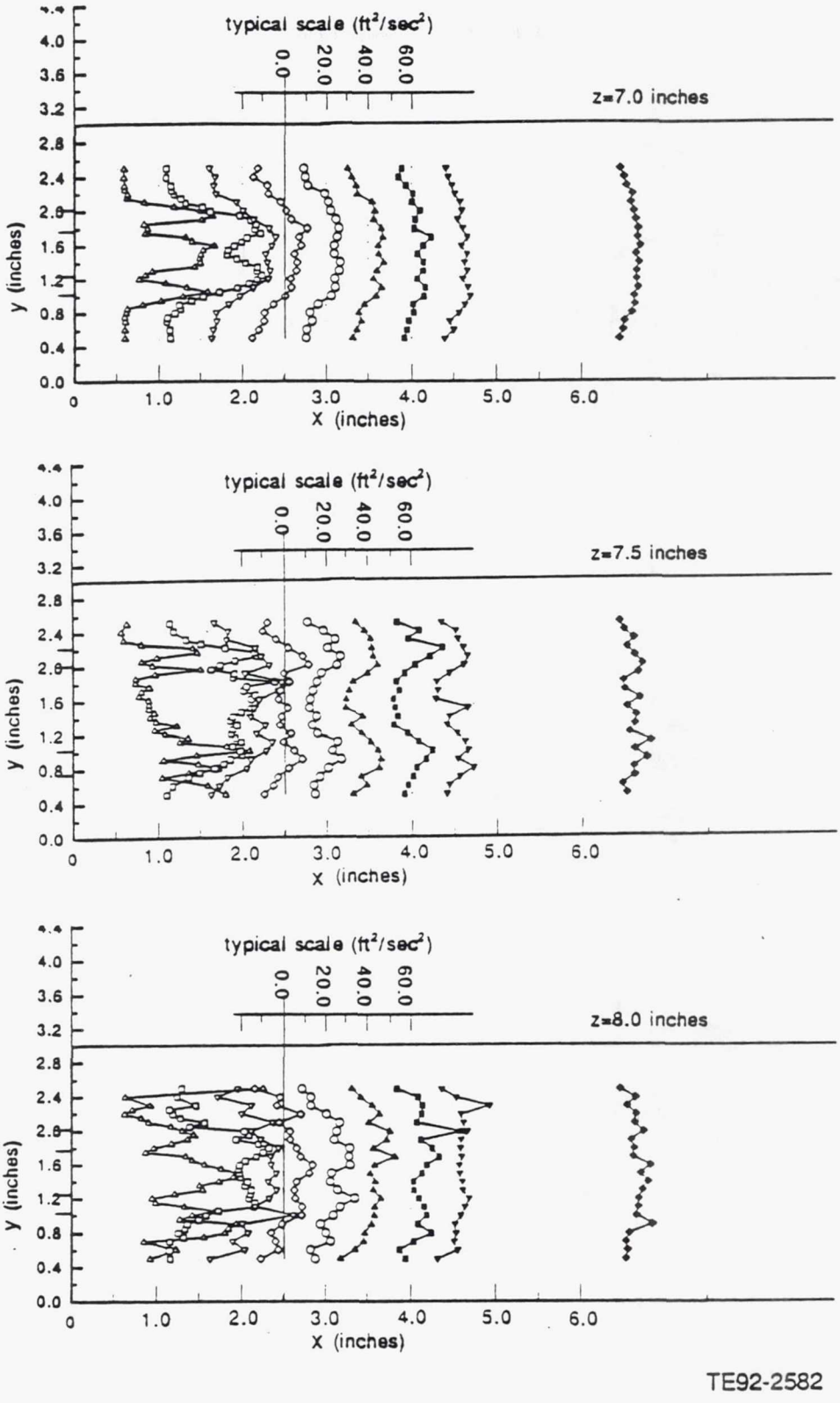

Figure 4.1.2-37. Annular jets only K' distribution.

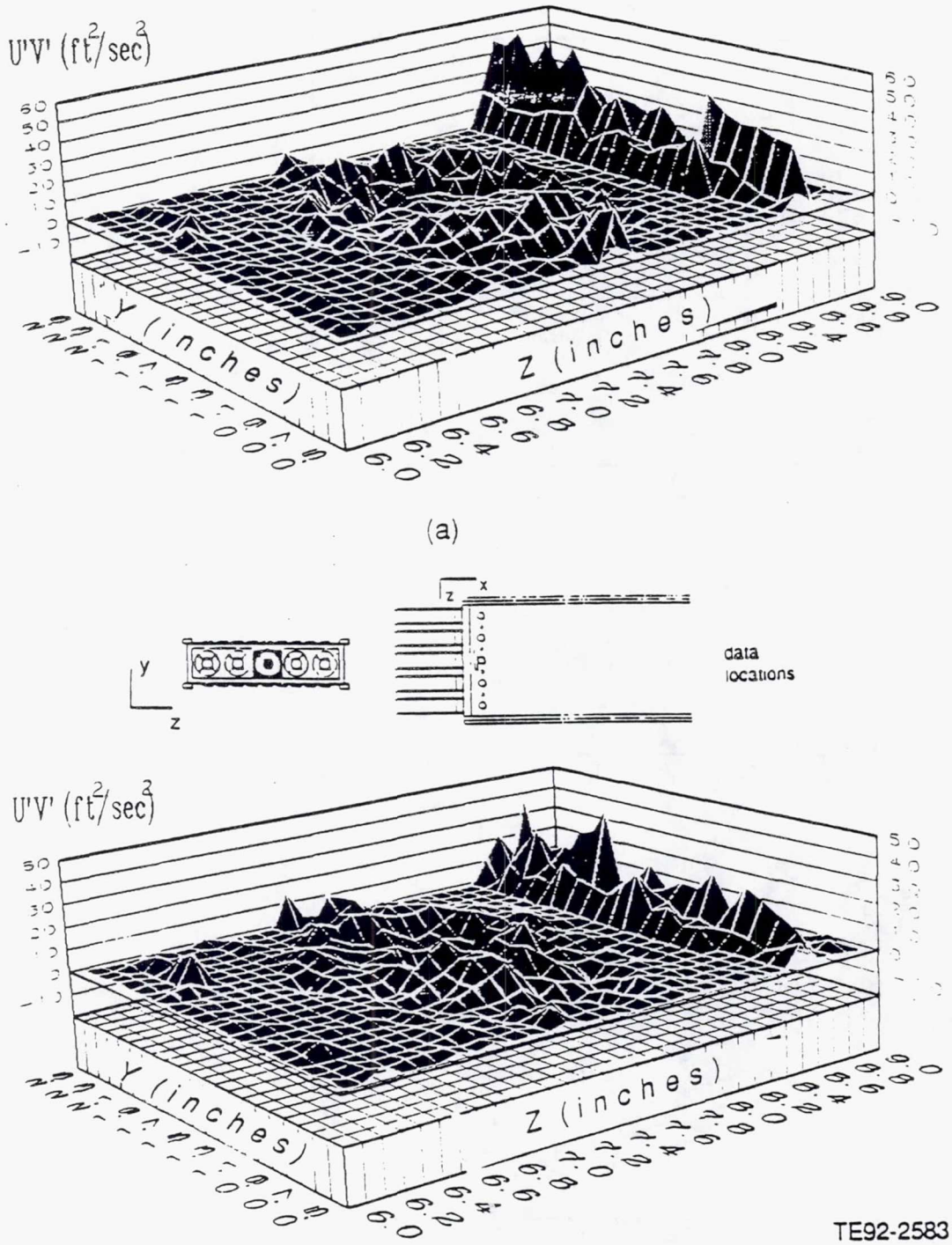

Figure 4.1.2-38. Annular jets only contour plot of U'V' at a) x=0.5 in. b) x=1.0 in.

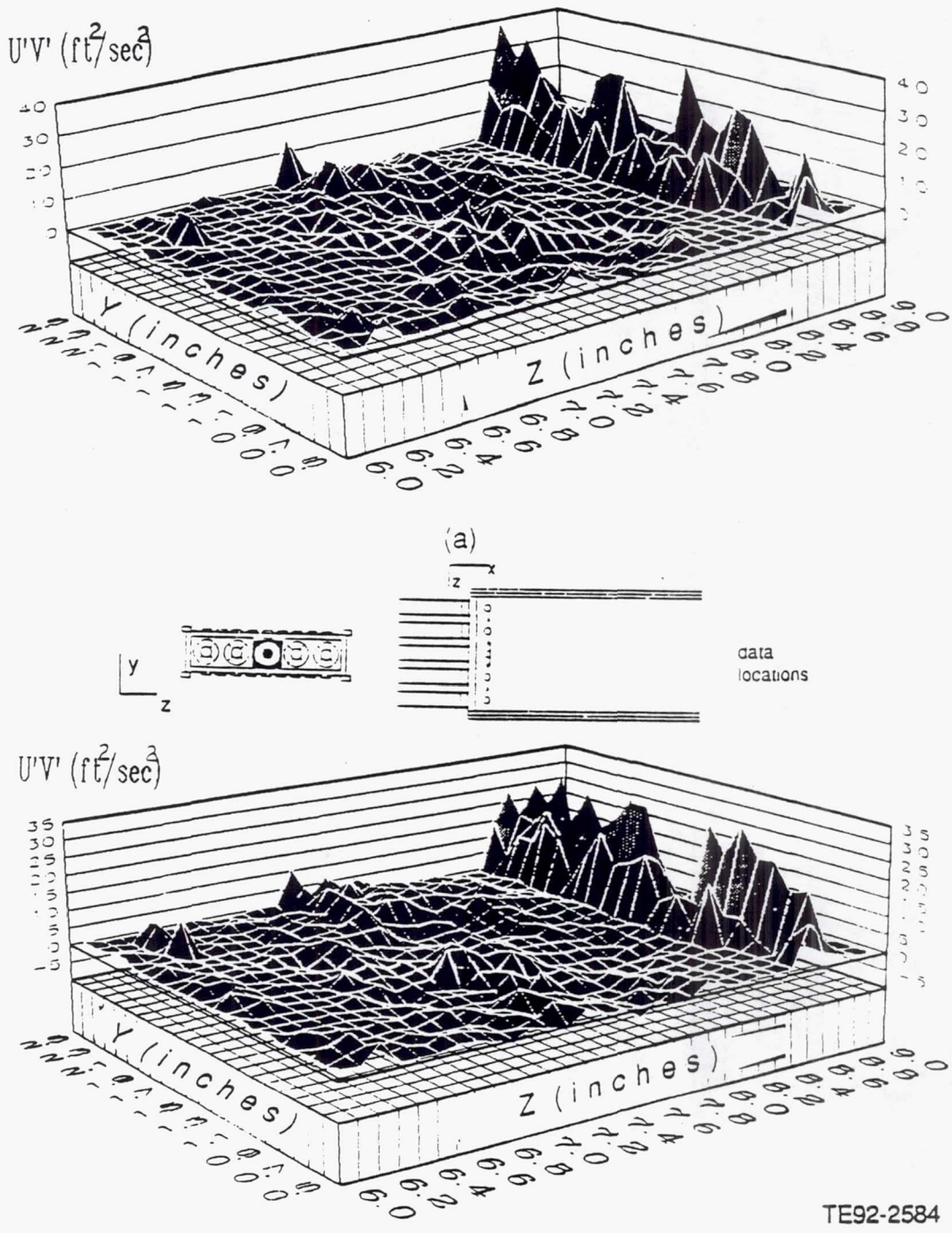

Figure 4.1.2-39. Annular jets only contour plot of U'V' at a) x=1.5 in. b) x=2.0 in.

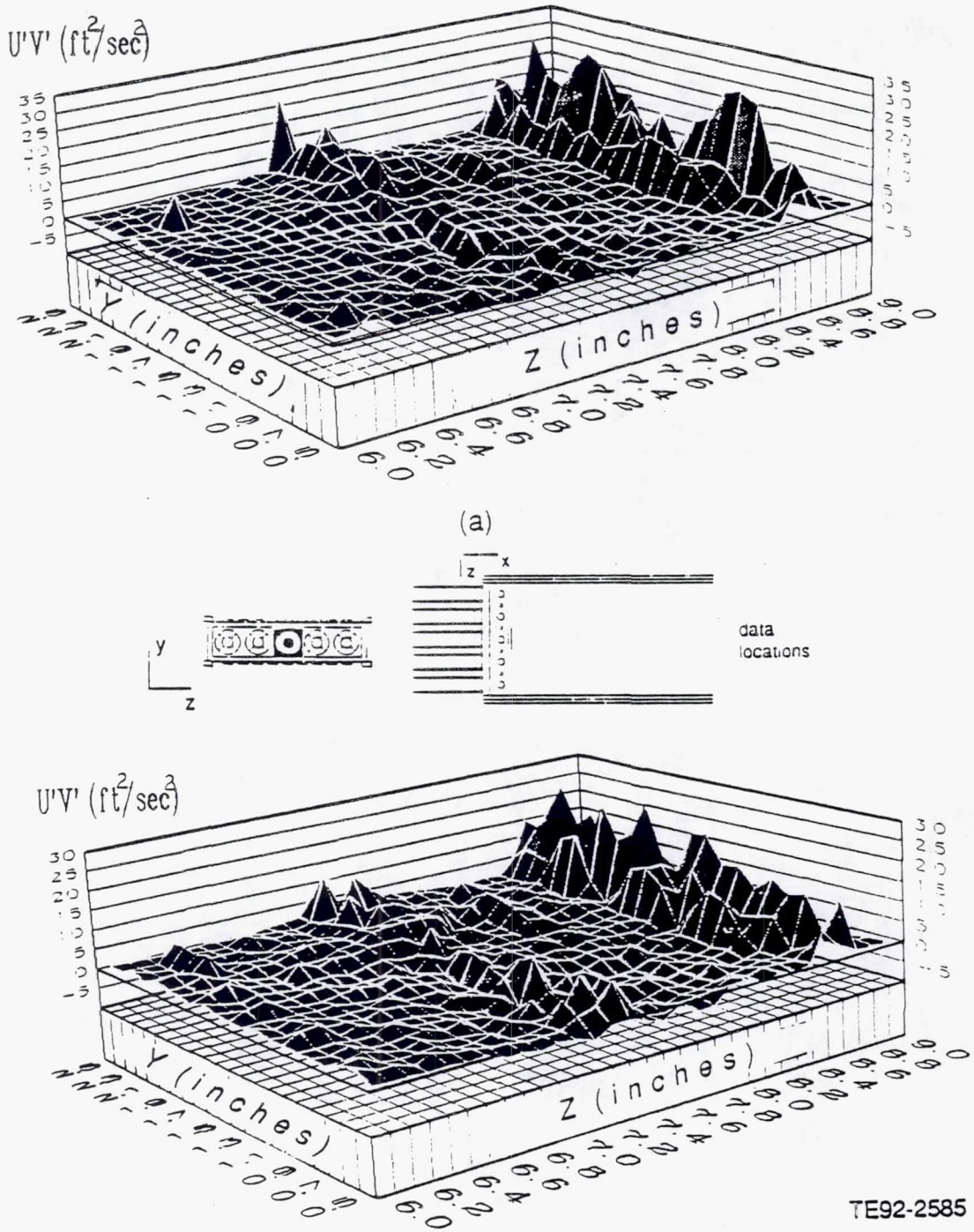

Figure 4.1.2-40. Annular jets only contour plot of U'V' at a) x=2.5 in. b) x=3.0 in.

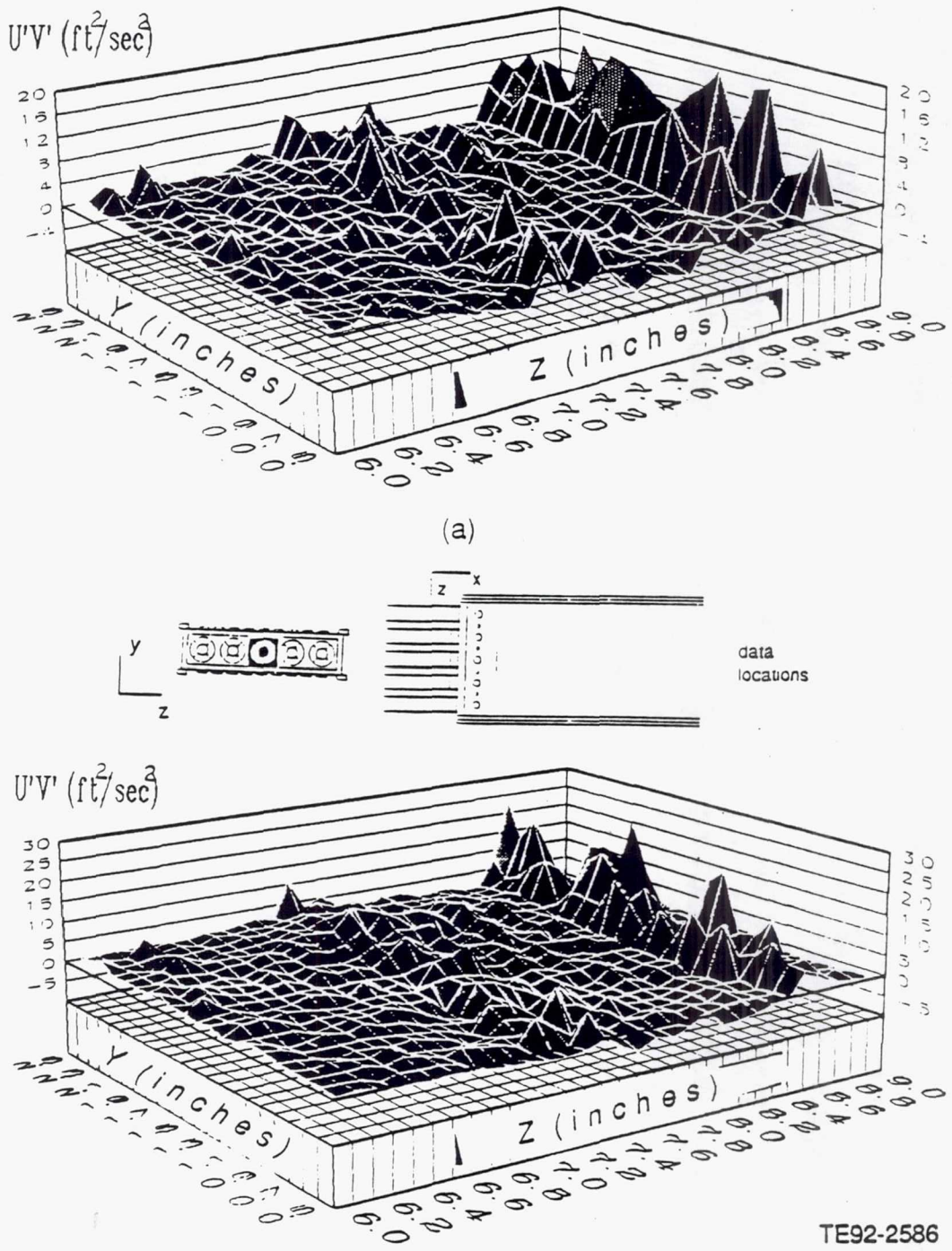

Figure 4.1.2-41. Annular jets only contour plot of U'V' at a) x=3.5 in. b) x=4.0 in.

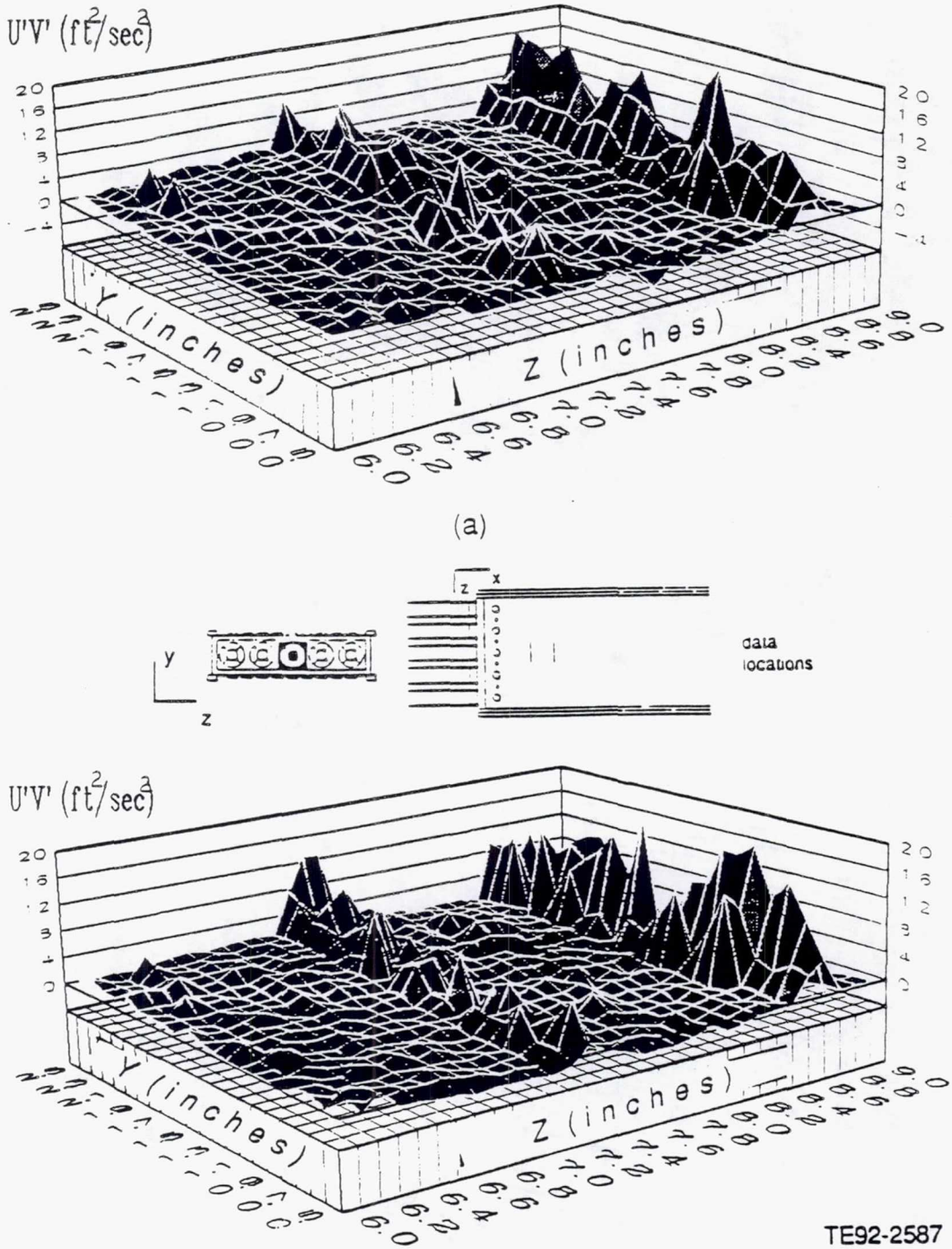

Figure 4.1.2-42. Annular jets only contour plot of U'V' at a) x=6.0 in. b) x=9.0 in.

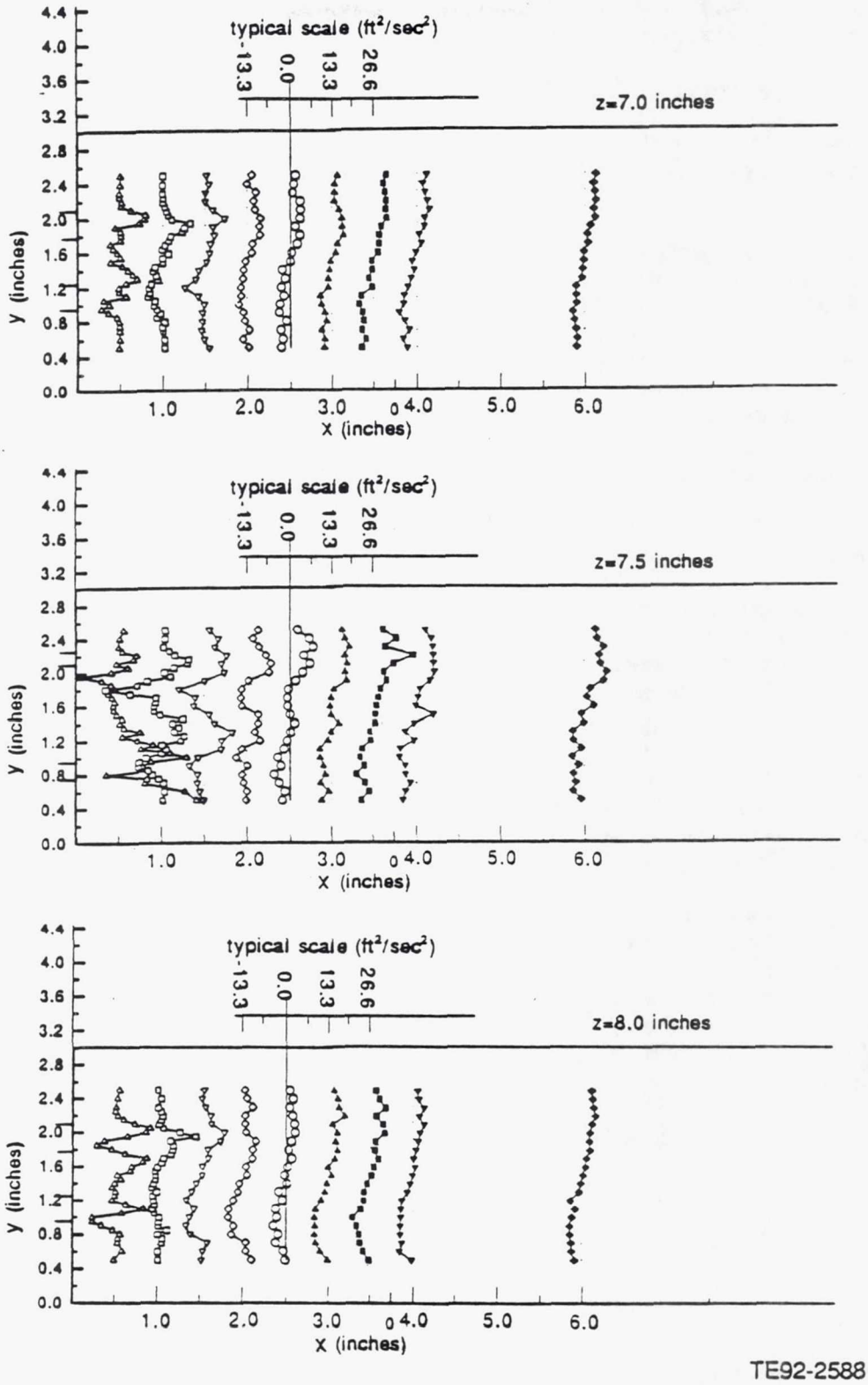

Figure 4.1.2-43. Annular jets only U'V' distribution.

4.2 PRIMARY JETS

Figure 4.2-1 shows a drawing of the primary jets only configuration. The next two subsections will present the concentration and velocity measurements, respectively.

4.2.1 Primary Jets - Concentration Measurements

Marker particles were introduced into the combustor model through the lower primary jet for this case. Data collected for this case will provide qualitative information about the mixing of the two primary jets.

Results for the primary jets only case are presented in Figures 4.2.1-1 through 4.2.1-12. Mean concentration values were obtained by averaging 127 frames of images of the xy plane. Figures 4.2.1-1 and 4.2.1-2 are single and 127 frame averages of images taken at z=7.5 in. The spread at the impingement region is less visible in the average picture due to oscillations of this region above and below the centerline. By averaging, the observable oscillations are reduced. Pictures in Figures 4.2.1-3 through 4.2.1-6 are 0.5 in. from the rig centerplane. The spreading of the jet impingement point can clearly be seen in all of the pictures, due to spreading of smoke in the xz plane. The turbulent nature of the flow is evident by the difference between single and averaged frame pictures. Symmetry should exist between averaged frames since each is the same distance from the rig centerplane.

Figures 4.2.1-7 through 4.2.1-12 present 3-D and line plots of the concentration inside the air rig. The line plots are taken at stations of constant x from the lower to upper wall of the rig. At z=7.5 in., the smoke entering the lower primary jet enters the rig up to the stagnation point with the opposing jet. Smoke is moved upstream and downstream by the jet stagnation point spreading radially in the xz plane. The line plots indicate that concentrations between upper and lower walls increase farther downstream and show a peak concentration near the rig centerline. Moving 0.5 in. away from the z=7.5 in. plane, z=7.0 and 8.0 in., line plots show an increased minimum concentration level at stations upstream and downstream of the primary jets. Peak concentrations still exist near the rig centerline at y=1.5 in. A peak can also be seen in the 3-D plots near x and y =1.5 in. due to the spreading of the smoke from the stagnation regions of the primary jets in the xz plane. Even farther away from the centerplane, z=6.5 and 8.5 in., the concentration levels spread out even more with peak values slightly above the rig centerline. As the smoke becomes completely mixed with air entering the upper primary jet, concentration levels are nearly equal from bottom to top walls of the rig downstream of x=1.0 in.

Figure 4.2.1-12 shows a line plot comparing measured concentrations along the primary jet axis of the different z planes. Planes equal distance from the center plane, z=7.5 in., should be symmetric due to rig symmetry. Planes at z=6.5 and 7.0 in. have peak concentrations placed closer to the upper wall of the rig than planes at z=8.0 and 8.5 in. A flapping motion of the stagnation region was observed in the xy plane. This flapping motion should also be present in the yz plane if symmetry is valid, and if more pronounced may cause a tilt of the stagnation region. Any slight misalignment in the jet could cause these asymmetries to arise.

4.2.2 Primary Jets - Velocity Measurements

A set of five pairs of opposing primary jets centered 1.5 in. (x/H = 0.5) downstream of the rig endplate was used. The annular jet endplate was replaced with a solid one-inch thick aluminum plate for this case. Figure 4.2.2-1 shows a drawing of the rig when annular jets are used in conjunction with the primary jets.

4.2.2.1 Inlet Conditions

To establish inlet conditions, velocity measurements of the primary jets were conducted. An extensive measurement of the lower primary jet was performed to observe the development of the jet as it enters the combustor model. A series of xy plane scans using the grid in Figure 4.2.2-2 were performed. These

scans were taken at 0.05 in. intervals in the z direction resulting in the xz plane grid shown in Figure 4.2.2-3. Since the average probe volume length was 0.05 in., the probe volume should not overlap between data points. Additionally, a measurement was taken of the upper and lower jets to determine the relative strengths of the two primary jets.

The mean and rms plots of the lower jet are presented in Figures 4.2.2-4 through 4.2.2-10. Figure 4.2.2-4 shows the axial velocity, distribution of the lower jet at y=0.1 in. From this plot it is evident that the entrance velocity has a flat top profile with mean velocity of 27.9 ft/sec. This yields a Reynolds number of 6,392 based on the jet diameter. The axial fluctuating velocity, V_{rms}, in Figure 4.2.2-4 indicates peak values along the edges of the jet at z=7.7 and z=7.3 in. and lower values at the edges of the jet at x=1.3 and x=1.7 in. This is caused by the length of the probe volume being approximately the same size as the grid spacings.

Measurements taken at y=0.25, 0.5, 0.75, 1.0, and 1.25 in. (Figures 4.2.2-5 through 4.2.2-9) show the maximum velocity at the center of the jet starts to gradually decrease and spread as more fluid is entrained into the jet and it nears the opposed jet. Also, the jet is seen to have a slight bend downstream due to the crossflow in the rig. The V_{rms} plots indicate that larger fluctuations occur at the jet edges as the jet emerges into the more turbulent flow. The upstream edge of the jet, x=1.3 in., shows larger fluctuations than any other part of the jet due to recirculating flow upstream of the jet entrance.

The plane at y=1.5 in. is at the center of the combustor model, Figure 4.2.2-11. Velocity fluctuations of -10 to 6 ft/sec are a result of the fluctuating stagnation point of the two opposing jets. Higher rms values due to increased turbulent mixing are also evident. Flow visualization revealed that the stagnation point of the two jets oscillated about the midpoint.

The velocity distribution 0.6 in. from the primary jet inlets is plotted in Figure 4.2.2-11, showing a comparison between the upper and lower primary jets. Approximately a 3% difference between the upper and lower jet maximum velocity is present. The rms values indicate that the upstream side of the jet has a slightly higher turbulence level due to recirculating flow.

4.2.2.2 Mean Flowfield Results

Perhaps the most helpful form of data presentation of the mean flow is xy plane vector plots. Vector plots at the various z locations provide a quick and informative view of the flow. With the addition of streamlines to the vector plots, recirculation zones and symmetry about the rig centerline is evident. Figure 4.2.2-12 provides details of the xy plane sampling grid. Figures 4.2.2-13 through 4.2.2-17 show vector plots for $7.1 \leq z \leq 7.9$ in. Symmetry should exist between upper and lower halves of the rig and between planes equal distance from the centerplane (z=7.5 in.).

Figure 4.2.2-13 shows the vector plot for the rig centerplane (z=7.5 in.). Clearly evident is the upper rear recirculation zone centered about x=3.5 in. and y=2.2 in. A lower recirculation zone also exists at approximately x=3.5 in. and y=0.75 in. Asymmetry between upper and lower halves is clear as the flow at the centerline tends toward the lower wall, resulting in a reattachment point of the lower recirculation zone farther upstream than the upper zone. This reattachment point will cause the upper recirculation zone to be larger than the lower recirculation zone. A larger recirculation zone will allow the flow to diffuse faster and cause the stagnation point of the recirculation zone to occur farther upstream.

Plots at the planes of z=7.4 and z=7.6 in. (Figure 4.2.2-14) should be the same due to symmetry of the rig. These two plots show the centers of the upper and lower rear recirculation zones occur at x=3.5, y=2.1 in. and x=3.75, y=0.7 in., respectively, for z=7.6 in. The same points for z=7.4 in. are at x=3.45, y=2.2 in. and x=3.75, y=0.7 in., respectively. Here symmetry between planes was seen to exist, while symmetry between upper and lower halves of the rig does not exist.

Comparison of the two planes at z=7.7 in. and z=7.3 in. (Figure 4.2.2-15) shows that the recirculation zones in the z=7.3 in. plane are centered slightly forward of the zones in the z=7.7 in. plane. In addition, the recirculation zones in the z=7.3 in. plane entrains fluid immediately downstream of the jet stagnation point, while in the z=7.7 in. plane the fluid immediately downstream of the jet stagnation point is allowed to move with the axial flow.

Different features of the flowfield are seen at the z=7.2 and z=7.8 in. planes. In Figure 4.2.2-16, flow forward of the jet inlet point, x=1.5 in., is not all entrained into the forward recirculation zones. Since the primary jets have a diameter of 0.43 in., the planes here are outside the boundaries of the jet. Thus, fluid is able to flow downstream and be entrained into the rear recirculation zones. Comparison between the two planes shows definite asymmetries. The rear recirculation zones in the z=7.2 in. plane are offset due to the reattachment point of the lower recirculation zone being farther upstream than the upper zone. While both planes see a bending of the flow toward the lower wall, only the plane at z=7.2 in. shows the dramatic offset of recirculation zones.

Figure 4.2.2-17 shows plots at z=7.1 and z=7.9 in., respectively. The plane at z=7.1 in. seems fairly symmetric with rear recirculation zones at approximately x=3.5 in. The flow between upper and lower halves of the rig is symmetrical as the fluid continues downstream. The plane at z=7.9 in. shows offset rear recirculation zones with the upper and lower zones centered around x=3.4 and 3.2 in., respectively. In addition, forward recirculation zones begin to become visible within the measured portion of the flow.

Additional vector plots of the flow between the planes z=6.0 and 7.0 in. and z=8.0 and 9.0 in. are presented in Figures 4.2.2-18 through 4.2.2-28. Table 4.2-I presents approximate forward and rear recirculation zone locations for the planes 6.5 in. $\leq z \leq$ 8.6 in. Some general trends of the recirculation zones can be seen from this table. Forward recirculation zones move downstream and toward the upper and lower walls farther away from the rig centerplane. Also, the forward recirculation zones tend to be fairly symmetric between upper and lower portions of the rig. These recirculation zones are clearly visible between the planes z=6.5 and 7.0 in. and z=8.0 and 8.5 in.

The center of the rear recirculation zones tends to move upstream and toward the upper and lower walls the farther away it is from the rig centerplane, z=7.5 in. Asymmetry between upper and lower recirculation zones is present in many of the plots. In addition, there seems to be a lot of variation in the occurrence of the recirculation zone centers between planes on different sides of the rig centerplane. Another very noticeable aspect in all the plots is the trend for the streamlines to bend quicker toward the lower wall of the rig. Reverse flow upstream of the jet entrance is evident even to the cell boundaries at z=6.0 and 9.0 in., indicating how influential the primary jets are throughout the cell.

4.2.2.3 Turbulent Flowfield Results

Figures 4.2.2-24 through 4.2.2-37 present the axial fluctuating, U_{rms}, and the vertical fluctuating, V_{rms}, velocities in the yz plane. At stations x=0.5 and x=1.0 in. peak values of the fluctuating components are seen at the center portion of the rig. The magnitudes of these quantities are seen to increase at station x=1.0 in. due to the measurements being closer to the impinging jets. The maximum value of the U_{rms} term is seen to be more and more concentrated in the center portion to the rig at x=1.0 in. than at x=0.5 in. The V_{rms} term seems to diffuse and spread out at the x=1.0 in. station while the magnitudes of the fluctuations in the center portion of the rig nearly doubles.

At the entrance of the primary jets, x=1.5 in., the influence of the primary jets can clearly be seen. In Figure 4.2.2-31, the U_{rms} velocity is seen to have a large decrease in magnitude between the upper and lower walls of the rig at z=7.5 in., indicating very low turbulence in this region. Two peaks can be seen on both sides of this dip, at z=6.6 in. and z=8.4 in., indicating increased turbulence in these regions due to the fluid flow accelerating around the jets downstream.

Table 4.2-I.
Primary jets only recirculation zone locations.

	Forward zones				Rear zones			
z (in.)	x (in.)	y (in.)	x (in.)	y (in.)	x (in.)	y (in.)	x (in.)	y (in.)
6.5	1.2	2.4	1.3	<0.5	--	--	--	--
6.6	1.0	2.25	1.0	0.75	2.9	>2.5	2.7	<0.5
6.7	0.85	2.15	0.85	0.85	3.15	2.35	3.0	<0.5
6.8	0.8	2.05	0.8	0.95	3.5	2.4	0.2	0.5
6.9	0.65	2.0	0.65	0.95	3.4	2.35	3.3	0.7
7.0	<0.5	2.1	<0.5	0.95	3.45	2.25	3.2	0.7
7.1	<0.5	2.0	<0.5	1.0	3.5	2.3	3.4	0.7
7.2	<0.5	2.0	<0.5	1.0	3.45	2.2	3.6	0.7
7.3	--	--	--	--	3.35	2.2	3.3	0.8
7.4	--	--	--	--	3.45	2.2	3.7	0.7
7.5	--	--	--	--	3.5	2.2	3.8	0.7
7.6	--	--	--	--	3.5	2.1	3.7	0.7
7.7	--	--	--	--	3.4	2.15	3.5	0.7
7.8	<0.5	2.0	<0.5	1.0	3.5	2.2	3.4	0.8
7.9	<0.5	2.0	<0.5	1.0	3.4	2.2	3.2	0.8
8.0	0.65	1.95	0.5	1.0	3.35	2.2	--	--
8.1	0.7	2.0	0.7	1.0	3.25	2.25	3.4	0.7
8.2	0.8	2.05	0.8	0.95	3.35	2.3	3.2	0.7
8.3	0.85	2.05	0.85	0.9	3.0	2.3	3.1	0.7
8.4	1.1	2.15	1.0	0.85	3.0	2.3	3.0	<0.5
8.5	1.3	2.35	1.3	0.7	2.7	>2.5	2.7	<0.5
8.6	1.5	2.5	1.5	0.6	--	--	--	--

The V_{rms} plot at x=1.5 in. shows a decrease in the V_{rms} velocity at the jet centerplane. However, this decrease in magnitude does not span the entire height of the rig. Peak values are seen at the middle of the rig at y=1.5 in., z=7.5 in. This is caused by increased turbulence due to the fluctuation of the jet stagnation point about y=1.5 in.

Downstream of the primary jet entrance, at x=2.0 in., the magnitude of the U_{rms} plot increases due to the acceleration of fluid from the jet stagnation point between the upper and lower recirculation zones. The V_{rms} term shows a decrease and diffusing of magnitudes toward the walls and cell boundaries. Similar results are seen at stations x=2.5, 3.0, 3.5, 4.0, and 6.0 in., see Figures 4.2.2-33 through 4.2.2-37.

Figures 4.2.2-38 and 4.2.2-39 show line plots of the U_{rms} and V_{rms} velocities at measurement locations between x=0.5 and 6.0 in. for planes at z=7.0, 7.5, and 8.0 in. The largest fluctuations in the U_{rms} term occur immediately upstream and downstream of the jet stagnation point. The largest V_{rms} fluctuations occur at the jet stagnation point, x=1.5 in. The U_{rms} and V_{rms} magnitudes decrease and diffuse downstream and farther from the rig centerline until nearly uniform magnitudes at x=6.0 in.

An alternate way to view the previous terms is through the two-dimensional turbulent kinetic energy term. Figures 4.2.2-40 through 4.2.2-44 show the results of the yz plane plots for K'. At station x=0.5 in., a central peak is observed in the middle regions of the rig indicating higher levels of turbulence than other regions of the flow. Similar results are seen at x=1.0 in. where the magnitude of K' increases

due to the acceleration of the fluid from the jet stagnation point between the forward recirculation zones.

The greatest magnitude of turbulence energy occurs at the primary jet impingement, Figure 4.2.2-41. A reduced magnitude of turbulence energy exists at z=7.5 in., where the primary jets enter, and larger peaks are on either side due to jet entraining fluid within the rig. Also visible are the two peaks on either side of the rig midpoint, see Figure 4.2.2-31 for the U_{rms} profile. Again, acceleration of fluid around the primary jets causes this increased turbulence.

Results at x=2.0 in. indicate a spreading of the turbulence energy in the z direction. Increased flow around the primary jets and downstream are responsible for this. Similar plots downstream are presented in Figures 4.2.2-42, 4.2.2-43, and 4.2.2-44.

Figure 4.2.2-45 represents line plots of K' at the z planes of 7.0, 7.5, and 8.0 in. It can be seen that the highest turbulence levels are around the stagnation region of the two jets. Turbulence levels decrease and spread towards the upper and lower walls of the rig as the flow continues downstream. Uniform turbulence is present by the time the flow is at x=6.0 in.

Figures 4.2.2-46 through 4.2.2-50 represent yz plane contour plots of the Reynolds shear stress component in the xy plane. Higher magnitudes of Reynolds stress occur in areas of higher velocity gradients where large momentum transfer occur. At the x=0.5 in. station peak values occur between z=6.7 in. and z=8.3 in. In addition, the sign of the Reynolds stress changes at the midpoint of the rig, y=1.5 in. These peak values occur in the regions where the forward recirculation zones occur. A similar plot is seen at the x=1.0 in. station. Only differences between this plot and at x=0.5 in. is that the magnitudes have increased.

A very different plot is seen at x=1.5 in. in Figure 4.2.2-47. Peak negative values occur at the z=7.5 in. plane where the primary jets enter. This indicates a large amount of momentum transfer taking place due to the fluid being entrained into the entering jet. Maximum positive values occur in the center of the rig on either side of the centerplane. Here, the stagnation point of the two jets results in large amount of shear stress and higher turbulence as the stagnation point fluctuates.

The plot at x=2.0 in. shows negative values of shear stress now occur on the lower half of the rig, while positive values occur on the upper half of the rig. Peak values can be seen to occur between z=6.7 and z=8.3 in., due to the recirculation zones in these regions. Additional plots downstream have similar trends and can be seen in Figures 4.2.2-48, 4.2.2-49, and 4.2.2-50.

Figure 4.2.2-51 shows the Reynolds shear stress distribution in the planes at z=7.0, 7.5, and 8.0 in. Peak values occur at the jet stagnation region. Magnitudes are seen to decrease farther away from the centerplane and a uniform distribution between upper and lower walls develops at x=6.0 in.

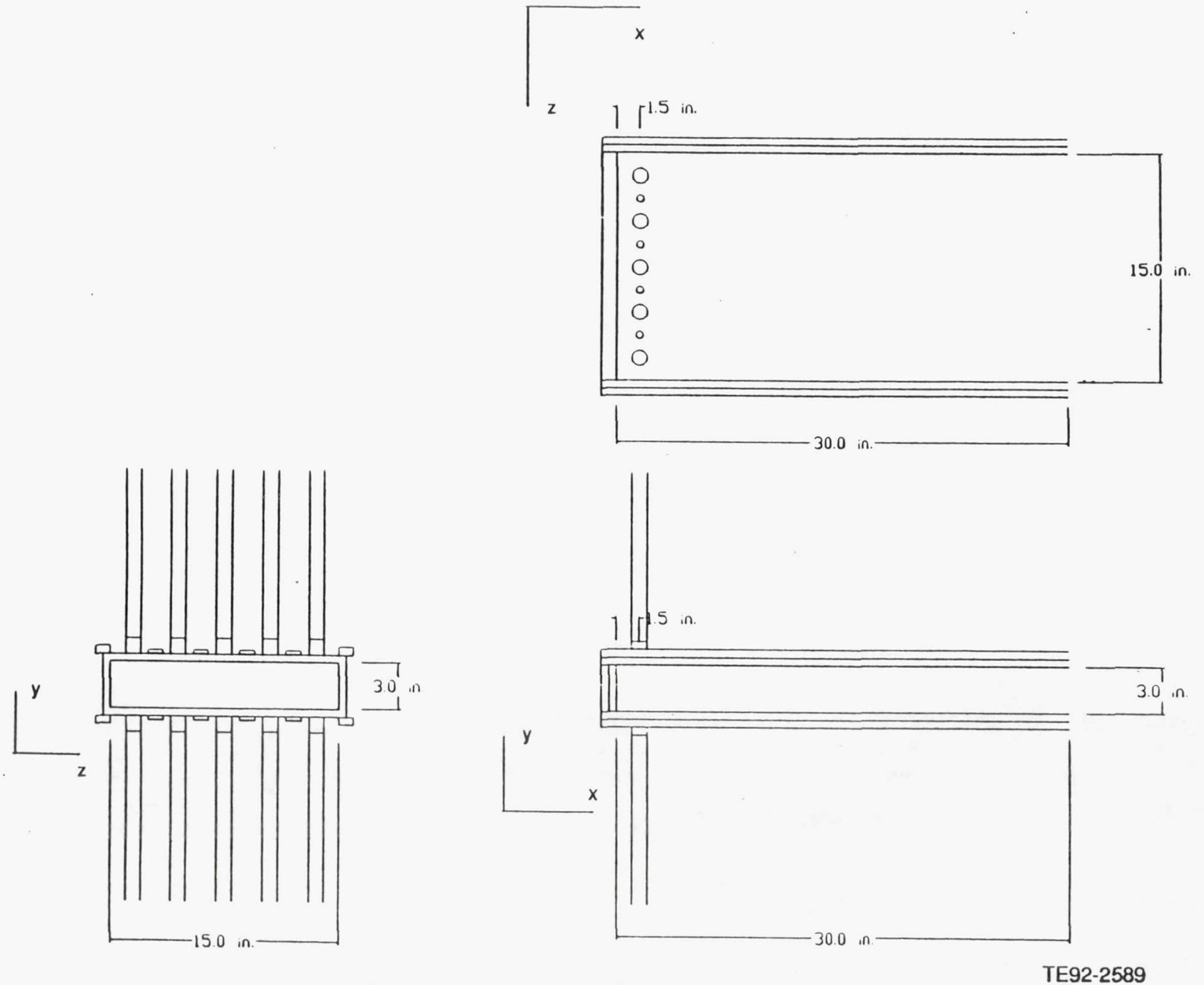

Figure 4.2-1. Primary jets only - three-view drawing.

Page intentionally left blank

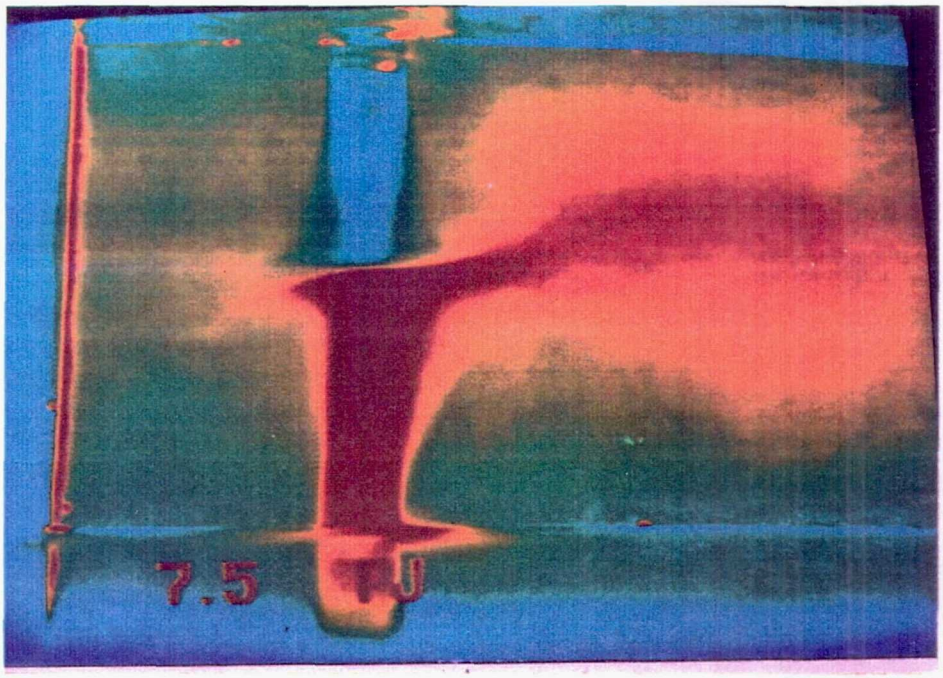

TE92-2590

Figure 4.2.1-1. Primary jets only single frame picture, z=7.5 in.

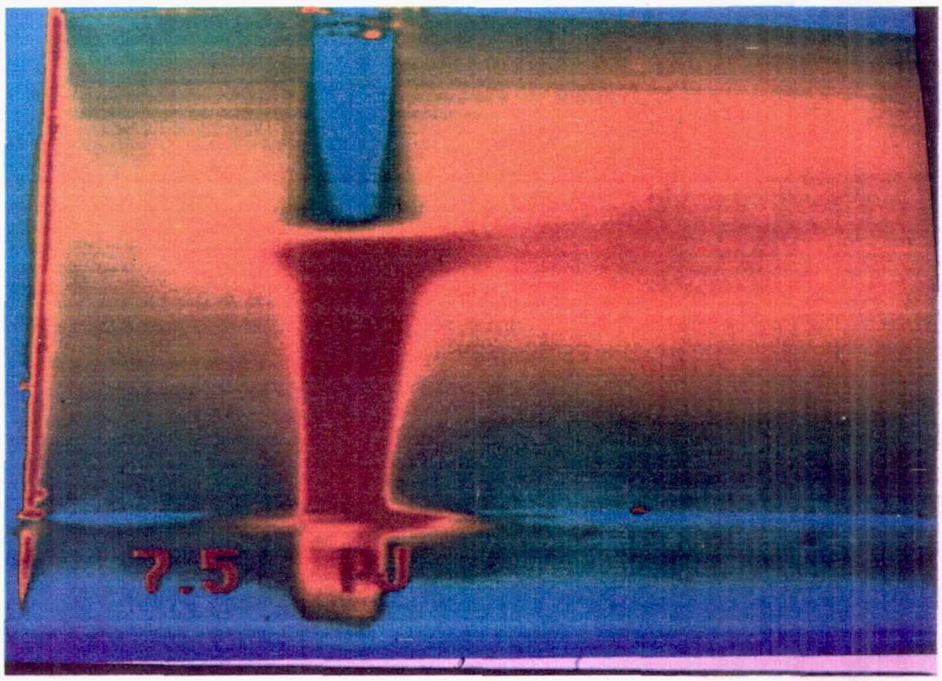

TE92-2591

Figure 4.2.1-2. Primary jets only 127 frame average picture, z=7.5 in.

Page intentionally left blank

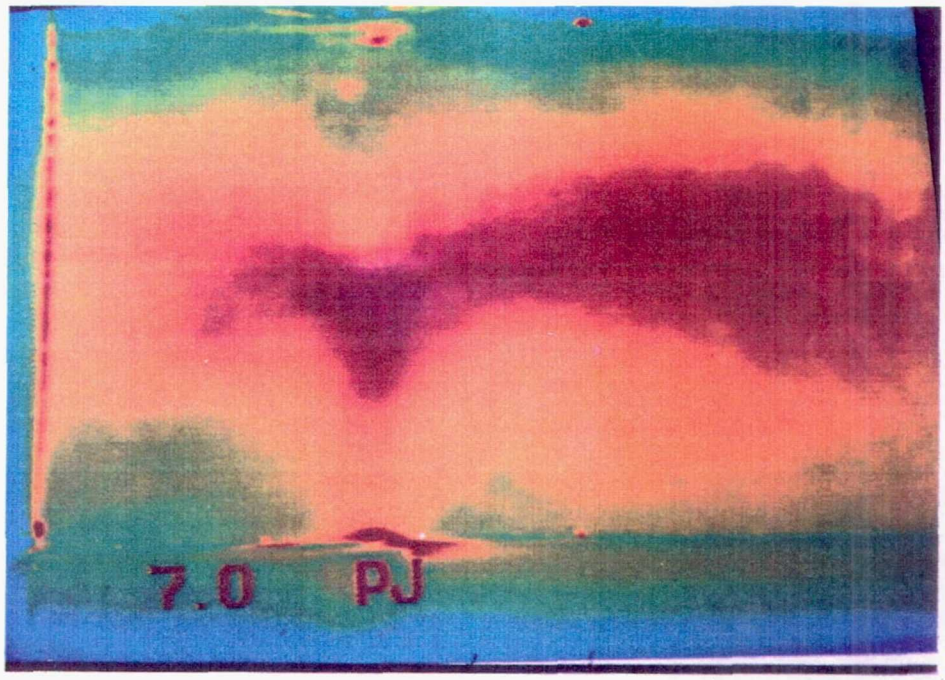

TE92-2592

Figure 4.2.1-3. Primary jets only single frame picture, z=7.0 in.

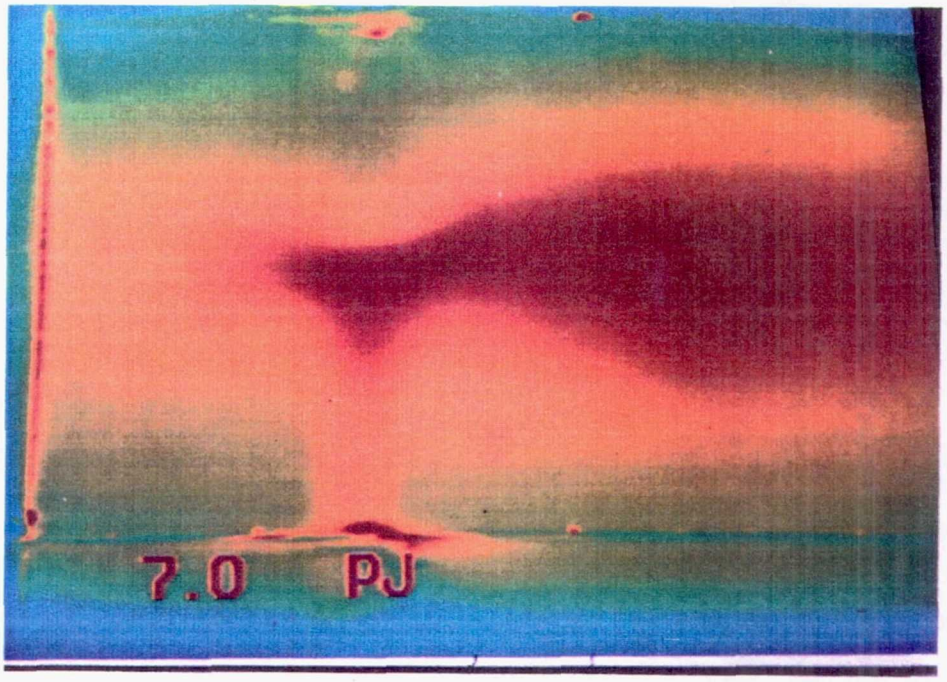

TE92-2593

Figure 4.2.1-4. Primary jets only 127 frame average picture, z=7.0 in.

Page intentionally left blank

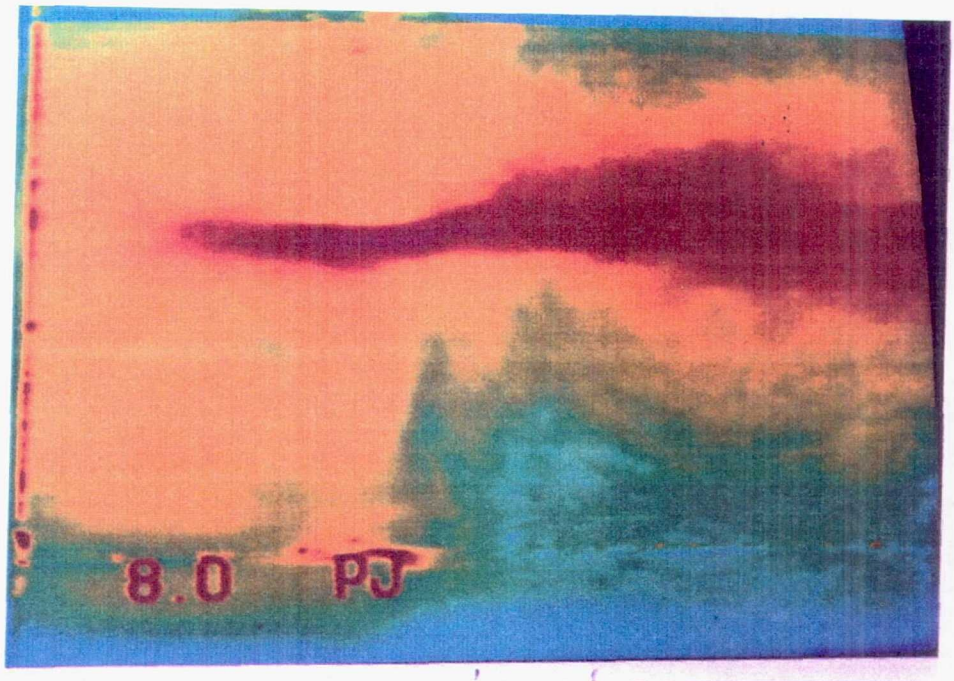

TE92-2594

Figure 4.2.1-5. Primary jets only single frame picture, z=8.0 in.

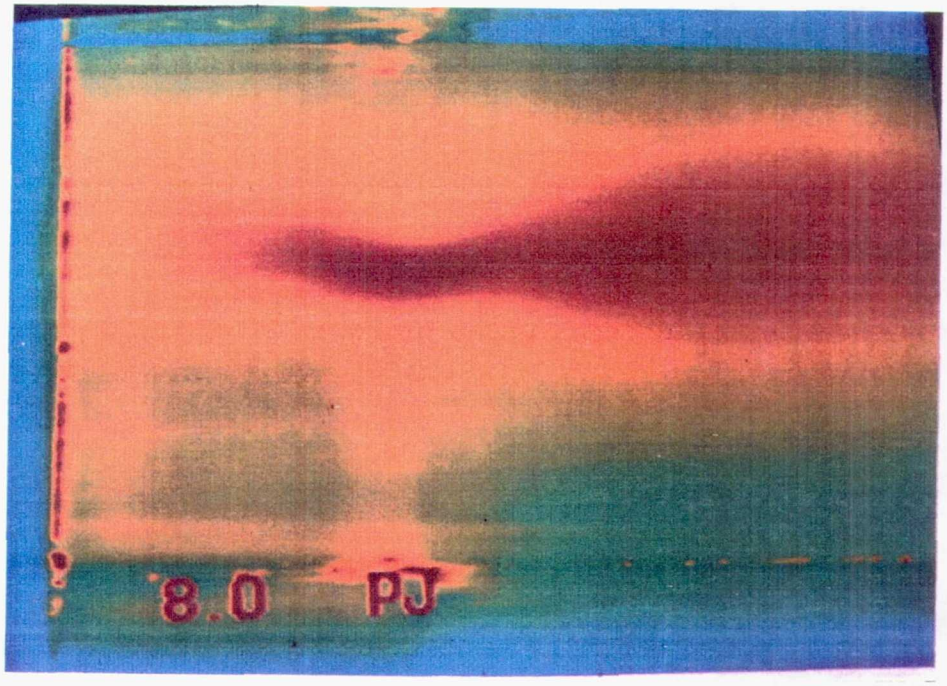

TE92-2595

Figure 4.2.1-6. Primary jets only 127 frame average picture, z=8.0 in.

Page intentionally left blank

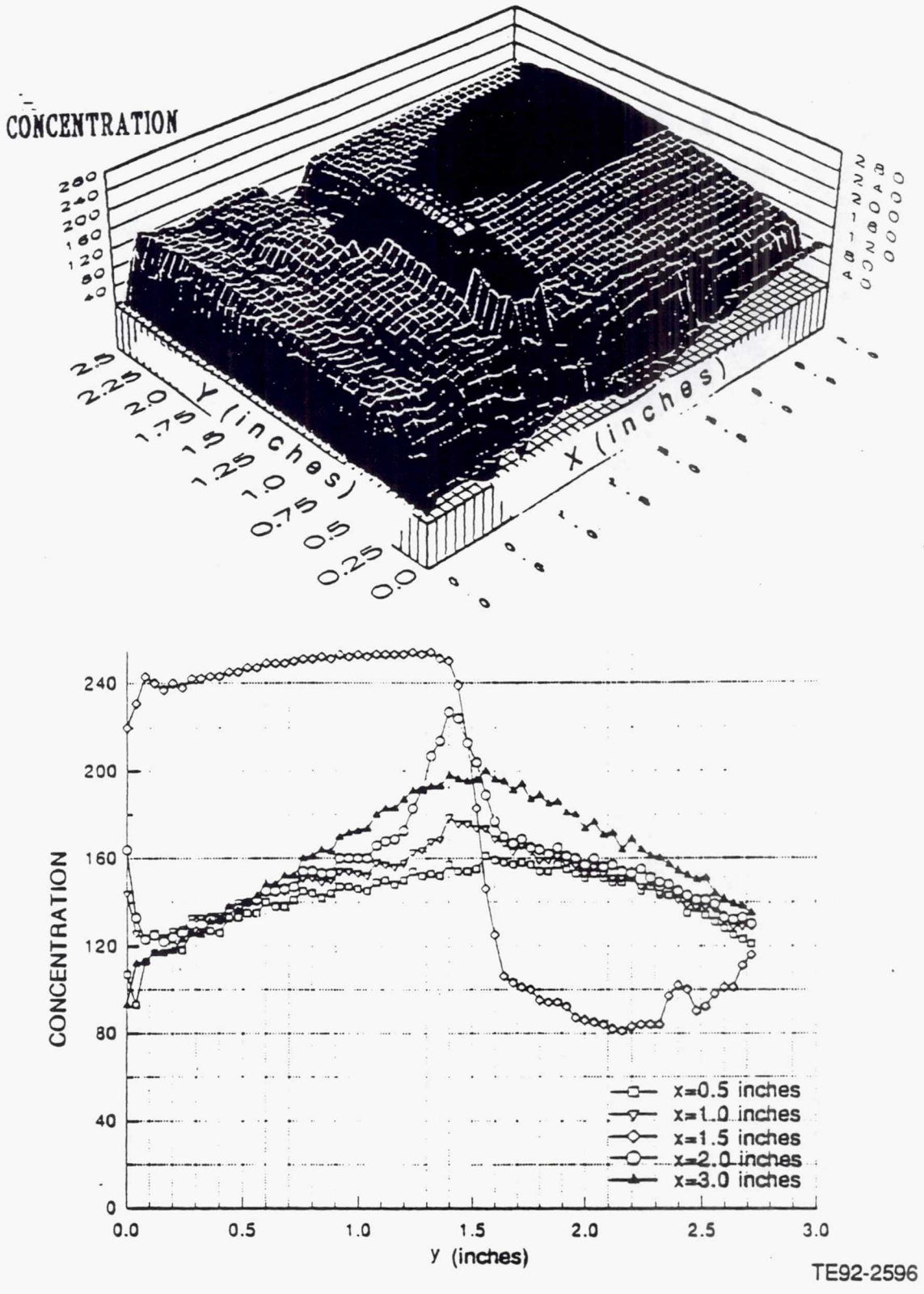

Figure 4.2.1-7. Primary jets only mean concentration distribution, z=7.5 in.

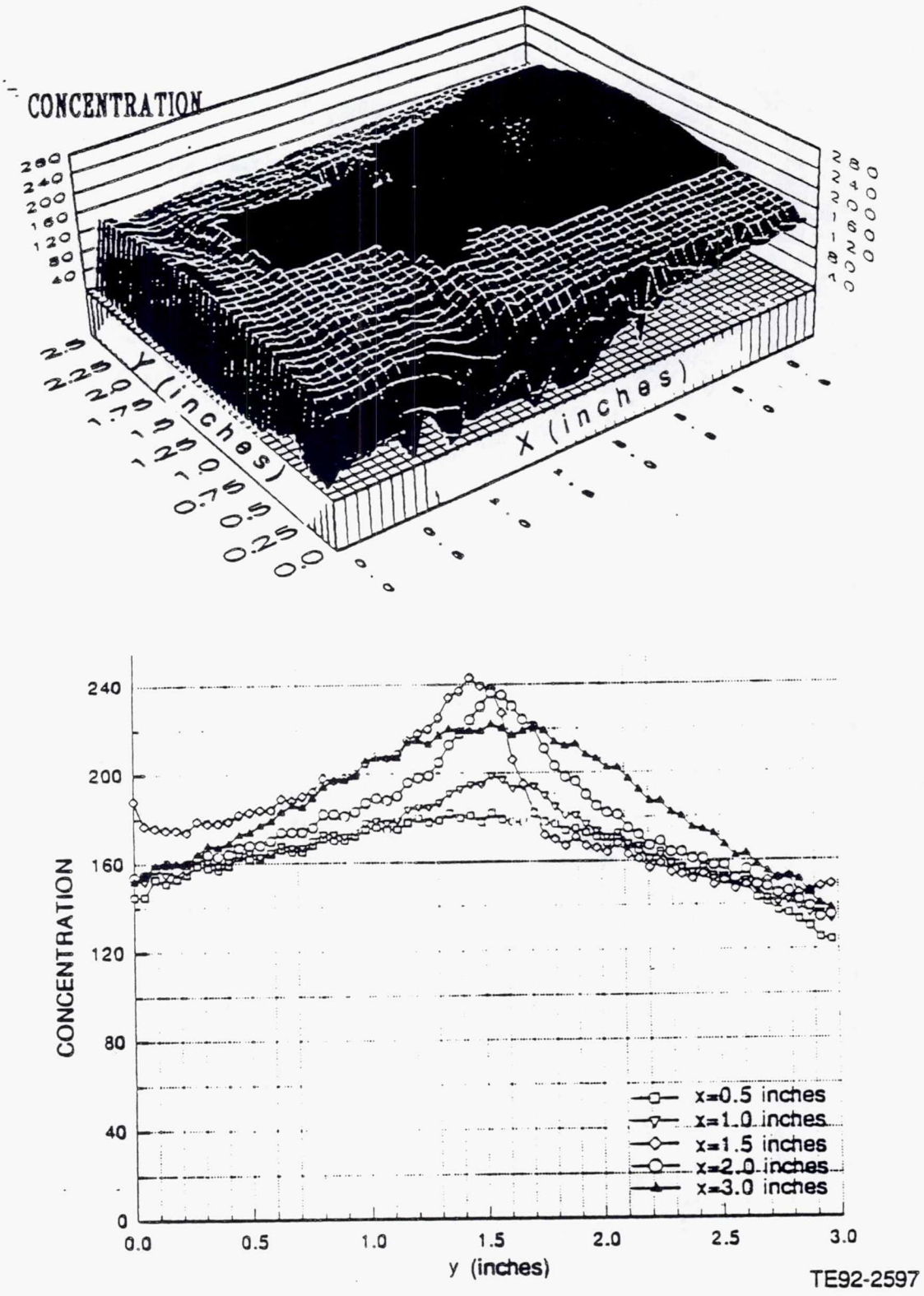

Figure 4.2.1-8. Primary jets only mean concentration distribution, z =7.0 in.

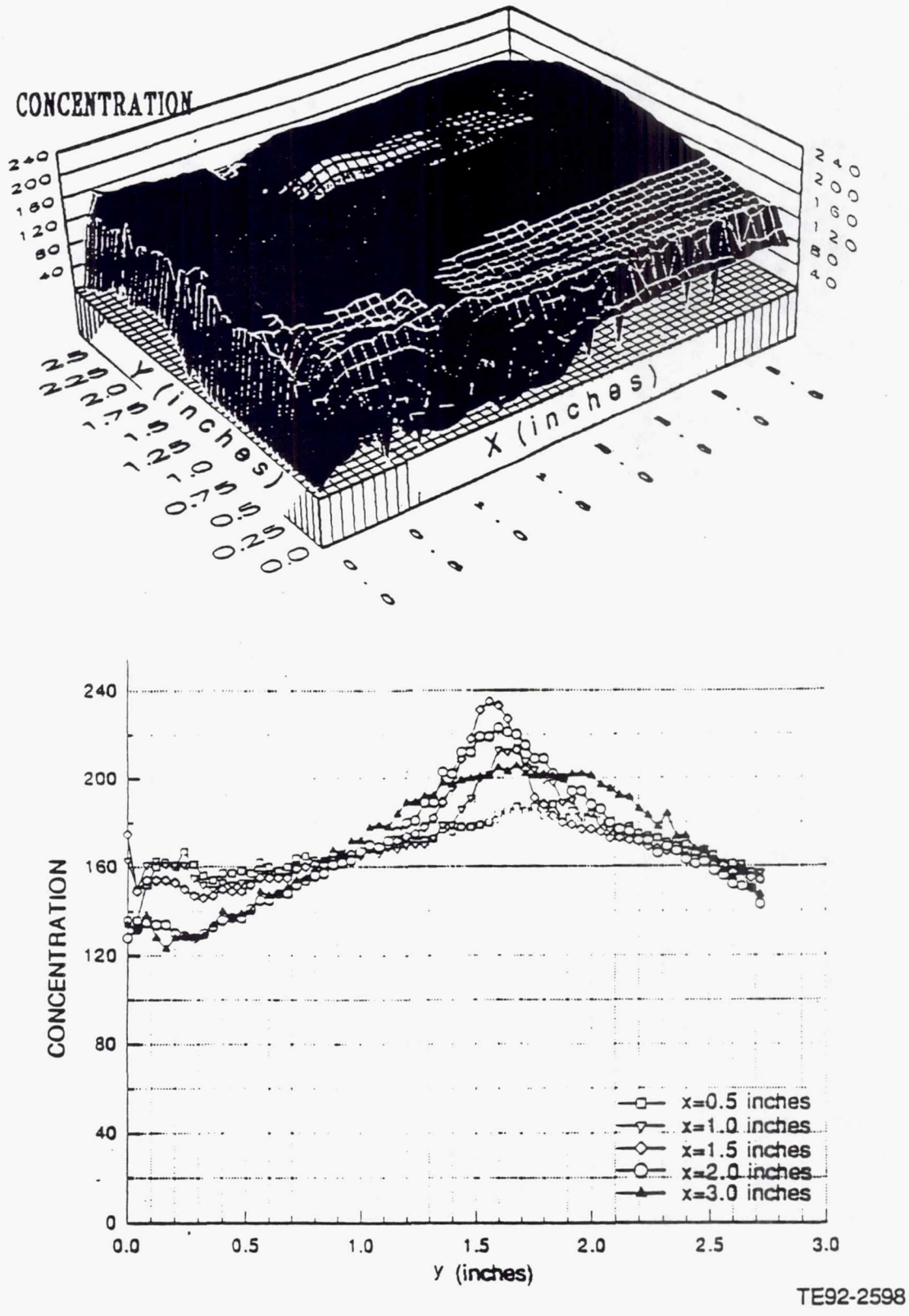

Figure 4.2.1-9. Primary jets only mean concentration distribution, z=8.0 in.

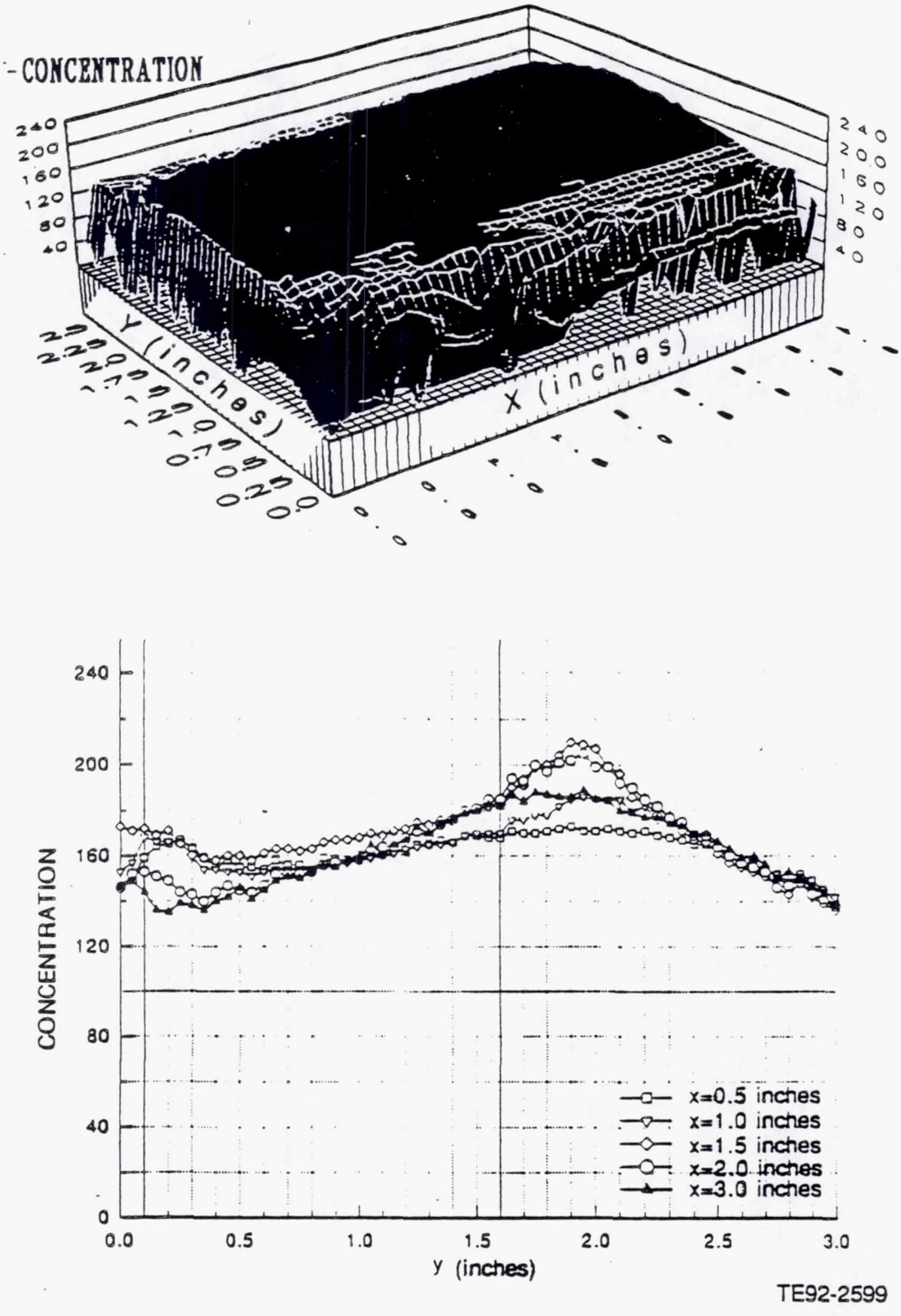

Figure 4.2.1-10. Primary jets only mean concentration distribution, z =6.5 in.

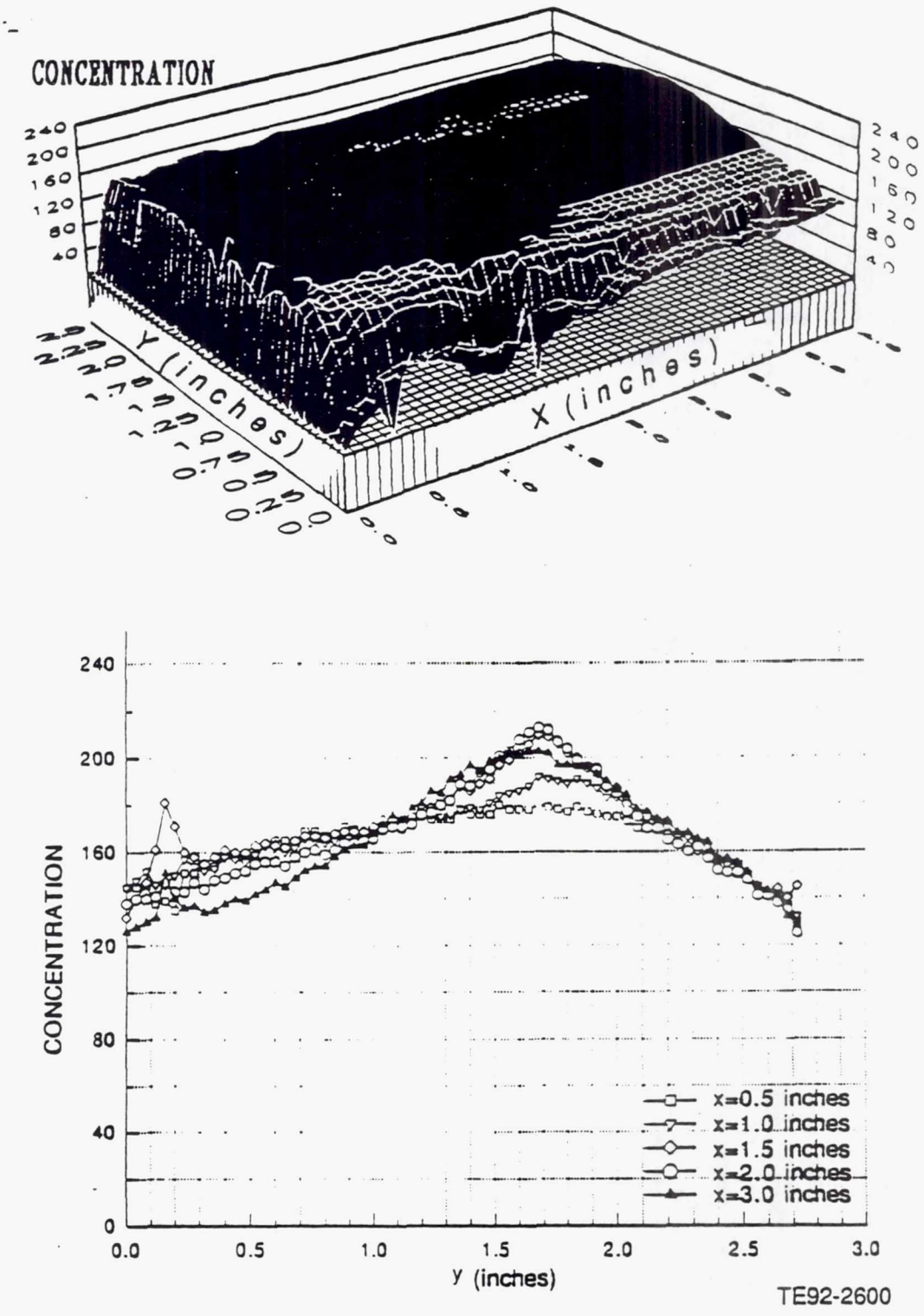

Figure 4.2.1-11. Primary jets only mean concentration distribution, z=8.5 in.

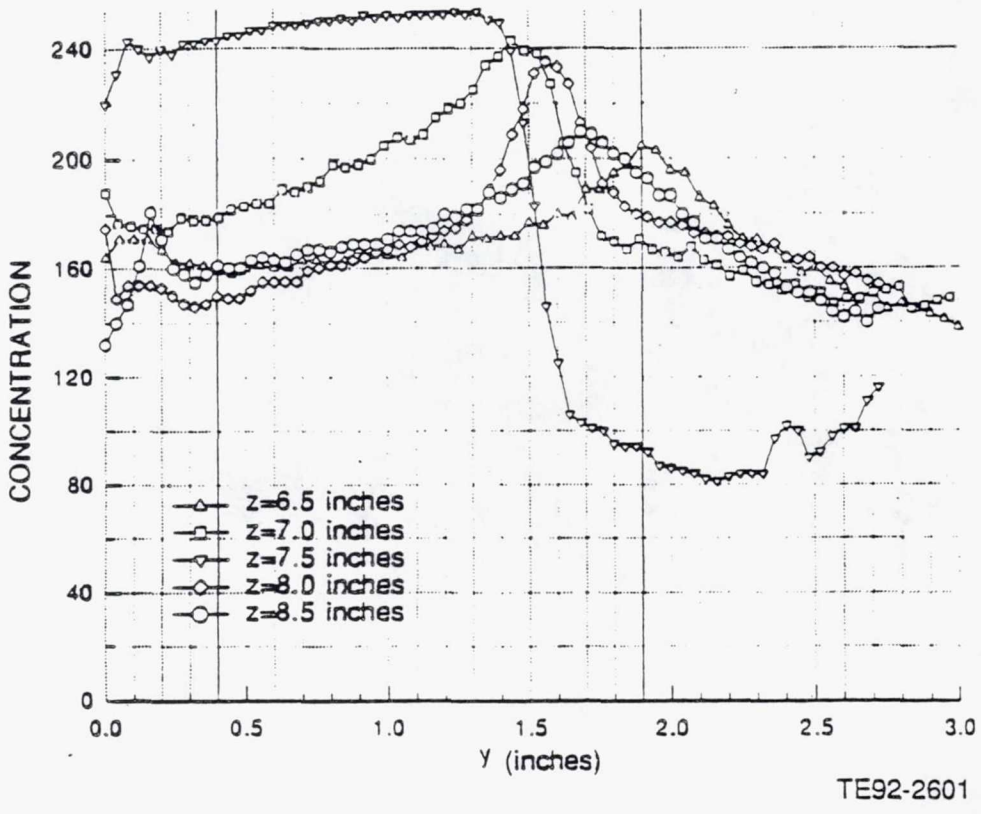

Figure 4.2.1-12. Primary jets only mean concentration along primary jet Axis, x=1.5 in.

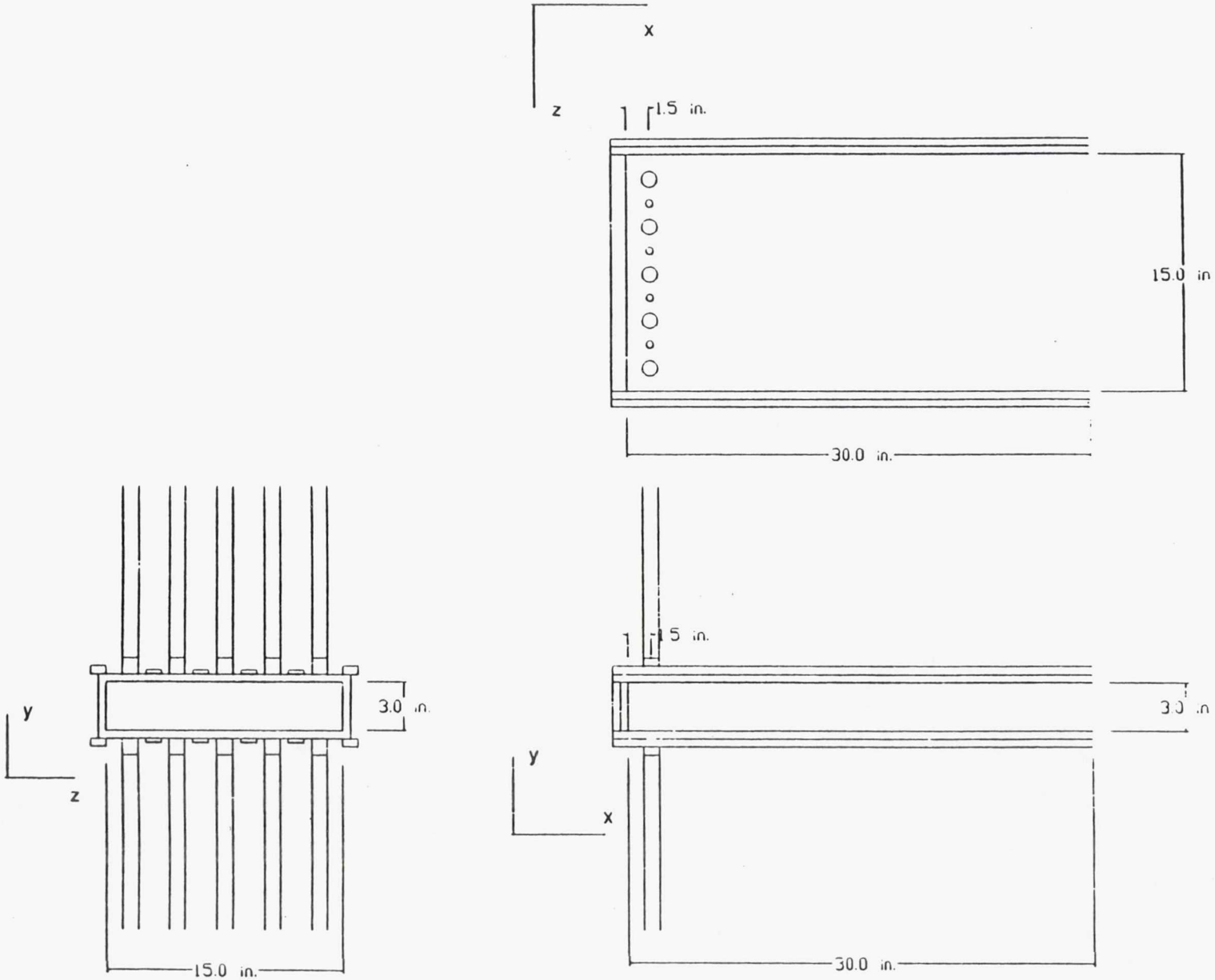

Figure 4.2.2-1. Primary jets only - three-view drawing.

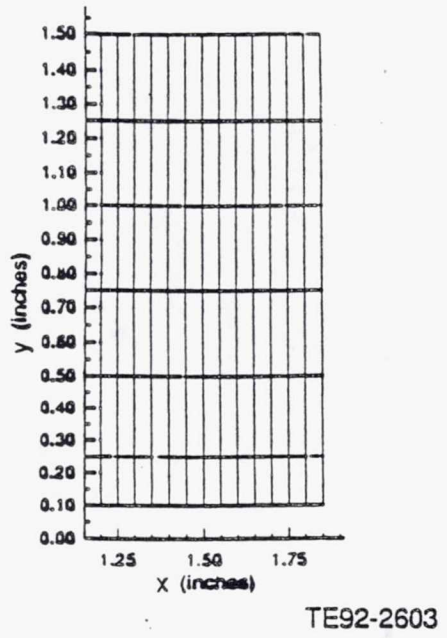

Figure 4.2.2-2. xy plane primary jets sampling grid.

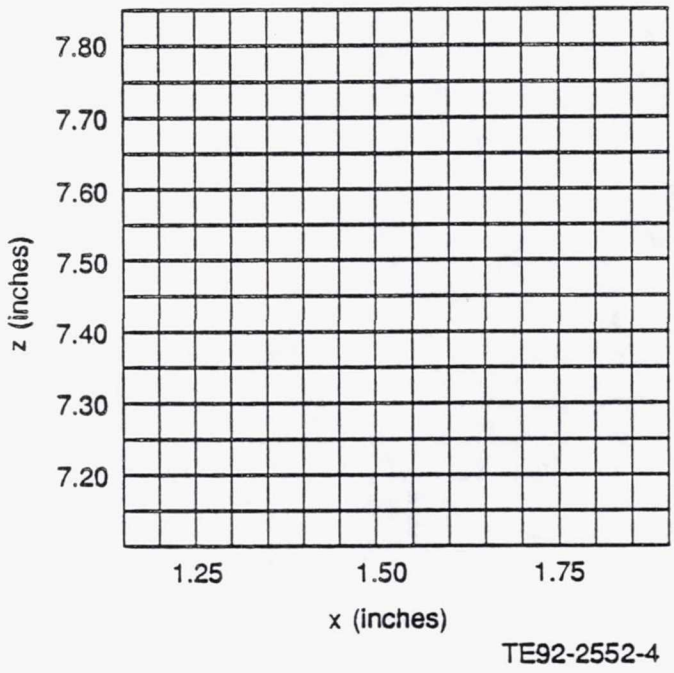

Figure 4.2.2-3. xz plane primary jets sampling grid.

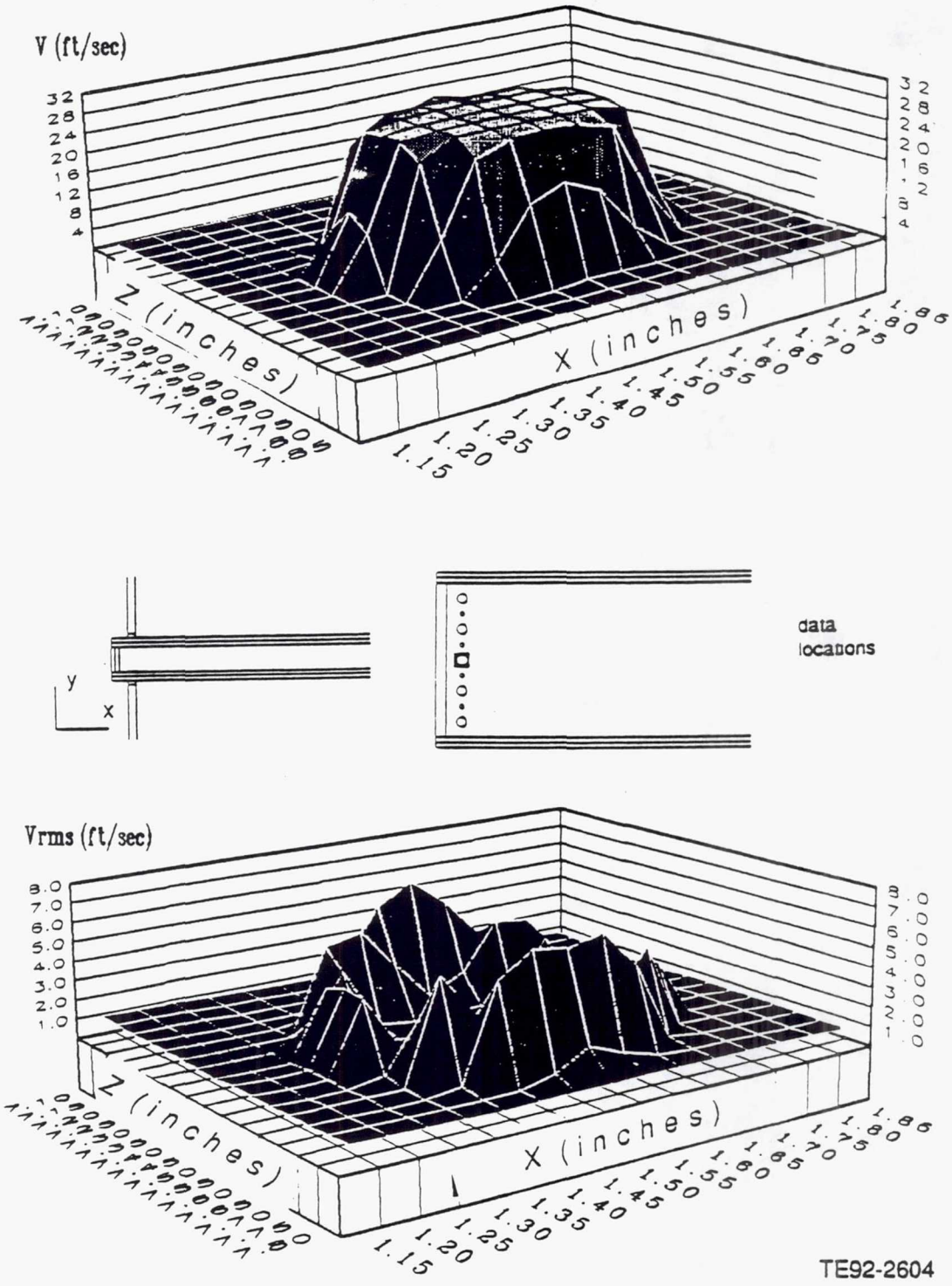

Figure 4.2.2-4. Primary jets only V and V_{rms} distribution of the primary jets at y=0.1 in.

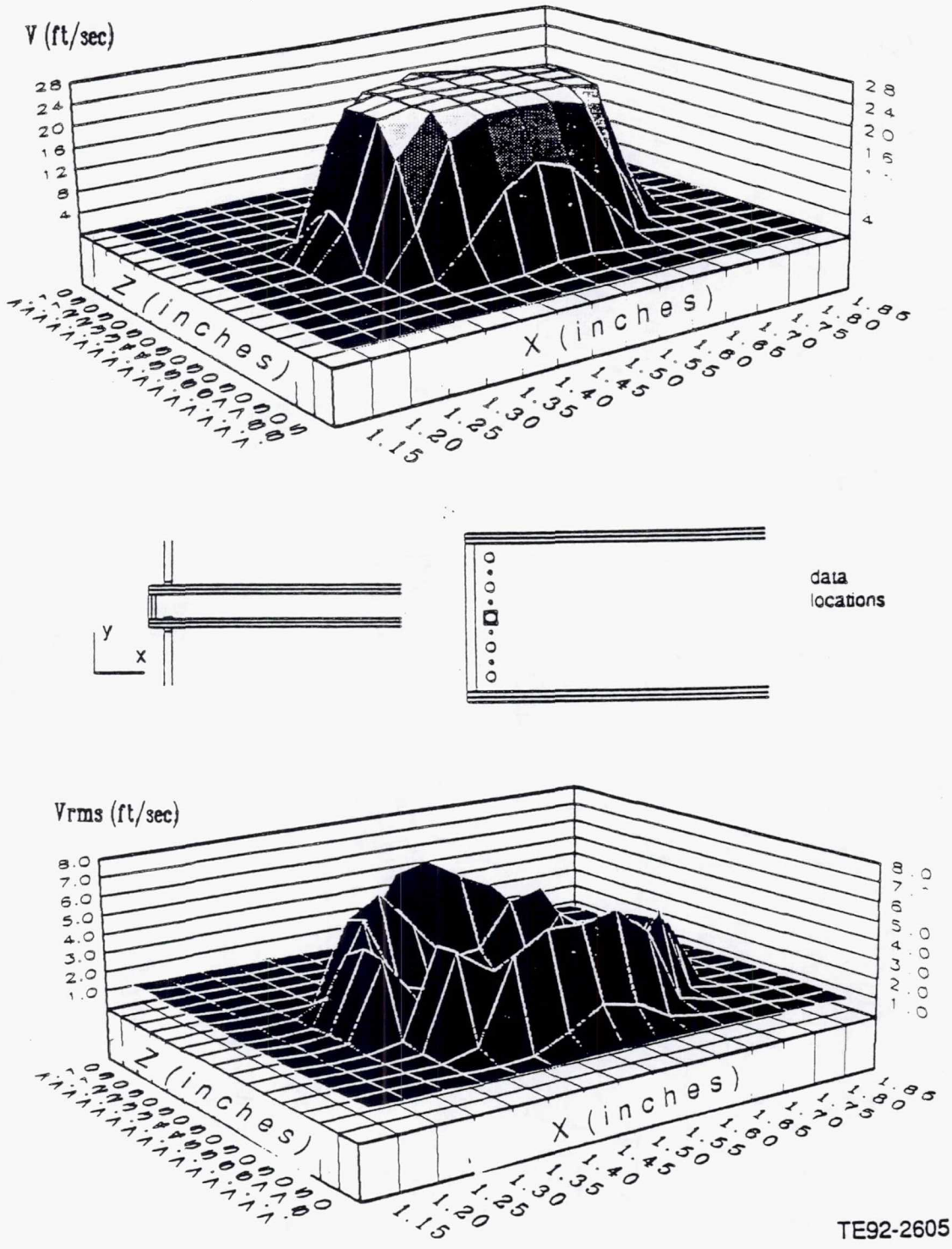

Figure 4.2.2-5. Primary jets only V and V_{rms} distribution of the primary jets at y=0.25 in.

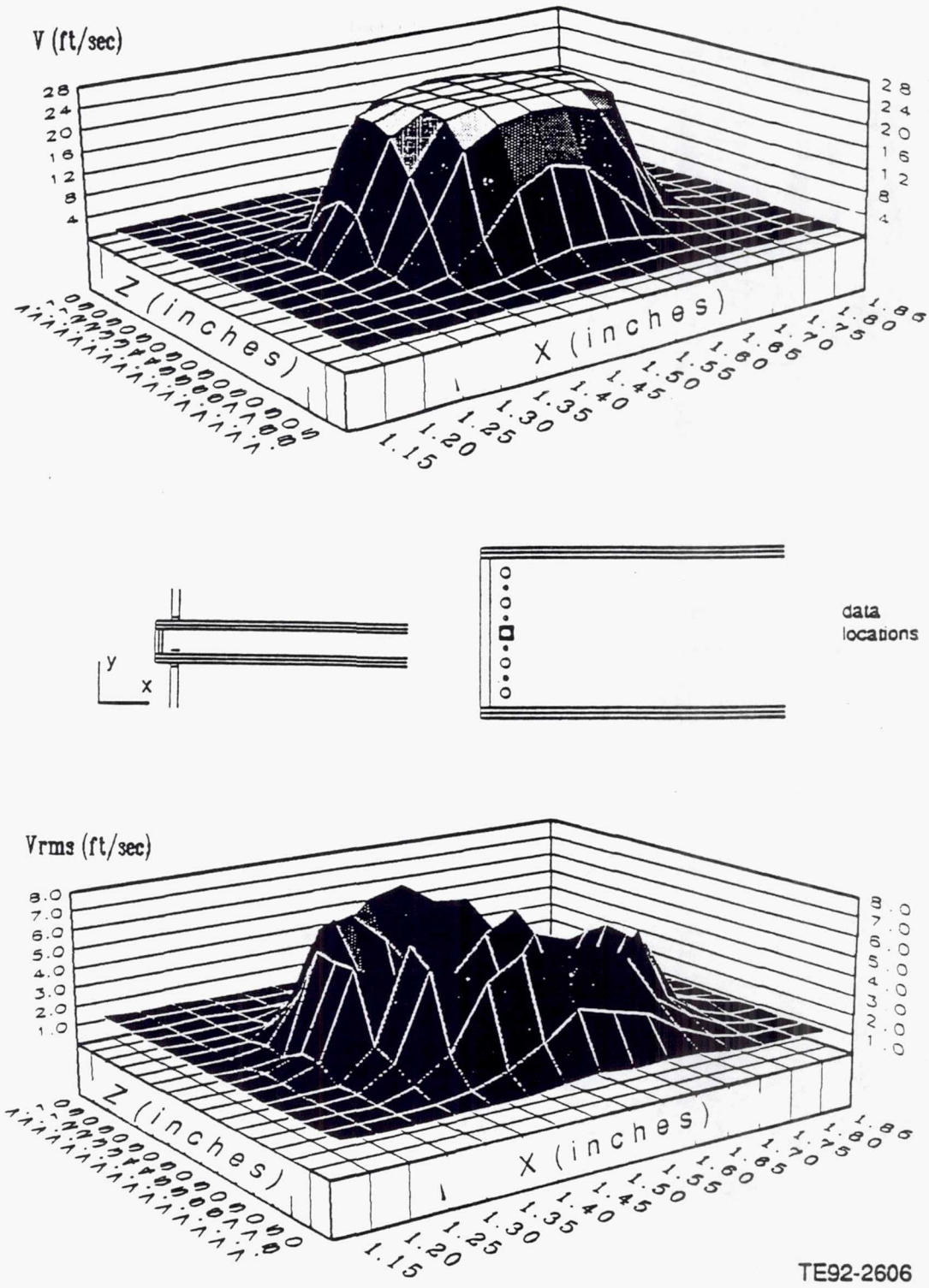

Figure 4.2.2-6. Primary jets only V and V_{rms} distribution of the primary jets at y=0.5 in.

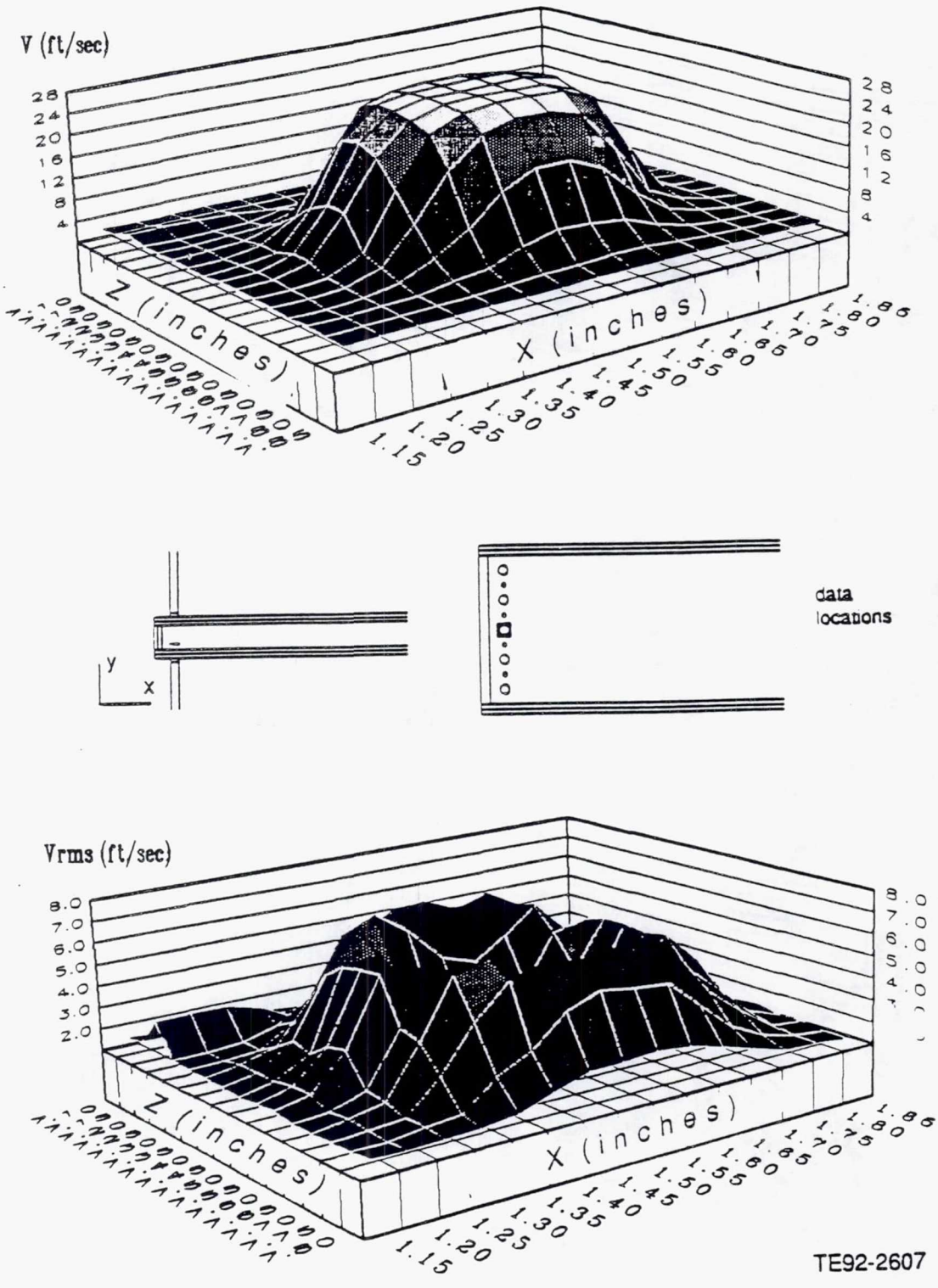

Figure 4.2.2-7. Primary jets only V and V_{rms} distribution of the primary jets at y=0.75 in.

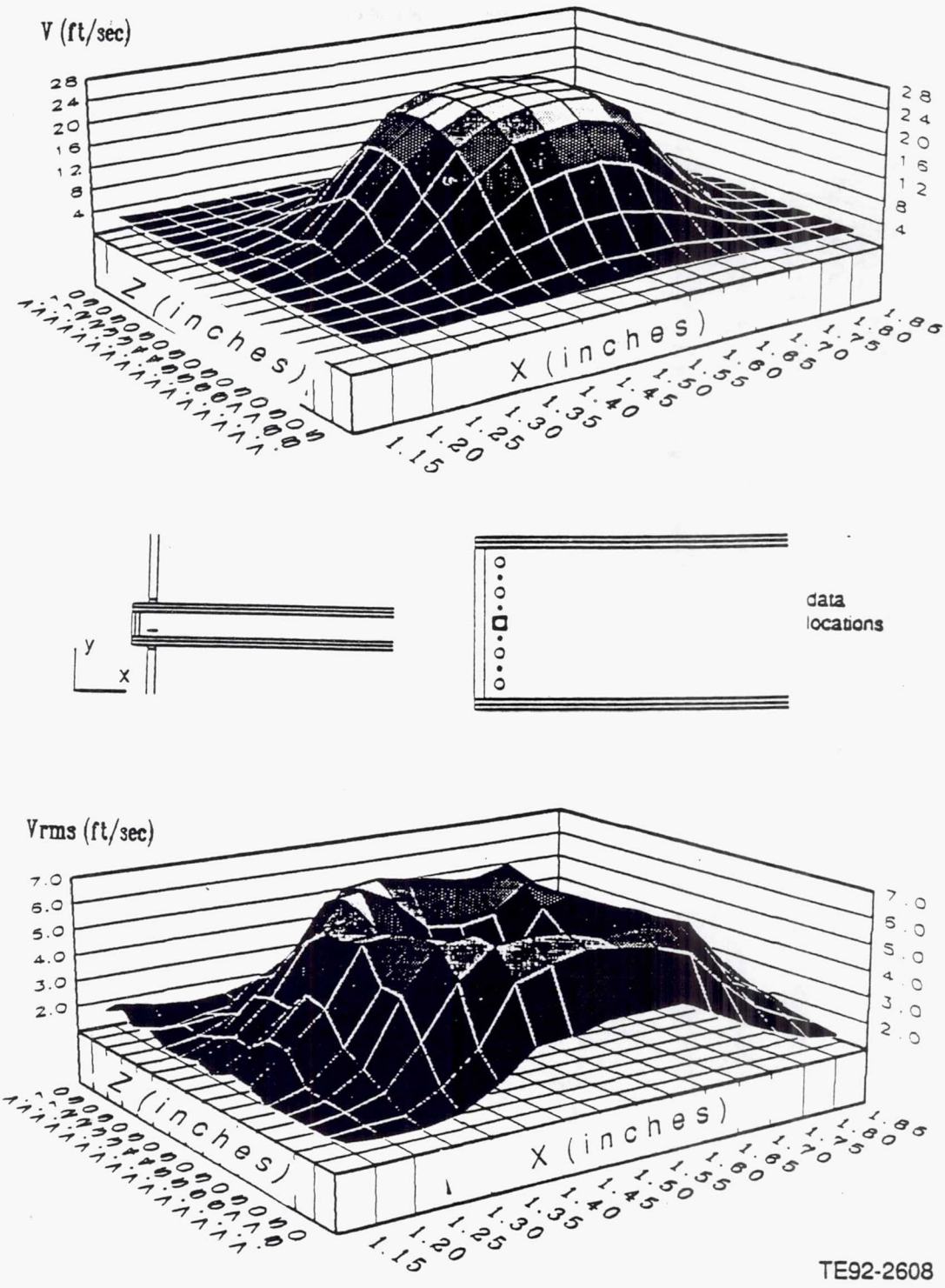

Figure 4.2.2-8. Primary jets only V and V_{rms} distribution of the primary jets at y=1.0 in.

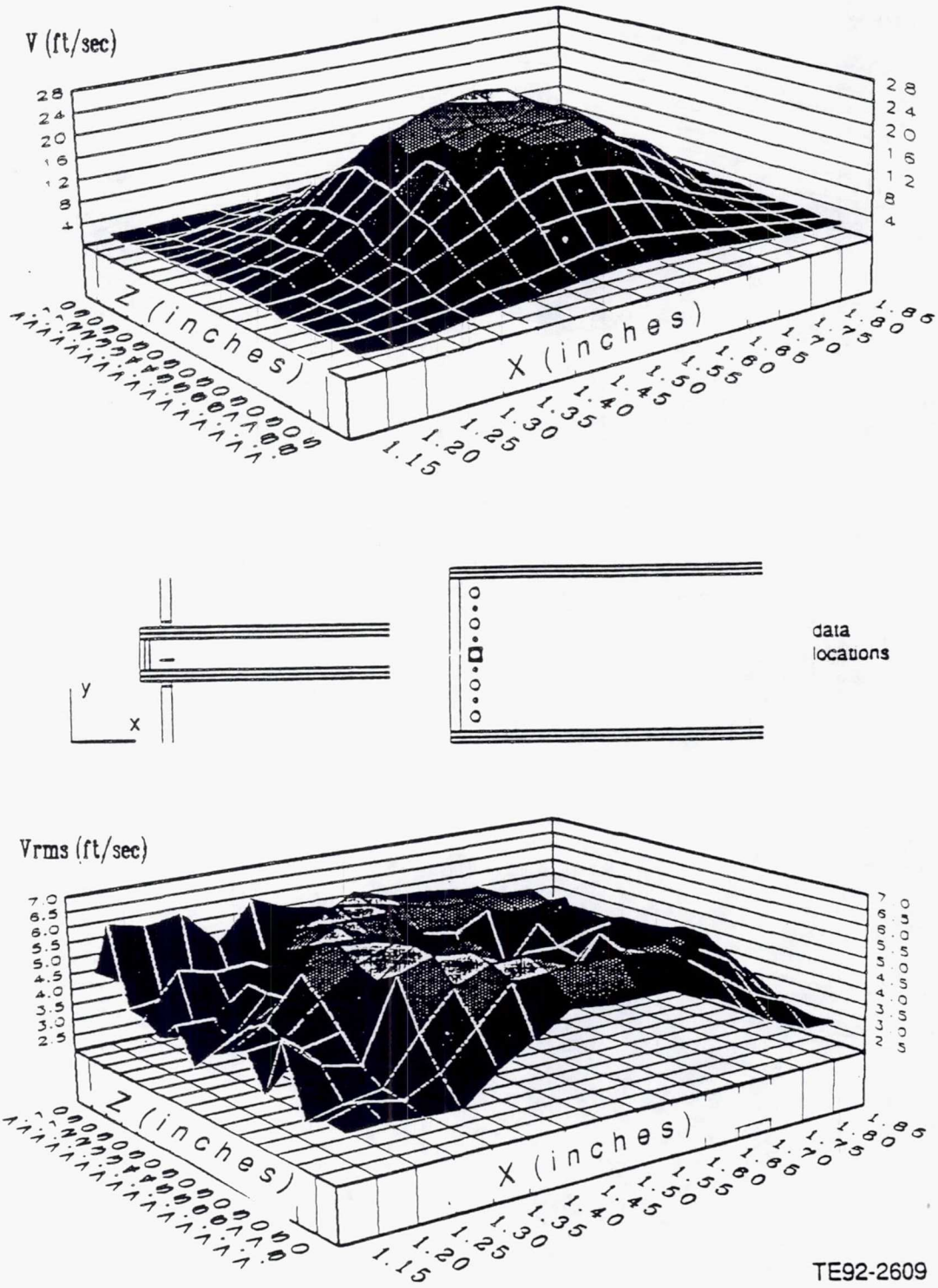

Figure 4.2.2-9. Primary jets only V and V_{rms} distribution of the primary jets at y=1.25 in.

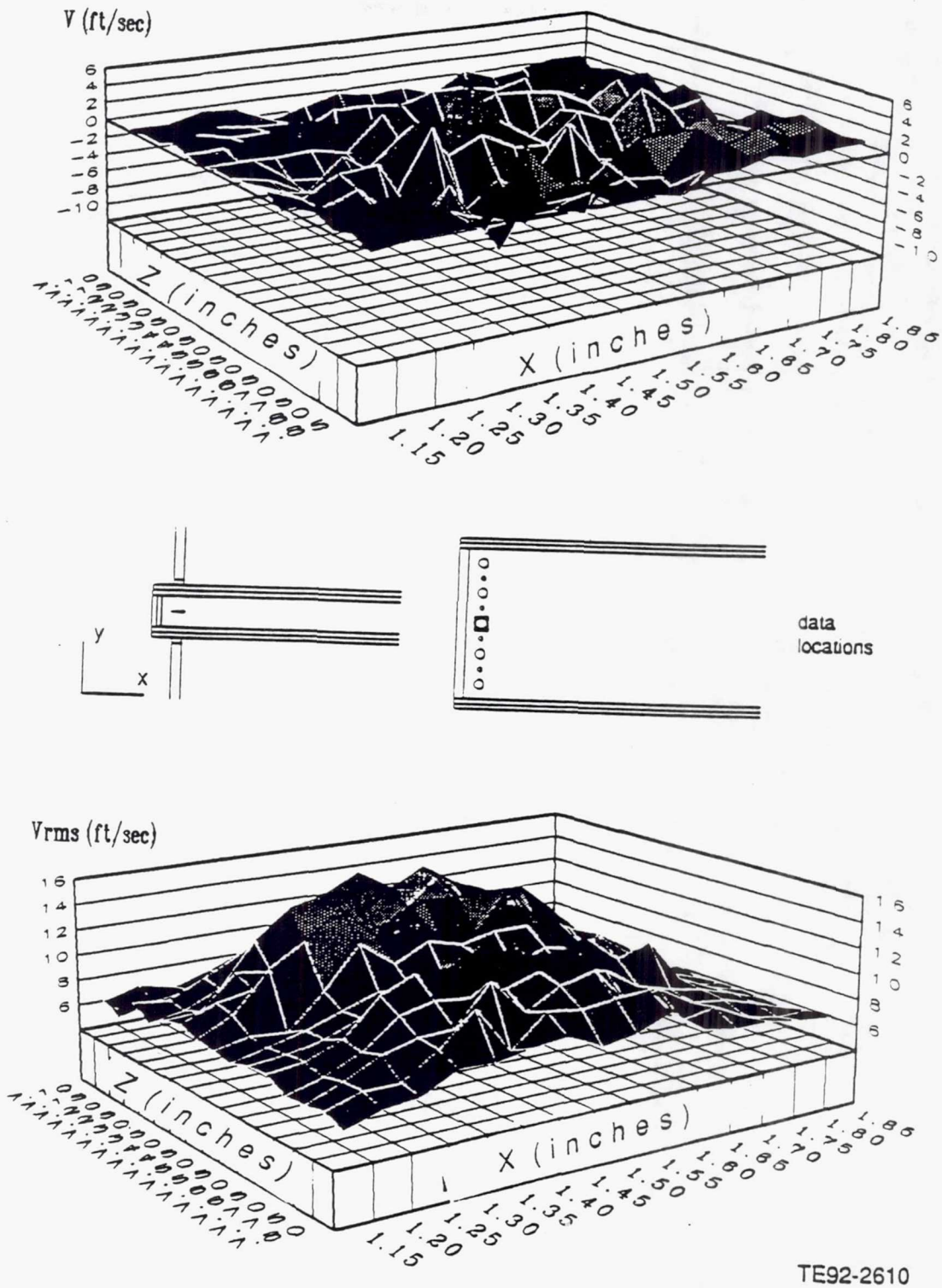

Figure 4.2.2-10. Primary jets only V and V_{rms} distribution of the primary jets at y=1.5 in.

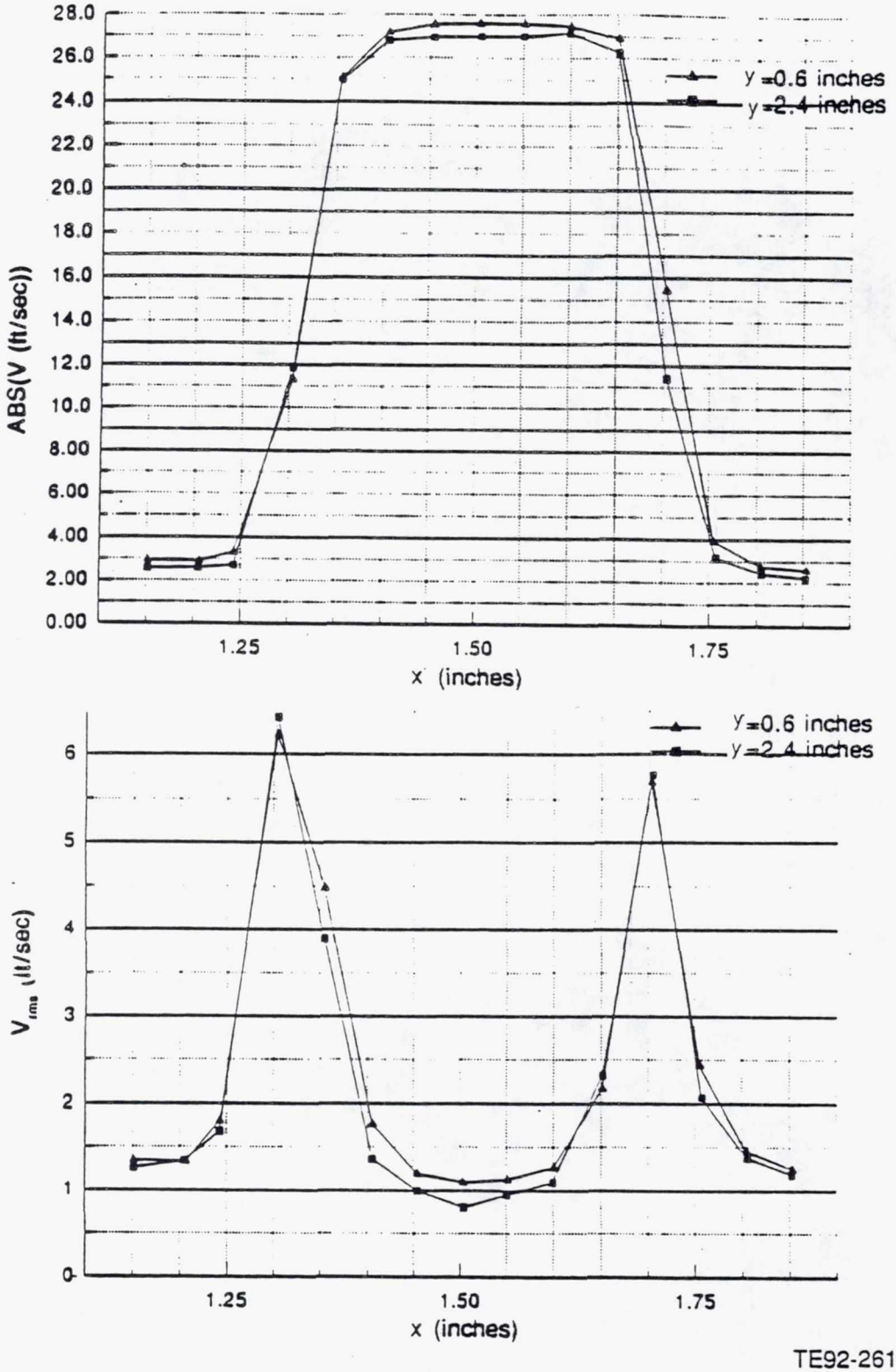

Figure 4.2.2-11. Primary jets only and V_{rms} distribution comparison of the primary jets at y=0.6 in. and y=2.4 in.

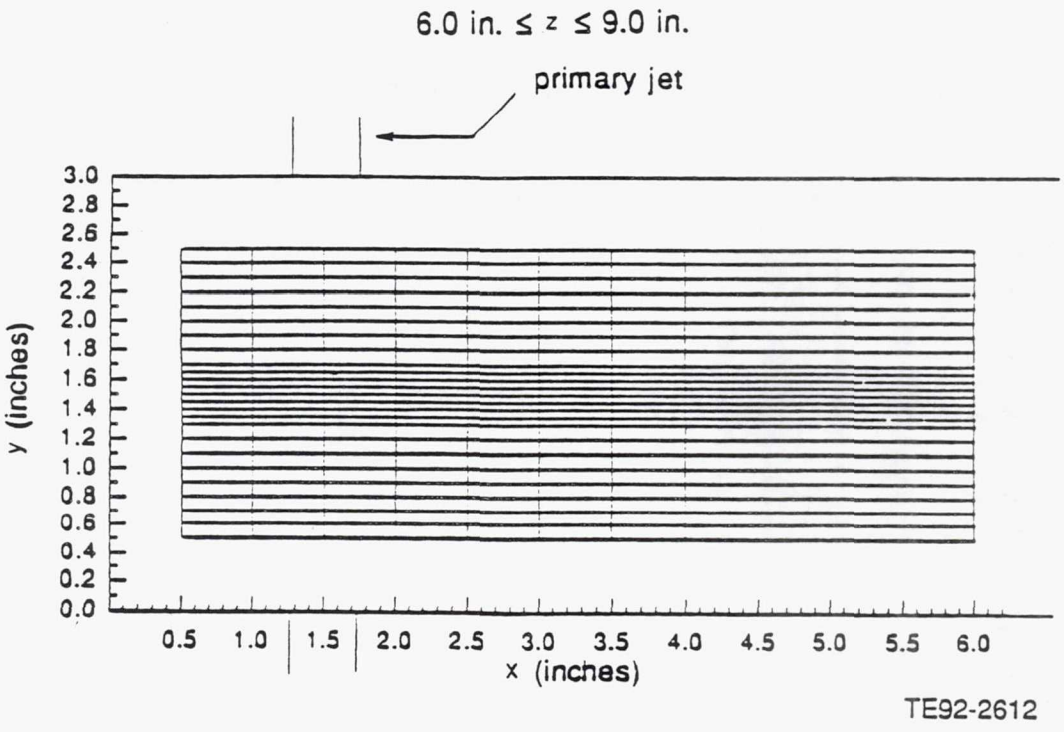

Figure 4.2.2-12. Primary jets only x y plane sampling grid.

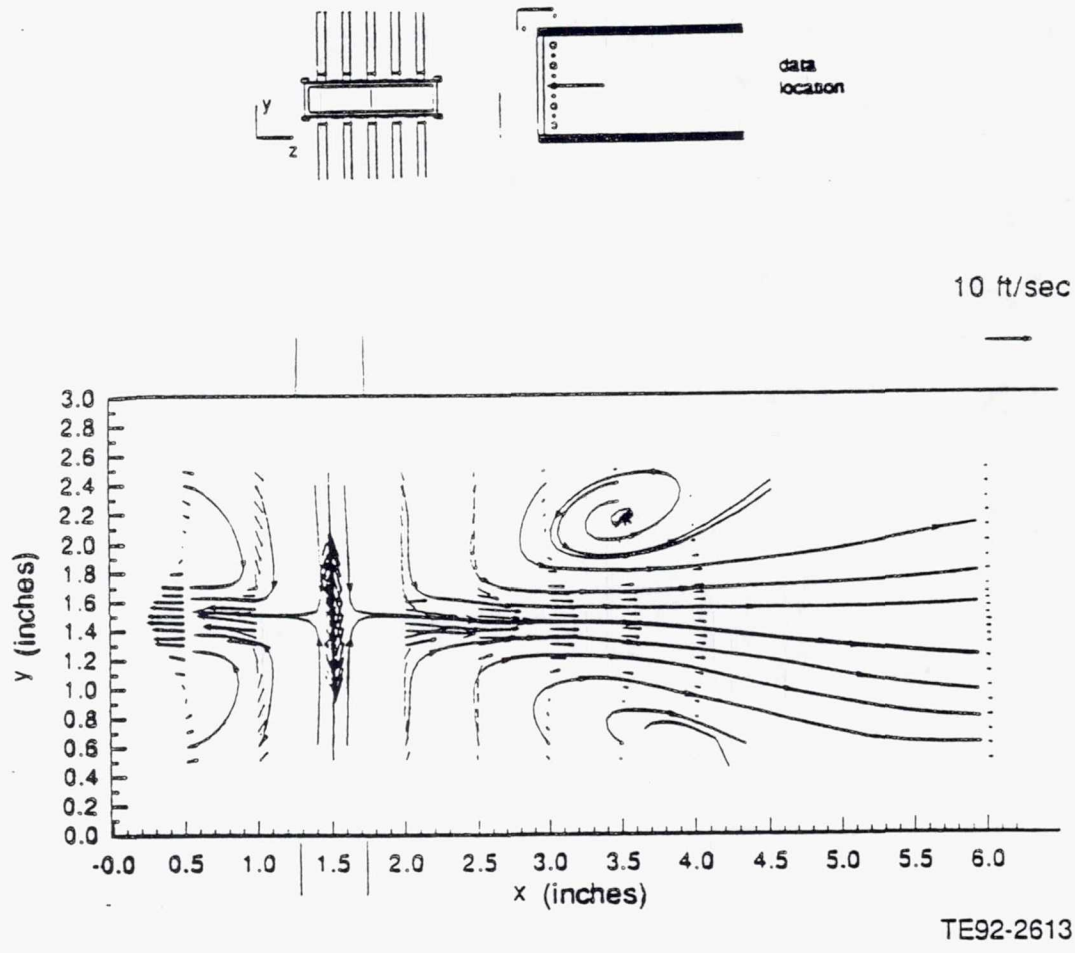

Figure 4.2.2-13. Primary jets only mean velocity vector plot at z=7.5 in.

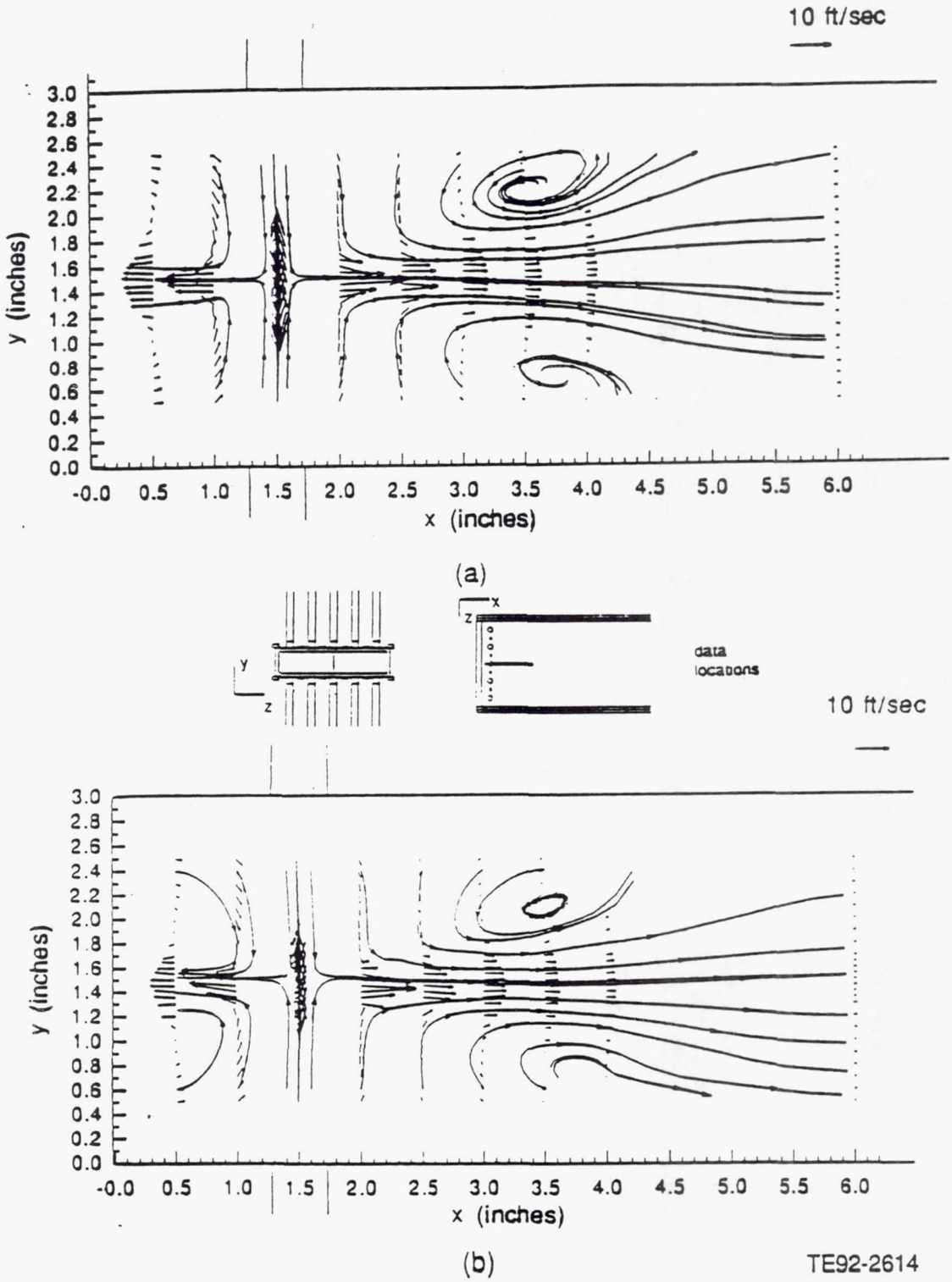

Figure 4.2.2-14. Primary jets only mean velocity vector plots a) z =7.4 in. b) z=7.6 in.

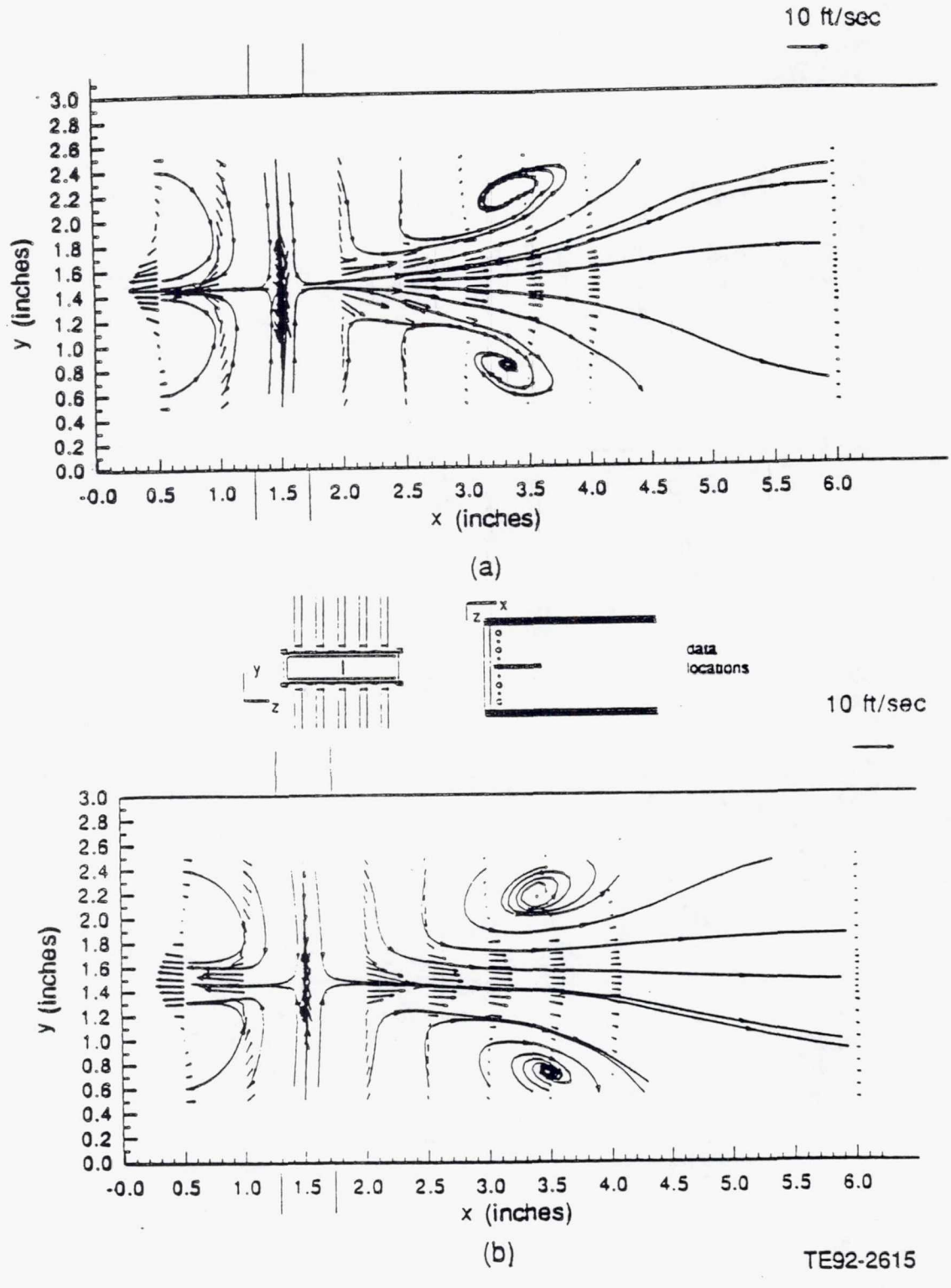

Figure 4.2.2-15. Primary jets only mean velocity vector plots a) z=7.3 in. b) z=7.7 in.

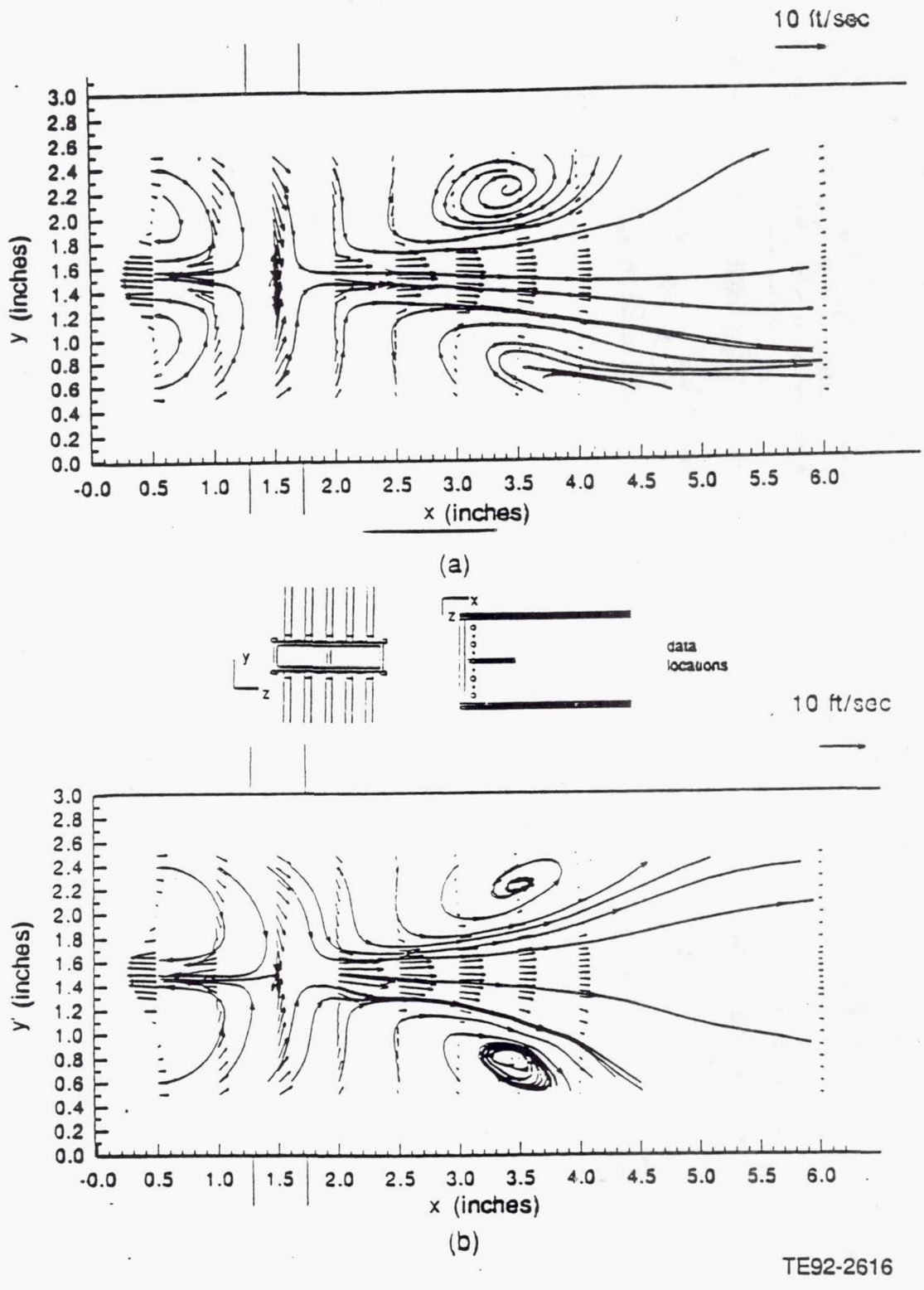

Figure 4.2.2-16. Primary jets only mean velocity vector plots a) z=7.2 in. b) z=7.8 in.

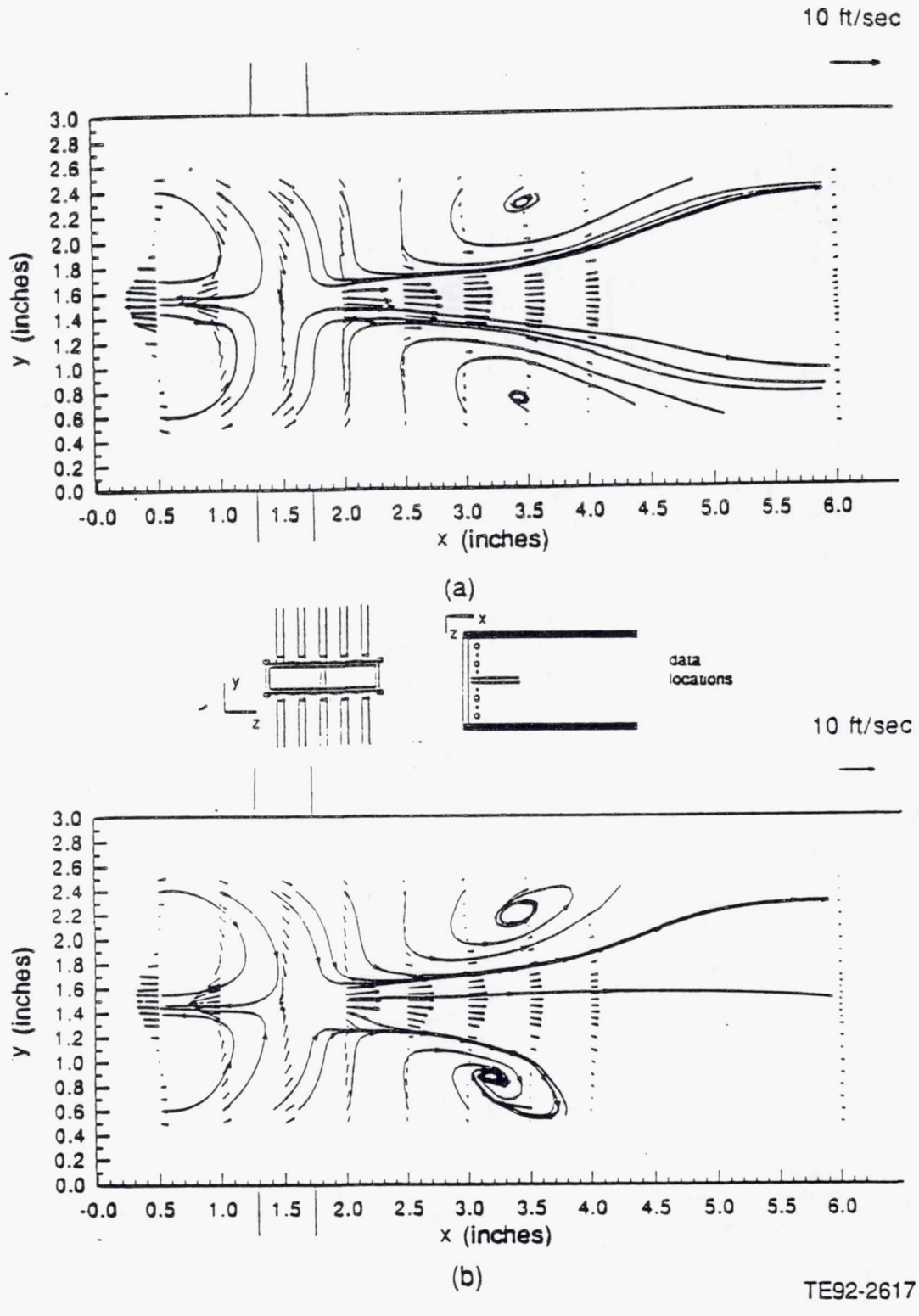

Figure 4.2.2-17. Primary jets only mean velocity vector plots a) z=7.1 in. b) z=7.9 in.

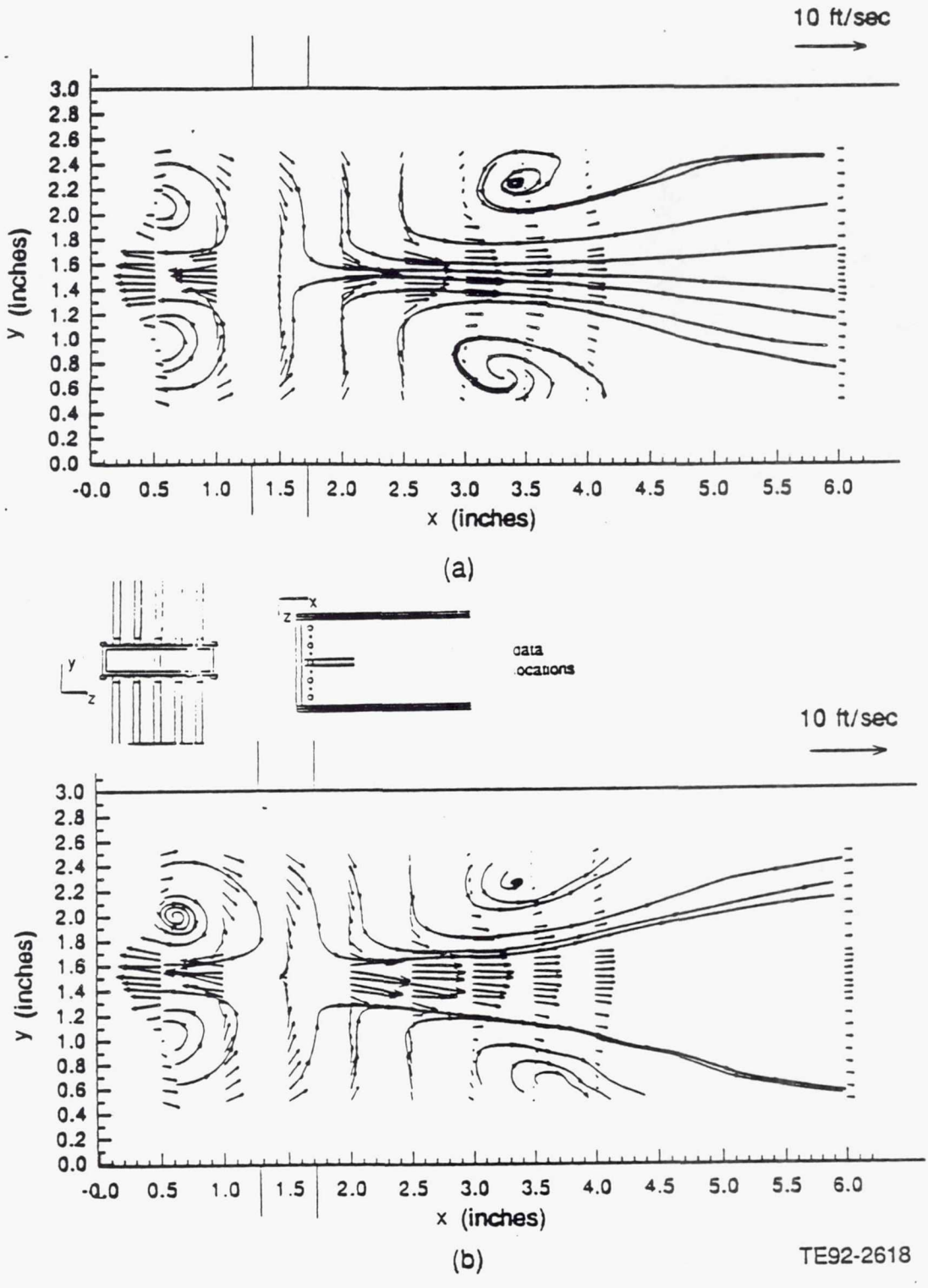

Figure 4.2.2-18. Primary jets only mean velocity vector plots a) z=7.0 in. b) z=8.0 in.

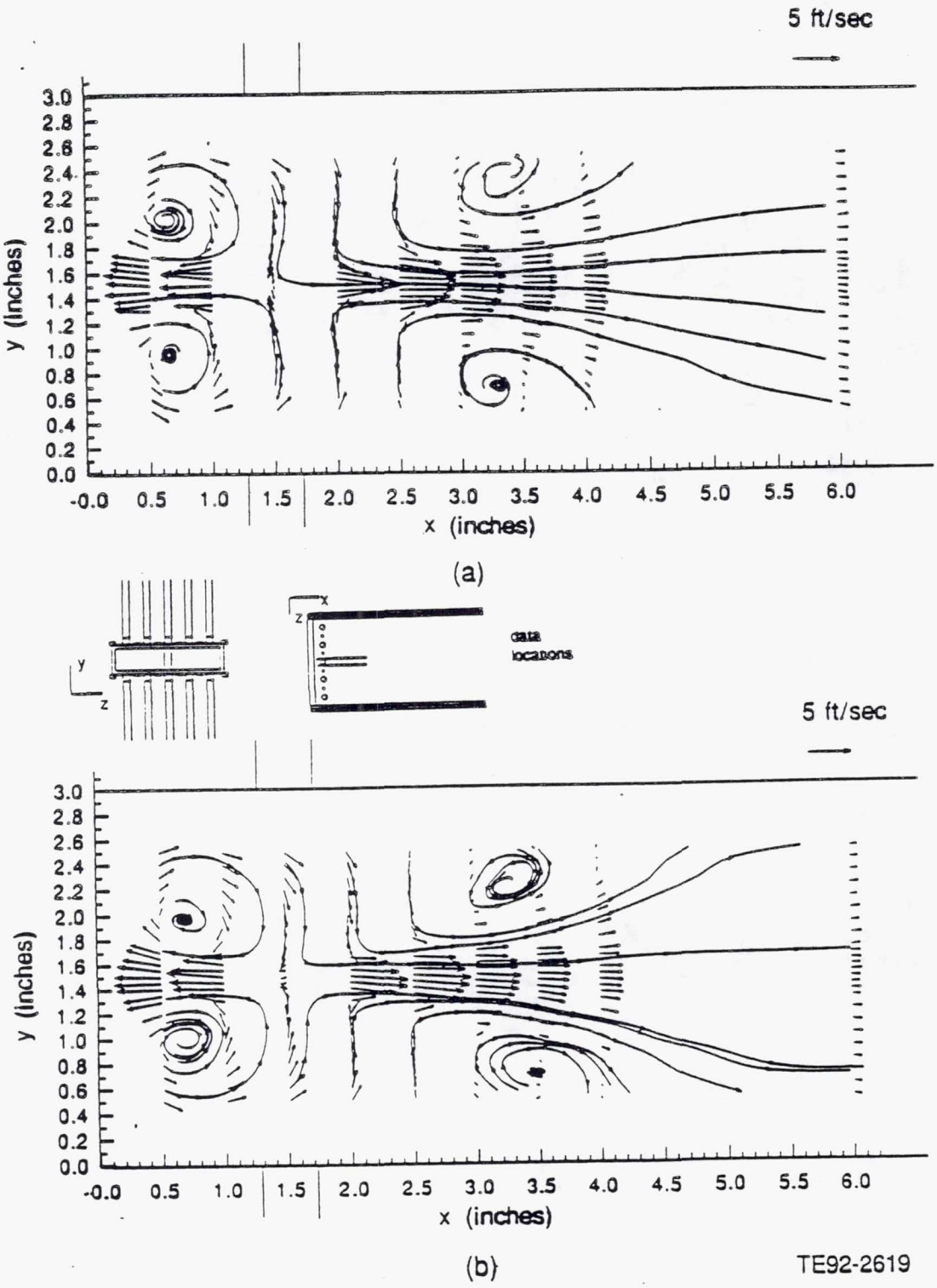

Figure 4.2.2-19. Primary jets only mean velocity vector plots a) z=6.9 in. b) z=8.1 in.

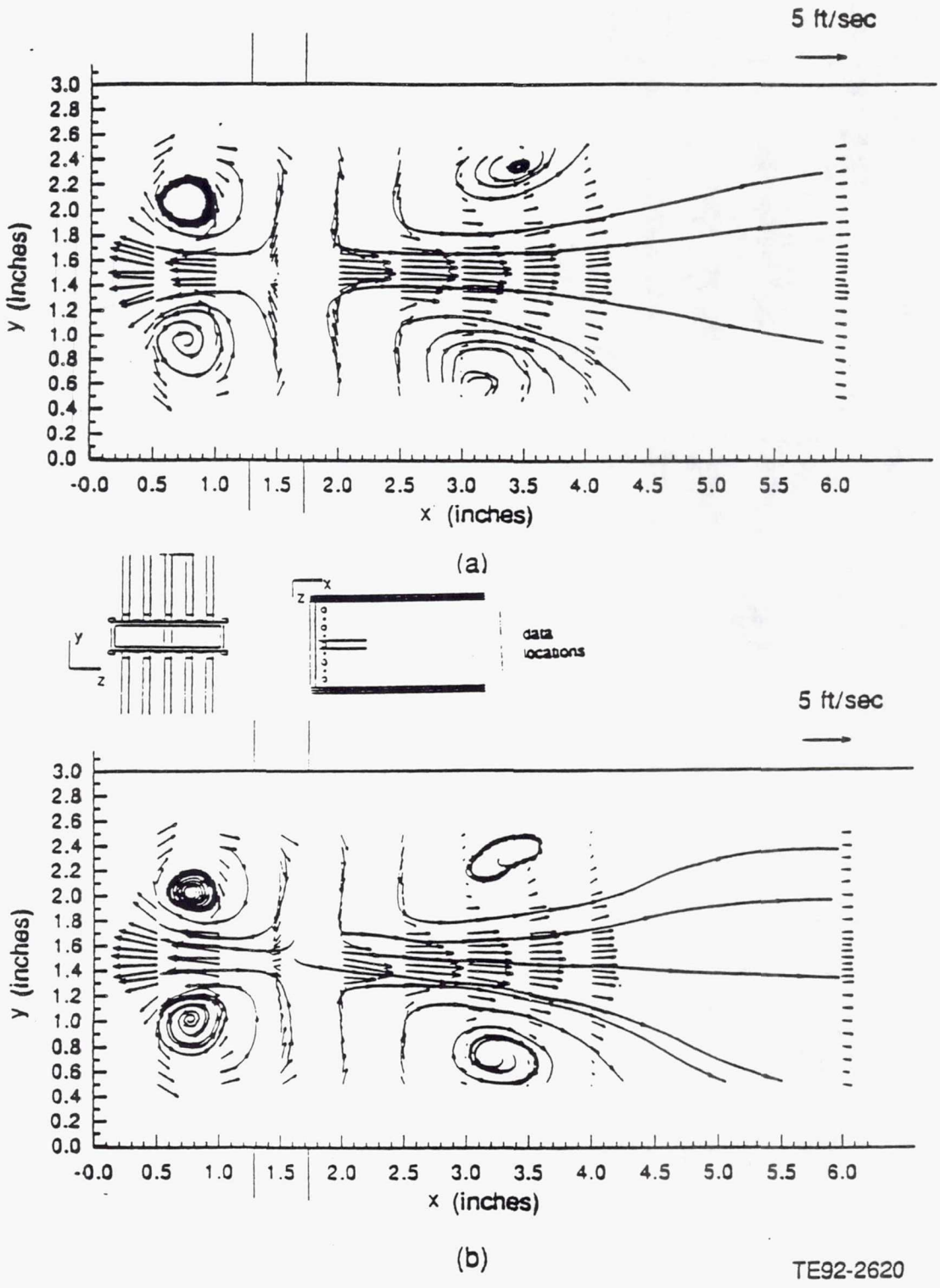

Figure 4.2.2-20. Primary jets only mean velocity vector plots a) z=6.8 in. b) z=8.2 in.

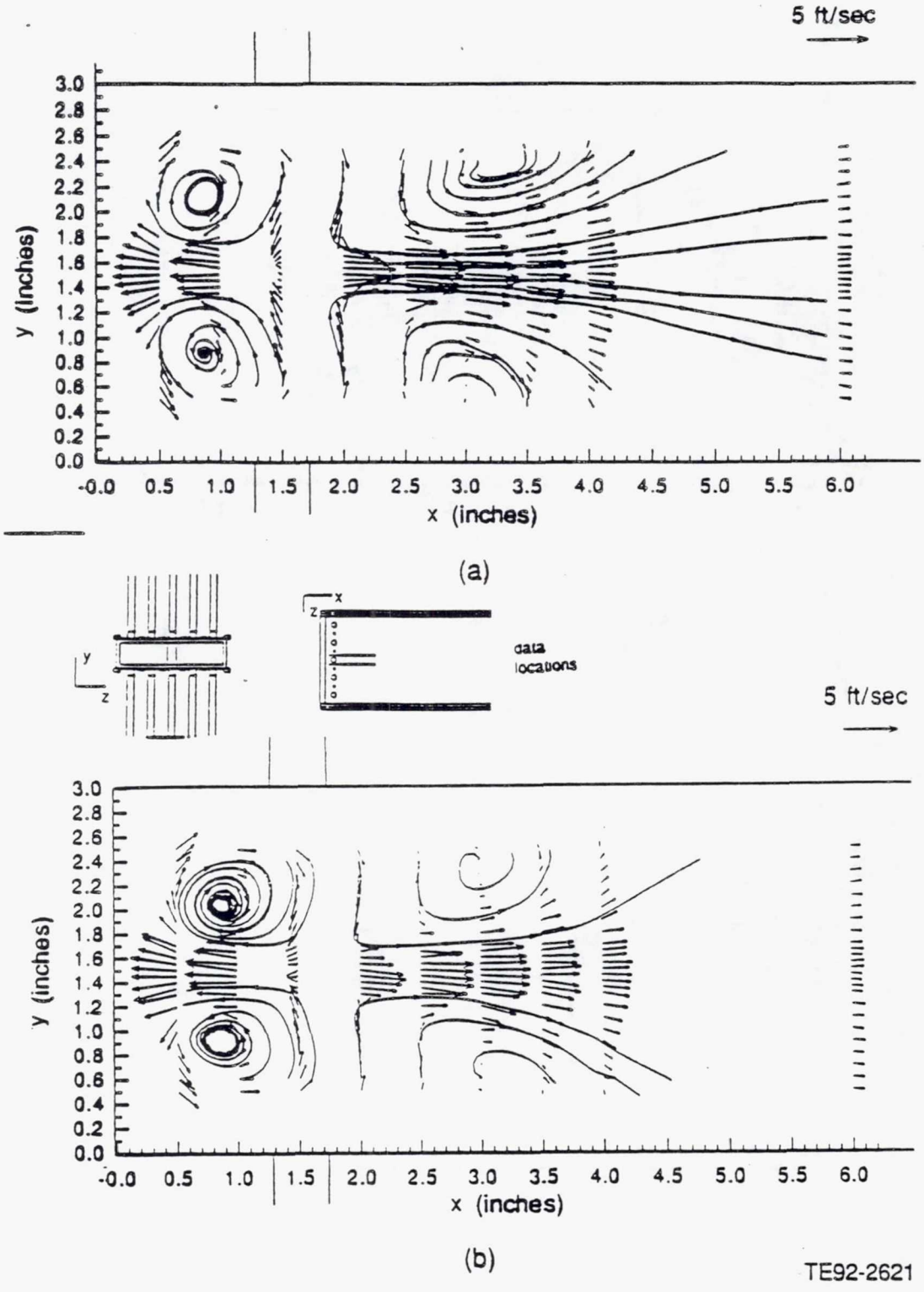

Figure 4.2.2-21. Primary jets only mean velocity vector plots a) z=6.7 in. b) z=8.3 in.

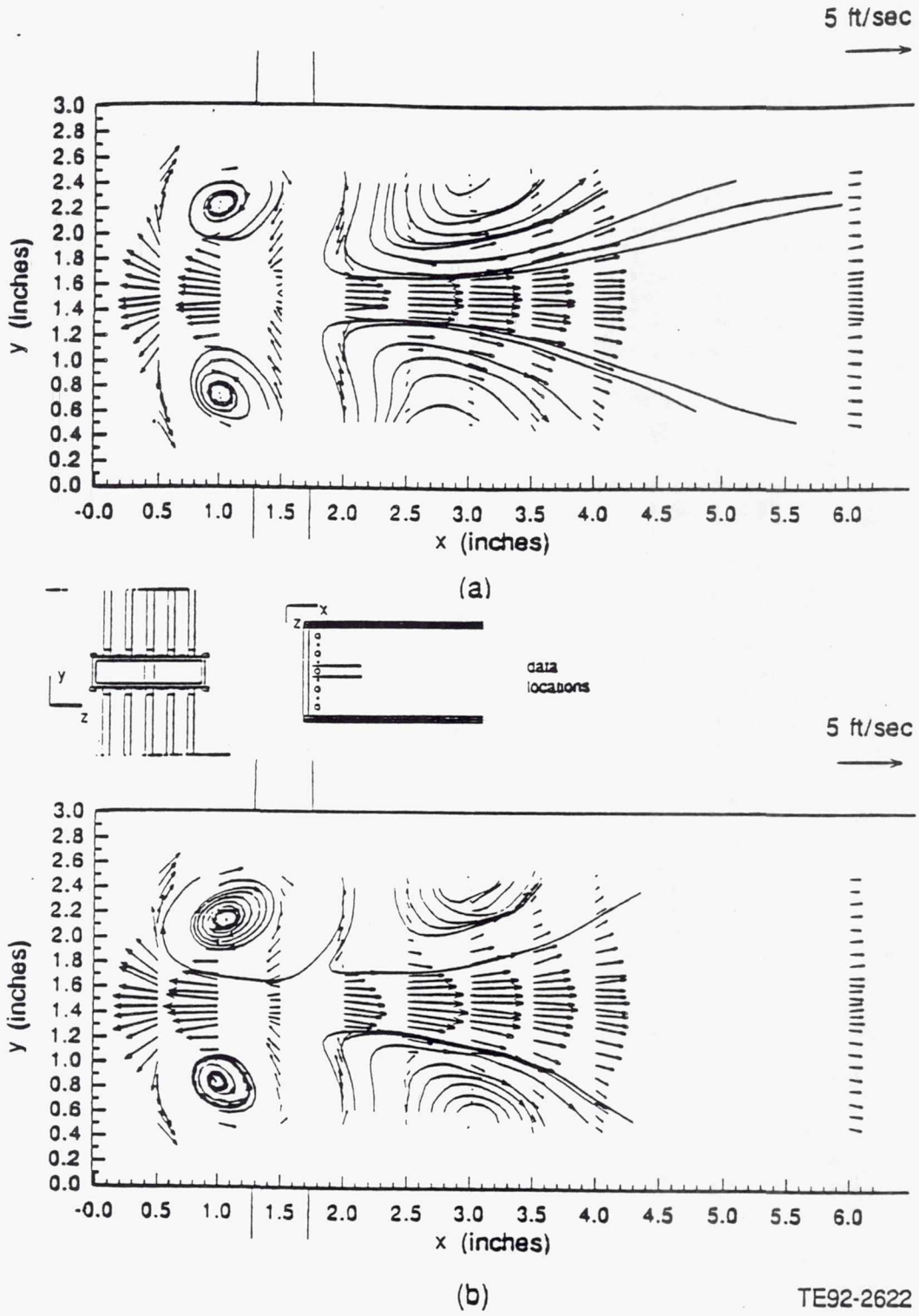

Figure 4.2.2-22. Primary jets only mean velocity vector plots a) z=6.6 in. b) z=8.4 in.

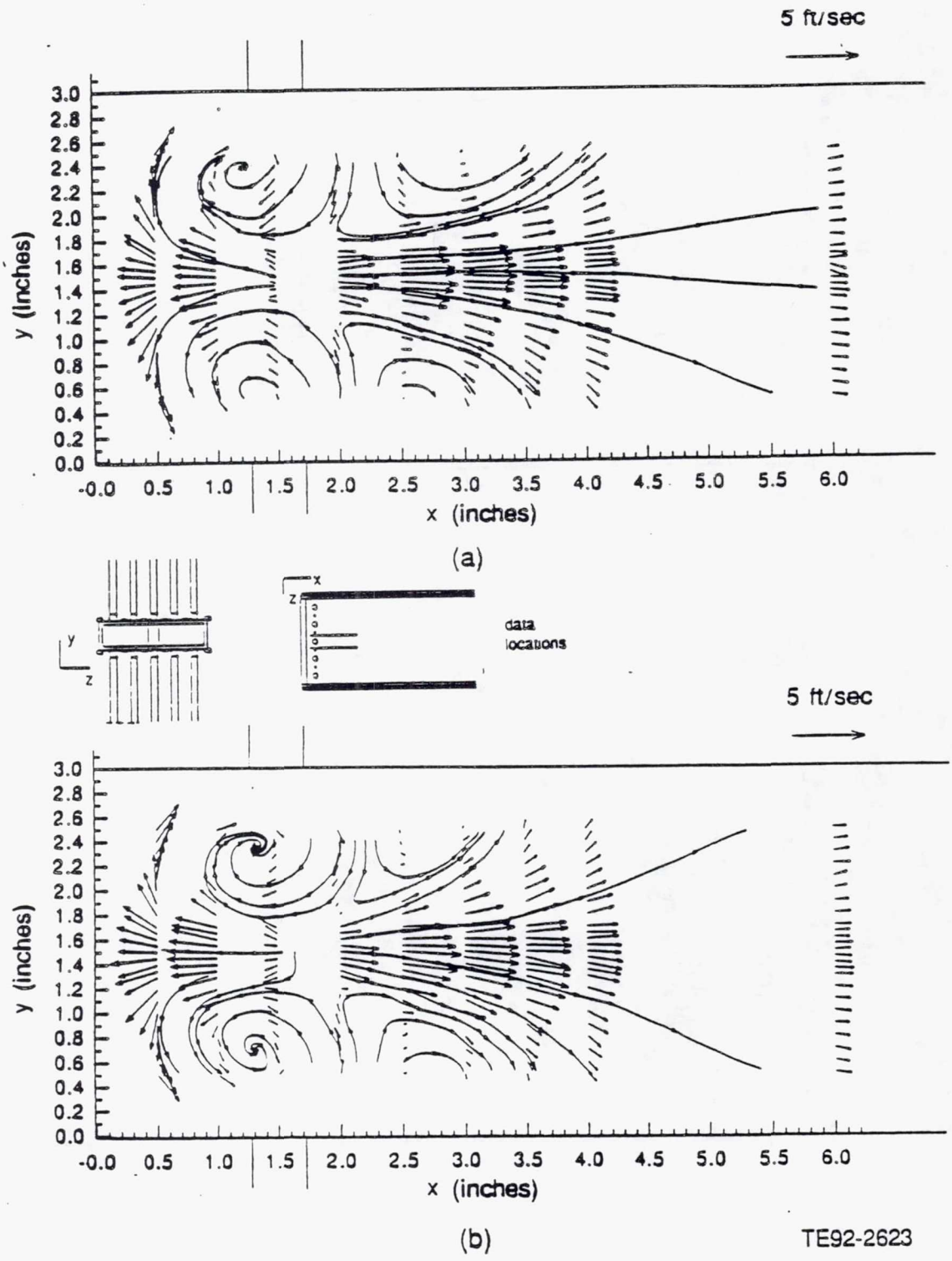

Figure 4.2.2-23. Primary jets only mean velocity vector plots a) z=6.5 in. b) z=8.5 in.

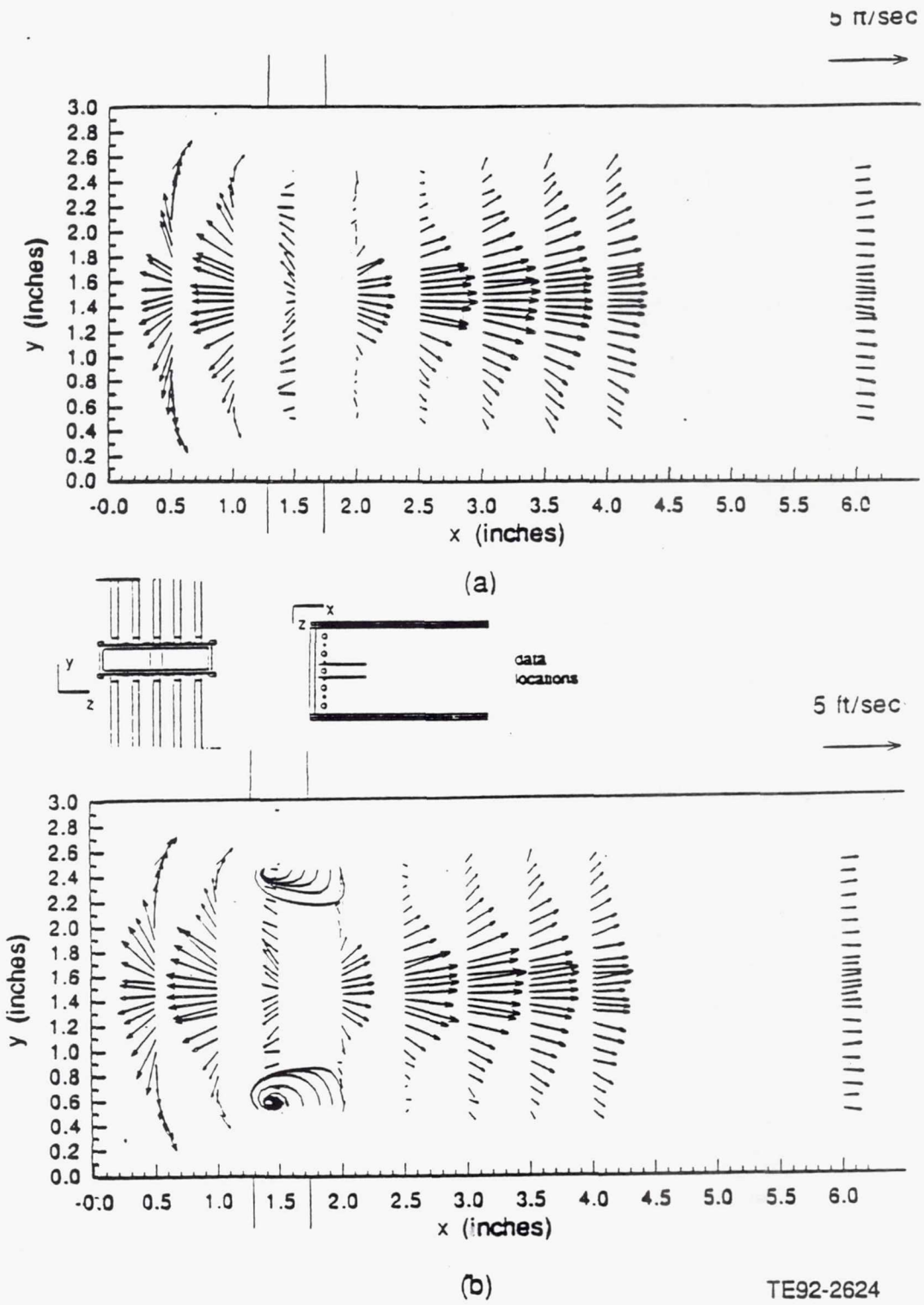

Figure 4.2.2-24. Primary jets only mean velocity vector plots a) z=6.4 in. b) z=8.6 in.

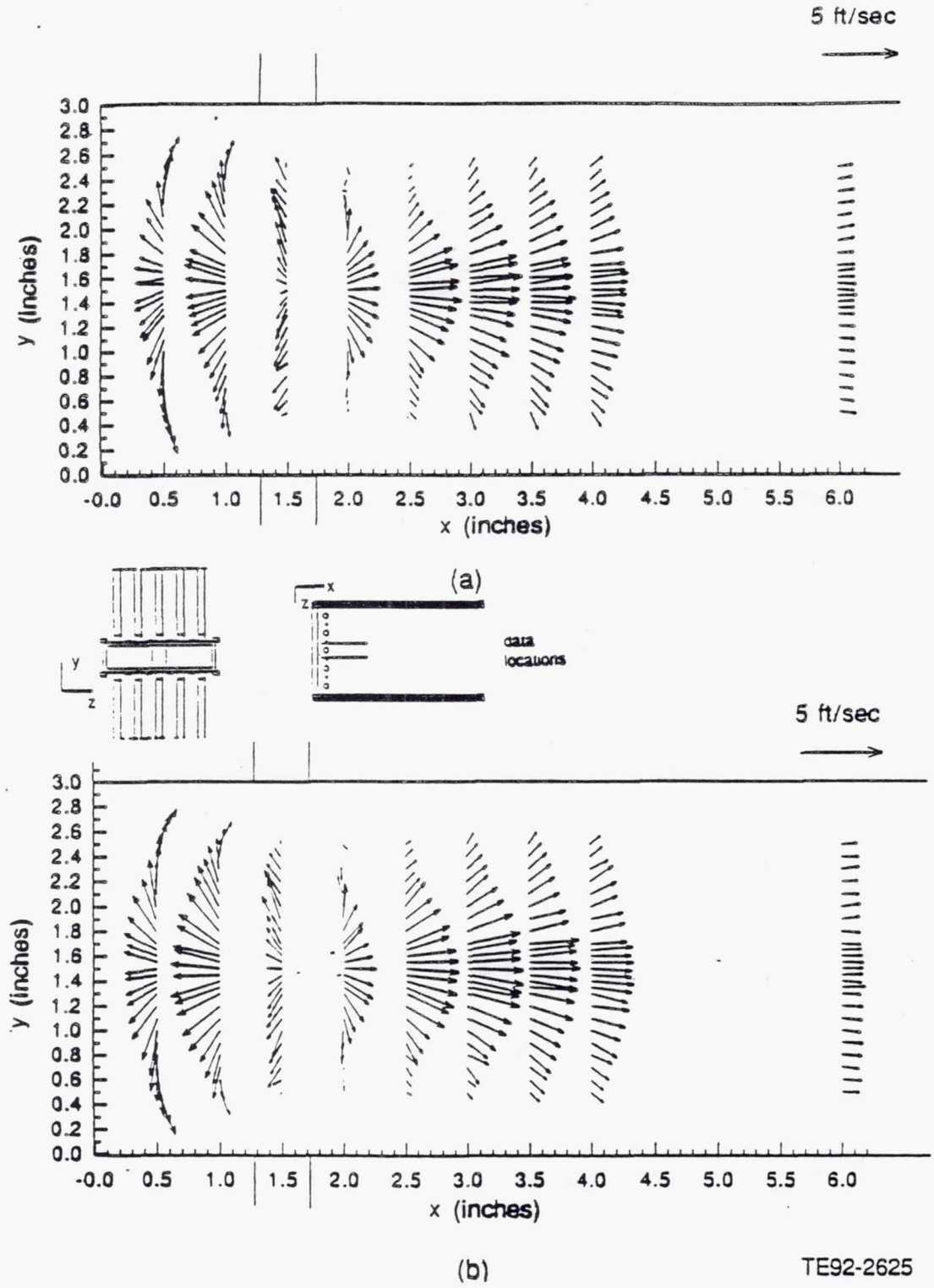

Figure 4.2.2-25. Primary jets only mean velocity vector plots a) z=6.3 in. b) z=8.7 in.

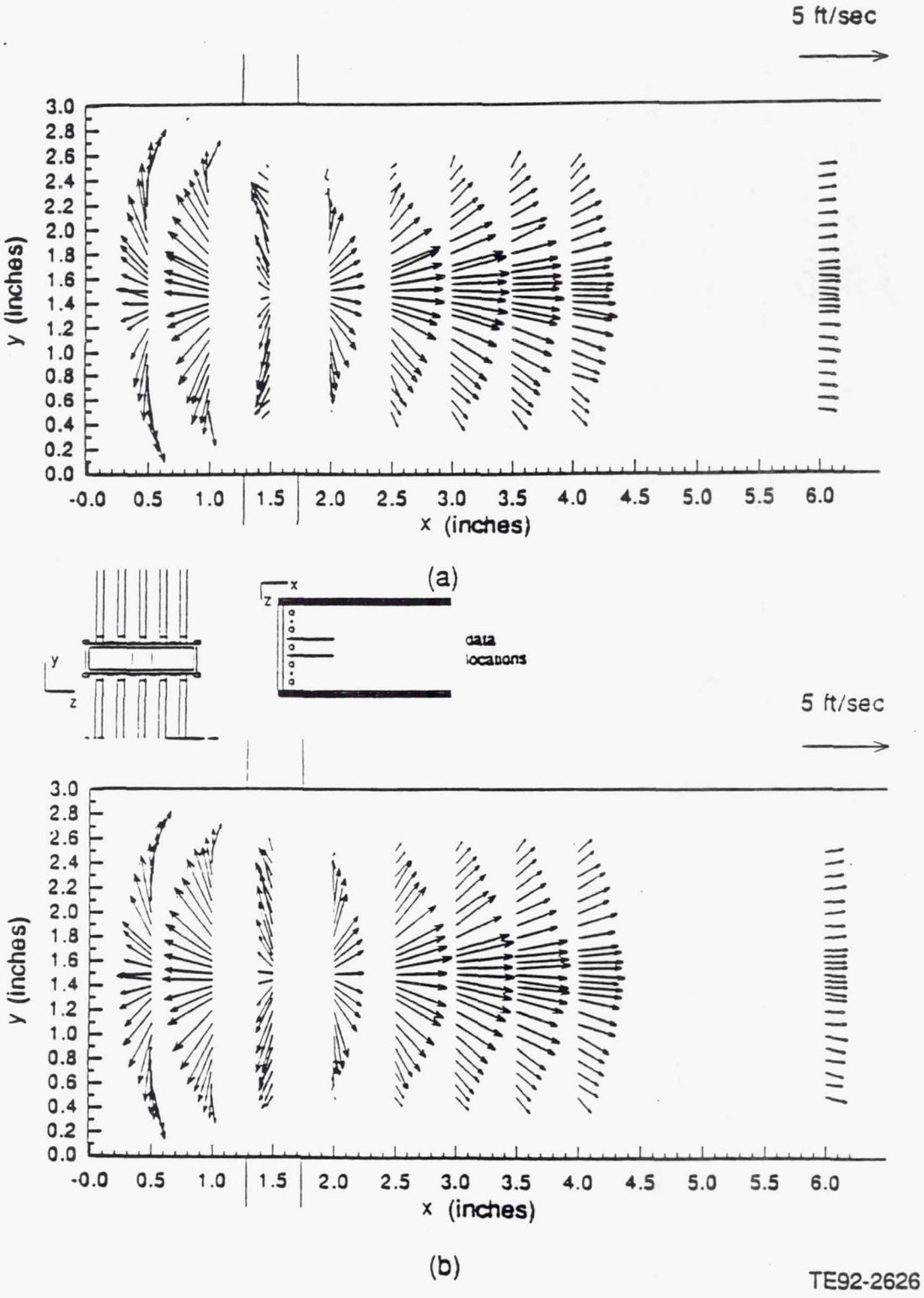

Figure 4.2.2-26. Primary jets only mean velocity vector plots a) z=6.2 in. b) z=8.8 in.

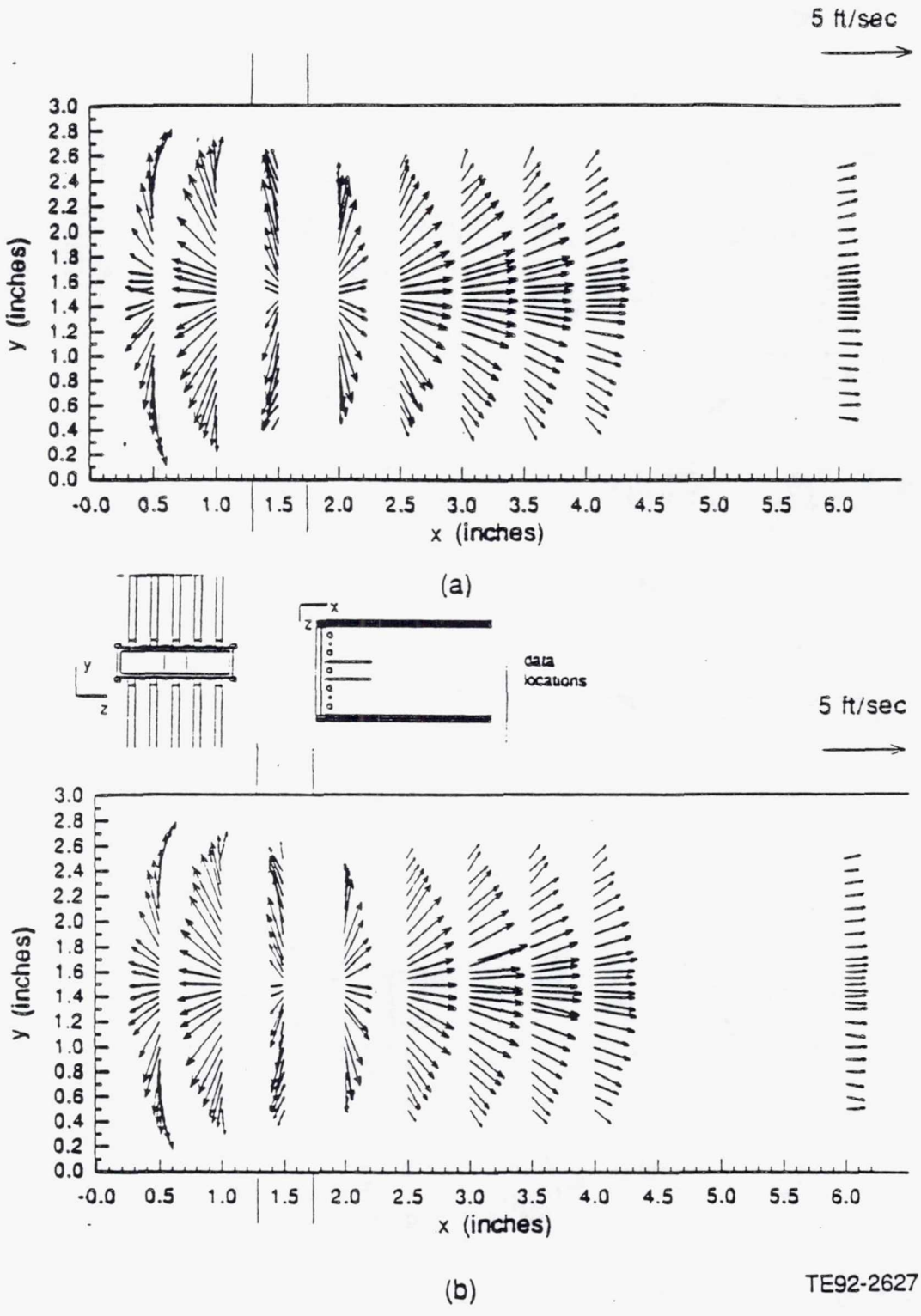

Figure 4.2.2-27. Primary jets only mean velocity vector plots a) z=6.1 in. b) z=8.9 in.

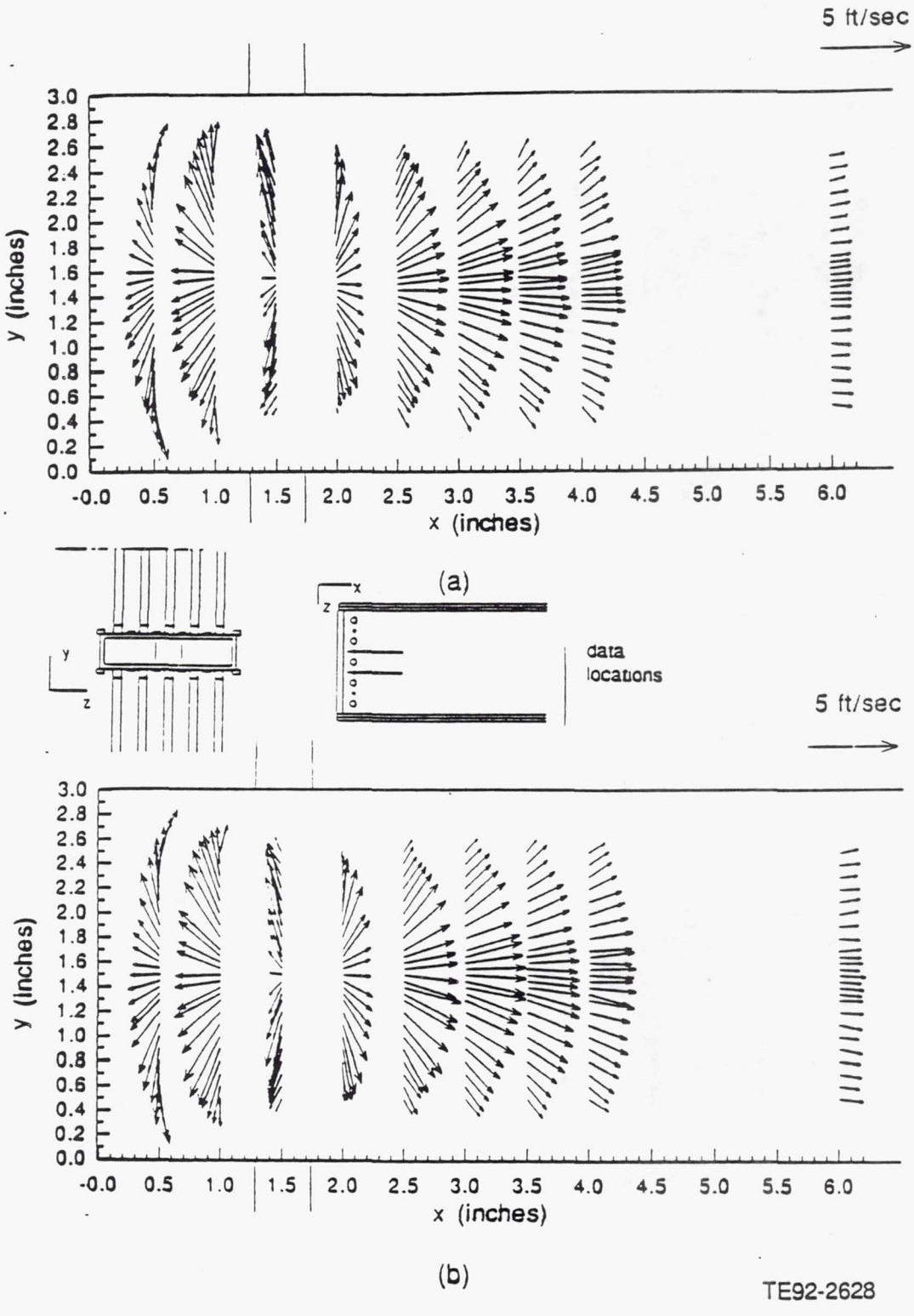

Figure 4.2.2-28. Primary jets only mean velocity vector plots a) z=6.0 in. b) z=9.0 in.

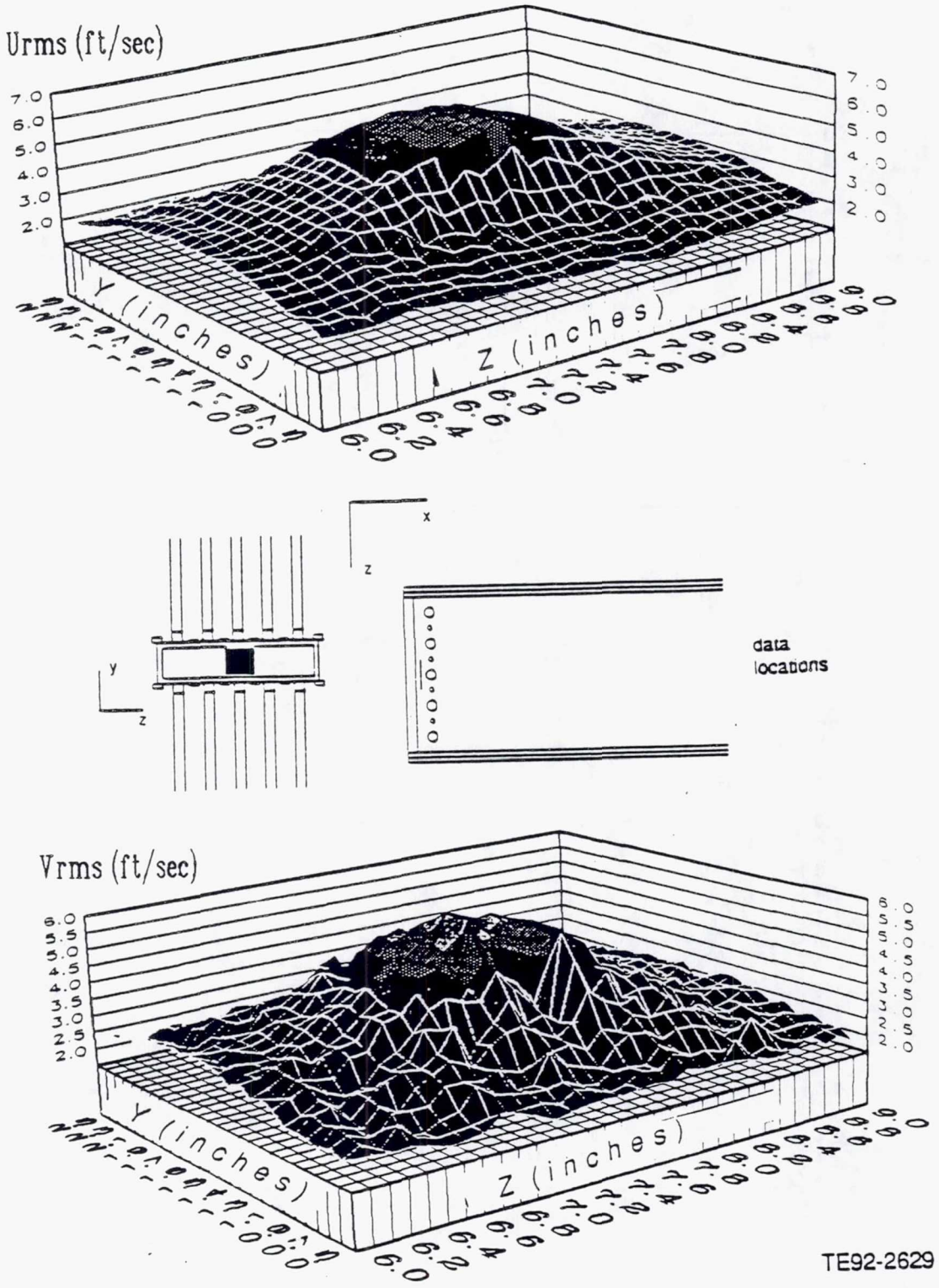

Figure 4.2.2-29. Primary jets only contour plot of U_{rms} and V_{rms} at x=0.5 in.

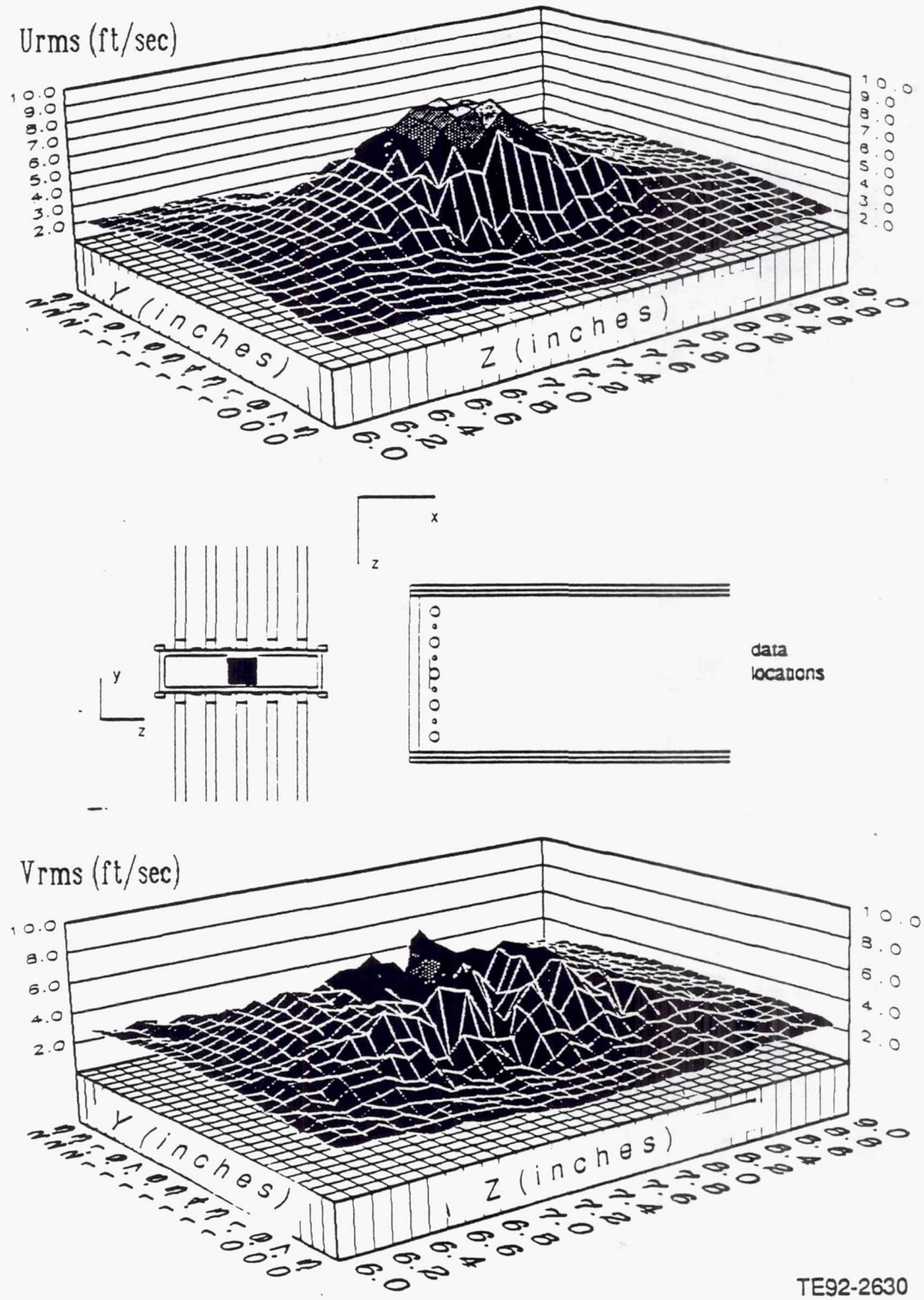

Figure 4.2.2-30. Primary jets only contour plot of U_{rms} and V_{rms} at x=1.0 in.

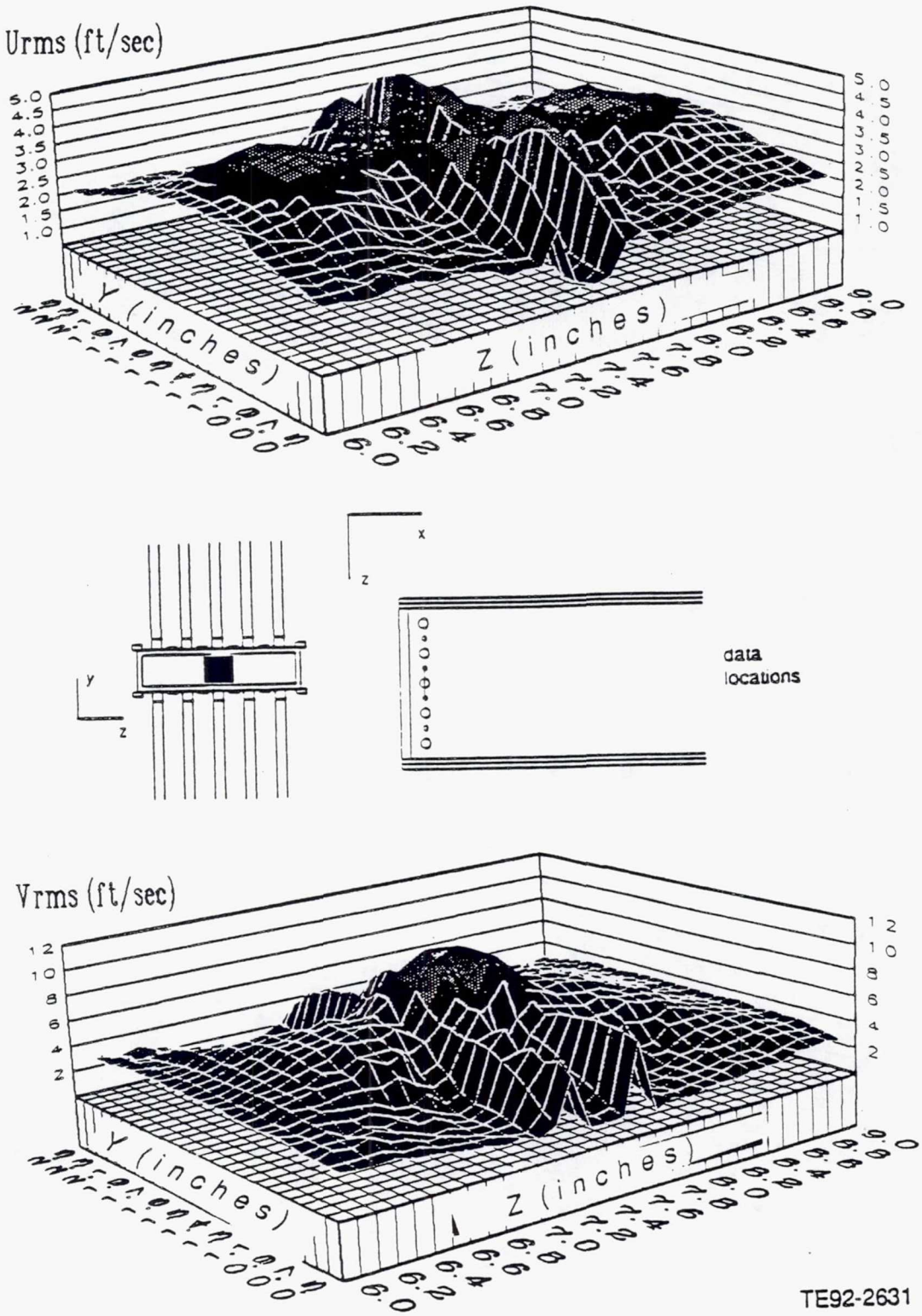

Figure 4.2.2-31. Primary jets only contour plot of U_{rms} and V_{rms} at x=1.5 in.

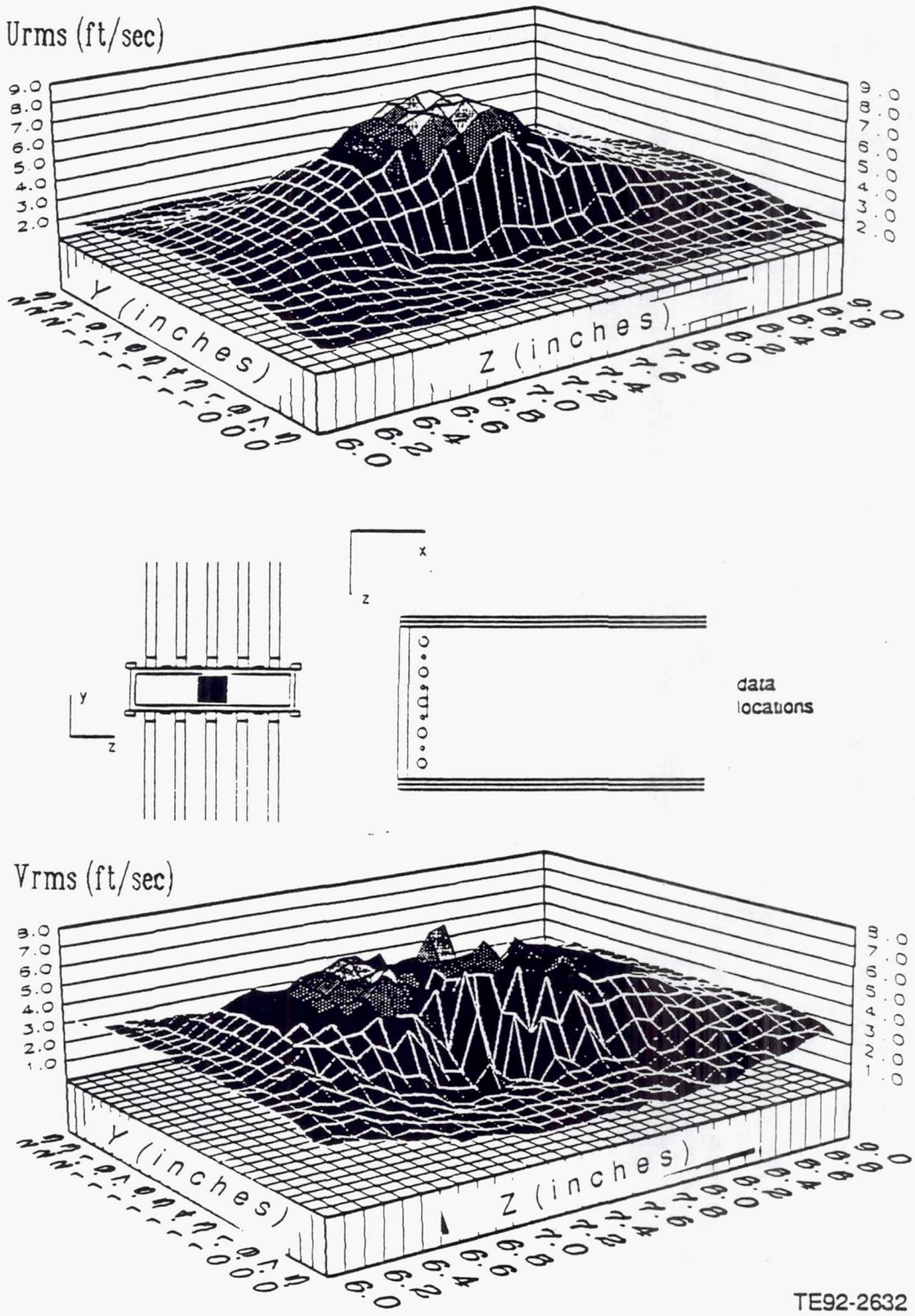

Figure 4.2.2-32. Primary jets only contour plot of U_{rms} and V_{rms} at x=2.0 in.

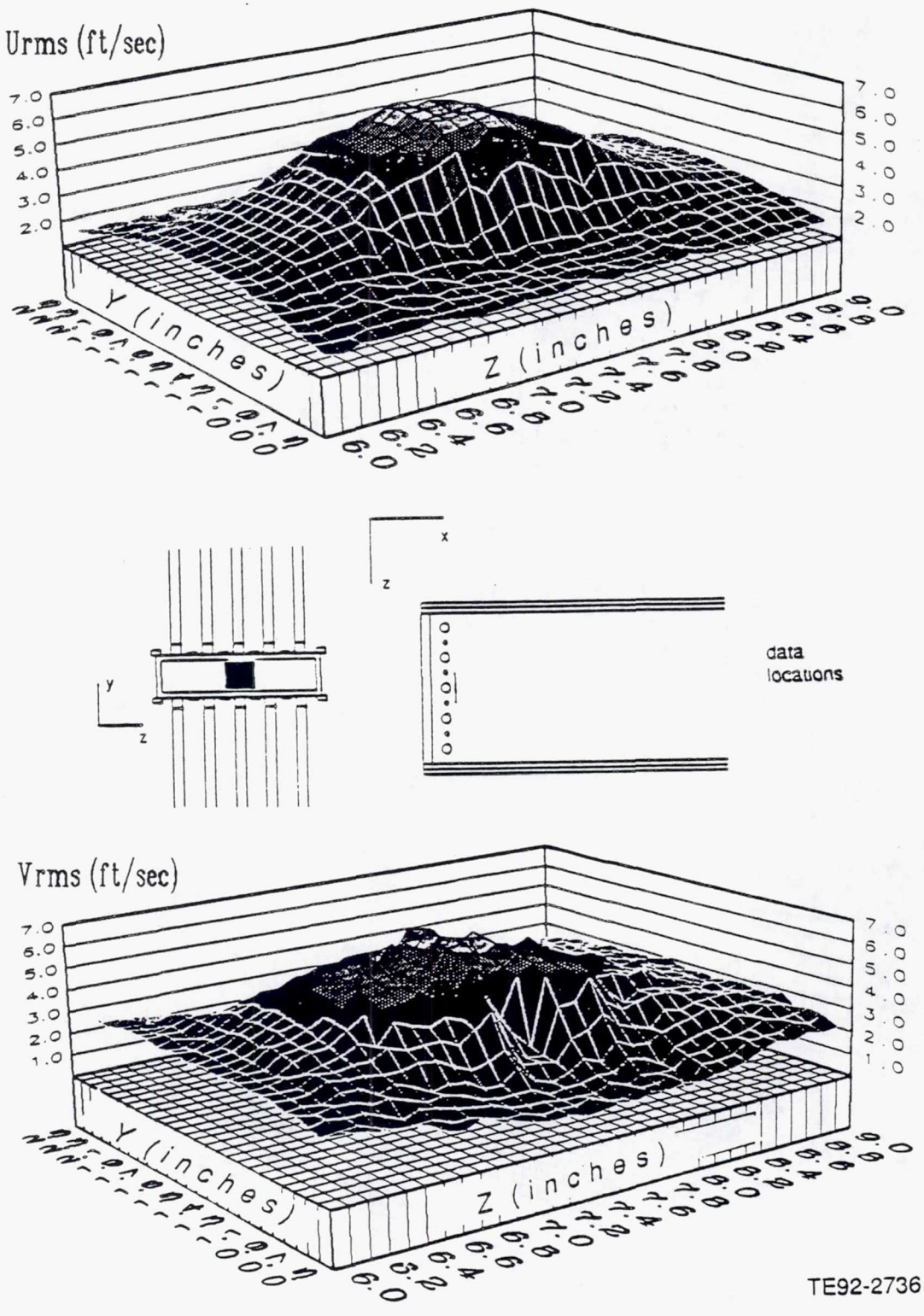

Figure 4.2.2-33. Primary jets only contour plot of U_{rms} and V_{rms} at x=2.5 in.

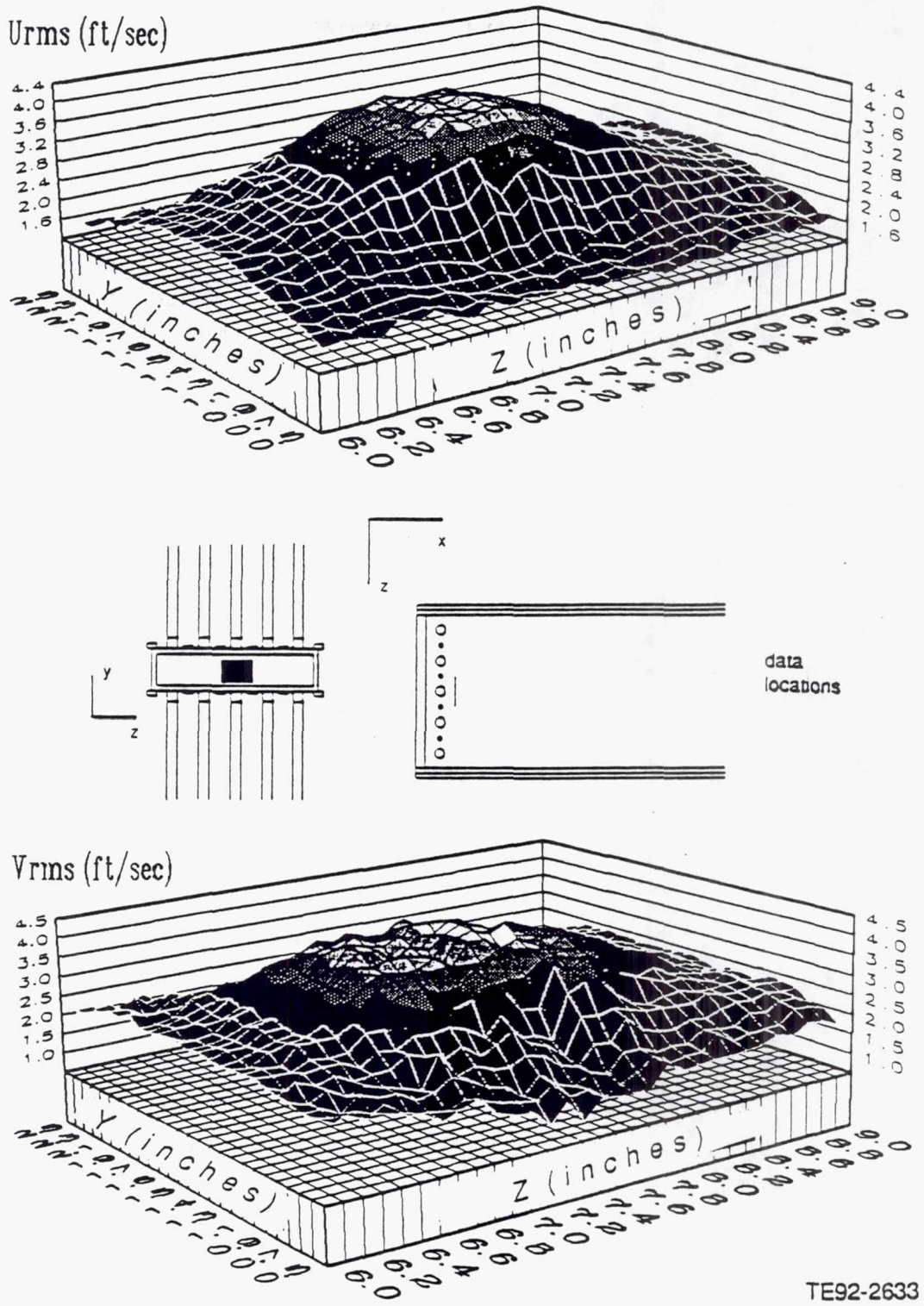

Figure 4.2.2-34. Primary jets only contour plot of U_{rms} and V_{rms} at x=3.0 in.

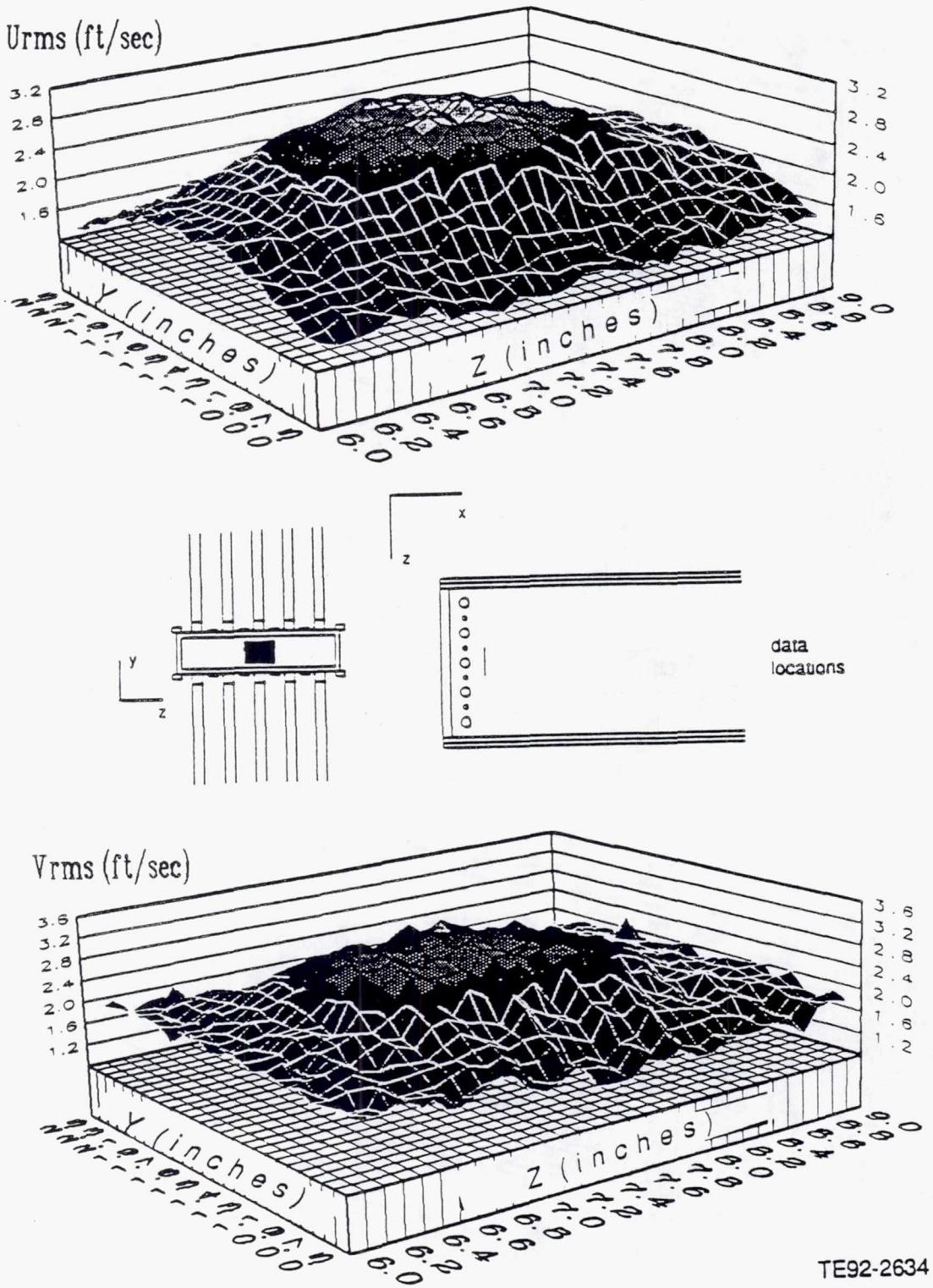

Figure 4.2.2-35. Primary jets only contour plot of U_{rms} and V_{rms} at x=3.5 in.

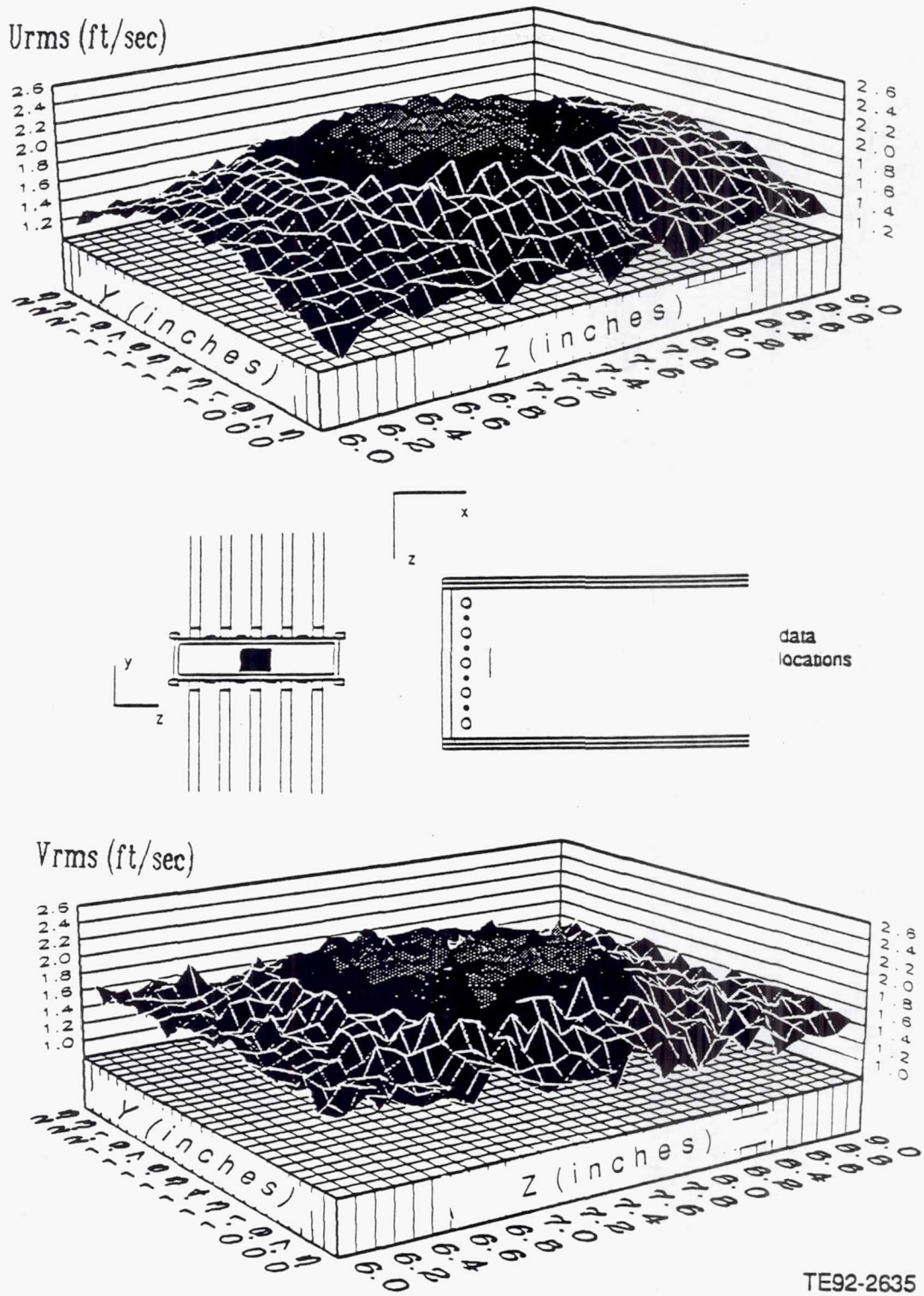

Figure 4.2.2-36. Primary jets only contour plot of U_{rms} and V_{rms} at x=4.0 in.

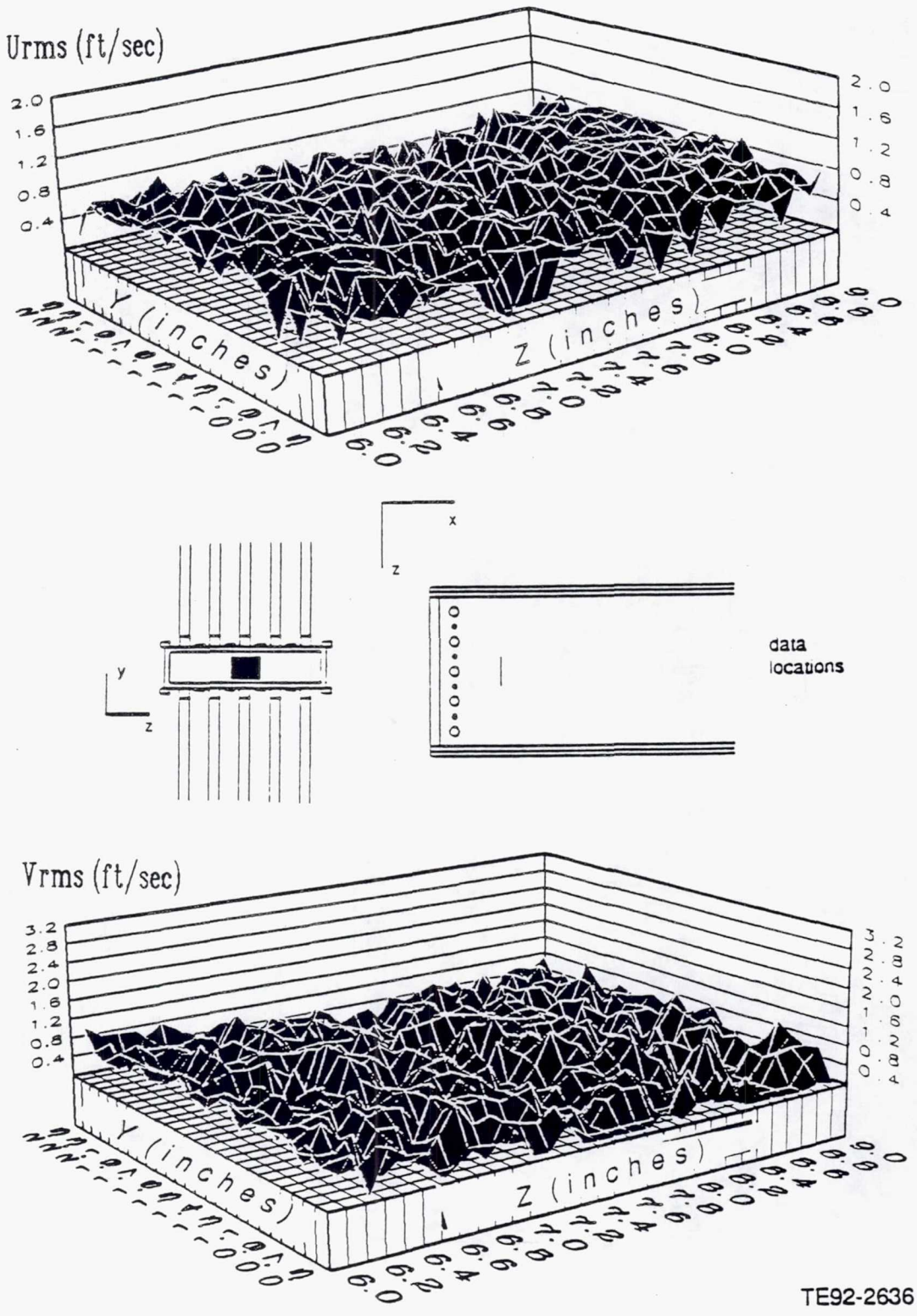

Figure 4.2.2-37. Primary jets only contour plot of U_{rms} and V_{rms} at x=6.0 in.

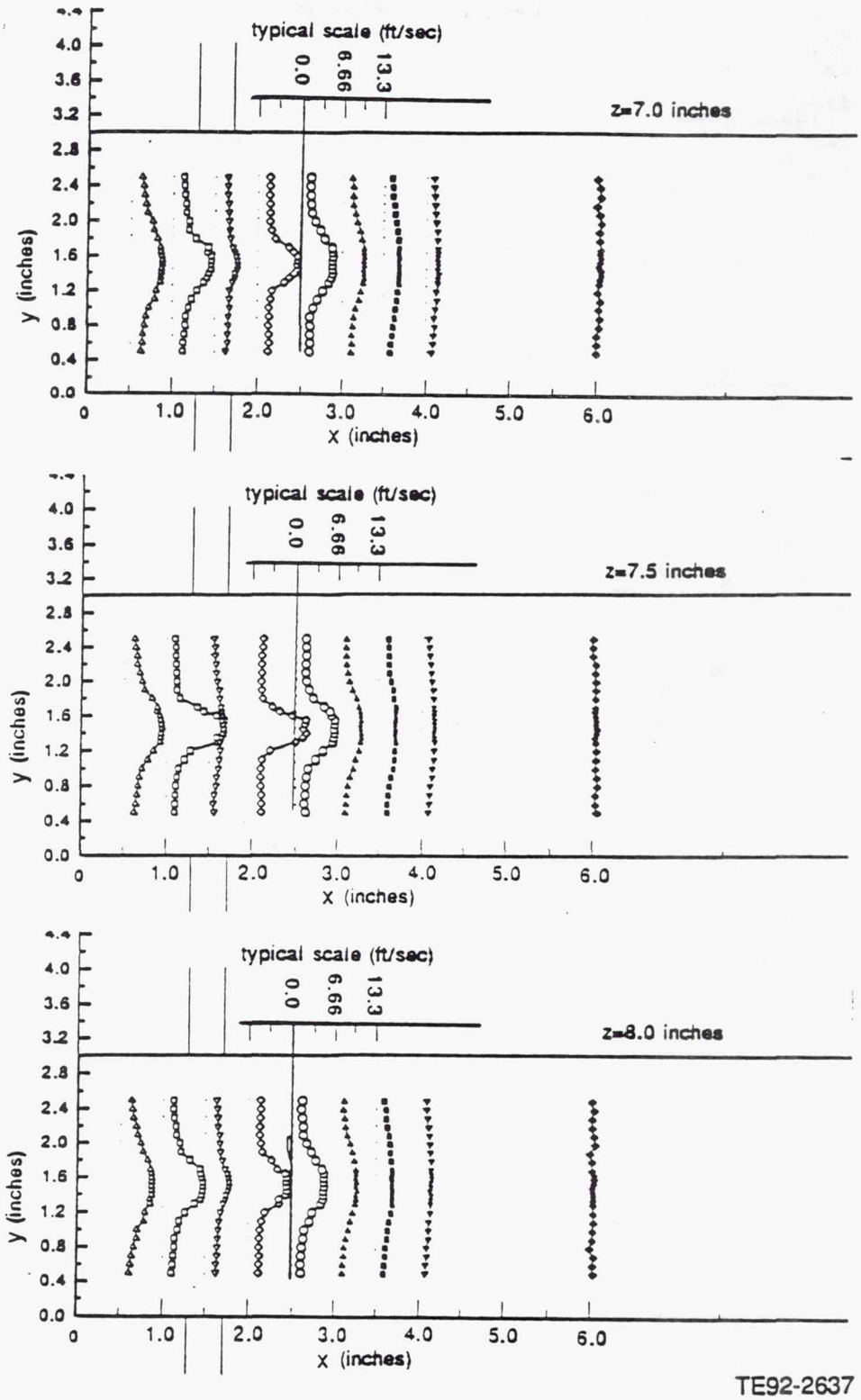

Figure 4.2.2-38. Primary jets only U_{rms} distribution.

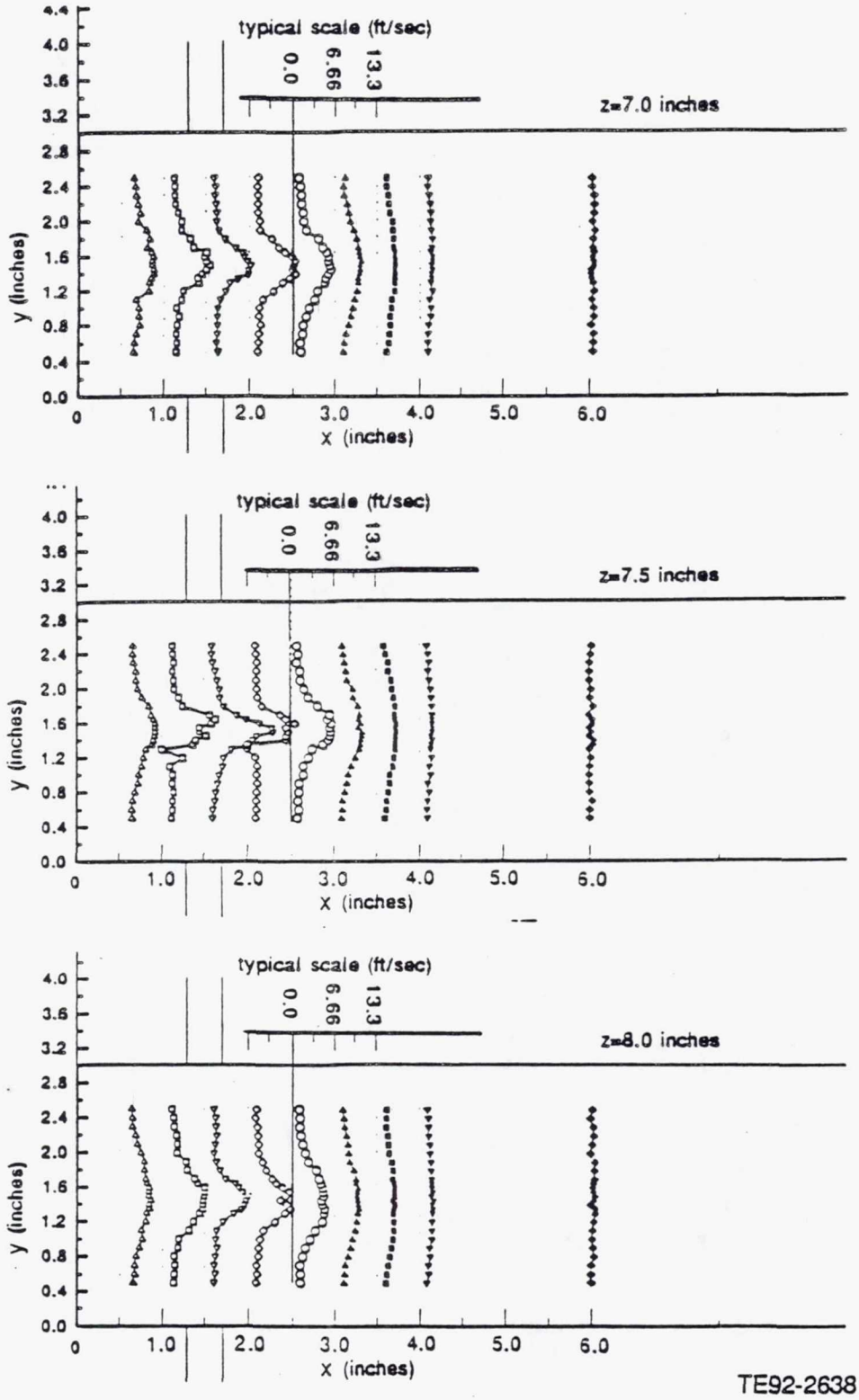

Figure 4.2.2-39. Primary jets only V_{rms} distribution.

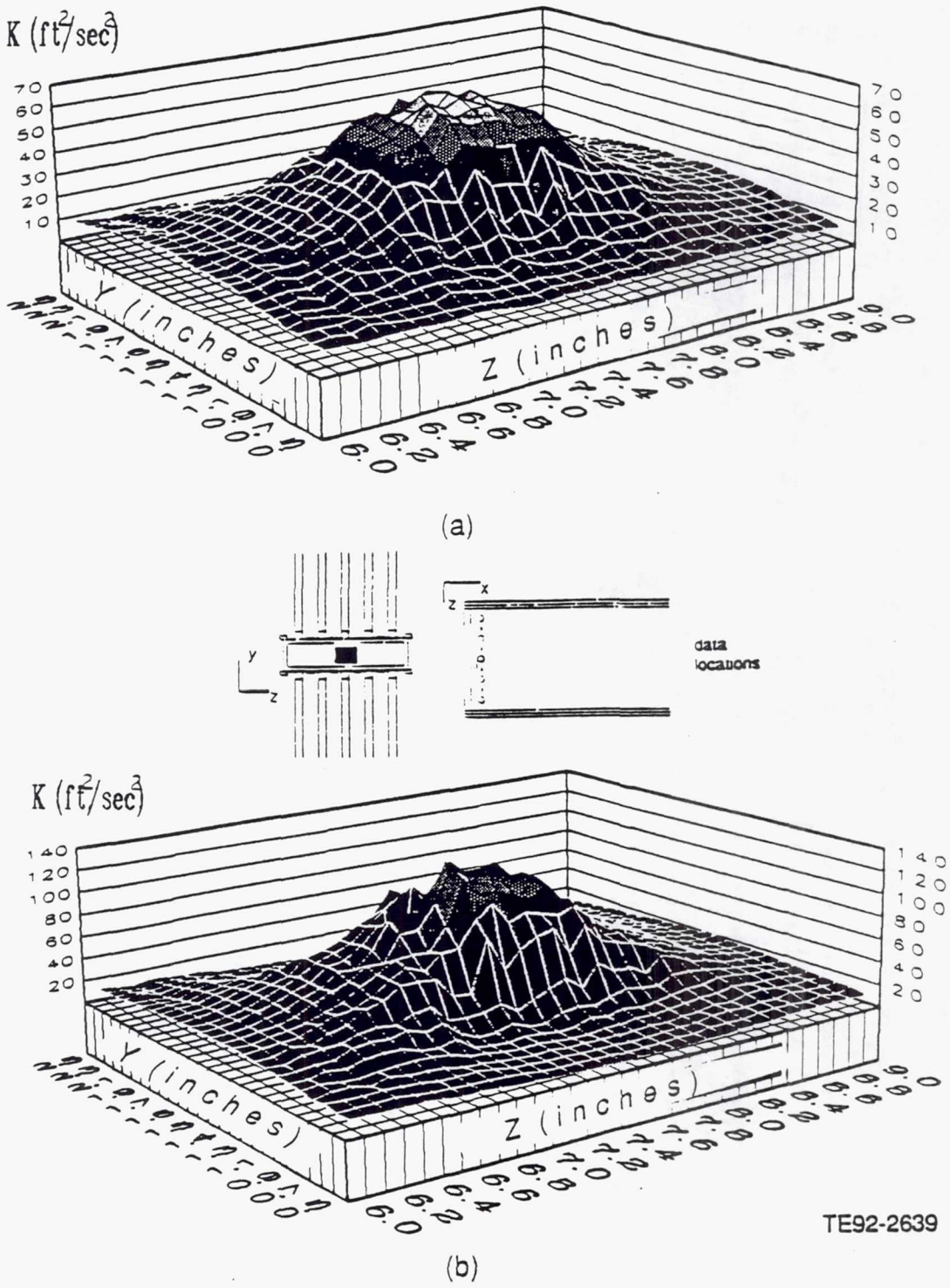

Figure 4.2.2-40. Primary jets only contour plot of K' at a) x=0.5 in. b) x=1.0 in.

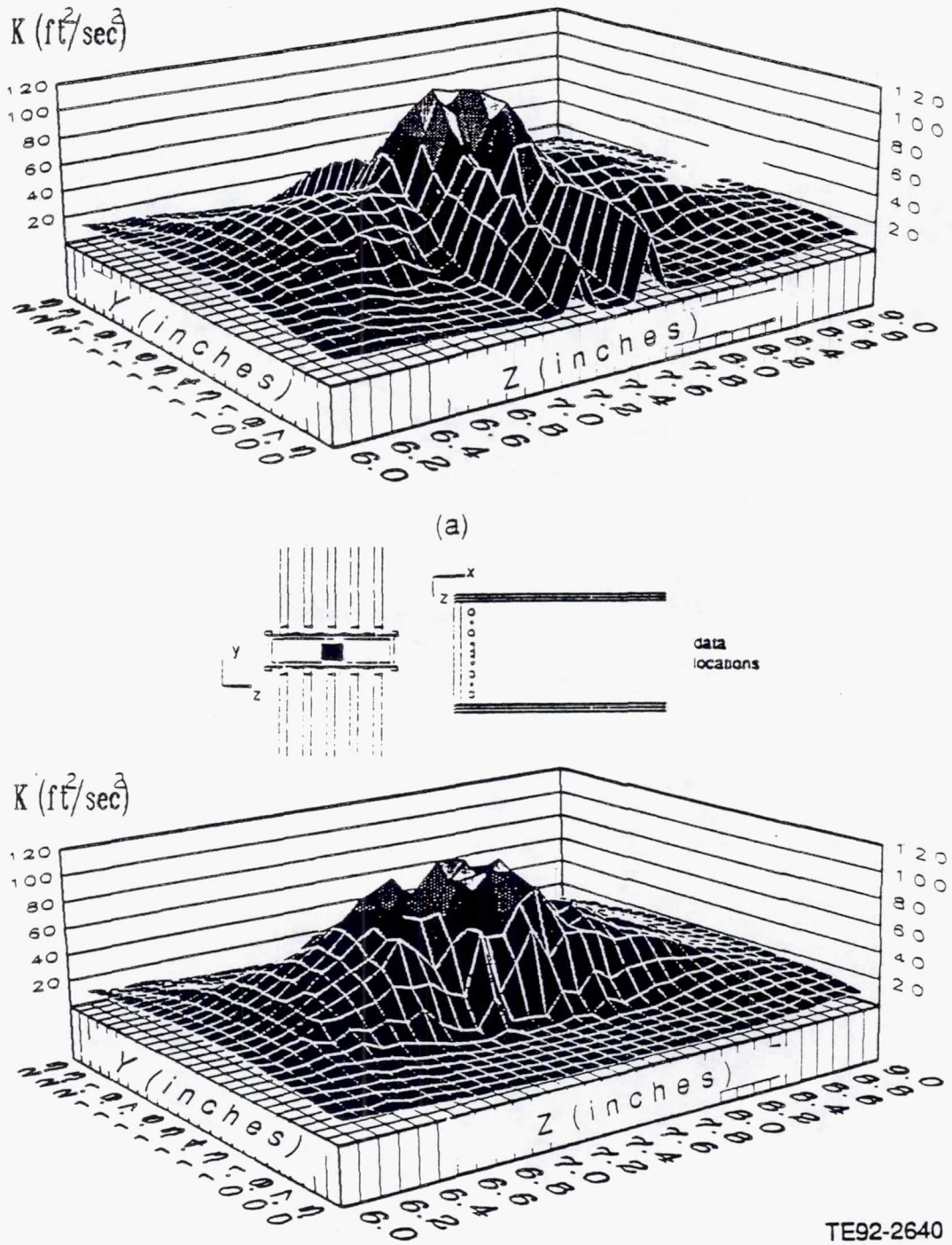

Figure 4.2.2-41. Primary jets only contour plot of K' at a) x=1.5 in. b) x=2.0 in.

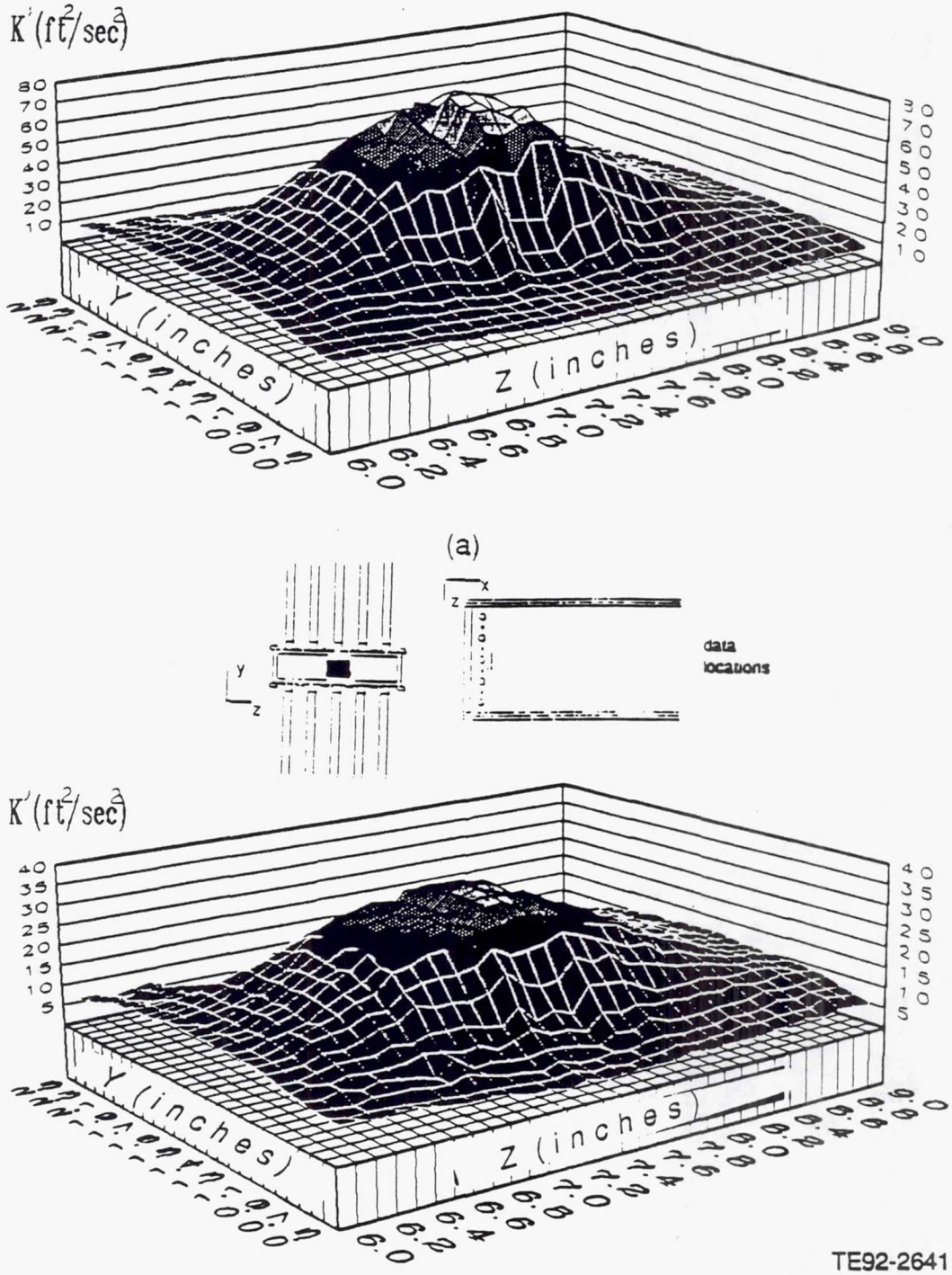

Figure 4.2.2-42. Primary jets only contour plot of K' at a) x=2.5 in. b) x=3.0 in.

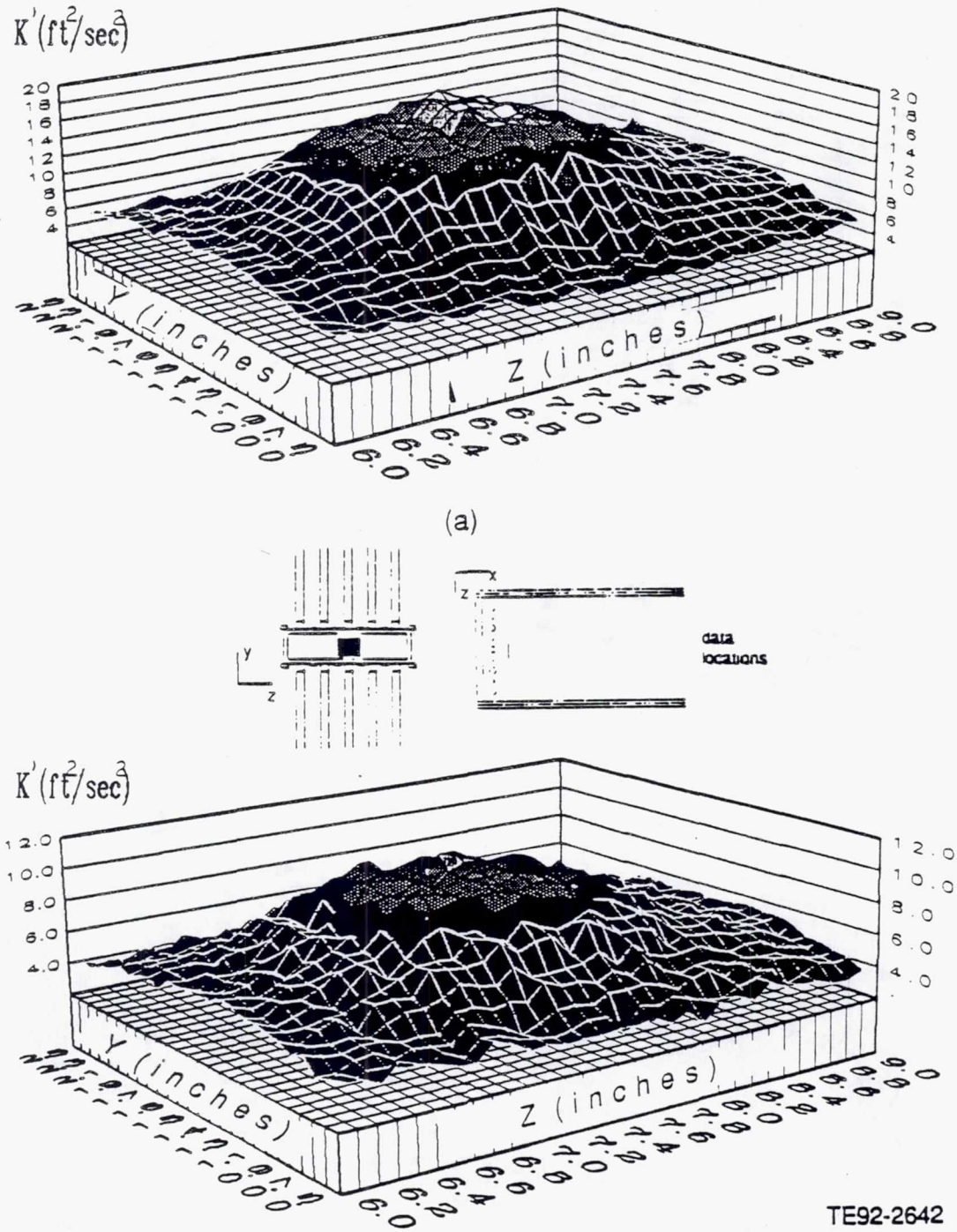

Figure 4.2.2-43. Primary jets only contour plot of K' at a) x=3.5 in. b) x=4.0 in.

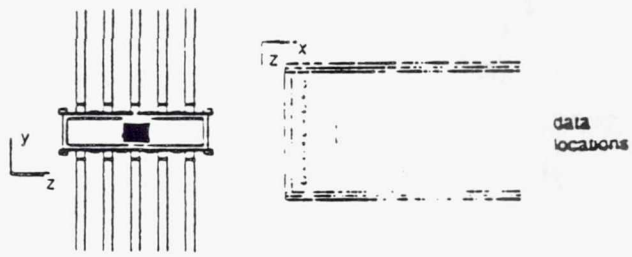

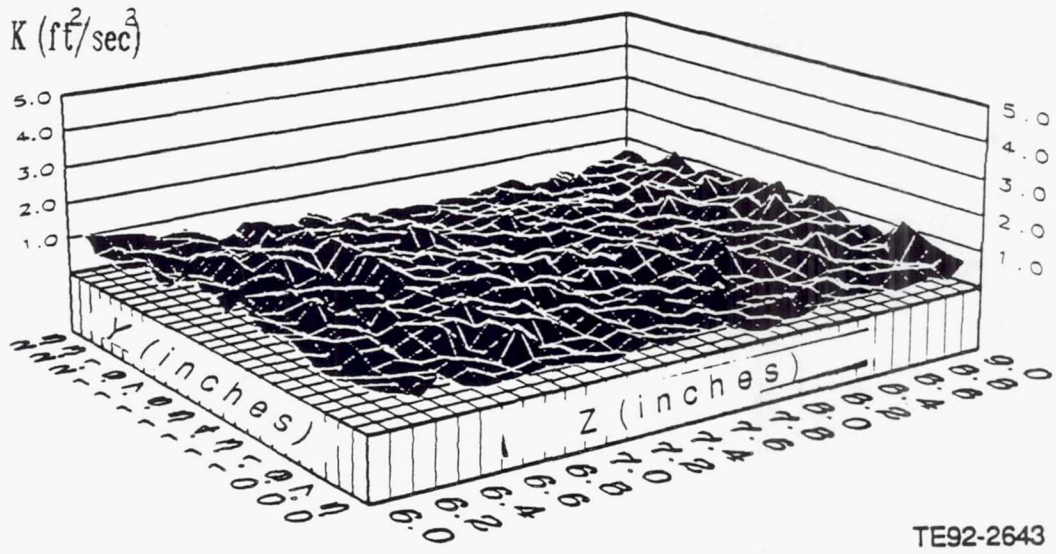

Figure 4.2.2-44. Primary jets only contour plot of K' at x=6.0 in.

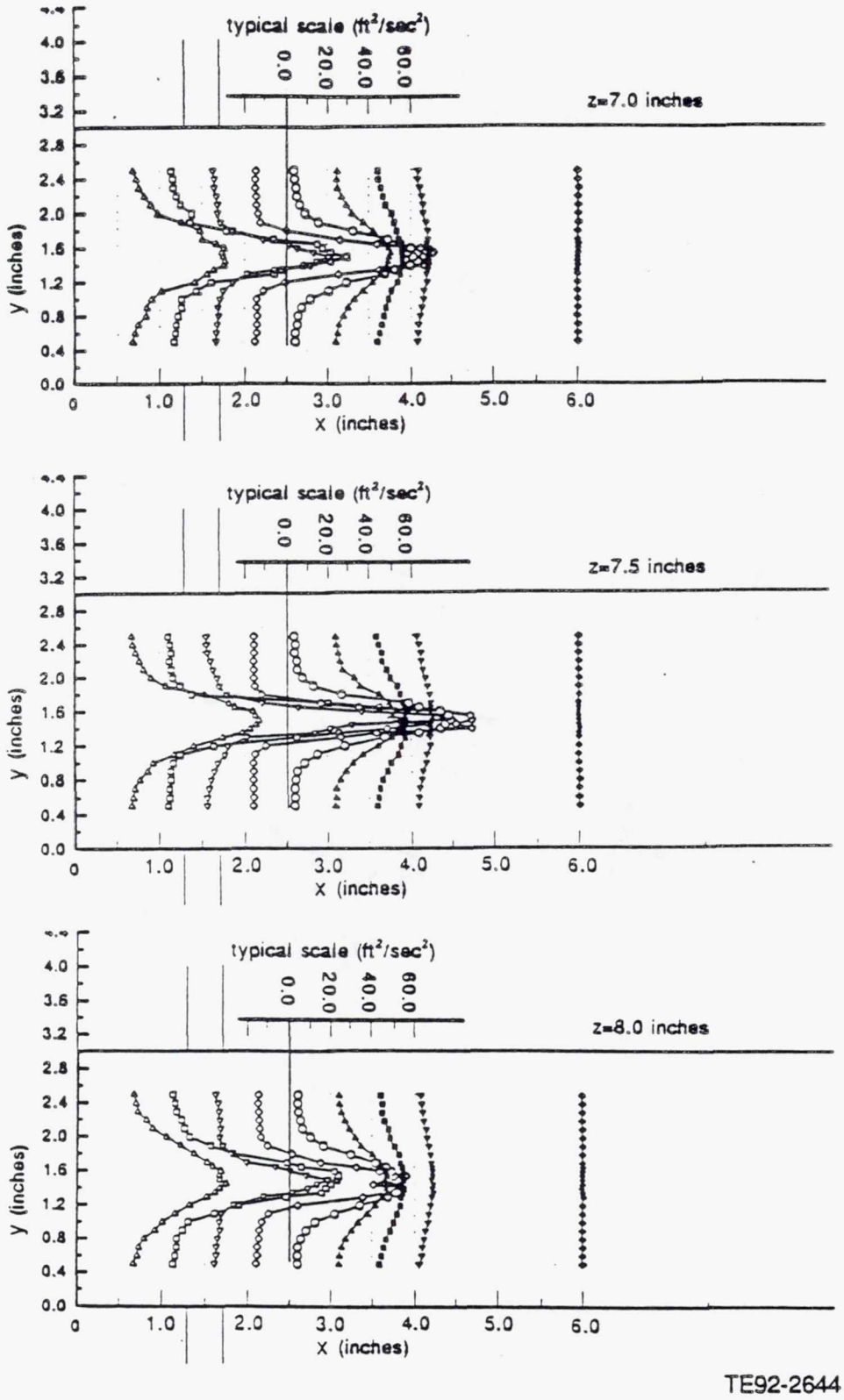

Figure 4.2.2-45. Primary jets only K' distribution.

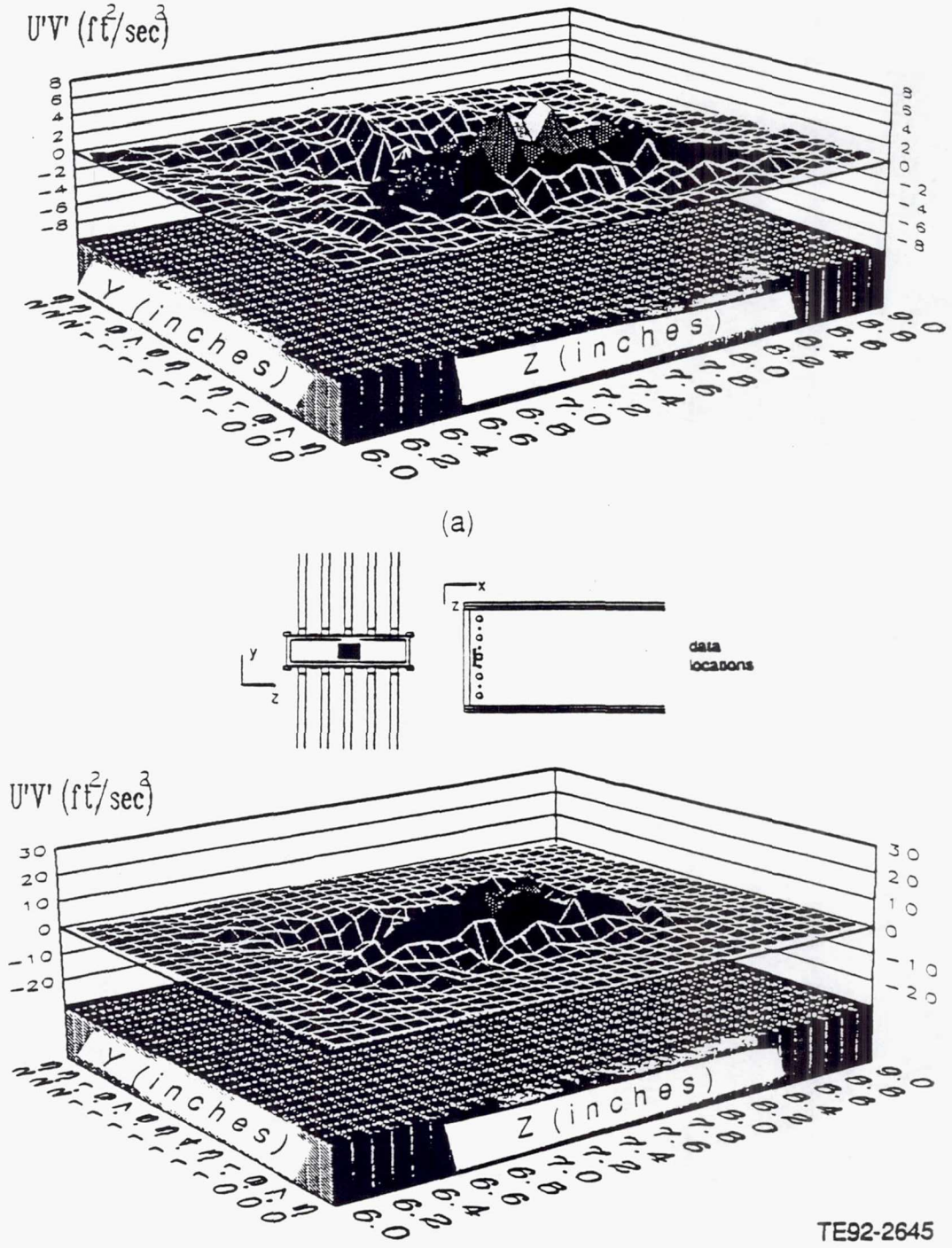

Figure 4.2.2-46. Primary jets only contour plot of U'V' at a) x=0.5 in. b) x=1.0 in.

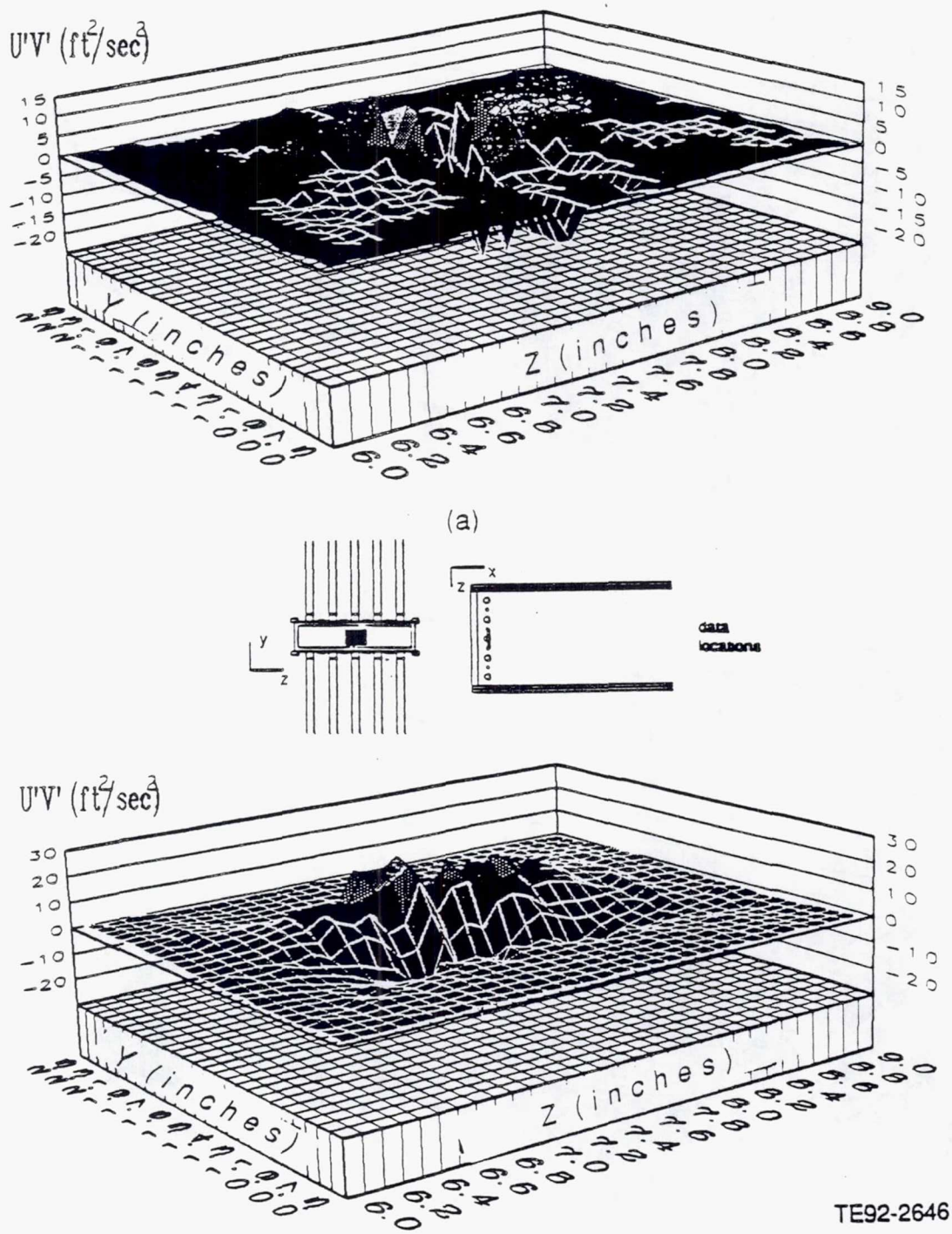

Figure 4.2.2-47. Primary jets only contour plot of U'V' at a) x=1.5 in. b) x=2.0 in.

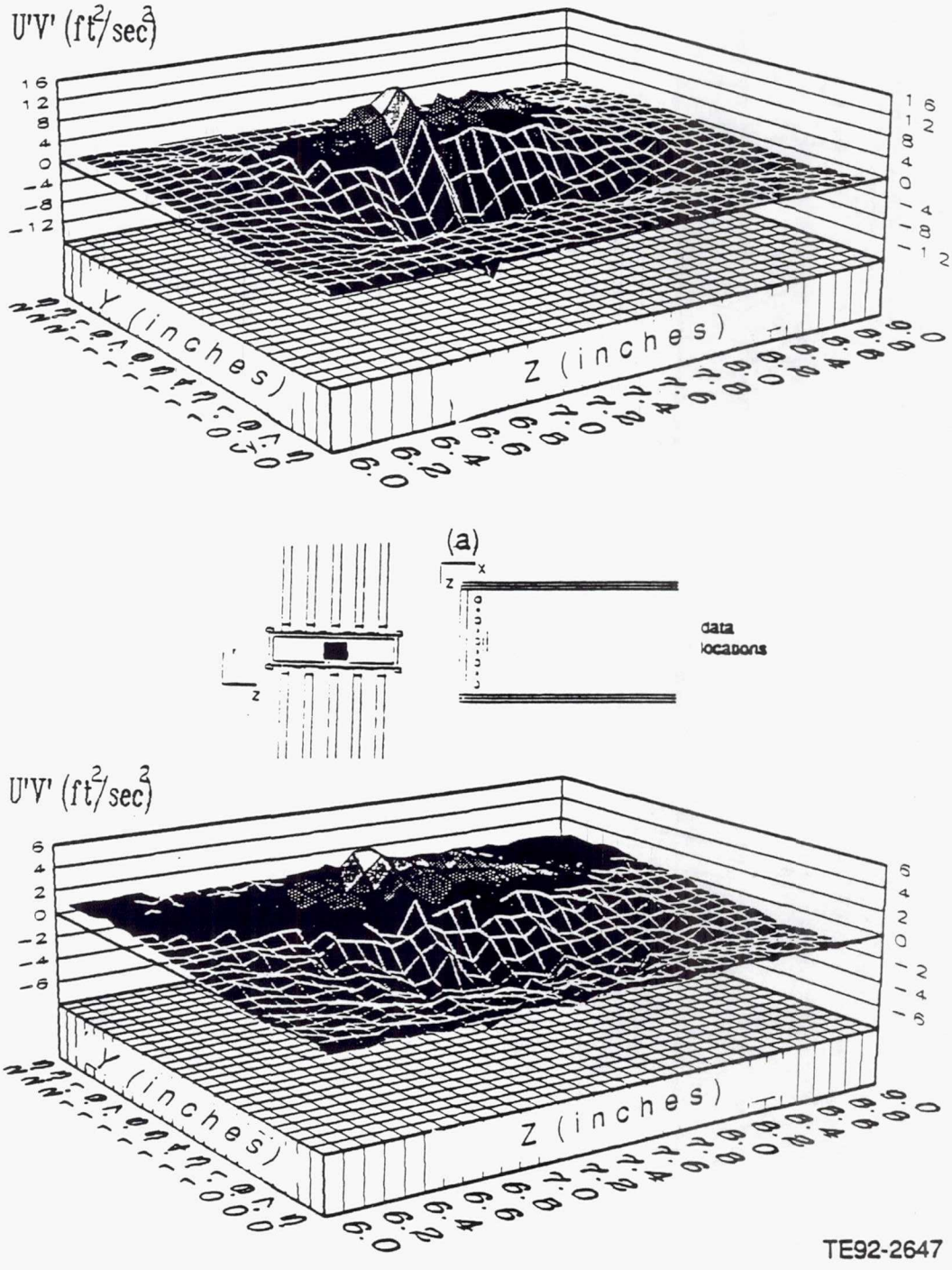

Figure 4.2.2-48. Primary jets only contour plot of U'V' at a) x=2.5 in. b) x=3.0 in.

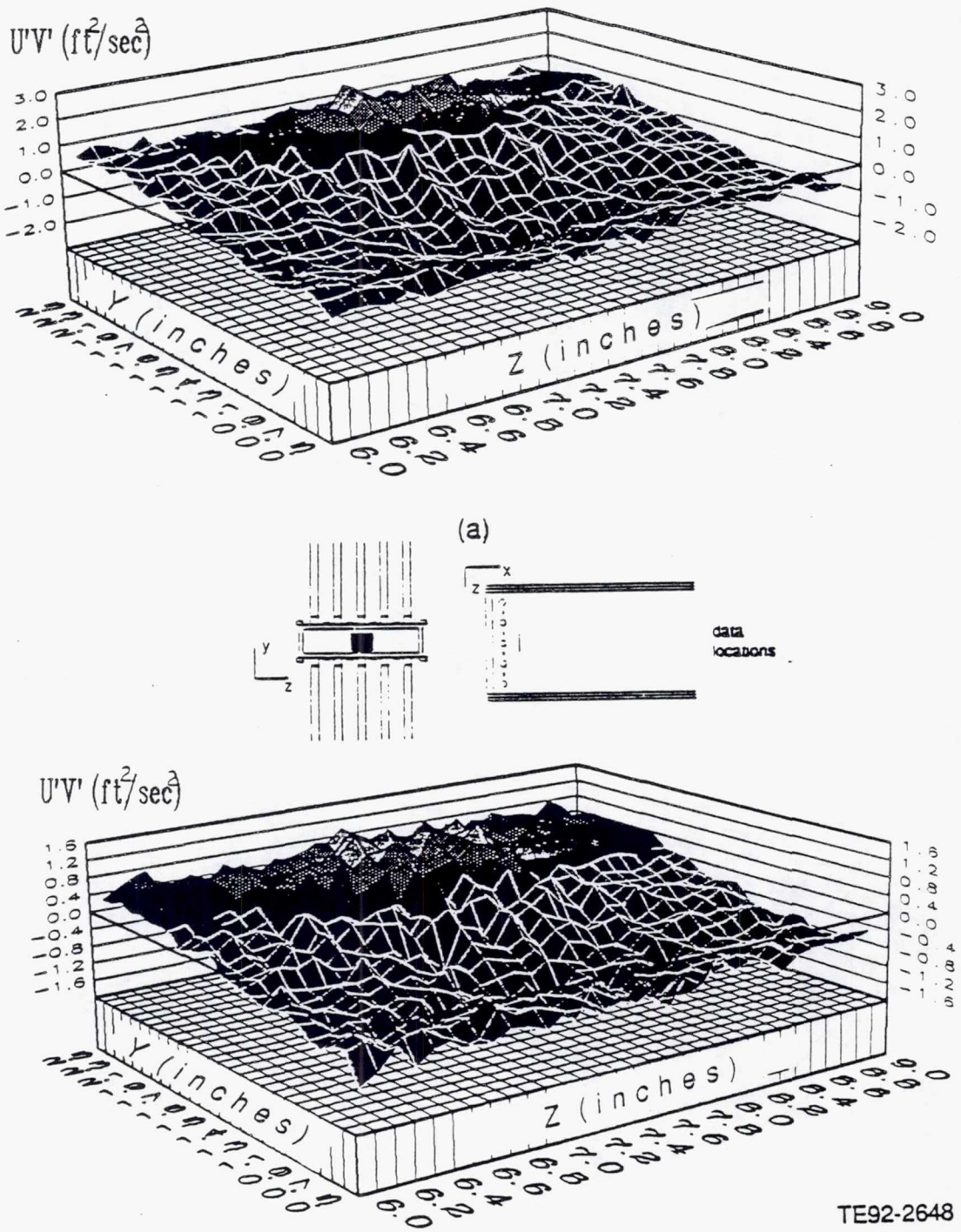

Figure 4.2.2-49. Primary jets only contour plot of U'V' at a) x=3.5 in. b) x=4.0 in.

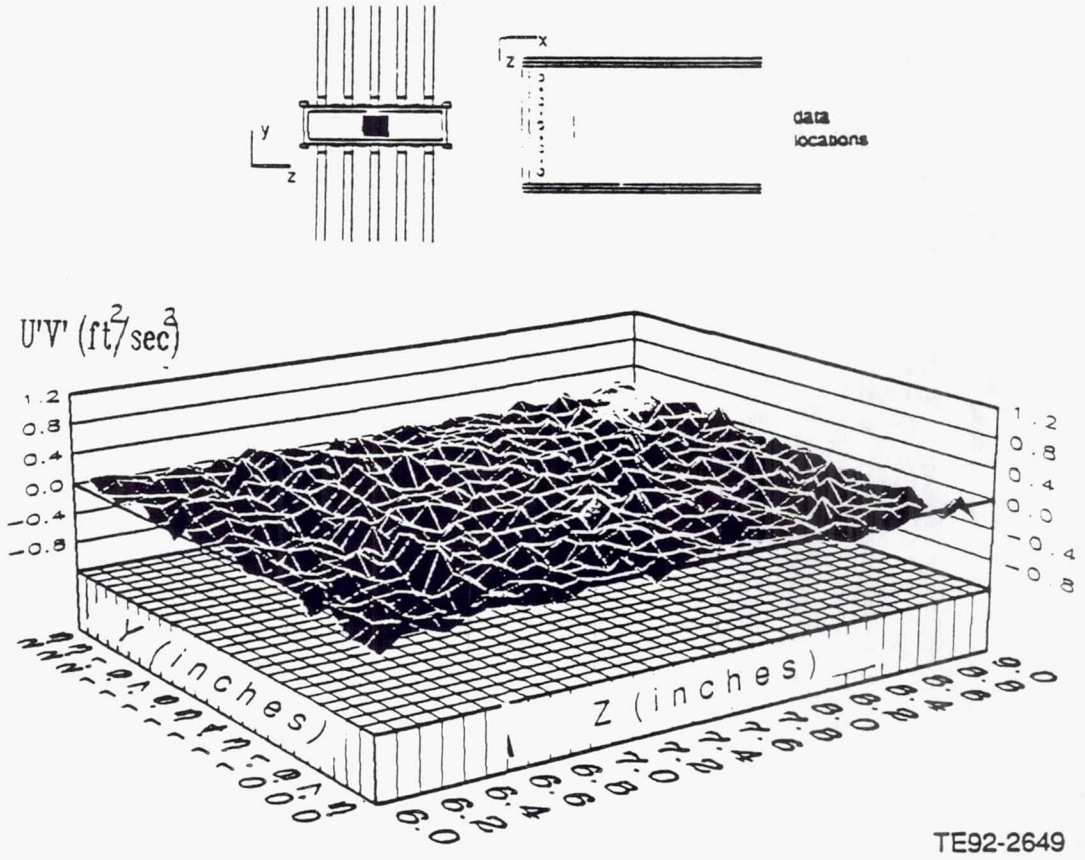

Figure 4.2.2-50. Primary jets only contour plot of U'V' at x=6.0 in.

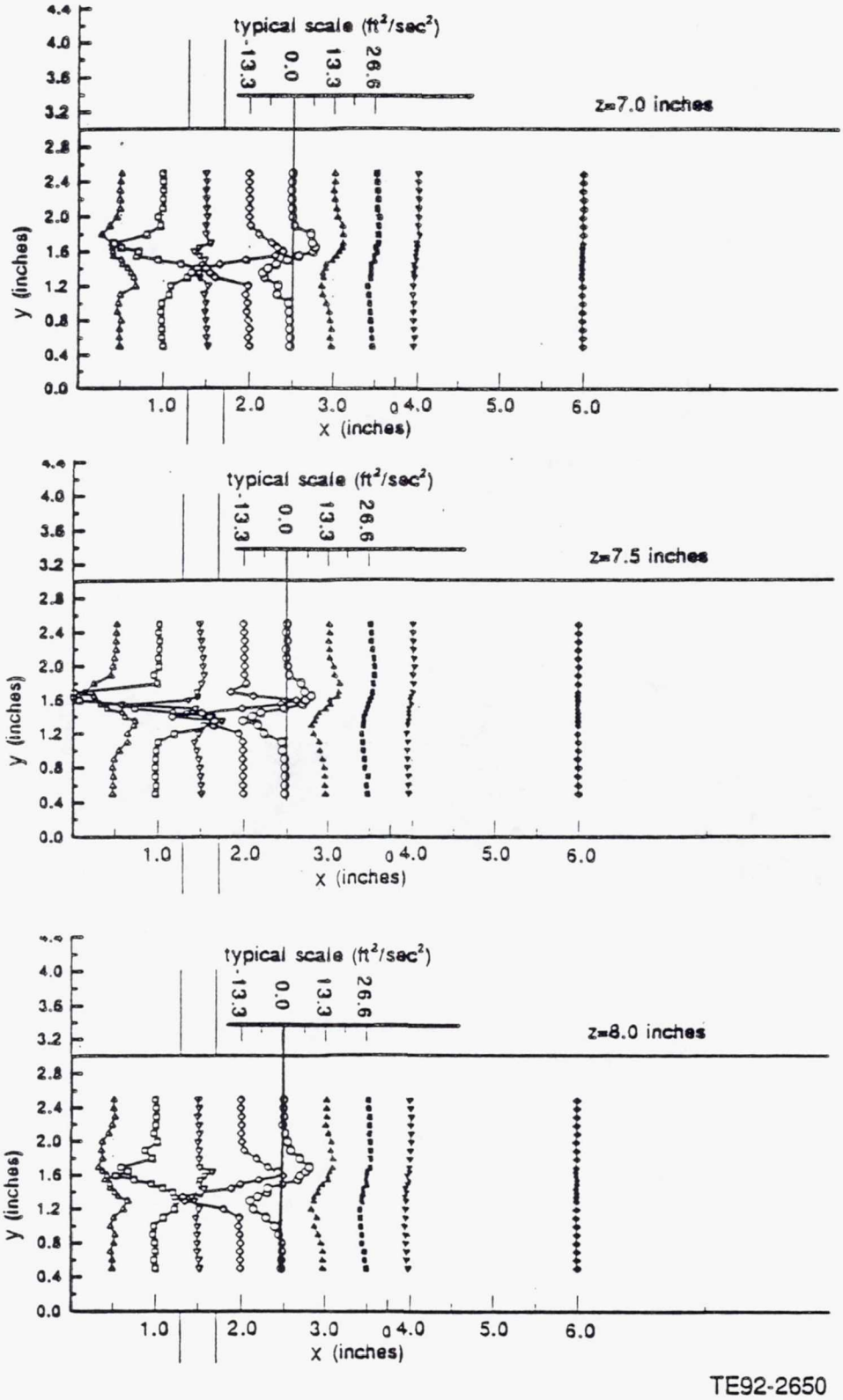

Figure 4.2.2-51. Primary jets only U'V' distribution.

4.3 DOME ANNULAR JETS AND PRIMARY JETS

Figure 4.3-1 shows a drawing of the annular and primary jet configuration. The following two subsections present the concentration and velocity measurements, respectively.

4.3.1 Dome Annular Jets and Primary Jets - Concentration Measurements

For the annular and primary jets, case marker particles were introduced into the combustor model through the annular jets only and through the lower primary jet. This allowed the observation of the mixing between the annular and primary jets.

4.3.1.1 Smoke in Primary Jets

Results for smoke in the lower primary jet with annular jet flow are shown in Figures 4.3.1-1 through 4.3.1-12. Figures 4.3.1-1 and 4.3.1-2 show single and 127 frame average at z=7.5 in. The effect of the annular jet can be seen by the bending of the flow from the primary jets downstream. The single frame picture has higher concentrations of smoke from the lower primary jet downstream than the averaged picture, thus demonstrating the unsteadiness of the flow. In the averaged pictures of the planes at z=7.0 and 8.0 in. (Figures 4.3.1-3 through 4.3.1-6) higher concentrations of smoke are seen in the corners and along the upper and lower walls. Similarity between planes is also seen as demonstrating symmetry.

Line and 3-D plots of the mean concentration are in Figures 4.3.1-7 through 4.3.1-12. At z=7.5 in., the influence of the annular jet on the primary jets is clearly apparent. Most of the smoke entering from the primary jet is pushed downstream, with very little smoke being mixed upstream of the upper primary jet. In comparison with Figure 4.3.1-7, with no annular flow, concentration levels of five to six times larger exist in the same area. Downstream of the primary jets, concentration profiles between the upper and lower walls smooth out with peak values on the lower side of the centerline. As the planes move farther away from the centerplane, the maximum concentration levels occur just above the rig centerline. Concentration levels along the upper half of the rig for $x < 1.5$ in. remain relatively small compared to the levels when no annular jet flow is used (Figures 4.3.1-7 through 4.3.1-11).

Figure 4.3.1-12 presents a comparison of concentration profiles along the primary jet axis for z=6.5 to 8.5 in. Symmetry between planes at z=7.0 and 8.0 in. and z=6.5 to 8.5 in. is seen to exist with the largest deviation between the plots along the upper wall of the rig. Comparison with Figure 4.3.1-12, with no annular jet flow, shows reduced concentration levels in the middle and upper half of the rig when the annular jet is on.

4.3.1.2 Smoke in Annular Jet

Results for smoke entering the annular jet with primary jets on are shown in Figures 4.3.1-13 through 4.3.1-23. Single frame and 127 frame averages for the z=7.5 in plane are given in Figures 4.3.1-13 and 4.3.1-14. Single and average frames are similar in appearance. Higher concentrations downstream of the primary jets is present for the single frame picture, while the average picture has a more uniform distribution between walls. At z=7.0 and 8.0 in. (Figures 4.3.1-15 through 4.3.1-18) the average frames show higher concentrations in the corners and along the upper and lower walls of the rig, similar to when smoke was in the primary jets.

Mean concentrations are plotted in Figures 4.3.1-19 through 4.3.1-23 with smoke in the annular jet. From the z=7.5 in. plane, the annular jet flow has a flat concentration distribution between upper and lower walls, up to the primary jet entrance. The smoke is then squeezed between the primary jets and gradually spreads out between upper and lower walls downstream. Farther from the centerplane, the concentration distribution flattens out. Distributions in the z=7.0 and 8.0 in. planes have constant values near the walls and flat top profiles across the annular jet inlet upstream of the primary jets. At z=6.5 and 8.5 in. this is not seen, and higher concentrations are downstream of x=1.5 in. Higher concentrations exist on

the upper than on the lower walls in all these plots, possibly indicating nonuniform smoke in the annular jet or Gaussian beam effects in the laser sheet.

4.3.2 Dome Annular Jets and Primary Jets - Velocity Measurements

Figure 4.3.2-1 presents the three-view drawing for this case. The five pairs of primary jets were centered 1.5 in. downstream of the annular jet entrance.

4.3.2.1 Inlet Conditions

To establish inlet conditions for this case the same type of measurements made on the primary jets for the primary jets only case were performed along with measurements of the annular jet described earlier. Figures 4.3.2-2 through 4.3.2-8 present contour plots of the mean and rms velocity of the lower primary jet. Figure 4.3.2-2 shows the mean velocity distribution at y=0.1 in. above the lower primary jet. Again, a flat top profile similar to the primary jets only results is seen. A mean velocity of 15.4 ft/sec is present resulting in a Reynolds number of 3528. The rms velocity shows peak values along the edges of the jet at z=7.7 in. and z=7.35 in. and lower peaks along edges at x=1.35 in. and x=1.7 in. Errors due to probe volume length and the grid spacing produce this result. In addition, higher fluctuations occur on the upstream side of the jet, $x < 1.3$ in., than on the downstream side, due to a recirculation zone at this edge of the jet.

Measurements taken in the planes at y=0.25, 0.5, 0.75, 1.0, and 1.25 in. (Figures 4.3.2-2 through 4.3.2-7) show the development of this jet as it enters the combustor model. The mean velocity of the jet can be seen to gradually decrease, and the jet appears to bend downstream as more and more fluid is entrained by the jet and the crossflow from the annular jet mixes with the jet. Comparison of these data with those obtained for the primary jets only case (Figures 4.2.2-5 through 4.2.2-9) demonstrates the effect of the annular jet on the primary jet flow. In addition, negative velocities are clearly evident on the upstream side of the primary jet for planes up to y=1.0 in., while the downstream side of the jet has velocities between 0.5 to 2 ft/sec. This is caused by a clockwise rotating recirculation zone between the endplate and the upstream side of the primary jet. These negative velocities are seen to disappear at y=1.0 in., due to the annular jet crossflow.

The rms velocities in Figures 4.3.2-2 through 4.3.2-7 show increased fluctuations on the upstream side of the primary jet until the y=1.0 in. plane is reached. Larger fluctuations are evident on the downstream side of the jet for y=1.0 and 1.25 in. This change in turbulence is due to the deflection of the primary jet by the annular jet and the formation of a rear recirculation zone at the downstream edge of the jet.

The jet stagnation point is reached at the y=1.5 in. plane (Figure 4.3.2-8). The mean velocity is similar to Figure 4.2.2-10 for the primary jets only case. The mean velocity is seen to fluctuate about zero due to the unsteady fluctuations of this stagnation point. A difference is visible between the rms velocities in Figure 4.3.2-8 and Figure 4.2.2-10 for the primary jets only case. For this case, the rms velocity steadily increases farther downstream, while for the primary jets only case the maximum fluctuations occur around the center of the jet. The annular jet crossflow causes a severe bending in the primary jet, producing this increased turbulence downstream farther than at the center of the plot.

A comparison between the upper and lower primary jets can be seen in Figure 4.3.2-9. Only approximately a 2.5 % difference is seen between the upper and lower jets maximum velocity. The rms velocity comparison again shows close agreement between upper and lower jets. Increased turbulence is also evident on the upstream side of the primary jet due to a recirculation zone.

Figure 4.3.2-10 shows the annular jet inlet velocities taken on four edges of the annular jet at 0.08 in. from the inlet. A very flat velocity distribution similar to Figure 4.1.2-2 for the annular jets only case can be seen. A mean velocity of 15.8 ft/sec is present in the center of the annular gap. The rms velocity

shows larger peak values for the right and left sides of the annular jet due to the probe volume length being nearly five times larger than the grid points.

4.3.2.2 Mean Flowfield Results

Figure 4.3.2-11 provides details of the xy plane sampling grids. Vector plots for the annular and primary jets case are presented in Figures 4.3.2-12 through 4.3.2-27. The centerplane is seen in Figure 4.3.2-12. The flow issuing from the annular jet can be seen entering at y=0.85 and y=2.15 in. This flow penetrates up to the primary jets inlet at x=1.5 in. and then is turned parallel to the primary jets forming recirculation zones outside the annular region, $y < 0.7$ in. and $y > 2.3$ in., and in the center of the annular region. The primary jets can be seen bending downstream due to the annular jet interaction. Downstream of the primary jet inlet, the flow accelerates between two recirculation zones on the upper and lower walls of the rig. This flow slowly diffuses as the recirculation zones shrink in size downstream.

The recirculation zones are clearly visible with the aid of streamlines. The rear recirculation zones show symmetric placement between upper and lower portions of the rig. The two forward recirculation zones centered in the annular region also show symmetric placement. Two additional recirculation zones outside of the annular region are also present, but since they are outside the measurement grid they do not stand out as clearly.

Comparison between planes at z=7.4 and z=7.6 in. (Figure 4.3.2-13) shows similar results. The rear recirculation zones at the z=7.4 in. plane can be seen to be slightly forward of the recirculation zones at the z=7.6 in. plane. In addition, the flow is seen to bend toward the lower wall at the z=7.4 in. plane, while there is no bending in the z=7.6 in. plane. The two forward recirculation zones are symmetric between planes at x=1.0 in., y=1.85 in. and x=1.0 in., y=1.1 in., for the upper and lower zones respectively.

Figure 4.3.2-14 shows plots at z=7.3 and 7.7 in. Symmetric flow between planes can be seen, while symmetry between upper and lower portions of the rig does not exist. Rear recirculation zones are located at approximately x=2.85 in., y=2.1 in. for the upper zone and x=3.05 in., y=0.9 in. for the lower zone. The placement of the upper recirculation zone forward of the lower recirculation zone indicates that the reattachment point occurs farther upstream for the lower recirculation zone. Asymmetry can also be seen for the forward recirculation zones in the z=7.7 in. plane. Placement of the forward recirculation zones in the z=7.3 in. plane is symmetric.

Planes at z=7.2 in and z=7.8 in. are seen in Figure 4.3.2-15. Rear recirculation zones here are symmetric between planes and between upper and lower halves of the rig. Forward recirculation zones are clearly present at z=7.2 in., but are very disordered at z=7.8 in. These planes are outside the primary jet inlet diameter, and therefore more of the flow moves directly downstream instead of being entrained into the forward recirculation zones.

More vector plots are seen in Figures 4.3.2-16 through 4.3.2-27. The annular jet inlet extends between 6.8 in $\leq z \leq$ 8.2 in., where a finer grid was used. Table 4.3-I presents approximate forward and rear recirculation zone centers. From this table, some trends are evident about the recirculation zones. The forward recirculation zones placement is steady between 7.2 in. $\leq z \leq$ 7.8 in. Outside these limits no center is well defined within the measured portion of the flow. Rear recirculation zones tend to move downstream and toward the upper and lower walls of the rig. Rear recirculation zone locations are visible between 6.8 in. $\leq z \leq$ 8.2 in. within the measured flow.

Backflow can be seen upstream of x=1.5 in., even out to the limits of the cell. Recirculating flow could exist in this region, but due to beam restrictions, points closer to the wall could not be measured. Measurements downstream of x=1.5 in. show that the flow velocity accelerates from x=1.5 in. on the way downstream between recirculation zones and then diffuses as the recirculation zones are passed. This is seen to happen to the cell boundaries.

Table 4.3-I.
Annular and primary jets recirculation zone locations.

	Forward zones				Rear zones			
z (in.)	x (in.)	y (in.)	x (in.)	y (in.)	x (in.)	y (in.)	x (in.)	y (in.)
6.8	--	>2.5	--	<0.5	--	>2.5	--	<0.5
6.9	--	>2.5	--	<0.5	3.4	2.4	--	<0.5
7.0	--	>2.5	--	<0.5	3.4	2.3	3.3	<0.5
7.1	--	>2.5	--	--	3.5	2.2	3.2	0.8
7.2	1.1	1.7	1.1	1.3	3.1	2.1	3.0	0.9
7.3	1.0	1.8	1.0	1.1	2.9	2.1	3.0	0.9
7.4	1.0	1.8	1.0	1.1	2.7	2.1	2.8	0.9
7.5	1.0	1.8	1.0	1.1	2.8	2.1	2.8	0.9
7.6	1.0	1.8	1.0	1.2	2.9	2.1	2.9	0.9
7.7	0.7	1.8	1.0	1.2	2.8	2.1	3.1	0.8
7.8	--	--	0.7	1.2	3.0	2.15	3.0	0.8
7.9	--	--	--	--	3.3	2.2	3.3	0.8
8.0	--	--	--	--	3.1	2.2	3.5	0.7
8.1	--	--	--	--	3.1	2.3	3.5	0.7
8.2	--	--	--	--	3.3	>2.5	3.5	0.7

Comparing vector plots to the primary jets only case, some similarities can be seen. The influence of the primary jets on the flowfield is seen downstream of x=1.5 in. Flow downstream of x=1.5 in., in the annular and primary jet case, is seen to be very similar to the flow in the primary jets only case. Recirculation zones for the annular and primary jet case are larger and extend downstream farther, but the flow is still seen to accelerate past the recirculation region and then diffuse. This is an indication of how much influence the primary jets have on the flow.

4.3.2.3 Turbulent Flowfield Results

The U_{rms} and V_{rms} yz plane contour plots are presented in Figures 4.3.2-28 through 4.3.2-37. Figure 4.3.2-28 contains plots for the station at x=0.5 in. Both plots show a flat profile outside of the annular jet inlet and inside the annular jet region. Peak fluctuations occur in the annular gap where fluid is entering.

The U_{rms} and V_{rms} plots at x=1.0 in. can be seen in Figure 4.3.2-29. The magnitude of the fluctuations increase and spread out from x=0.5 in. to x=1.0 in. Fluctuations at the center of the annular region have increased due to the pair of counterrotating recirculation zones formed in this region. Magnitudes outside the annular jet remain small compared to the annular jet region.

Plots at x=1.5 in. show a definite change in the U_{rms} and V_{rms} velocity distribution due to primary jet interaction (Figure 4.3.2-30). The U_{rms} plot shows decreased turbulence at the centerplane, z=7.5 in., from the top to bottom walls of the rig due to the primary jets. Three pairs of peak fluctuations occur on the sides of the centerplane. The peaks at the bottom and top walls are caused by the flow above and below the annular jets accelerating around the primary jets and flowing downstream. The pair of peaks at the center of the rig correspond to increased flow around the primary jets from recirculating fluid in the center of the annular jet. The turbulence diffuses as the edges of the cell are reached.

The V_{rms} plot at x=1.5 in. shows decreased magnitudes at the upper and lower walls at the rig centerplane. A peak is observed at the center of the cell due to the fluctuation of the stagnation point of the primary jets. The magnitudes dissipate as the cell boundaries are reached.

The U_{rms} component at x=2.0 in. (Figure 4.3.2-31) shows a decrease at both upper and lower walls in the rig center and peak magnitudes occur along the rig centerline between z=7.0 in. and z=8.3 in. The drop in magnitude along the upper and lower walls is due to a recirculation zone, while the peaks at the center of the rig are caused from fluid being accelerated between the upper and lower recirculation zones. The V_{rms} component at x=2.0 in. shows peak velocities along the rig centerline between z=7.0 in. and z=7.9 in. Similar results are evident at downstream locations (Figures 4.3.2-32 through 4.3.2-37).

Figures 4.3.2-38 and 4.3.2-39 show line plots of U_{rms} and V_{rms} velocities as they develop in the rig for planes at z=7.0, 7.5, and 8.0 in. Peak U_{rms} fluctuations are at the annular jet exit and immediately downstream of the primary jets. Peak V_{rms} fluctuations can be seen in the region of the primary jet stagnation. On downstream, the magnitudes decrease and spread out. Uniform fluctuations from the bottom to the top walls can be seen at x=6.0 in. Magnitudes at x=6.0 in. are slightly larger than the primary jets case and much smaller than the annular jet case.

The 2-D turbulent kinetic energy contour plots are presented in Figures 4.3.2-40 through 4.3.2-44. The K' distribution at x=0.5 and 1.0 in. (Figure 4.3.2-40) shows similar distributions. Peak turbulence occurs at the edges of the annular jet where large shear stress is present. Outside the annular inlet, the turbulence is uniform to the cell boundaries and walls. The plot at x=1.0 in. shows peak magnitudes nearly doubling with increased turbulence within the annular region. Distributions toward the cell boundaries continue to be uniform.

The plot at x=1.5 in. shows peak turbulence occurring at the rig center and at the top and bottom walls. The decrease seen in the rms plots is also seen here in Figure 4.3.2-41. The trends seen in this plot correspond to the trends explained in the rms plots in Figure 4.3.2-30.

At x=2.0 in., peak turbulence values can be seen at the center of the rig with a sharp drop in turbulence energy between z=7.0 and 8.0 in. at the upper and lower walls. The formation of the downstream recirculation regions in these areas are responsible for the drop in turbulence energy. Magnitudes decrease as cell boundaries and walls are reached. Similar trends are present in plots downstream (Figures 4.3.2-42, 4.3.2-43, and 4.3.2-44).

Figure 4.3.2-45 contains the 2-D turbulent kinetic energy distribution throughout the rig at the planes z=7.0, 7.5, and 8.0 in. The largest turbulence energy can be seen concentrated in the region of annular and primary jet intersection at x=1.5 and 2.0 in. Magnitudes decay and spread downstream and away from the rig centerplane. Uniform turbulence energy between upper and lower walls is present at x=6.0 in.

yz plane contour plots of the xy plane Reynolds shear stress are in Figures 4.3.2-46 through 4.3.2-50. The U'V' distribution at x=0.5 in. is seen in Figure 4.3.2-46. Negative stresses are observed at the edges of the annular jet inlet due to the transfer of momentum from the edges of the annular jet to the fluid within the rig. A constant distribution is seen throughout the rest of the plane indicating very little momentum transfer. Similar results occur at x=1.0 in. Here, the magnitudes of the stresses have nearly doubled and spread to the inner annular jet region. A uniform region is still seen throughout the rest of the plane.

At the x=1.5 in. plane, three regions of decreased, or negative, stress is seen separated by a strip of increased U'V' at z=7.5 in. The three regions of decreased magnitude occurs in the same area as the peak fluctuations occurred for the U_{rms} plot in Figure 4.3.2-30. The negative values are therefore caused by the increased velocity gradients in these regions as the flow accelerates around the primary jets. The

central peak must be caused by the cross jets entering in this location. Outside of the annular jet inlet, z=6.8 and z=8.2 in., a uniform shear stress extends to the cell boundaries.

At x=2.0 in., a region of peak positive U'V' occurs along the upper half of the rig while negative U'V' occurs through the lower half of the rig. The magnitudes continue to decrease and the peaks tend to spread toward the walls and boundaries of the rig on downstream. The peak through the rig at z=7.5 in. seems to exist on downstream. Similar distributions are present downstream of x=2.0 in. Figures 4.3.2-48, 4.3.2-49, and 4.3.2-50 contain these plots.

Figure 4.3.2-51 shows line plots of the Reynolds shear stress as it develops downstream at planes z=7.0, 7.5, and 8.0 in. The largest fluctuation of shear stress is present at x=1.5 in. Here, primary and annular jet interaction produces large velocity gradients and momentum transfer. Downstream and away from the centerplane, magnitudes decay and approach a uniform distribution of shear stress at x=6.0 in.

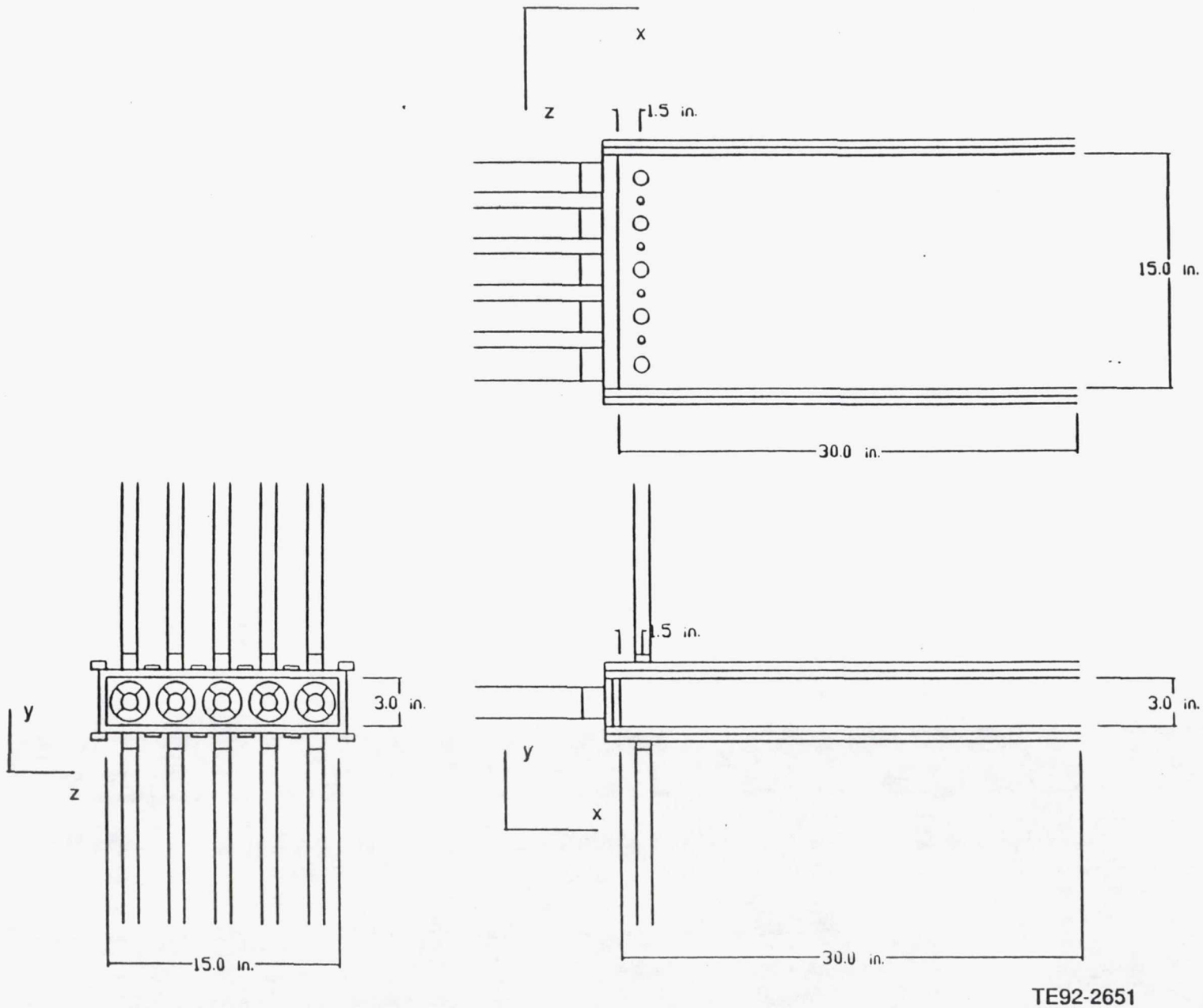

Figure 4.3-1. Annular and primary jets - three-view drawing.

Page intentionally left blank

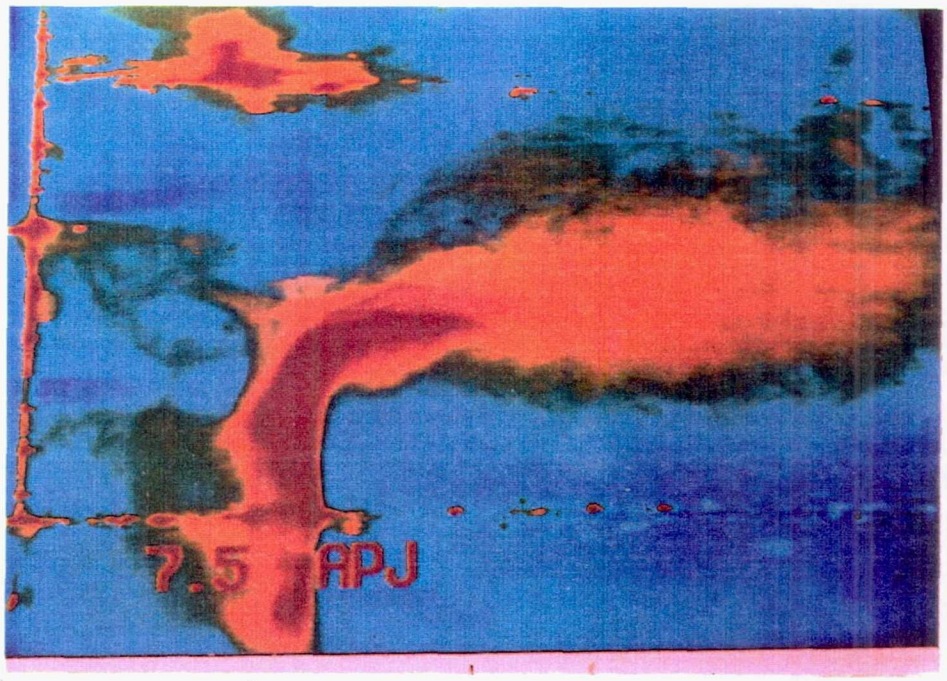

TE92-2652

Figure 4.3.1-1. Annular and primary jets with smoke in primary jet, single frame picture, z=7.5 in.

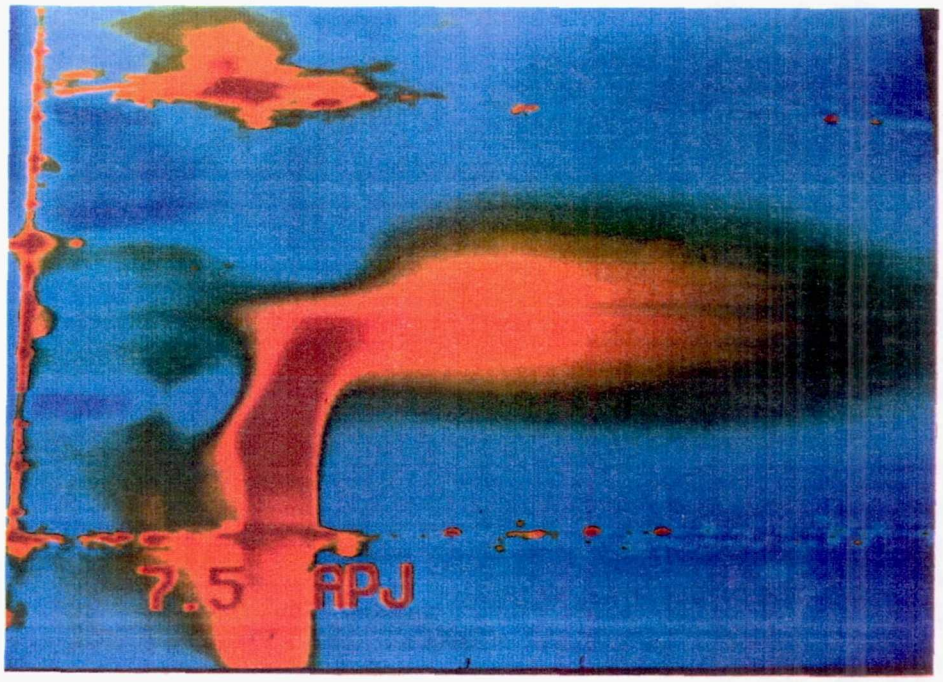

TE92-2653

Figure 4.3.1-2. Annular and primary jets with smoke in primary jet, 127 frame average picture, z=7.5 in.

Page intentionally left blank

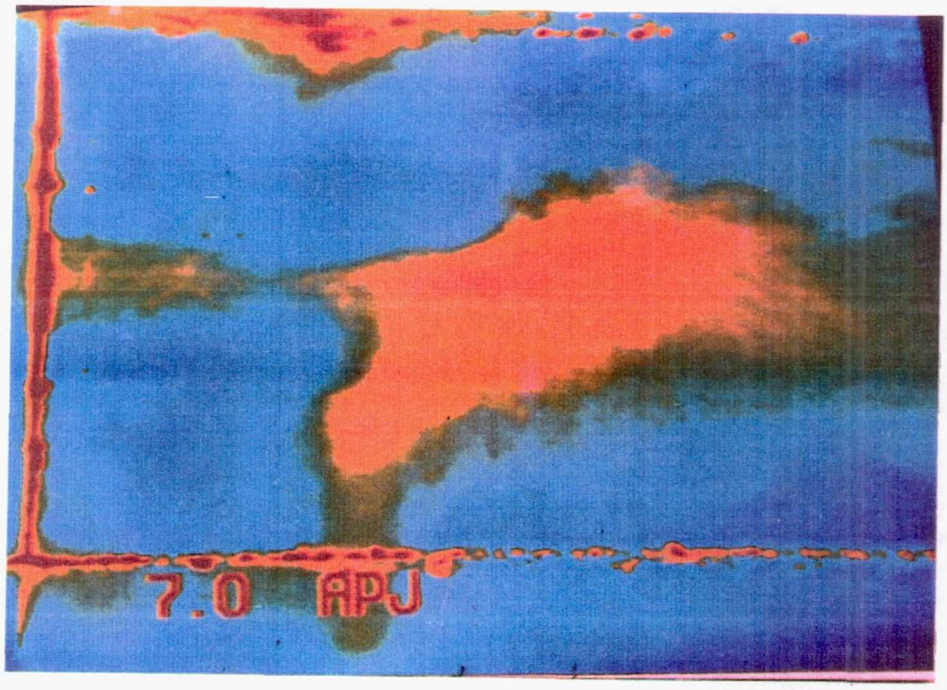

TE92-2654

Figure 4.3.1-3. Annular and primary jets with smoke in primary jet, single frame picture, z=7.0 in.

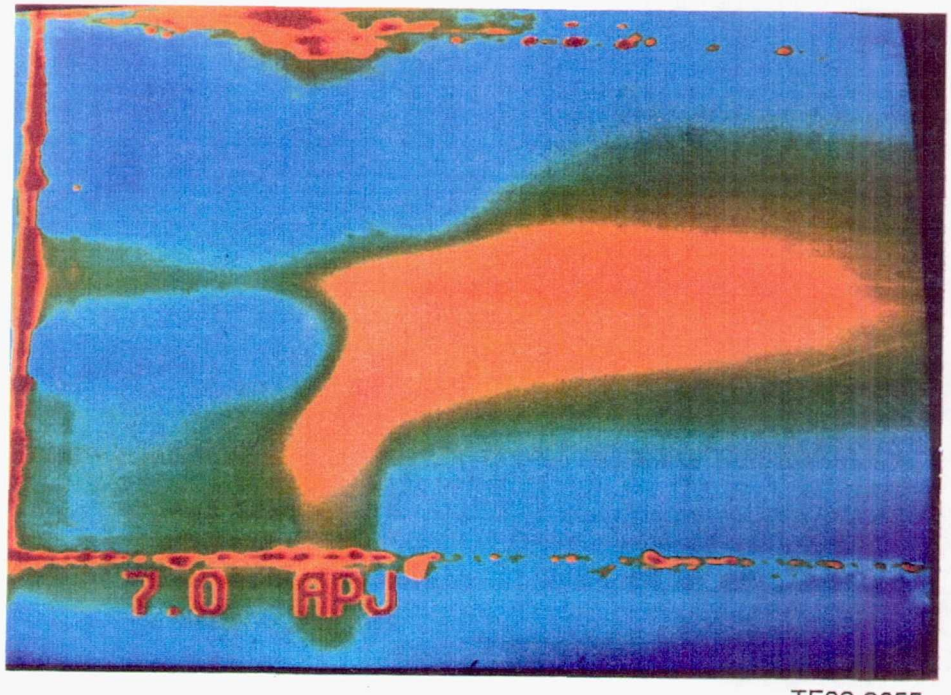

TE92-2655

Figure 4.3.1-4. Annular and primary jets with smoke in primary jet, 127 frame average picture, z=7.0 in.

Page intentionally left blank

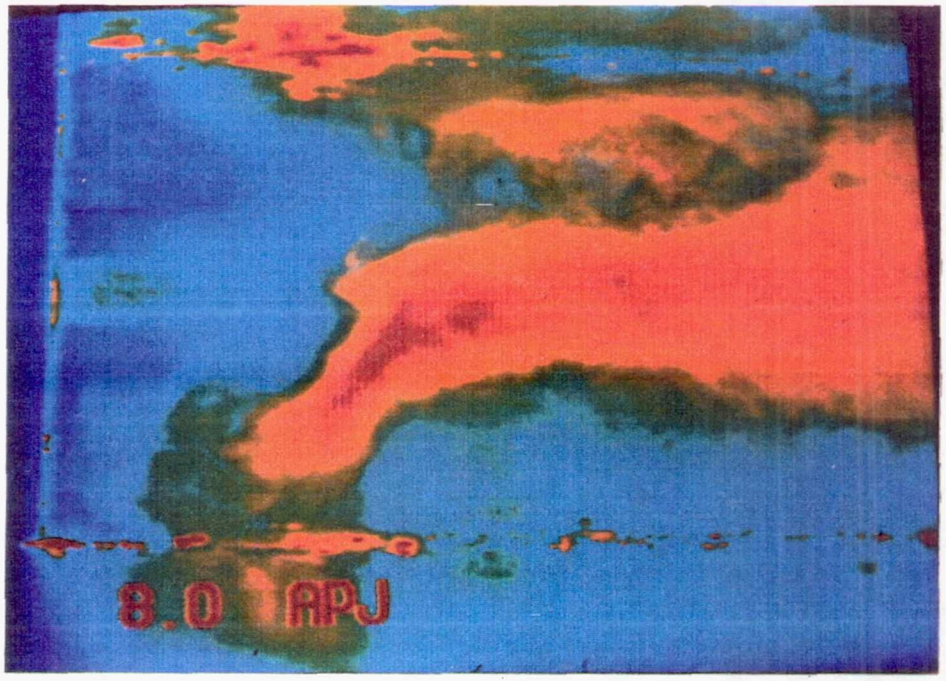

TE92-2656

Figure 4.3.1-5. Annular and primary jets with smoke in primary jet, single frame picture, z=8.0 in.

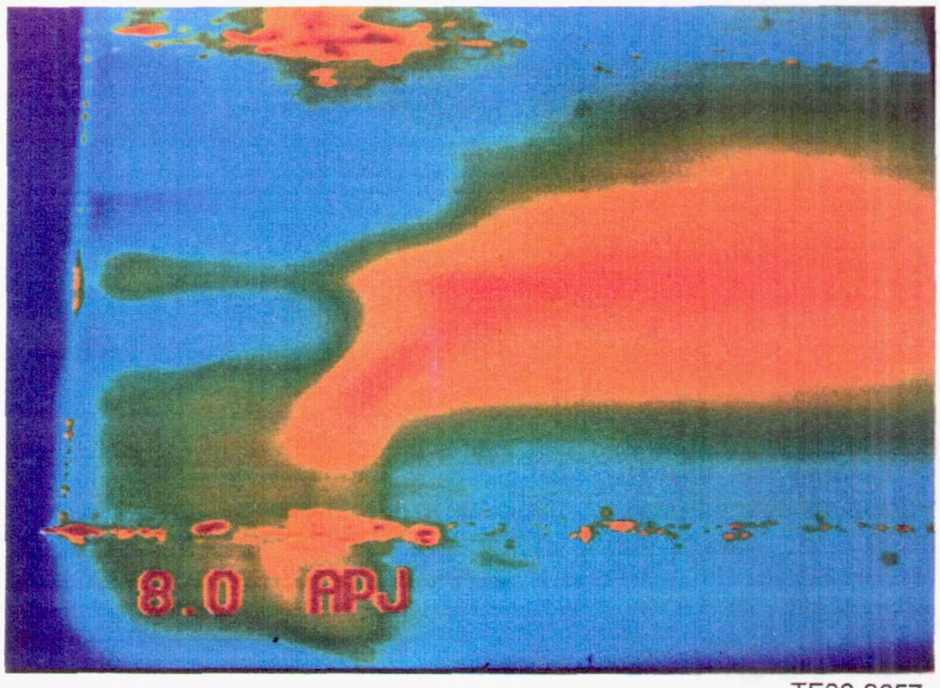

TE92-2657

Figure 4.3.1-6. Annular and primary jets with smoke in primary jet, 127 frame average picture, z=8.0 in.

Page intentionally left blank

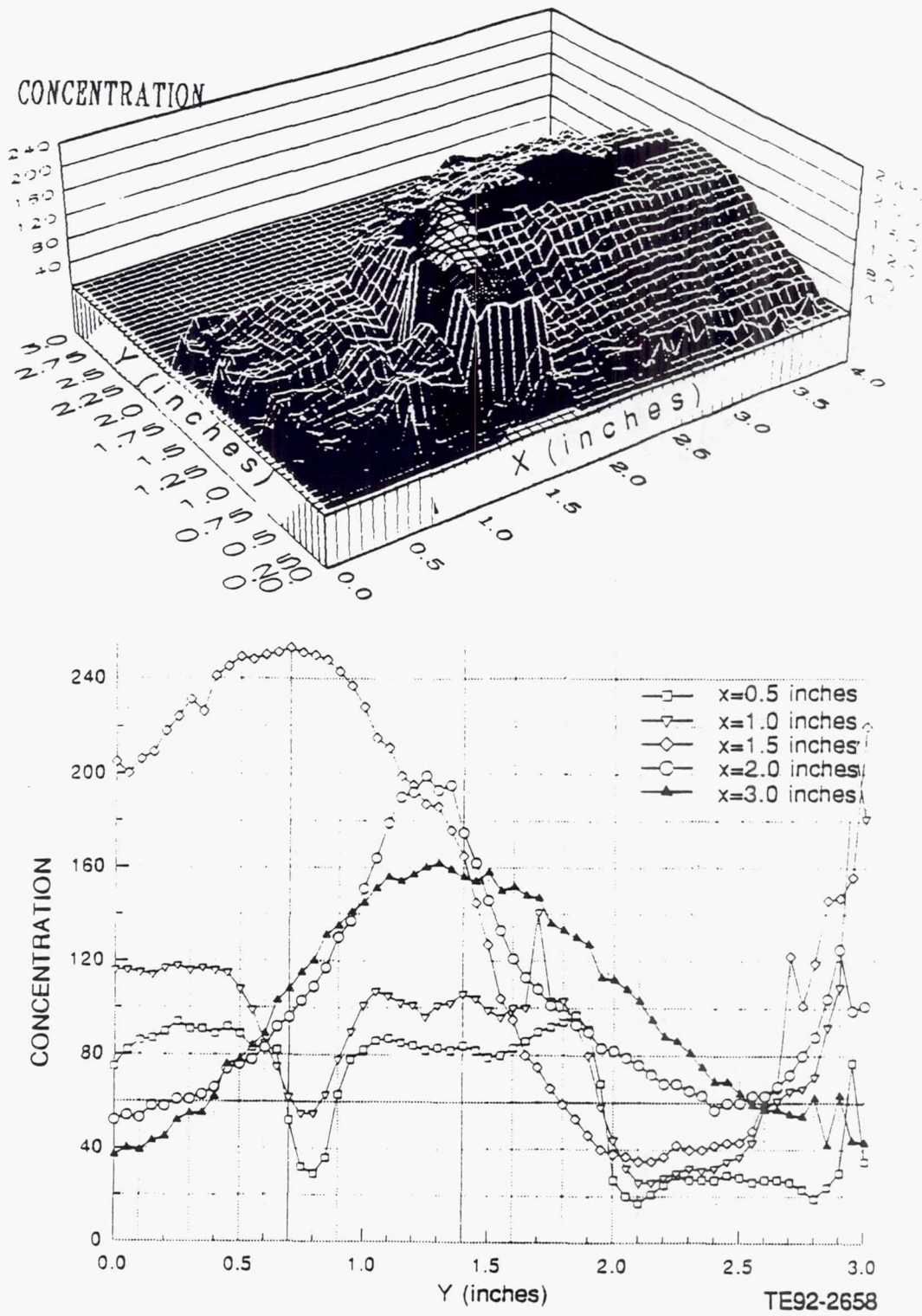

Figure 4.3.1-7. Annular and primary jets mean concentration distribution with smoke in lower primary jet, z=7.5 in.

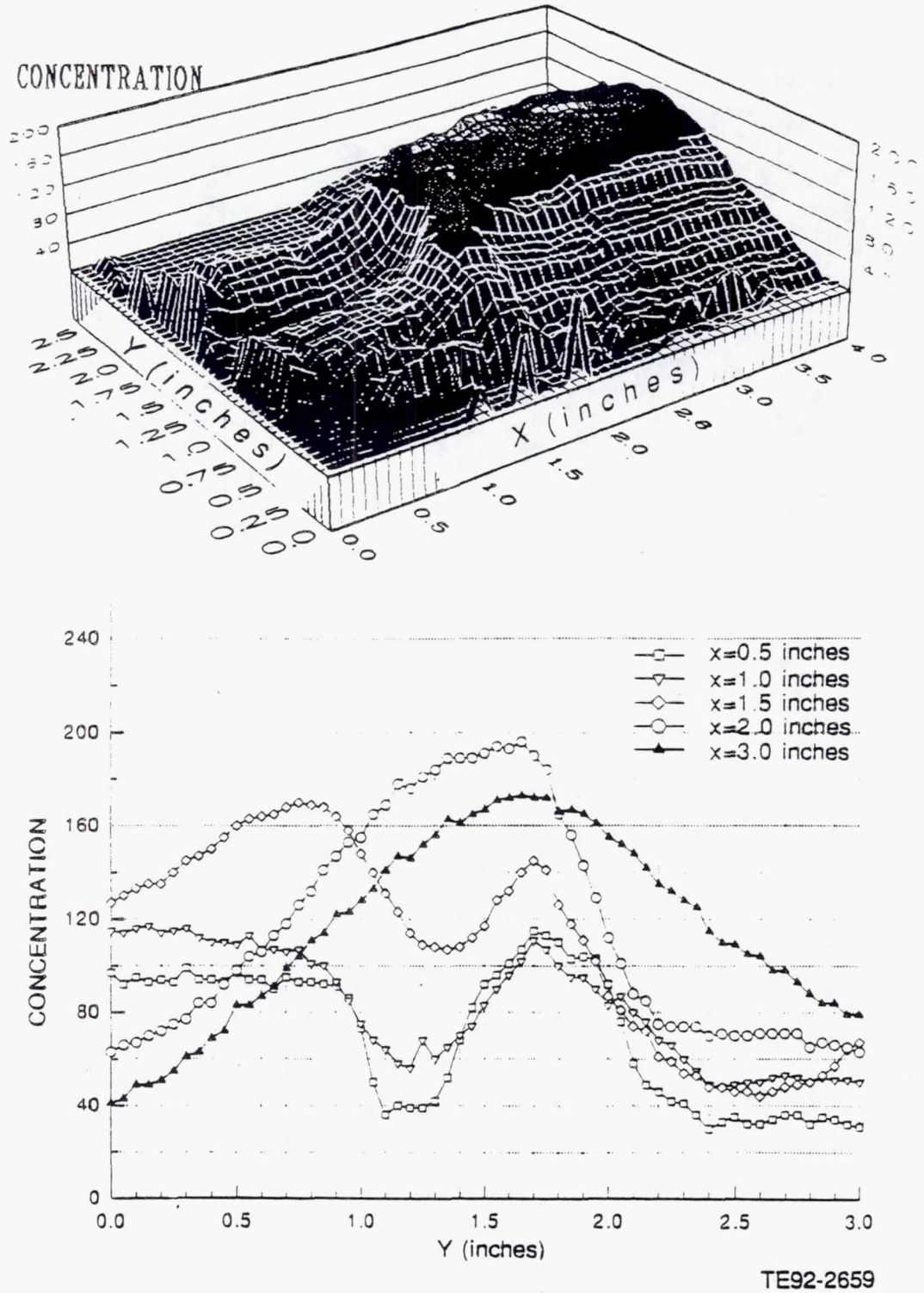

Figure 4.3.1-8. Annular and primary jets mean concentration distribution with smoke in lower primary jet, z=7.0 in.

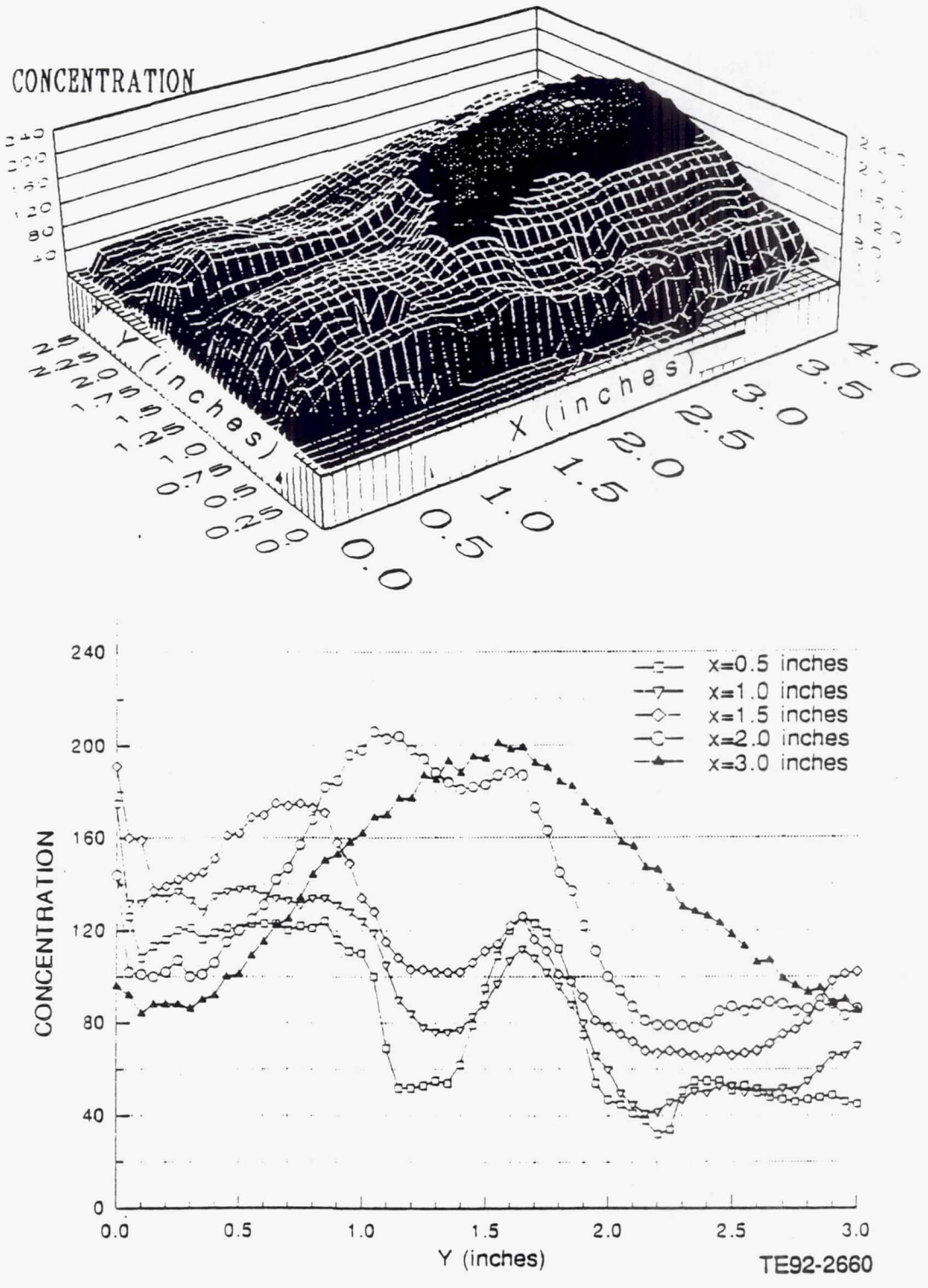

Figure 4.3.1-9. Annular and primary jets mean concentration distribution with smoke in lower primary jet, z=8.0 in.

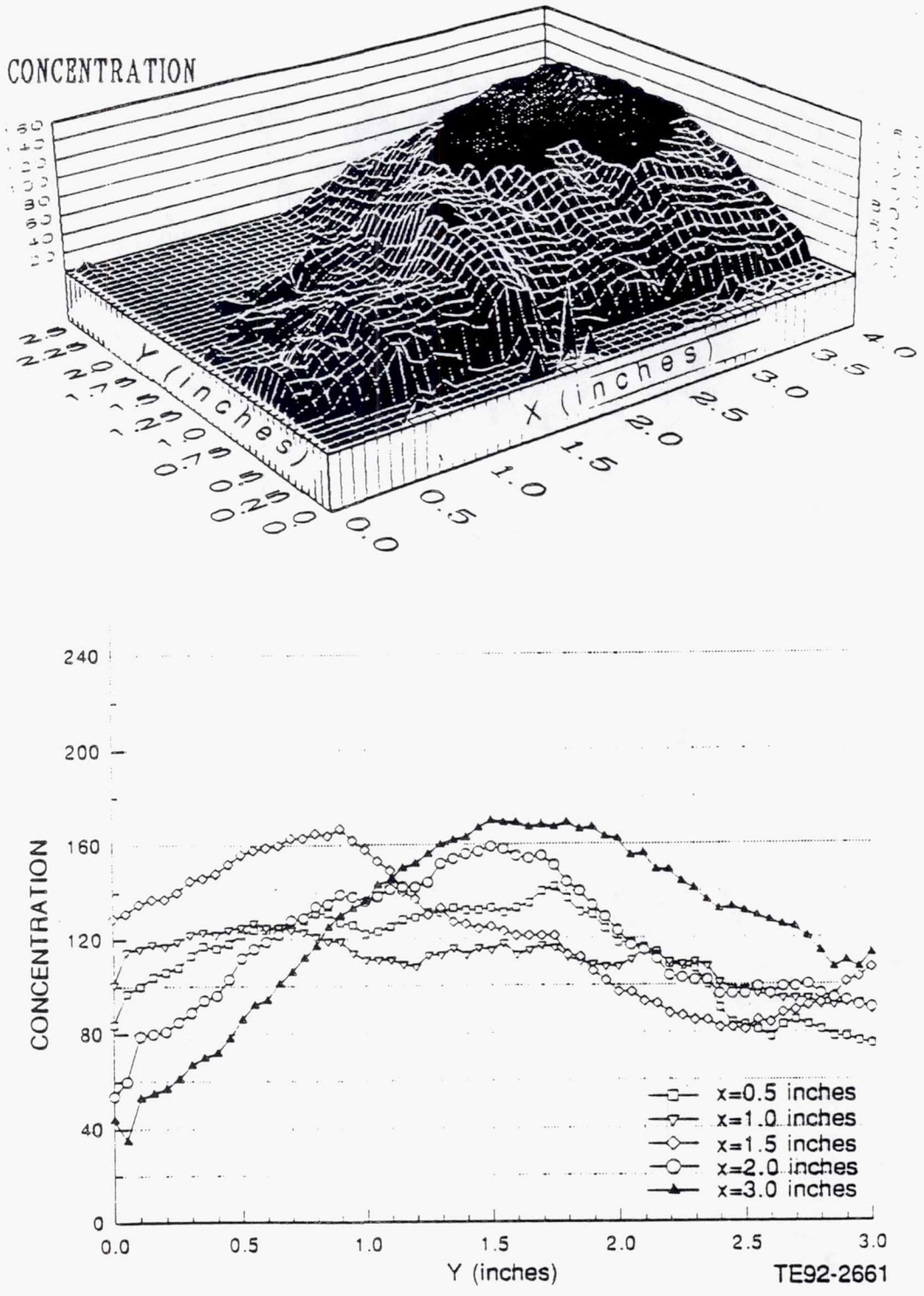

Figure 4.3.1-10. Annular and primary jets mean concentration distribution with smoke in lower primary jet, z=6.5 in.

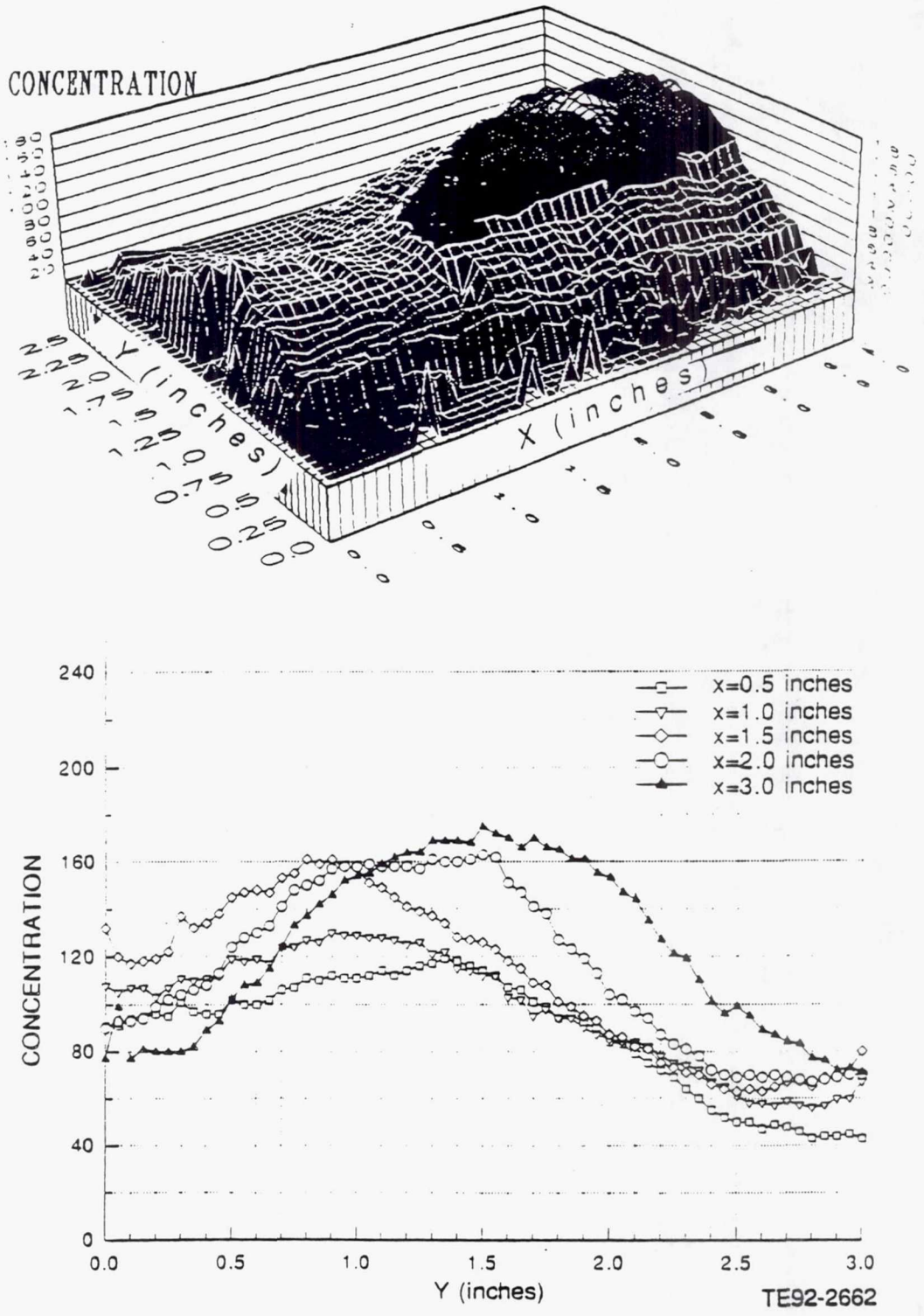

Figure 4.3.1-11. Annular and primary jets mean concentration distribution with smoke in lower primary jet, z=8.5 in.

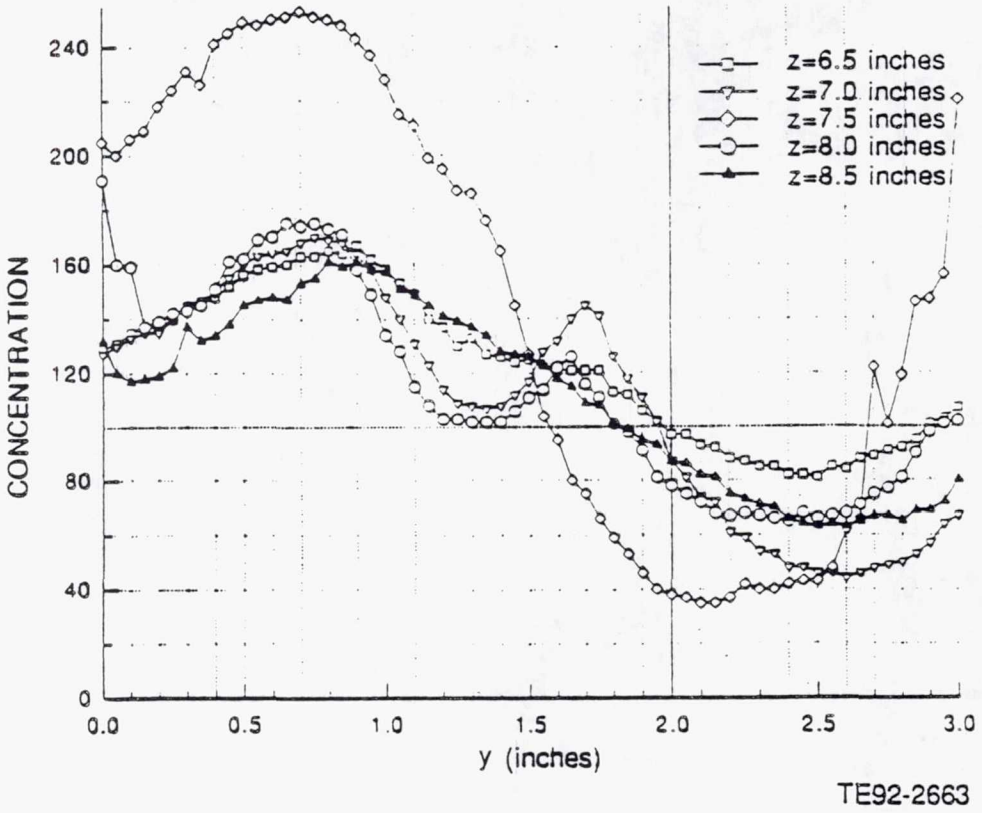

Figure 4.3.1-12. Annular and primary jets mean concentration along primary jet axis with smoke in lower primary jet, x=1.5 in.

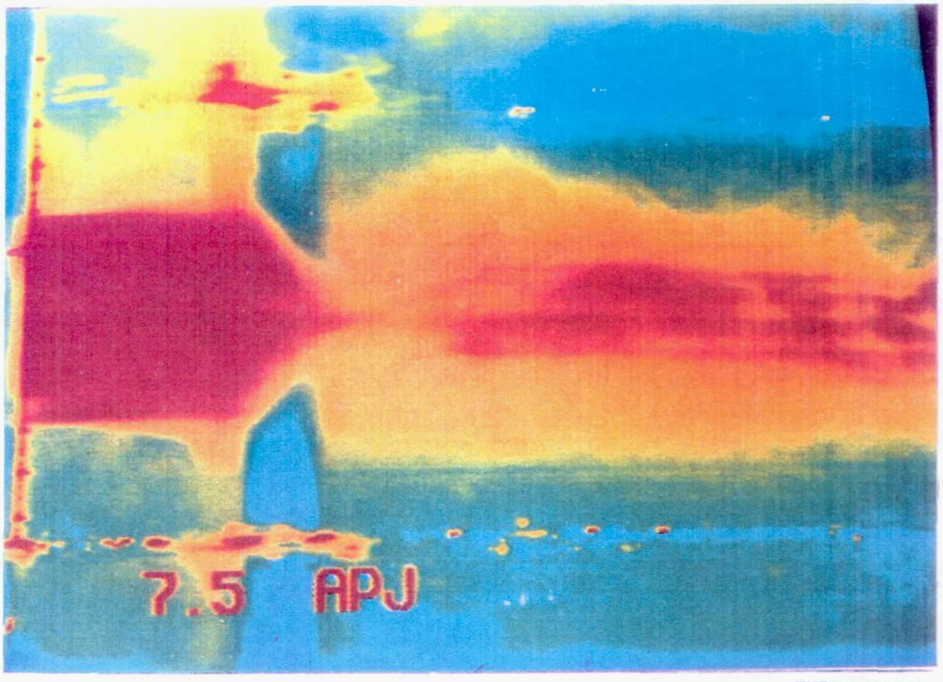

TE92-2664

Figure 4.3.1-13. Annular and primary jets with smoke in annular jet, single frame picture, z=7.5 in.

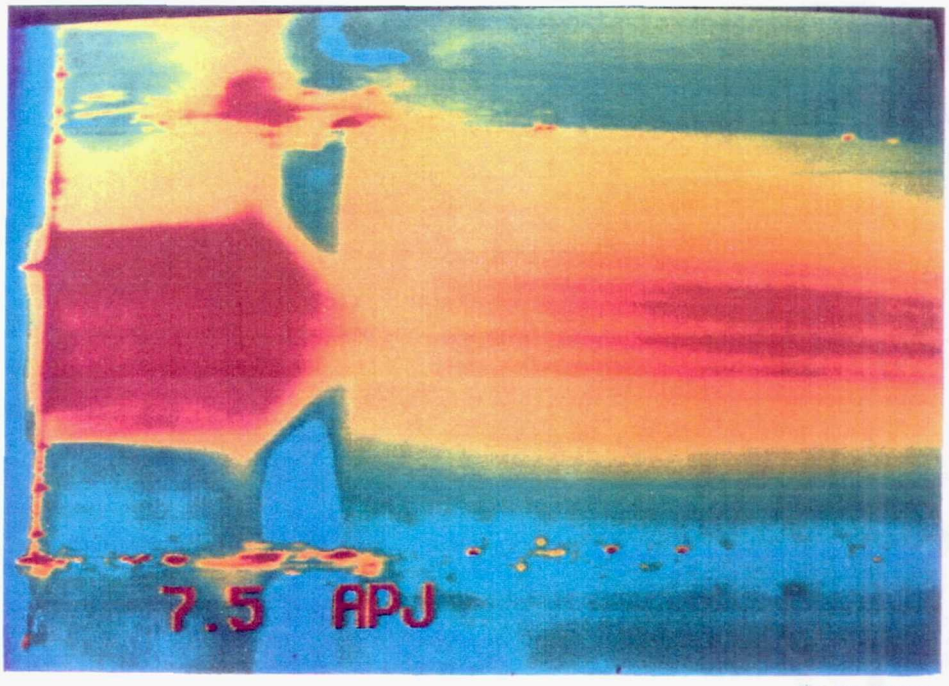

TE92-2665

Figure 4.3.1-14. Annular and primary jets with smoke in annular jet, 127 frame average picture, z=7.5 in.

Page intentionally left blank

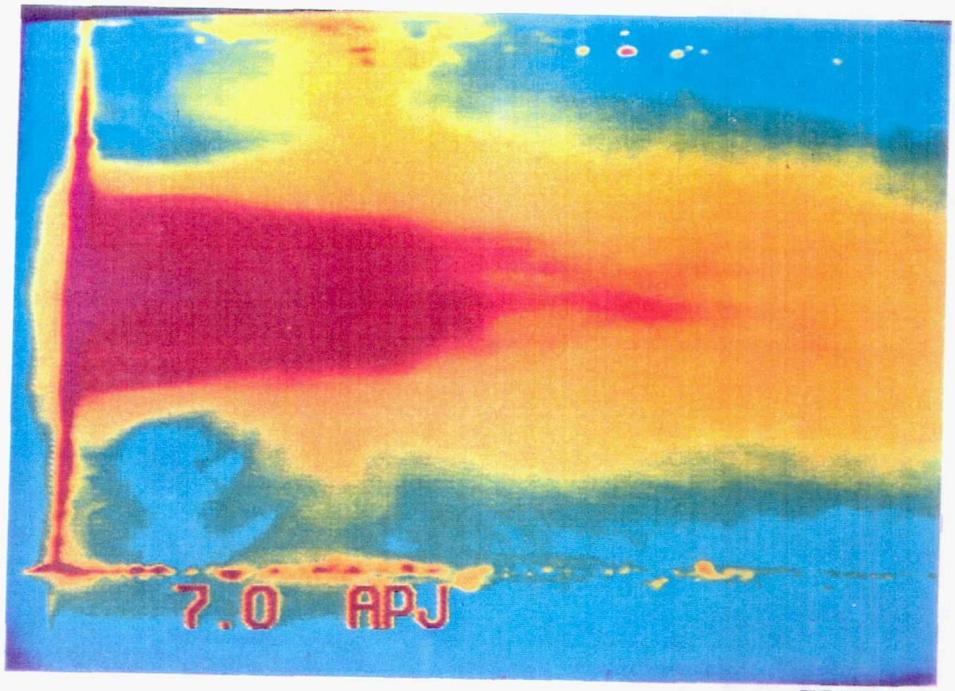

TE92-2666

Figure 4.3.1-15. Annular and primary jets with smoke in annular jet, single frame picture, z=7.0 in.

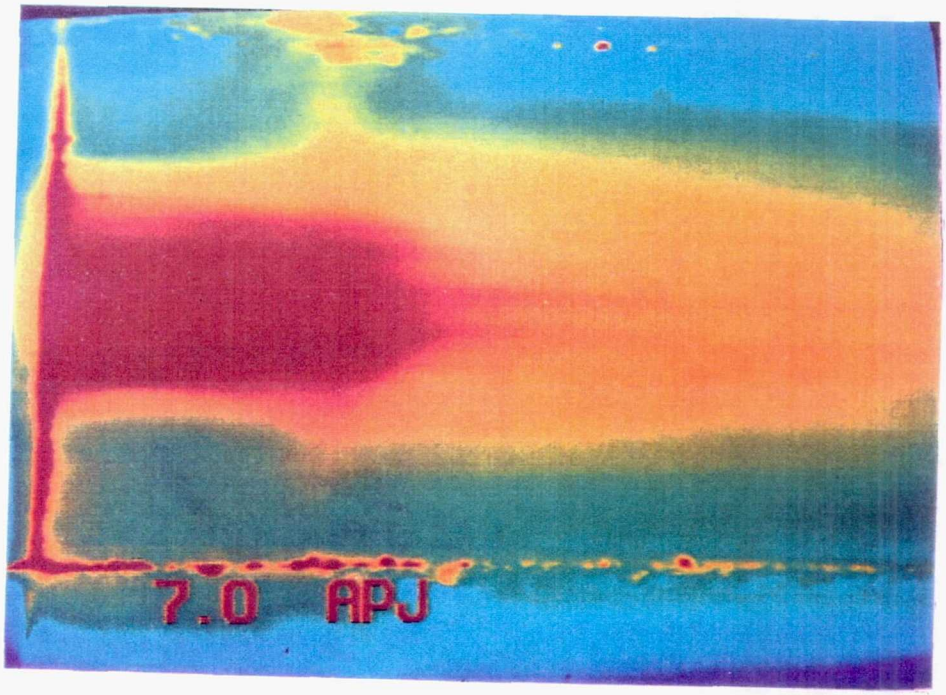

TE92-2667

Figure 4.3.1-16. Annular and primary jets with smoke in annular jet, 127 frame average picture, z=7.0 in.

Page intentionally left blank

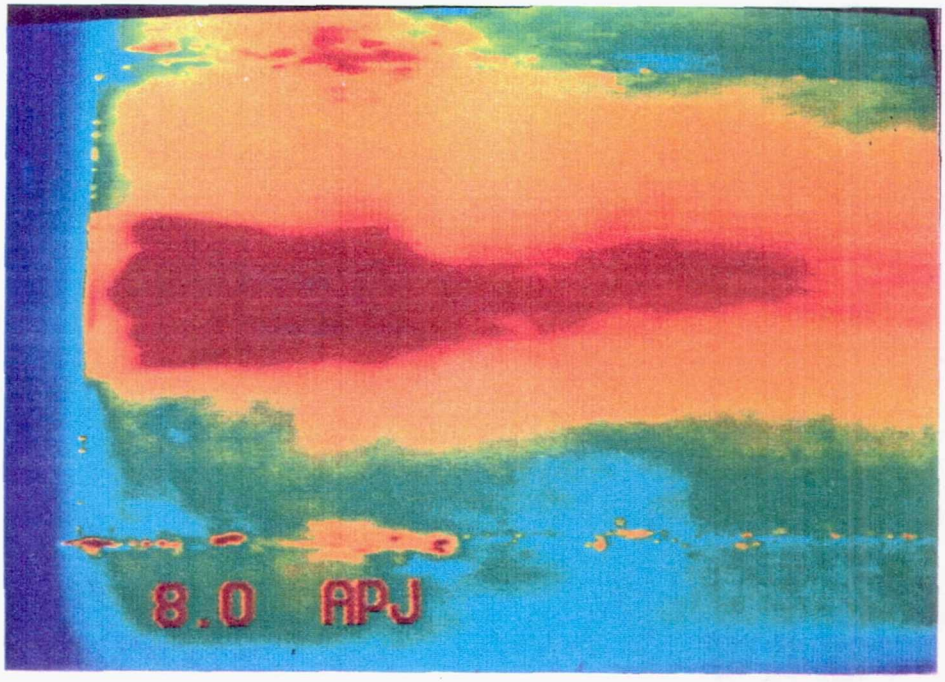

TE92-2668

Figure 4.3.1-17. Annular and primary jets with smoke in annular jet, single frame picture, z=8.0 in.

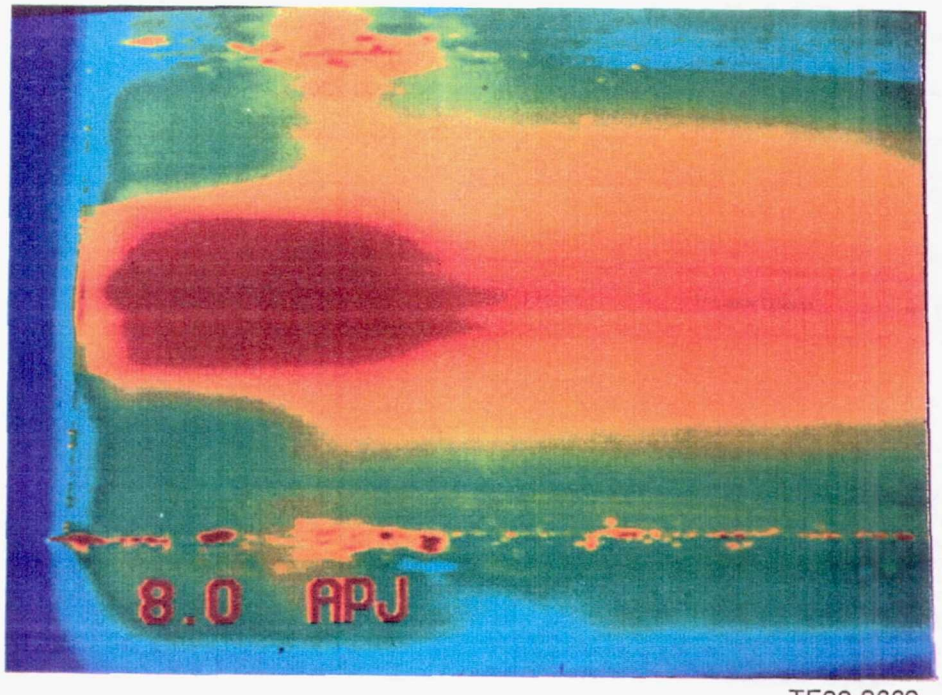

TE92-2669

Figure 4.3.1-18. Annular and primary jets with smoke in annular jet, 127 frame average picture, z=8.0 in.

Page intentionally left blank

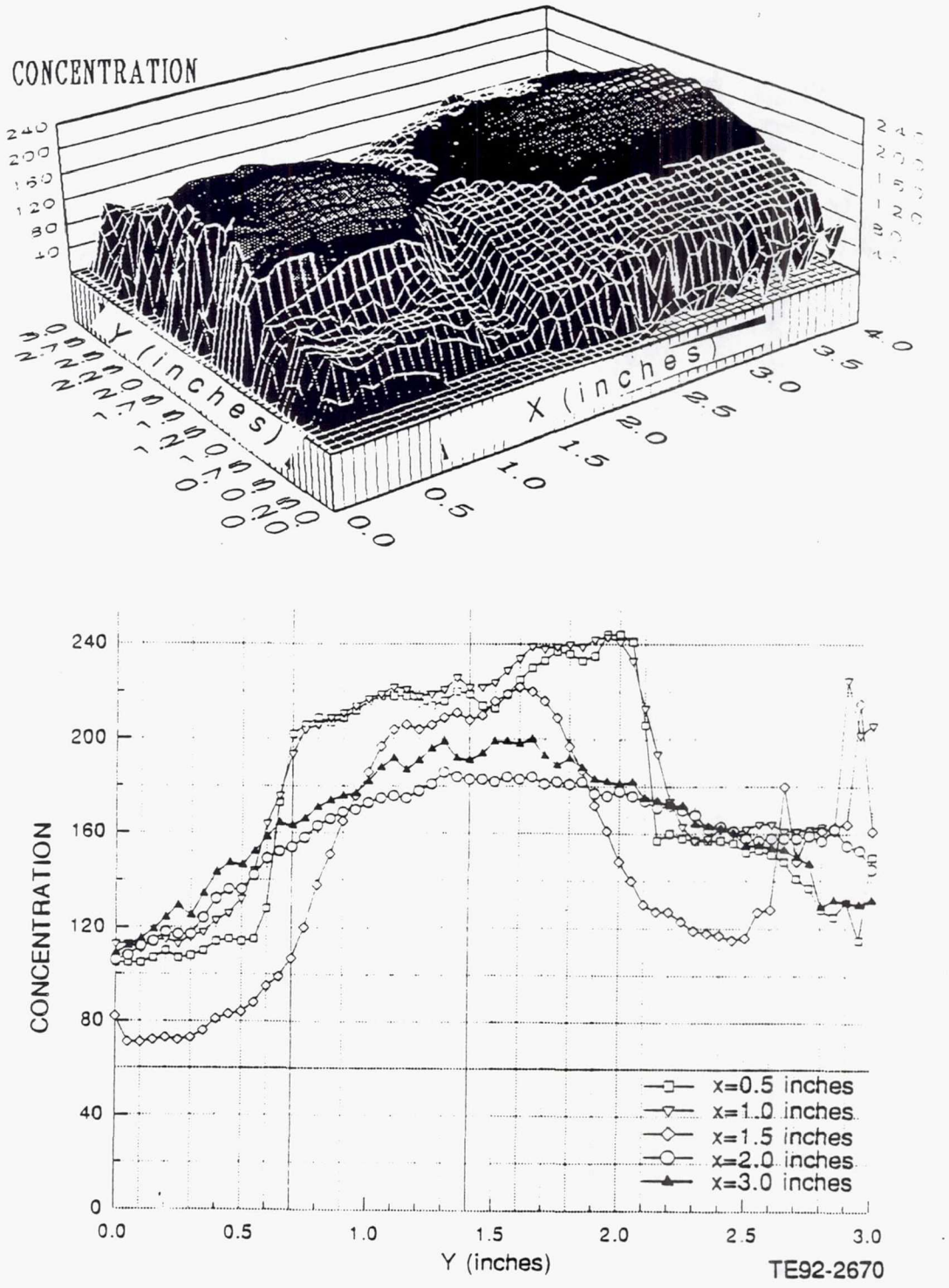

Figure 4.3.1-19. Annular and primary jets mean concentration distribution with smoke in annular jet, z=7.5 in.

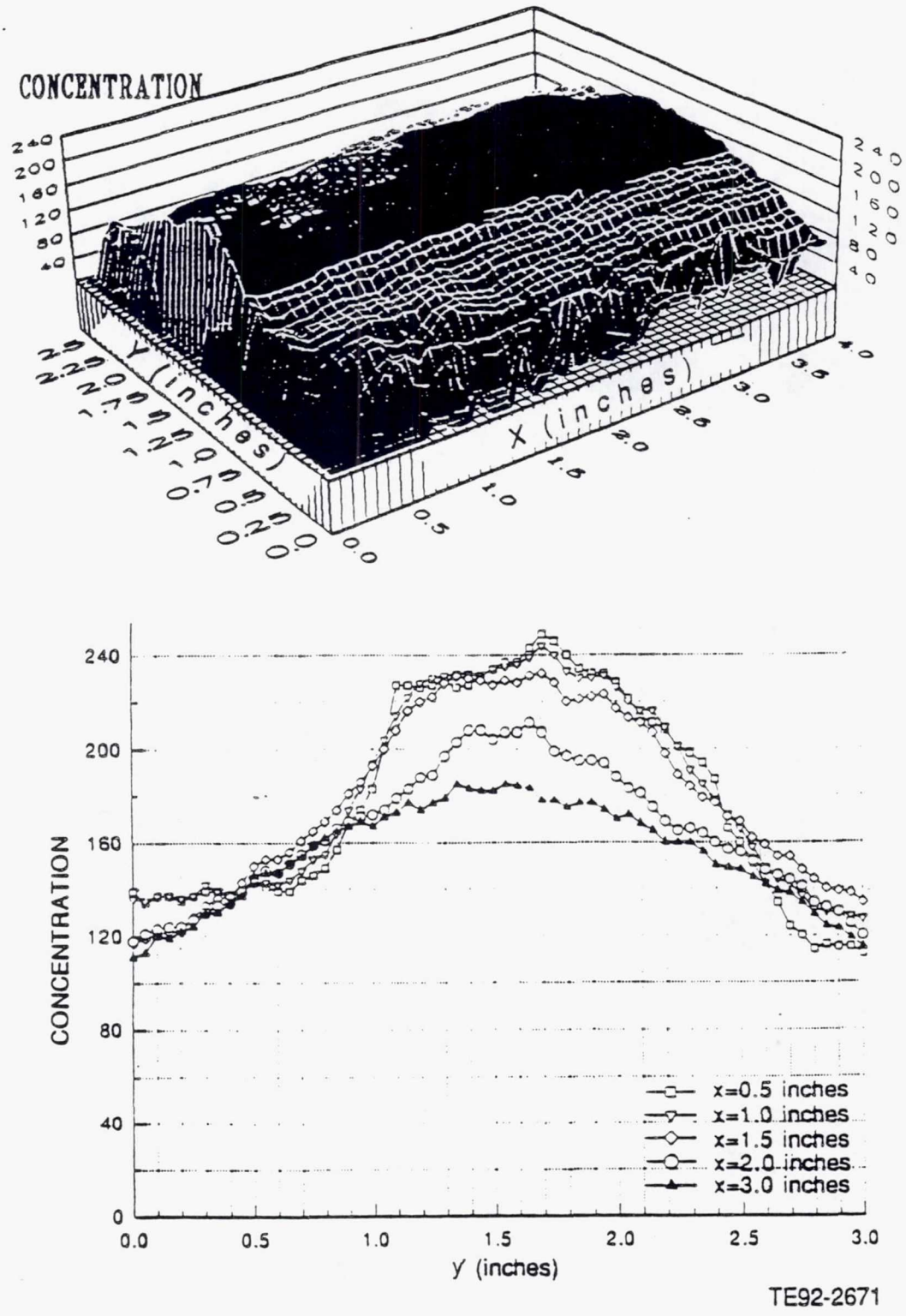

Figure 4.3.1-20. Annular and primary jets mean concentration distribution with smoke in annular jet, z=7.0 in.

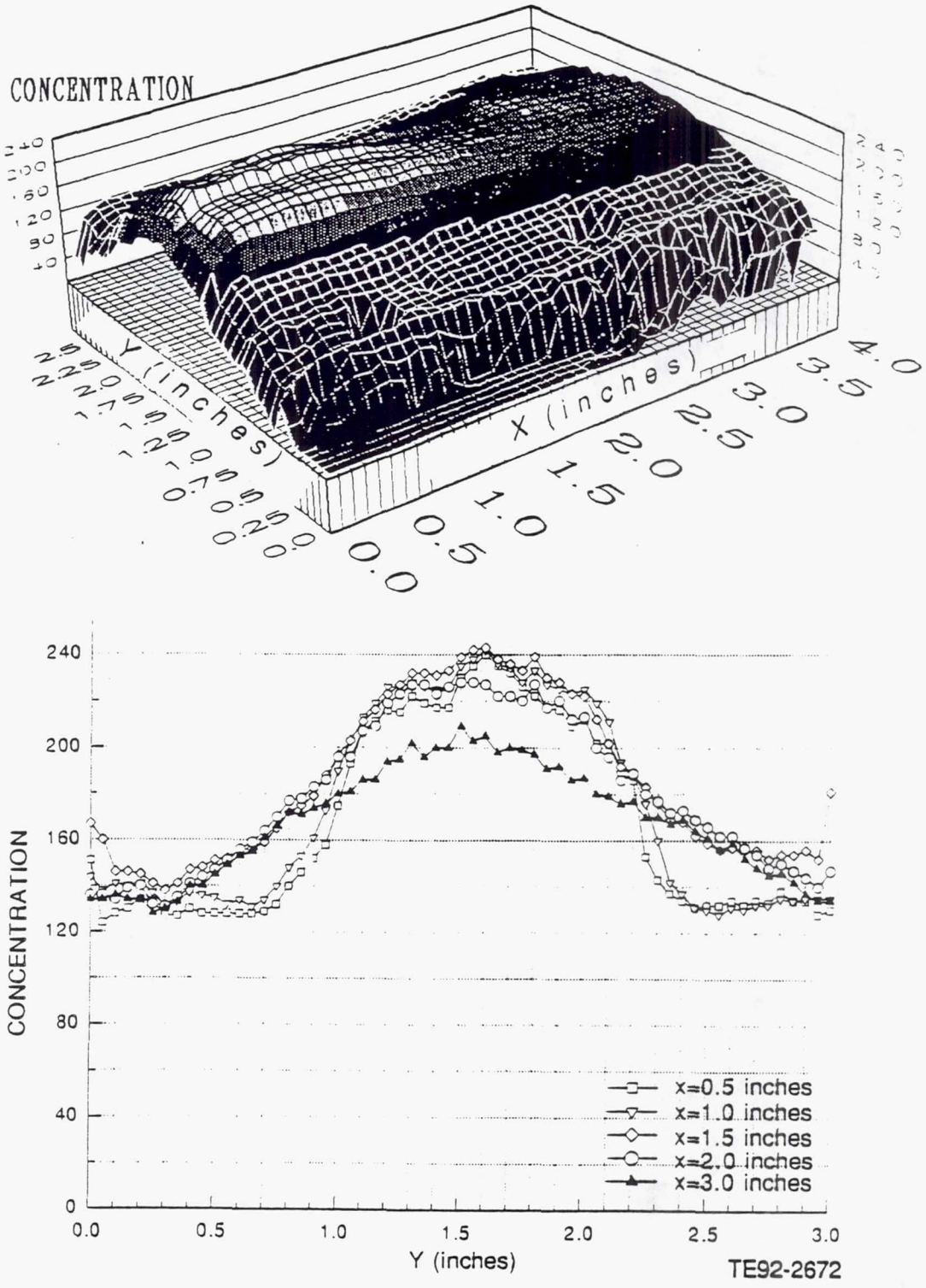

Figure 4.3.1-21. Annular and primary jets mean concentration distribution with smoke in annular jet, z=8.0 in.

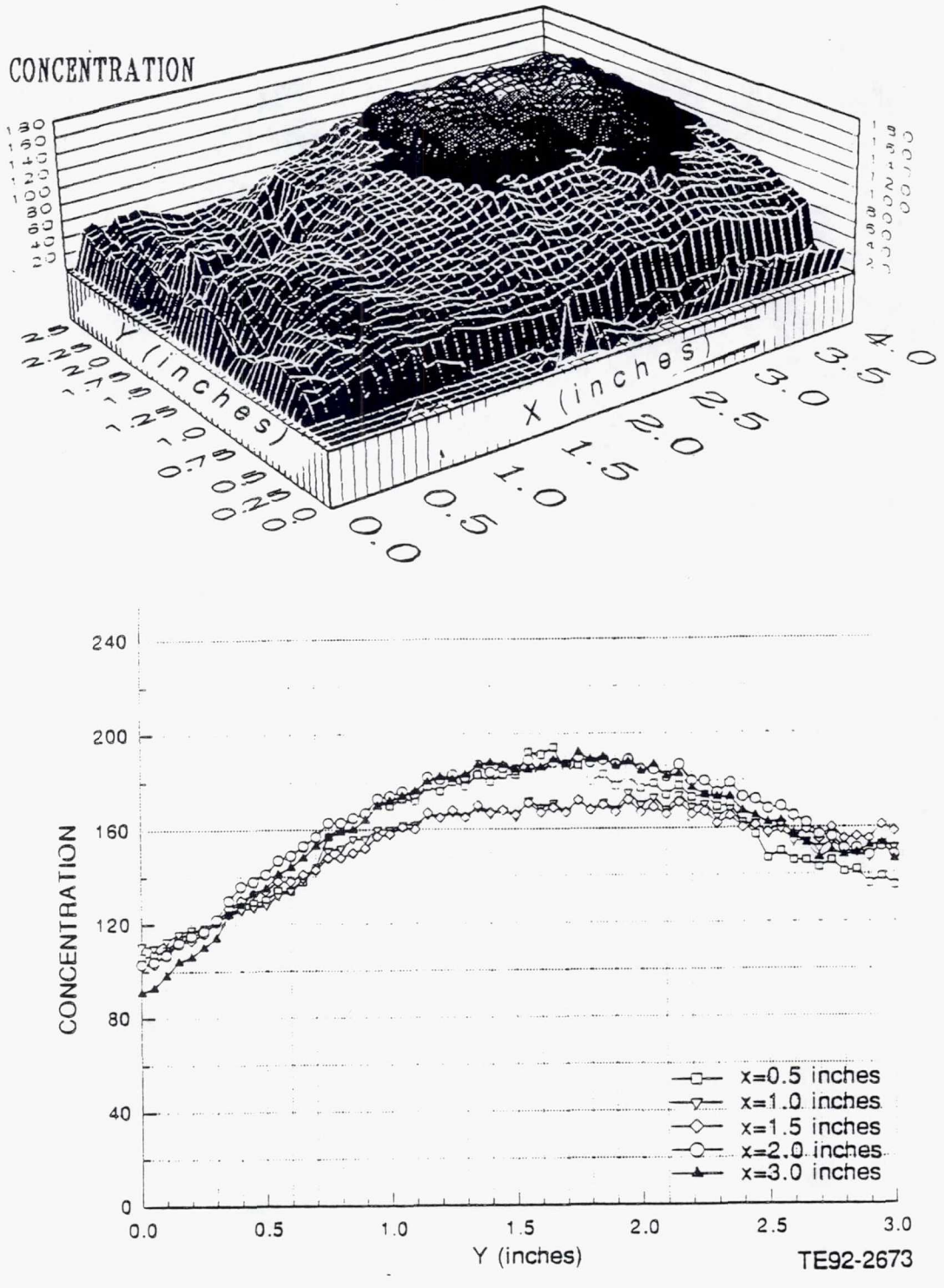

Figure 4.3.1-22. Annular and primary jets mean concentration distribution with smoke in annular jet, z=6.5 in.

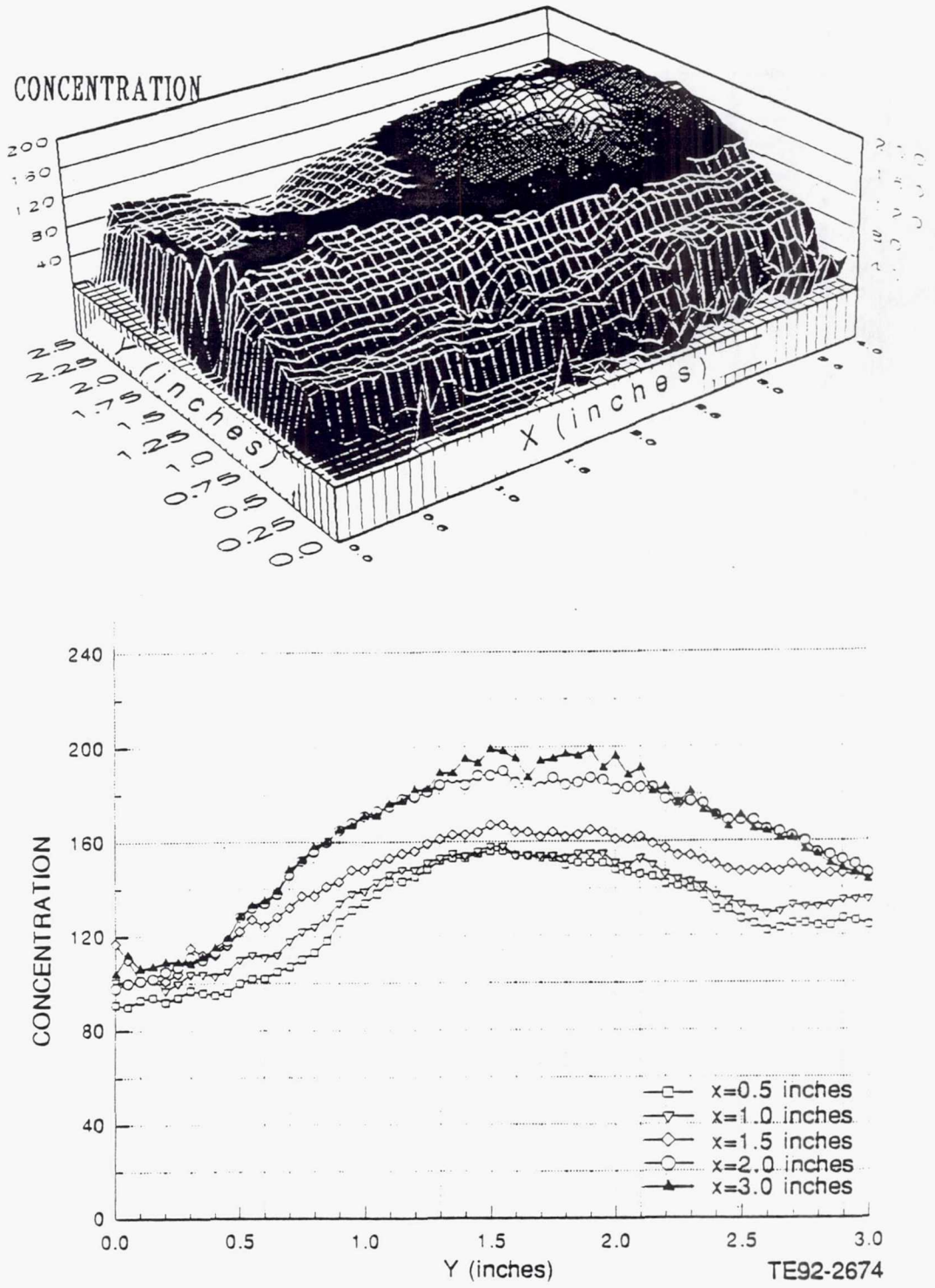

Figure 4.3.1-23. Annular and primary jets mean concentration distribution with smoke in annular jet, z=8.5 in.

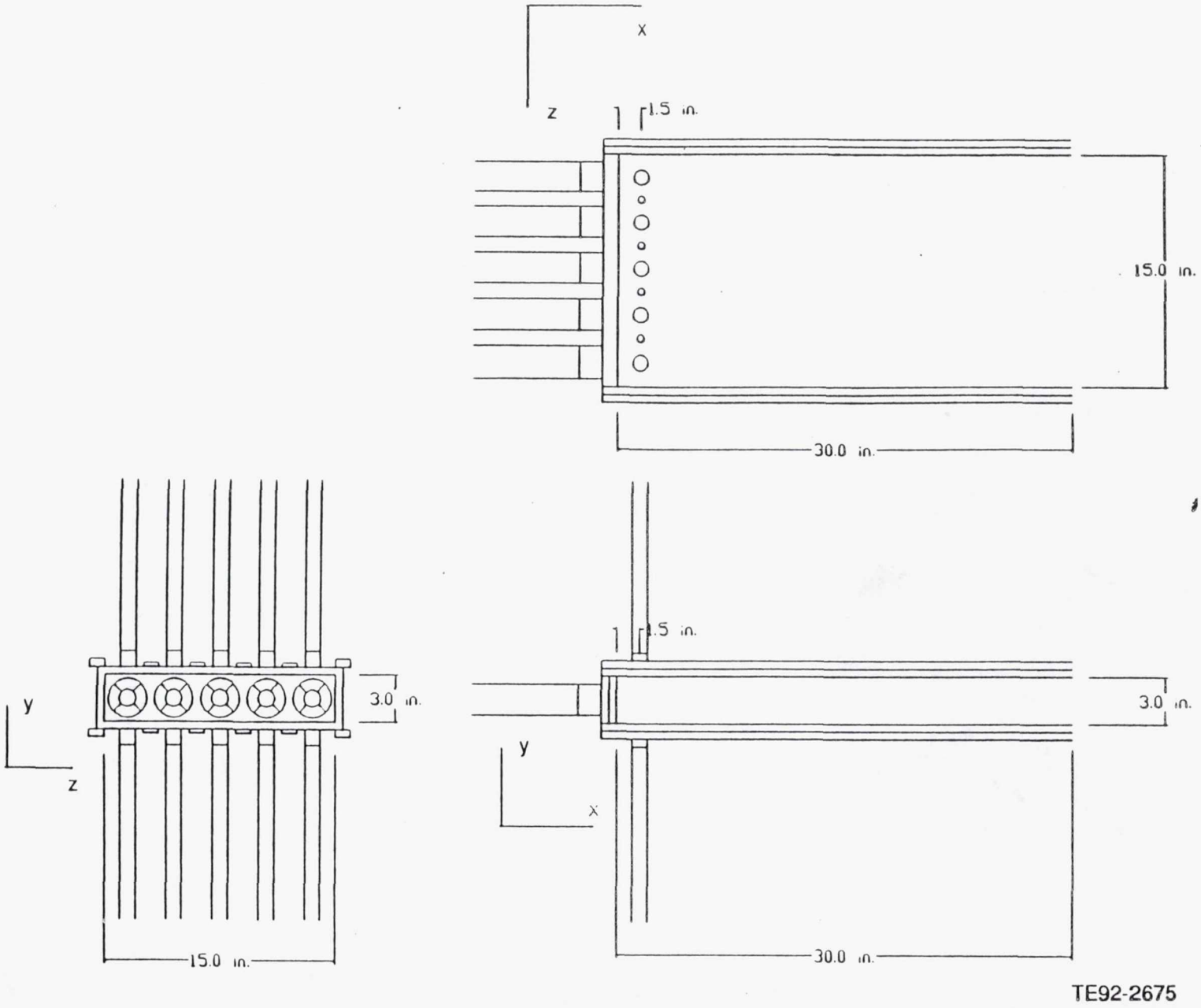

Figure 4.3.2-1. Annular and primary jets - three-view drawing.

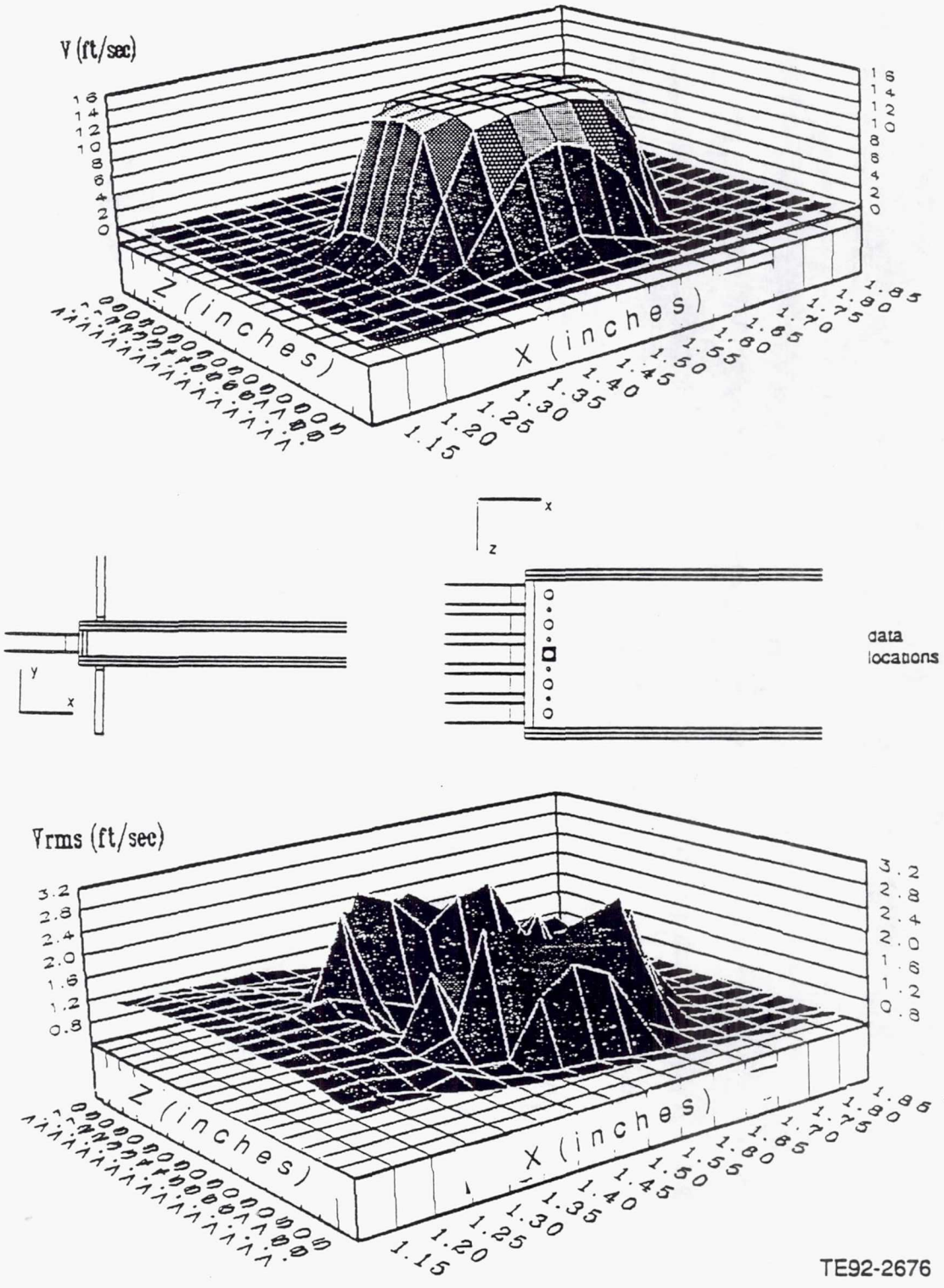

Figure 4.3.2-2. Annular and primary jets V and V_{rms} distribution of the primary jets at y=0.1 in.

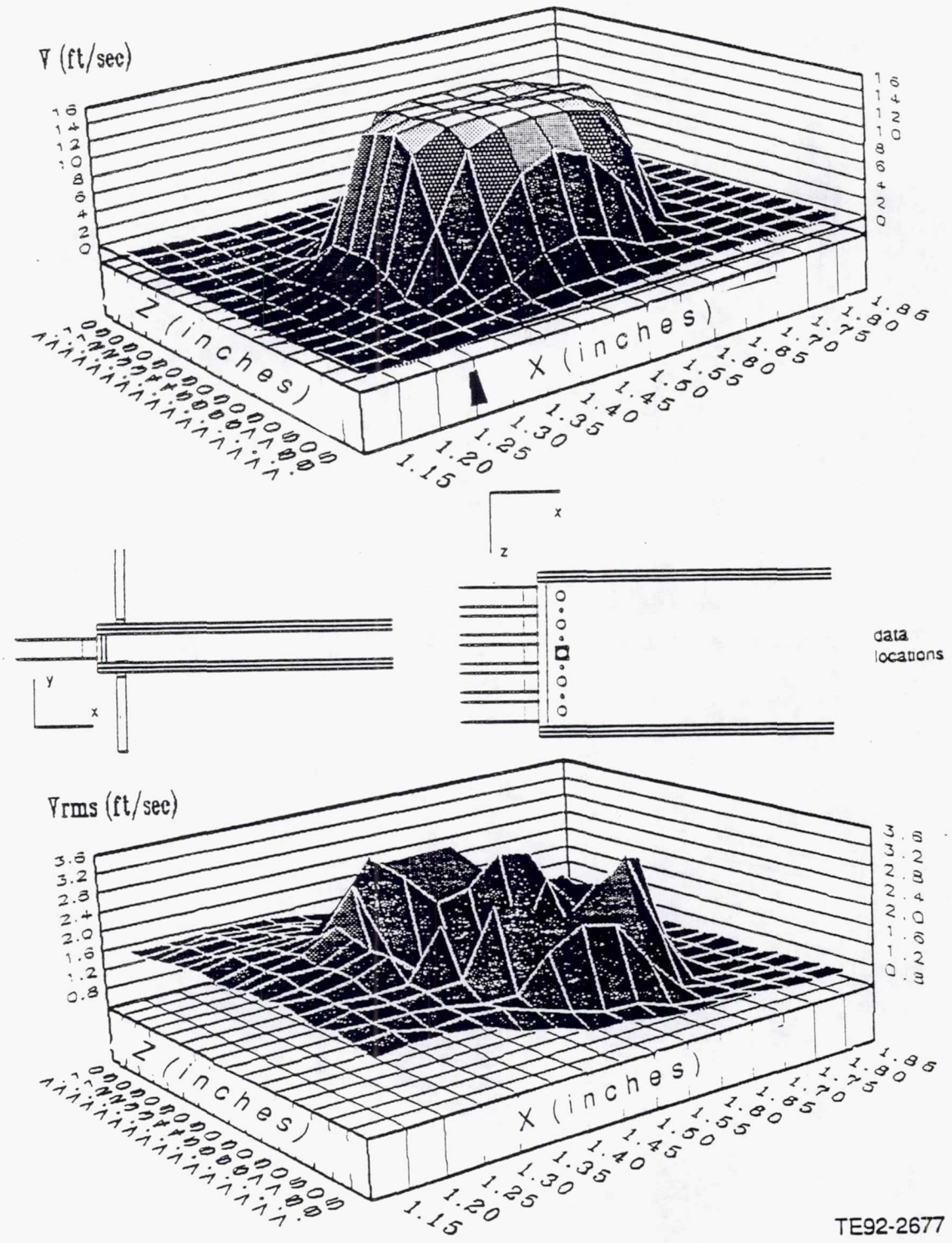

Figure 4.3.2-3. Annular and primary jets V and V_{rms} distribution of the primary jets at y=0.25 in.

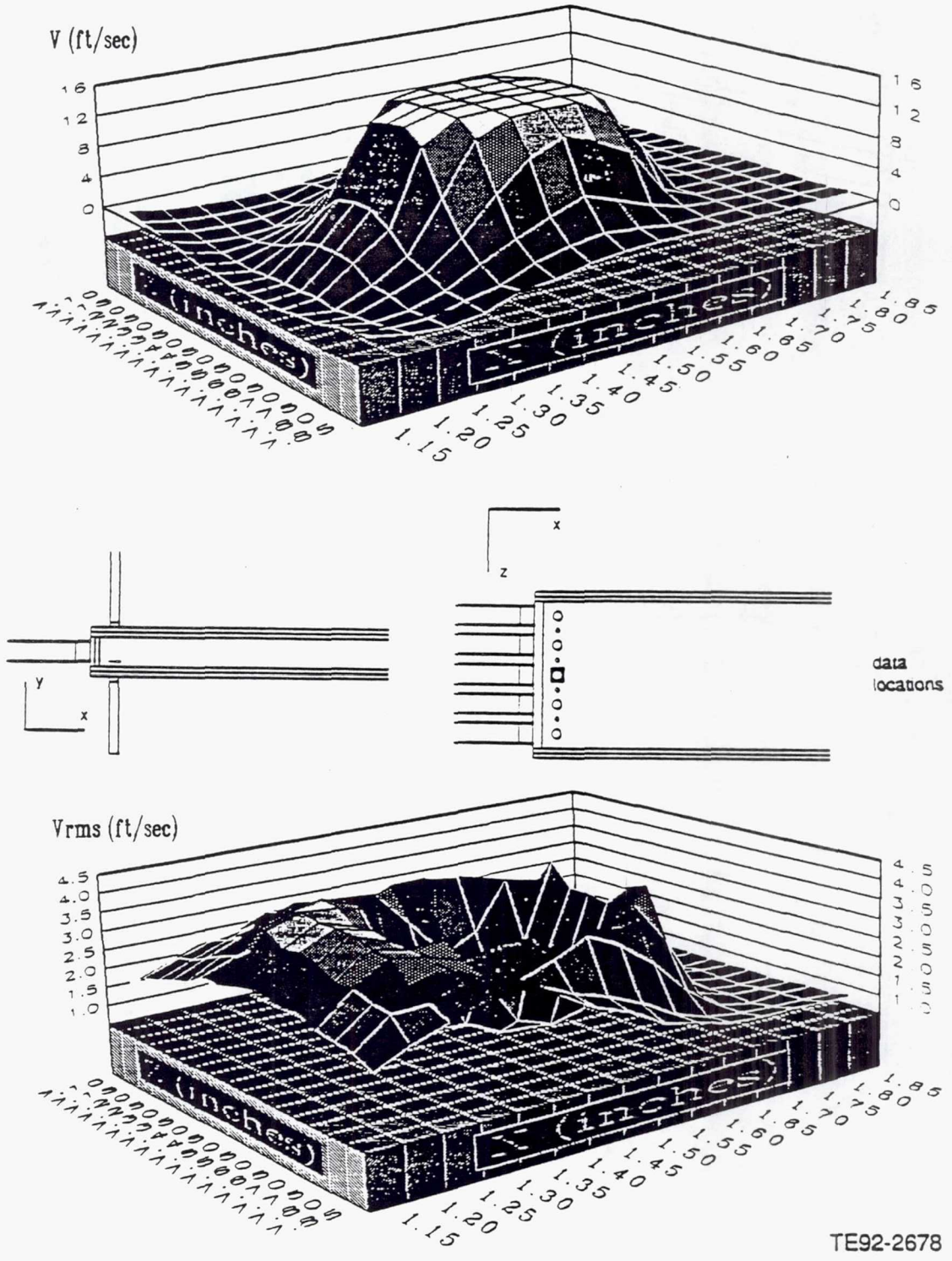

Figure 4.3.2-4. Annular and primary jets V and V_{rms} distribution of the primary jets at y=0.5 in.

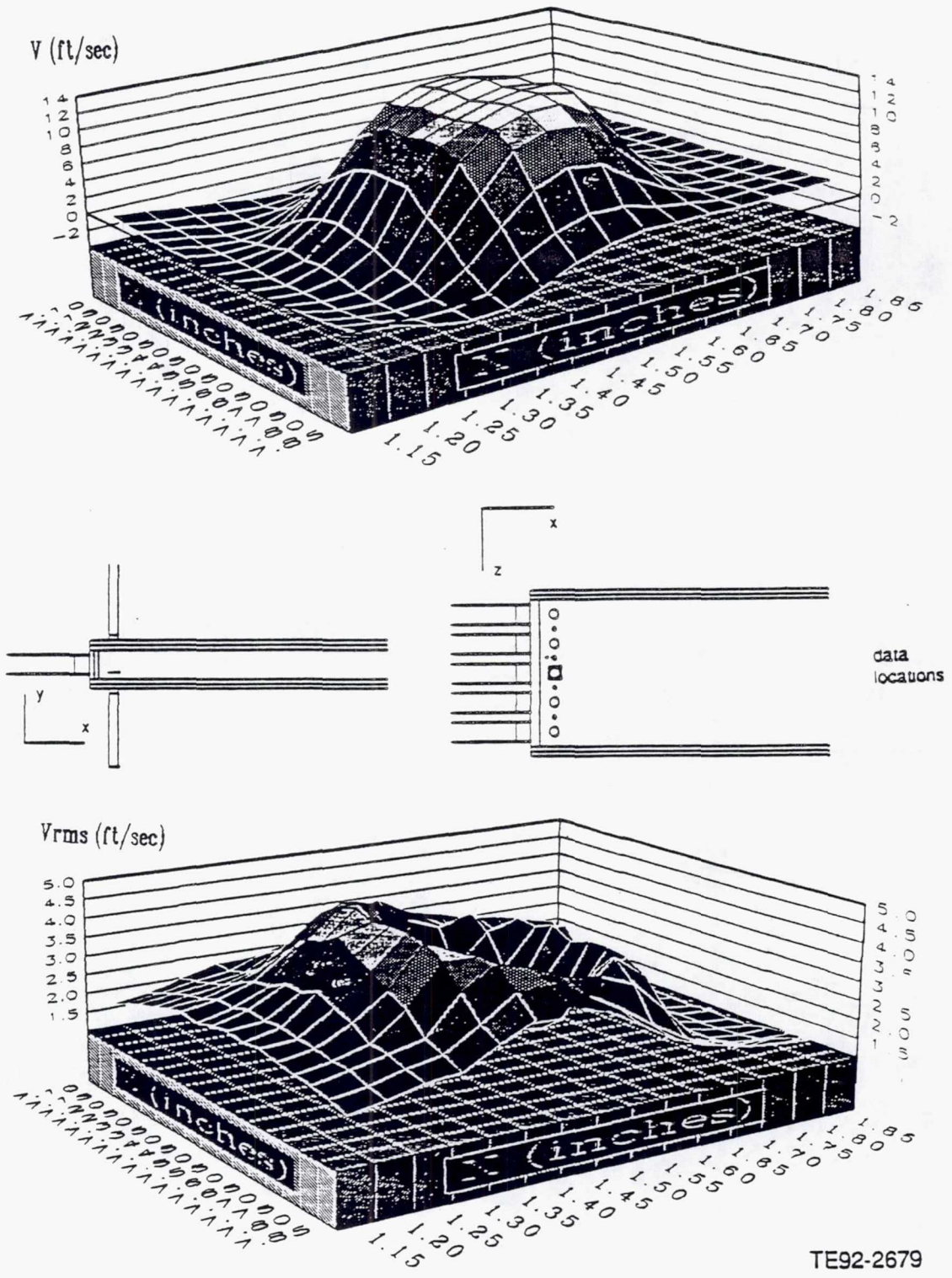

Figure 4.3.2-5. Annular and primary jets V and V_{rms} distribution of the primary jets at y=0.75 in.

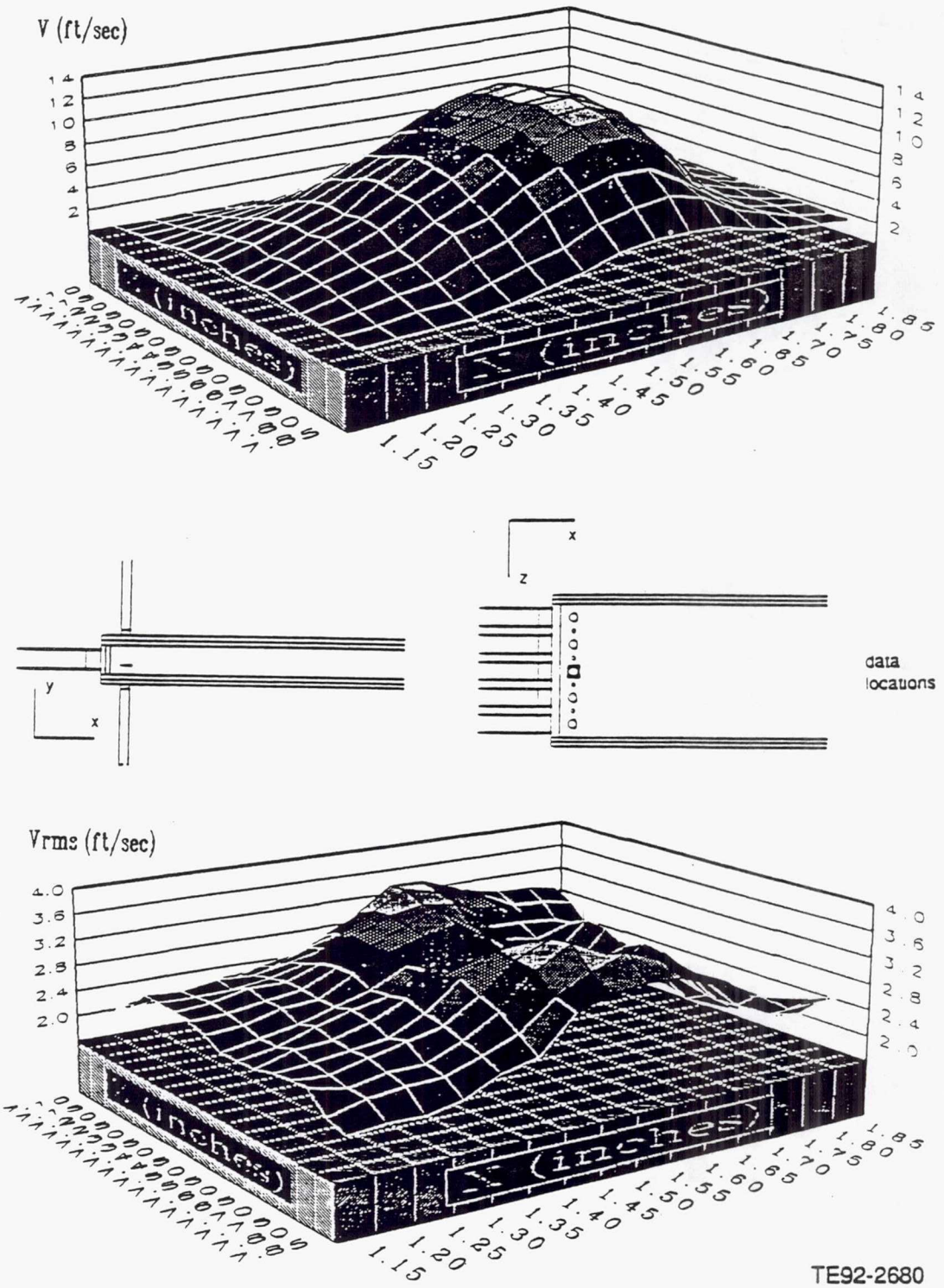

Figure 4.3.2-6. Annular and primary jets V and V_{rms} distribution of the primary jets at y=1.0 in.

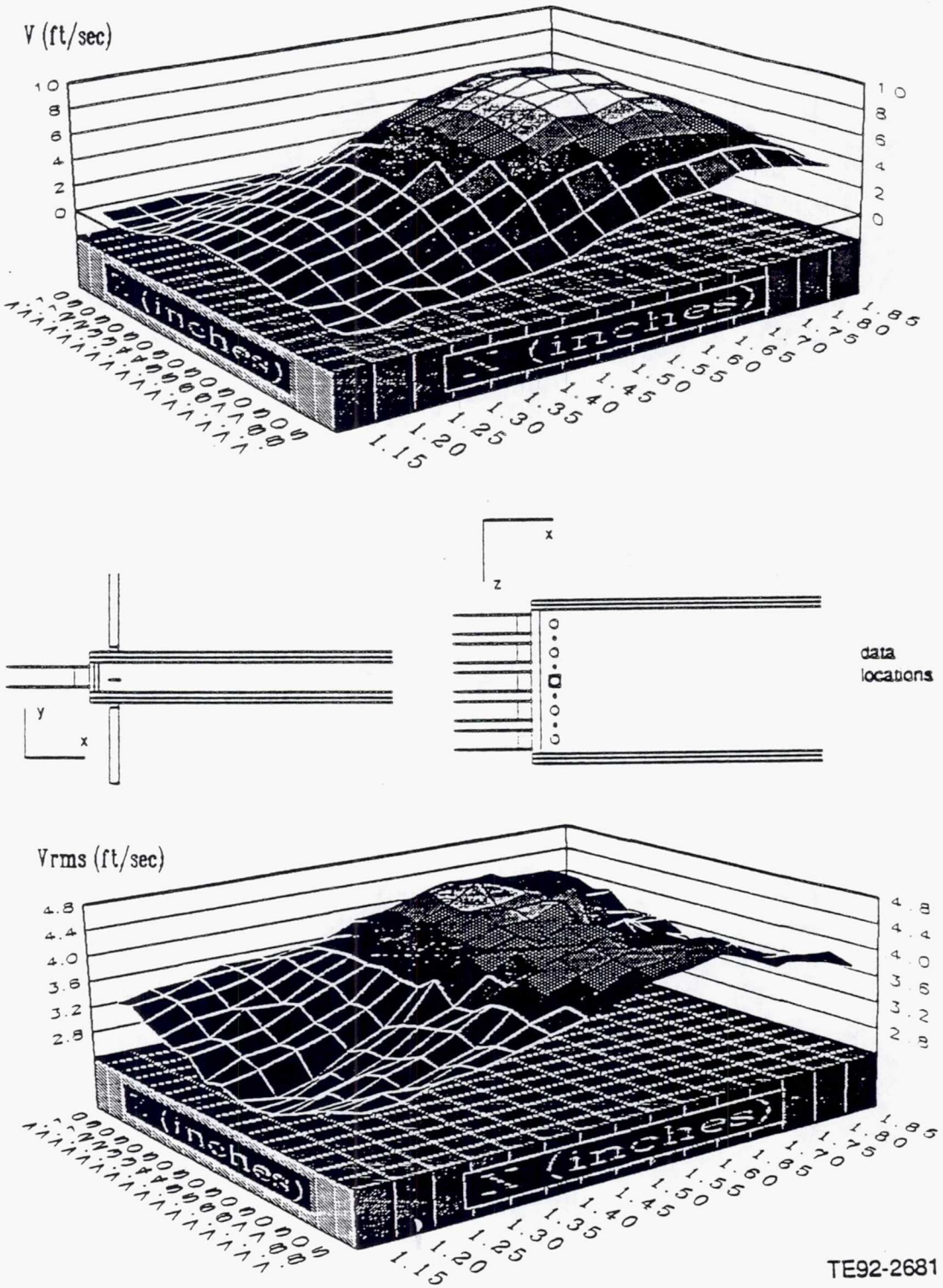

Figure 4.3.2-7. Annular and primary jets V and V_{rms} distribution of the primary jets at y=1.25 in.

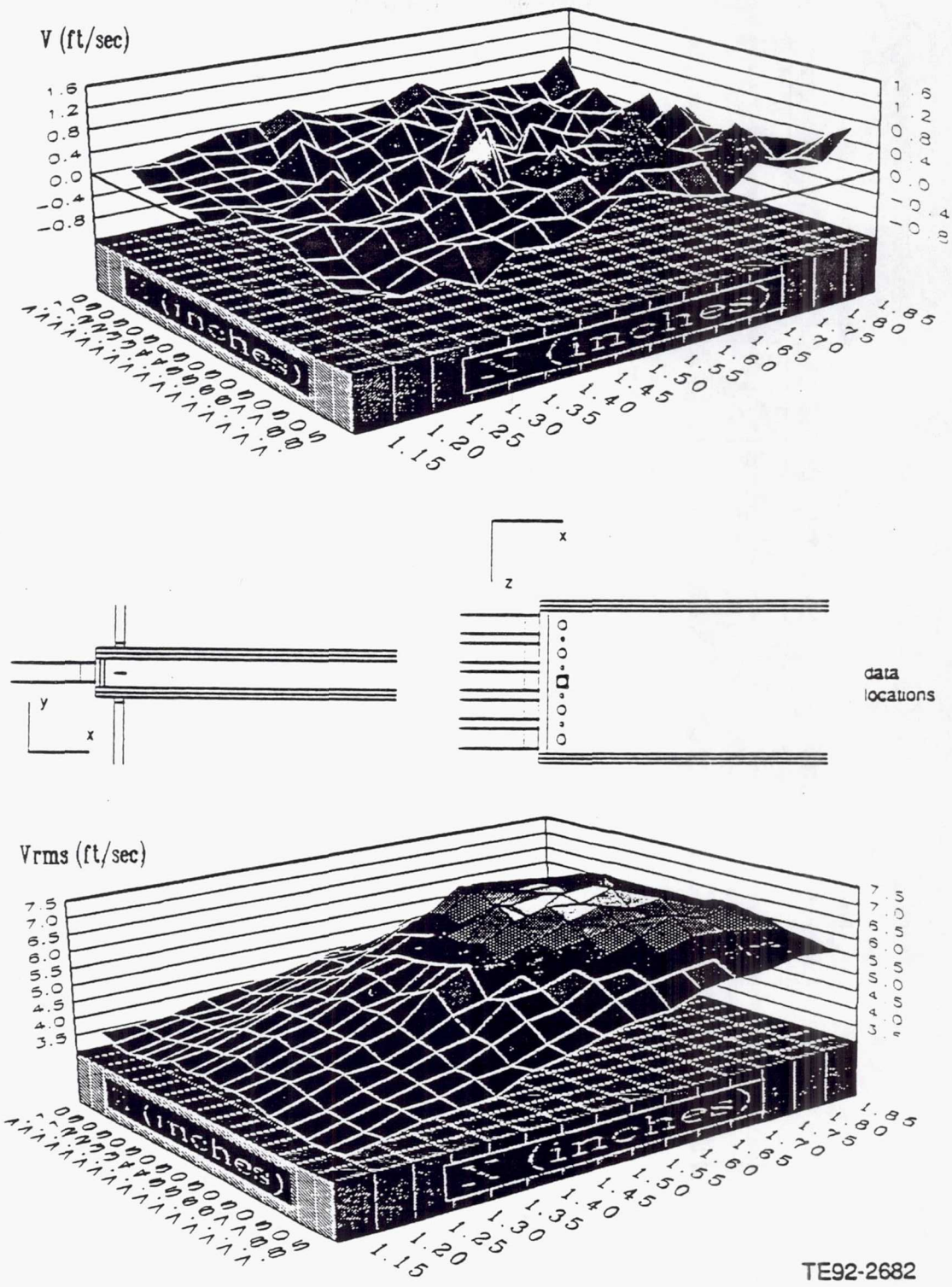

Figure 4.3.2-8. Annular and primary jets V and V_{rms} distribution of the primary jets at y=1.5 in.

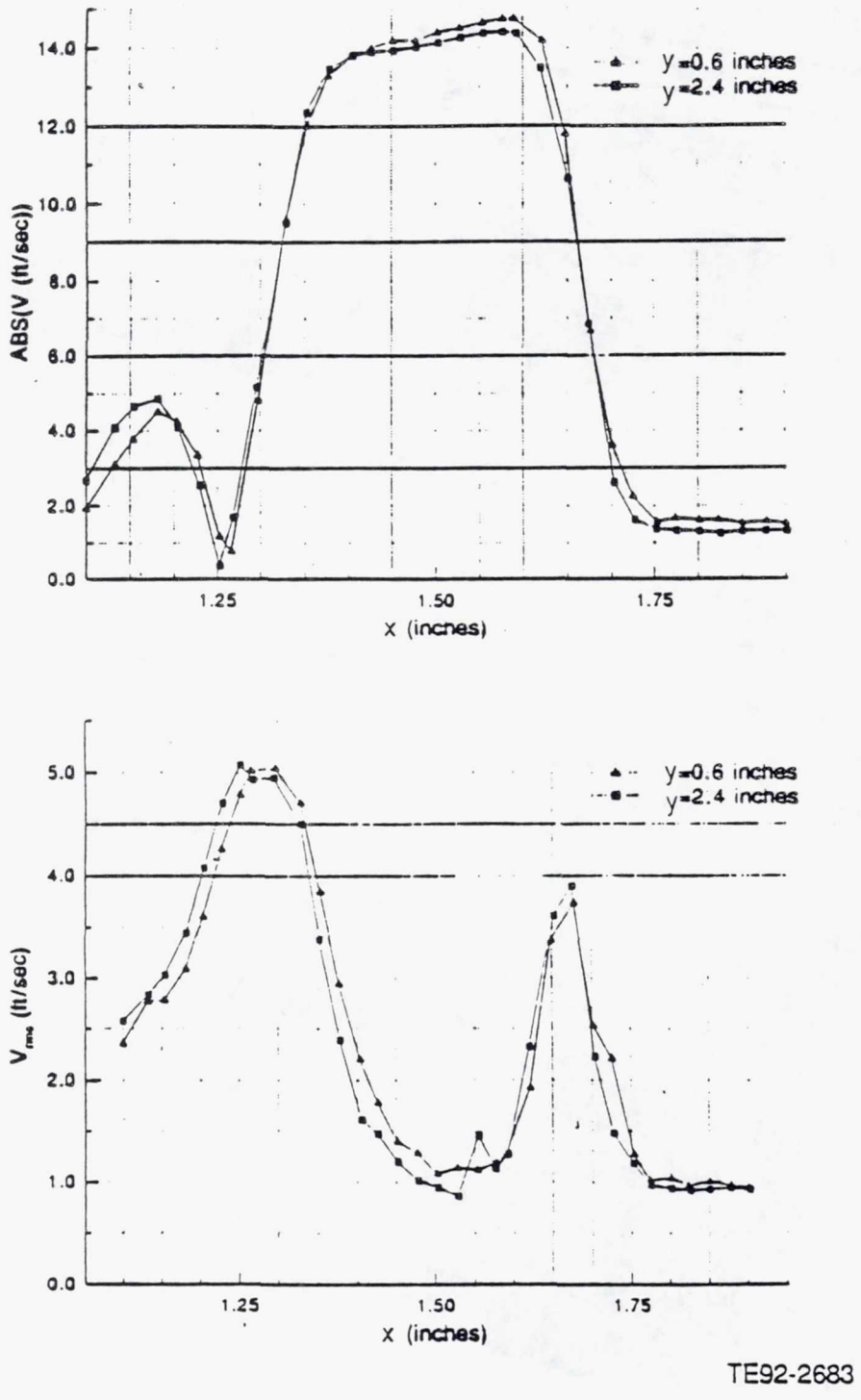

Figure 4.3.2-9. Annular and primary jets and V_{rms} distribution comparison of the primary jets at y=0.6 in. and y=2.4 in.

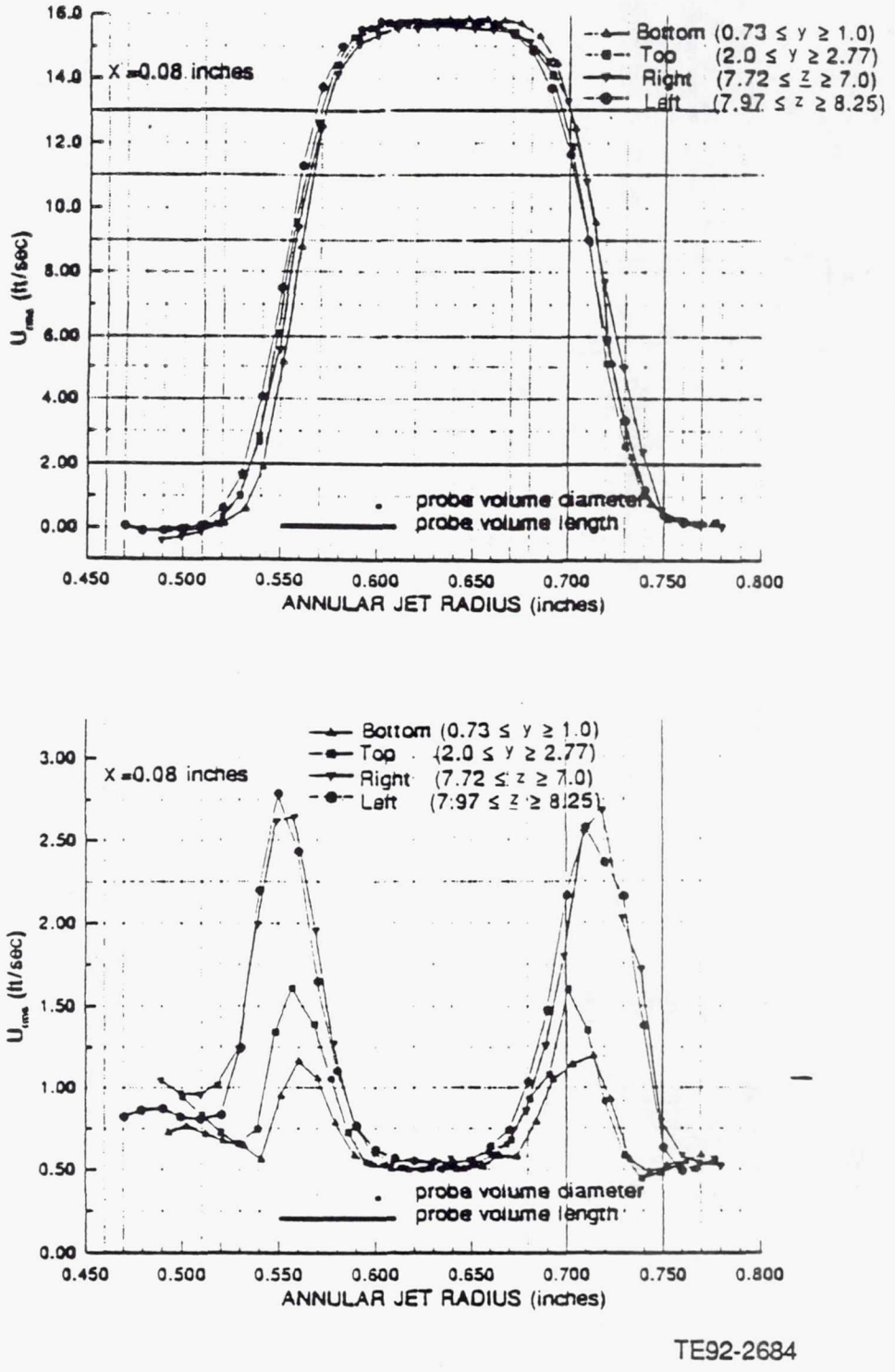

Figure 4.3.2-10. Annular and primary jets and U_{rms} distribution of the annular jets at x =0.08 in.

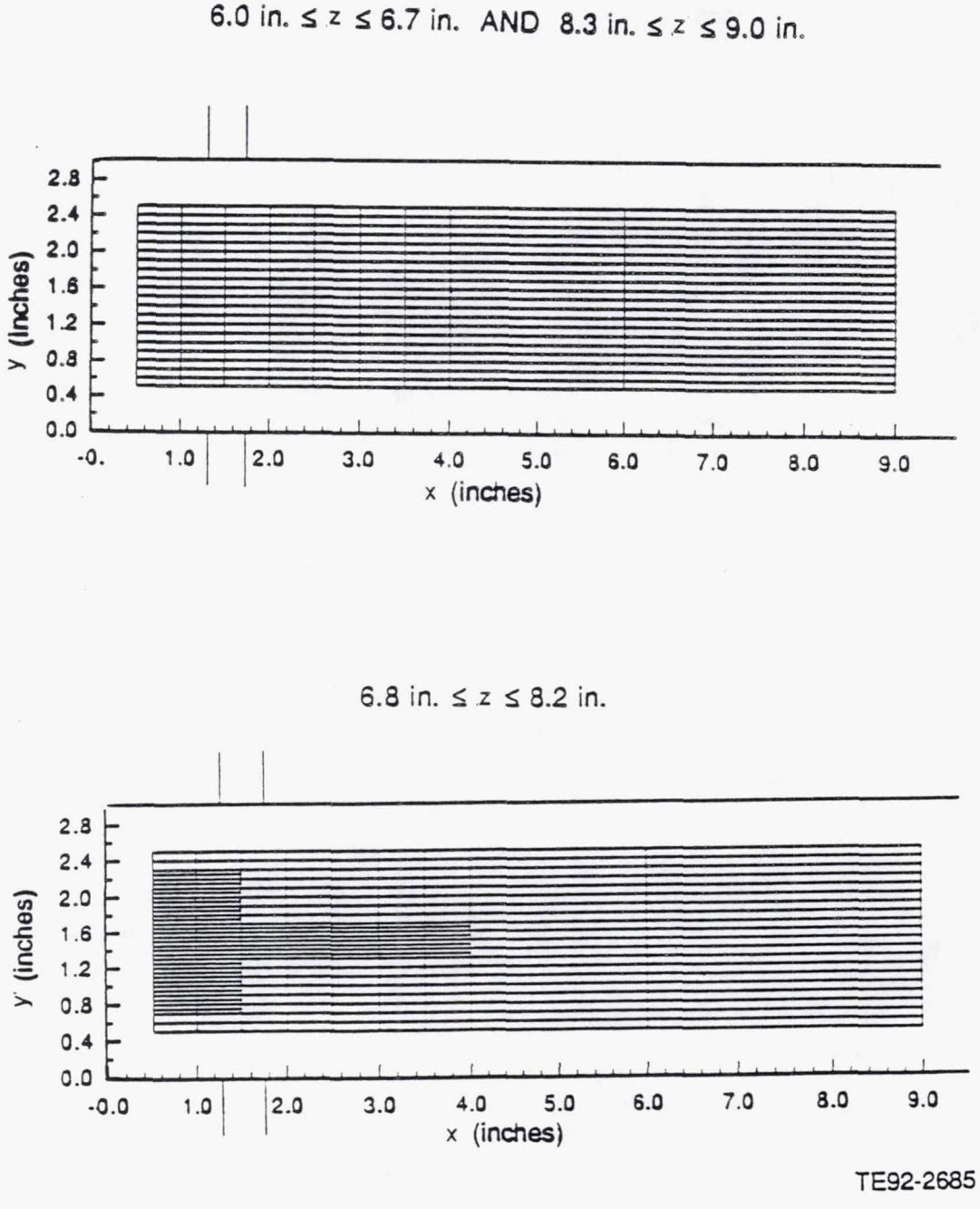

Figure 4.3.2-11. Annular and primary jets x y plane sampling grid.

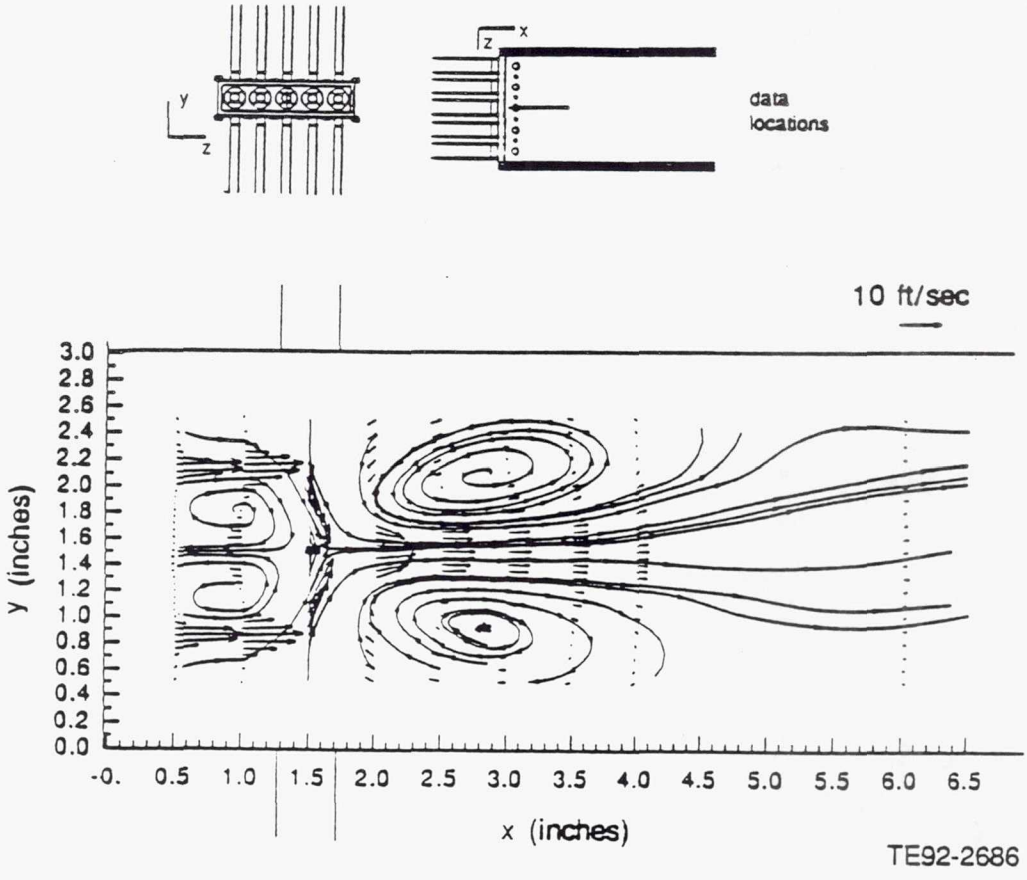

Figure 4.3.2-12. Annular and primary jets mean velocity vector plot at z=7.5 in.

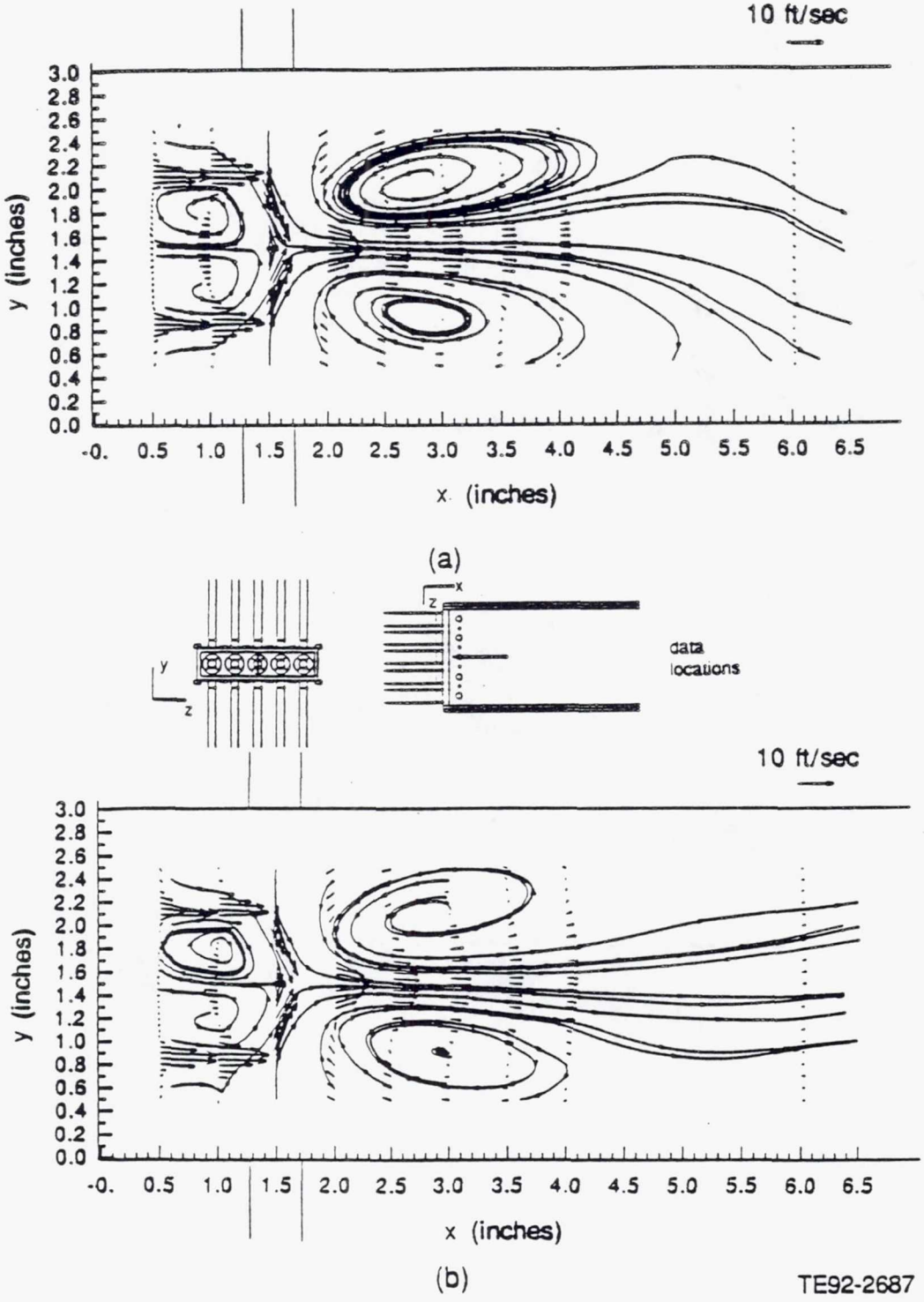

Figure 4.3.2-13. Annular and primary jets mean velocity vector plot at a) z=7.4 in. b) z=7.6 in.

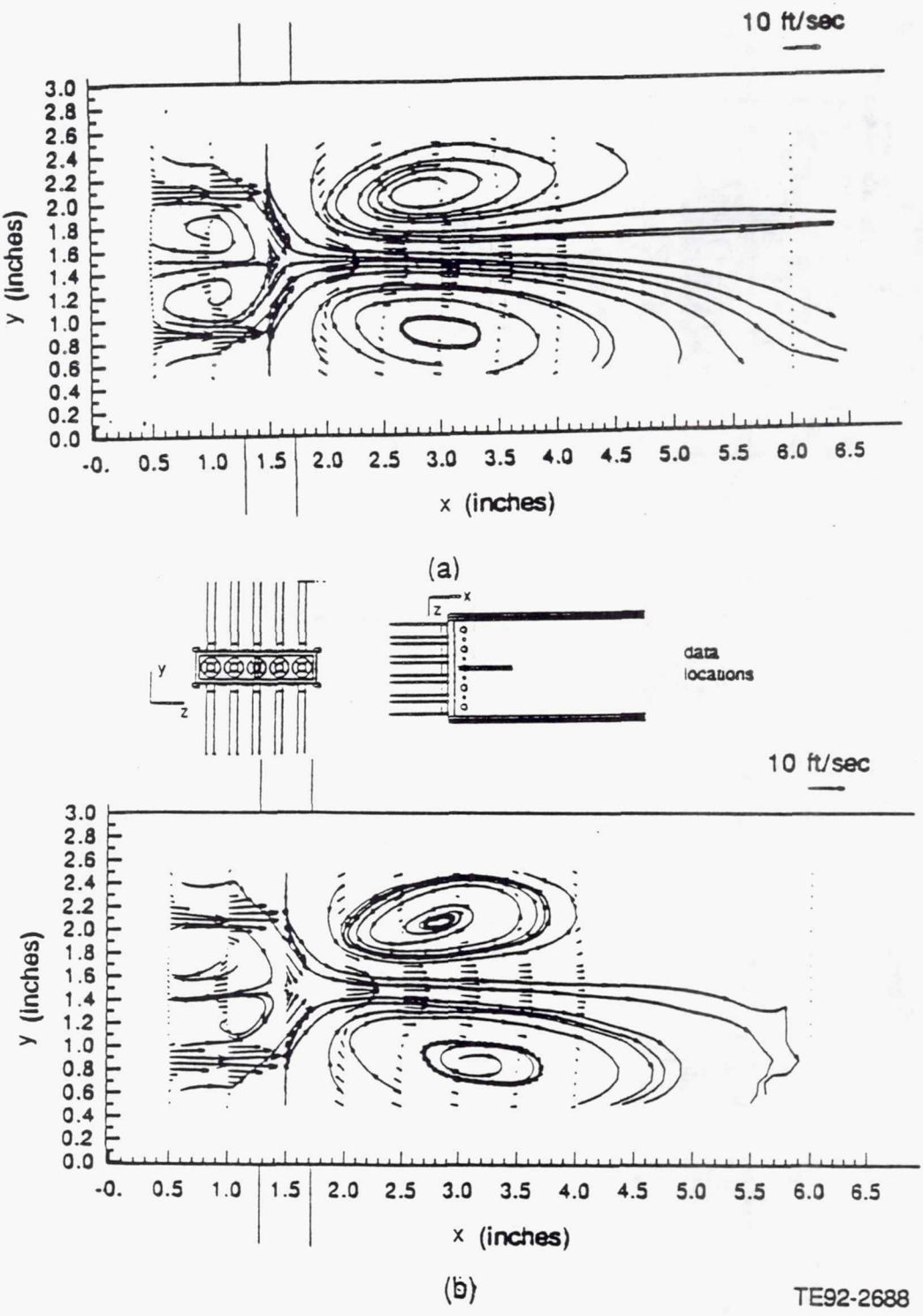

Figure 4.3.2-14. Annular and primary jets mean velocity vector plot at a) z=7.3 in. b) z=7.7 in.

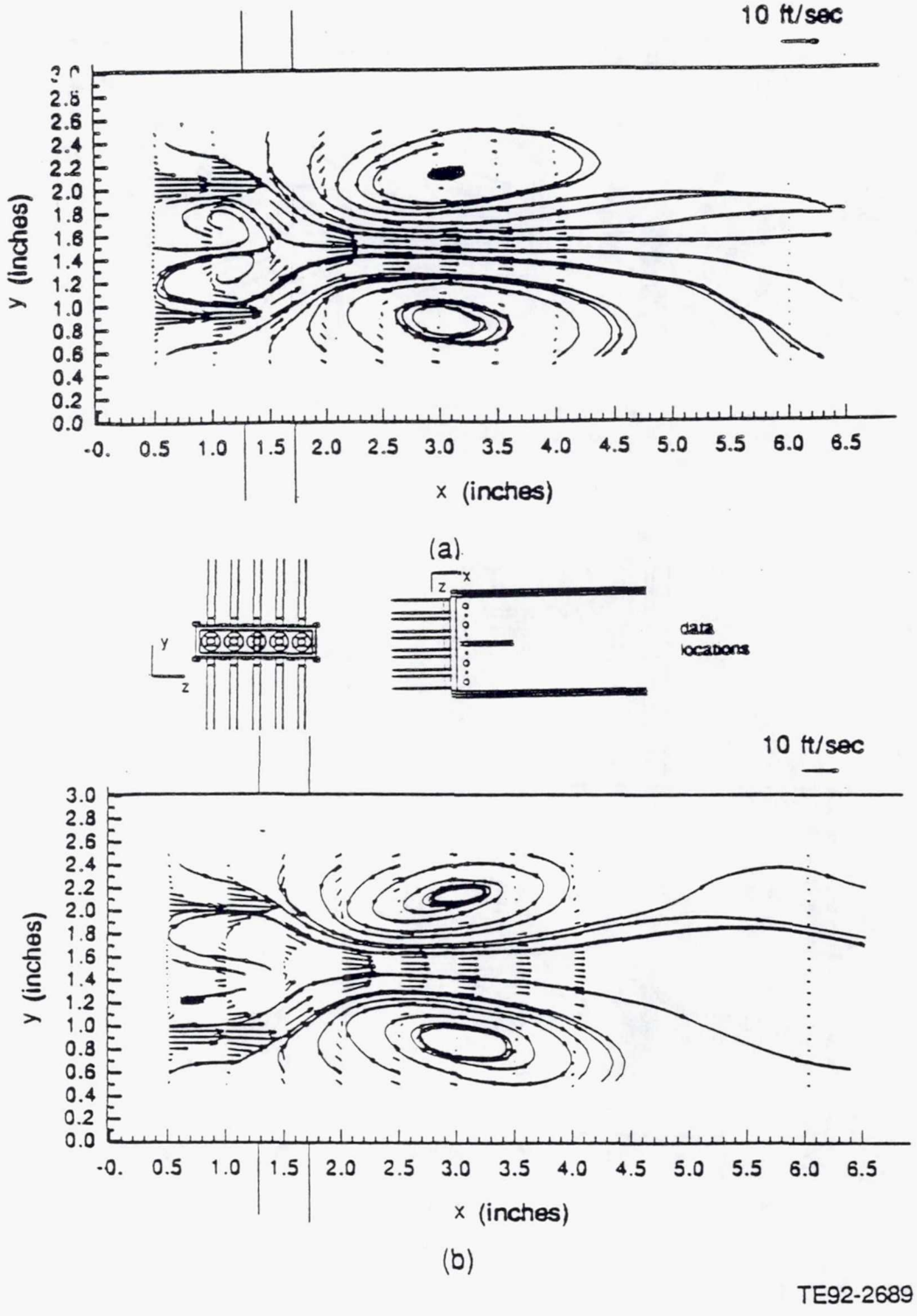

Figure 4.3.2-15. Annular and primary jets mean velocity vector plot at a) z=7.2 in. b) z=7.8 in.

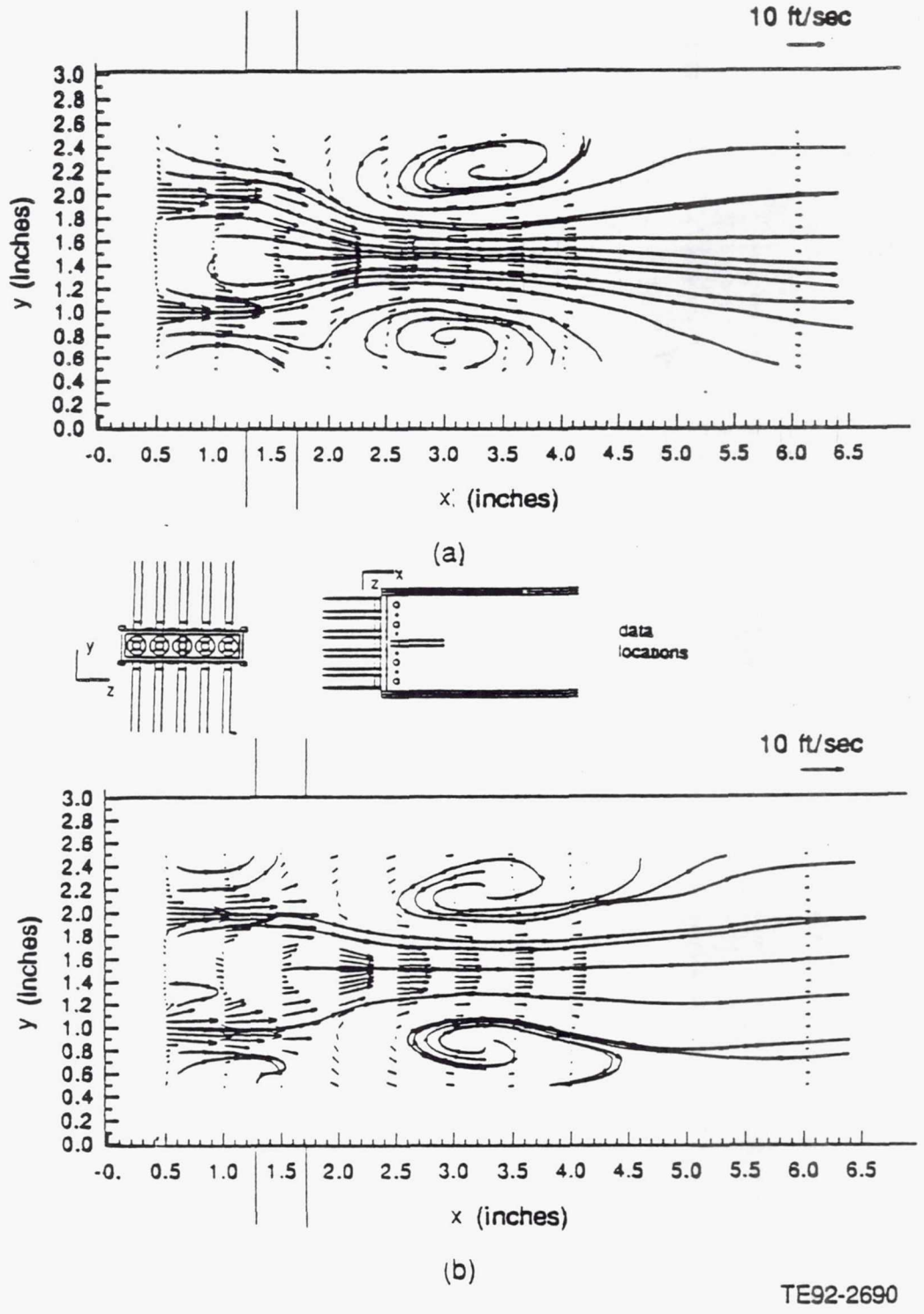

Figure 4.3.2-16. Annular and primary jets mean velocity vector plot at a) z=7.1 in. b) z=7.9 in.

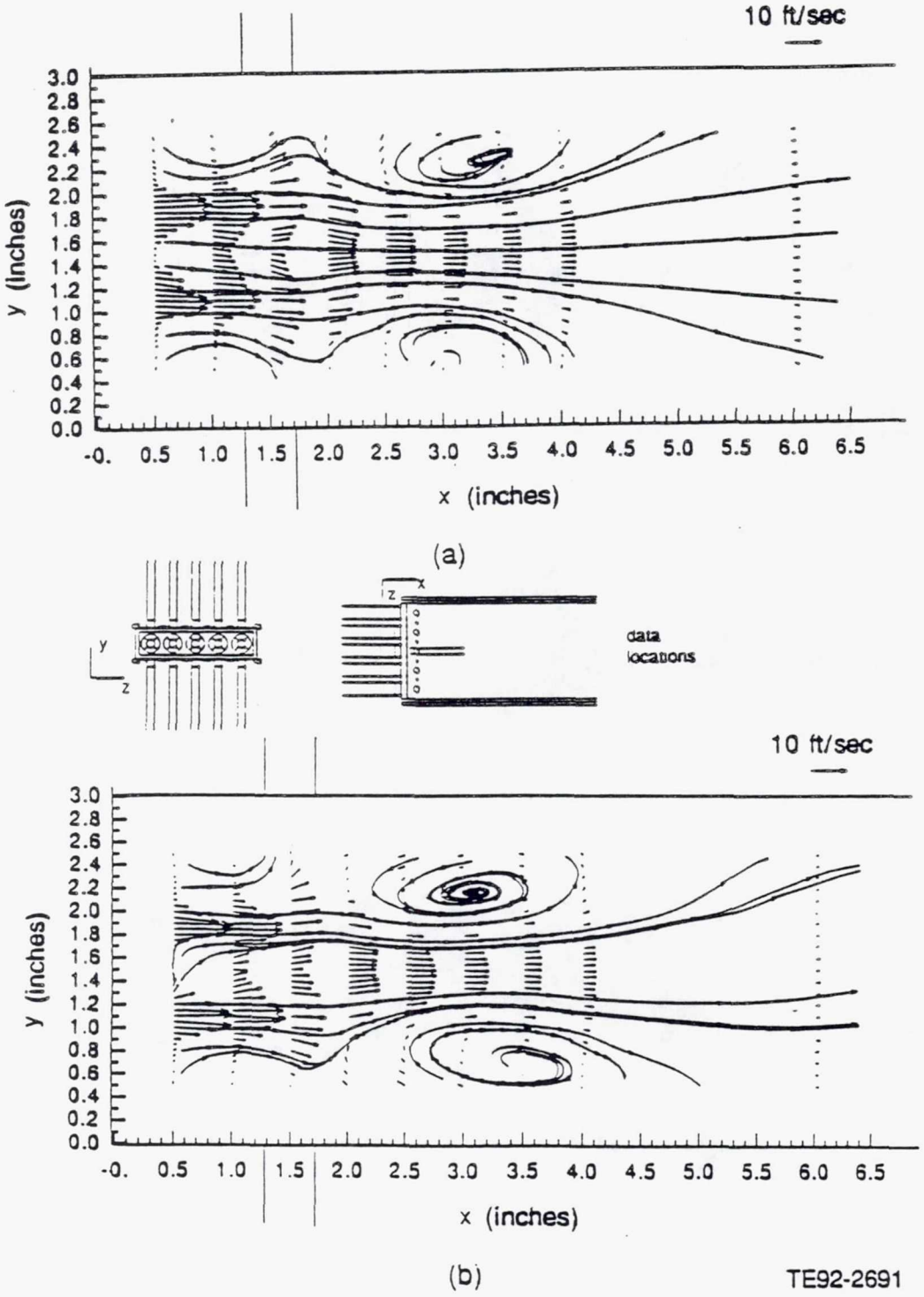

Figure 4.3.2-17. Annular and primary jets mean velocity vector plot at a) Z=7.0 in. b) z=8.0 in.

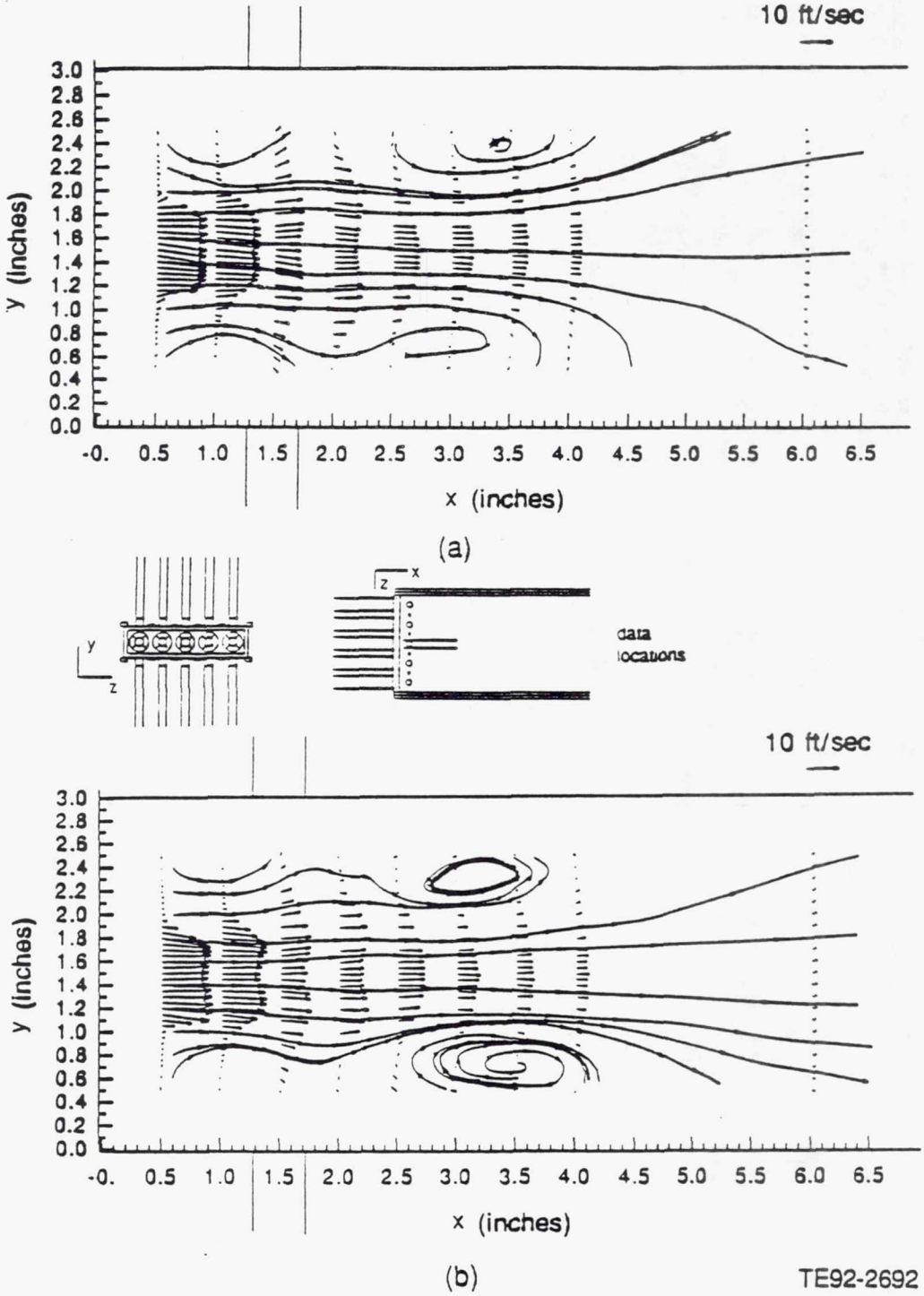

Figure 4.3.2-18. Annular and primary jets mean velocity vector plot at a) z=6.9 in. b) z=8.1 in.

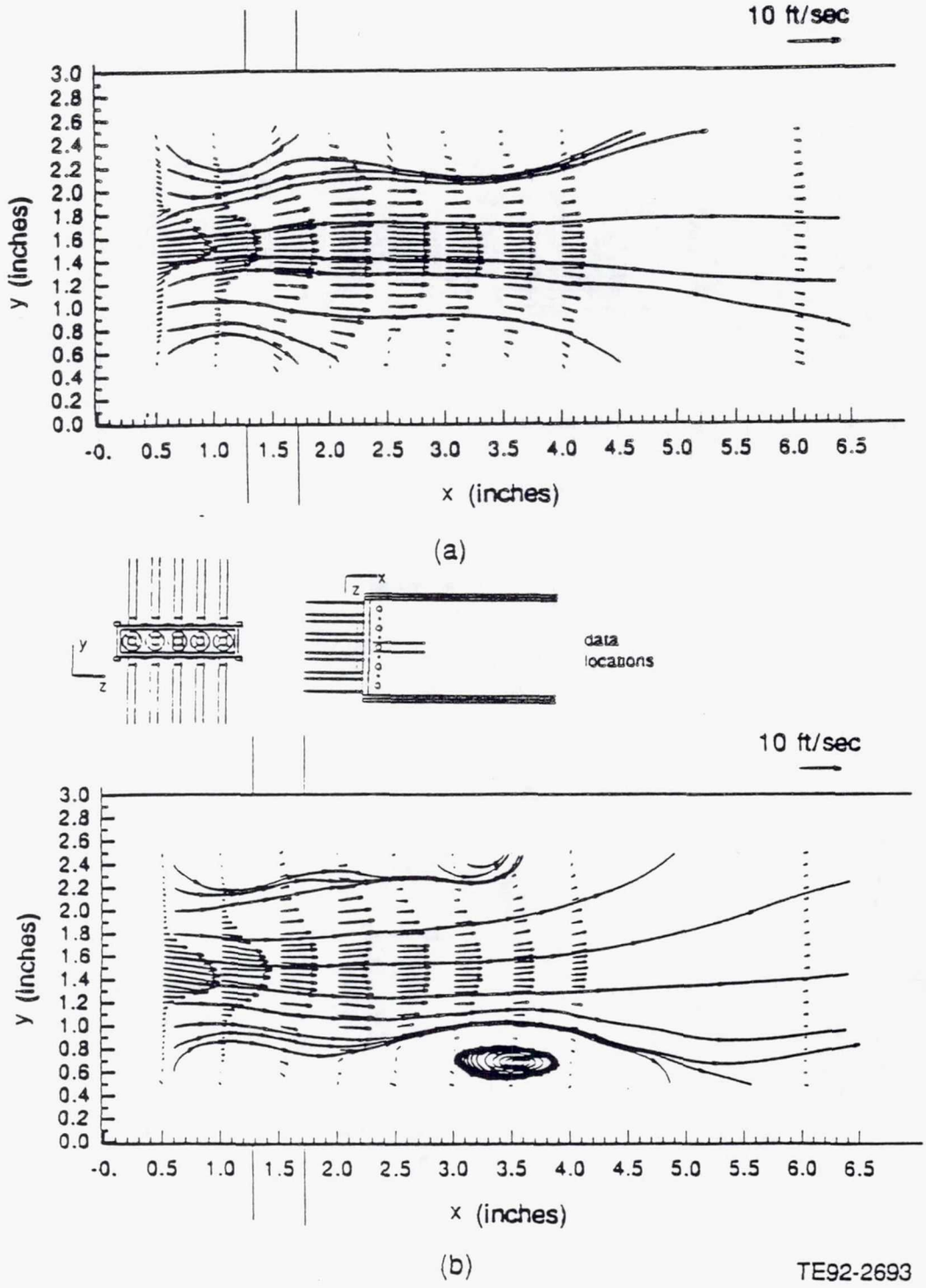

Figure 4.3.2-19. Annular and primary jets mean velocity vector plot at a) z=6.8 in. b) z=8.2 in.

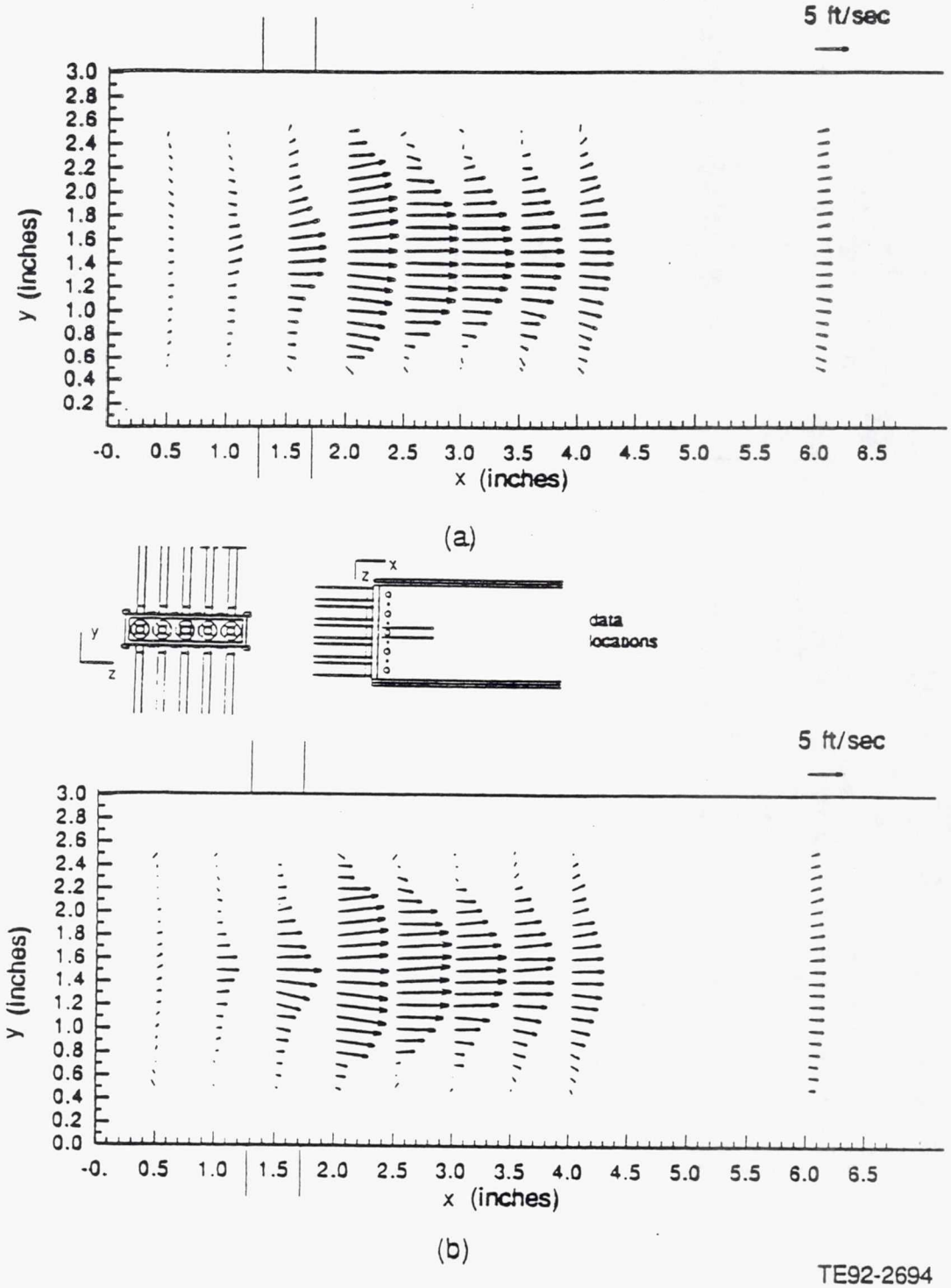

Figure 4.3.2-20. Annular and primary jets mean velocity vector plot at a) z=6.7 in. b) z=8.3 in.

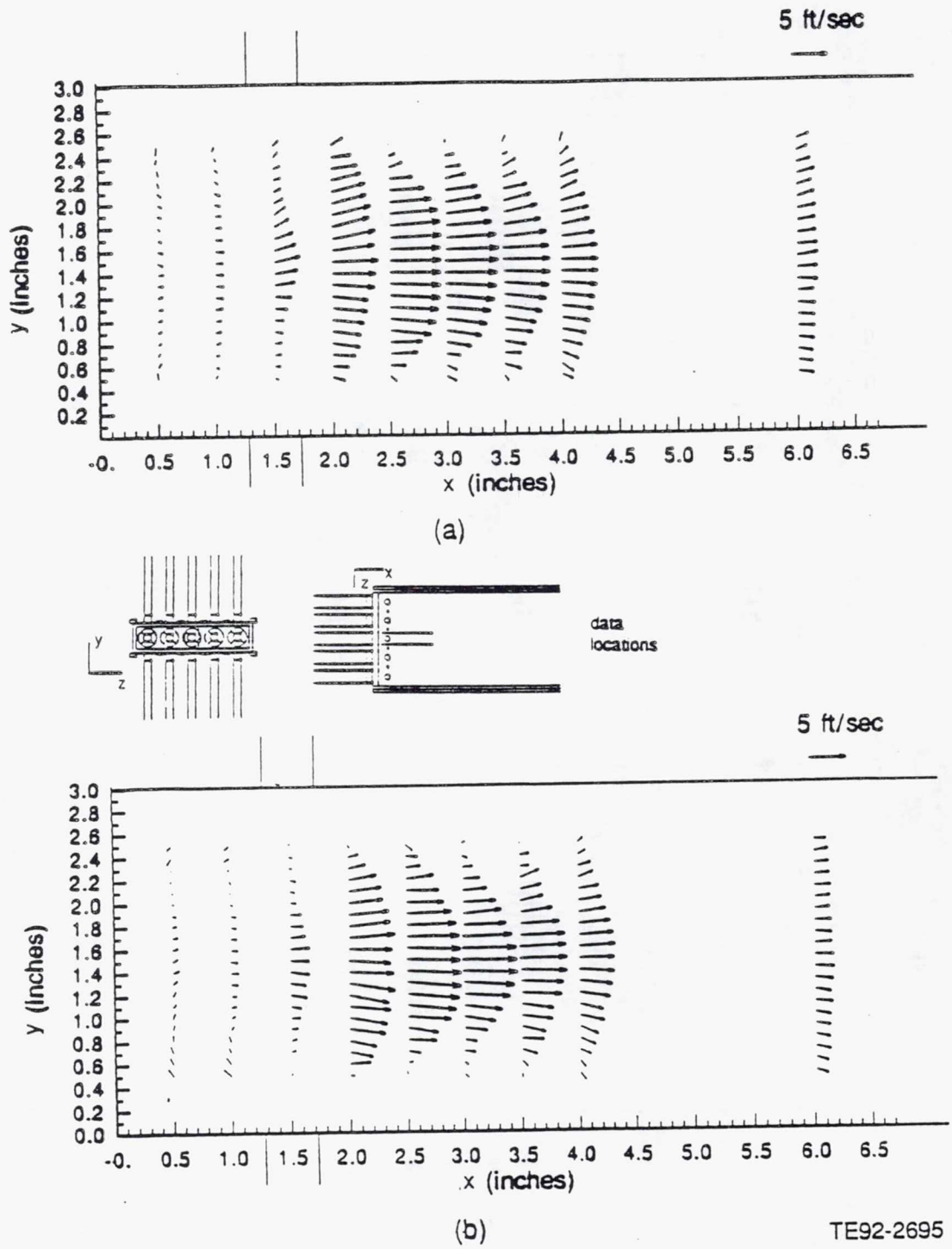

Figure 4.3.2-21. Annular and primary jets mean velocity vector plot at a) z=6.6 in. b) z=8.4 in.

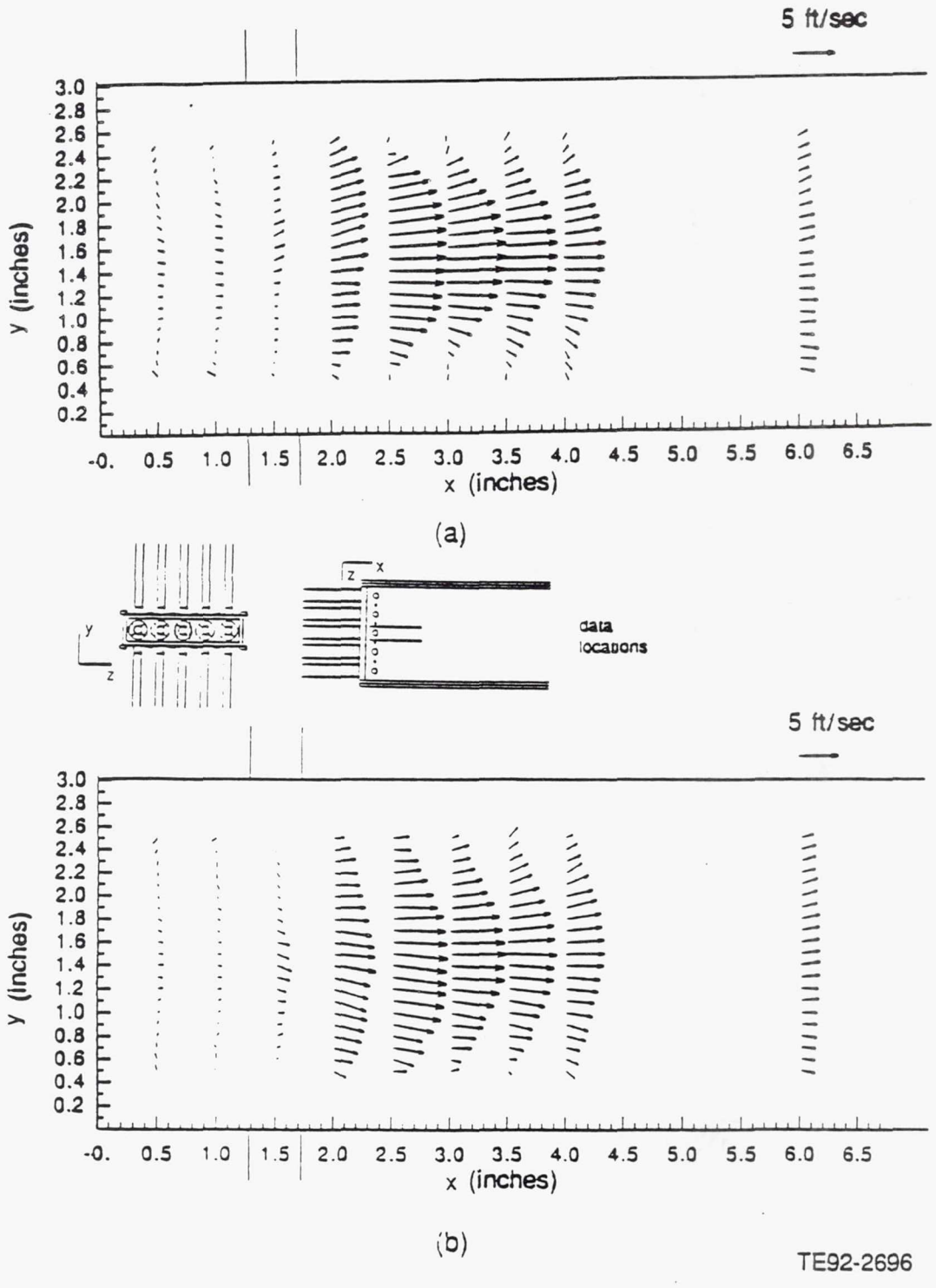

Figure 4.3.2-22. Annular and primary jets mean velocity vector plot at a) z=6.5 in. b) z=8.5 in.

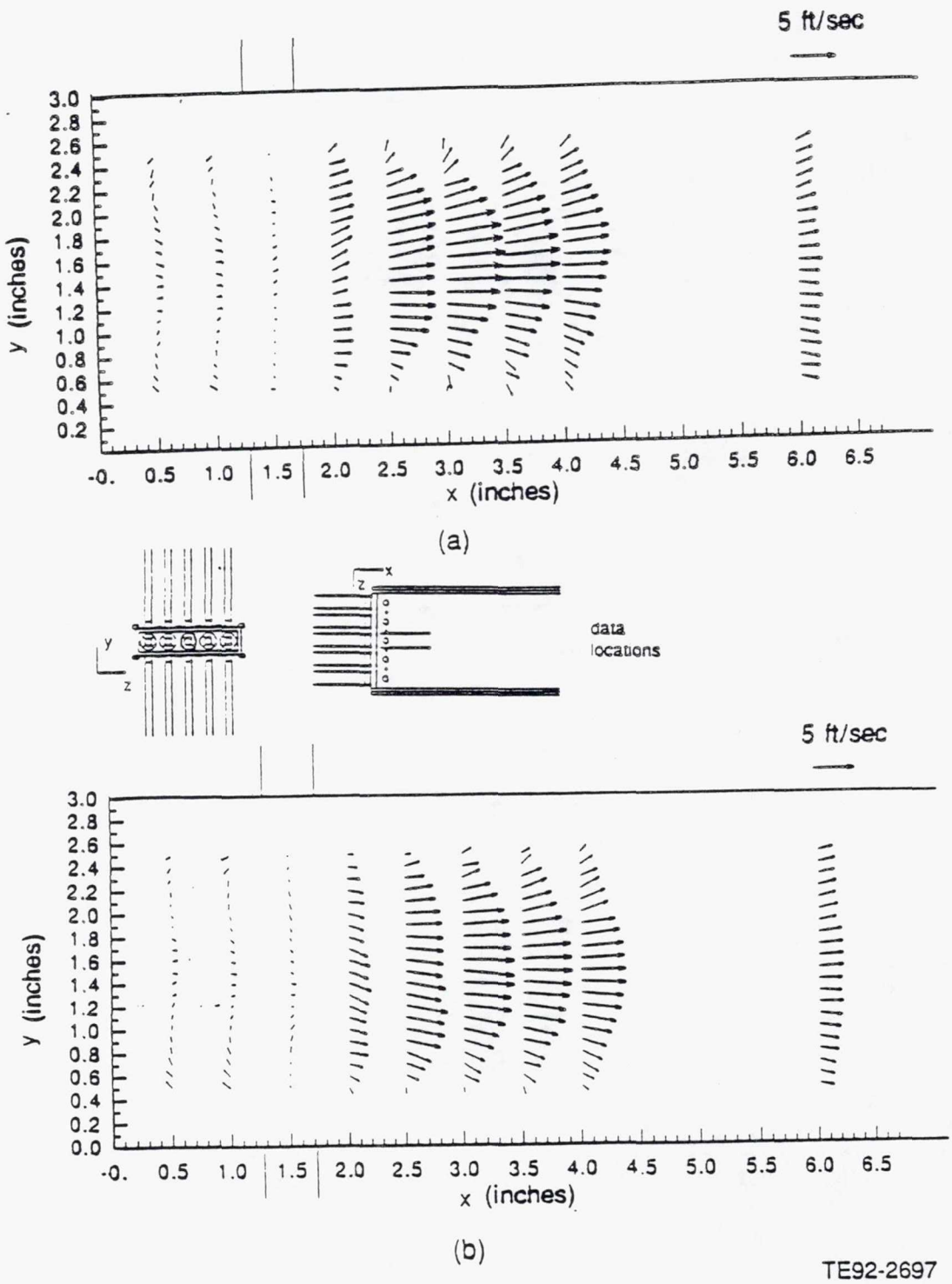

Figure 4.3.2-23. Annular and primary jets mean velocity vector plot at a) z=6.4 in. b) z=8.6 in.

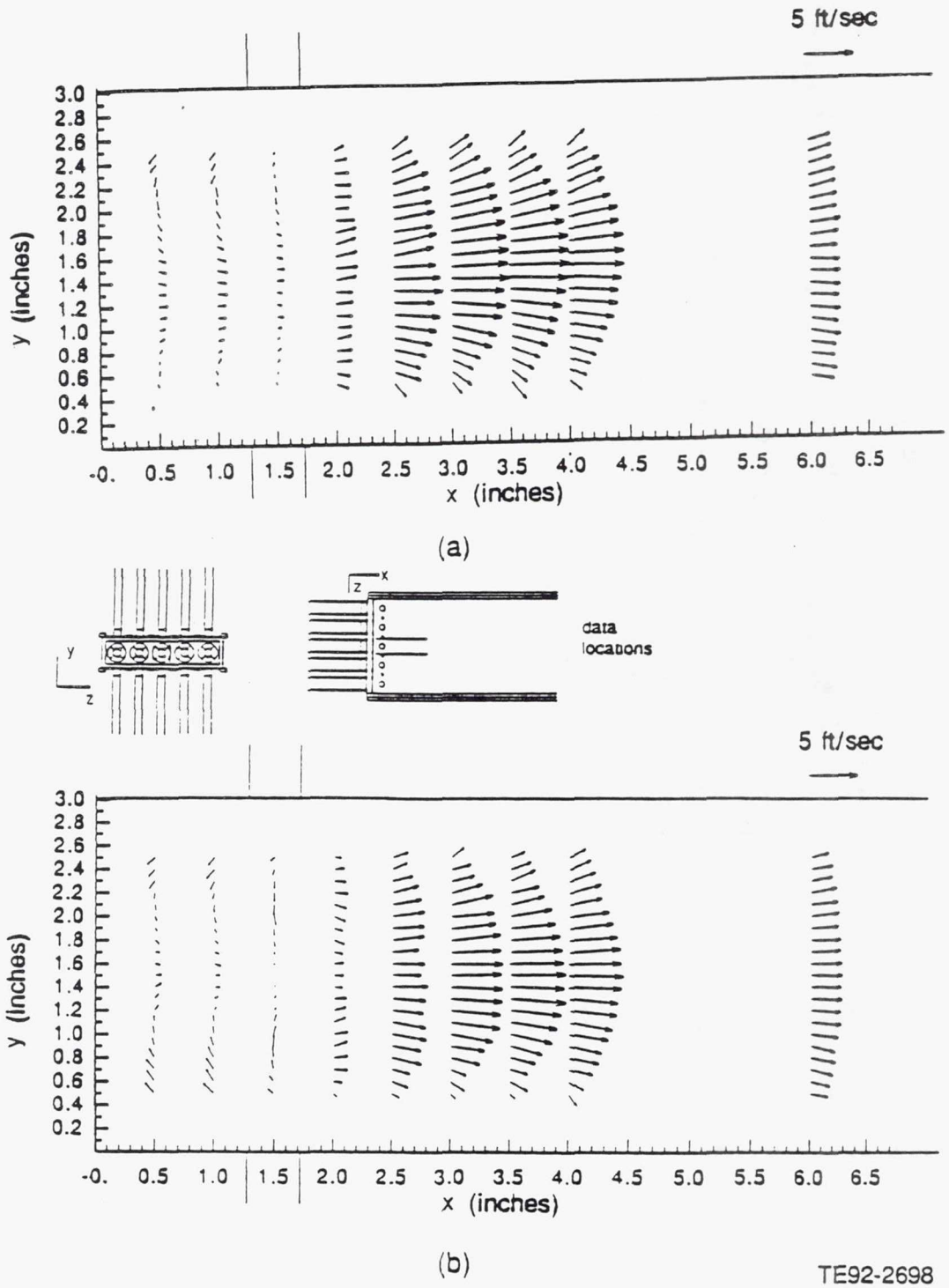

Figure 4.3.2-24. Annular and primary jets mean velocity vector plot at a) z=6.3 in. b) z=8.7 in.

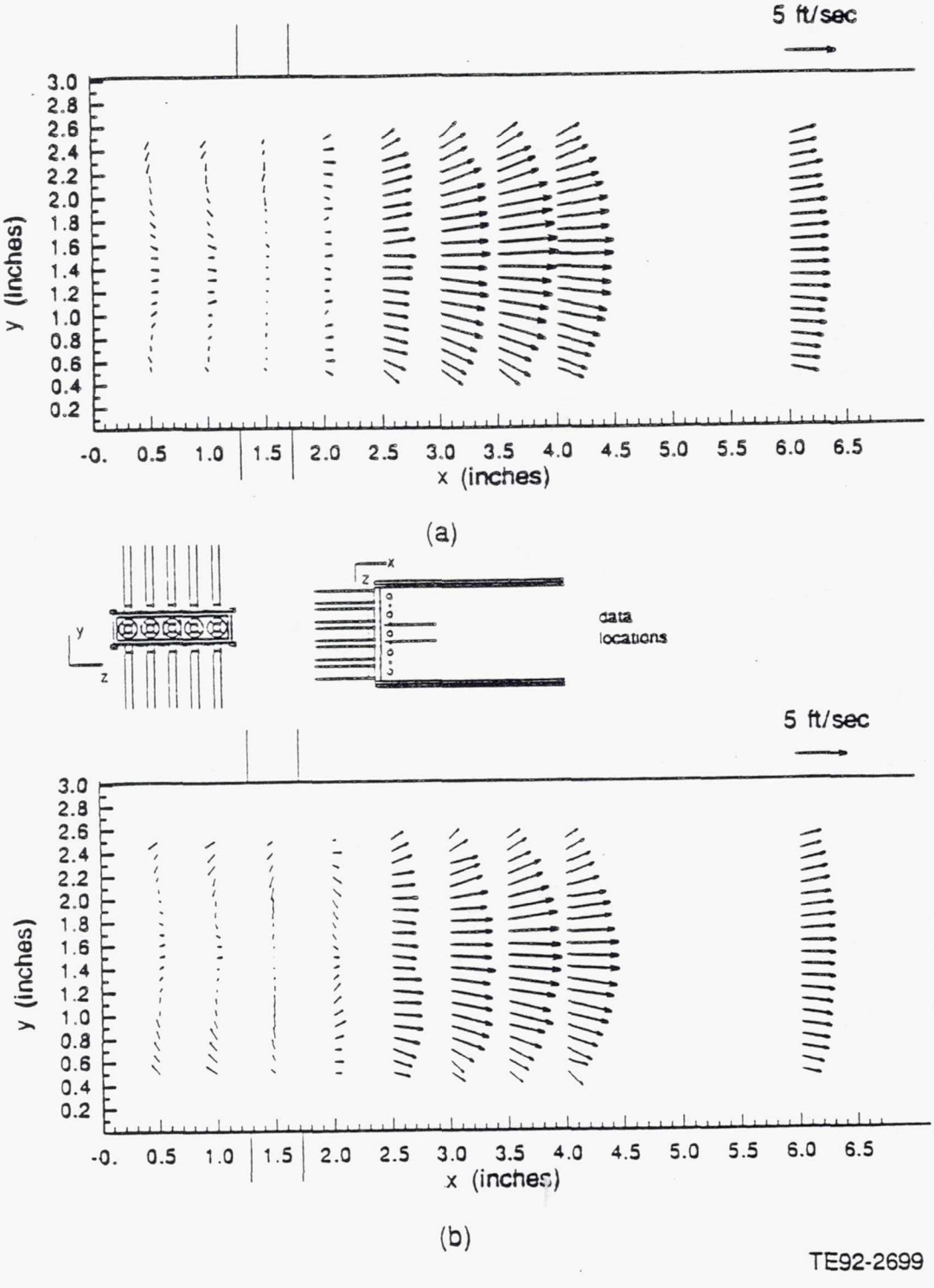

Figure 4.3.2-25. Annular and primary jets mean velocity vector plot at a) z=6.2 in. b) z=8.8 in.

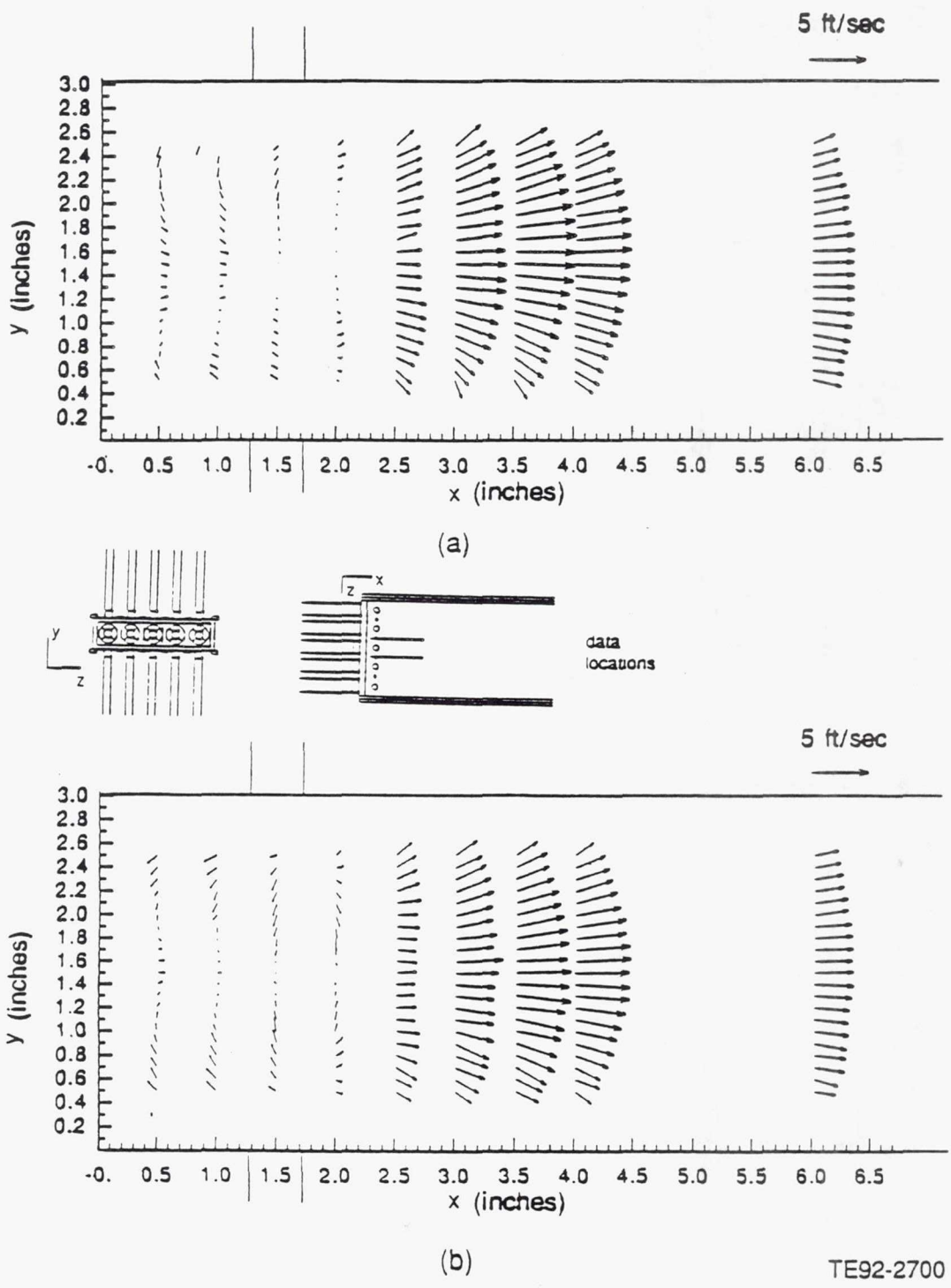

Figure 4.3.2-26. Annular and primary jets mean velocity vector plot at a) z=6.1 in. b) z=8.9 in.

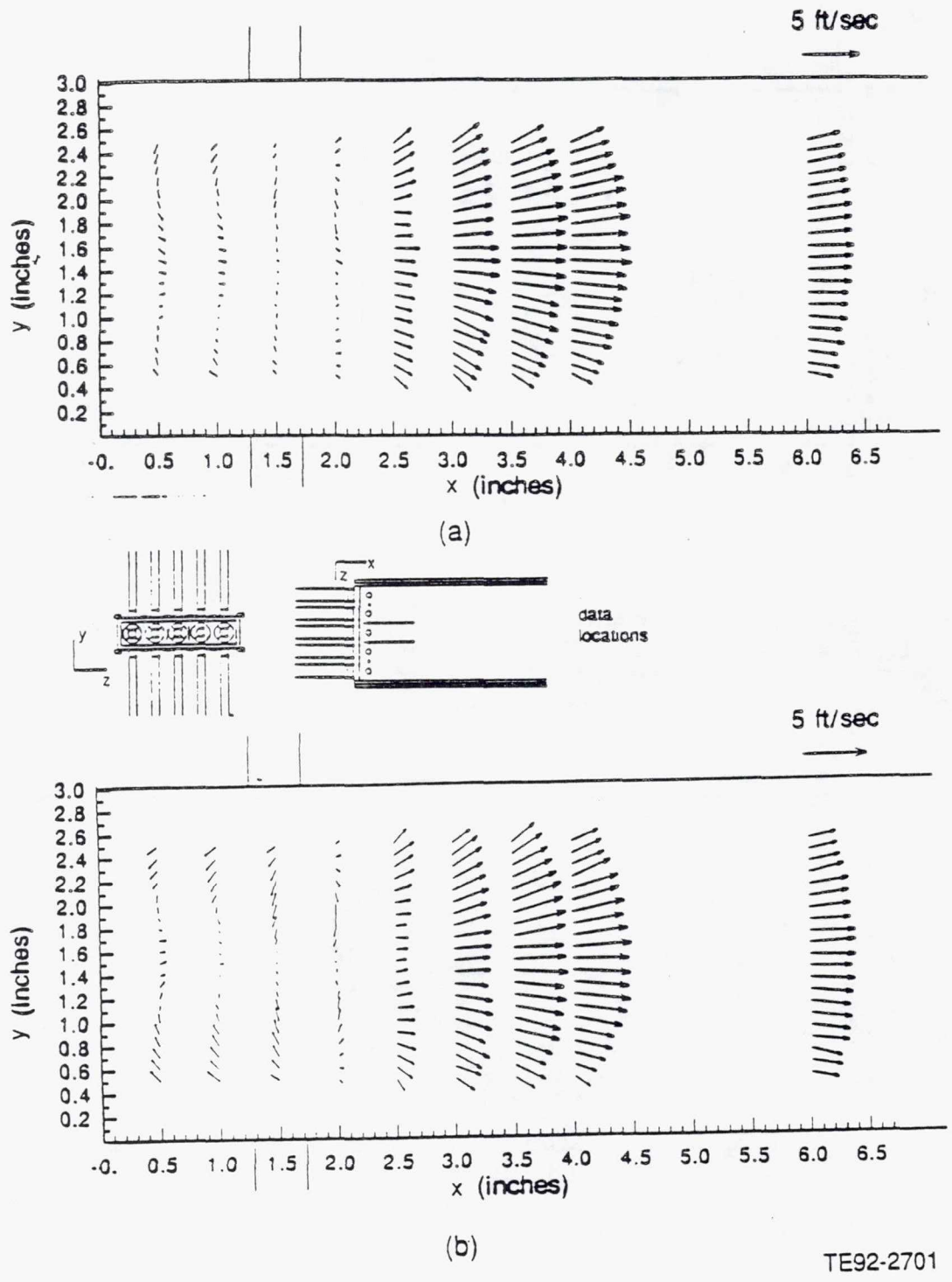

Figure 4.3.2-27. Annular and primary jets contour plot of U_{rms} and V_{rms} at x=0.5 in.

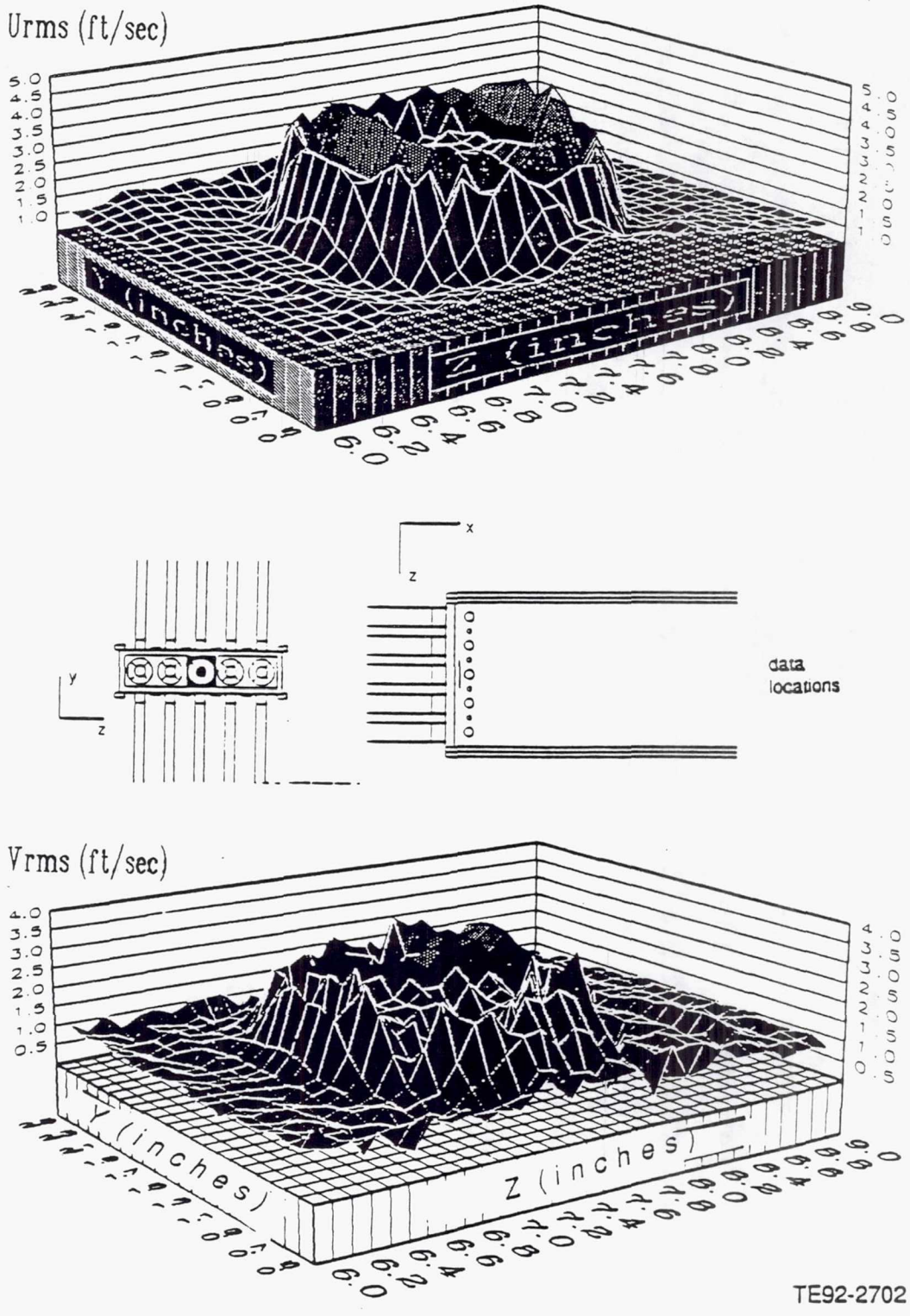

Figure 4.3.2-28. Annular and primary jets contour plot of U_{rms} and V_{rms} at x=1.0 in.

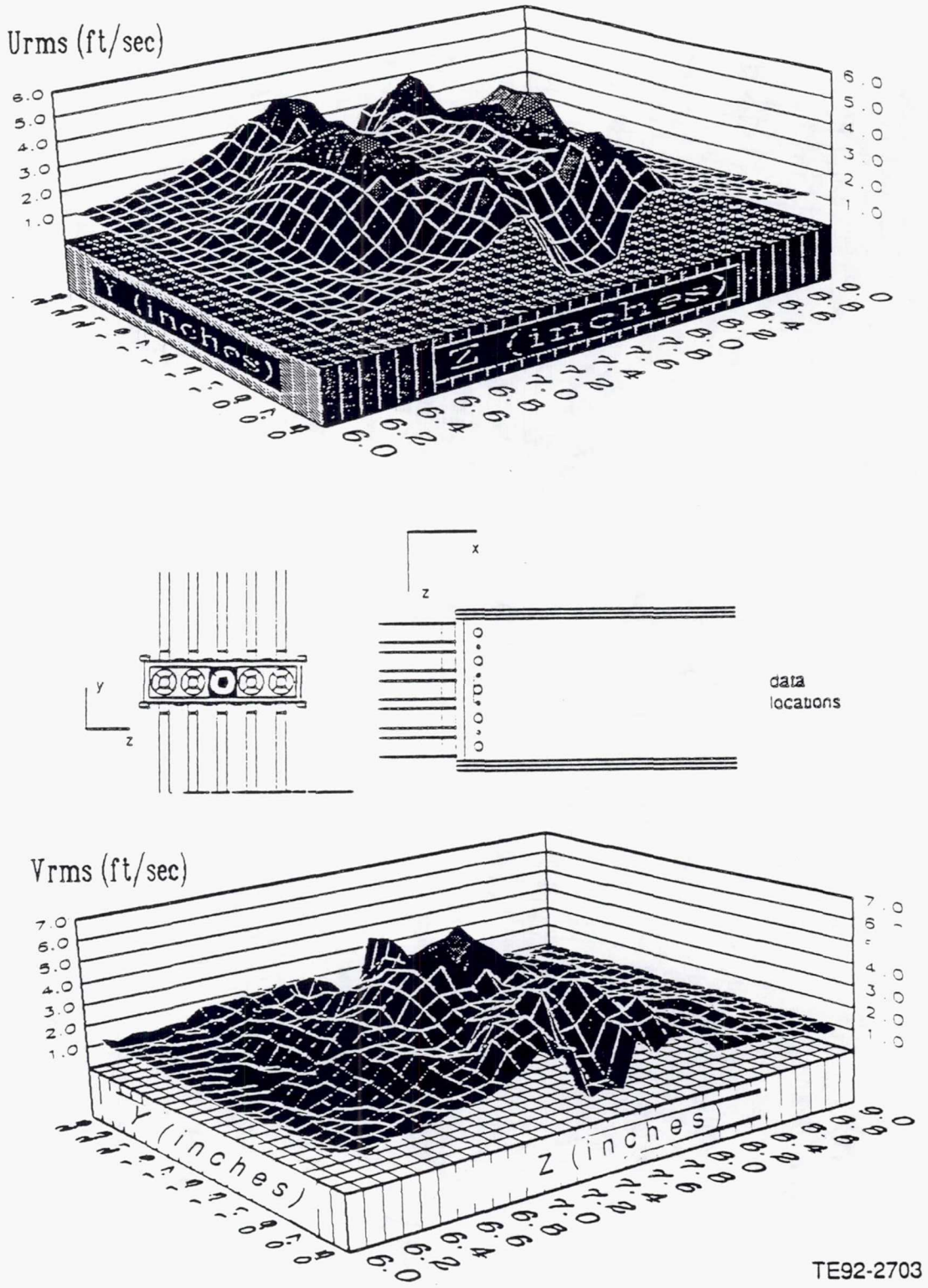

Figure 4.3.2-29. Annular and primary jets contour plot of U_{rms} and V_{rms} at x=1.5 in.

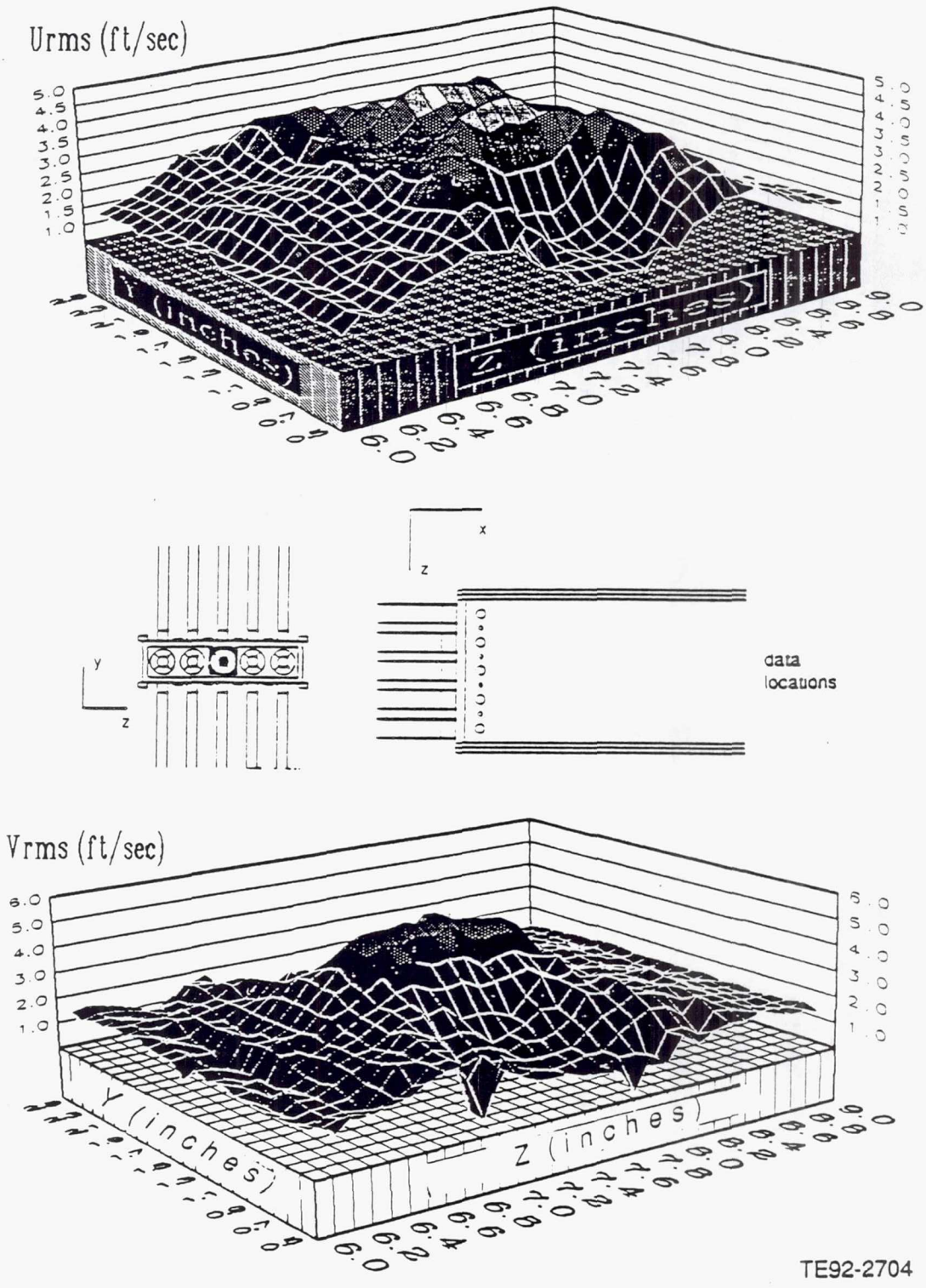

Figure 4.3.2-30. Annular and primary jets contour plot of U_{rms} and V_{rms} at x=2.0 in.

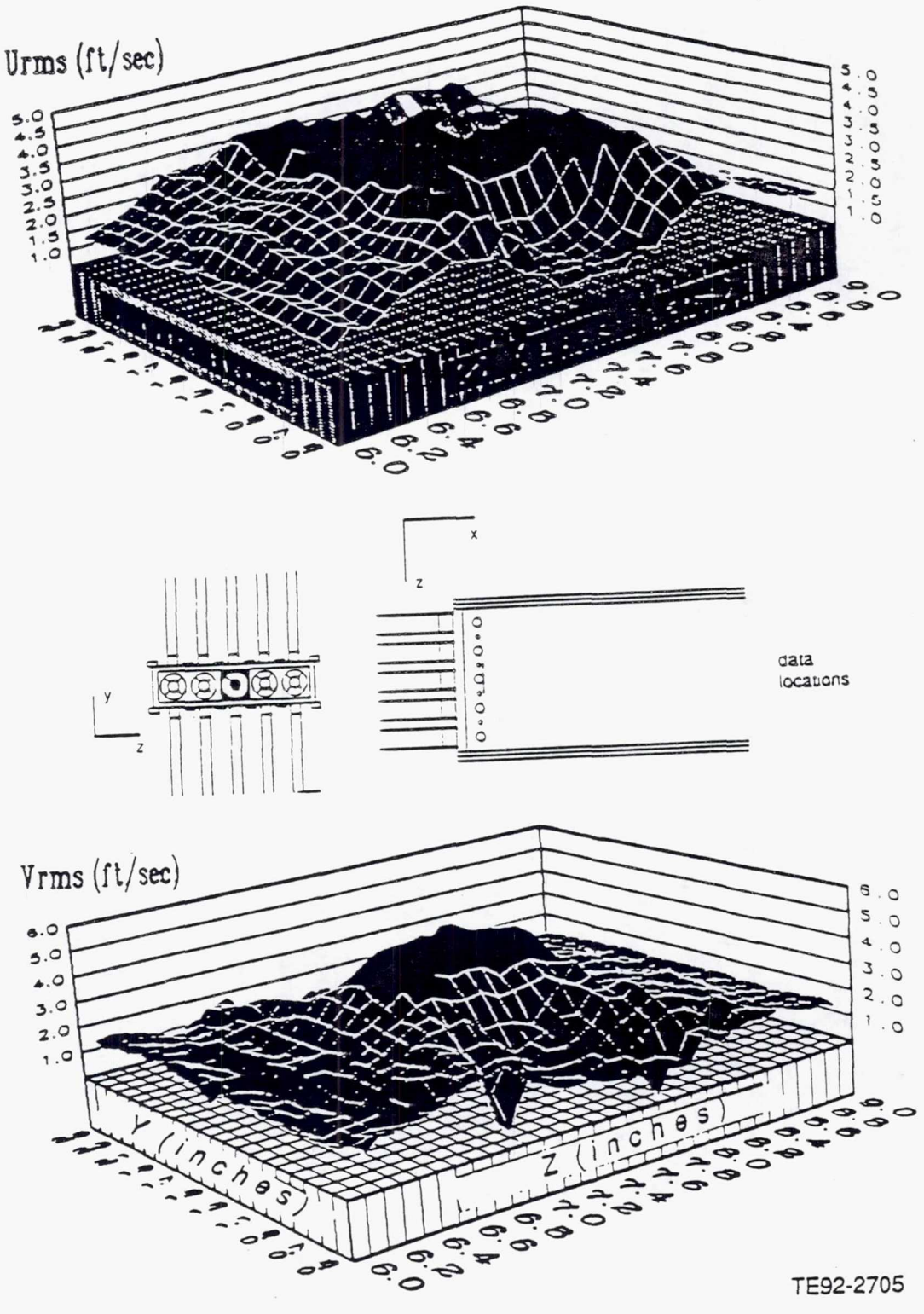

Figure 4.3.2-31. Annular and primary jets mean velocity vector plot at a) z=6.0 in. b) z=9.0 in.

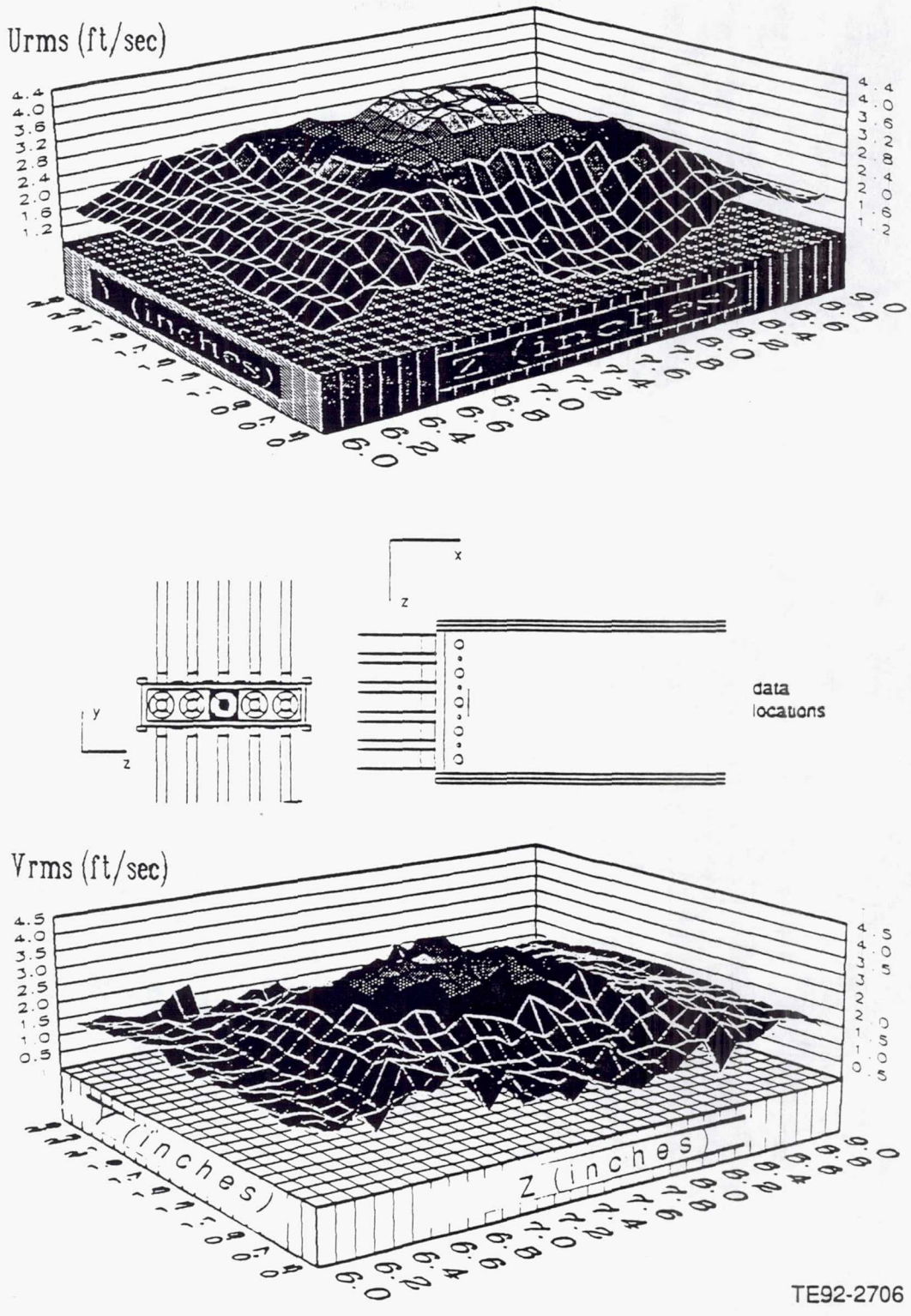

Figure 4.3.2-32. Annular and primary jets contour plot of U_{rms} and V_{rms} at x=2.5 in.

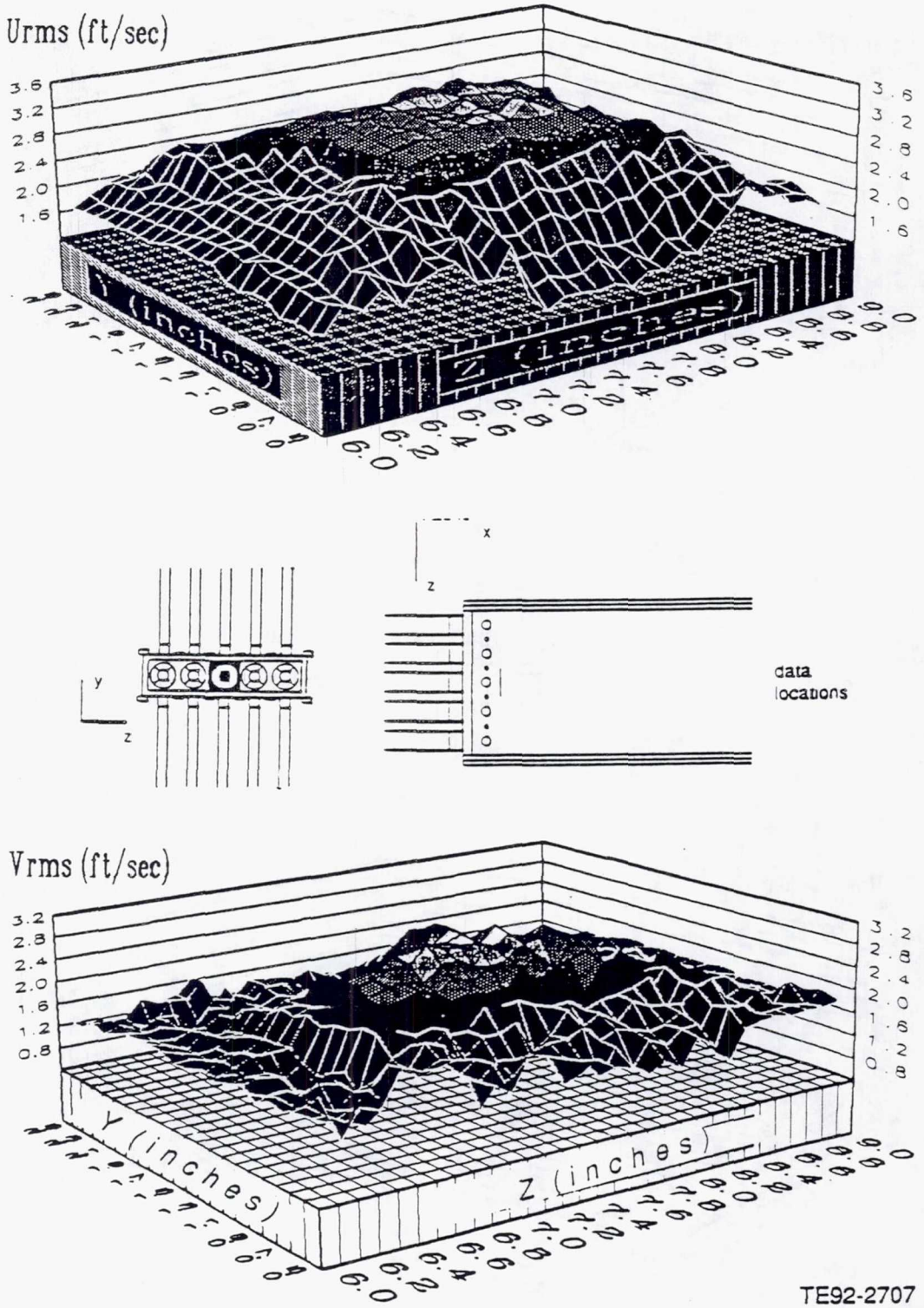

Figure 4.3.2-33. Annular and primary jets contour plot of U_{rms} and V_{rms} at x=3.0 in.

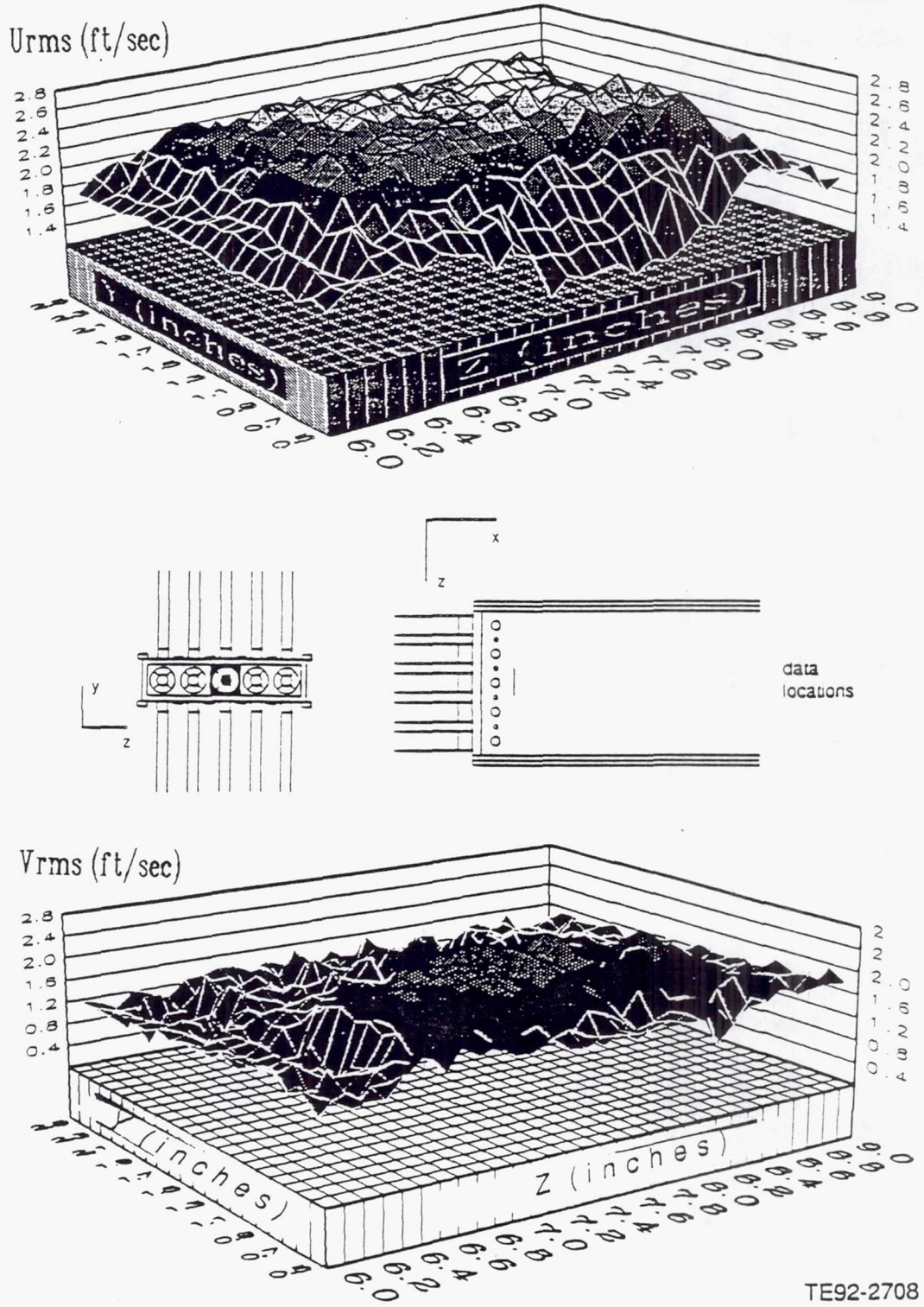

Figure 4.3.2-34. Annular and primary jets contour plot of U_{rms} and V_{rms} at x=3.5 in.

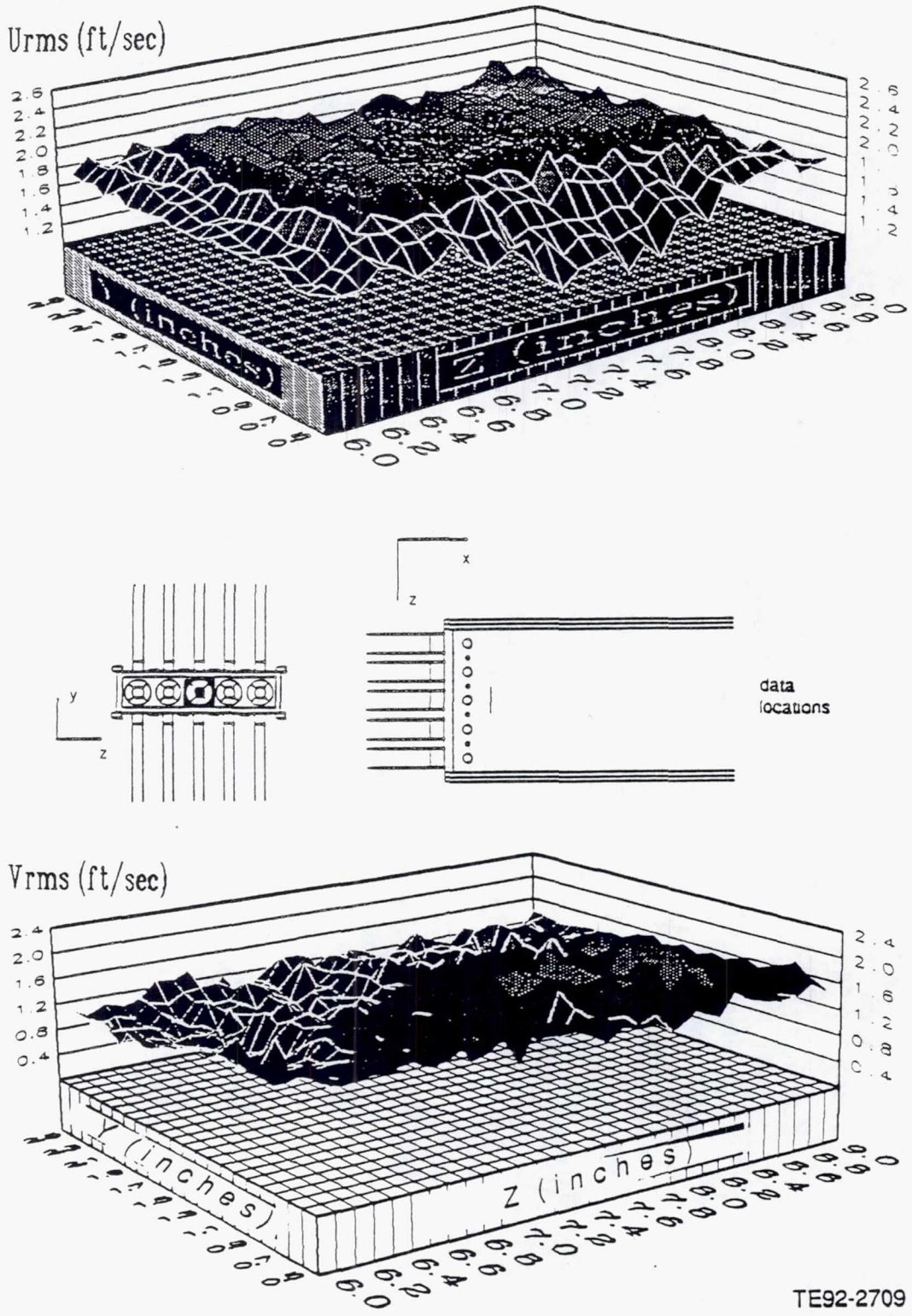

Figure 4.3.2-35. Annular and primary jets contour plot of U_{rms} and V_{rms} at x=4.0 in.

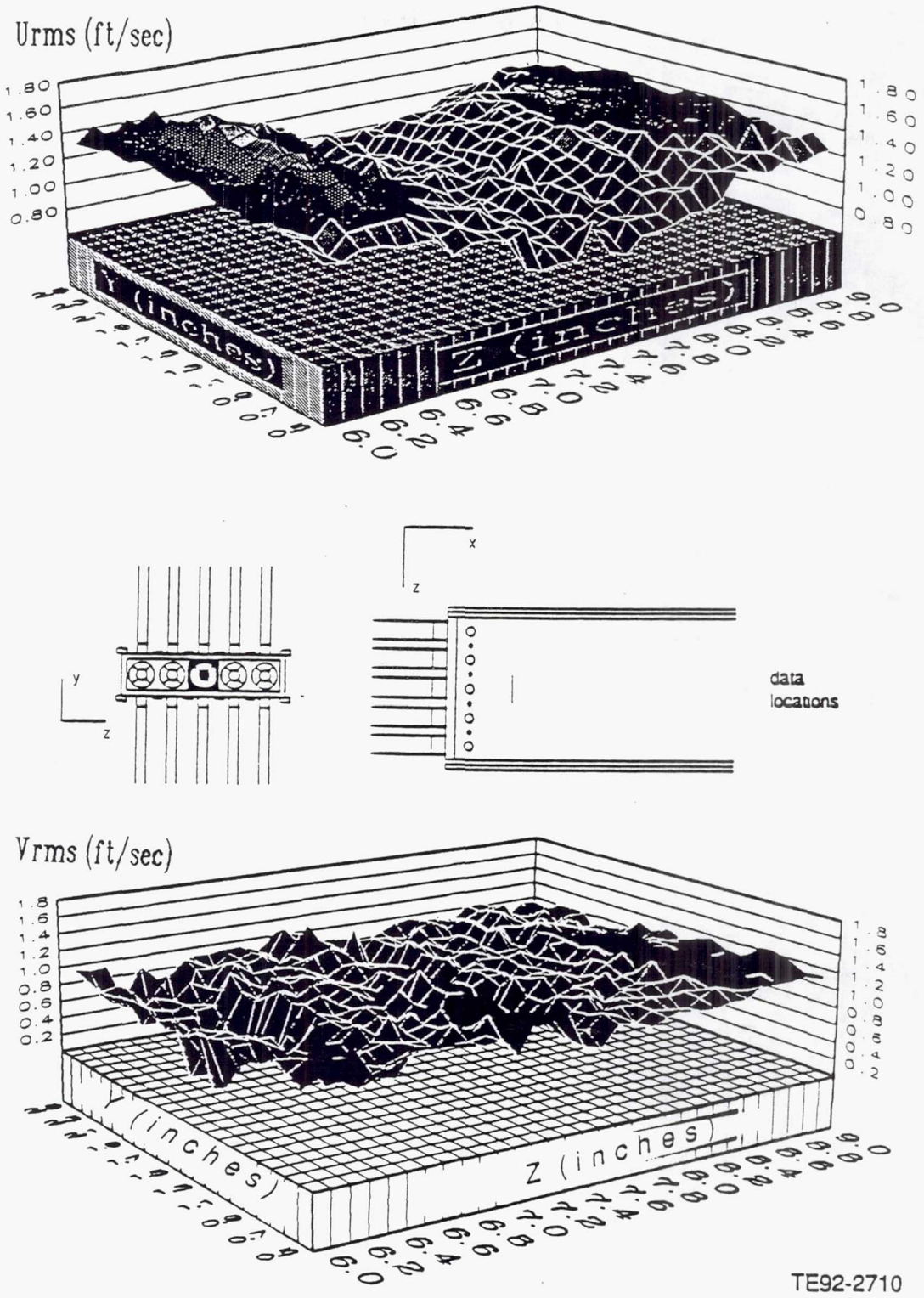

Figure 4.3.2-36. Annular and primary jets contour plots of U_{rms} and V_{rms} at x=6.0 in.

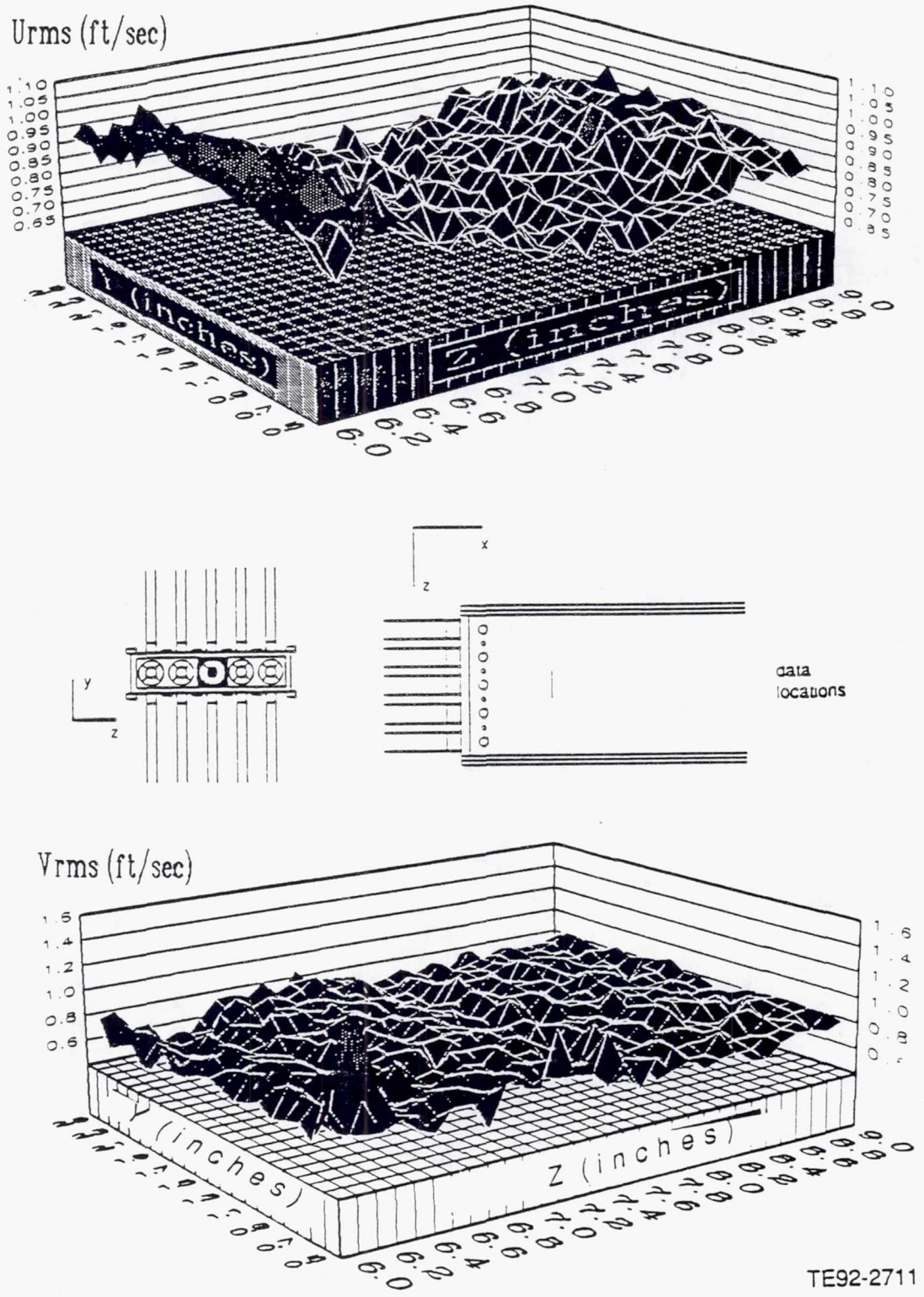

Figure 4.3.2-37. Annular and primary jets contour plots of U_{rms} and V_{rms} at x=9.0 in.

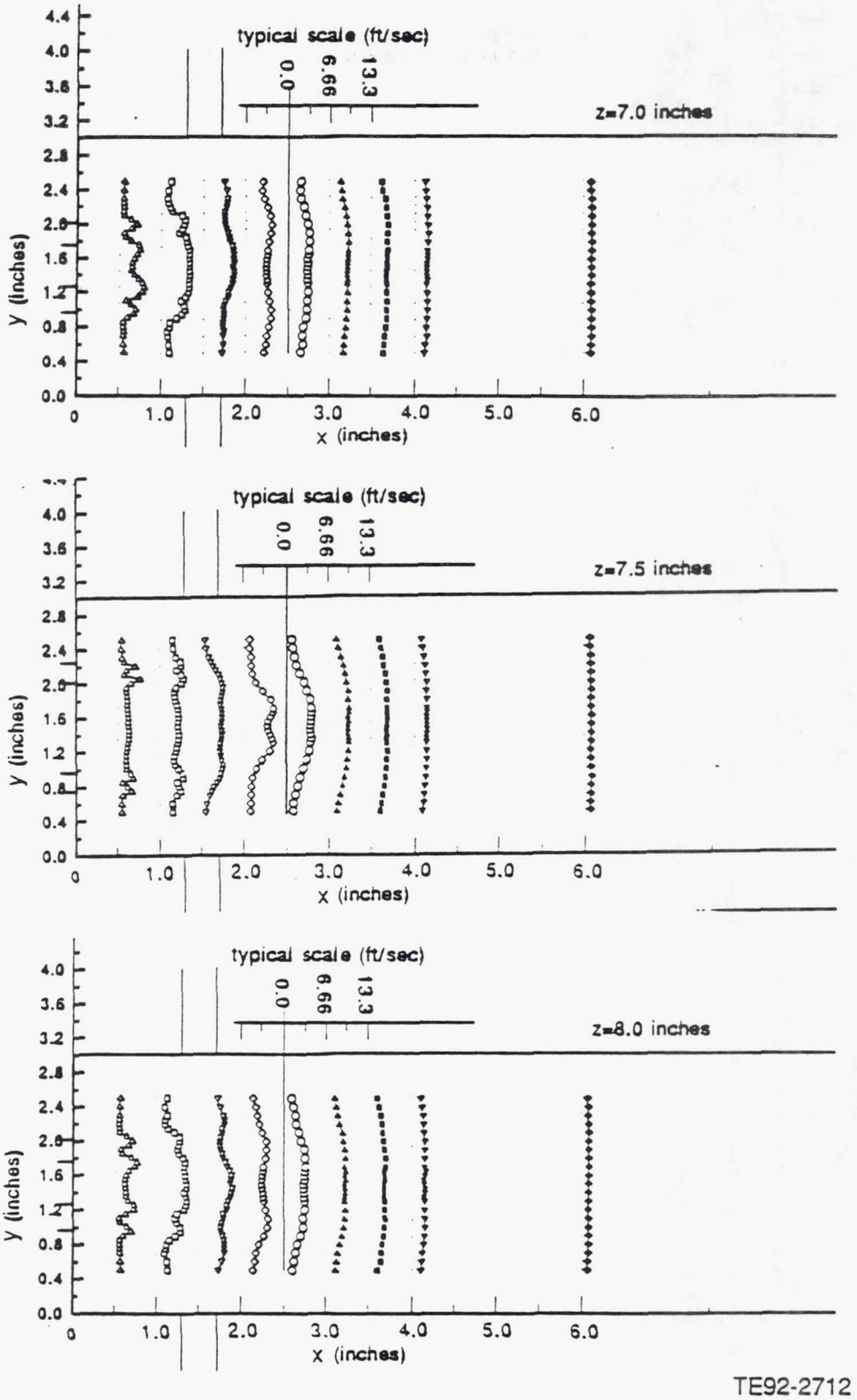

Figure 4.3.2-38. Annular and primary jets U_{rms} distribution.

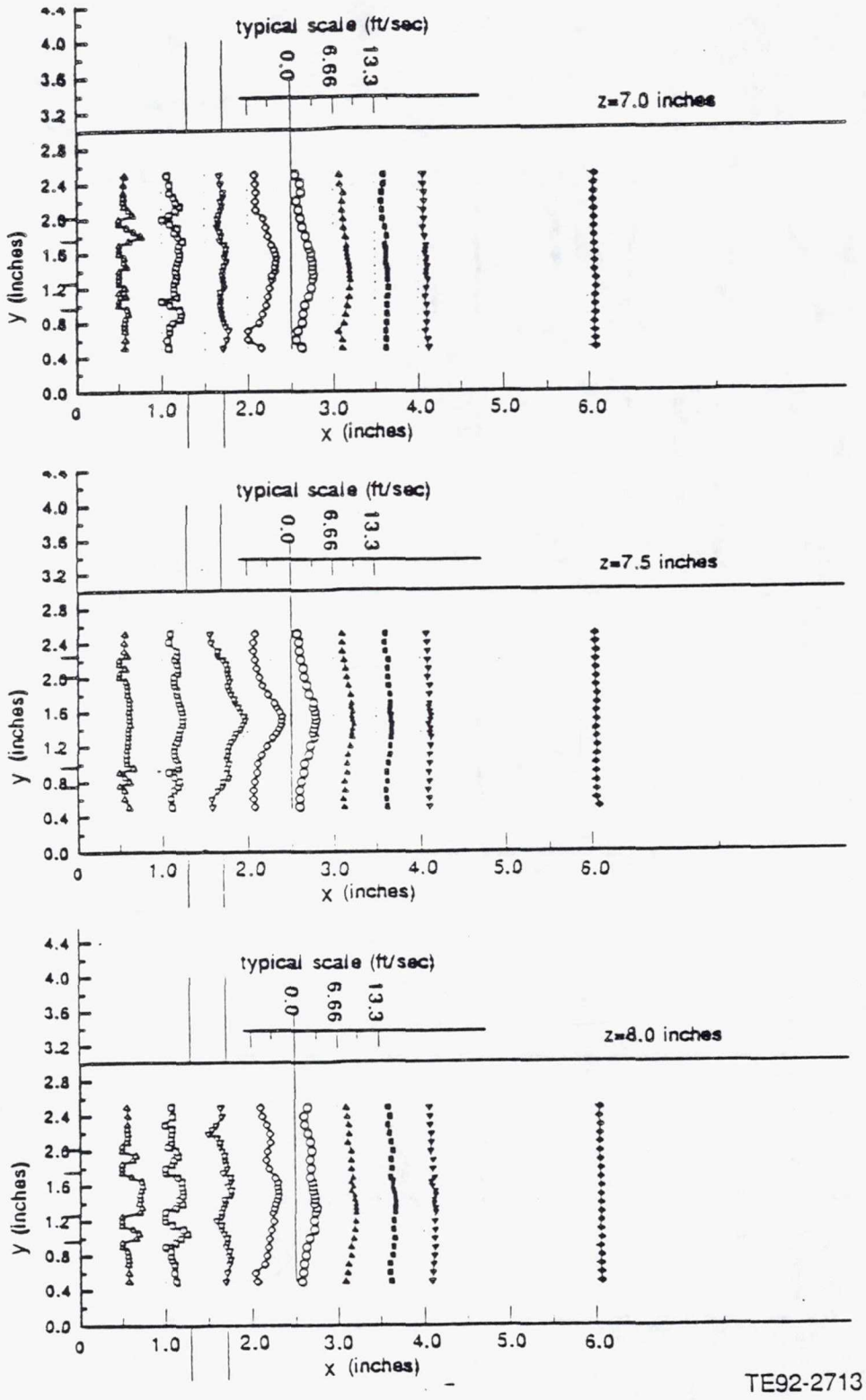

Figure 4.3.2-39. Annular and primary jets V_{rms} distribution.

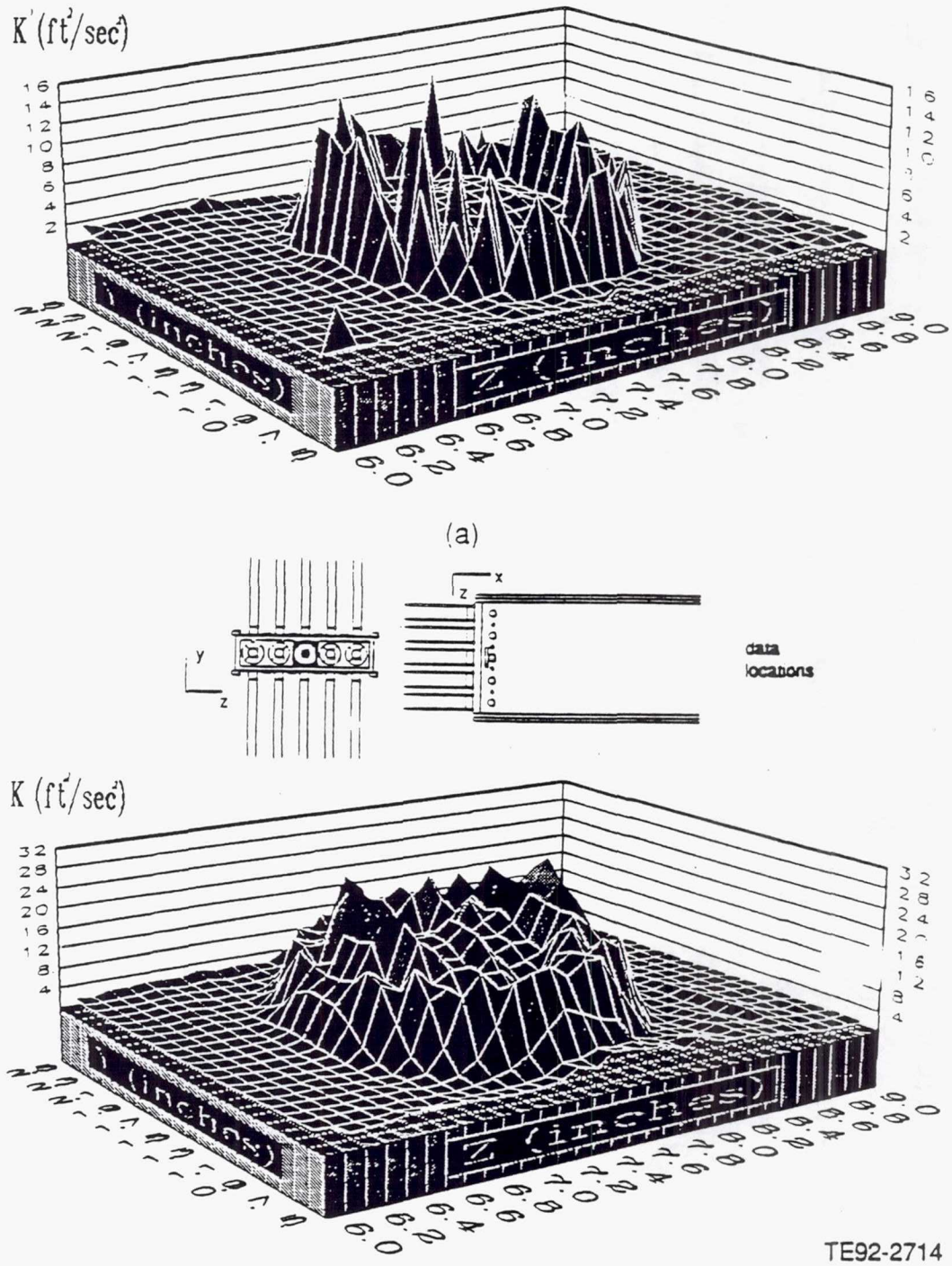

Figure 4.3.2-40. Annular and primary jets contour plots of K' at a) x=0.5 in. b) x=1.0 in.

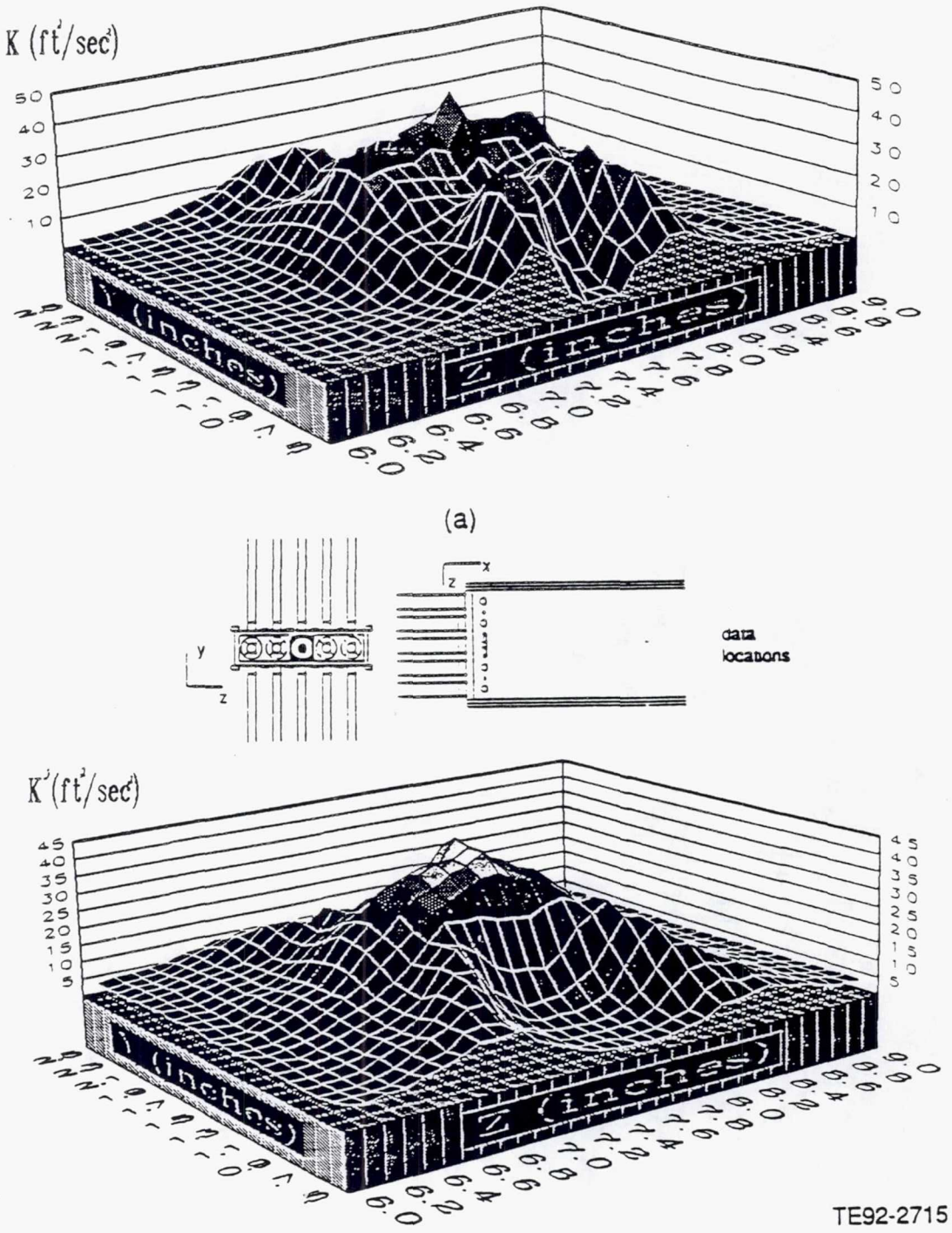

Figure 4.3.2-41. Annular and primary jets contour plots of K' at a) x=1.5 in. b) x=2.0 in.

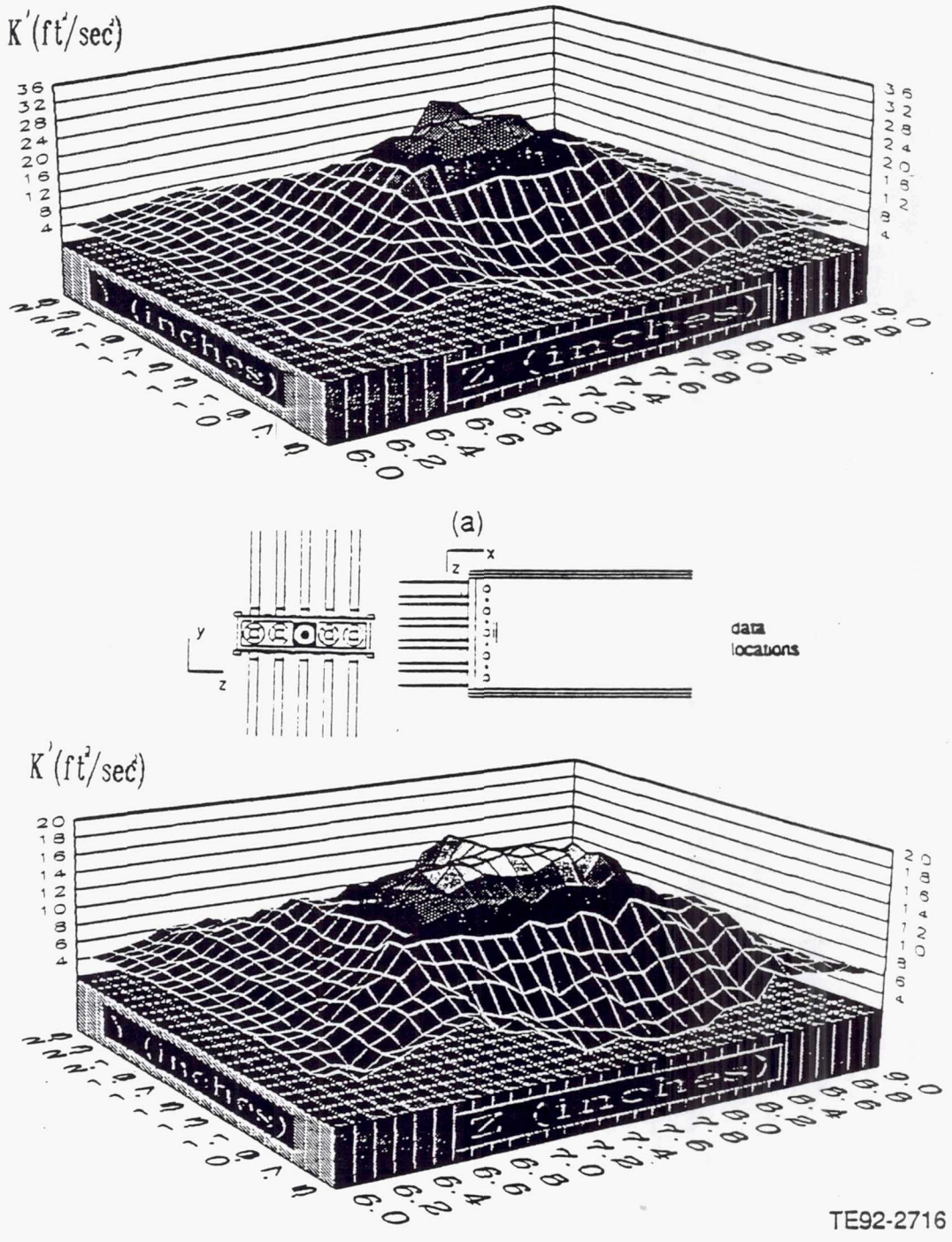

Figure 4.3.2-42. Annular and primary jets contour plots of K' at a) x=2.5 in. b) x=3.0 in.

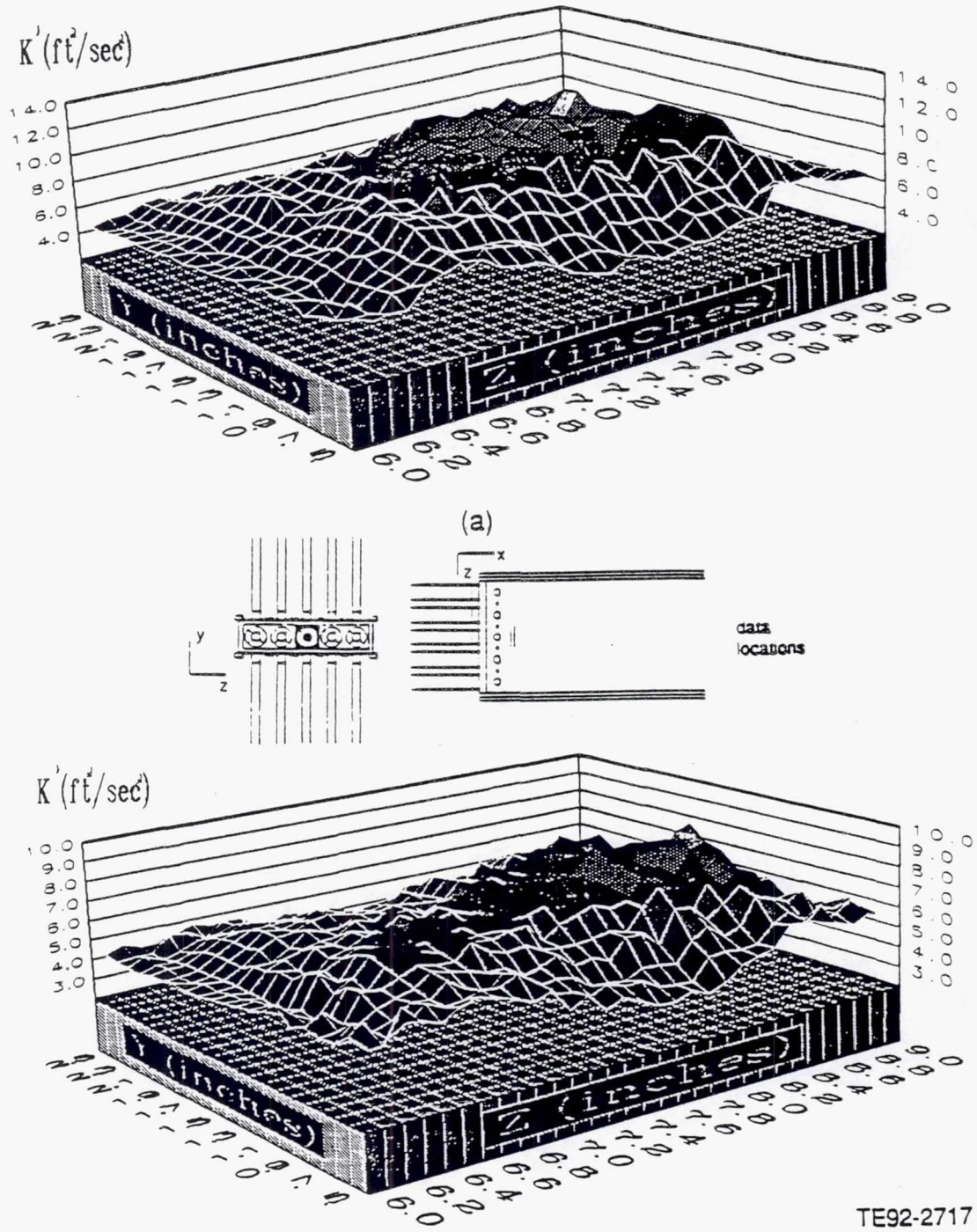

Figure 4.3.2-43. Annular and primary jets contour plots of K' at a) x=3.5 in. b) x=4.0 in.

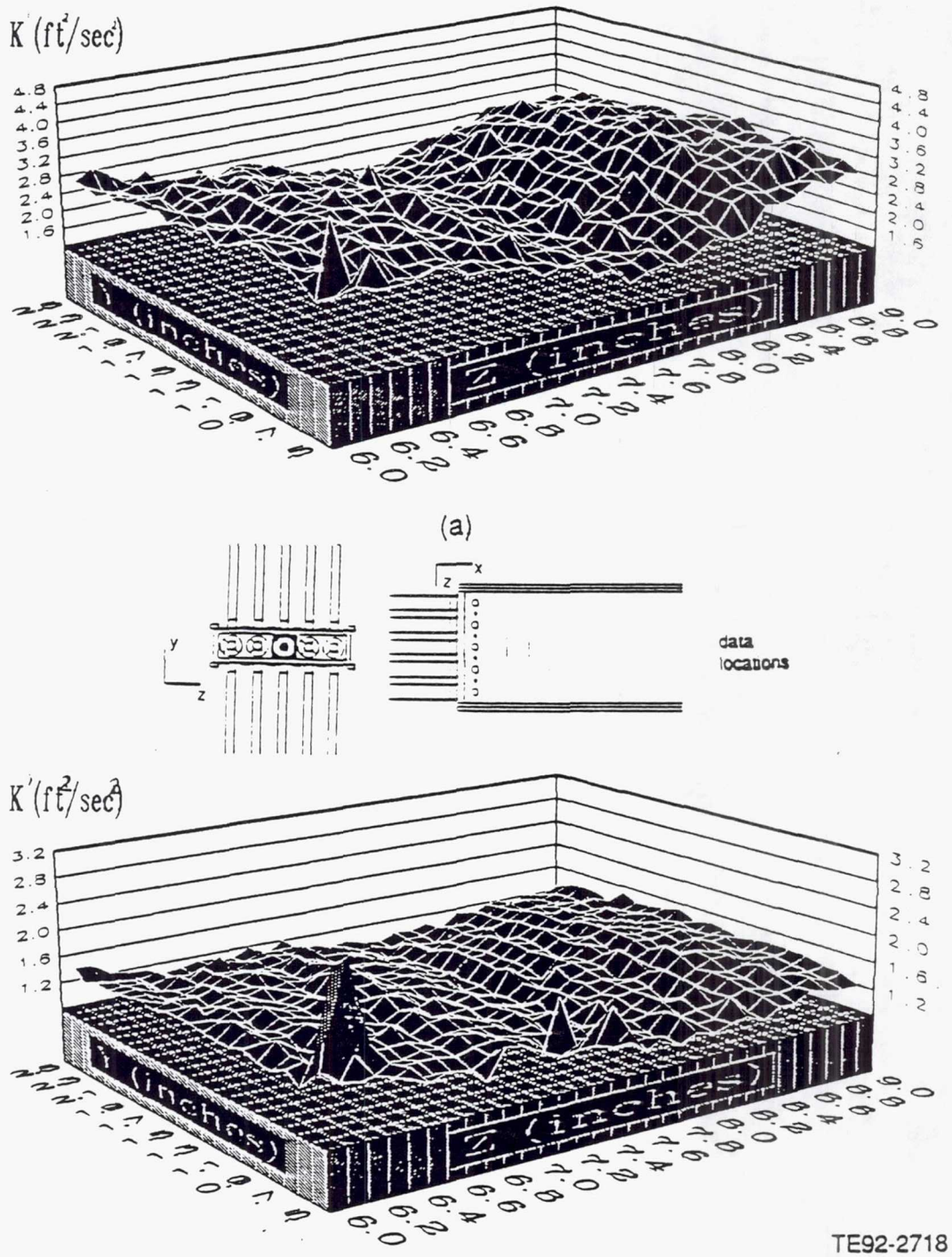

Figure 4.3.2-44. Annular and primary jets contour plots of K' at a) x=6.0 in. b) x=9.0 in.

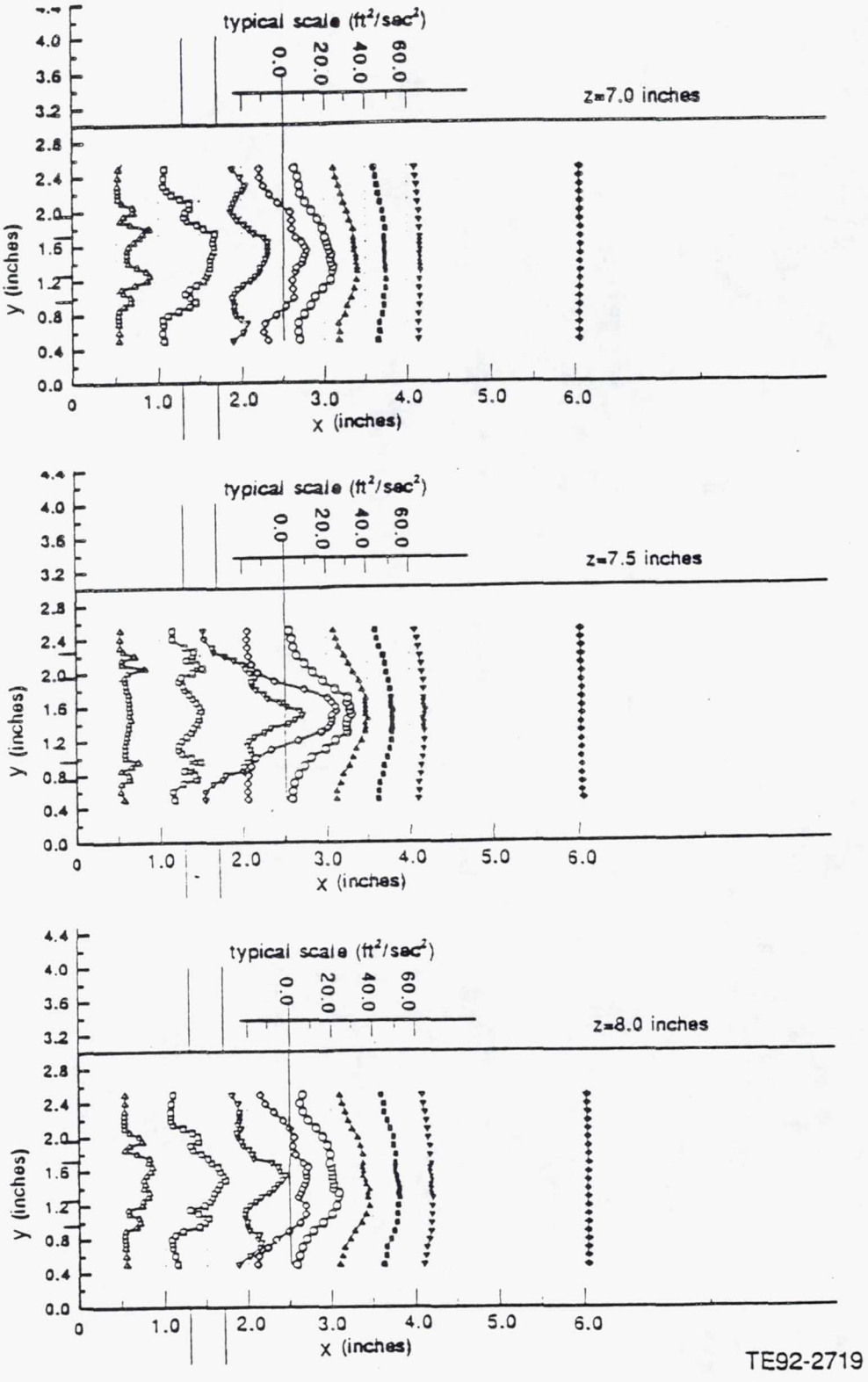

Figure 4.3.2-45. Annular and primary jets K' distribution.

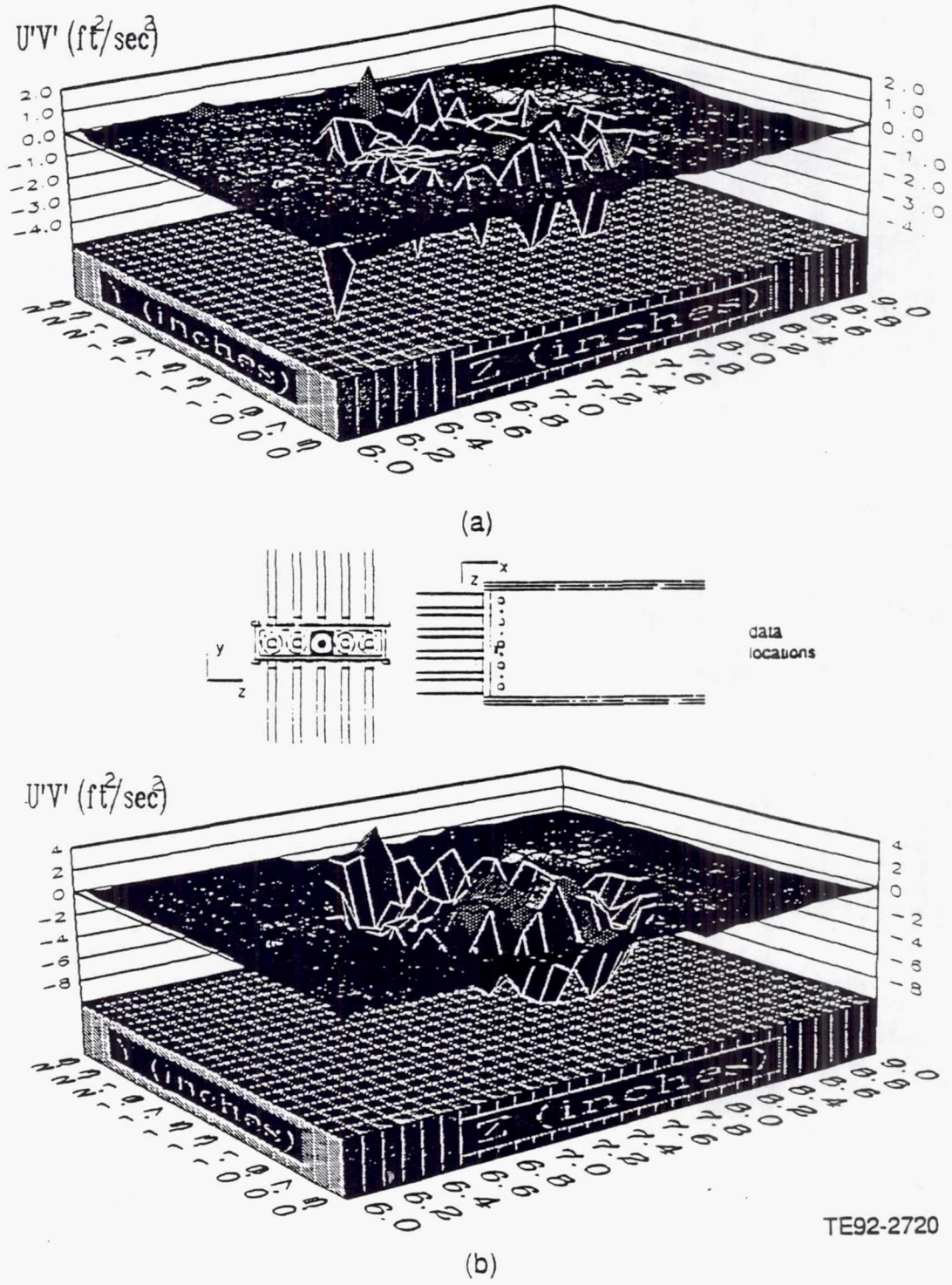

Figure 4.3.2-46. Annular and primary jets contour plots of U'V' at a) x=0.5 in. b) x=1.0 in.

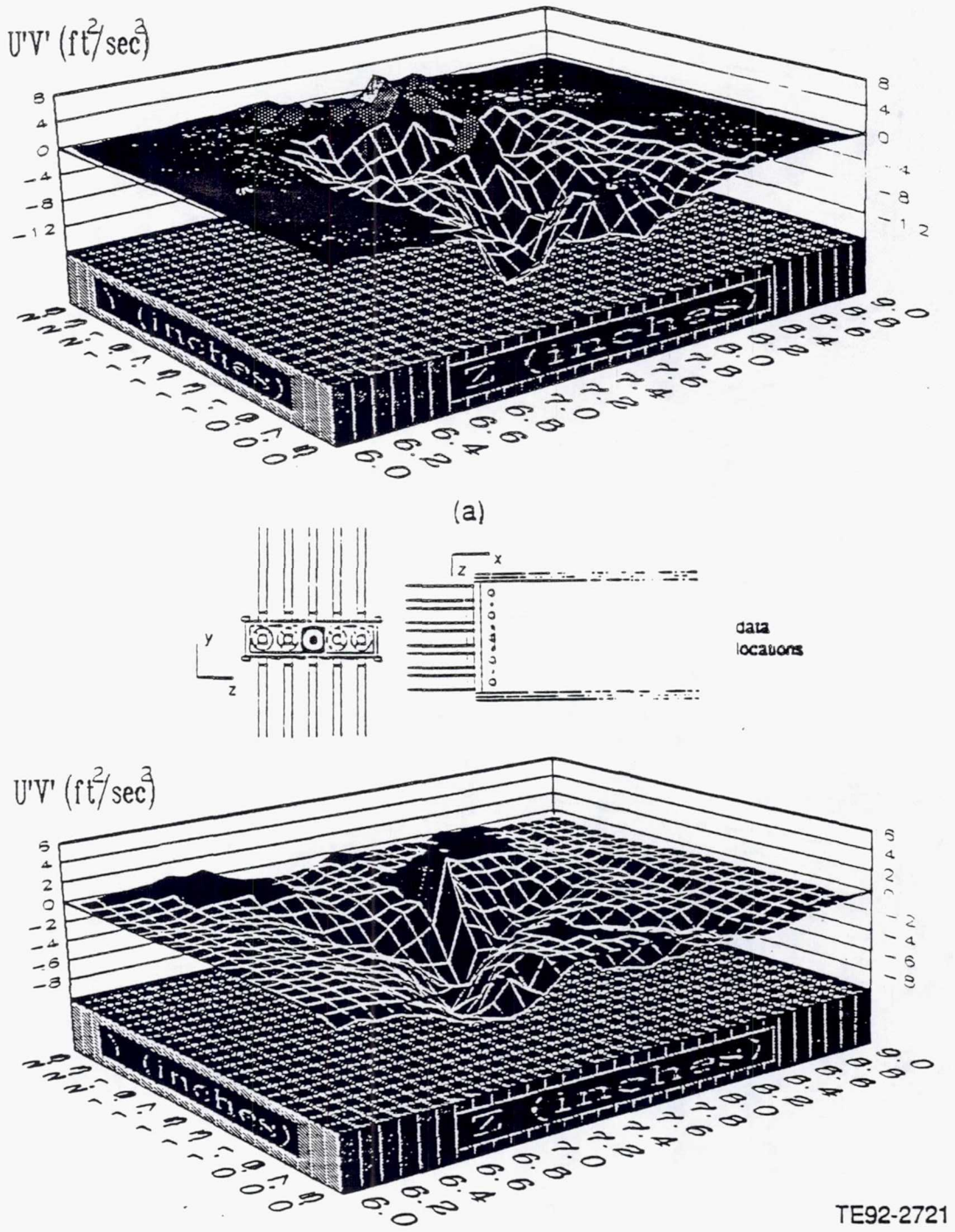

Figure 4.3.2-47. Annular and primary jets contour plot of U'V' at a) x=1.5 in. b) x=2.0 in.

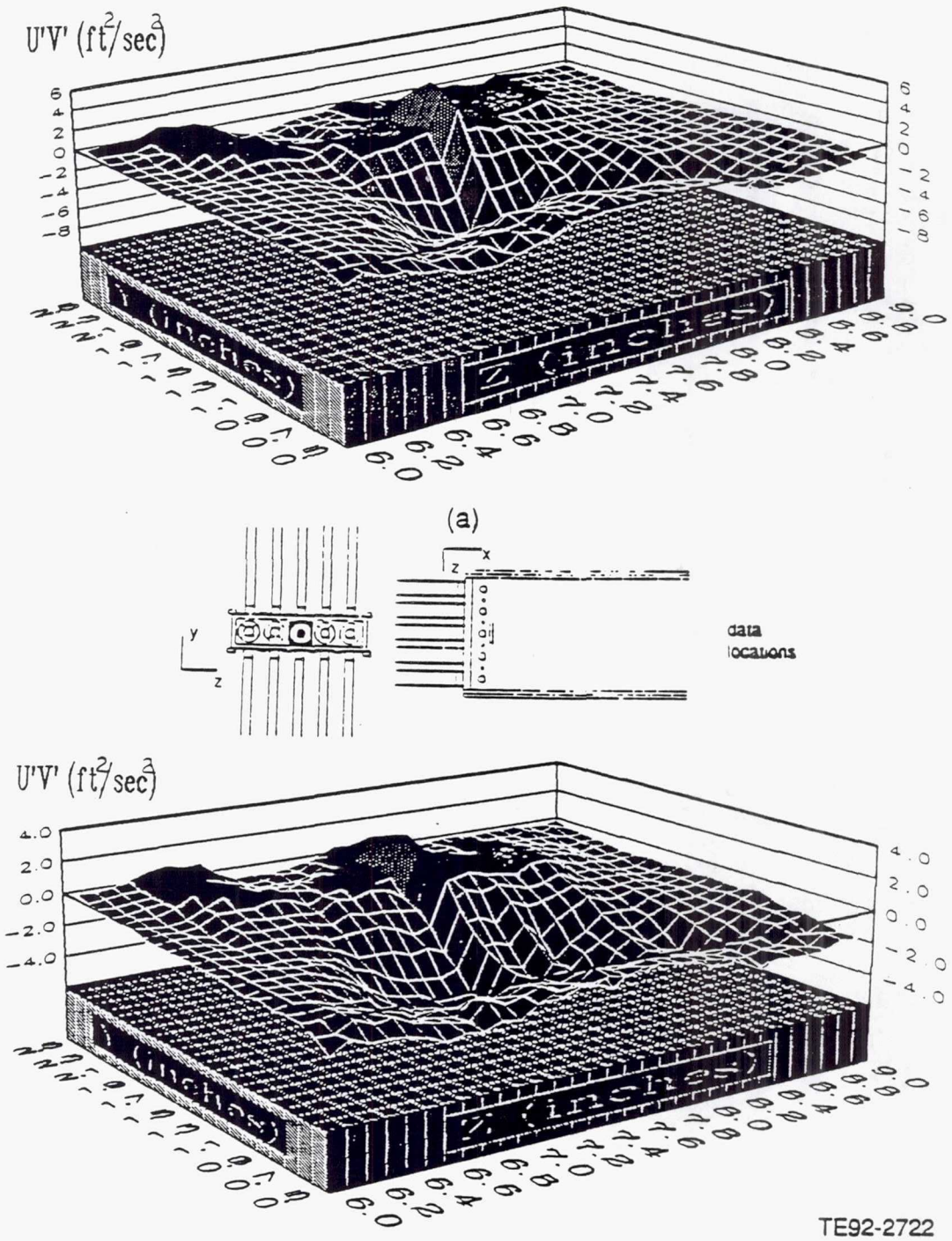

Figure 4.3.2-48. Annular and primary jets contour plot of U'V' at a) x=2.5 in. b) x=3.0 in.

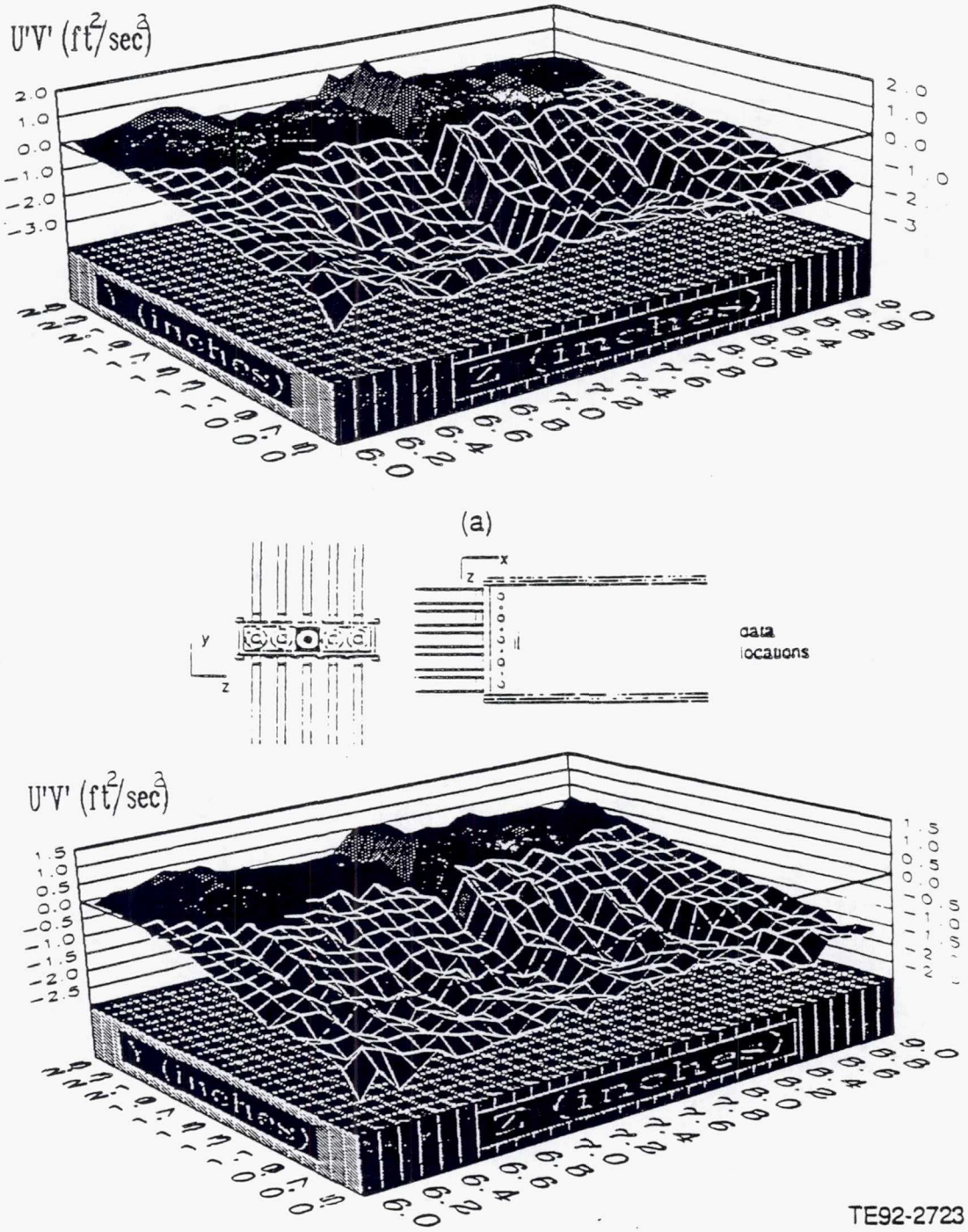

Figure 4.3.2-49. Annular and primary jets contour plot of U'V' at a) x=3.5 in. b) x=4.0 in.

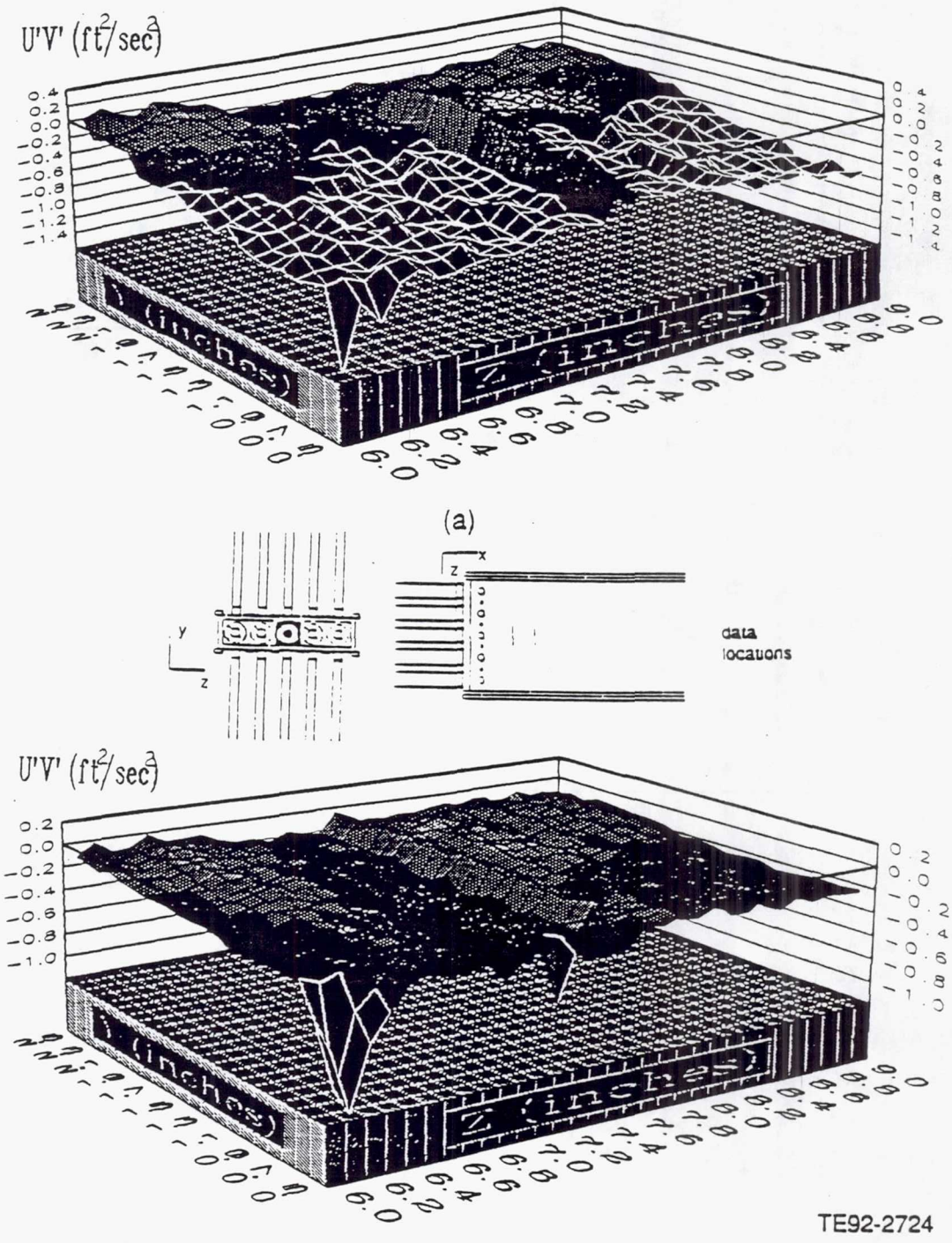

Figure 4.3.2-50. Annular and primary jets contour plot of U'V' at a) x=6.0 in. b) x=9.0 in.

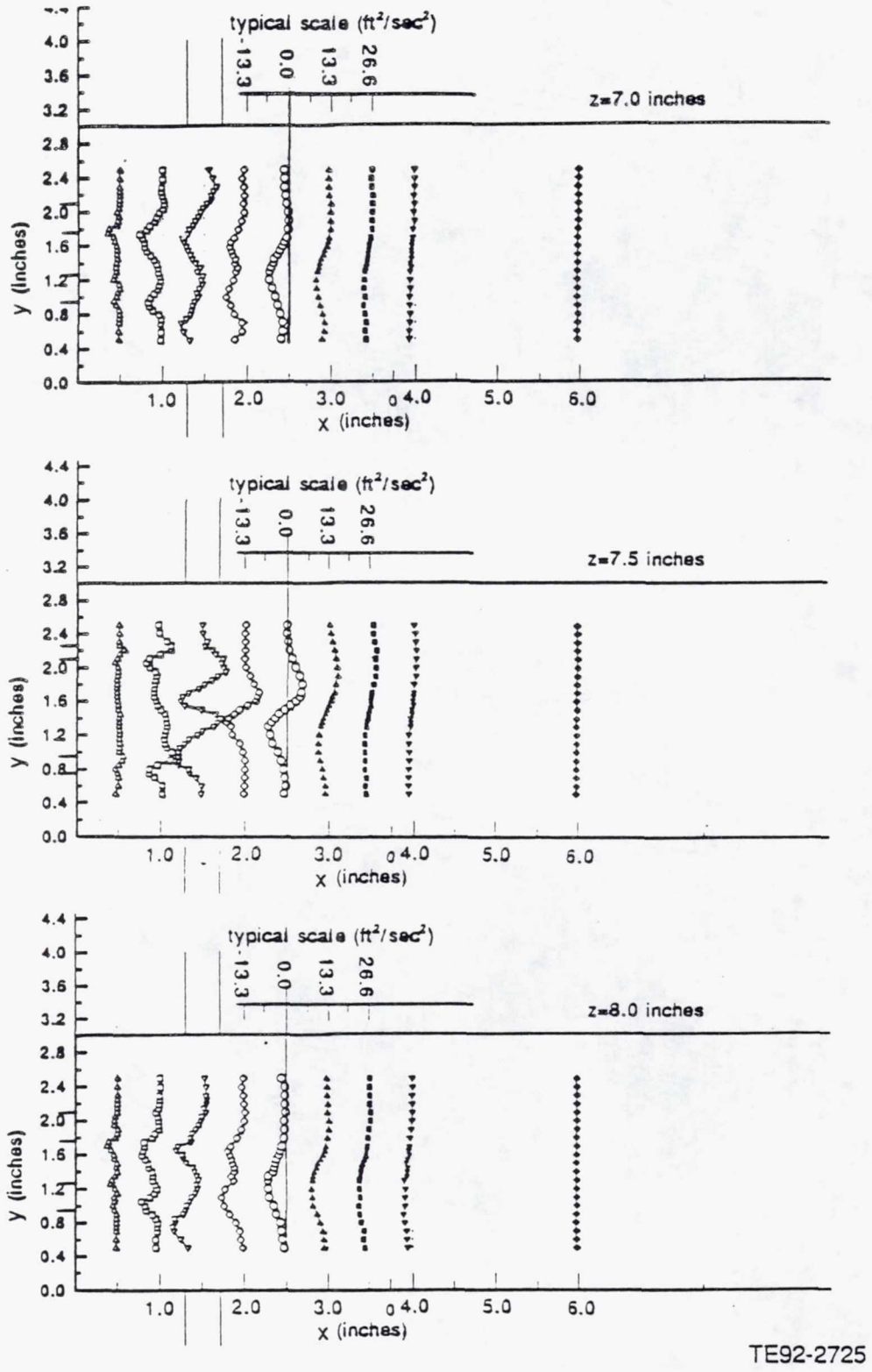

Figure 4.3.2-51. Annular and primary jets U'V' distribution.

REFERENCES

Becker, H. A., Hottel, H. C., and Williams, G. C., 1967, "The Nozzle-Fluid Concentration Field of the Round, Turbulent, Free Jet," *Journal of Fluid Mechanics*, Vol 30, Part 2, pp 285-303.

Becker, H. A., 1977, "Mixing, Concentration Fluctuations, and Marker Nephelometry," *Studies in Convection*, Vol 2, edited by B. E. Launder, Academic Press, new York, pp 45-139.

Beer, J. M., and Chigier, N. A., 1983, *Combustion Aerodynamics*, Robert E. Krieger Publishing.

Birch, A. D., Brown, D. R., Dodson, M. G., and Thomas, J. R., 1978, "The Turbulent Concentration Field of a Methane Jet," *Journal of Fluid Mechanics*, Vol 88, Part 3, pp 431-449.

Borleteau, J. P., 1983, "Concentration Measurement with Digital Image Processing," ICIASF 1983 Record, pp 37-42.

Borrego, C., and Olivari, D., 1980, "A Method for the Measurements of Mixing Properties in a Flow," AGARD CP-281, *Testing and Measurement Techniques in Heat Transfer and Combustion*, September.

Brondum, D. C., and Bennett, J. C., 1986, "Numerical and Experimental Investigation of Nonswirling and Swirling Confined Jets," AIAA Paper No. 86-0040, Presented at AIAA 24th Aerospace Sciences meeting, Reno, Nevada, January.

Brum, R. D., and Samuelson, G. S., 1987, "Two-Component Laser Anemometry Measurements of Non-Reacting and Reacting Complex Flows in a Swirl-Stabilized Model Combustor," *Experiments in Fluids*, Vol 5, pp 95-102.

Dahm, W. J. A., and Dimotakis, P. E., 1985, "Measurements of Entrainment and Mixing in Turbulent Jets," AIAA Paper No. 85-0056.

Durst, F., Melling, A., and Whitelaw, J. H., 1976, *Principles and Practice of Laser Doppler Anemometry*, Academic Press.

Edwards, Robert V., 1987, "Report of the Special Panel on Statistical Partical Bias Problems in Laser Anemometry," *Journal of Fluids Engineering*, Vol 109, pp 89-93, June.

Forstall, W. Jr., and Shapiro, A. H., 1950, "Momentum and Mass Transfer in Coaxial Gas Jets," ASME Transactions, *Journal of Applied Mechanics*, Vol 17, pp 399-408.

Gore, R. W., and Ranz, W. E., 1964, "Backflows in Rotating Fluids Moving Axially Through Expanding Cross Sections," *AIChE Journal*, Vol 10, pp 83-88, January.

Gupta, A. K., Lilley, D. G., and Syred, N., 1984, *Swirl Flows*, Abucus Press.

Hinze, J. O., 1975, *Turbulence*, McGraw-Hill, New York,.

Koochesfahani, M. M. and Dimotakis, P. E., 1984, "Laser Induced Fluorescence Measurements of Concentration in a Plane Mixing Layer," AIAA paper No. 84-0198, AIAA 22nd Aerospace Sciences Meeting, Reno, Nevada, January.

Laufer, J., 1954, "The Structure of Turbulence in Fully Developed Pipe Flow," NACA Report 1174.

Long, M. B., Chu, B. T., and Chang, R. K., 1981, "Instantaneous Two-Dimensional Gas Concentration Measurements by Light Scattering," AIAA Journal, Vol 19, No. 9, pp 1151-1157.

Mathur and Maccallum, 1967, "Swirling Air Jets From Vane Swirlers. Part 1: Free Jets," *Journal of the Institute of Fuel*, May.

McLaughlin, D. K., and Tiederman, W. G., 1973, "Biasing Correction for Individual Realization of Laser Velocimeter Measurements in Turbulent Flows," *Physics of Fluids*, Vol 16, No. 12, pp 2082-2088, December.

Roesler, T. C., 1980, "Investigation of Bias Errors in Laser Doppler Velocimeter Measurements," MS Thesis, Purdue University, August.

Rosenweig, R. N., 1966, Sc.D. dissertation, Massachusetts Institute of Technology, 1966.

Rosenweig, R. E., Hottel, H. C., and Williams, G. C., 1961, "Smoke Scattered Light Measurements of Turbulent Concentration Fluctuations," *Chemical Engineering Science*, Vol 15, pp 111-129, July.

Schaughnessy, E. J., and Morton, J. B., 1977, "Light Scattering Measurements of Particle Concentration in a Turbulent Jet," *Journal of Fluid Mechanics*, Vol 80, Part 1, pp 129-148.

Schlichting, H., 1979, *Boundary-Layer Theory*, McGraw-Hill.

Squire, H. B., and Trouncer, J., 1944, "Round Jets in a General Stream," ARC Technical Report R&M No. 1974.

Tennekes, H., and Lumley, J. L., 1973, *A First Course in Turbulence*, MIT Press.

Vu, B. T., and Gouldin, F. C., 1982, "Flow Measurement in a Model Swirl Combustor," *AIAA Journal*, Vol 20, pp 642-651, May.

Walker, D. A., 1987, "A Fluorescence Technique for Measurement of Concentration in Mixing Liquids," *Journal of Physics E: Scientific Instruments*, Vol 20, pp 217-224.

TABLE OF CONTENTS

V. PHYSICAL AND MATHEMATICAL MODELS

5.1 GOVERNING EQUATIONS AND TURBULENCE MODELS

In this subsection, the equations which govern the distribution of the mean quantities are summarized. These equations are derived from the conservation laws of mass and momentum using time averaging and are expressed in tensor notation for steady and constant density flow as

$$\frac{\partial U_i}{\partial X_i} = 0 \tag{62}$$

$$\frac{\partial (U_i U_j)}{\partial X_j} = -\frac{1}{\rho}\frac{\partial P}{\partial X_i} - \frac{\partial}{\partial X_j}(\overline{u_i u_j}) \tag{63}$$

where U_i and u_i are the mean and fluctuating velocities along the x_i direction, respectively, p is the mean pressure, and the bar is used to denote time-averaged quantities.

As a consequence of the nonlinearity of Equation 63, the averaging process used introduces unknown correlations $u_i u_j$ which can be made known through the assumption of turbulence modeling.

Three different types of turbulence closures are investigated, namely, the standard k-ε model, algebraic second-moment closure (ASM), and differential second-moment closure (DSM).

The k-ε model is a simple closure based on the gradient transport relations. In this model, the turbulent fluxes are related to the mean fields through the assumption of an isotropic eddy viscosity and a turbulent Prandtl/Schmidt number as:

$$-\rho\overline{u_i u_j} = \mu_t\left(\frac{\partial U_i}{\partial X_j} + \frac{\partial U_j}{\partial X_i}\right) - \frac{2}{3}\delta_{ij}\rho k \tag{64}$$

The eddy viscosity (μ_t) is obtained from the turbulent kinetic energy (k) and its dissipation rate (ε) using the relation:

$$\mu_t = c_\mu \rho k^2/\varepsilon \tag{65}$$

In order to close the set of Equations 62 through 64, two additional equations governing the transport of k and ε are required. These are

$$\rho U_j\frac{\partial k}{\partial X_j} = \frac{\partial}{\partial X_j}\left(\frac{\mu_t}{\sigma_k} + \mu\right)\frac{\partial k}{\partial X_j} - (\rho\overline{u_i u_j})\frac{\partial U_i}{\partial X_j} - \rho\varepsilon \tag{66}$$

$$\rho U_j\frac{\partial \varepsilon}{\partial X_j} = \frac{\partial}{\partial X_j}\left(\frac{\mu_t}{\sigma_\varepsilon} + \mu\right)\frac{\partial \varepsilon}{\partial X_j} - C_{\varepsilon 1}\frac{\varepsilon}{k}(\rho\overline{u_i u_j})\frac{\partial U_i}{\partial X_j} - C_{\varepsilon 2}\rho\frac{\varepsilon^2}{k} \tag{67}$$

where σ_k and σ_ε are turbulent Schmidt numbers and $C_{\varepsilon 1}$ and $C_{\varepsilon 2}$ are model constants. The constants used in this model have been taken from Launder and Spalding (1974*) and are given in Table 5.1-I.

---

* References for Section V are listed at the end of the section.

Table 5.1-I.
Values of constants in the k-ε model.

C_m	0.09
$C_{\varepsilon 1}$	1.44
$C_{\varepsilon 2}$	1.92
σ_k	1.0
σ_ε	1.3

The k-ε model is the simplest model which is suitable for recirculating flow calculations. It allows the characteristic length scale of a wide range of complex flow fields to be determined. The k-ε model has been used with success in the calculation of various free shear flows and recirculating flows with and without swirl (e.g., Rodi, 1980). However, in flows with significant streamline curvature, the isotropic eddy viscosity assumption may not be able to describe the turbulent diffusion effects adequately. The three-dimensional form of the turbulent flow equations is given in Appendix A for the k-ε model.

To allow for the nonisotropic behavior of the eddy viscosity and to account for the effect of body forces (e.g., buoyancy, rotation), the k-ε model is refined by introducing ASM. This model is based on a simplification of the Reynolds stress transport equation which relates the individual stresses to mean velocity gradient, turbulent kinetic energy, and its dissipation rate by way of algebraic expressions. The ASM model adopted here is based on Rodi's hypothesis (Rodi, 1976) which approximate the connection and diffusion transport of turbulent stresses in terms of the transport of k.

The result can be summarized as:

$$a_{ij} = \frac{1 - C_2}{C_1 - 1 + \frac{P_k}{\rho\varepsilon}} \cdot \frac{P_{ij} - \frac{2}{3}\delta_{ij}P_k}{\rho\varepsilon} \tag{68}$$

where

$$P_{ij} = \rho\overline{u_j u_k}\frac{\partial U_i}{\partial X_k} - \rho\overline{u_i u_k}\frac{\partial U_j}{\partial X_k} \tag{69}$$

$$P_k = \frac{1}{2}P_{ii} \tag{70}$$

C_1 and C_2 are model constants, and a_{ij} is the nondimensional measure of anisotropy and is given by the following expression.

$$a_{ij} = \frac{\overline{u_i u_j}}{k} - \frac{2}{3}\delta_{ij} \tag{71}$$

Since the quantities k and ε are present in these equations, their transport equations also have to be solved. These are determined by:

$$\rho U_j \frac{\partial k}{\partial X_j} = \frac{\partial}{\partial X_j}\left(C_k \rho \frac{k}{\varepsilon}\overline{u_j u_n}\frac{\partial k}{\partial X_n}\right) - P_k - \rho\varepsilon \tag{72}$$

$$\rho U_j \frac{\partial \varepsilon}{\partial X_j} = \frac{\partial}{\partial X_j}\left(C_\varepsilon \rho \frac{k}{\varepsilon} \overline{u_j u_n} \frac{\partial \varepsilon}{\partial X_n}\right) + C_{\varepsilon 1} \frac{\varepsilon}{k} P_k - C_{\varepsilon 2} \rho \frac{\varepsilon^2}{k} \tag{73}$$

C_k, C_ε, $C_{\varepsilon 1}$, and $C_{\varepsilon 2}$ are all model constants and are given in Table 5.1-II.

The k-ε and ASM models assume that the local state of turbulence can be characterized by one velocity scale. In order to allow for the different development of the various Reynolds stresses representing various velocity scales in complex flows, and to account properly for their transport, models which employ transport equations for the individual stresses must be applied.

The Reynolds stress equations can be written in tensor notation form as

$$\rho U_k \frac{\partial}{\partial X_k} \overline{u_i u_j} - d_{ij} = P_{ij} + \phi_{ij} - \rho \varepsilon_{ij} \tag{74}$$

Here, P_{ij} is the production of Reynolds stress $u_i u_j$, ε_{ij} represents viscous dissipation, ϕ_{ij} controls the redistribution of turbulence energy among the normal stresses through the interaction of pressure and strain, and d_{ij} stands for turbulence diffusion. Since P_{ij} is exact, it does not need modeling. However, closure assumptions are required for d_{ij}, ϕ_{ij}, and ε_{ij}. The assumption of local isotropy allows the dissipation tensor to be approximated by

$$\varepsilon_{ij} = \frac{2}{3}\delta_{ij}\varepsilon \tag{75}$$

where ε is the turbulence energy dissipation rate. The diffusion term is approximated by the gradient-diffusion model of Daly and Harlow (1970)

$$d_{ij} = -\frac{\partial}{\partial X_k}\left(C_k \rho \overline{u_k u_n} \frac{k}{\varepsilon} \frac{\partial \overline{u_i u_j}}{\partial X_n}\right) \tag{76}$$

where C_k is a model constant and $k = 1/2\ u_i u_i$ is the turbulent kinetic energy. The pressure redistribution term (ϕ_{ij}) is modeled in three parts, ϕ_{ij1} resulting from purely turbulence interactions known as return-to-isotropy, ϕ_{ij2} involving interactions between the mean strain rate and turbulence known as rapid part, and ϕ_{ijw} representing the effects of rigid boundaries on both ϕ_{ij1} and ϕ_{ij2}. The presence of a rigid wall affects the flow field near that region by impeding the transfer of turbulent energy from the streamwise direction to that normal to the wall, and as a result reduces the relative magnitude of the shear stress. In the present study, Rotta's linear model (Rotta, 1951) for the turbulence part of ϕ_{ij} is adopted:

Table 5.1-II.
Values of constants in the ASM and DSM closures.

$C_{\varepsilon 1}$	1.44
$C_{\varepsilon 2}$	1.92
C_ε	0.18
C_k	0.22
C_1	1.8
C_2	0.6
C_{1w}	0.05
C_{2w}	0.006

$$\phi_{ij1} = - C_1 \rho \frac{\varepsilon}{k} \left(\overline{u_i u_j} - \frac{2}{3} \delta_{ij} k \right) \tag{77}$$

The simple linear form for ϕ_{ij1} is widely accepted and used dispite the fact that the actual return-to-isotropy process is highly nonlinear (Bradshaw, 1968). More sophisticated nonlinear forms, such as Lumely and Khayeh-Nouri's proposal (1974), have been suggested, but these have shown no significant improvement over Rotta's proposal. The rapid part is approximated using the simple model suggested by Naot et al (1970), known as the isotropization production (IP) model

$$\phi_{ij2} = - C_2 \left(P_{ij} - \frac{2}{3} \delta_{ij} P_k \right) \tag{78}$$

A more sophisticated version of ϕ_{ij2} is the linear quasi-isotropic (QI) model (Launder et al, 1975)

$$\begin{aligned} \phi_{ij2} = & - \left(\frac{C_2 + 8}{11} \right) \left(P_{ij} - \frac{2}{3} \delta_{ij} P_k \right) - \left(\frac{8C_2 - 2}{11} \right) \left(D_{ij} - \frac{2}{3} \delta_{ij} P_k \right) \\ & - \left(\frac{30C_2 - 2}{55} \right) \rho k \left(\frac{\partial U_i}{\partial X_j} + \frac{\partial U_j}{\partial X_i} \right) \end{aligned} \tag{79}$$

where

$$D_{ij} = - \rho \left(\overline{u_i u_k} \frac{\partial U_k}{\partial X_j} + \overline{u_j u_k} \frac{\partial U_k}{\partial X_i} \right) \tag{80}$$

This model includes both the symmetric and antisymmetric mean strain effects on redistribution modeling.

The effects of solid boundaries on pressure redistribution term are included using the wall correction proposed by Launder et al (1975), or

$$\phi_{ijw} = \frac{k^{1.5}}{\varepsilon X_n} \left[C_{1w} \frac{\varepsilon}{k} \left(\overline{u_i u_j} - \frac{2}{3} \delta_{ij} P_k \right) + C_{2w} \left(P_{ij} - D_{ij} \right) \right] \tag{81}$$

where x_n is the normal distance from the wall and the model constants C_{1w} and C_{2w} are specified in Table 5.1-II. The modeled Reynolds stress transport equations for three-dimensional flow are given in Appendix B.

5.2 MATHEMATICAL FORMULATION

The calculation procedure used in this study is based on the primitive variable formulation of the Navier-Stokes equations. The conservation equations are discretized using a control-volume approach. The coupling between the continuity and momentum equations is handled via the SIMPLER algorithm. The procedure is described in detail in Karki et al (1988), Patankar (1980), and Varejao (1979).

The conservation equations for all dependent variables may be expressed in the following general form

$$\frac{\partial}{\partial X}(\rho U\phi) + \frac{\partial}{\partial Y}(\rho V\phi) + \frac{\partial}{\partial Z}(\rho V\phi) = \frac{\partial}{\partial X}(\Gamma\frac{\partial \phi}{\partial X}) + \frac{\partial}{\partial Y}(\Gamma\frac{\partial \phi}{\partial Y}) + \frac{\partial}{\partial Z}(\Gamma\frac{\partial \phi}{\partial Z}) + S \qquad (82)$$

where ϕ is the particular variable of interest, Γ is the diffusion coefficient, and S is the source term.

5.2.1 Discretization

Equation 82 can be written as:

$$\frac{\partial}{\partial X}J_x + \frac{\partial}{\partial Y}J_y + \frac{\partial}{\partial Z}J_Z = S \qquad (83)$$

where J_x, J_y, and J_z, are the total (convection and diffusion) fluxes defined by

$$J_x = \rho U\phi - \Gamma\frac{\partial \phi}{\partial X} \qquad (84a)$$

$$J_y = \rho V\phi - \Gamma\frac{\partial \phi}{\partial Y} \qquad (84b)$$

$$J_z = \rho V\phi - \Gamma\frac{\partial \phi}{\partial Z} \qquad (84c)$$

The integration of Equation 83 over the control volume surrounding the grid point P (Figure 5.2.1-1*) gives

$$(J_{x,e} - J_{x,w})\,\Delta Y\,\Delta Z + (J_{y,n} - J_{y,s})\,\Delta X\,\Delta Z + (J_{z,t} - J_{z,b})\,\Delta X\,\Delta Y = S\,\Delta X\,\Delta Y\,\Delta Z \qquad (85)$$

A discretization scheme is needed to relate the flux at each control-volume face to the values of the dependent variable at the neighboring grid points. The results presented in this report have been obtained using the power-law differencing scheme and flux-spline scheme. A brief description of these schemes is presented next.

5.2.2 Power-Law Differencing Scheme

This scheme is based on a curve fit to the exact solution of the one-dimensional convection-diffusion equation without a source. Since this formulation is based on a purely one-dimensional flux balance, it leads to significant numerical errors in the presence either of strong source terms or crossflow gradients

---

* Figures for Section V appear at the end of each subsection. The figure number identifies the subsection in which the figure is discussed.

in multidimensional flows coupled with the grid-to-flow skewness. The flux-spline scheme includes these effects in the interpolation profile between the grid points.

5.2.3 Flux-Spline Differencing Scheme

The flux-spline scheme considered here is based on the assumption that within a control volume the total flux in a given direction varies linearly along the coordinate direction. For example, the flux in the x direction for the control volume around the grid point P (Figure 5.2.3-1) is given by

$$J_x = \rho U\phi - \Gamma \frac{\partial \phi}{\partial X} = J_{x,w} + \left(\frac{J_{x,e} - J_{x,w}}{\Delta X} \right) X \tag{86}$$

The integration of Equation 50 leads to the following expression for the variation of ϕ in the x direction

$$\phi = a + b \exp(\rho U X/\Gamma) + c X \tag{87}$$

where the constants a, b, and c for a given control volume can be expressed in terms of $J_{x,e}$, $J_{x,w}$, and ϕ_P.

Equation 87 gives the variation of ϕ within a control volume. For two adjacent control volumes the ϕ-profiles are such that they imply the same total flux at the common interface. In addition, these profiles must also give a unique value of ϕ at the common interface. This continuity-of-ϕ (spline continuity) condition for the interface between the grid points W and P can be expressed as:

$$J_{x,w} = (D_{x,w}\phi_W - E_{x,w}\phi_P) + B_{x,w}(J_{x,w} - J_{x,e}) + C_{x,w}(J_{x,w} - J_{x,ww}) \tag{88}$$

Here, the expression $(D_{x,w}\phi_W - E_{x,w}\phi_P)$ is identical to that obtained from the lower-order exponential scheme (e.g., Patankar, 1980) which is based on the assumption that the total flux is uniform within a control volume. The extra terms involving B_x and C_x result from the linear variation of flux. For ease of presentation, Equation 88 is rewritten as

$$J_{x,w} = (D_{x,w}\phi_W - E_{x,w}\phi_P) + \hat{J}_{x,w} \tag{89}$$

It should be noted that additional terms such as $J_{x,w}$ involve the difference in flux values at adjacent faces of the control volume. That there is a difference in flux indicates the presence of a source term and/or multidimensionality (a change of flux in one direction is felt as a source term in another direction).

Similar expressions can also be derived for fluxes in other coordinate directions. Substituting these expressions in Equation 85 and utilizing the discrete form of the continuity equation, the following discretization equation for ϕ is obtained

$$a_P\phi_P = \Sigma a_{nb}\phi_{nb} + b + \hat{S} \tag{90}$$

The values of the influence coefficients a_{nb} are identical to the coefficients obtained from the exponential scheme. The contribution of the flux-spline formulation is contained in the term S, which is given

$$\hat{S} = (\hat{J}_{x,w} - \hat{J}_{x,e})\,\Delta y\,\Delta z + (\hat{J}_{y,s} - \hat{J}_{y,n})\,\Delta x\,\Delta z + (\hat{J}_{z,b} - \hat{J}_{z,t})\,\Delta x\,\Delta y \tag{91}$$

A three-dimensional situation is governed by three field variables: ϕ, J_x, and J_y. The four sets of equations that determine these variables are:

(1) the conservation equation for ϕ
(2) the spline-continuity condition in the x direction
(3) the spline-continuity condition in the y direction
(4) the spline-continuity condition in the z direction

The solution of these equations is obtained in an iterative manner. In the beginning, J_x, J_y, and J_z are set equal to zero, then the conservation equation for ϕ reduces to the lower-order formulation and can be easily solved. The solution leads to new estimates for the fluxes J_x, J_y, and J_z from which new J_x J_y, and J_z can be calculated. The ϕ-equation is now solved with the flux-spline contribution to the source term. This process is repeated until convergence is achieved.

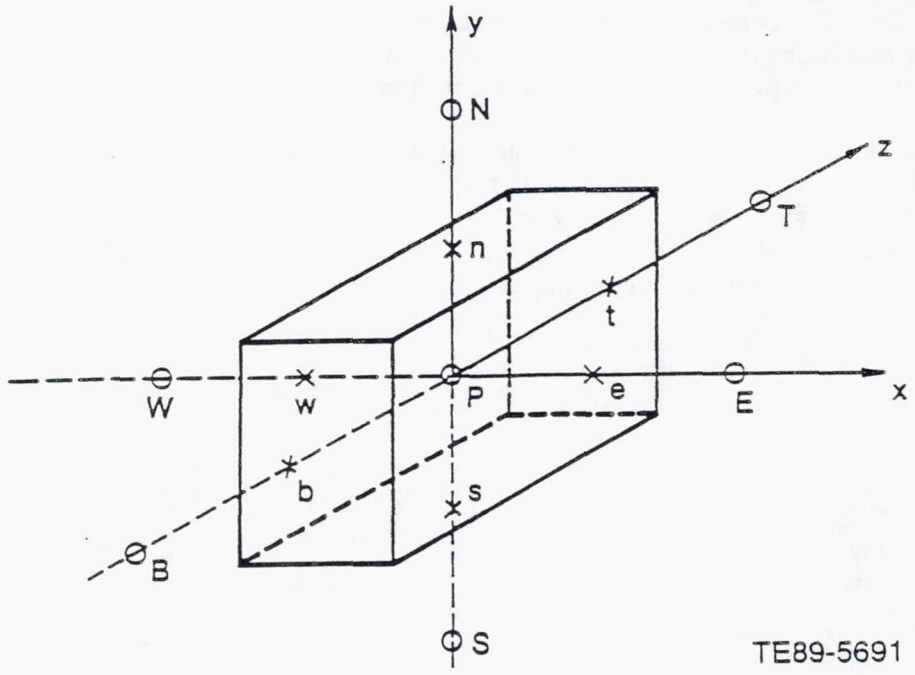

Figure 5.2.1-1. Control volume around the grid point P.

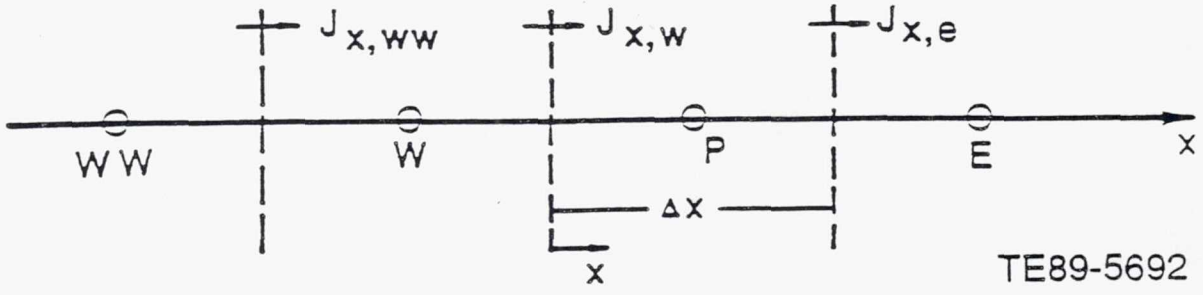

Figure 5.2.3-1. One-dimensional condition.

REFERENCES

Bradshaw, P., 1968, "Outlook for 3-Dimensional Procedures," *Proc. AFOSR-IP-Stanford Boundary Layer Conf.*, 1, 427.

Daly, B. J. and Harlow, F. H., 1970, "Transport Equations of Turbulence," *Phys, Fl.*, 13, 2634-2649.

Karki, K. C., Patankar, S. V., Runchal, A. K., and Mongia, H. C., 1988, "Improved Numerical Methods for Turbulent Viscous Recirculating Flows," *Aerothermal Modeling Phase II Final Report*, NASA CR-182169.

Launder, B. E. and Spalding, D. B., 1974, "The Numerical Computation of Turbulent Flows," *Computer Methods in Applied Mechanics and Engineering*, 3, 269-289.

Launder, B. E., Reece, G. J., and Rodi, W., 1975, "Progress in the Development of a Reynolds Stress Turbulence Closure," *JFM*,, 68, 537-577.

Lumley, J. L. and Khajeh-Nouri, B. J., 1974, "Computational Modeling of Turbulent Transport," *Adv. Geophys.*, 18A, 169.

Naot, D., Shavit, A., and Wolfshtein, M., 1970, "Interactions Between Components of the Turbulent Velocity Correlation Tensor," *Israel J. Tech.*, 8, 259-269.

Patankar, S. V., 1980, *Numerical Heat Transfer and Fluid Flows*, Hemisphere, New York.

Rodi, W., 1976, "A New Algebraic Relation for Calculating the Reynolds Stresses," *Zeitschrift fuer Angewandte Mathematik and Mechanik*, 56, 219-221.

Rodi, W., 1980, *Turbulence Models and Their Application in Hydraulics, Inter*national Association of Hydraulic Research, Delft, The Netherlands.

Rotta, J. C., 1951, "Statistische Theorie Nichthomogener Turbulenz," *Zeitschrift fur Physik*,, 129, 547-572.

Varejao, L. M. C., 1979, "Flux-Spline Method for Heat, Mass, and Momentum Transfer", Ph.D. thesis, University of Minnesota.

Page intentionally left blank

TABLE OF CONTENTS

VI. MODEL VALIDATION

This section presents the results of the comparisons of the various models for three-dimensional recirculating flows. Predictions obtained with each of the turbulence models are discussed and compared with experimental data. The goals of this study require a careful selection of the test cases. They have to provide reliable mean flow and turbulence data in the recirculation and recovery regions. A detailed specification of the flow parameters in the upstream region is also essential, since these are used as inlet conditions to start the computations. The test problems used encompass the range of complexities involved in combustor flows. Theses are:

- dome annular jets
- primary jets
- dome annular jets and primary jets

All data sets meet the criteria for acceptable measurements in terms of adequate experimental facility, appropriate instrumentation, and agreement with generally accepted flow trends.

6.1 DOME ANNULAR JETS

This subsection presents the comparison of the computational results with the experimental data obtained for three-dimensional annular flow. The experiment was conducted in an air rig (Figure 6.1-1*) consisting of five annular swirling or nonswirling streams issuing into a duct of rectangular cross section. Five jets were used in the experiment in order to allow for any interaction between jets and to remove wall effects. The test section was of rectangular cross section, 3.0 x 15.0 in., and extended 10 duct heights (76.2 cm) downstream from the headplate. The top, bottom, and sides were constructed of glass and Plexiglas to facilitate easy access with the laser. There were provisions for radial jets at specified axial locations. For the present case, all streams were nonswirling and there were no primary jets.

The elliptic nature of the flow required the boundary conditions to be specified on the six sides of the solution domain. Four kinds of boundaries needed consideration: inlet, axis of symmetry, wall, and the outlet. In an ideal annular combustor, geometric symmetry exists between annular jets. The volume between the annular jets extends downstream of the combustor inlet. Due to the symmetry of the problem, the computational domain includes only one quarter of the annular stream. In the cross section, the computational domain is bounded by symmetry lines in the z direction, and by a symmetry line and a wall in the y direction. At the inlet boundary, which is located at the exit of the annular streams (x=0.0), the experimentally measured profiles of axial velocity and kinetic energy, assuming isotropic turbulence, are prescribed. The inlet dissipation rate is calculated based on the turbulent kinetic energy and constant length scale. The computational domain extends from the inlet plane to four duct heights (4H) downstream of the jet exit. Since the measured flow does not show any x dependence at x>3H, the specified condition, $\partial/\partial x = 0$, at the exit plane of the calculation domain is realistic. At the axis of symmetry, the radial velocity, turbulent shear stress, and the radial gradients of other variables are set to zero. The conventional logarithmic law, which is based on the local equilibrium assumption, is applied to the wall boundary condition. The inlet profiles and the grid distribution are displayed in Figures 6.1-2 and 6.1-3.

Computations are made on two grids, 37 x 27 x 27 and 52 x 42 x 42, which are referred to as medium and fine grids, respectively. In the refined grid, a finer spacing is used within and near the jet. In both cases, the grid spacing in the x direction is finer near the inlet.

---

* Figures for Section VI appear at the end of each subsection. The figure number identifies the subsection in which the figure is discussed.

The accuracy of a numerical simulation is dictated by the differencing scheme and the physical models embodied in the computational method. The use of first-order differencing schemes for transport terms in the conservation equations introduces significant false-diffusion in the numerical solution (Patankar, 1980*). The presence of false diffusion makes accurate predictions of complex flows difficult, as it may completely mask the effects of physical diffusion. In principle, false diffusion can be reduced to negligibly low levels by using a very fine grid. However, the necessary degree of grid refinement is almost impractical for complex three-dimensional flows. The need for an excessively fine grid can be avoided by using an improved differencing scheme for the transport terms in the conservation equations. The improved schemes take into account the effects of flow skewness, lateral transport, and the sources. For the same accuracy, these schemes require a smaller number of grid points than the first-order schemes (Varejao, 1979; Karki, 1988).

Two different numerical schemes, namely the first-order power-law differencing scheme (PLDS) and higher-order flux-spline differencing scheme (FSDS), are applied for the calculations. Here, the emphasis is being placed on the differences between the results obtained from these schemes. Thus, the disagreements between the numerical and experimental results may be attributed to the numerical inaccuracy or the inadequacy of the turbulence model. However, for a given turbulence model, the flux-spline results are more accurate.

Three different turbulence models, namely the k-ε model, algebraic second-moment (ASM), and differential second-moment (DSM), were applied with grid size of 37 x 27 x 27 to predict the mean and turbulence quantities. Figure 6.1-4 shows the axial velocity profiles in the vertical center plane (xy plane at z = 7.5 in.) predicted by the k-ε model at the selected axial locations obtained from the medium grid solution. The results show differences in the prediction of peak and centerline values in the developing region. The calculated velocity field shows higher peaks and a longer recirculation at the centerplane when the FSDS is applied. At all streamwise locations, the profiles resulting from the power-law are more smeared than those from the FSDS. This trend indicates the presence of excessive numerical diffusion in the power-law solution. The experimental data show a portion of the fluid from the upper and lower sections of the annular jet. The main portion of the fluid can be seen converging at the middle of the rig and accelerating as the flow is squeezed between recirculation regions of flow along the upper and lower walls of the rig (Figure 6.1-4). Downstream, the main flow then decelerates as the recirculation zones are passed. The computational results show recirculating flow along the upper and lower walls of the rig, this behavior has been observed experimentally through flow visualization studies.

The comparison of the predicted centerline velocity distribution with the experimental data is presented in Figure 6.1-5. It is seen that the FSDS results in better agreement with the measurement at locations near the inlet. However, further downstream the velocity is underpredicted by both schemes. The underprediction for a centerline velocity stems from the incorrect representation of the turbulent diffusion process. As shown by Ribeiro (1976), the radial normal stress is particularly important in the upstream region and, as a consequence, the isotropic viscosity hypothesis is inadequate.

The predicted axial velocity profiles in the xy plane at y = 1.5 in. (horizontal centerplane), which contains the centerline of the annular jet, at various streamwise locations obtained from the k-ε model are shown in Figure 6.1-6. The experimental data show that the maximum velocity in the xz plane is slightly higher than the peak value in the xy plane. The calculations show that the FSDS resulted in higher maximum velocity and a larger recirculation zone. Away from the centerline, the measurement shows recirculation zones between the annular jets. The fluid is converged at the middle of the rig and increases the velocity. The computations show the recirculations between the jets start to form at approximately x = 1.0 in. from the inlet. At all axial locations, the false diffusion associated with the first-order numerical scheme causes the PLDS to predict smaller peak velocity and, as a result, a shorter recirculation region.

---

* References for Section VI are listed at the end of the section.

Having demonstrated the effect of the isotropic diffusion assumption and compared the k-ε model with data, attention was turned to the performance of the DSM closure. It seems somewhat paradoxical that the more advanced types of turbulence models have been least successful in the complex flows associated with flow recirculation for which in theory they have the most to offer compared with eddy viscosity based closures. Comparisons of the predicted mean velocity profiles by DSM closure with measurements are shown in Figures 6.1-7 and 6.1-8. The results have been illustrated in xy (Figure 6.1-7) and xz (Figure 6.1-8) centerplanes and calculated by both PLDS and FSDS. One of the main differences between these results and those obtained from the k-ε model is apparent near the inlet plane (x = 0.2 in.), where the PLDS resulted in a larger negative velocity despite the fact that a smaller peak velocity was predicted. However, the velocity profile was squeezed near the centerline in order to satisfy the global mass conservation.

The second difference observed in the calculations is that the FSDS predicted a longer recirculation length up to one-third of the channel height. The agreement between the calculated and measured results improved in the upstream region when the advanced numerical scheme was applied. The underprediction of the centerline velocity (Figure 6.1-9) has been noted at several axial locations and probably reflects a deficiency of the turbulence model. Some further diagnostic runs were carried out by varying the inlet turbulence kinetic energy and dissipation length scale, but these changes had minor influence on the centerline velocity.

Figures 6.1-10 through 6.1-14 are plots of velocity at various lateral locations away from the centerplane, and the results are shown for selected axial stations. The experimental results similar to those at z = 7.5 in. are seen at z = 7.4 and 7.6 in. The recirculation zones along the upper and lower are apparent. The flow visualization shows the existence of recirculating flow in the center annular jet region, and also shows that the convergence and acceleration of the main flow between the recirculating flow along the upper and lower walls still exist. Similar results are seen farther away from the centerplane between $6.2 \leq z \leq 8.2$ in. several general trends can be observed from these figures. The first trend is the movement of the two velocity peaks at the annular jet exit toward the centerline and the disappearance of the recirculation zone behind the center of the annular jet. The cause of both of these is due to the annular jet curvature. The second observable trend is the widening of the recirculation zones along the upper and lower walls. Both recirculation zones are clearly evident farther away from the rig centerplane. Third, a decrease in the main flow velocity along the centerline is seen. The flow is still seen to accelerate between the upper and lower recirculation zones. At planes outside of the annular jet, $6.0 \leq z \leq 6.6$ in. and $8.4 \leq z \leq 9.0$ in., there is a breakdown of any organized pattern of flow. In these planes some general trends are still noticeable in the plots. Downstream flow is reduced and completely disappears by the time the planes at z = 6.4 and 8.6 in. are reached.

Comparisons of the mean velocity and root mean square (rms) velocity profiles predicted by the ASM and DSM closures with the measured values are presented in Figures 6.1-15 through 6.1-18. The results have been shown for eight axial stations along the centerplane. In general, the results of the ASM and DSM are similar in the upstream region ($x \leq 0.8$ in.). At subsequent downstream locations there are substantial differences between the two models in the prediction of centerline velocity. Both models predicted similar recirculation length, however, use of the ASM promotes higher centerline velocity relative to the DSM. The reason is attributed to the turbulent diffusion process, which depends on the Reynolds stress gradients. In the outer flow region the ASM and DSM predict similar axial turbulence intensity distribution, but, the maximum turbulence levels were better predicted by the DSM model.

With regard to the comparison between the FSDS and PLDS, the predictions by the FSDS seem to be better, especially near the inlet, for turbulence field (Figure 6.1-19). Examination of the calculated rms profiles indicates that the FSDS results mimic the experimental data better near the centerline region. The maximum turbulence intensity predicted by both models are very close and are underpredicted as flow proceeds towards the downstream region. Overall, the turbulence intensities were qualitatively well predicted and their behaviors were in agreement with the measured profiles.

The predictions for the finer grid (52 x 42 x 42) using the standard k-ε model are displayed in Figure 6.1-20, and similar trends are noticed. The FSDS results in higher peak values than all the previous calculations. To some extent, the fine grid solution obtained from the PLDS is as good as the result of the FSDS for medium grid. The computed centerline velocity variations of the fine grid (Figure 6.1-21) indicate a strong recirculation zone. However, in the accelerating region the centerline values calculated from the FSDS are in closer agreement with the experimental data.

Comparisons of the predicted streamwise turbulent kinetic energy using both schemes is shown in Figure 6.1-22. The results are normalized with the inlet axial velocity (U_o = 98.2 ft/sec). A wide disparity exists between the calculation and the measurement. Numerical study indicates that the inlet ε profile is a very important factor in predicting the maximum values of turbulence quantities (Nikjooy et al, 1989). The calculated and measured turbulence fields show two different trends. The experimental profiles show further increase of the peak values extending from the inlet plane to the end of the central recirculation zone without any significant change of turbulence intensity at the centerline. The turbulence intensity then gradually tends to diffuse towards the wall. Secondly, the calculated profiles indicate the continuous growth of the turbulence intensity at the centerline.

Predictions of the axial velocity profiles in the xz centerplane (y = 1.5 in.) show similar behavior seen previously in the xy plane (Figure 6.1-23). The use of the FSDS generated higher maximum velocities and a longer recirculation length. The predicted peak values in the xy and xz planes are almost identical, showing that the top and bottom walls did not significantly affect the potential region. On the other hand, the experiment shows higher peaks in the xz plane. The wake region created by the dividing lip between the two streams is the probable reason for this behavior. In order for mass to be conserved, the recirculation zone created in the wake region accelerated the flow in the potential region and resulted in higher velocities.

The CPU time needed to achieve the fine grid solution was about 20 hours on a CRAY2 machine. The criteria selected for a convergent solution was based on the absolute sums of the mass and momentum residuals at all internal grid points, normalized by inlet mass and momentum fluxes. With this assumption, the maximum relative residual errors for all calculations is found to be 0.01%.

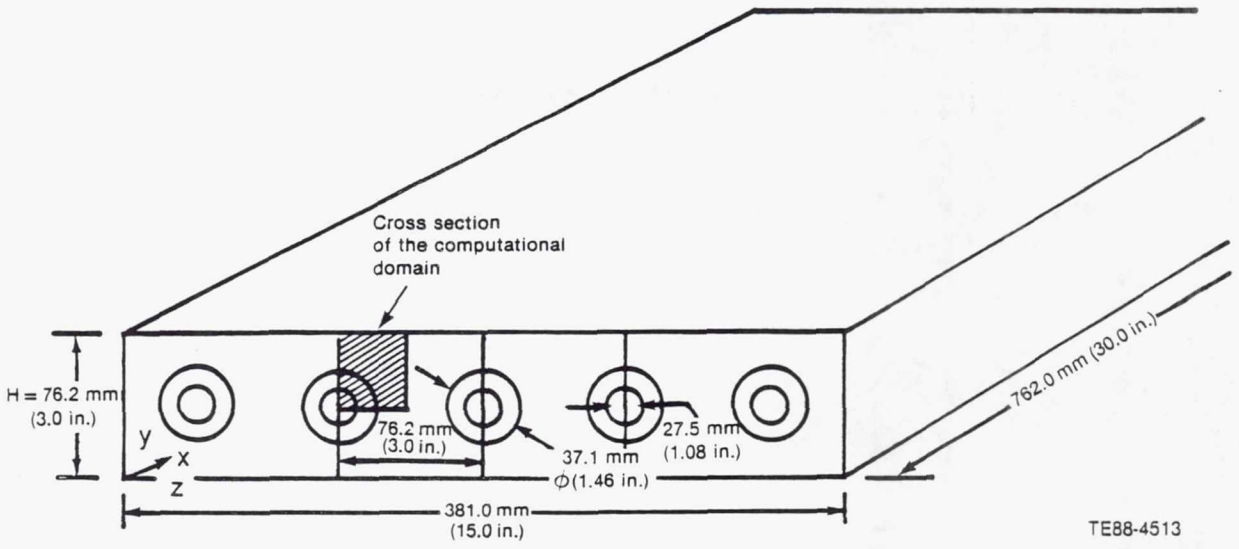

Figure 6.1-1. Geometry for an annular jet-induced flow in a duct.

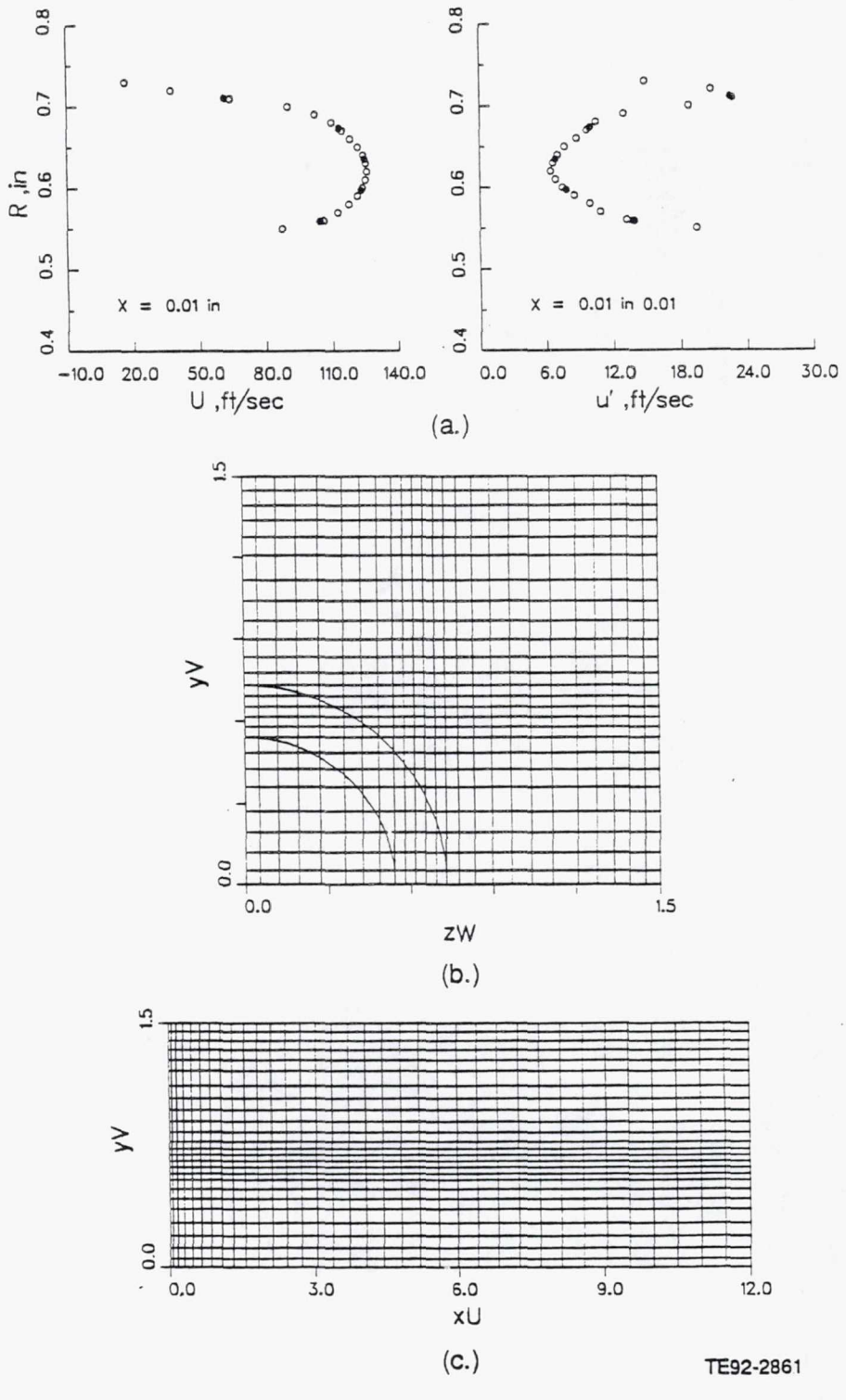

Figure 6.1-2. Inlet conditions for the medium-grid.

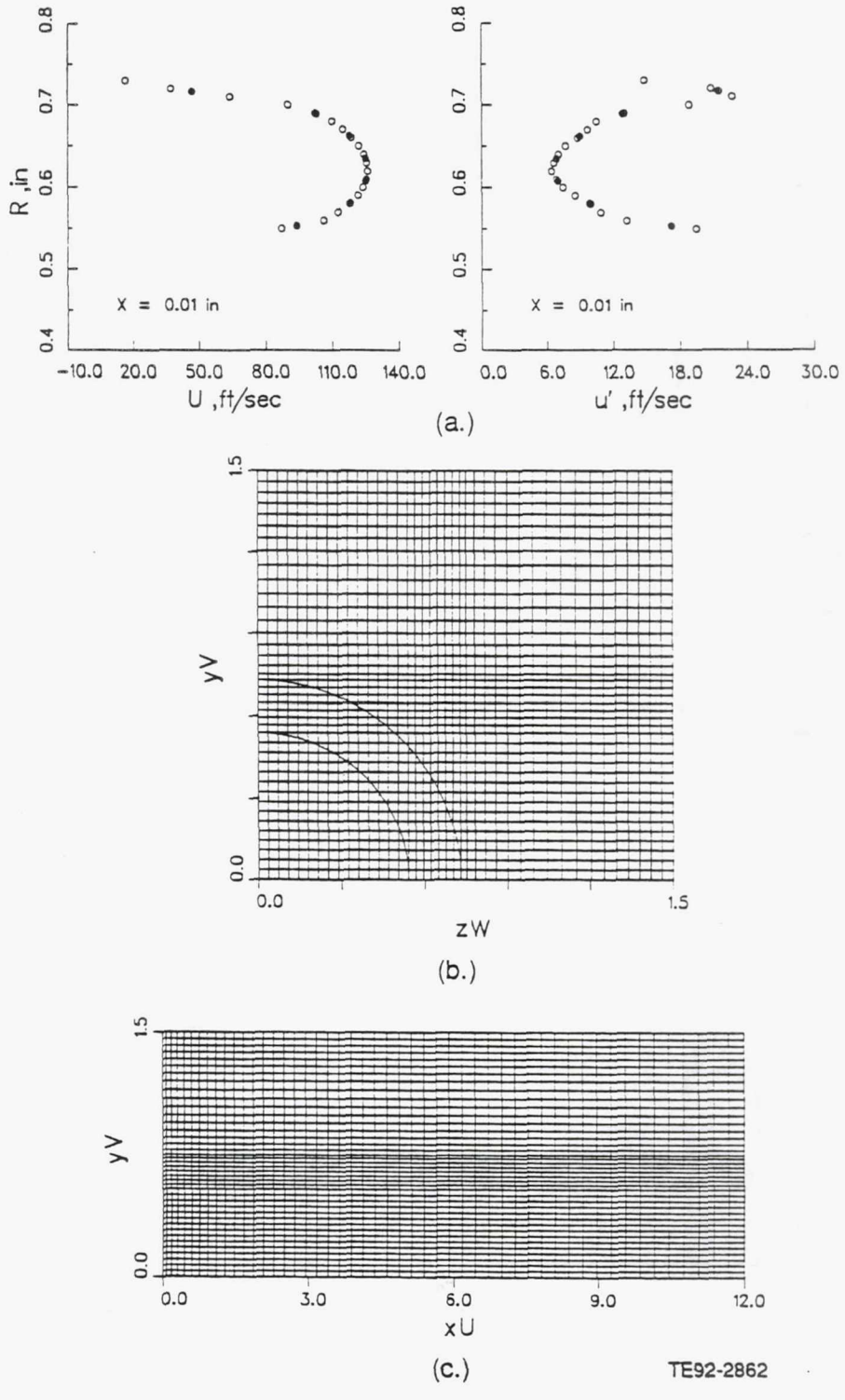

Figure 6.1-3. Inlet conditions for the fine-grid.

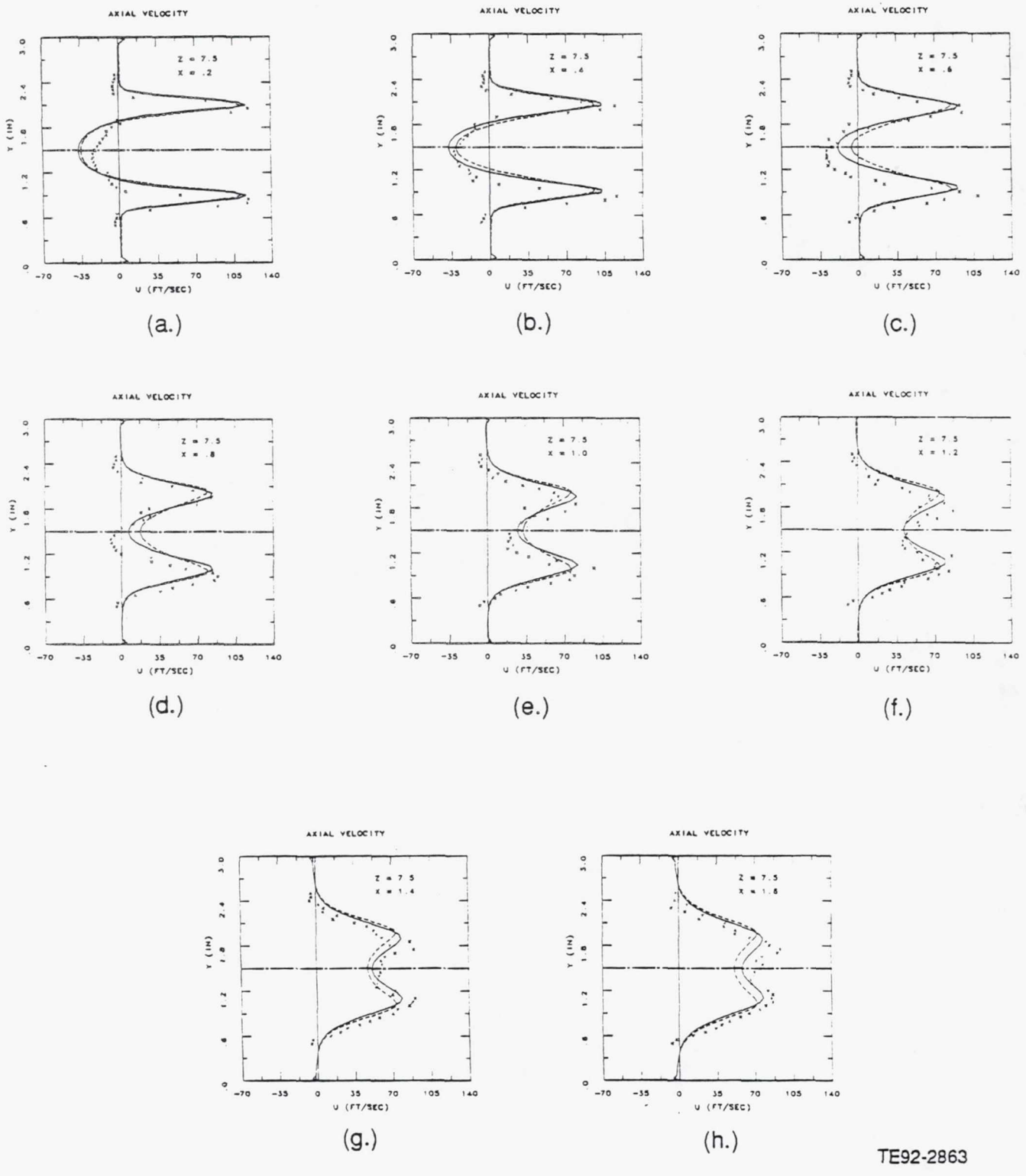

Figure 6.1-4. Axial velocity profiles at z = 7.5 in. plane, medium grid (k-ε model; ——flux spline---- power-law).

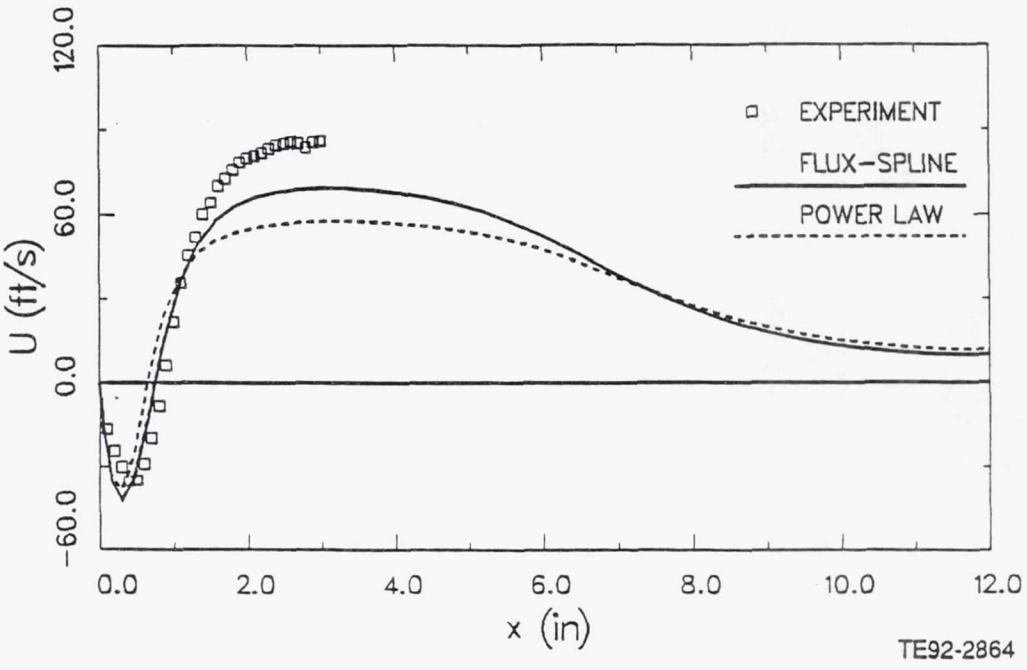

Figure 6.1-5. Variations of the centerline axial velocity, medium grid (k-ε model).

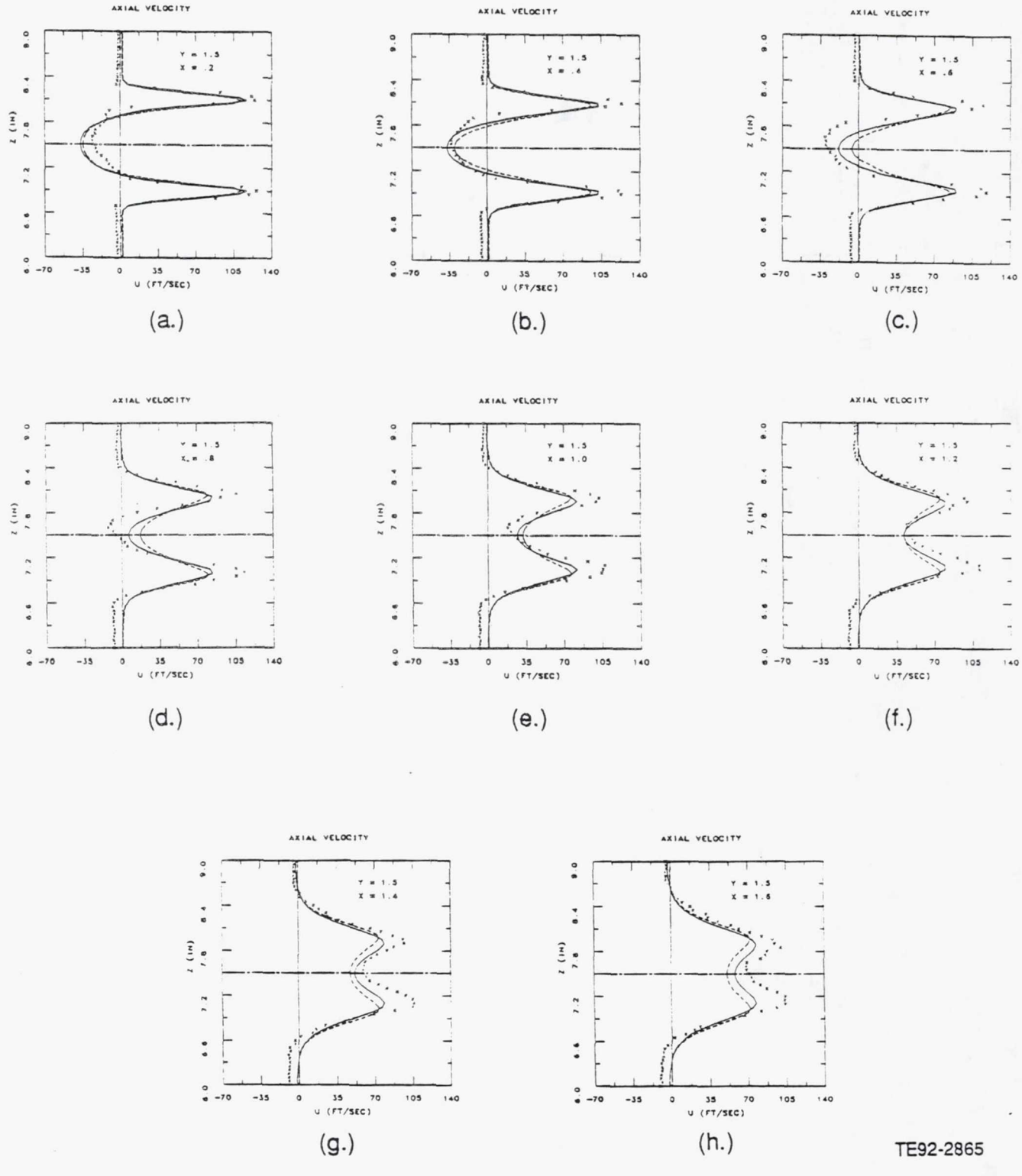

Figure 6.1-6. Axial velocity profiles at y = 1.5 in. plane, medium grid (k-ε model; ——flux spline–– power-law).

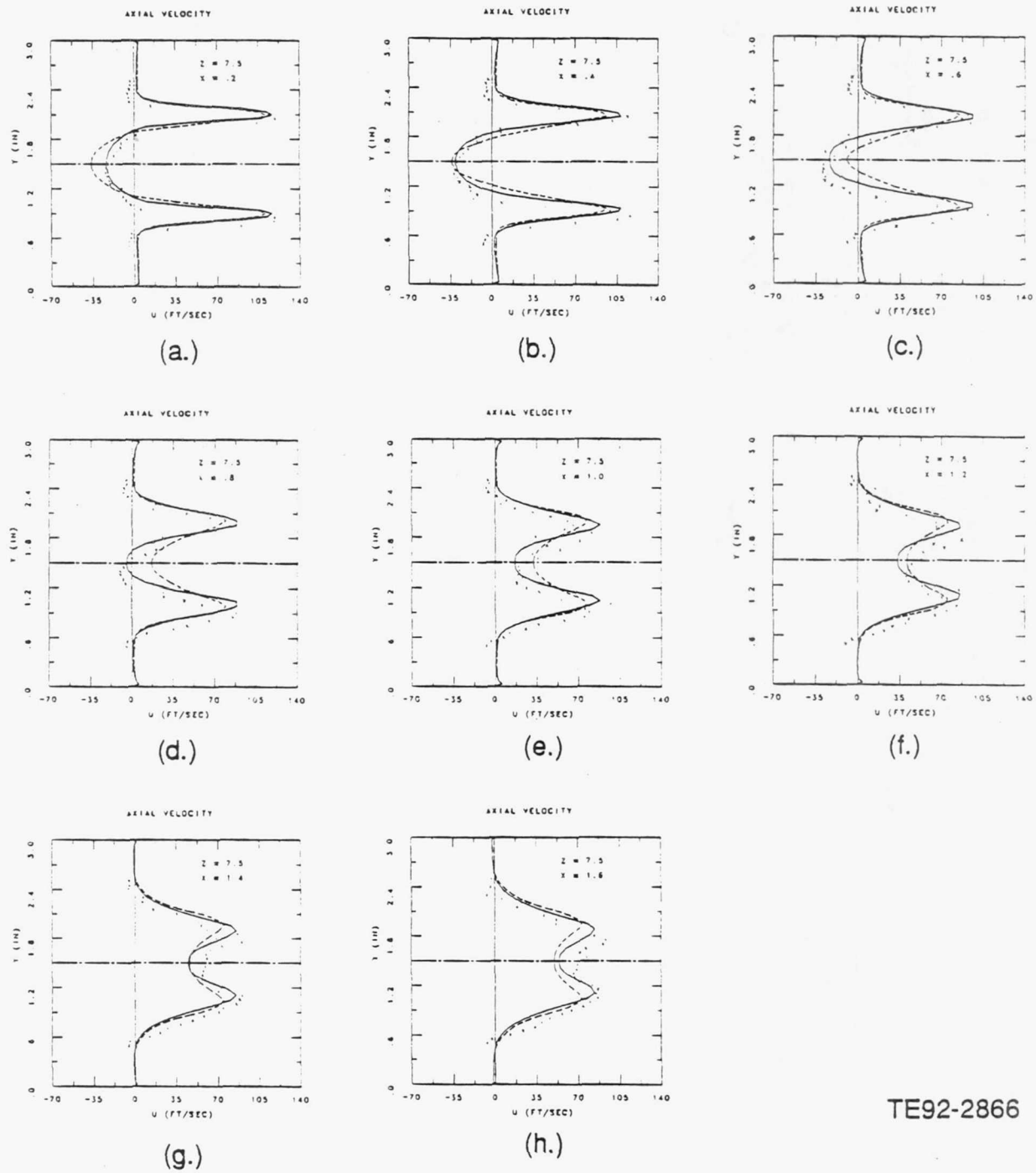

Figure 6.1-7. Axial velocity profiles at z = 7.5 in. plane, (DSM; ——flux spline——power-law).

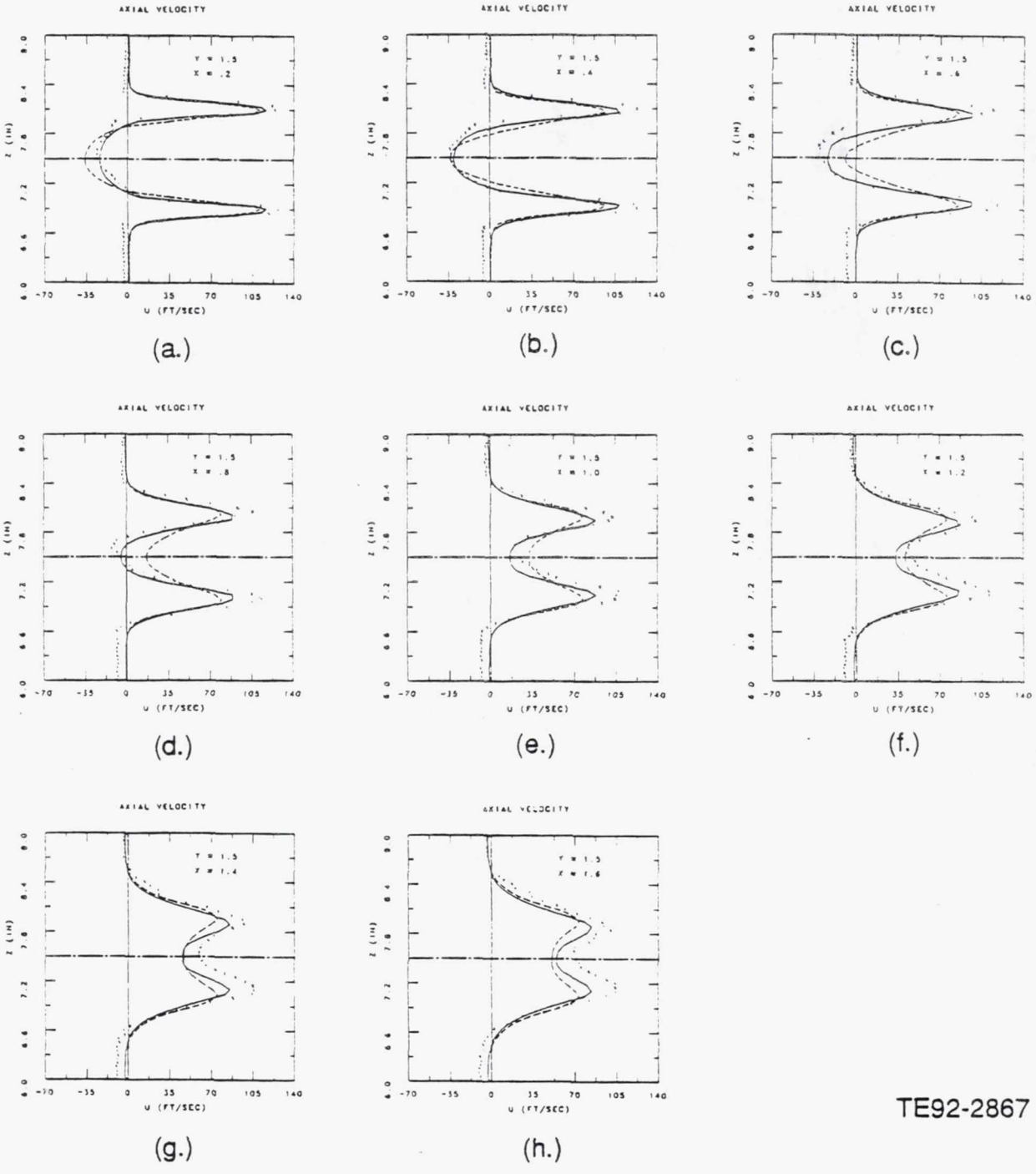

Figure 6.1-8. Axial velocity profiles at y = 1.5 in. plane, (DSM; ——flux spline----power-law).

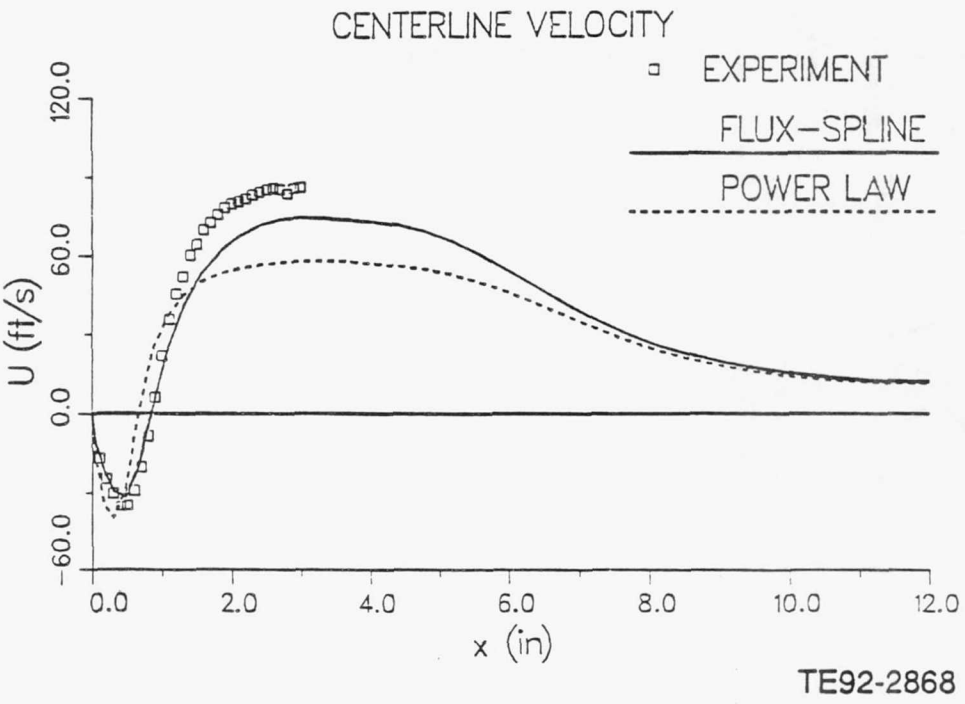

Figure 6.1-9. Centerline axial velocity profiles predicted by DSM using flux-spline and power-law schemes.

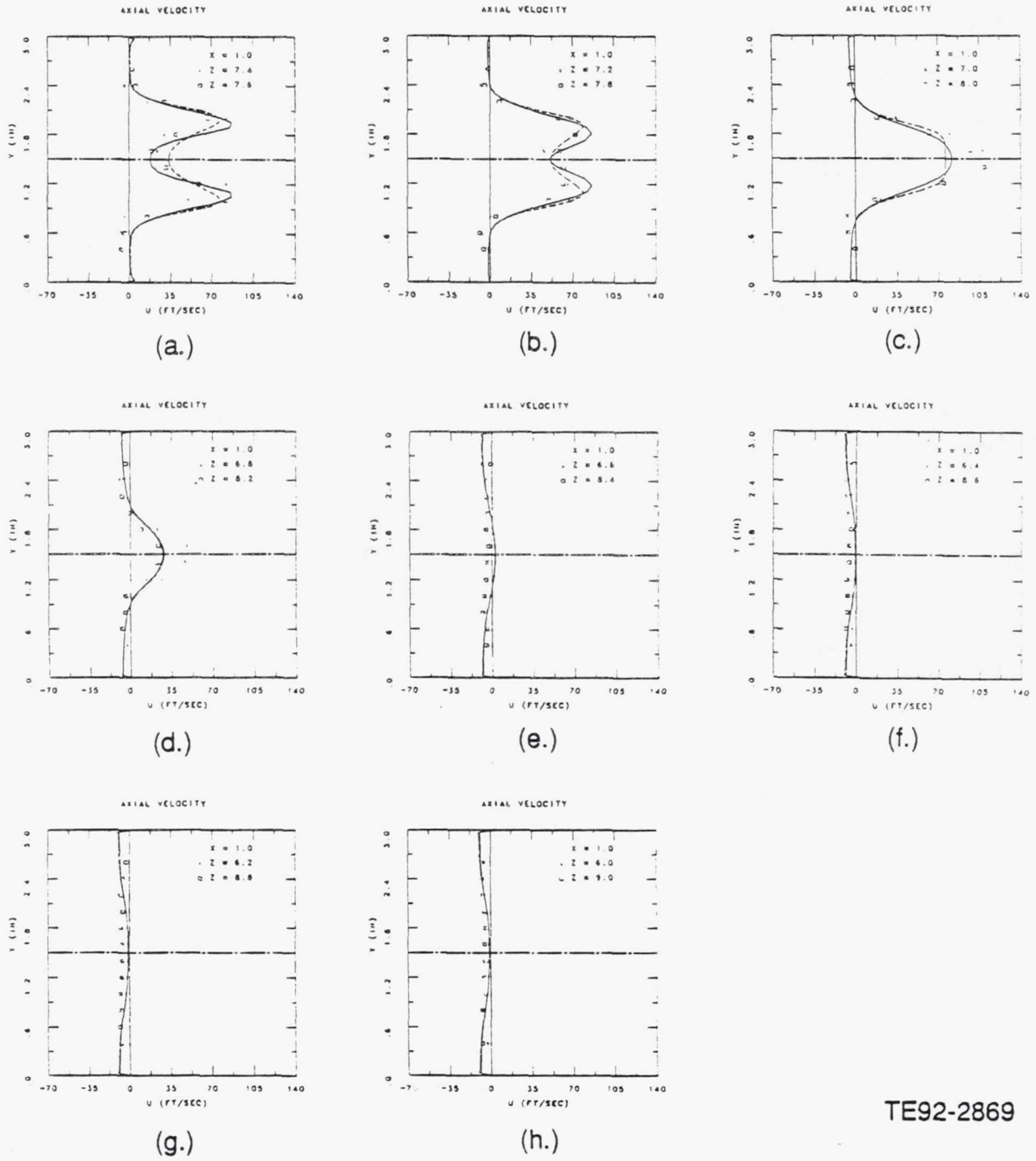

Figure 6.1-10. Axial velocity profiles predicted by DSM (—— flux-spline—power law).

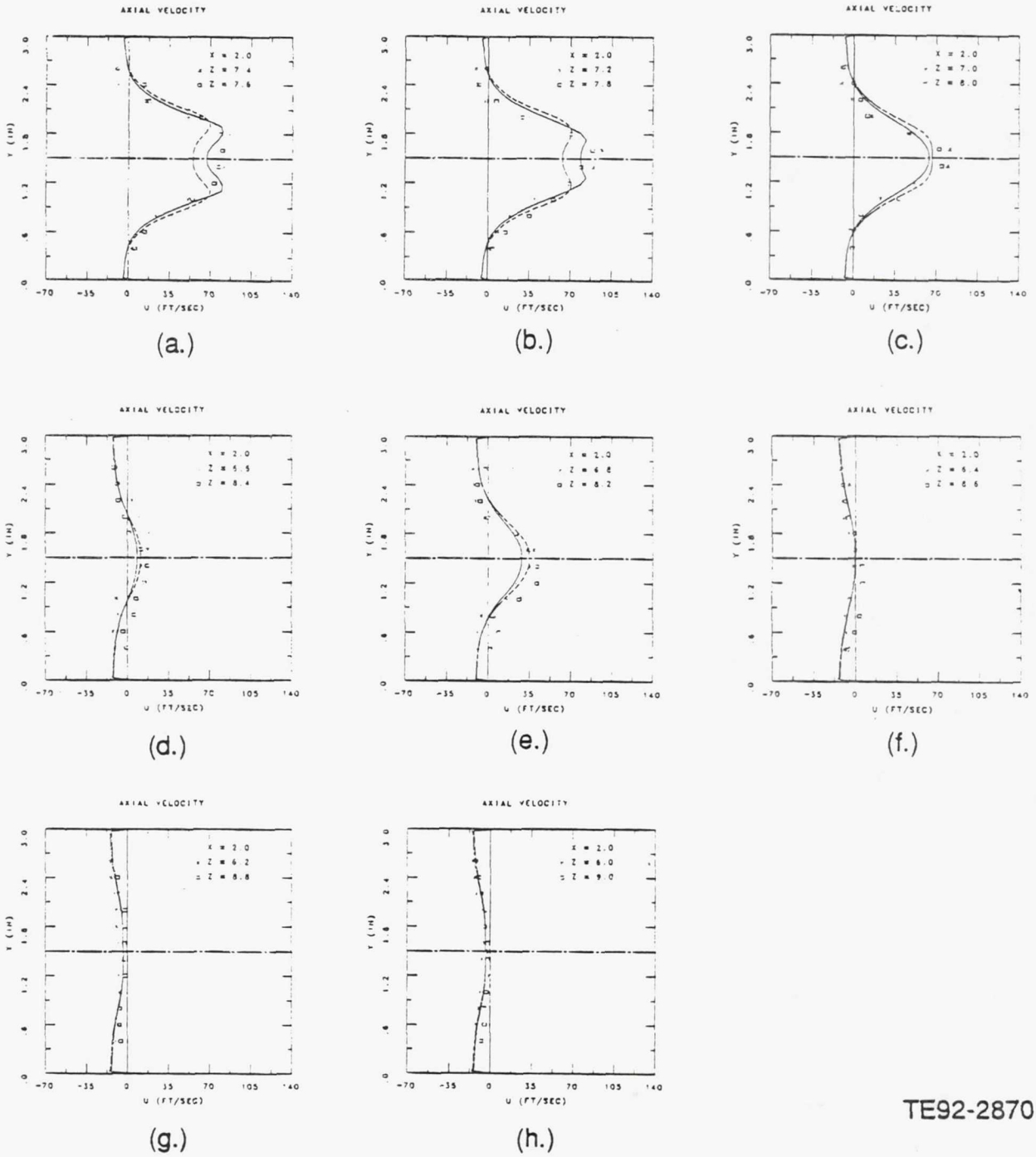

Figure 6.1-11. Axial velocity profiles predicted by DSM (—— flux-spline—power law).

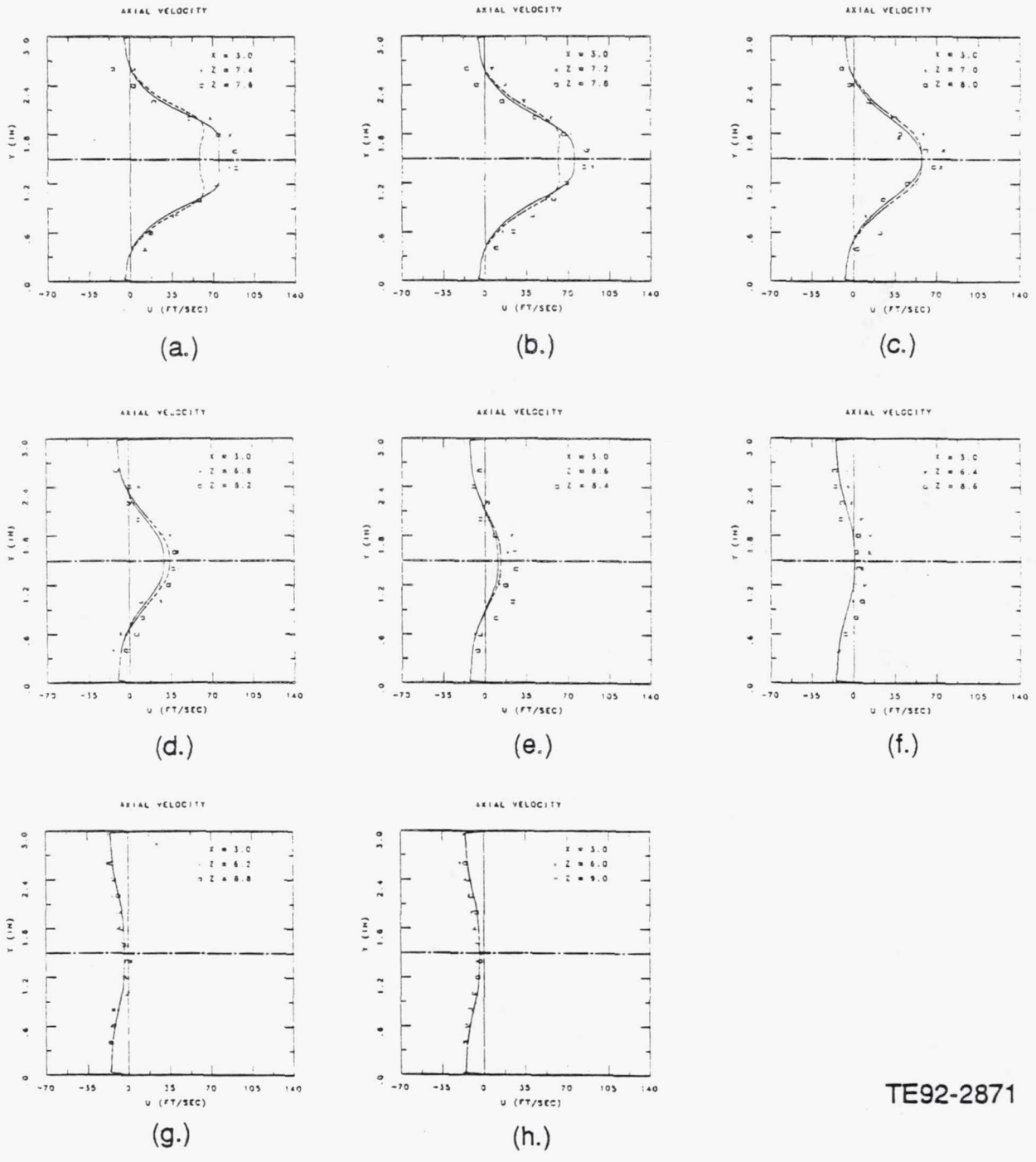

Figure 6.1-12. Axial velocity profiles predicted by DSM (—— flux-spline---power law).

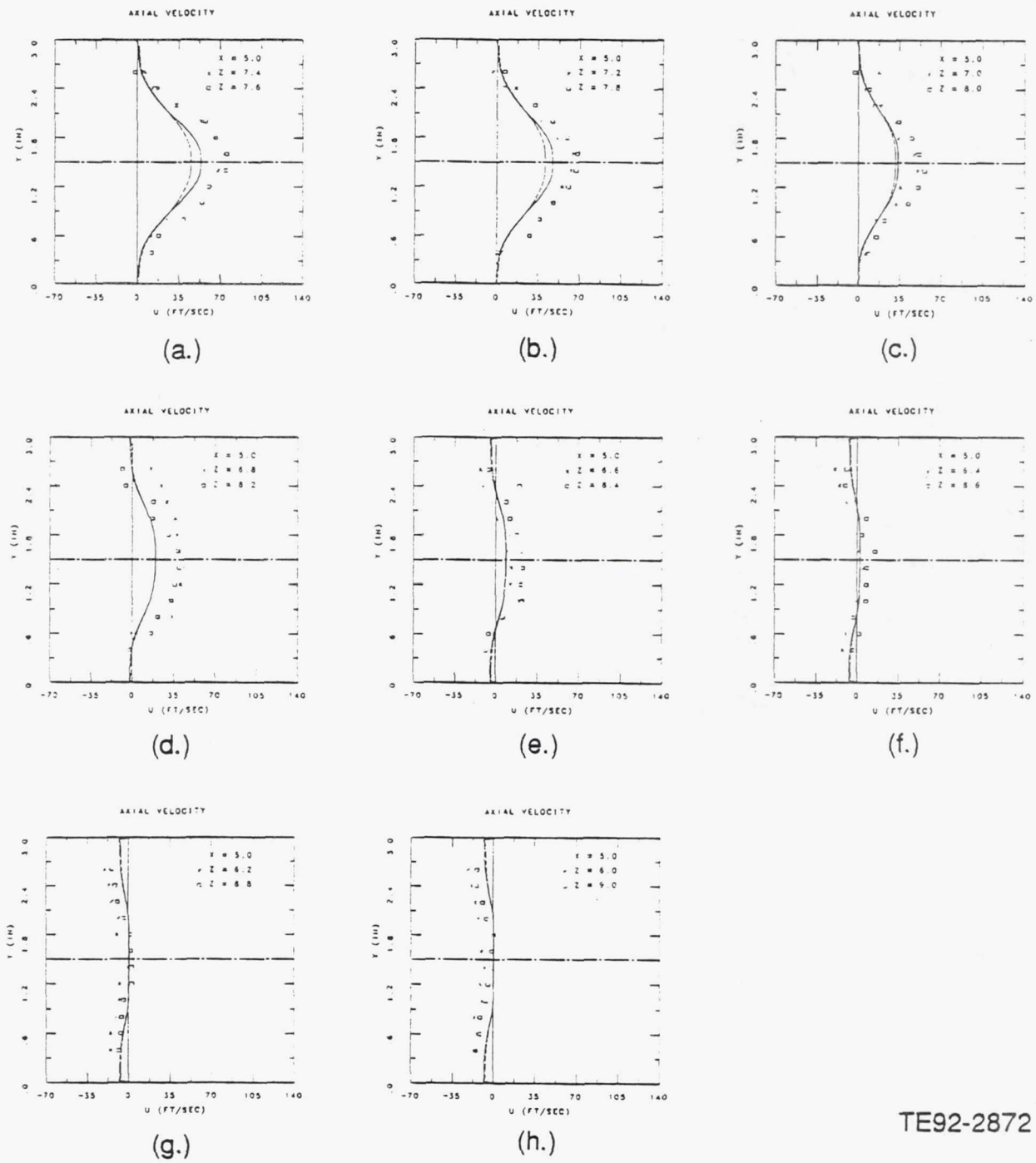

Figure 6.1-13. Axial velocity profiles predicted by DSM (—— flux-spline—power law).

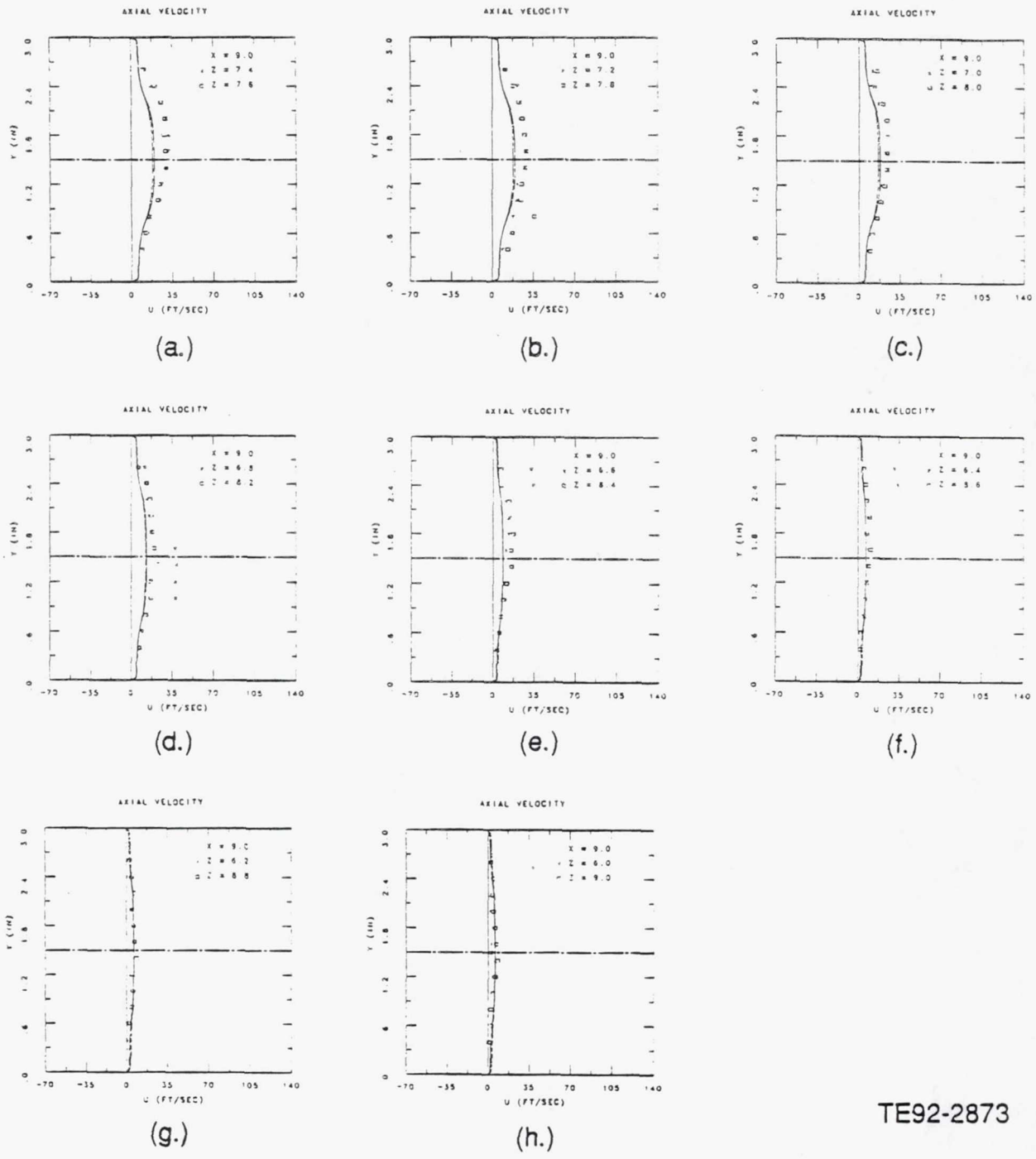

Figure 6.1-14. Axial velocity profiles predicted by DSM (—— flux-spline—power law).

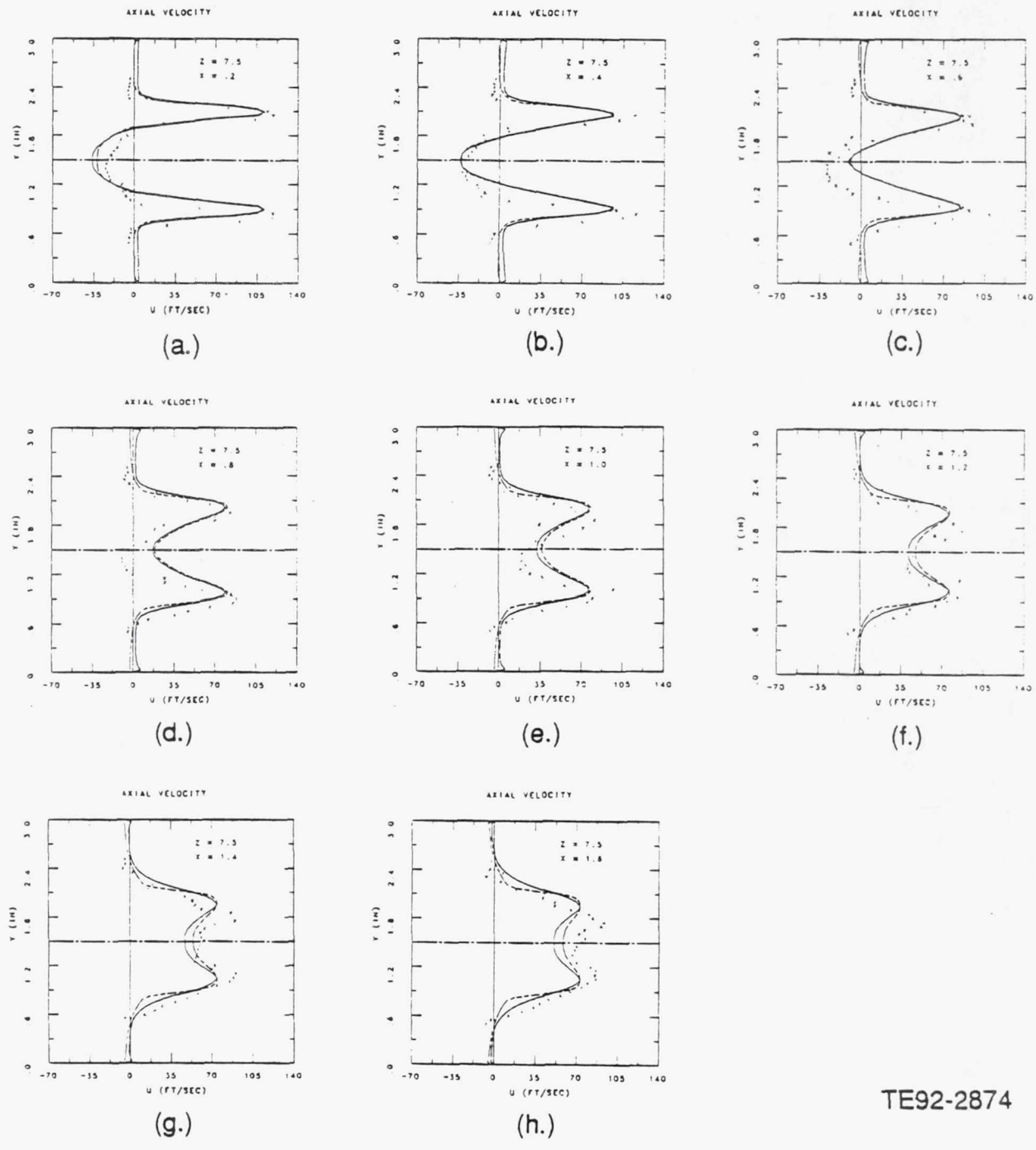

Figure 6.1-15. Axial velocity profiles predicted by DSM and ASM using power-law at z = 7.5 in. plane (—— DSM–––ASM).

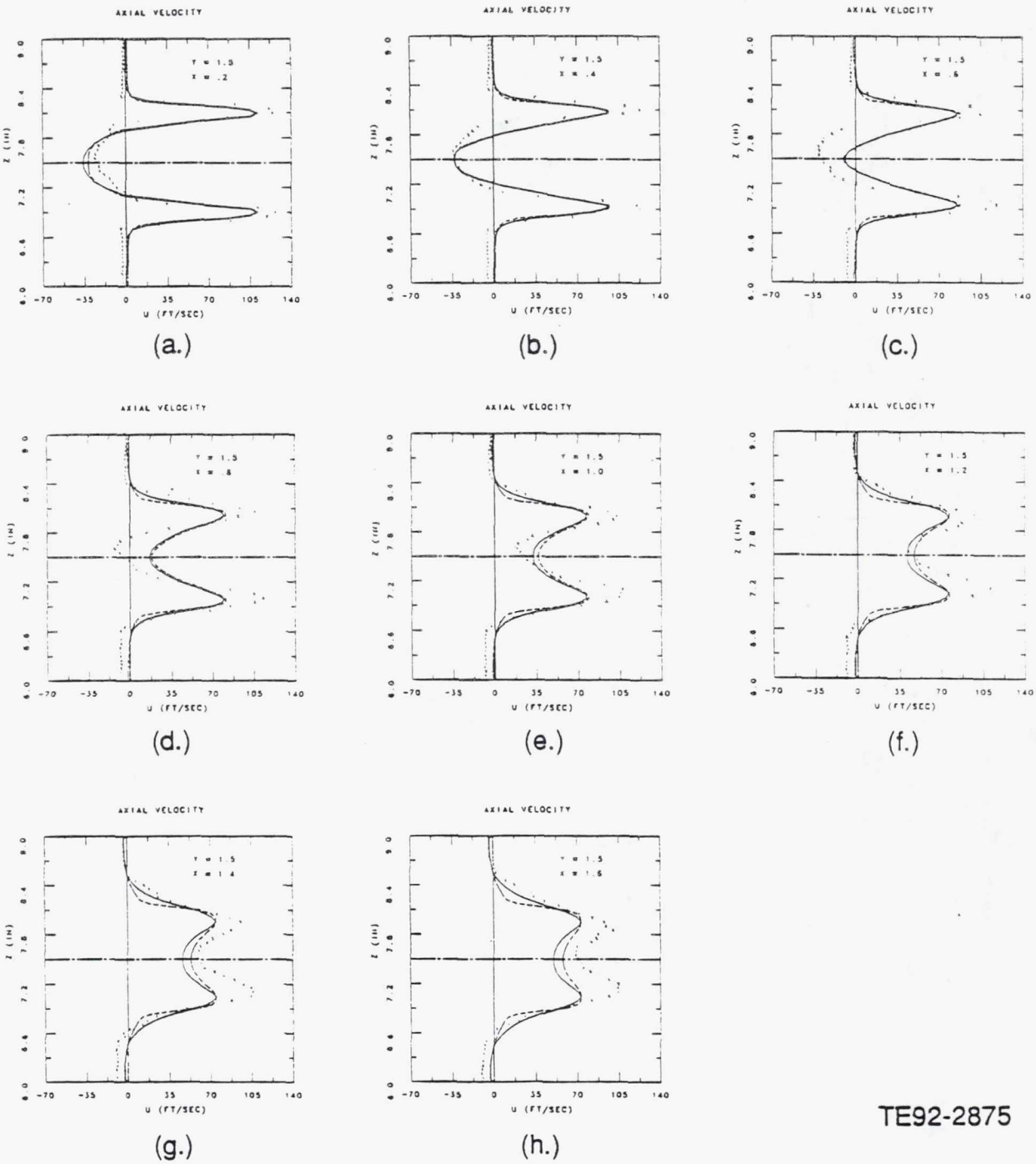

Figure 6.1-16. Axial velocity profiles predicted by DSM and ASM using power-law at y = 1.5 in. plane (—— DSM---ASM).

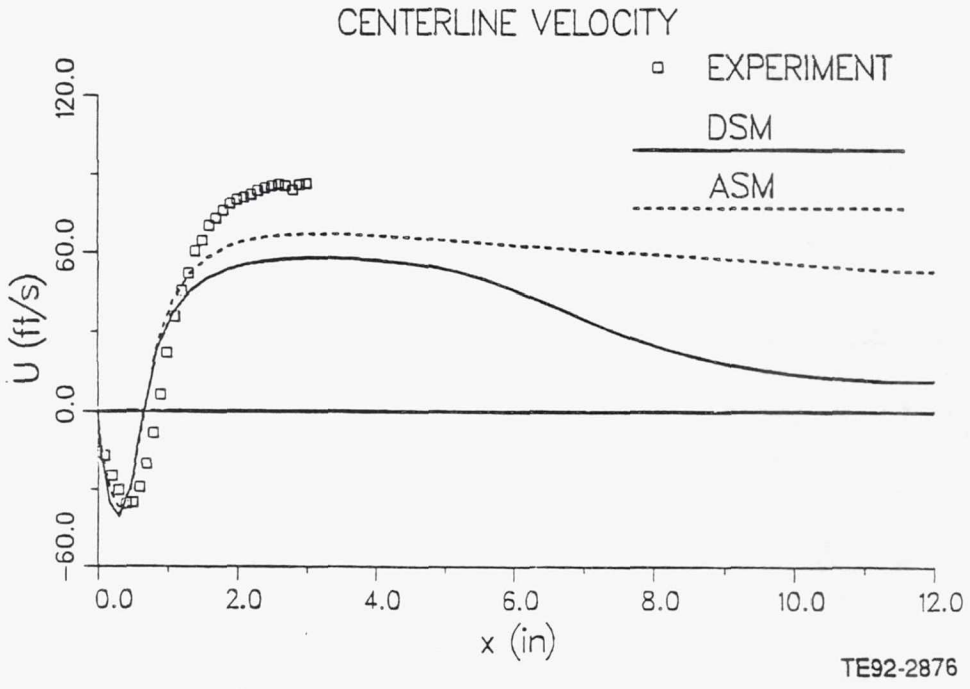

Figure 6.1-17. Centerline velocity profiles predicted by DSM and ASM using the power-law scheme.

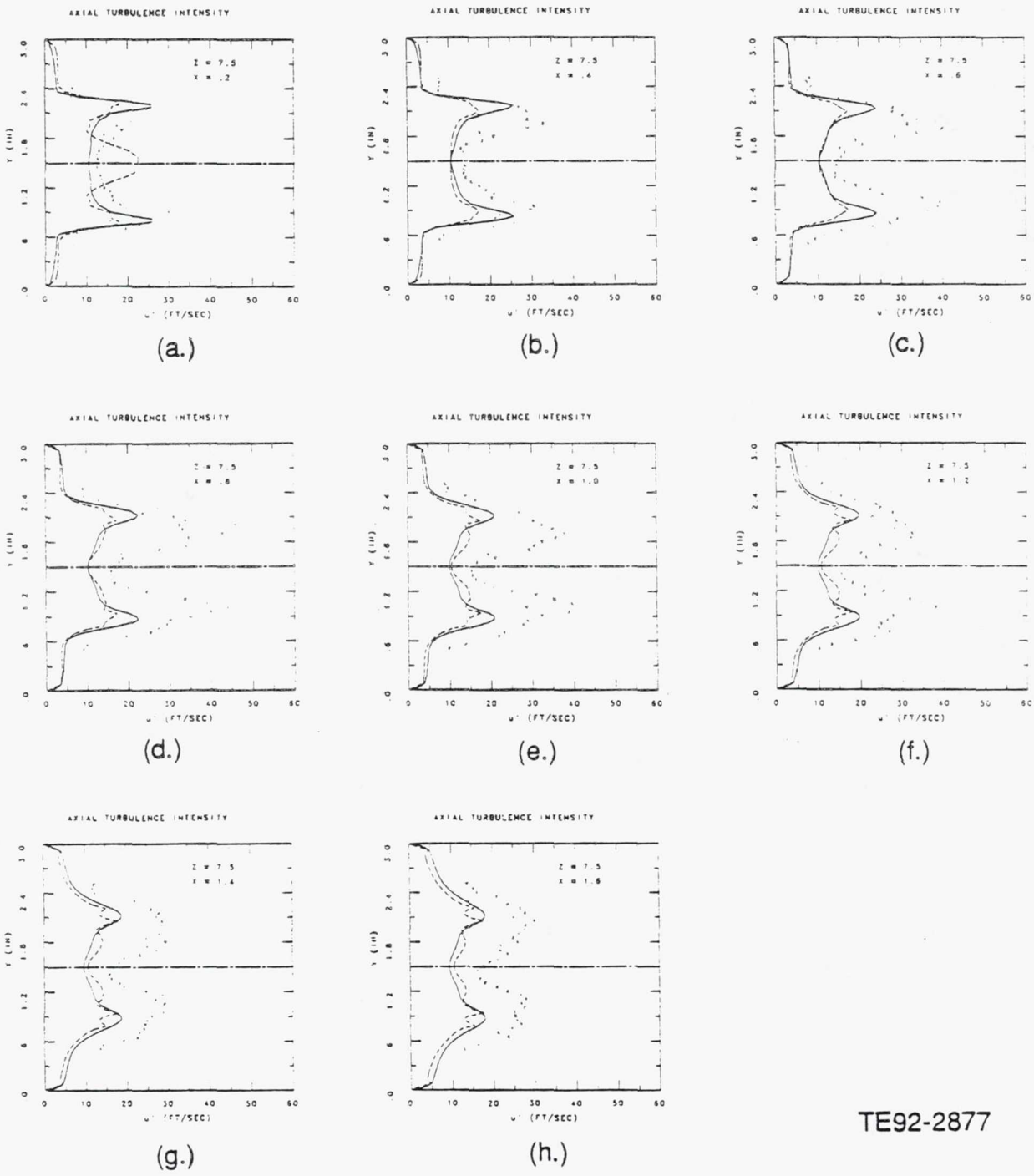

Figure 6.1-18. Axial turbulence intensity profiles predicted by DSM and ASM using power-law at z = 7.5 in. plane (—— DSM—ASM).

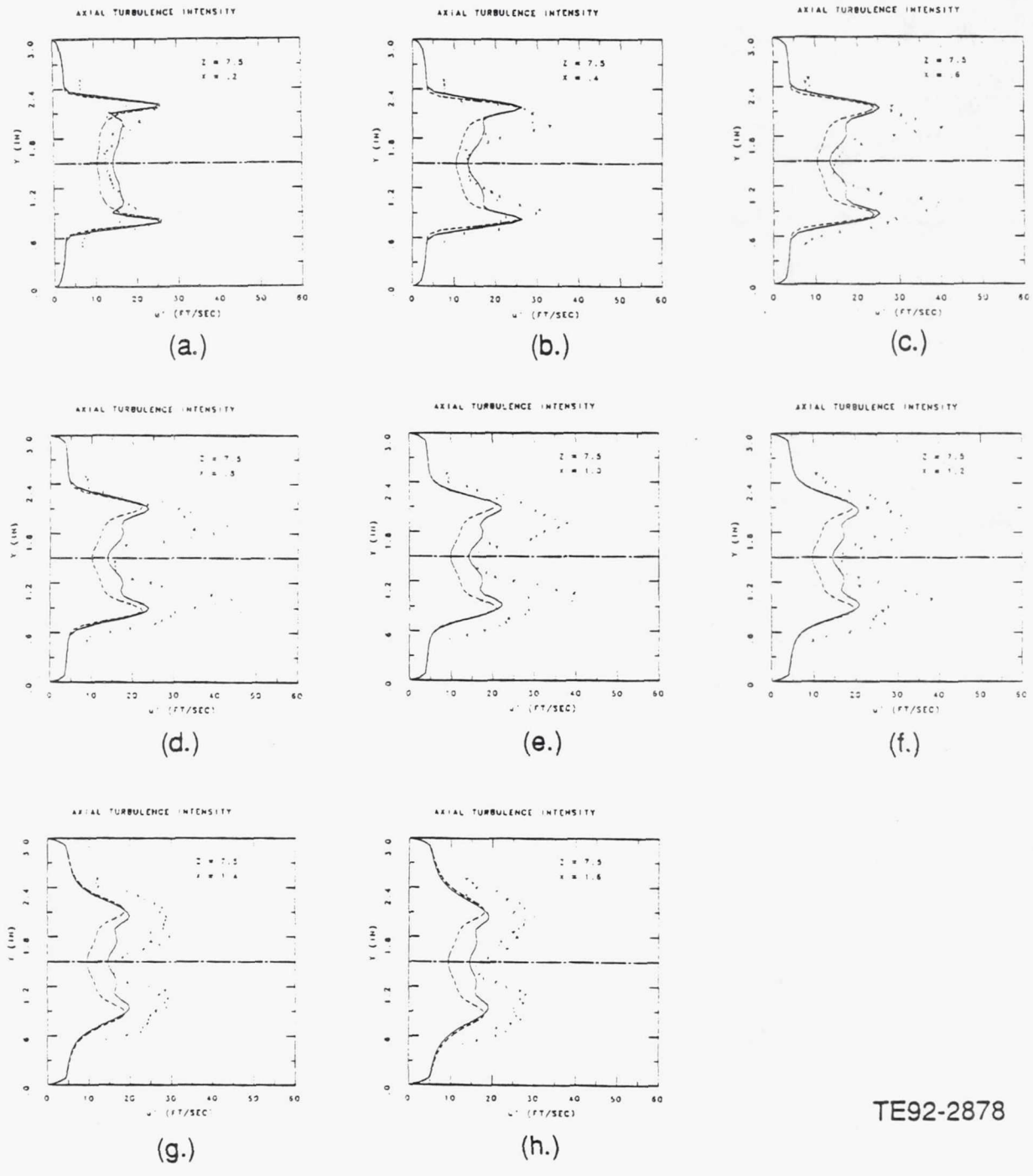

Figure 6.1-19. Axial turbulence intensity profiles predicted by DSM using flux-spline and power-law at z = 7.5 in. plane (—— flux-spline—power-law).

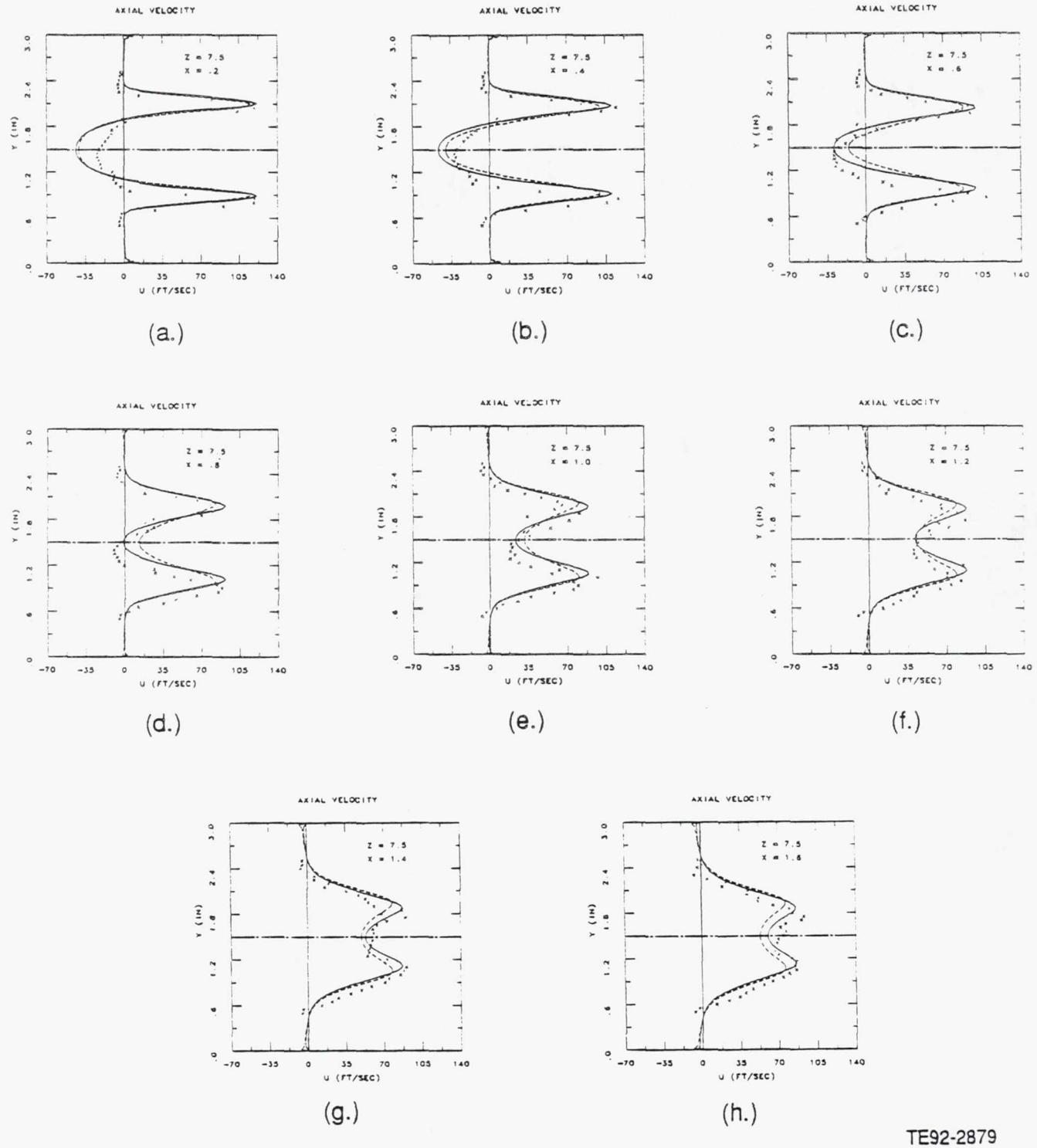

Figure 6.1-20. Axial velocity profiles at z = 7.5 in. plane, fine-grid (k-ε; —— flux-spline---power-law).

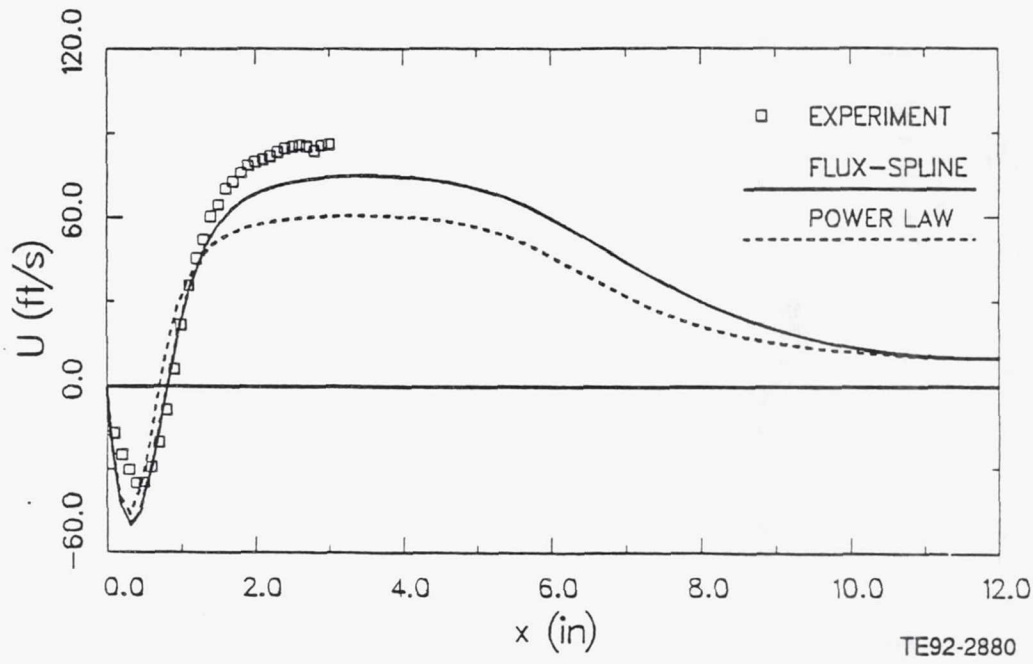

Figure 6.1-21. Variations of the centerline axial velocity, fine grid (k-ε model).

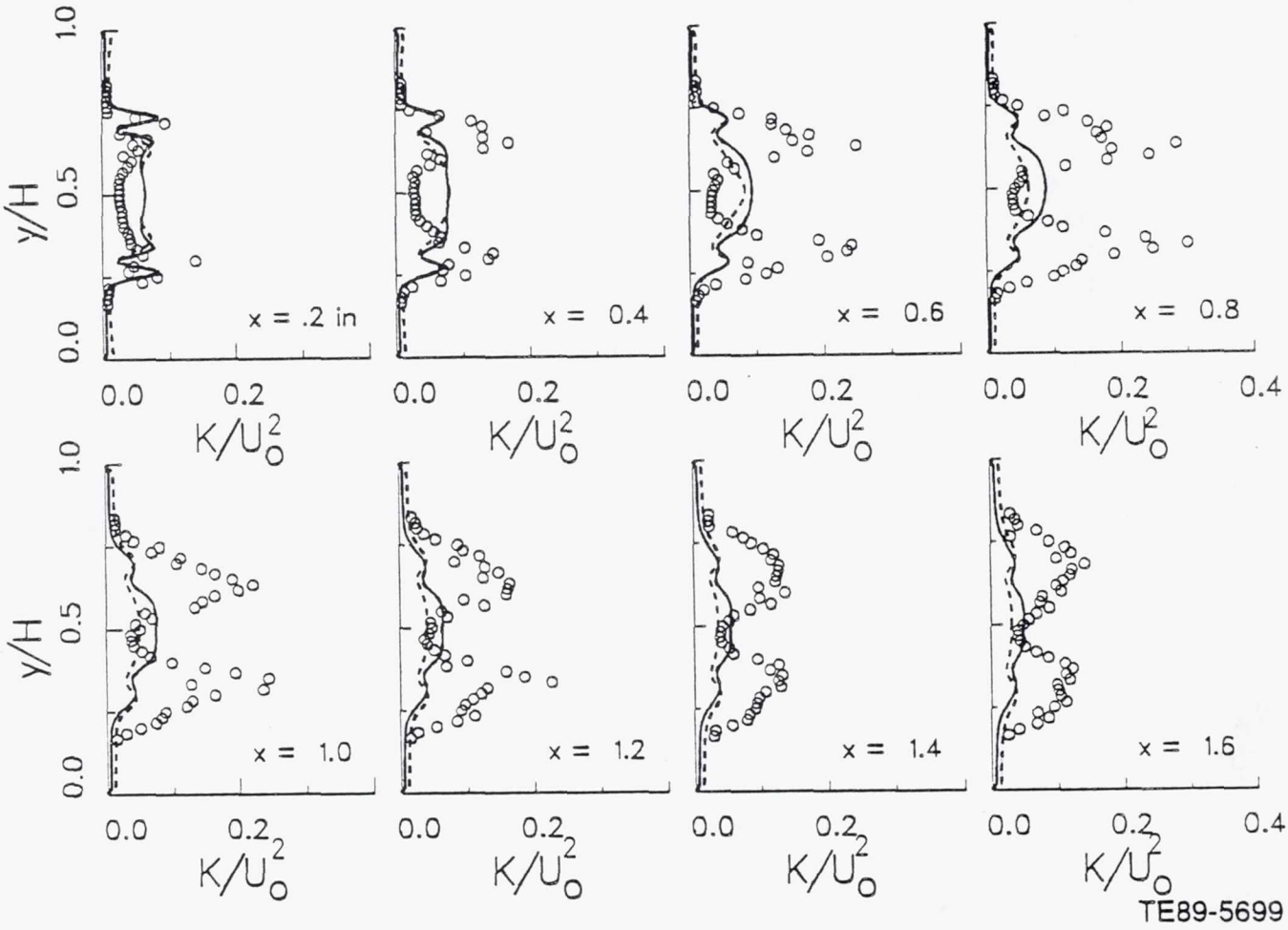

Figure 6.1-22. Turbulent kinetic energy at z = 7.5 in., fine-grid (—— flux-spline---power-law).

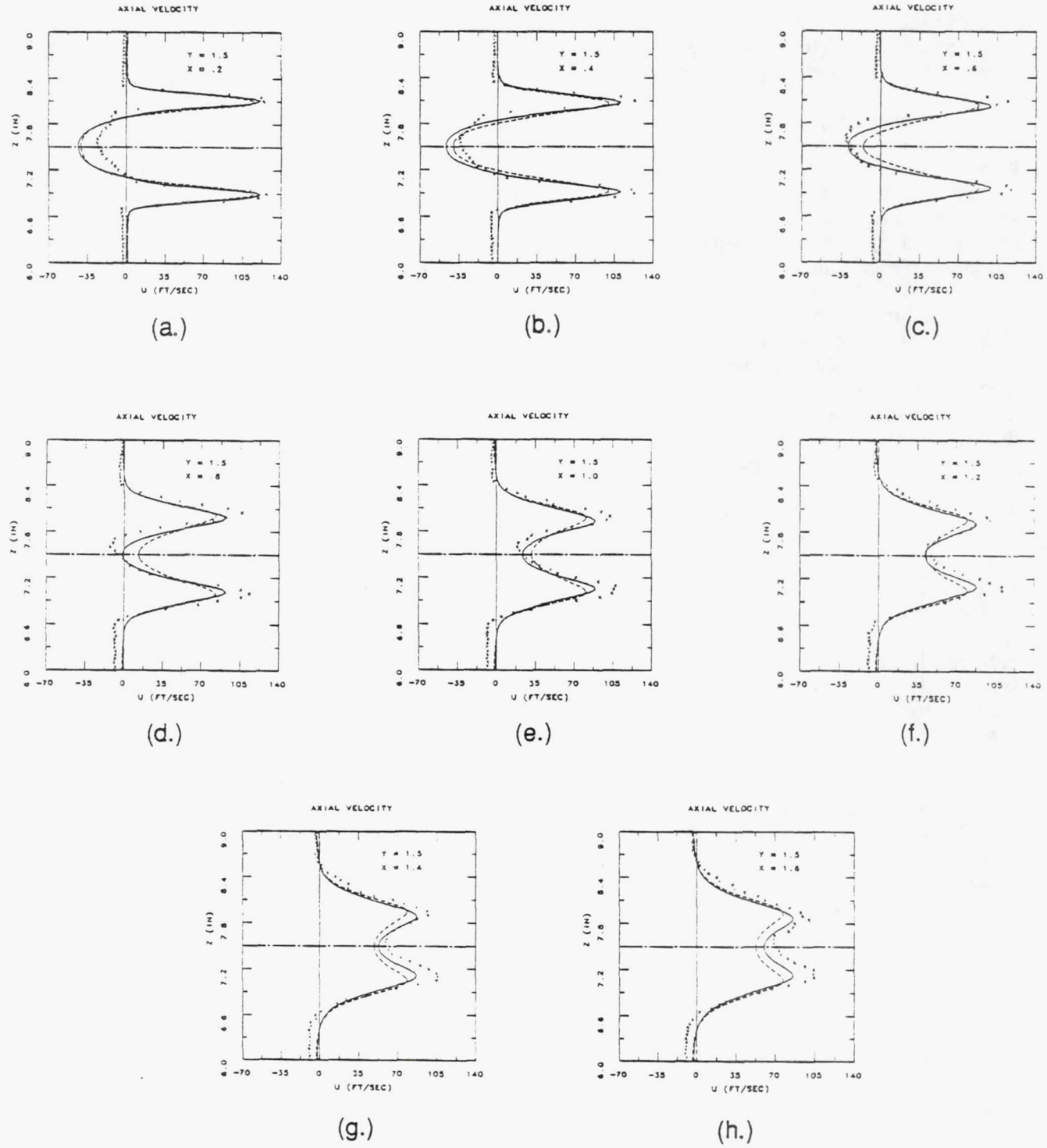

Figure 6.1-23. Axial velocity profiles at y = 1.5 in. plane, fine grid (k-ε; —— flux-spline----power-law).

6.2 PRIMARY JETS

In this subsection the comparisons of numerical results with measured values obtained for opposed primary jets are presented. The experiment was conducted in an air rig (Figure 6.2-1) using a set of five pairs of opposing primary jets centered 1.5 in. from the rig endplate. The test section was of rectangular cross section, 3.0 x 15.0 in., and extended 10 duct heights (76.2 cm) downstream from the headplate. Also in this case, all streams were nonswirling.

The set of governing partial differential equations for isothermal, constant density, three-dimensional flow consists of equations for continuity, axial, vertical, and lateral momenta, dissipation rate, and six Reynolds stress components. These equations are coupled and are nonlinear. The finite volume method (Patankar, 1980) has been used to reduce the continuous equations of motion to a set of coupled algebraic equations. The numerical solutions have been obtained using both the PLDS and the FSDS. The PLDS is based on a curve fit to the exact solution of the one-dimensional convection-diffusion equation without source terms. This scheme becomes identical to the hybrid scheme for mesh Peclet number (Pe) greater than 10. The PLDS can be considered as approximations to the exponential scheme (Patankar, 1980) which results from the exact solution to the one-dimensional convection-diffusion equation. In the derivation of this scheme, the total flux (convection + diffusion) is assumed to be uniform between two grid points. The FSDS improves upon this approximation by assuming a piecewise linear variation of the total flux. This leads to a scheme in which the discretization coefficients are identical to those from the exponential scheme, but there is an additional source term which involves the differences of fluxes at the control volume faces. The presence of this extra source term enables the FSDS to respond to the source terms in the governing equations and/or to the multidimensional effects.

A calculation procedure for elliptic flow requires boundary conditions on all boundaries of the computational domain. Four kinds of boundaries need consideration, namely inlet, plane of symmetry, wall, and the outlet. Due to the symmetry of the problem, the computational domain includes only one-half of the primary jet. In the cross section, the computational domain is bound by symmetry lines in the z direction and by a symmetry plane, wall, and inflow in the y direction. All dependent variables must be specified at the inflow boundary. The inlet conditions were derived from the experimentally measured profiles. The inlet dissipation rate is calculated based on the turbulent kinetic energy and constant length scale. The computational domain extends from 1.5 in. upstream of the primary jets plane to 4 duct heights downstream. At the downstream plane, the gradients of all dependent variables in the axial direction are set to zero. At the symmetry plane Neumann boundary conditions are specified. The normal gradients of all dependent variables except the zero radial velocity and shear stresses are taken to be zero. At the wall, the conventional logarithmic law, which is based on the local equilibrium assumption, is applied. The inlet profile and the grid distribution in xy and yz planes are presented in Figures 6.2-1 and 6.2-2. The coupled equations and boundary conditions are solved numerically in a sequential manner using the staggered grids for velocities and shear stresses. The main advantage of staggering the locations of stresses is to enhance numerical stability, a result of high coupling between the shear stresses and related mean strains. The iteration sequence employes the SIMPLER algorithm (Patankar, 1980) to handle the coupling between the continuity and momentum equations. The algebraic equations are solved using a line-by-line tridiagonal matrix algorithm. Iterations are carried out until the absolute sums of the mass and momentum residuals at all internal grid points, normalized by inlet mass and momentum, are less than 10^{-3}%.

The predicted mean axial velocity obtained from the k-ε model is compared with the experimental data (Figure 6.2-3). A nonuniform grid of 40 x 28 x 24 along the x, y, and z directions, respectively, was used for all calculations. The symmetry of the flow in the lateral (z) direction allows the computations to be confined between the jet centerline and the centerline between the jets.

Two different numerical schemes, namely FSDS and PLDS, were applied for the calculations. Figure 6.2-3 shows the streamwise mean velocity profiles on the z = 7.5 in. (containing the centerline of the

primary jets) at the selected axial locations. The purpose of this calculation is to address the differences between the results found from these schemes. Comparison of the data with the measurement reveals differences near the centerline. The velocity profiles predicted by both schemes were underestimated upstream and downstream of the primary jets. There are, however, minor differences observed between the schemes which demonstrate the presence of false diffusion. The measured data show asymmetry between the upper and lower halves. As a result, the flow at the centerline tends toward the lower wall resulting in a reattachment point of the lower recirculation zone farther upstream than the upper zone. This will cause the upper recirculation zone to be larger than the lower recirculation zone. A larger recirculation zone will allow the flow to diffuse faster and cause the stagnation point of the recirculation zone to occur farther upstream.

Figure 6.2-4 shows the comparison of the predicted centerline velocity distribution with the experimental data. The flux-spline results are in relatively better agreement with experimental data at locations near the centerline. Near the impingement region, the velocity is considerably underpredicted.

Figure 6.2-5 shows the turbulent kinetic profiles on the z = 7.5 in. plane at various streamwise locations obtained using the k-ε model with the FSDS. Although differences between the calculated and experimental results are significant, the predicted results reasonably well mimic the behavior of the experimental data. A central peak is observed in the middle regions of the test section indicating higher levels of turbulence than in other regions of the flow. The magnitude of turbulent kinetic energy increases from x = 0.5 in. to x = 1.0 in. due to the acceleration of the fluid from the jet stagnation point between the forward recirculation zones. The greatest magnitude of turbulence energy occurs at the primary jet impingement (x = 1.5 in.). A spreading of the turbulence energy occurs farther downstream due to the increased flow around the primary jets.

The differences between the predictions and the experimental data may be due to the coarseness of the mesh used and/or the inadequacy of the turbulence model. To reduce the numerical errors, calculations were repeated on a finer grid (Figures 6.2-6, 6.2-7, and 6.2-8). The use of the fine grid reduces the differences between the results from the two differencing schemes. The smeared (coarse grid) power-law profile indicates the presence of excessive numerical diffusion. Although differences between the fine grid power-law calculations and the experimental results still exist, change of the differencing scheme to flux-spline did not improve the predictions (Figure 6.2-8). This clearly shows that the present calculations are grid independent.

Computations were also made on a 40 x 28 x 24 grid using the DSM and ASM closures. Figure 6.2-9 shows the axial velocity profiles on centerplane at selected axial locations obtained using the FSDS. For this calculation, plug profiles were prescribed at the inlet plane. At all streamwise locations, the profiles resulting from the DSM and ASM are more smeared than those from the k-ε model. This trend indicates the presence of excessive diffusion in the ASM and DSM solutions. Figures 6.2-10 and 6.2-11 show the comparison of the predicted axial and vertical turbulence intensities obtained from the DSM and ASM closures. A wide disparity existing between the two models. At all axial stations, the DSM results mimic the behavior of the experimental data better than those obtained from the ASM. At stations x = 0.5 and x = 1.0 in. peak values of the fluctuating components are seen at the center portion of the rig. The magnitudes of these quantities are seen to increase at station x = 1.0 in. due to the closer effects of the impinging jets. The maximum value of the axial component predicted by the ASM is seen to be off the center portion of the rig at x = 1.0 in. The radial component seems to diffuse and spread out at the x = 1.0 in. station while the magnitudes of the fluctuations in the center portion of the rig nearly double.

At the entrance of the primary jet, x = 1.5 in., the influence of the primary jets can clearly be seen. Only the behaviors of the results obtained from the DSM are consistent with the experimental data. The radial turbulence intensity at x = 1.5 in. shows the a decrease in the v at the jet centerplane. However, this decrease in magnitude does not span the entire height of the test section. The maximum values are seen at the middle of the rig, which is caused by increased turbulence due to the fluctuation of the jet stagnation point. Downstream of the primary jet entrance, the data show that the magnitude of the ax-

ial turbulence intensity increases due to the acceleration of fluid from the jet stagnation point between the upper and lower recirculation zones. This phenomena has been only partially predicted by DSM. Similar results are seen at further downstream stations.

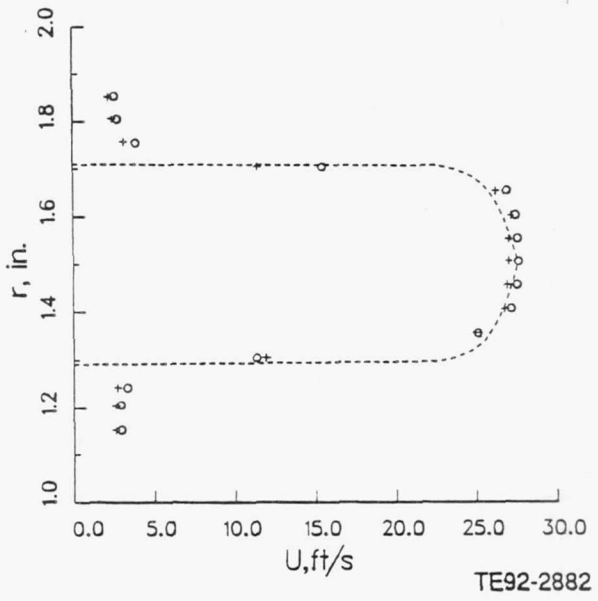

Figure 6.2-1. Inlet velocity profile.

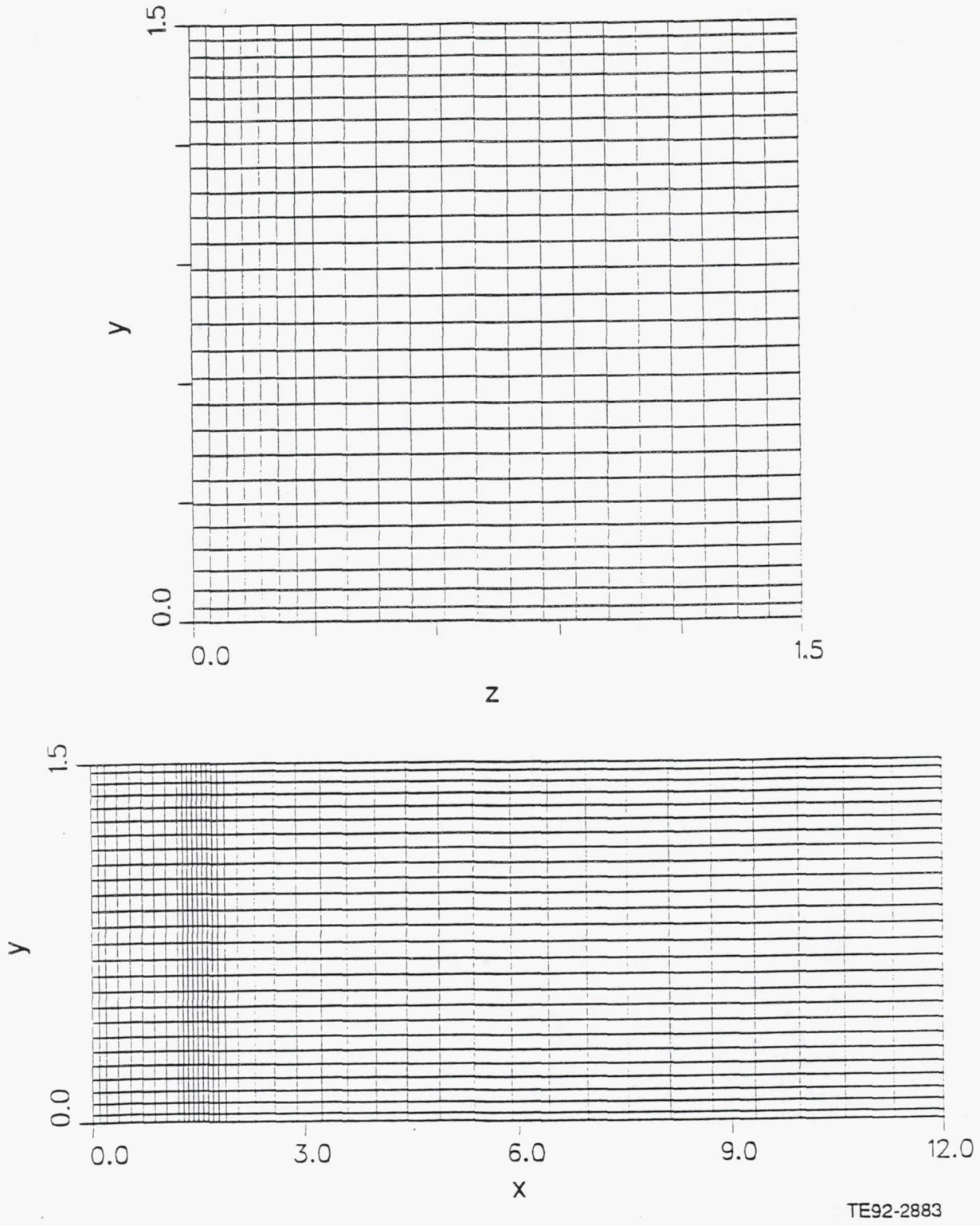

Figure 6.2-2. Opposed jets grid layout.

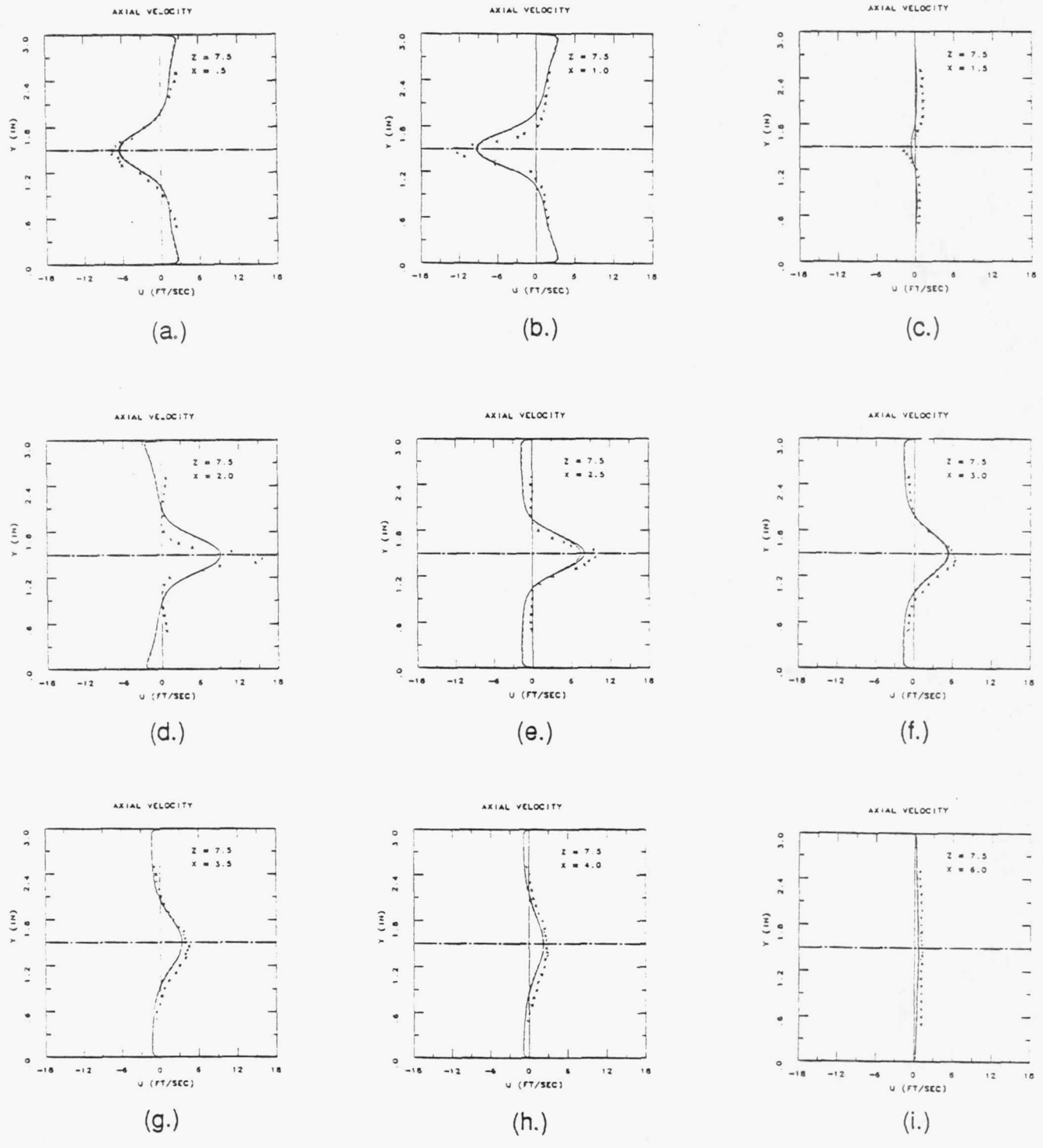

Figure 6.2-3. Axial velocity profiles at z = 7.5 in. plane (k-ε model; —— flux-spline---power-law).

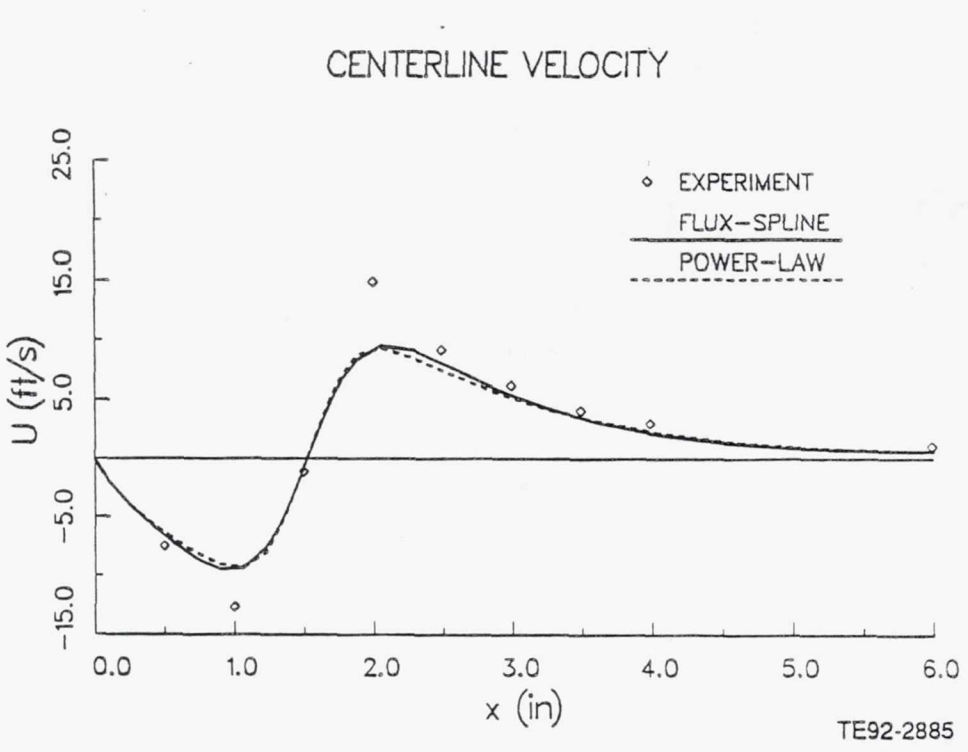

Figure 6.2-4. Centerline axial velocity profiles predicted by k-ε model (—— flux-spline----power-law).

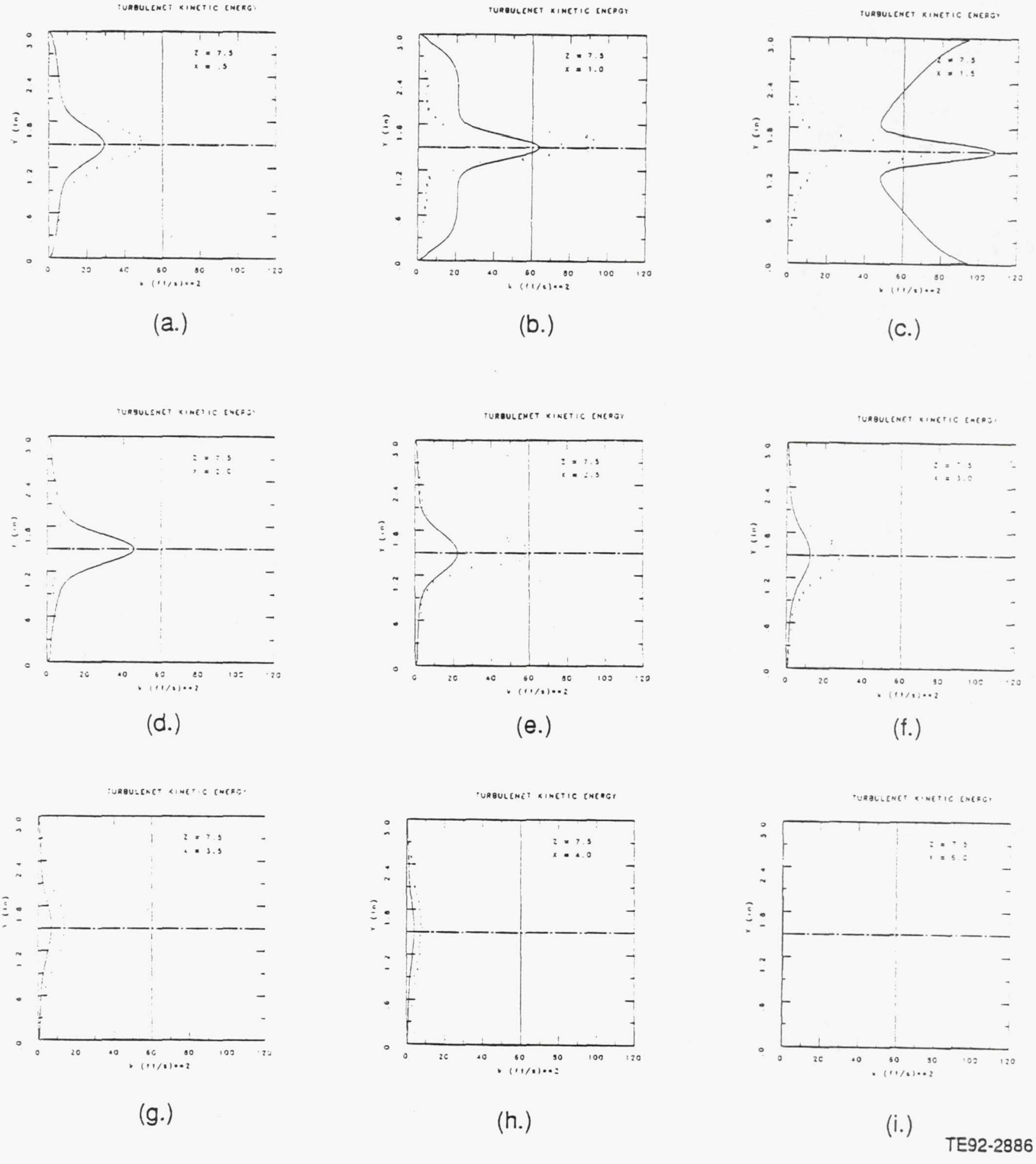

Figure 6.2-5. Turbulent kinetic energy predicted by k-ε model and flux-spline scheme.

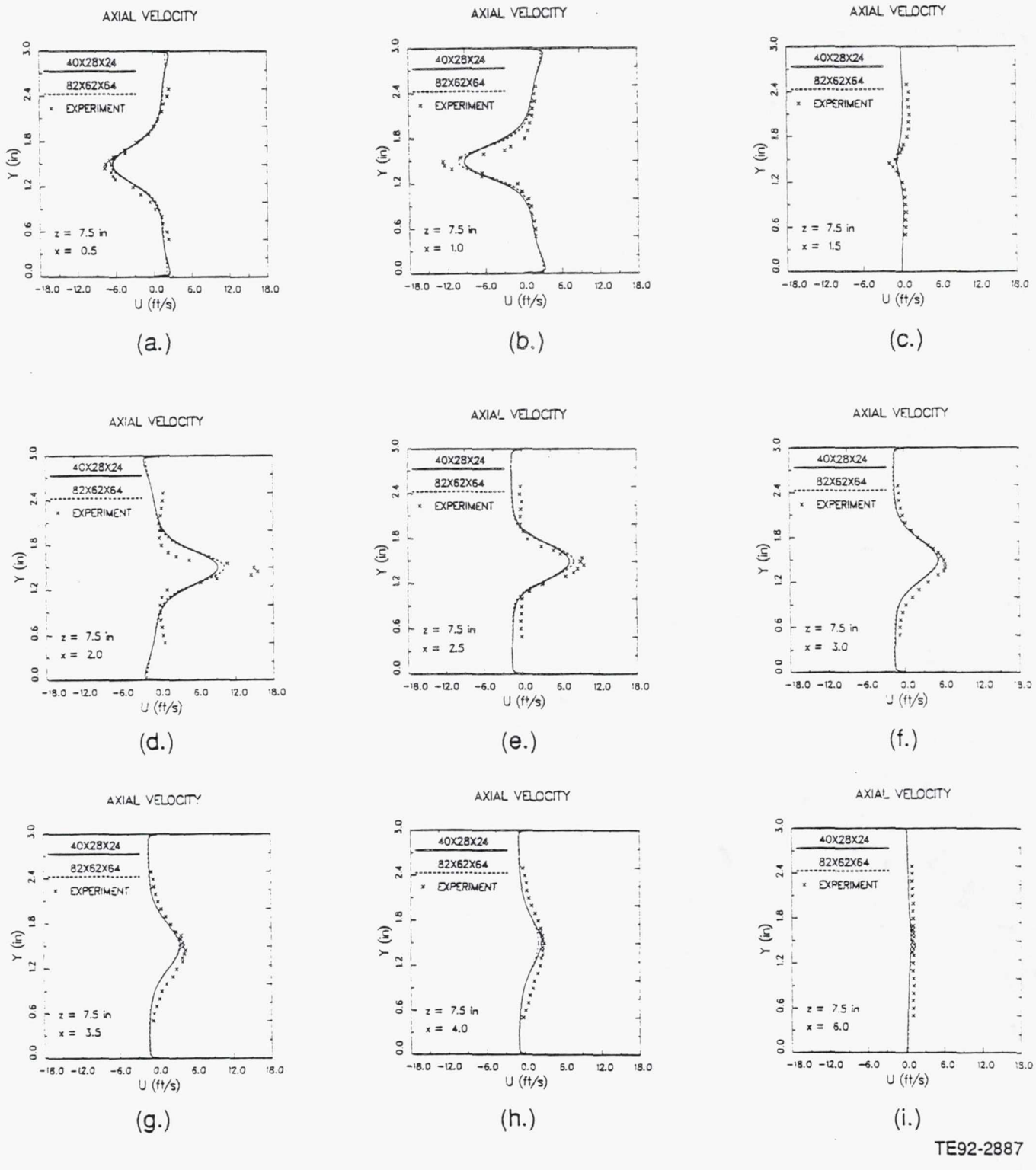

Figure 6.2-6. Axial velocity profiles predicted by k-ε model and power-law at z = 7.5 in. plane.

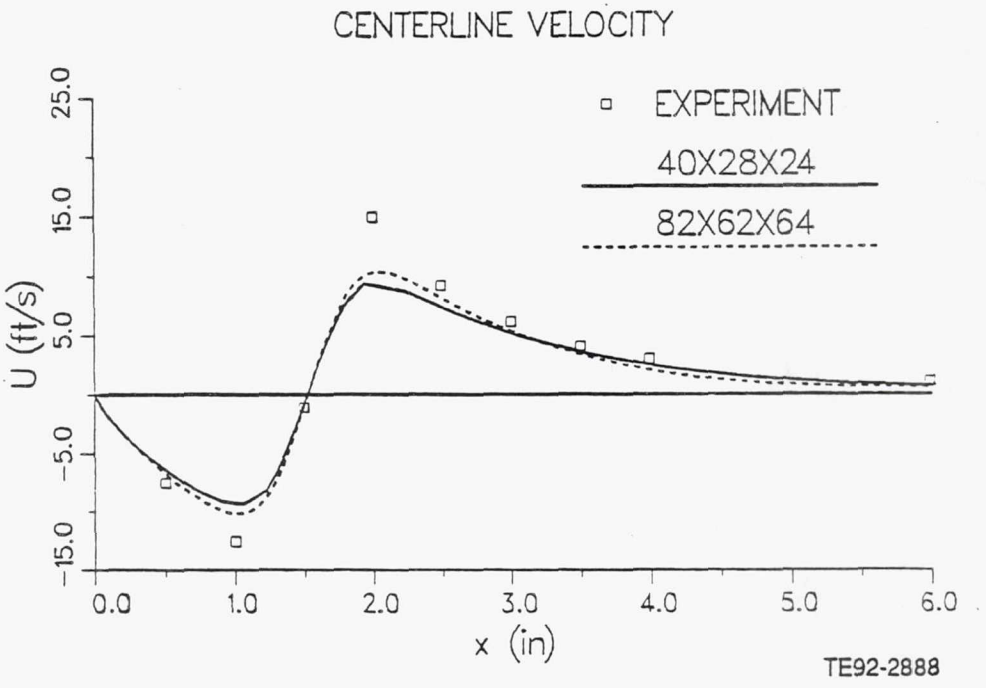

Figure 6.2-7. Centerline axial velocity profiles predicted by k-ε model and power-law scheme (—— coarse grid— fine grid).

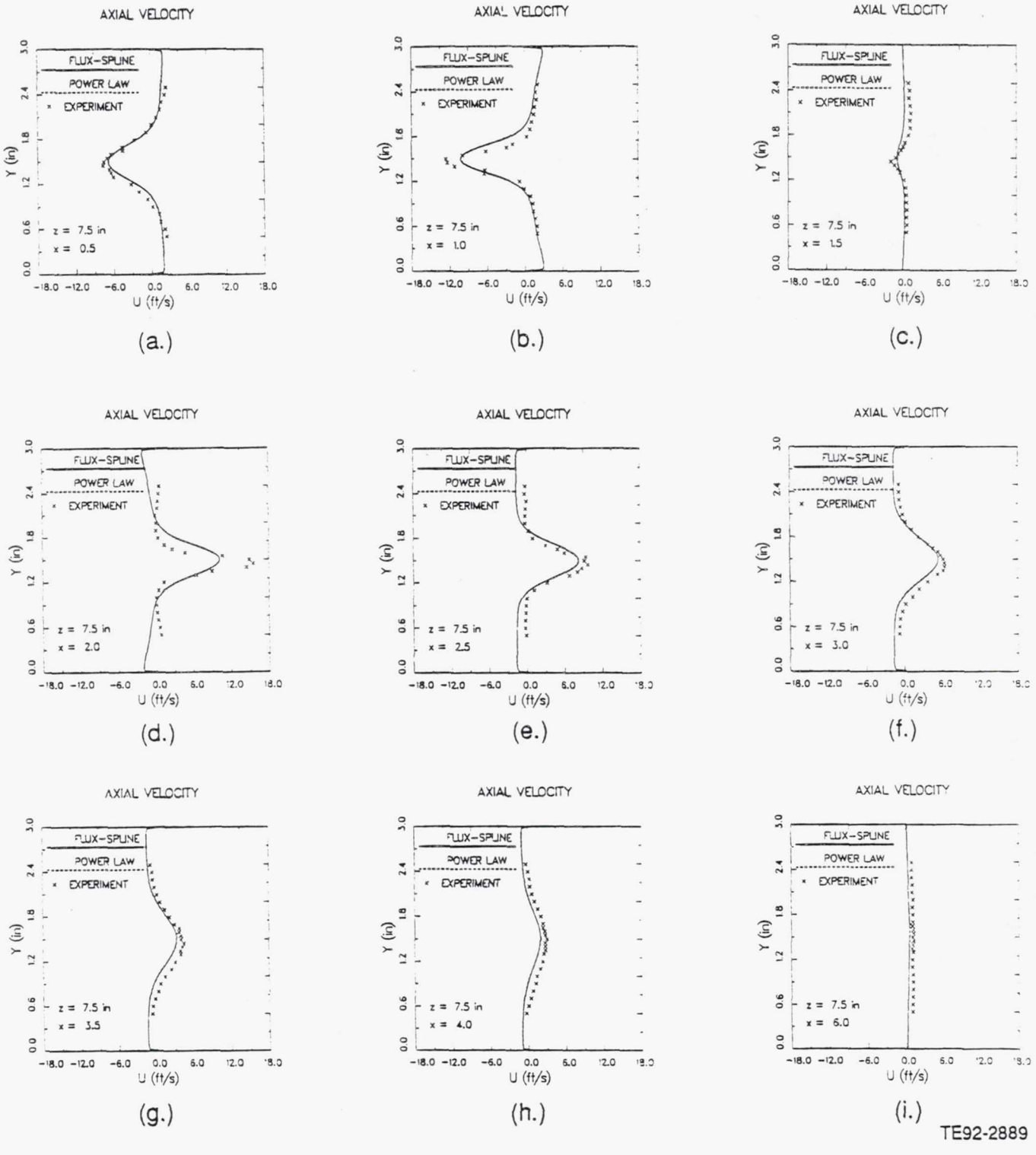

Figure 6.2-8. Axial velocity profiles predicted by k-ε model (—— flux-spline—— power-law).

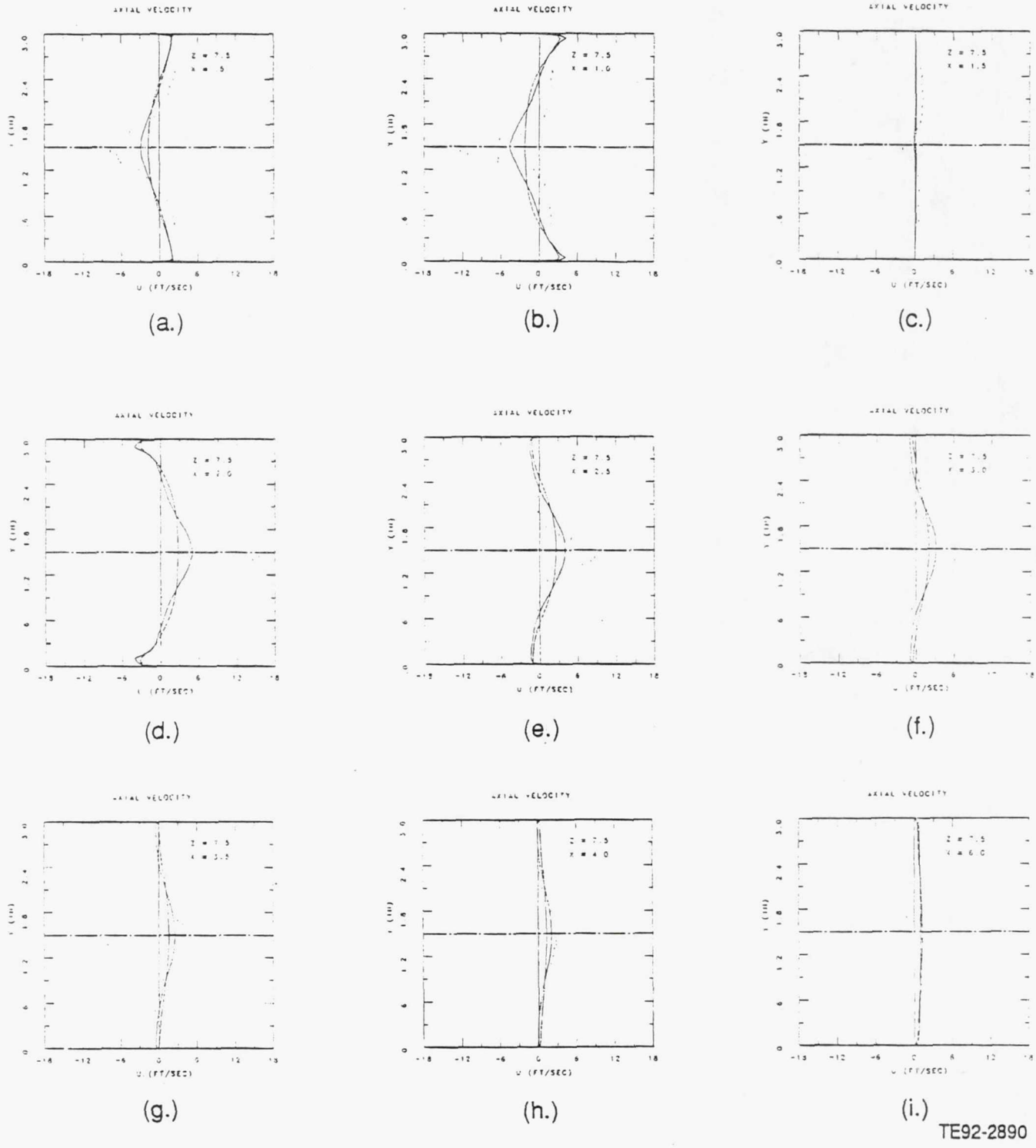

Figure 6.2-9. Axial velocity profiles predicted by DSM and ASM (—— DSM--- ASM).

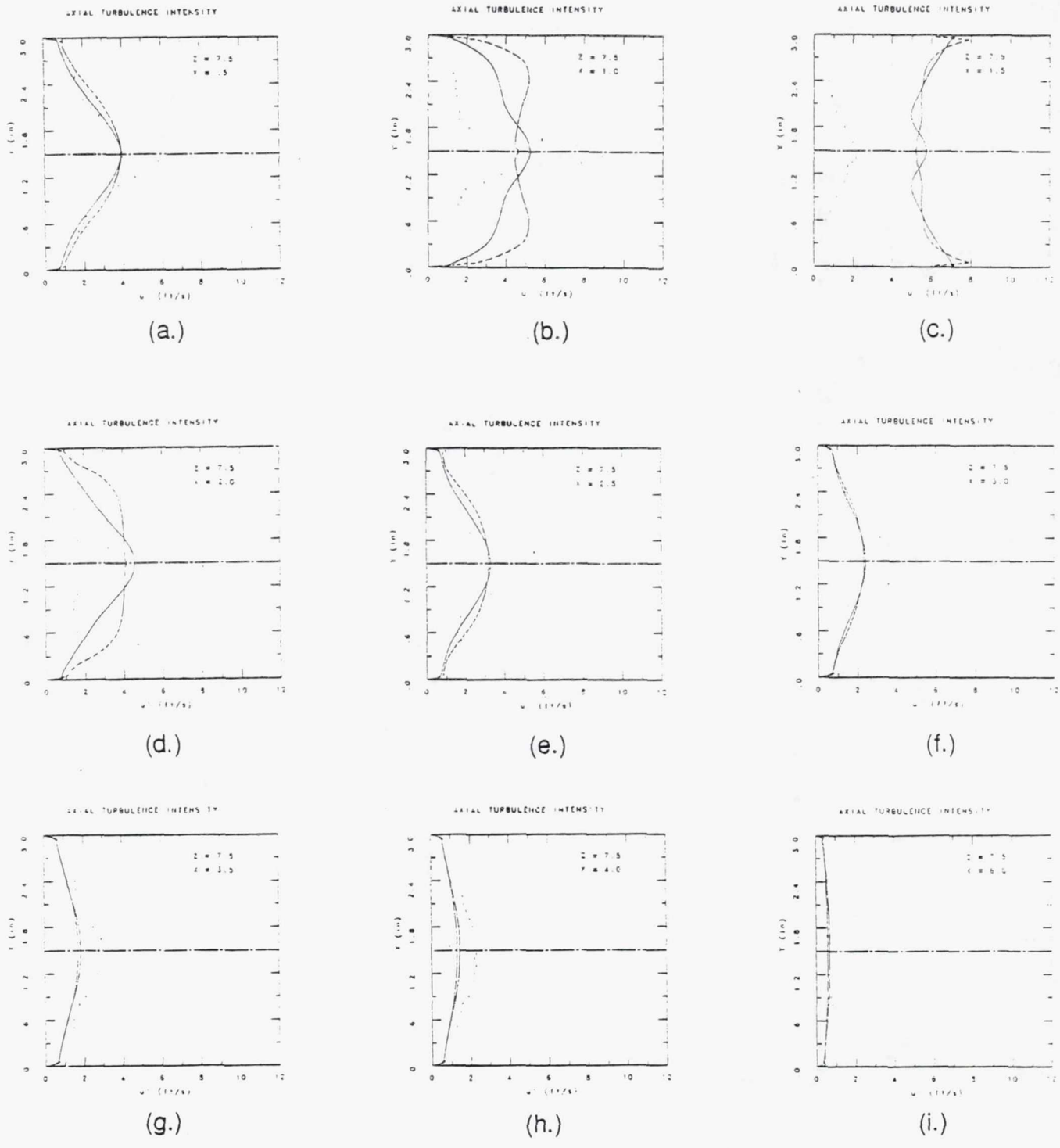

Figure 6.2-10. Axial turbulence intensity profiles predicted by DSM and ASM (—— DSM----ASM).

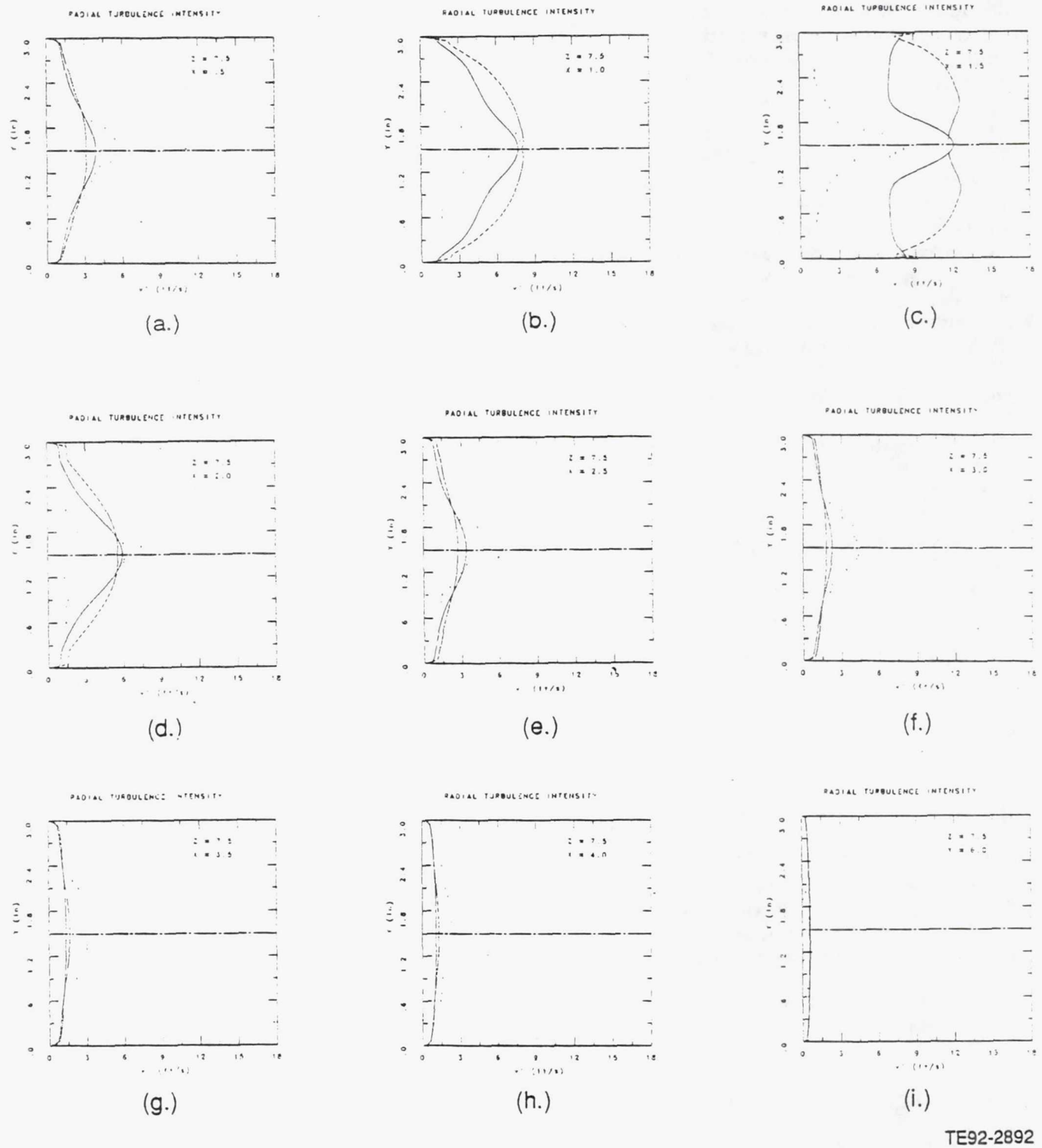

Figure 6.2-11. Radial turbulence intensity profiles predicted by DSM and ASM (—— DSM—ASM).

6.3 DOME ANNULAR JETS AND PRIMARY JETS

In this subsection, a numerical study of a jet-in-cross-flow configuration is presented. The purpose of this study is to assess the performance of the DSM closure for complex three-dimensional flow. Both first and second-order discretization schemes were employed. The experiments were performed in an air rig (Figure 6.1-1) consisting of five annular nonswirling streams issuing into a duct of rectangular cross section 3.0 x 15.0 in. There are also five pairs of primary jets centered 1.5 in. downstream of the annular jet entrance.

The set of governing partial differential equations for isothermal, constant density, three-dimensional flow consists of equations for continuity, axial, radial, and tangential momenta, ε, and six Reynolds stress components; these equations are coupled and are nonlinear. It is not possible to obtain analytical solutions, so numerical techniques have to be used. The finite volume method (Patankar, 1980) has been used to reduce the continuous equations of motion to a set of coupled algebraic equations. The numerical solutions have been obtained using both the PLDS and FSDS (Varejao, 1979). In the FSDS, the total flux is assumed to vary in a piecewise linear manner within a control volume. This assumption leads to a scheme in which the discretization coefficients are identical to those from the exponential scheme (Patankar, 1980), but there is an additional source term that involves the differences in fluxes at adjacent faces of a control volume. The presence of this source term enables the FSDS to respond to the presence of sources and/or multidimensionality of the flow.

The elliptic nature of this flow required the boundary conditions be specified on the six sides of the solution domain. Four kinds of boundaries need consideration: inlet, plane of symmetry, wall, and the outlet. Due to the symmetry of the problem, the computational domain includes only one quarter of the annular stream. In the cross section, the computational domain is bounded by symmetry lines in the z direction and by a symmetry plane, wall, and inflow in the y direction. All dependent variables must be specified at the inflow boundary. The upstream boundary, which is placed at the exit of the annular stream (x = 0.0), the experimentally measured profiles of axial velocity and normal Reynolds stress components are prescribed. The inlet dissipation rate is calculated based on the turbulent kinetic energy and constant length scale. The computational domain extends from the inlet plane to four duct heights downstream of the jet exit. The reason for this selection was to prevent recirculation at the exit. At the downstream plane the gradients of all dependent variables in the axial direction are equal to zero. At the symmetry plane Neumann boundary conditions are specified. The normal gradients of all dependent variables, except the zero radial velocity and shear stress components, are taken to be zero. The conventional logarithmic law, which is based on the local equilibrium assumption, is applied to the wall boundary condition. The inlet profiles and the grid distribution in the xy and yz planes are displayed in Figures 6.3-1 and 6.3-2.

The coupled equations and boundary conditions are solved numerically in a sequential manner using the staggered grids for velocities and shear stresses. The main advantage of staggering the locations of stresses is to enhance numerical stability, a result of high coupling between the shear stresses and related mean streams. The iteration sequence employs the SIMPLER algorithm (Patankar, 1980) to handle the coupling between the continuity and momentum equations. The algebraic equations are solved using a line-by-line tridiagonal matrix algorithm. Iterations are carried out until the absolute sums of the mass and momentum residuals at all internal grid points, normalized by inlet mass and momentum, are less than 0.01%.

The predicted mean and turbulence fields obtained for jet-in-cross flow are compared here with the experimental data. The jet-to-cross stream velocity ratio investigated is almost equal to 1. A nonuniform grid of 52 x 42 x 42 x, y, and z directions, respectively, was used for all calculations. The symmetry of the flow in the lateral (z) direction allows the computations to be confined between the jet centerline and the centerline between the jets. Figure 6.3-3 shows the streamwise mean velocity profiles on the z = 7.5 in., containing the centerline of the annular jet and primary jets, at the selected axial locations obtained from the DSM solution. Two different numerical schemes, namely the PLDS and FSDS, are ap-

plied for the calculations. Here, the emphasis is being placed on the differences between the results obtained from these schemes. The results show differences in the prediction of peak and centerline values in the developing region. The predicted velocity profiles indicate higher maximum and a longer recirculation at the centerplane when the FSDS is applied. In the lower order schemes, the physical diffusion may be dominated by the false diffusion and the physical diffusion may have no influence on the numerical solution. At all streamwise locations, the profiles resulting from the PLDS are more smeared than those from the FSDS due to excessive numerical diffusion in the power-law solution. If a diffusive scheme, such as the PLDS, is used for discretizing the equations and if the flow is recirculating, which creates sufficient internal production of turbulence, the numerical experiment shows that the results are not strongly sensitive to the inlet profiles for k and ε. The differences between the two solutions diminish as the grid is refined.

The data show that the annular jets penetrate up to the primary jets inlet at x = 1.5 in. and then are turned parallel to the primary jets forming recirculation zones outside and in the center of the annular region. This behavior has been well predicted by the DSM closure. The primary jets can be seen bending downstream due to the annular jet interaction. Downstream of the primary jet inlet, the flow accelerates between two recirculation zones on the upper and lower walls. This flow slowly diffuses as the recirculation zones shrink in size downstream. The recirculation zones show symmetric placement between upper and lower portions of the test section. The two forward recirculation zones centered in the annular region also show symmetric placement.

Figures 6.3-4 and 6.3-5 show the axial and radial turbulence intensity profiles along the axial direction on centerplane (z = 7.5 in.). Again the agreement is less in the peak and centerline region. Examination of the calculated turbulent distributions indicates that both schemes have similar trends and the differences between them are minimized as flow proceeds towards the downstream. The rms velocities show increased fluctuations on the upstream side of the primary jet, fluctuations created by the inner and outer walls. Larger fluctuations are evident on the downstream side of the primary jet. The change in turbulence is due to the deflection of the primary jet by the annular jet and the formation of a rear recirculation zone at the downstream edge of the jet. It should be noted that the rms velocity steadily increases farther downstream. The reason is that the annular jet cross flow causes a severe bending in the primary jet producing this increased turbulence. At x = 0.5 in. both the axial and radial rms velocities plots show a flat profile outside of the annular jet inlet and inside the annular jet region. Peak fluctuations occur in the annular gap where fluid is entering. The magnitude of the fluctuations increase and spread out from x = 0.5 in. to x = 1.0 in. Fluctuations at the center of the annular region have increased due to the pair of counter rotating recirculation zones formed in the region. Magnitudes outside the annular jet remain small compared to the annular jet region. Plots at x = 1.5 in. show a definite change in the axial and radial rms velocities due to primary jet interaction. The axial rms velocity plot shows decreased turbulence at the centerplane, z = 7.5 in., across the test section due to the primary jets. The experimental data show two pairs of peak fluctuations occur on the sides of the centerplane. However, the DSM closure could only predict one pair of peak values. The peaks at the bottom and top walls are caused by the flow above and below the annular jets accelerating around the primary jets and flowing downstream. The pair of peaks at the center of the rig correspond to increased flow around the primary jets from recirculating fluid in the center of the annular jet. The radial rms velocity plot at x = 1.5 in. shows decreased magnitudes at the upper and lower walls of the rig centerplane. A peak is observed at the center of the test section due to the fluctuation of the stagnation point of the primary jets. The axial rms velocity component at x = 2.0 in. shows a decrease at both upper and lower walls in the rig center and peak magnitudes occuring along the rig centerline. The drop in magnitude along the upper and lower walls is due to a recirculation zone, while the peaks at the center of the test section are caused by fluid being accelerated between the upper and lower recirculation zones. The radial rms velocity component at x = 2.0 in. shows peak velocities along the rig centerline. Similar results are evident at downstream locations.

Comparison of predicted turbulent shear stress by DSM with the data is shown in Figure 6.3-6. The improved scheme showed higher peaks over the PLDS. Negative stresses are observed at the edges of the

annular jet inlet due to the transfer of momentum from the edges of the annular jet to the fluid. Both schemes predicted such a process and FSDS showed a higher negative value. In comparison to the measurement, the locations of maximum and minimum are shifted. Near the inlet, the experimental data show a constant distribution around the centerline indicating very little momentum transfer. At most of the locations, the calculated profiles are similar to the exhibited data trend. The largest values of shear stress are present at x = 1.5 in. Here, primary and annular jet interaction produces large velocity gradients and momentum transfer. Downstream and away from the centerplane, magnitudes decay and approach a uniform distribution of shear stress at x = 6.0 in. The experiment shows a region of peak positive shear stress along the upper half of the test section, while negative value occurs through the lower half of the test rig at x = 2.0 in. The magnitudes continue to decrease and the peaks tend to spread toward the walls and boundaries of the rig on downstream.

The profiles at various lateral locations are displayed in Figures 6.3-7 through 6.3-16. The results have been shown at selected axial stations. The computed results obtained from the PLDS and FSDS are very similar close to the centerplane between the annular jets. The FSDS results in higher peak values and a longer recirculation zone. The profiles resulting from the power-law are more smeared than those from the FSDS. This behavior indicates the presence of false diffusion in the power-law solution. The data between planes at z = 7.4 in. and z = 7.6 in. show similar results. The rear recirculation zones at the z = 7.4 in. plane are slightly forward of the recirculation zones at the z = 7.6 in. plane. In addition, the flow is seen to bend toward the lower wall at the z = 7.4 in. plane. The two forward recirculation zones are symmetric between planes for the upper and lower zones. The experimental data show that while symmetric flow between z = 7.3 and z = 7.7 in. exists, there is no symmetry between upper and lower portions of the test rig. The annular jet inlet extends between 6.8 in. $\leq z \leq$ 8.2 in. The forward recirculation zones placement is steady between 7.2 in. $\leq z \leq$ 7.8 in.

The influence of the primary jets on the flowfield is seen downstream of x = 1.5 in. Flow downstream of x = 1.5 in., in the annular and primary jet case, is seen to be very similar to the flow in the primary jets only case. Recirculation zones for the annular and primary jet case are larger and extend downstream farther, but the flow is still seen to accelerate past the recirculation region and then diffuse. This is an indication of how much influence the primary jets have on the flow.

Figure 6.3-17 shows the axial velocity profiles on the z = 7.5 in. plane, containing the centerline of the annular stream and primary jets, at several streamwise locations using the standard k-ε model. Both the PLDS and FSDS differencing profiles were applied. For this calculation experimental profiles were prescribed at the inlet plane. The use of the FSDS results in sharper peaks and a longer recirculation zone at the center. The computational results simulate the behavior of the measured data. However, the flux-spline results are in better agreement with the experimental data at locations near the inlet. At all axial stations, the predicted profiles by PLDS are more smeared than those from the FSDS. This trend shows the presence of excessive numerical diffusion in the power-law solution.

Comparison of the predicted streamwise turbulent kinetic energy using both schemes is shown in Figure 6.3-18. A wide disparity exists between the calculation and the measurement. The energy distribution at x = 0.5 and 1.0 in. shows similar behaviors. Peak turbulence occurs at the edges of the annular jet where large shear stress is present. Outside the annular inlet the turbulence is uniform to the boundaries and walls. The plots at x= 1.5 and 2.0 in. show peak turbulence occurring at the rig center and at the top and bottom walls. The largest turbulence energy can be seen concentrated in the region of annular and primary jet intersection at x = 1.5 and 2.0 in. Magnitudes decay and spread downstream and away from the rig centerplane. Uniform turbulence energy between the upper and lower walls is present at x = 6.0 in.

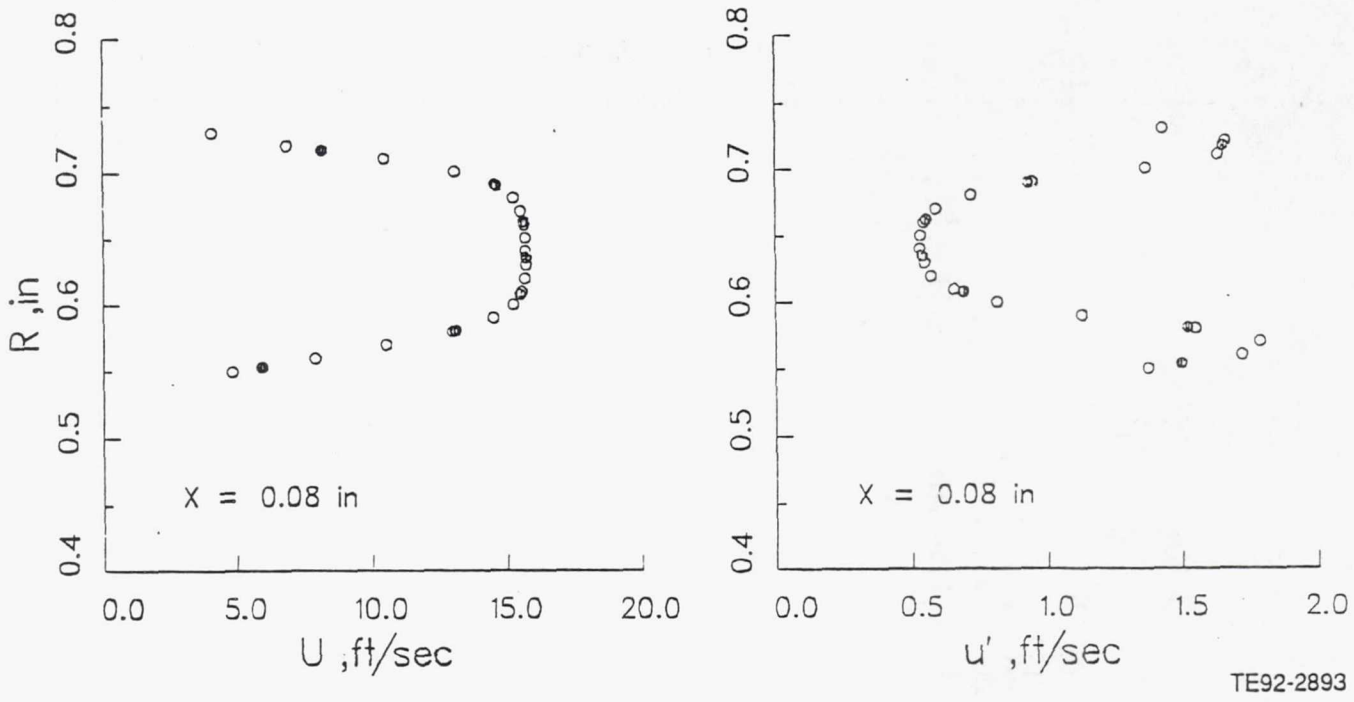

Figure 6.3-1. Inlet profiles.

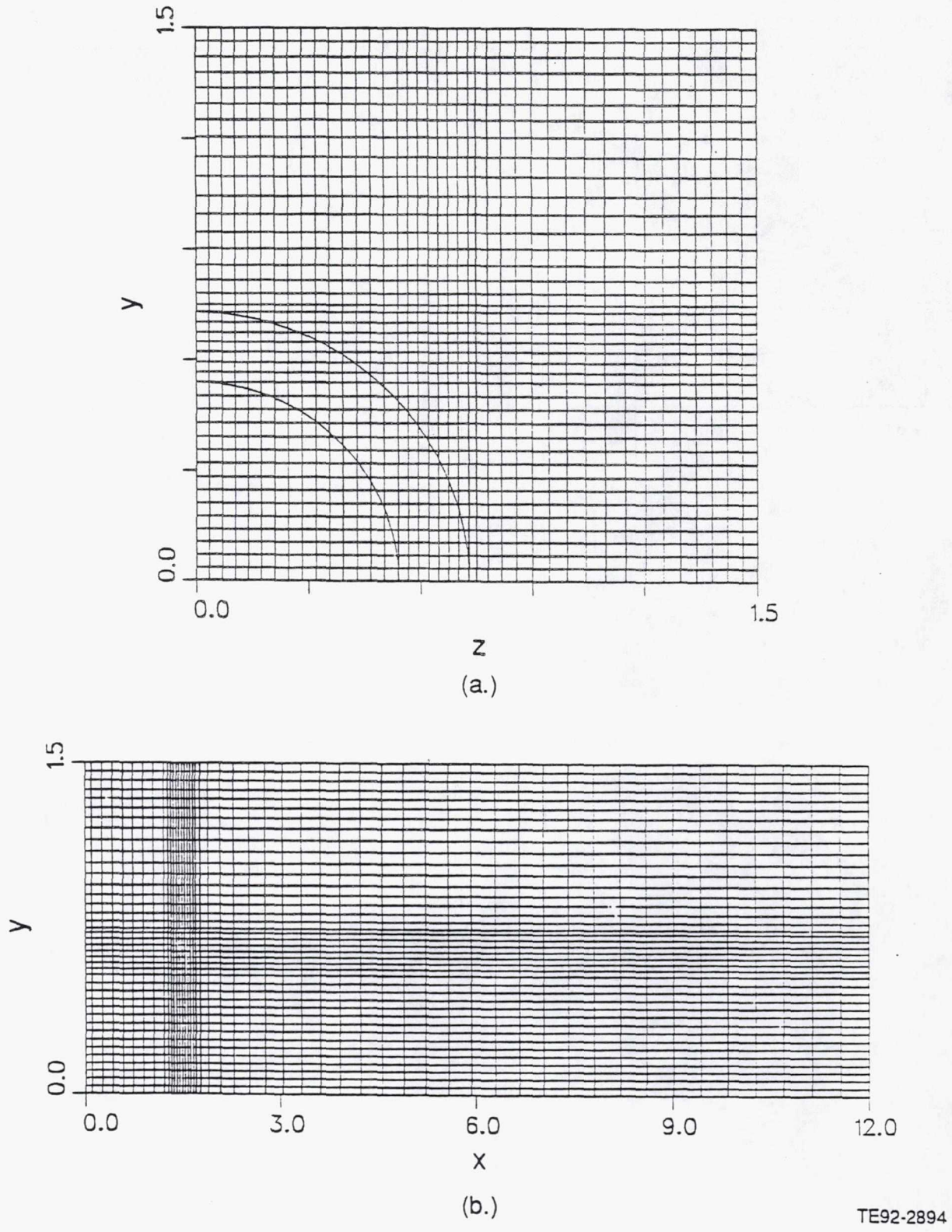

Figure 6.3-2. Annular and primary jets grid layout.

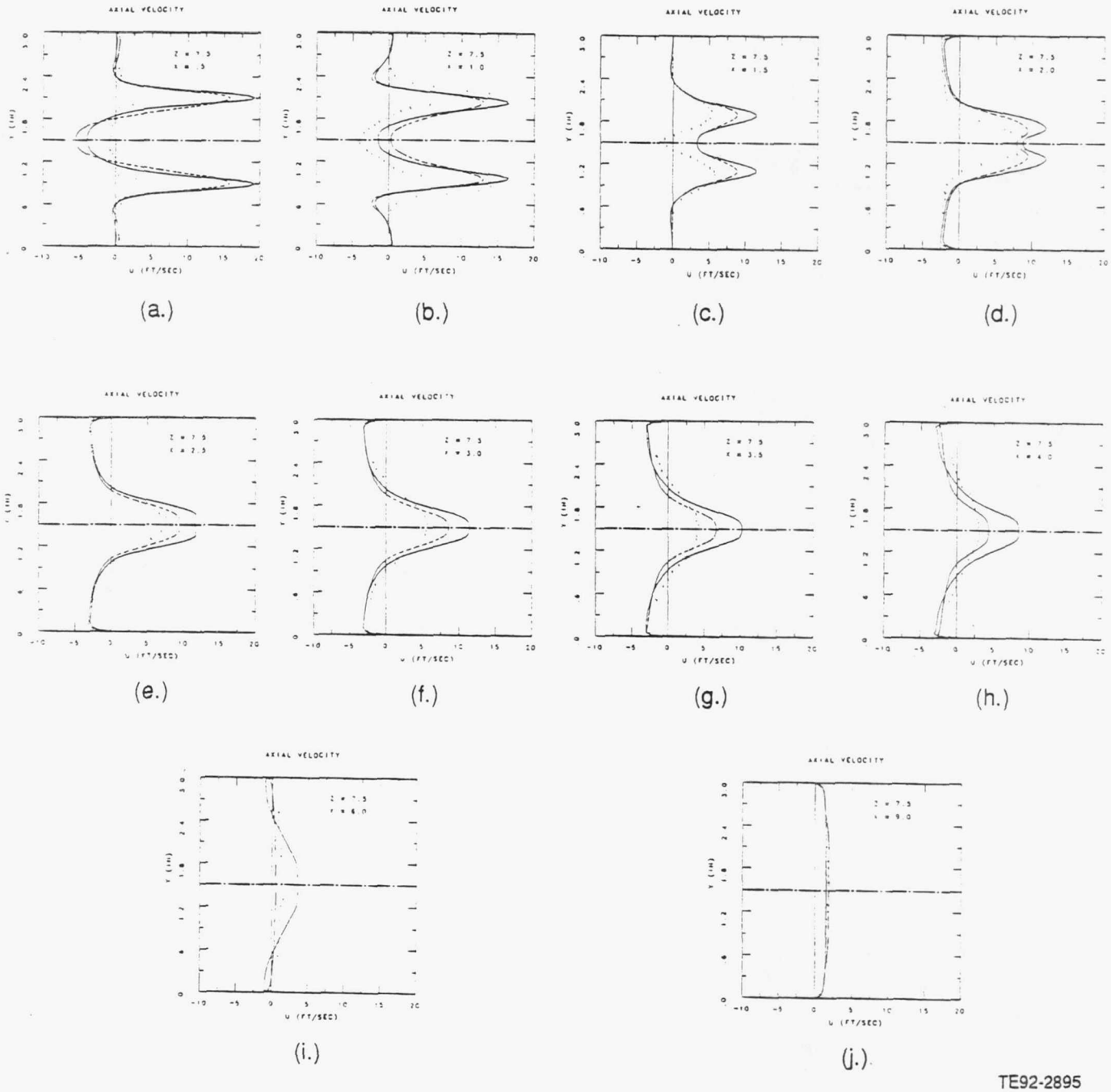

Figure 6.3-3. Axial velocity profiles at z = 7.5 in. plane (DSM; —— flux-spline---power-law).

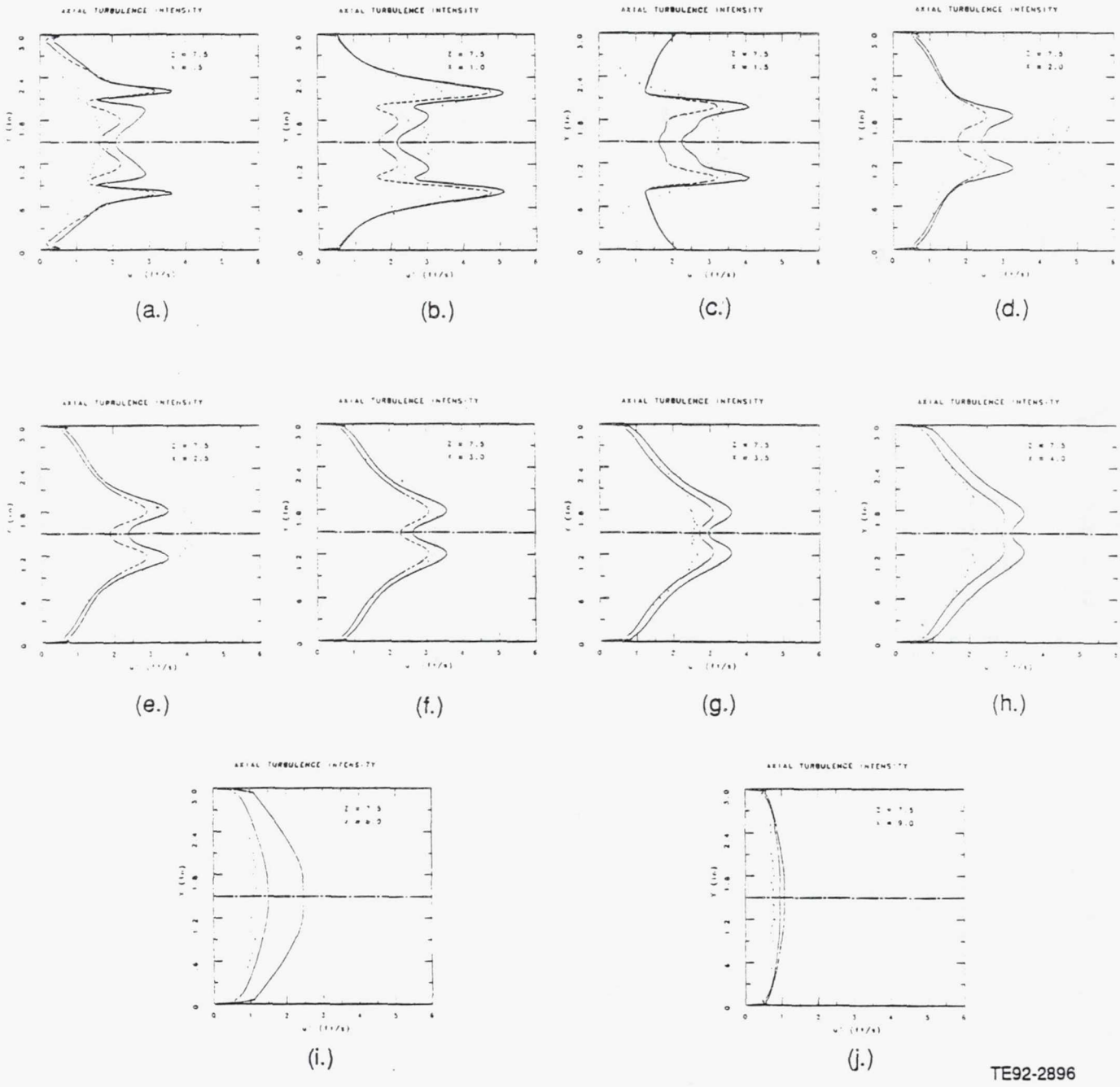

Figure 6.3-4. Axial turbulence intensity profiles at z = 7.5 in. plane (DSM; —— flux-spline—— power-law).

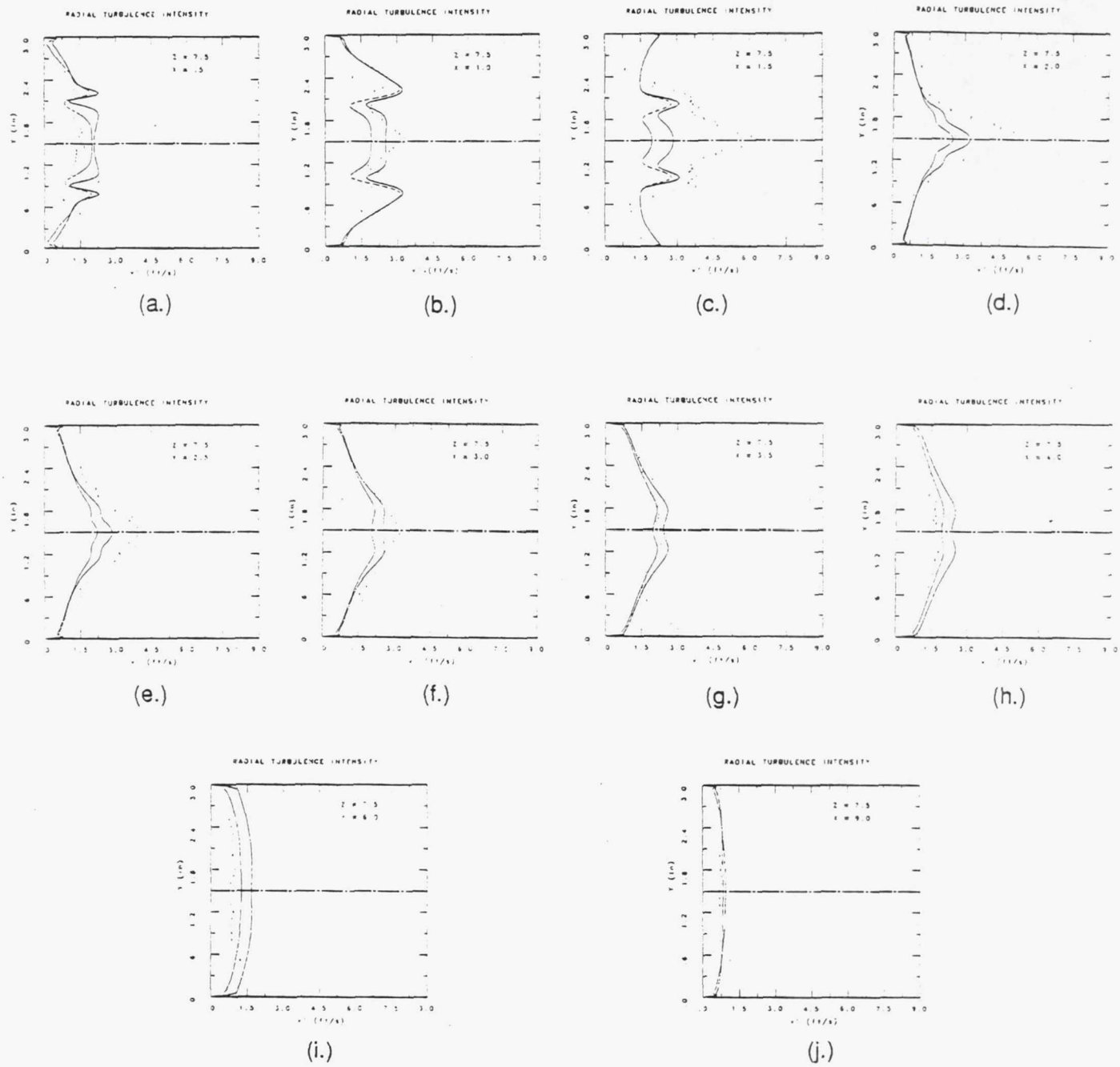

Figure 6.3-5. Radial turbulence intensity profiles at z = 7.5 in. plane (DSM; —— flux-spline—— power-law).

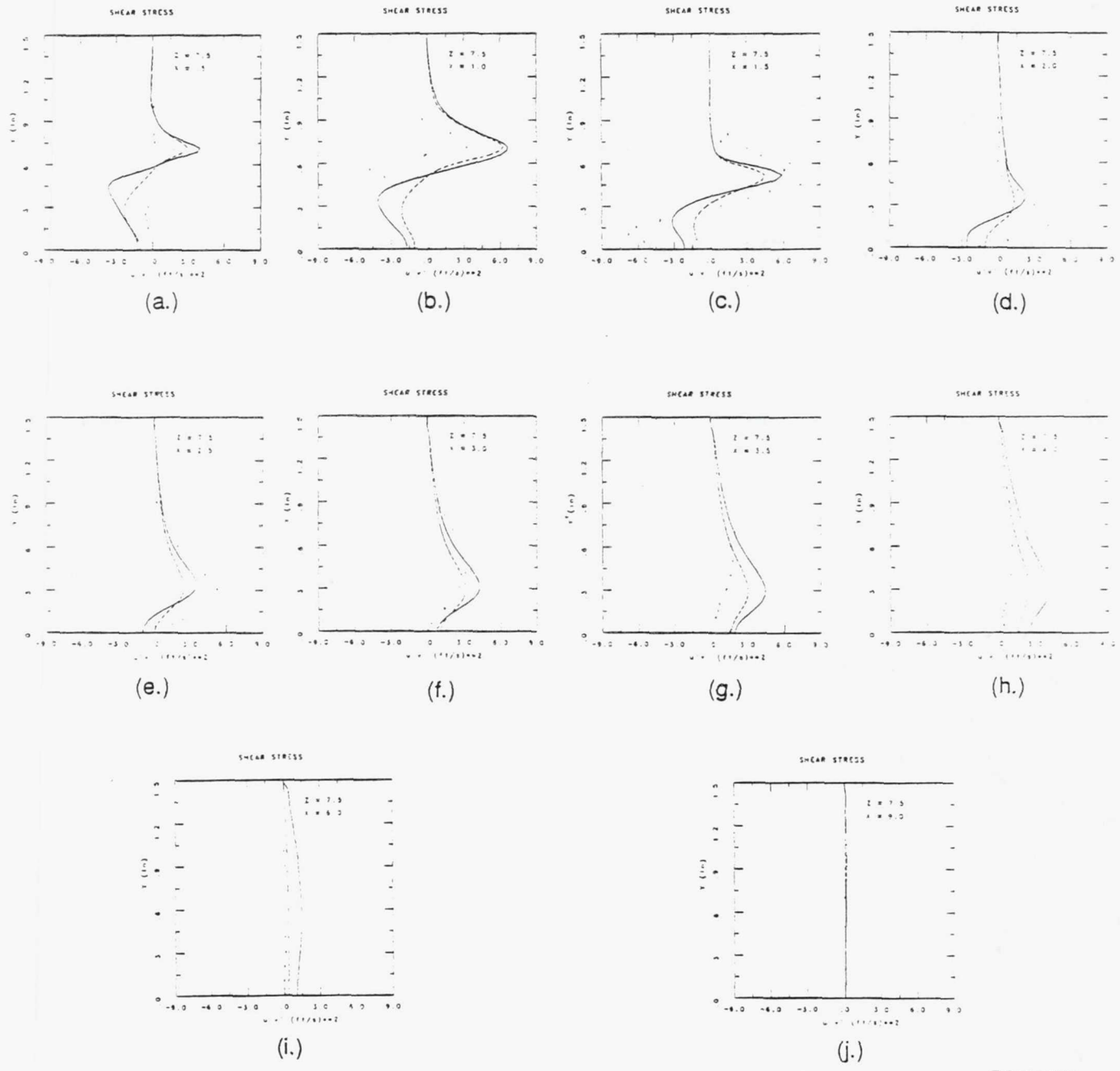

Figure 6.3-6. Turbulent shear stress profiles at z = 7.5 in. plane (DSM; —— flux-spline—— power-law).

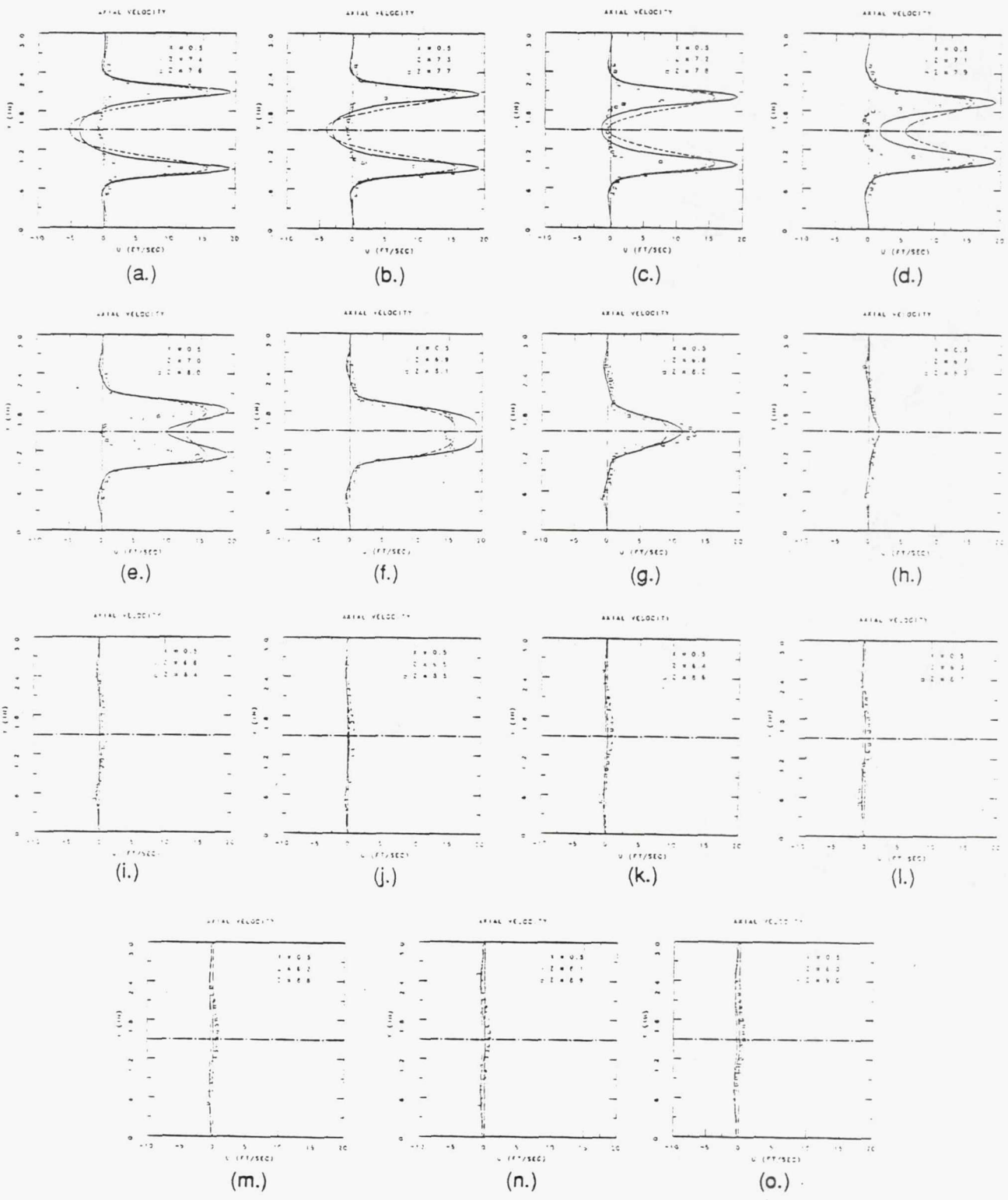

Figure 6.3-7. Axial velocity profiles at x = 0.5 in. and various lateral stations (DSM; —— flux-spline– -- power-law).

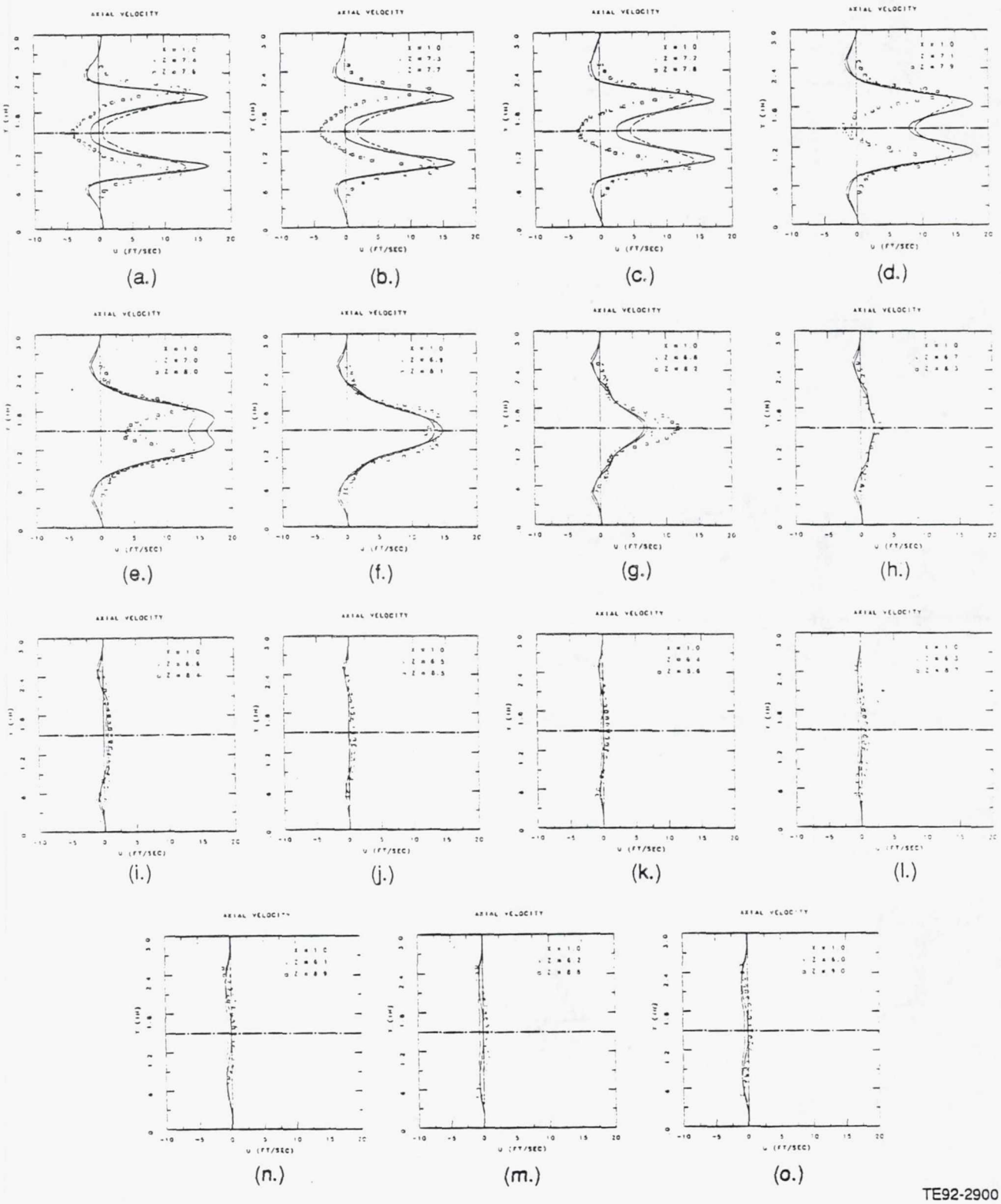

Figure 6.3-8. Axial velocity profiles at x = 1.0 in. and various lateral stations (DSM; —— flux-spline-- -- power-law).

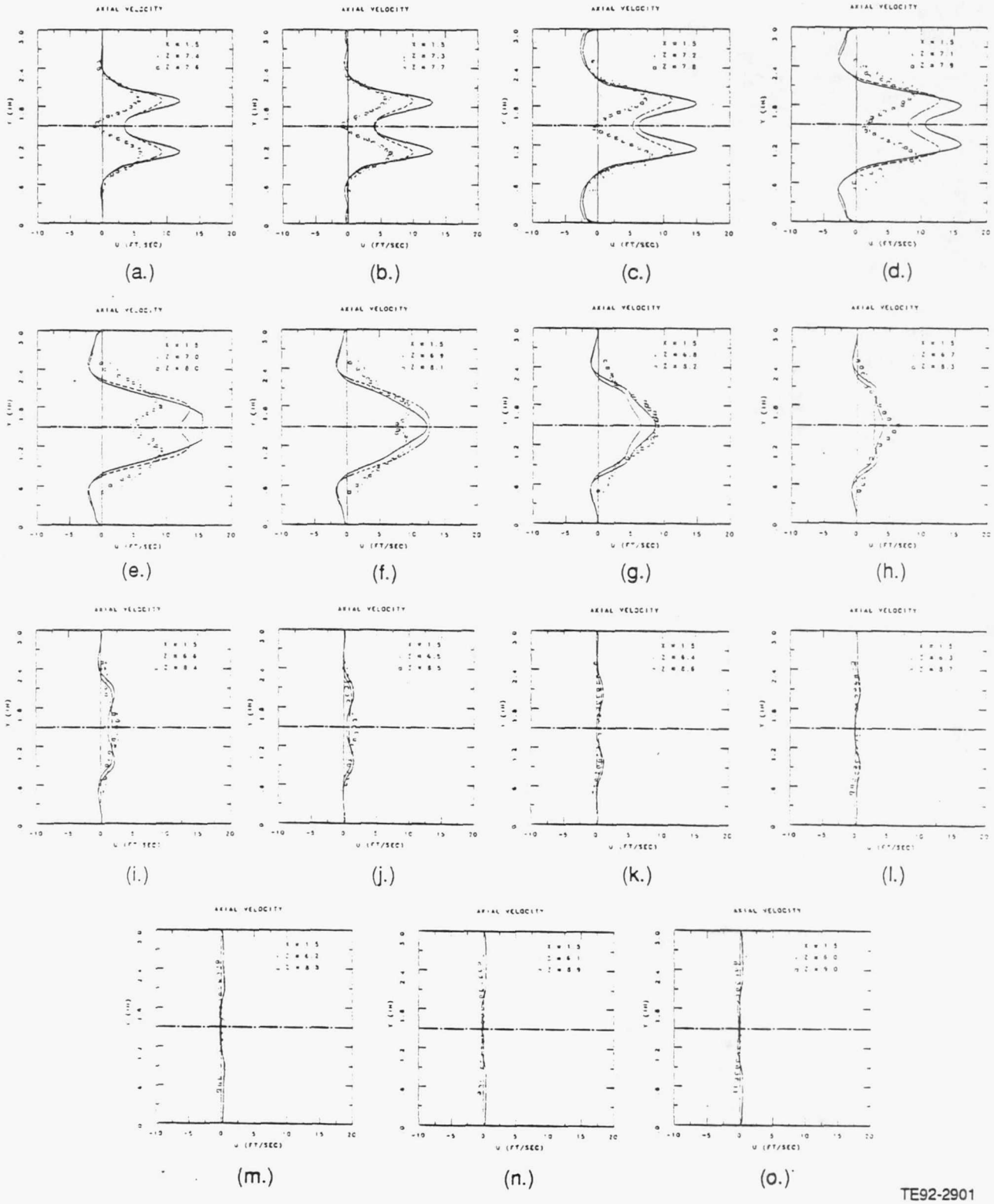

Figure 6.3-9. Axial velocity profiles at x = 1.5 in. and various lateral stations (DSM; —— flux-spline-- -- power-law).

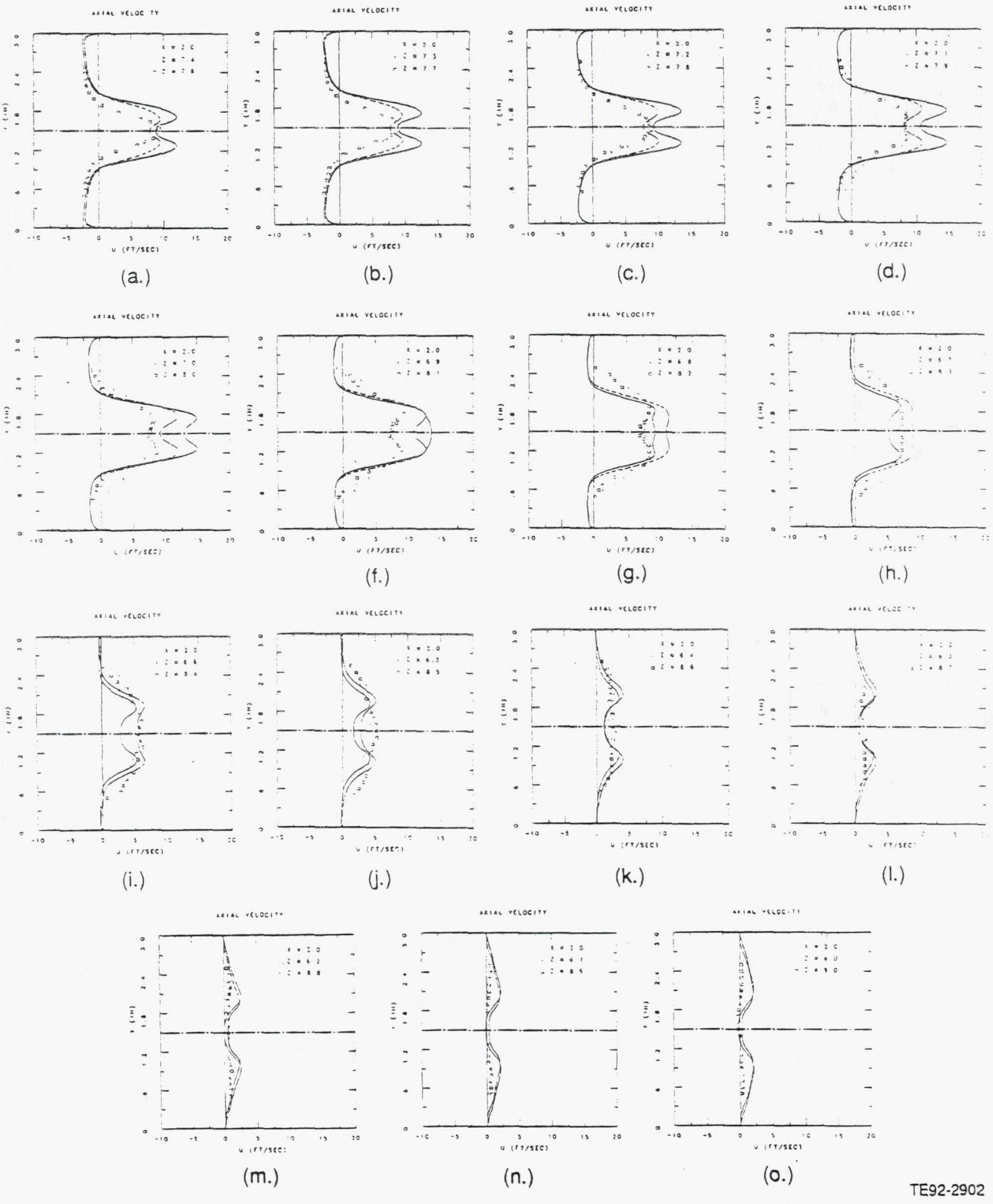

Figure 6.3-10. Axial velocity profiles at x = 2.0 in. and various lateral stations (DSM; —— flux-spline- — power-law).

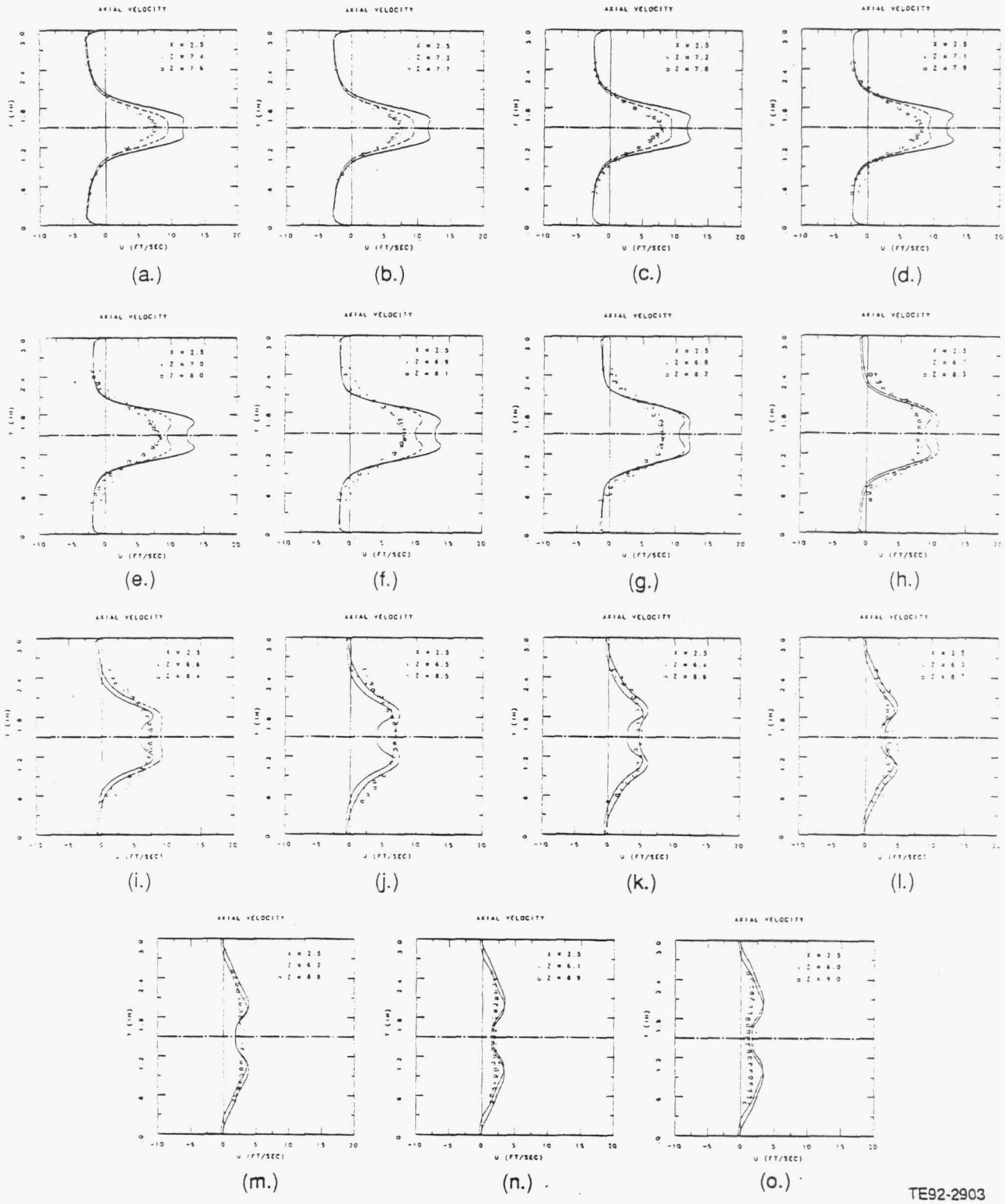

Figure 6.3-11. Axial velocity profiles at x = 2.5 in. and various lateral stations (DSM; —— flux-spline- — power-law).

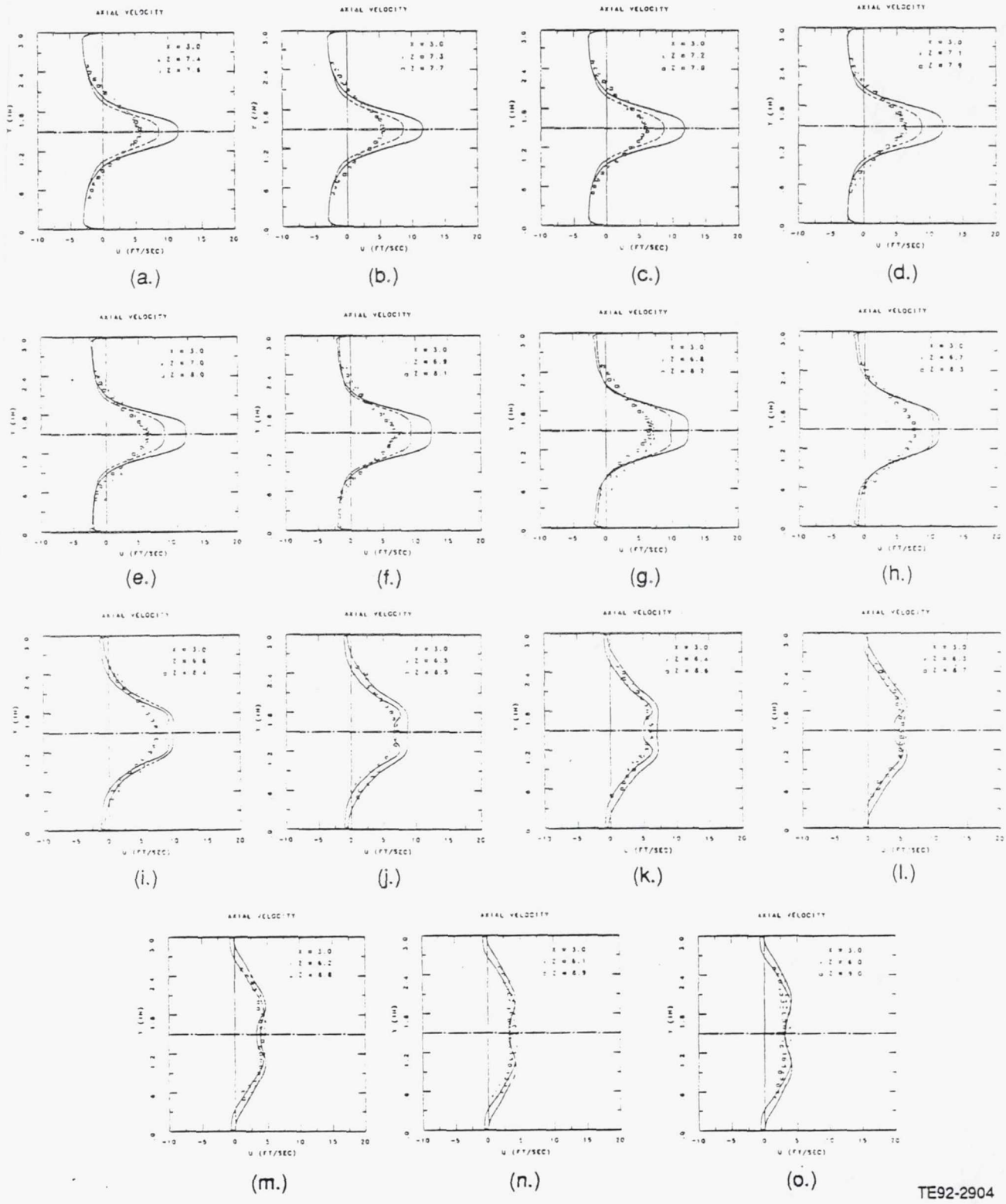

Figure 6.3-12. Axial velocity profiles at x= 3.0 in. and various lateral stations (DSM; —— flux-spline-- -- power-law).

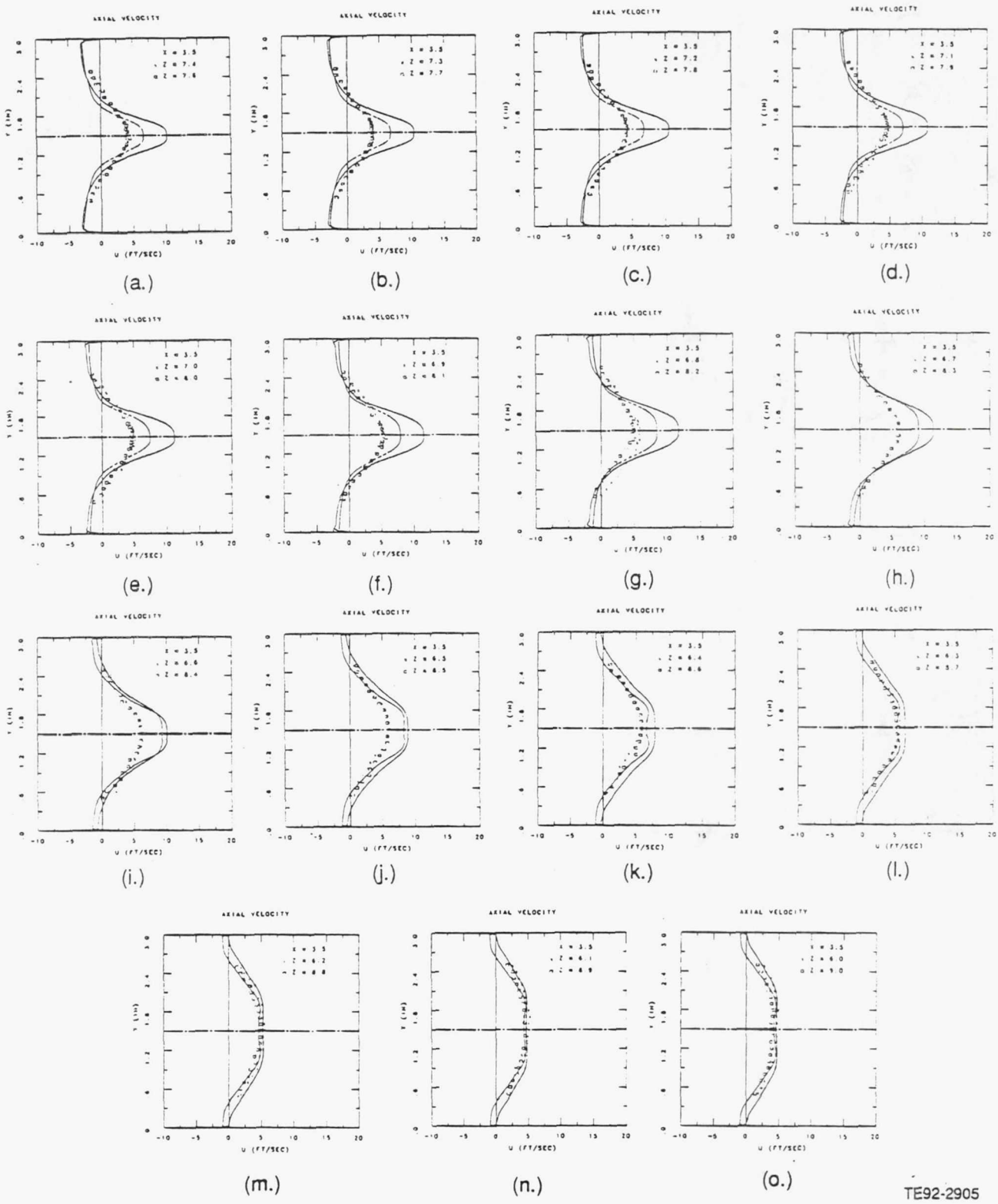

Figure 6.3-13. Axial velocity profiles at x = 3.5 in. and various lateral stations (DSM; —— flux-spline- — power-law).

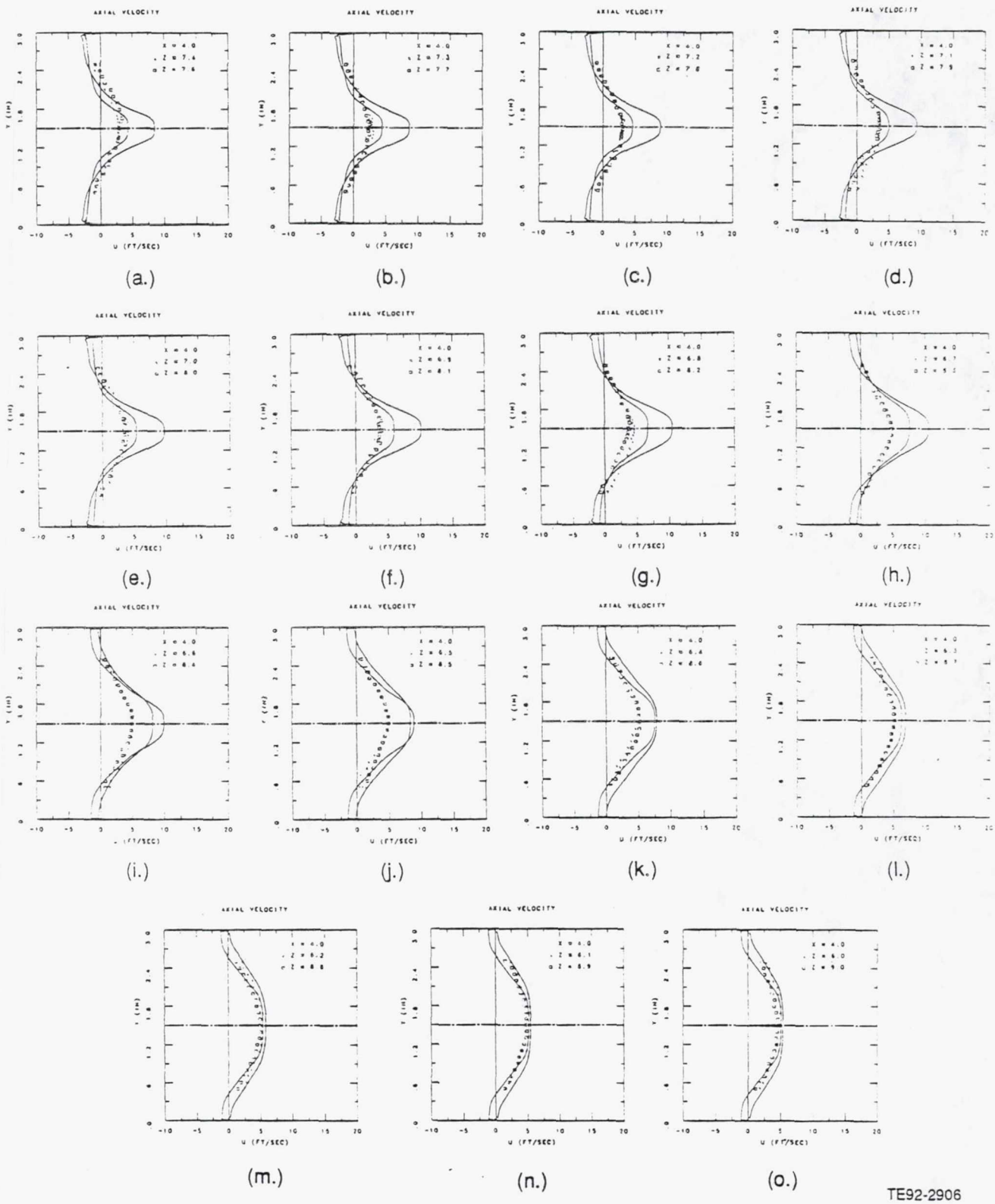

Figure 6.3-14. Axial velocity profiles at x = 4.0 in. and various lateral stations (DSM; —— flux-spline- — power-law).

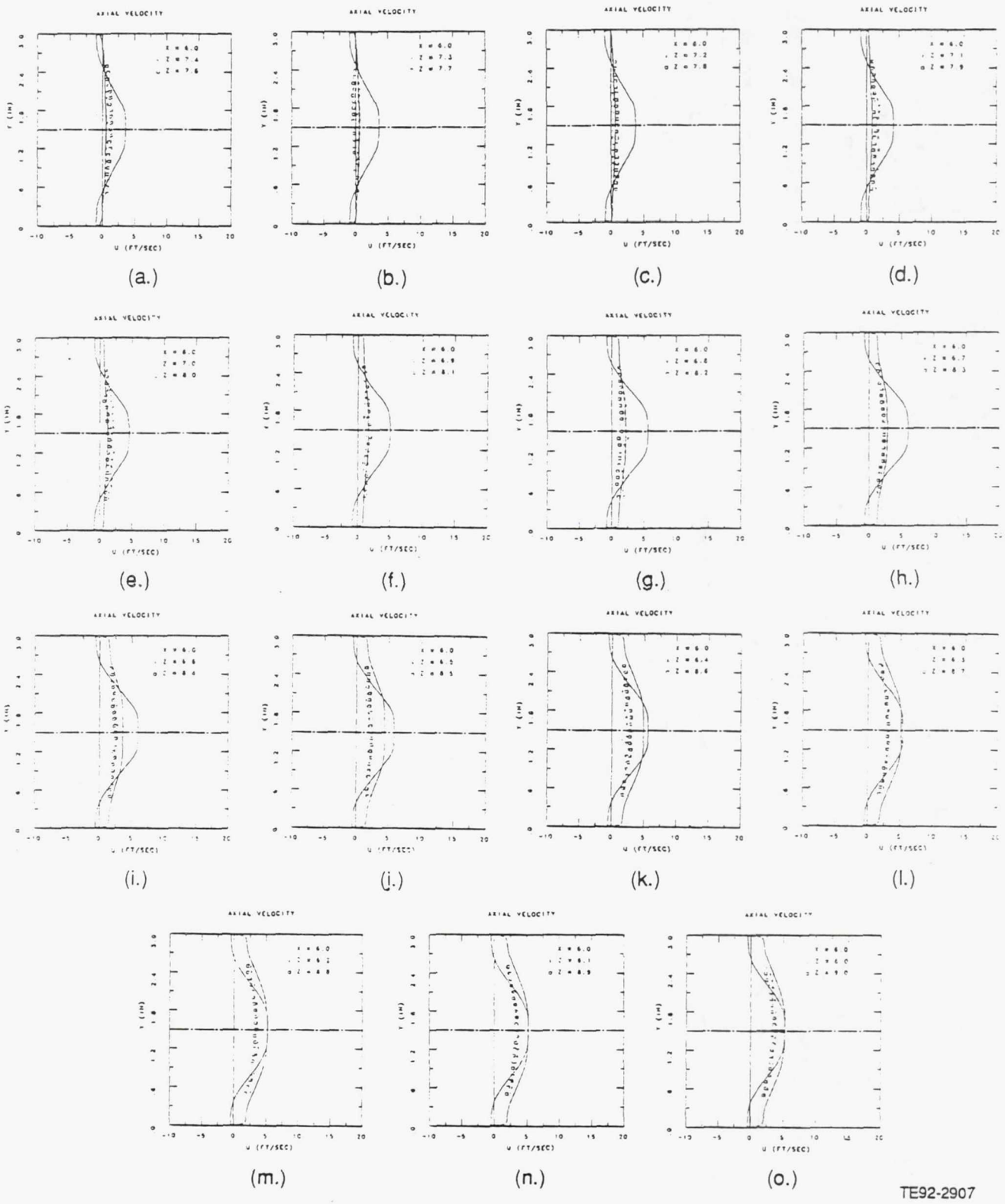

Figure 6.3-15. Axial velocity profiles at x = 6.0 in. and various lateral stations (DSM; —— flux-spline- -- power-law).

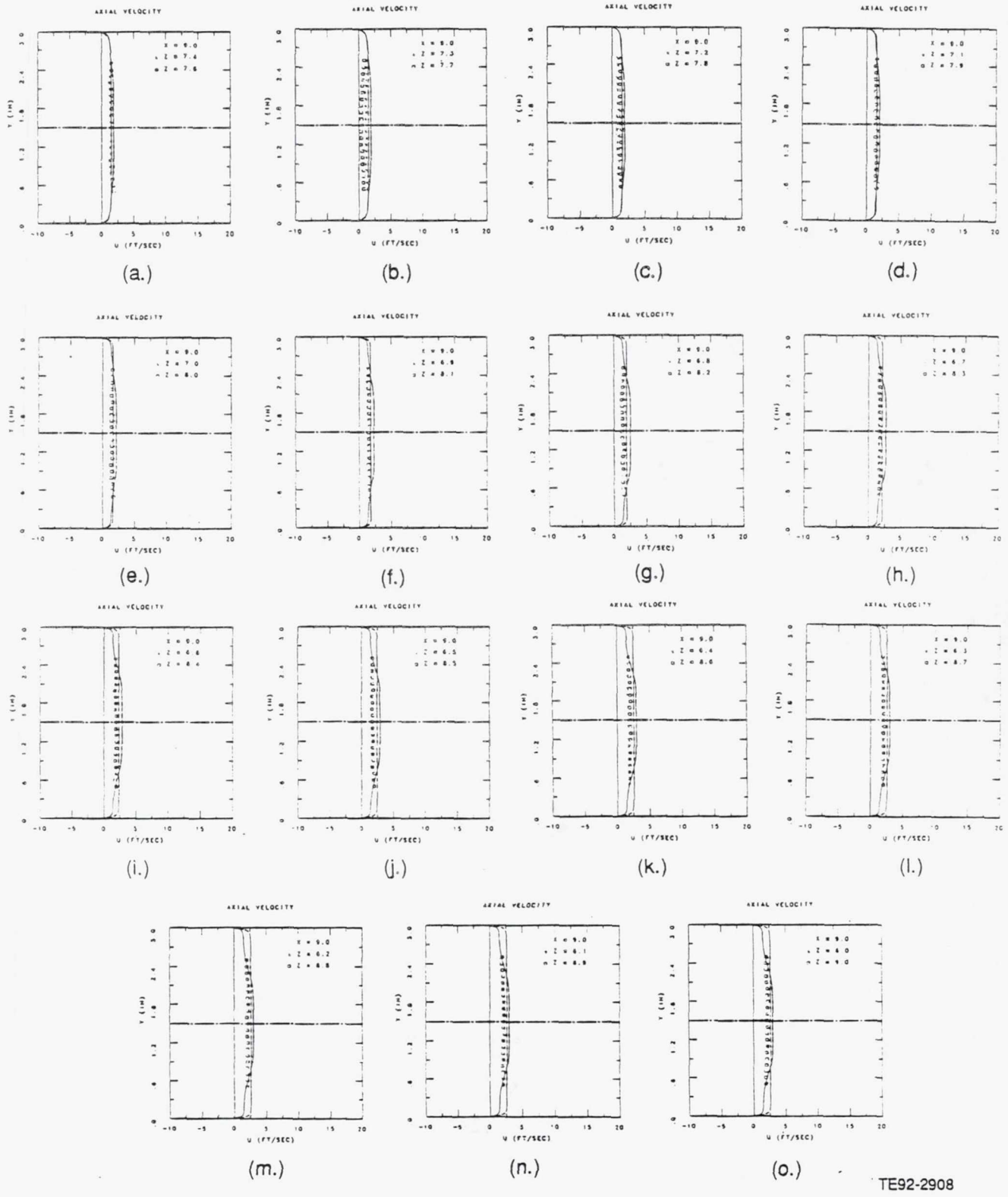

Figure 6.3-16. Axial velocity profiles at x = 9.0 in. and various lateral stations (DSM; —— flux-spline- — power-law).

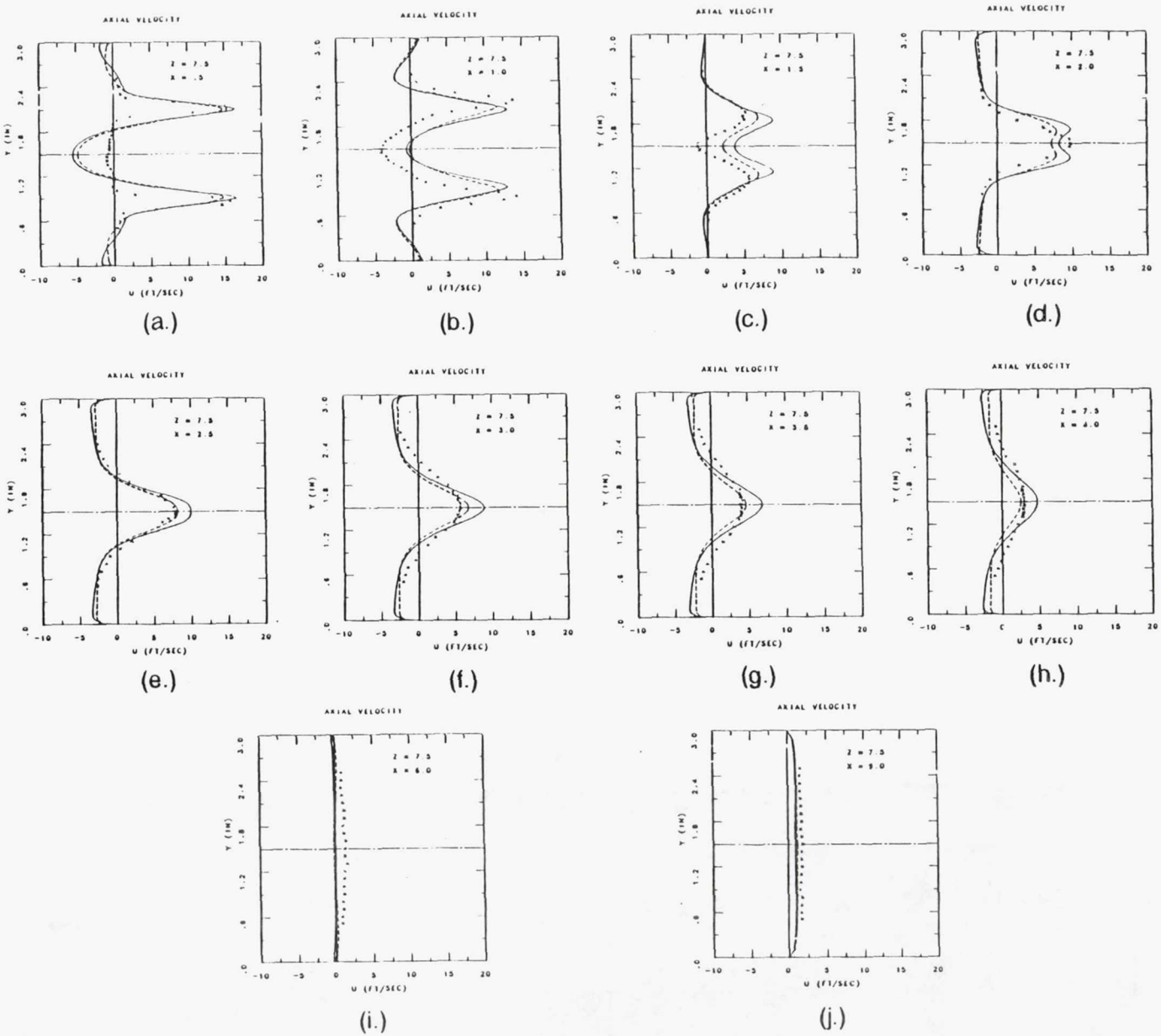

Figure 6.3-17. Axial velocity profiles at z = 7.5 in. plane (k-ε model; —— flux-spline---- power-law).

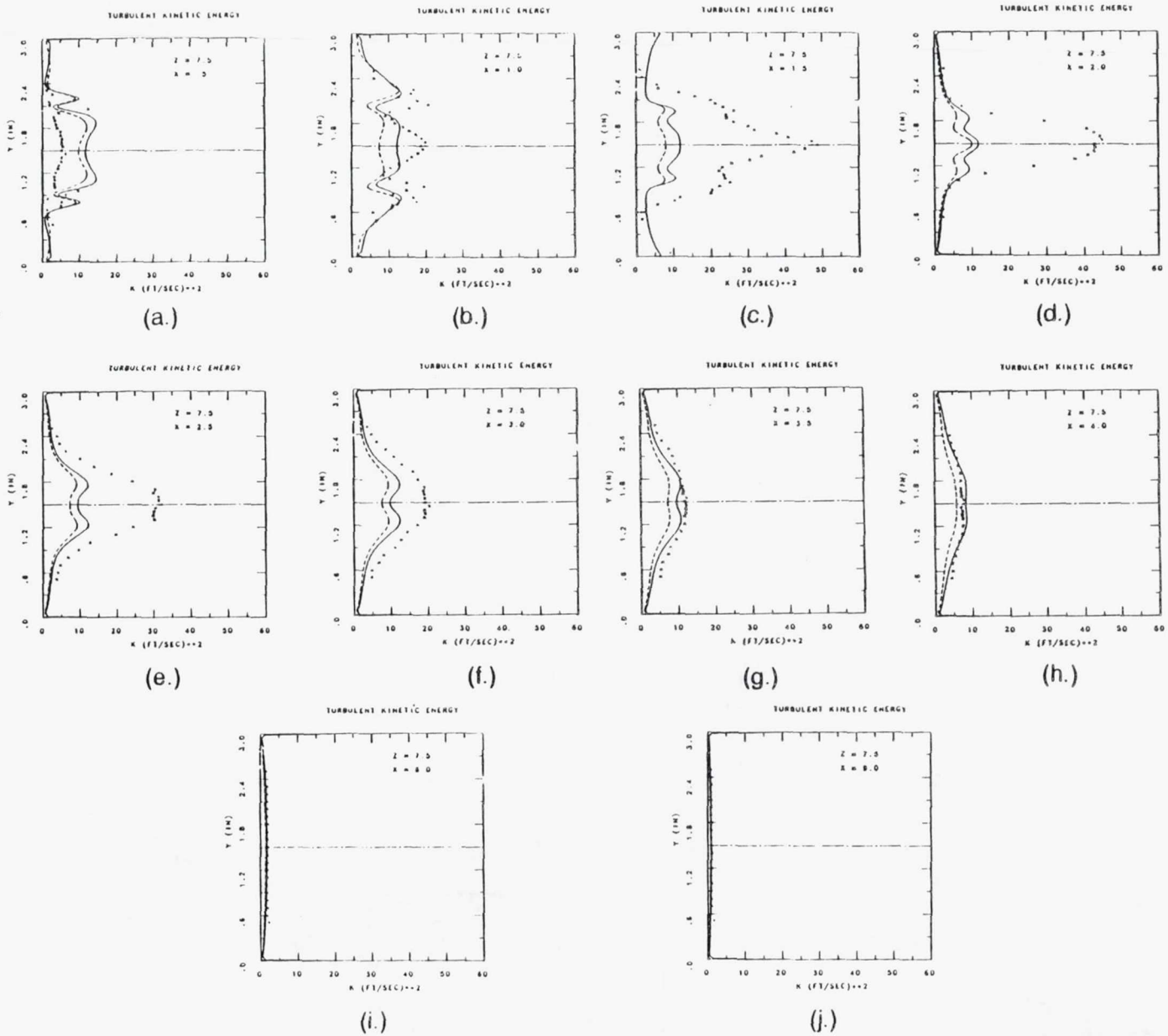

Figure 6.3-18. Turbulent kinetic energy profiles at z = 7.5 in. plane (k-ε model; —— flux-spline ---- power-law).

REFERENCES

Karki, K. C., Patankar, S. V., Runchal, A. K., and Mongia, H. C., 1988, "Improved Numerical Methods for Turbulent Viscous Recirculating Flows," *Aerothermal Modeling Phase II Final Report*, NASA CR-182169.

Nikjooy, M., Karki, K. C., Mongia, H. C., McDonell, V. G., and Samuelsen, G. S., 1989, "A Numerical and Experimental Study of Coaxial Jets," *Int. J. Heat and Fluid Flow*, 10, No. 3, pp. 253-261.

Patankar, S. V., 1980, *Numerical Heat Transfer and Fluid Flows*, Hemisphere, New York.

Ribeiro, M. M., 1976, *The Turbulence Structure of Free Jet Flows with and without Swirls*, University of London.

Varejao, L. M. C., 1979, "Flux-Spline Method for Heat, Mass, and Momentum Transfer," Ph.D. thesis, University of Minnesota1979.

Page intentionally left blank

TABLE OF CONTENTS

VII. SUMMARY AND CONCLUSIONS

A combined experimental/analytical investigation was conducted to validate conventional and improved turbulence models. A systematic experimental program was carried out to collect benchmark quality data for the mean and fluctuating quantities in the developing region of an annular-type gas turbine combustor. A laser-Doppler velocimeter was used to provide nonintrusive detailed measurements of the mean velocity components and the corresponding turbulence intensities in an annular combustor model. A detailed specification of the flow parameters in the upstream region was provided and was used as the inlet conditions to start the computations. Three different geometrical configurations of the annular combustor model were investigated. These configurations consisted of primary jets only, annular jets only, and annular and primary jets together.

Major features of the flowfield include the recirculating region, the primary and annular jet interaction, and the high turbulence region. In the primary jets only configuration, four recirculation zones were observed. Two counterrotating recirculation zones were set up between the endplate and the primary jets on the upper and lower halves of the rig. These zones were observed to move toward the primary jets and the upper and lower walls. Another two counterrotating recirculation zones also formed downstream of the primary jets on the upper and lower halves of the rig. These recirculation zones moved upstream and toward the upper and lower walls of the rig. The turbulent energy was mainly concentrated at the center of the test cell between the endplate and the primary jet entrance. The turbulence slowly decayed further downstream.

For the annular jets only case, two recirculation zones were formed along the upper and lower walls of the combustor. These recirculation zones extend downstream from the annular jet entrance and showed no definite center as the recirculation zones did in the primary jets only case. The greatest turbulent energy and shear stress existed at the inlet of the annular jet. As in the primary jets only case, the turbulence decayed farther downstream.

For the primary and annular jets case, four recirculation zones occurred in the combustor. Two large recirculation zones downstream of the primary jets along the upper and lower walls and two zones upstream of the primary jets between the edges of the annular jet and the upper and lower walls were present. Two additional recirculation zones were formed behind the center of the annular jet. The highest turbulent energy and shear stress met at $x = 1.5$ inches, where the annular and primary jets interact. Turbulence levels decayed and dispersed downstream, as in the primary jets only case.

The most pronounced result from the data is the effect the primary jets had on the flowfield. The annular jets only case had more scattered data than any of the other geometries. When the primary jets and annular jets were used together, the resulting data were much more symmetric than in the annular jets only case. In addition, recirculation zones were much more defined with the primary jets only. The combustor model was designed to model the primary zone of a typical gas turbine engine combustor and to help understand the flow within the combustor. The objective of this program was to provide data that can be used for turbulence model validation.

Three different levels of turbulence models (k-ε, algebraic second-moment [ASM], and differential second-moment [DSM] closure) were applied for computations. To reduce the effect of numerical (false) diffusion on the predicted results, the linear flux-spline scheme was used to solve several three-dimensional flows. For a given number of grid points, the flux-spline scheme produces results that are superior to those from the (lower-order) power-law differencing scheme. In addition, it has the potential of providing a grid independent solution without requiring an excessive number of grid points. It should be noted that the effectiveness of turbulence model predictions could be obscured to some extent by competing factors such as boundary conditions, oscillatory phenomena, and numerical diffusion. A significant contribution from any

of these factors tends to invalidate conclusions regarding the superiority or inferiority of a given turbulence model. The turbulence model cannot compensate for inadequacy in this area.

Although some of the models described in this study, in particular the k-ε model, have been shown to work well in many situations, there is much room for further development. The ε-equation in its present form appears not to be sufficiently universal and should be improved. As observed by many, this equation is responsible for the performance of most models. The model assumption for the pressure-strain correlation is also not very satisfactory and needs improvement. Proposals for the behavior of Φ_{ij1} in homogeneous flaws have only gone further than that of Rotta's linear model by including further terms in a series expansion about the isotropic homogeneous state. However, optimization of the coefficients of the terms in the expansion on the basis of available experimental data is a very difficult tasks indeed. It seems unlikely that any serious proposal for Φ_{ij1} will be made in the near future, and emphasis should be placed on developing a better approximation for Φ_{ij2}.

Unfortunately, in many instances there is a lack of quality data relevant to gas turbine combustion. Many modeling assumptions are similar to the constant-density, Reynolds stress closure. Therefore, further experiments with more emphasis on turbulent scalar fluxes and density correlations are needed to support or to improve these assumptions.

CONTENTS

APPENDICES

Page intentionally left blank

APPENDIX A

TURBULENT FLOW EQUATIONS FOR THE k-ε MODEL

Page intentionally left blank

TURBULENT FLOW EQUATIONS FOR THE k-ε MODEL

The transport equations presented in the previous sections reduce in three-dimensional coordinates (x, y, z) to the following:

Continuity Equation:

$$\frac{\partial}{\partial x}(\rho U)+\frac{\partial}{\partial y}(\rho V)=0 \tag{A-1}$$

x - Momentum Equation:

$$\frac{\partial}{\partial x}(\rho UU)+\frac{\partial}{\partial y}(\rho UV)+\frac{\partial}{\partial z}(\rho UW)=-\frac{\partial P}{\partial x}+\frac{\partial}{\partial x}(\tau_{uu})+\frac{\partial}{\partial y}(\tau_{uv})+\frac{\partial}{\partial z}(\tau_{uw}) \tag{A-2}$$

y - Momentum Equation:

$$\frac{\partial}{\partial x}(\rho UV)+\frac{\partial}{\partial y}(\rho VV)+\frac{\partial}{\partial z}(\rho VW)=-\frac{\partial P}{\partial y}+\frac{\partial}{\partial x}(\tau_{uv})+\frac{\partial}{\partial y}(\tau_{vv})+\frac{\partial}{\partial z}(\tau_{vw}) \tag{A-3}$$

z - Momentum Equation:

$$\frac{\partial}{\partial x}(\rho UW)+\frac{\partial}{\partial y}(\rho VW)+\frac{\partial}{\partial z}(\rho WW)=-\frac{\partial P}{\partial z}+\frac{\partial}{\partial x}(\tau_{uw})+\frac{\partial}{\partial y}(\tau_{vw})+\frac{\partial}{\partial z}(\tau_{ww}) \tag{A-4}$$

k - Transport Equation:

$$\frac{\partial}{\partial x}(\rho Uk)+\frac{\partial}{\partial y}(\rho Vk)+\frac{\partial}{\partial z}(\rho Wk)=P_k-\rho\varepsilon+\frac{\partial}{\partial x}\left[\left(\frac{\mu_t}{\sigma_k}+\mu\right)\frac{\partial k}{\partial x}\right]+\frac{\partial}{\partial y}\left[\left(\frac{\mu_t}{\sigma_k}+\mu\right)\frac{\partial k}{\partial y}\right]+\frac{\partial}{\partial z}\left[\left(\frac{\mu_t}{\sigma_k}+\mu\right)\frac{\partial k}{\partial z}\right] \tag{A-5}$$

ε - Transport Equation:

$$\frac{\partial}{\partial x}(\rho U\varepsilon)+\frac{\partial}{\partial y}(\rho V\varepsilon)+\frac{\partial}{\partial z}(\rho W\varepsilon)=C_{\varepsilon 1}\frac{\varepsilon}{k}P_k-C_{\varepsilon 2}\rho\frac{\varepsilon^2}{k}+\frac{\partial}{\partial x}\left[\left(\frac{\mu_t}{\sigma_\varepsilon}+\mu\right)\frac{\partial \varepsilon}{\partial x}\right]+$$
$$\frac{\partial}{\partial y}\left[\left(\frac{\mu_t}{\sigma_\varepsilon}+\mu\right)\frac{\partial \varepsilon}{\partial y}\right]+\frac{\partial}{\partial z}\left[\left(\frac{\mu_t}{\sigma_\varepsilon}+\mu\right)\frac{\partial \varepsilon}{\partial z}\right] \tag{A-6}$$

where

$$\mu_t=c_\mu\rho\frac{k^2}{\varepsilon} \tag{A-7}$$

$$\tau_{uu}=2\mu_T\frac{\partial U}{\partial x} \tag{A-8}$$

$$\tau_{uv} = \mu_T \left(\frac{\partial U}{\partial y} + \frac{\partial V}{\partial x} \right) \tag{A-9}$$

$$\tau_{uw} = \mu_T \left(\frac{\partial U}{\partial z} + \frac{\partial W}{\partial x} \right) \tag{A-10}$$

$$\tau_{vv} = 2\mu_T \frac{\partial V}{\partial y} \tag{A-11}$$

$$\tau_{vw} = \mu_T \left(\frac{\partial V}{\partial z} + \frac{\partial W}{\partial y} \right) \tag{A-12}$$

$$\tau_{ww} = 2\mu_T \frac{\partial W}{\partial z} \tag{A-13}$$

$$\mu_T = \mu_t + \mu \tag{A-14}$$

$$P_k = \left[2 \left[\left(\frac{\partial U}{\partial x} \right)^2 + \left(\frac{\partial V}{\partial y} \right)^2 + \left(\frac{\partial W}{\partial z} \right)^2 \right] + \left(\frac{\partial U}{\partial y} + \frac{\partial V}{\partial x} \right)^2 + \left(\frac{\partial U}{\partial z} + \frac{\partial W}{\partial x} \right)^2 + \left(\frac{\partial V}{\partial z} + \frac{\partial W}{\partial y} \right)^2 \right] \tag{A-15}$$

APPENDIX B

TURBULENT FLOW EQUATIONS FOR DSM CLOSURE

Page intentionally left blank

TURBULENT FLOW EQUATIONS FOR DSM CLOSURE

The modeled Reynolds stress transport equations presented in the tensor notation reduce in 3-D coordinates (x, y, z) to the following equations.

Equation for $\overline{u^2}$:

$$\frac{\partial}{\partial x}\left(\rho U\overline{u^2}\right)+\frac{\partial}{\partial y}\left(\rho V\overline{u^2}\right)+\frac{\partial}{\partial z}\left(\rho W\overline{u^2}\right)=\frac{\partial}{\partial x}\left[\left(C_k\rho\frac{k}{\varepsilon}\overline{u^2}\right)\frac{\partial\overline{u^2}}{\partial x}\right]+$$
$$\frac{\partial}{\partial y}\left[\left(C_k\rho\frac{k}{\varepsilon}\overline{v^2}\right)\frac{\partial\overline{u^2}}{\partial y}\right]+\frac{\partial}{\partial z}\left[\left(C_k\rho\frac{k}{\varepsilon}\overline{w^2}\right)\frac{\partial\overline{u^2}}{\partial z}\right]+P_{11}+\Phi_{11}-\frac{2}{3}\rho\varepsilon \qquad \text{(B-1)}$$

Equation for $\overline{v^2}$:

$$\frac{\partial}{\partial x}\left(\rho U\overline{v^2}\right)+\frac{\partial}{\partial y}\left(\rho V\overline{v^2}\right)+\frac{\partial}{\partial z}\left(\rho W\overline{v^2}\right)=\frac{\partial}{\partial x}\left[\left(C_k\rho\frac{k}{\varepsilon}\overline{u^2}\right)\frac{\partial\overline{v^2}}{\partial x}\right]+$$
$$\frac{\partial}{\partial y}\left[\left(C_k\rho\frac{k}{\varepsilon}\overline{v^2}\right)\frac{\partial\overline{v^2}}{\partial y}\right]+\frac{\partial}{\partial z}\left[\left(C_k\rho\frac{k}{\varepsilon}\overline{w^2}\right)\frac{\partial\overline{v^2}}{\partial z}\right]+P_{22}+\Phi_{22}-\frac{2}{3}\rho\varepsilon \qquad \text{(B-2)}$$

Equation for $\overline{w^2}$:

$$\frac{\partial}{\partial x}\left(\rho U\overline{w^2}\right)+\frac{\partial}{\partial y}\left(\rho V\overline{w^2}\right)+\frac{\partial}{\partial z}\left(\rho W\overline{w^2}\right)=\frac{\partial}{\partial x}\left[\left(C_k\rho\frac{k}{\varepsilon}\overline{u^2}\right)\frac{\partial\overline{w^2}}{\partial x}\right]+$$
$$\frac{\partial}{\partial y}\left[\left(C_k\rho\frac{k}{\varepsilon}\overline{v^2}\right)\frac{\partial\overline{w^2}}{\partial y}\right]+\frac{\partial}{\partial z}\left[\left(C_k\rho\frac{k}{\varepsilon}\overline{w^2}\right)\frac{\partial\overline{w^2}}{\partial z}\right]+P_{33}+\Phi_{33}-\frac{2}{3}\rho\varepsilon \qquad \text{(B-3)}$$

Equation for $\overline{uv}$:

$$\frac{\partial}{\partial x}\left(\rho U\overline{uv}\right)+\frac{\partial}{\partial y}\left(\rho V\overline{vw}\right)+\frac{\partial}{\partial z}\left(\rho W\overline{uv}\right)=\frac{\partial}{\partial x}\left[\left(C_k\rho\frac{k}{\varepsilon}\overline{u^2}\right)\frac{\partial\overline{uv}}{\partial x}\right]+$$
$$\frac{\partial}{\partial y}\left[\left(C_k\rho\frac{k}{\varepsilon}\overline{v^2}\right)\frac{\partial\overline{uv}}{\partial y}\right]+\frac{\partial}{\partial z}\left[\left(C_k\rho\frac{k}{\varepsilon}\overline{w^2}\right)\frac{\partial\overline{uv}}{\partial z}\right]+P_{12}+\Phi_{12} \qquad \text{(B-4)}$$

Equation for $\overline{vw}$:

$$\frac{\partial}{\partial x}\left(\rho U\overline{vw}\right)+\frac{\partial}{\partial y}\left(\rho V\overline{vw}\right)+\frac{\partial}{\partial z}\left(\rho W\overline{vw}\right)=\frac{\partial}{\partial x}\left[\left(C_k\rho\frac{k}{\varepsilon}\overline{u^2}\right)\frac{\partial\overline{vw}}{\partial x}\right]+$$
$$\frac{\partial}{\partial y}\left[\left(C_k\rho\frac{k}{\varepsilon}\overline{v^2}\right)\frac{\partial\overline{vw}}{\partial y}\right]+\frac{\partial}{\partial z}\left[\left(C_k\rho\frac{k}{\varepsilon}\overline{w^2}\right)\frac{\partial\overline{vw}}{\partial z}\right]+P_{23}+\Phi_{23} \qquad \text{(B-5)}$$

Equation for $\overline{uw}$:

$$\frac{\partial}{\partial x}\left(\rho U\overline{uw}\right)+\frac{\partial}{\partial y}\left(\rho V\overline{uw}\right)+\frac{\partial}{\partial z}\left(\rho W\overline{uw}\right)=\frac{\partial}{\partial x}\left[\left(C_k\rho\frac{k}{\varepsilon}\overline{u^2}\right)\frac{\partial\overline{uw}}{\partial x}\right]+$$
$$\frac{\partial}{\partial y}\left[\left(C_k\rho\frac{k}{\varepsilon}\overline{v^2}\right)\frac{\partial\overline{uw}}{\partial y}\right]+\frac{\partial}{\partial z}\left[\left(C_k\rho\frac{k}{\varepsilon}\overline{w^2}\right)\frac{\partial\overline{uw}}{\partial z}\right]+P_{13}+\Phi_{13} \tag{B-6}$$

where

$$P_{11}=-2\rho\left(\overline{u^2}\frac{\partial U}{\partial x}+\overline{uv}\frac{\partial U}{\partial y}+\overline{uw}\frac{\partial U}{\partial z}\right) \tag{B-7}$$

$$P_{22}=-2\rho\left(\overline{uv}\frac{\partial V}{\partial x}+\overline{v^2}\frac{\partial V}{\partial y}+\overline{vw}\frac{\partial V}{\partial z}\right) \tag{B-8}$$

$$P_{33}=-2\rho\left(\overline{uw}\frac{\partial W}{\partial x}+\overline{vw}\frac{\partial W}{\partial y}+\overline{w^2}\frac{\partial W}{\partial z}\right) \tag{B-9}$$

$$P_{12}=-\rho\left(\overline{u^2}\frac{\partial V}{\partial x}+\overline{v^2}\frac{\partial U}{\partial y}-\overline{uv}\frac{\partial W}{\partial z}+\overline{uw}\frac{\partial V}{\partial z}+\overline{vw}\frac{\partial U}{\partial z}\right) \tag{B-10}$$

$$P_{13}=-\rho\left(\overline{u^2}\frac{\partial W}{\partial x}+\overline{w^2}\frac{\partial U}{\partial z}-\overline{uw}\frac{\partial V}{\partial y}+\overline{uv}\frac{\partial W}{\partial y}+\overline{vw}\frac{\partial U}{\partial y}\right) \tag{B-11}$$

$$P_{23}=-\rho\left(\overline{v^2}\frac{\partial W}{\partial y}+\overline{w^2}\frac{\partial V}{\partial z}-\overline{vw}\frac{\partial U}{\partial x}+\overline{uv}\frac{\partial W}{\partial x}+\overline{uw}\frac{\partial V}{\partial x}\right) \tag{B-12}$$

$$\Phi_{11}=-C_1\rho\frac{\varepsilon}{k}\left(\overline{u^2}-\frac{2}{3}k\right)-C_2\left(P_{11}-\frac{2}{3}P_k\right) \tag{B-13}$$

$$\Phi_{22}=-C_1\rho\frac{\varepsilon}{k}\left(\overline{v^2}-\frac{2}{3}k\right)-C_2\left(P_{22}-\frac{2}{3}P_k\right) \tag{B-14}$$

$$\Phi_{33}=-C_1\rho\frac{\varepsilon}{k}\left(\overline{w^2}-\frac{2}{3}k\right)-C_2\left(P_{33}-\frac{2}{3}P_k\right) \tag{B-15}$$

$$\Phi_{12}=-C_1\rho\frac{\varepsilon}{k}\overline{uv}-C_2P_{12} \tag{B-16}$$

$$\Phi_{13}=-C_1\rho\frac{\varepsilon}{k}\overline{uw}-C_2P_{13} \tag{B-17}$$

$$\Phi_{23} = -C_1\rho\frac{\varepsilon}{k}\overline{vw} - C_2P_{23} \tag{B-18}$$

$$P_k = 0.5\left(P_{11} + P_{22} + P_{33}\right) \tag{B-19}$$

Page intentionally left blank

APPENDIX C

PUBLICATIONS PARTIALLY SUPPORTED BY THIS STUDY

Page intentionally left blank

PUBLICATIONS PARTIALLY SUPPORTED BY THIS STUDY

1. Barron, D. A., 1986, "LDV Measurements in an Annular Combustor Model," M. Sc Thesis, Purdue University.

2. Seal II, M. D., 1988, "An Experimental Study of Swirling Flows as Applied to Annular Combustors," M. Sc Thesis, Purdue University.

3. Sullivan, J. P., Barron, D. A., Seal, M. D., Morgan, D., and Murthy, S. N. B., 1989, "Primary Zone Dynamics in a Gas Turbine Combustor," AIAA-89-0480.

4. Dwenger, R. D., 1990, "Laser Doppler Velocimeter Measurements and Laser Sheet Imaging in an Annular Combustor Model," M. Sc Thesis, Purdue University.

5. Morgan, D. C., 1988, "Concentration Measurement in Cold Flow Model Annular Combustor Using Laser-Induced Fluorescent," NASA-CR 182252.

6. Nikjooy, M., Karki, K. C., and Mongia, H. C., 1990, "Calculation of Turbulent Three-Dimensional Jet-Induced Flow in a Rectangular Enclosure," AIAA-90-0684.

REPORT DOCUMENTATION PAGE

Form Approved
OMB No. 0704-0188

1. AGENCY USE ONLY (*Leave blank*)	2. REPORT DATE	3. REPORT TYPE AND DATES COVERED
	November 1993	Final Contractor Report

4. TITLE AND SUBTITLE

Flow Interaction Experiment
Aerothermal Modeling Phase II
Final Report–Volume II

5. FUNDING NUMBERS

WU–505–62–52
C–NAS3–24350

6. AUTHOR(S)

M. Nikjooy, H.C. Mongia, J.P. Sullivan, and S.N.B. Murthy

7. PERFORMING ORGANIZATION NAME(S) AND ADDRESS(ES)

General Motors Corporation
Allison Gas Turbine Division
P.O. Box 420
Indianapolis, Indiana 46206–0420

8. PERFORMING ORGANIZATION REPORT NUMBER

E–8180
EDR 16026

9. SPONSORING/MONITORING AGENCY NAME(S) AND ADDRESS(ES)

National Aeronautics and Space Administration
Lewis Research Center
Cleveland, Ohio 44135–3191

10. SPONSORING/MONITORING AGENCY REPORT NUMBER

NASA CR–189192

11. SUPPLEMENTARY NOTES

M. Nikjooy and H.C. Mongia, General Motors Corporation; and J.P. Sullivan and S.N. B. Murthy, Purdue University, School of Engineering, West Lafayette, Indiana 47907. Project Manager, James D. Holdeman, Internal Fluid Mechanics Division, (216) 433–5846.

12a. DISTRIBUTION/AVAILABILITY STATEMENT

Unclassified - Unlimited
Subject Category 07

12b. DISTRIBUTION CODE

13. ABSTRACT *(Maximum 200 words)*

An experimental and computational study is reported for the flow of a turbulent jet discharging into a rectangular enclosure. The experimental configurations consisting of primary jets only, annular jets only, and a combination of annular and primary jets are investigated to provide a better understanding of the flow field in an annular combustor. A laser Doppler velocimeter is used to measure mean velocity and Reynolds stress components. Major features of the flow field include recirculation, primary and annular jet interaction, and high turbulence. A significant result from this study is the effect the primary jets have on the flow field. The primary jets are seen to create statistically larger recirculation zones and higher turbulence levels. In addition, a technique called marker nephelometry is used to provide mean concentration values in the model combustor. Computations are performed using three levels of turbulence closures, namely k-ϵ model, algebraic second moment (ASM), and differential second moment (DSM) closure. Two different numerical schemes are applied. One is the lower-order power-law differencing scheme (PLDS) and the other is the higher-order flux-spline differencing scheme (FSDS). A comparison is made of the performance of these schemes. The numerical results are compared with experimental data. For the cases considered in this study, the FSDS is more accurate than the PLDS. For a prescribed accuracy, the flux-spline scheme requires a far fewer number of grid points. Thus, it has the potential for providing a numerical error-free solution, especially for three-dimensional flows, without requiring an excessively fine grid. Although qualitatively good comparison with data was obtained, the deficiencies regarding the modeled dissipation rate (ϵ) equation, pressure-strain correlation model, and the inlet ϵ profile and other critical closure issues need to be resolved before one can achieve the degree of accuracy required to analytically design combustion systems.

14. SUBJECT TERMS

Turbulence modeling; Jet-in-cross flow; Three-dimensional flow; Gas turbine combustion; Experimental data; Turbulent flow model validation

15. NUMBER OF PAGES

315

16. PRICE CODE

A14

17. SECURITY CLASSIFICATION OF REPORT	18. SECURITY CLASSIFICATION OF THIS PAGE	19. SECURITY CLASSIFICATION OF ABSTRACT	20. LIMITATION OF ABSTRACT
Unclassified	Unclassified	Unclassified	